Mathematical Problems in Engineering

Recent Progress in Sliding Mode Control Theory and Applications

Lead Guest Editor: Shihong Ding
Guest Editors: Haibo Du, Chih-Chiang Chen, and Jyoti Mishra

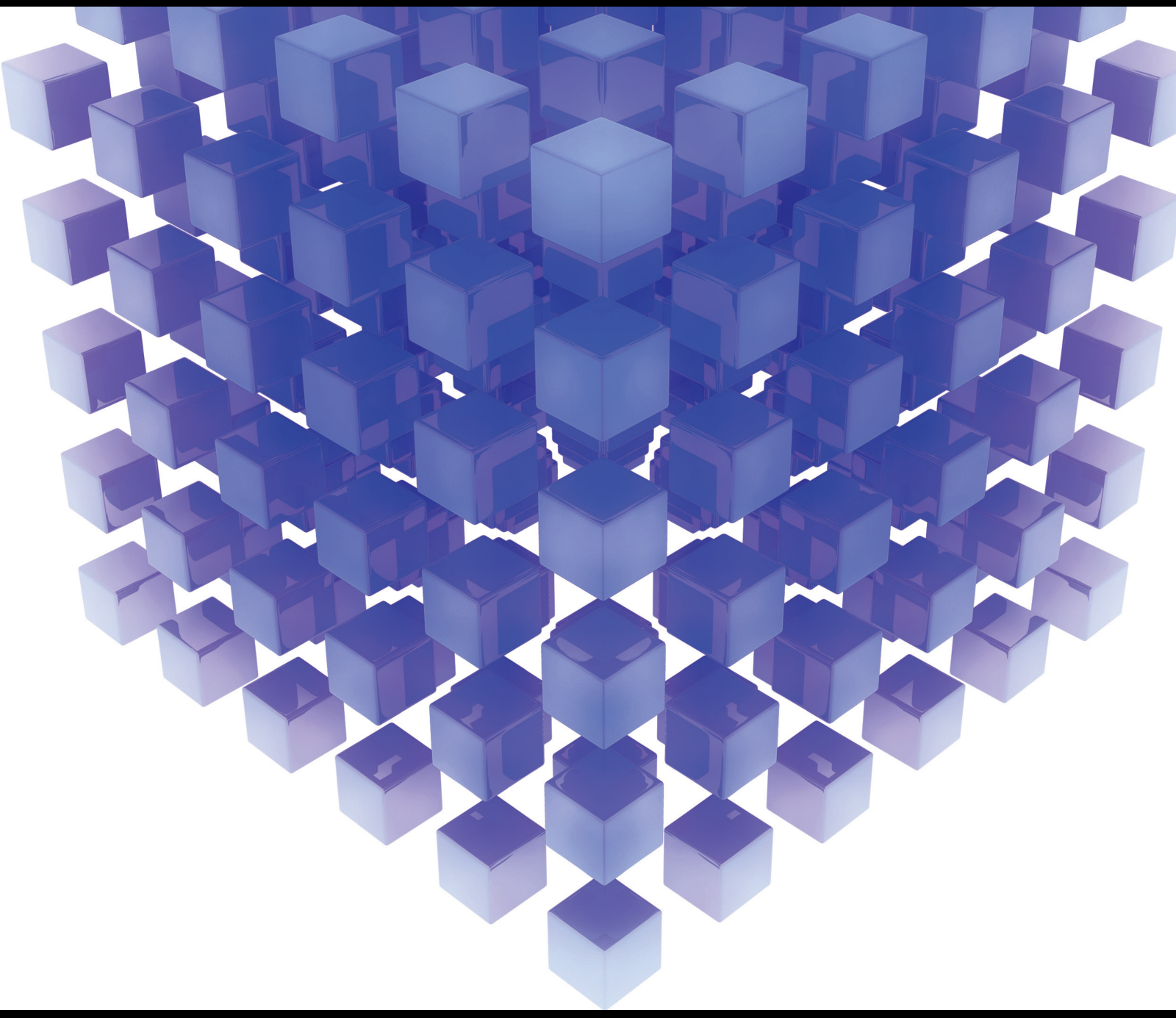

Recent Progress in Sliding Mode Control Theory and Applications

Mathematical Problems in Engineering

Recent Progress in Sliding Mode Control Theory and Applications

Lead Guest Editor: Shihong Ding
Guest Editors: Haibo Du, Chih-Chiang Chen, and Jyoti Mishra

Chief Editor

Academic Editors

Contents

Hindawi
Mathematical Problems in Engineering
Volume 2021, Article ID 8883752, 10 pages
https://doi.org/10.1155/2021/8883752

Research Article

Fault-Tolerant Control for *N*-Link Robot Manipulator via Adaptive Nonsingular Terminal Sliding Mode Control Technology

Nannan Shi,[1] Fanghui Luo,[1] Zhikuan Kang,[1] Lihui Wang,[1] Zhuo Zhao,[1] Qiang Meng ,[2,3] and Weiqin Hou[2,3]

[1]*Seismic Engineering and Structure Key Laboratory of Beijing, Beijing University of Technology, Beijing 100124, China*
[2]*Guangdong RULEBIT Intelligent Robot Technology Co., Ltd., Zhuhai 519000, China*
[3]*Shenzhen RULEBIT Intelligent Robot Technology Co., Ltd., Shenzhen 518000, China*

Correspondence should be addressed to Qiang Meng; qiang.meng@rulebittech.com

Received 24 September 2020; Revised 19 May 2021; Accepted 22 June 2021; Published 6 July 2021

Academic Editor: Shihong Ding

An adaptive nonsingular terminal sliding mode control (ANTSMC) scheme for the *n*-link robot manipulator is presented in this study, which can achieve faster convergence and higher precision tracking compared with the linear hyperplane-based sliding mode control. Novel adaptive updating laws based on the actual tracking error are employed to online adjust the upper bound of uncertainty, which comprehensively consider both the tracking performance and chattering eliminating problem. The stability analysis of the proposed ANTSMC is verified using the Lyapunov method with the existence of the parameter uncertainty and the actuator faults. Numerical simulation studies the comparison of performance between ANTSMC and the conventional nonsingular terminal sliding mode control (NTSMC) scheme to validate the advantages of the proposed control algorithm.

1. Introduction

Robot manipulators play a pivotal role in the modern industrial field, whose dynamics are typically multi-input multioutput (MIMO) nonlinear systems. In practice, parameter variations and external disturbances are inevitable for the mechanical systems. Moreover, high accuracy and safety demands of the robot manipulator cause a greatly increasing attention to the unpredictable faults. Recently, many fault detection methods have been successfully employed for the robot manipulators [1–6], such as the prediction-error-based approach [1], second-order sliding mode observer [2, 3], nonlinear observer [4], optimal unknown input observer [6], and power consumption modeling based method [5]. Besides, the fault-tolerant control research applied in the robot manipulators has been a hot topic. Song introduced a multilayered feed-forward neural network to identify the faults for robot manipulator and then achieved the tracking performance in the presence of uncertainty [7]. Siqueira et al. [8] proposed an output-feedback H_∞ fault-tolerant controller for robot manipulators by linearizing the dynamic model around the operation point. In 2009, Siqueira and Terra [9] further derived H_2, H_∞, and mixed H_2/H_∞ Markovian algorithms for the robot manipulator, but their drawbacks are still the linearization problems. Liu et al. [10] published a novel robust fixed-time fault-tolerant tracking controller for the uncertain robot manipulator. Hagh et al. [11] gave an active fault-tolerant control design for actuator fault mitigation in robotic manipulators. In this paper, we aim to develop a simple and effective passive fault-tolerant control algorithm for the robot manipulator without the fault detection and diagnosis (FDD) module.

Sliding mode control (SMC) schemes are well known for their robustness to the parameter variation and disturbances and have been successfully adopted in many nonlinear systems [12–16]. To assure the finite-time convergence, the terminal sliding mode control (TSMC) has been derived to reach the equilibrium point within a finite time to realize high accuracy control [17]. Besides, the singularity problem of the conventional TSMC has been overcome by indirect [17, 18] and direct approaches [19]. Nowadays, researchers

focus on the unknown functions estimated or designed for the TSMC. Since neural networks and fuzzy logic are universal function approximations, the mixed control algorithms combining them and the TSMC technologies have been extensively employed. Lin proposed an adaptive nonsingular TSMC method for the robotic systems using fuzzy wavelet networks and verified the corresponding controller on a six-link robot manipulator [20]. A dynamics estimation method based on an adaptive algorithm and fuzzy logic is introduced to the nonsingular TSMC for a class of MIMO uncertain nonlinear systems [21]. Xu et al. derived a TSMC based on adaptive fuzzy-neural observer for nonaffine nonlinear system [22]. Cao et al. also used the adaptive fuzzy algorithm to achieve an adaptive nonsingular TSMC for the fault-tolerant small satellite attitude control [23]. Moreover, other adaptive TSMC schemes using different adaptive updating laws without the neural networks and fuzzy logic have also been successfully adopted in many nonlinear systems, such as the electromechanical actuator [24], spacecraft formation flying [25], uncertain nonlinear single-input single-output (SISO) systems [26], and nonlinear differential inclusion systems [27]. However, for the robot manipulator, only the nonsingular TSMC control schemes have been developed [18, 28], though the upper bound of the uncertainty is usually unknown in most of the real systems (especially in the faulty conditions). In fact, the upper bound uncertainty of the nonsingular TSMC for the robot manipulator is conventionally designed as a fixed one, which will bring a trade-off problem between the control accuracy and the control chattering. Therefore, we hope to derive a novel adaptive nonsingular TSMC for the robot manipulator by combining an adaptive updating law to consider both the control accuracy and the control chattering.

Motivated by the above discussion, an adaptive nonsingular TSMC scheme for the robot manipulators with the existence of the parameter uncertainty and the actuator faults is derived in this paper, which can online tune the upper bound of the uncertainty to ensure the high precise tracking performance, finite time convergence, and Lyapunov stability.

2. Problem Formulation

The n-link robot manipulator dynamics can be formulated as

$$\mathbf{M}(\mathbf{q})\ddot{q} + \mathbf{C}(\mathbf{q}, \dot{q}) + \mathbf{G}(\mathbf{q}) = \boldsymbol{\tau}, \tag{1}$$

where $\mathbf{M}(\mathbf{q})$, $\mathbf{C}(\mathbf{q}, \dot{q})$, and $\mathbf{G}(\mathbf{q})$ denote the inertia matrix, Coriolis and centrifugal forces, and gravitational torque, respectively, $\mathbf{q}$ represents the generalized coordinates, and τ is the joint torque.

Considering the uncertainties and actuator faults, the dynamics of the uncertain robot manipulator can be rewritten as

$$(\mathbf{M}_0 + \Delta\mathbf{M})\ddot{q} + (\mathbf{C}_0 + \Delta\mathbf{C}) + (\mathbf{G}_0 + \Delta\mathbf{G}) = \boldsymbol{\delta}_a(\boldsymbol{\tau} + \boldsymbol{\delta}_f), \tag{2}$$

where $\mathbf{M}_0$, $\mathbf{C}_0$, and $\mathbf{G}_0$ represent the estimated terms; $\Delta\mathbf{M}$, $\Delta\mathbf{C}$, and $\Delta\mathbf{G}$ denote the uncertain terms; δ_a and δ_f are the multiplicative and additive faults.

Equation (2) can be further rearranged as

$$\mathbf{M}_0\ddot{q} + \mathbf{C}_0 + \mathbf{G}_0 = \boldsymbol{\tau} + \boldsymbol{\delta}_{\text{total}}, \tag{3}$$

$$\begin{aligned}\boldsymbol{\delta}_{\text{total}} = {} & \left(\boldsymbol{\delta}_a\left(\boldsymbol{\tau} + \boldsymbol{\delta}_f\right) - \boldsymbol{\tau}\right) \\ & - \Delta\mathbf{G} - \Delta\mathbf{C} - \Delta\mathbf{M}\ddot{q}\end{aligned}, \tag{4}$$

where δ_{total} denotes the total uncertainty of the robot manipulator.

3. Nonsingular Terminal Sliding Mode Control (NTSMC)

In this section, the nonsingular terminal sliding mode control (NTSMC) proposed by Man and Yu [18] is briefly described, which solves the singular problem of the TSMC by direct approach.

Lemma 1 (see [18]). *For the uncertain n-link manipulator (described by equation (3)), if the NTSMC manifold and its input command are formulated by equations (5)–(8) and Assumption 1 holds, then the system tracking error ε will converge to zero in finite time.*

$$\mathbf{s} = \boldsymbol{\varepsilon} + \boldsymbol{\Lambda}\dot{\varepsilon}^{p/q}, \tag{5}$$

where

$$\begin{aligned}\boldsymbol{\tau}_{\text{ntsmc}} = {} & \mathbf{M}_0\ddot{q}_d + \mathbf{C}_0 \\ & + \mathbf{G}_0 - \frac{q}{p}\mathbf{M}_0\boldsymbol{\Lambda}^{-1}\dot{\varepsilon}^{2-(p/q)} - \frac{\left[\mathbf{s}^T\mathbf{W}\right]^T}{\left\|\mathbf{s}^T\mathbf{W}\right\|^2}\|\mathbf{s}\|\|\mathbf{W}\|\Gamma_{\text{constant}},\end{aligned} \tag{6}$$

$$\Gamma_{\text{constant}} = b_1 + b_2\|\mathbf{q}\| + b_3\|\dot{q}\|^2, \tag{7}$$

$$\mathbf{W} = \boldsymbol{\Lambda}\text{diag}\left(\dot{\varepsilon}^{(p/q)-1}\right)\mathbf{M}_0^{-1}, \tag{8}$$

where $\varepsilon = \mathbf{q} - \mathbf{q}_d$; $\mathbf{q}$ and $\mathbf{q}_{\text{d}}$ represent the actual input and desired input, respectively; p and q are positive odd integers, which satisfy $1 < p/q < 2$; and $\Lambda = diag[\lambda_1, \ldots, \lambda_n]$ denotes a design matrix.

Assumption 1. The total uncertainty δ_{total} of the robot manipulator can be bounded, which can be formulated as [18]

$$\left\|\boldsymbol{\delta}_{\text{total}}\right\| < b_1 + b_2\|\mathbf{q}\| + b_3\|\dot{q}\|^2, \tag{9}$$

where b_1, b_2, and b_3 are positive numbers.

Remark 1. Lemma 1 gives a conventional NTSMC scheme for the robot manipulator based on Assumption 1, and the design parameters (b_1, b_2, and b_3) of the upper bound Γ_{constant} are constant. In practice, the high upper bound can obtain the high-quality tracking performance at the cost of serious chattering, and the low upper bound owns the

opposite characteristic. Moreover, unpredictable faults may cause the great change of the uncertainty upper bound satisfying Assumption 1. Therefore, it is a hard task to choose an appropriate upper bound Γ_{constant} for the NTSMC.

4. Adaptive Nonsingular Terminal Sliding Mode Control

To appropriately select the uncertainty upper bound of the NTSMC, adaptive updating methods are natural choices. Considering the mechanical systems, there are some special stages: (1) in the start-up phase, the initial trajectory error causes the large starting torque, which appears to be serious chattering phenomenon for the SMC control schemes; (2) in the stability phase, the tracking performance is affected by the system uncertainty; and (3) in the faulty condition, the uncertainty of the nonlinear system may generate great change. Therefore, the uncertainty upper bound of the NTSMC should be chosen to be a low one, a moderate one, and a high one for the above three stages, respectively.

In this section, we introduce adaptive updating laws based on the tracking errors to online adjust the uncertainty upper bound, which are summarized as follows.

Theorem 1. *For the uncertain n-link robot manipulator (described by equation (3)), if the adaptive nonsingular terminal sliding mode control (ANTSMC) manifold and its input command are formulated by equations (10)–(16) and Assumption 1 holds, then the system tracking error ε will converge to zero in finite time.*

$$\mathbf{s} = \boldsymbol{\varepsilon} + \boldsymbol{\Lambda}\dot{\varepsilon}^{p/q}, \tag{10}$$

$$\begin{aligned}\boldsymbol{\tau}_{\text{antsmc}} = {} & \mathbf{M}_0\ddot{q}_d + \mathbf{C}_0 + \mathbf{G}_0 - \frac{q}{p}\mathbf{M}_0\boldsymbol{\Lambda}^{-1}\dot{\varepsilon}^{2-(p/q)} \\ & - \frac{\left[\mathbf{s}^T\mathbf{W}\right]^T}{\left\|\mathbf{s}^T\mathbf{W}\right\|^2}\|\mathbf{s}\|\|\mathbf{W}\|\widehat{\Gamma}_{\text{adaptive}},\end{aligned} \tag{11}$$

$$\mathbf{W} = \boldsymbol{\Lambda}\text{diag}\left(\dot{\varepsilon}^{(p/q)-1}\right)\mathbf{M}_0^{-1}. \tag{12}$$

Moreover, the updating laws are chosen as

$$\widehat{\Gamma}_{\text{adaptive}} = \widehat{b}_1 + \widehat{b}_2\|\mathbf{q}\| + \widehat{b}_3\|\dot{q}\|^2, \tag{13}$$

$$\dot{\widehat{b}}_1 = d_1 \cdot \frac{p}{q}\|\mathbf{W}\|\|\mathbf{s}\|, \tag{14}$$

$$\dot{\widehat{b}}_2 = d_2 \cdot \frac{p}{q}\|\mathbf{W}\|\|\mathbf{s}\|\|\mathbf{q}\|, \tag{15}$$

$$\dot{\widehat{b}}_3 = d_3 \cdot \frac{p}{q}\|\mathbf{W}\|\|\mathbf{s}\|\|\dot{q}\|^2, \tag{16}$$

where $\widehat{\Gamma}_{\text{adaptive}}$, $\widehat{b}_1$, $\widehat{b}_2$, and $\widehat{b}_3$ denote the adaptive estimated values and d_1, d_2, and d_3 are constants.

Proof. Consider the following Lyapunov function:

$$V_{\text{antsmc}} = \frac{1}{2}\left(s^T s + \frac{1}{d_1}\widetilde{b}_1^T\widetilde{b}_1 + \frac{1}{d_2}\widetilde{b}_2^T\widetilde{b}_2 + \frac{1}{d_3}\widetilde{b}_3^T\widetilde{b}_3\right), \tag{17}$$

where $\widetilde{b}_1$, $\widetilde{b}_2$, and $\widetilde{b}_3$ represent the mismatch between the actual and estimated parameters.

$$\widetilde{b}_1 = b_1 - \widehat{b}_1, \tag{18}$$

$$\widetilde{b}_2 = b_2 - \widehat{b}_2, \tag{19}$$

$$\widetilde{b}_3 = b_3 - \widehat{b}_3. \tag{20}$$

Differentiating V_{antsmc} with respect to time and substituting equation (10) and equations (18)–(20) into it yield

$$\dot{V}_{\text{antsmc}} = \mathbf{s}^T\left(\dot{\varepsilon} + \frac{p}{q}\boldsymbol{\Lambda}\text{diag}\left(\dot{\varepsilon}^{(p/q)-1}\right)\ddot{\varepsilon}\right) - \frac{1}{d_1}\widetilde{b}_1^T\dot{\widehat{b}}_1 - \frac{1}{d_2}\widetilde{b}_2^T\dot{\widehat{b}}_2 - \frac{1}{d_3}\widetilde{b}_3^T\dot{\widehat{b}}_3. \tag{21}$$

Substituting equation (3) into equation (21) gives

$$\dot{V}_{\text{antsmc}} = \mathbf{s}^T\left(\dot{\varepsilon} + \frac{p}{q}\boldsymbol{\Lambda}\text{diag}\left(\dot{\varepsilon}^{(p/q)-1}\right)\left(\mathbf{M}_0^{-1}\left(\boldsymbol{\tau}_{\text{antsmc}} + \boldsymbol{\delta}_{\text{total}} - \mathbf{C}_0 - \mathbf{G}_0\right) - \ddot{q}_d\right)\right) - \frac{1}{d_1}\widetilde{b}_1^T\dot{\widehat{b}}_1 - \frac{1}{d_2}\widetilde{b}_2^T\dot{\widehat{b}}_2 - \frac{1}{d_3}\widetilde{b}_3^T\dot{\widehat{b}}_3. \tag{22}$$

Substituting equation (11) into equation (22), equation (22) can be further rearranged as

$$\dot{V}_{\text{antsmc}} = \mathbf{s}^T\left(\dot{\varepsilon} + \frac{p}{q}\boldsymbol{\Lambda}\text{diag}\left(\dot{\varepsilon}^{(p/q)-1}\right)\left(\begin{array}{c} -\frac{q}{p}\boldsymbol{\Lambda}^{-1}\dot{\varepsilon}^{2-(p/q)} \\ \mathbf{M}_0^{-1}\left(\begin{array}{c} -\frac{\left[\mathbf{s}^T\mathbf{W}\right]^T}{\left\|\mathbf{s}^T\mathbf{W}\right\|^2}\|\mathbf{s}\|\|\mathbf{W}\|\widehat{\Gamma}_{\text{adaptive}} \\ +\boldsymbol{\delta}_{\text{total}} \end{array}\right) \end{array}\right)\right) - \frac{1}{d_1}\tilde{b}_1^T\dot{\hat{b}}_1 - \frac{1}{d_2}\tilde{b}_2^T\dot{\hat{b}}_2 - \frac{1}{d_3}\tilde{b}_3^T\dot{\hat{b}}_3$$
$$= \mathbf{s}^T\left(\frac{p}{q}\boldsymbol{\Lambda}\text{diag}\left(\dot{\varepsilon}^{(p/q)-1}\right)\mathbf{M}_0^{-1}\left(-\frac{\left[\mathbf{s}^T\mathbf{W}\right]^T}{\left\|\mathbf{s}^T\mathbf{W}\right\|^2}\|\mathbf{s}\|\|\mathbf{W}\|\widehat{\Gamma}_{\text{adaptive}} + \boldsymbol{\delta}_{\text{total}}\right)\right) - \frac{1}{d_1}\tilde{b}_1^T\dot{\hat{b}}_1 - \frac{1}{d_2}\tilde{b}_2^T\dot{\hat{b}}_2 - \frac{1}{d_3}\tilde{b}_3^T\dot{\hat{b}}_3. \tag{23}$$

Substituting equation (12) into equation (23) yields

$$\dot{V}_{\text{antsmc}} = \mathbf{s}^T\left(\frac{p}{q}\mathbf{W}\left(-\frac{\left[\mathbf{s}^T\mathbf{W}\right]^T}{\left\|\mathbf{s}^T\mathbf{W}\right\|^2}\|\mathbf{s}\|\|\mathbf{W}\|\widehat{\Gamma}_{\text{adaptive}} + \boldsymbol{\delta}_{\text{total}}\right)\right) - \frac{1}{d_1}\tilde{b}_1^T\dot{\hat{b}}_1 - \frac{1}{d_2}\tilde{b}_2^T\dot{\hat{b}}_2 - \frac{1}{d_3}\tilde{b}_3^T\dot{\hat{b}}_3$$
$$= -\frac{p}{q}\|\mathbf{s}\|\|\mathbf{W}\|\widehat{\Gamma}_{\text{adaptive}} + \frac{p}{q}\mathbf{s}^T\mathbf{W}\boldsymbol{\delta}_{\text{total}} - \frac{1}{d_1}\tilde{b}_1^T\dot{\hat{b}}_1 - \frac{1}{d_2}\tilde{b}_2^T\dot{\hat{b}}_2 - \frac{1}{d_3}\tilde{b}_3^T\dot{\hat{b}}_3. \tag{24}$$

Substituting equations (14)–(16) into equation (24), equation (24) can be rewritten as

$$\dot{V}_{\text{antsmc}} = -\frac{p}{q}\|\mathbf{s}\|\|\mathbf{W}\|\left(\widehat{\Gamma}_{\text{adaptive}} + \tilde{b}_1^{\text{T}} + \tilde{b}_2^{\text{T}}\|\mathbf{q}\| + \tilde{b}_3^{\text{T}}\|\dot{q}\|^2\right) + \frac{p}{q}\mathbf{s}^{\text{T}}\mathbf{W}\boldsymbol{\delta}_{\text{total}}. \tag{25}$$

Substituting equation (13) and equations (18)–(20) into equation (25) gives

$$\dot{V}_{\text{antsmc}} = -\frac{p}{q}\|\mathbf{s}\|\|\mathbf{W}\|\left(b_1 + b_2\|\mathbf{q}\| + b_3\|\dot{q}\|^2\right) + \frac{p}{q}\mathbf{s}^T\mathbf{W}\boldsymbol{\delta}_{\text{total}}. \tag{26}$$

Equation (25) can be further rearranged as

$$\dot{V}_{\text{antsmc}} \le \frac{p}{q}\|\mathbf{s}\|\|\mathbf{W}\|\left(\left\|\boldsymbol{\delta}_{\text{total}}\right\| - b_1 - b_2\|\mathbf{q}\| - b_3\|\dot{q}\|^2\right). \tag{27}$$

Therefore, $\dot{V}_{\text{antsmc}} < 0$ can be satisfied using Assumption 1. This completes the proof. □

Remark 2. The initial uncertainty upper bound of the ANSMC can be designed as a low value, and it can adaptively change based on the actual tracking errors to consider both of the tracking performance and chattering phenomenon.

Remark 3. The convergence speed of the ANSMC is mainly affected by the choice of the parameters p, q, and $\Lambda = \text{diag}[\lambda_1, \ldots, \lambda_n]$. The controller tracking performances including the accuracy and chattering are mainly designed by the choice of the parameters (b_1, b_2, b_3, $\hat{b}_1$, $\hat{b}_2$, and $\hat{b}_3$ of the upper bound Γ_{constant}).

Moreover, the finite-time converge characteristic of the NTSMC has been approved for trajectory stabilization of the SISO nonlinear systems in [18]; we further extended the corresponding study to the trajectory tracking of the MIMO systems.

Equation (10) leads to

$$s_i = \varepsilon_i + \lambda_i\dot{\varepsilon}_i^{p/q}, \tag{28}$$

where $(^*)_i$ denotes the ith element of $(^*)$ and $\varepsilon_i = q_i - q_{d,i}$.

The final time $t_{s,i}$ that is taken to travel from $t_{r,i}$ to $\varepsilon_i(t_{r,i} + t_{s,i}) = 0$ for the ith element of system states can be formulated by

$$t_{s,i} = -\lambda_i^{q/p}\int_{\varepsilon_i(t_{r,i})}^{0}\varepsilon_i^{-(q/p)}\text{d}\varepsilon_i = \lambda_i^{q/p}\left(\frac{p}{p-q}\right)\left|\varepsilon_i^{1-(q/p)}{}_{(t_{r,i})}\right|, \tag{29}$$

where $t_{r,i}$ is the time when the sliding mode $s_i(t_{r,i}) = 0$ is reached.

Therefore, the convergence time for the MIMO nonlinear systems can be given by

$$t_s = \max\{t_{s,1}, \ldots, t_{s,n}\}. \tag{30}$$

This means that the system states $\mathbf{q}$ will converge to the desired $\mathbf{q}_d$ in finite time t_s after the sliding mode $\mathbf{s} = 0$ is reached.

Remark 4. To eliminate chattering, the following algorithm is introduced for the NTSMC and ANTSMC control schemes at the cost of introducing tracking errors and deteriorating the perfect stability conditions.

$$\frac{\|\mathbf{s}\|\|\mathbf{W}\|}{\|\mathbf{s}^T\mathbf{W}\|^2} = \frac{\|\mathbf{s}\|\|\mathbf{W}\|}{\left(\|\mathbf{s}^T\mathbf{W}\| + \xi\right)^2}, \tag{31}$$

where ξ is a small constant.

Remark 5. For the robot manipulator, the implementation complexity of the proposed ANSMC is mainly decided by the calculation accuracy of the estimated terms $\mathbf{M}_0$, $\mathbf{C}_0$, and $\mathbf{G}_0$. The estimated terms $\mathbf{M}_0$, $\mathbf{C}_0$, and $\mathbf{G}_0$ are calculated by the multibody dynamics of the robot manipulators. The more components of the robot manipulator are considered in the dynamic analysis of the robot system and will induce the higher implementation complexity of the proposed ANSMC controller. Generally speaking, the main components of the robot manipulator should be computed, such as the thirteen moving rigid bodies of the Stewart Platform [29]. Fortunately, the controller proposed in this paper can obtain a satisfactory performance by introducing adaptive updating laws to compensate the unmodeled dynamics influences. In practice, the calculation accuracy of the estimated terms $\mathbf{M}_0$, $\mathbf{C}_0$, and $\mathbf{G}_0$ can be chosen by comprehensively considering the difficulty of the robot multibody dynamic analysis and the implementation hardware platform capability.

5. Simulation Studies

A two-link robot manipulator is employed to evaluate the performance of the proposed ANTSMC control scheme. Its dynamic model can be formulated by equation (32) with the following parameters: r_1, r_2, J_1, J_2, m_1, and m_2 are 1 m, 0.8 m, 5 kg·m, 5 kg·m, 0.5 kg, and 1.5 kg, respectively [18].

$$\mathbf{M}_{\text{rob}}(\mathbf{q}_{\text{rob}})\ddot{q}_{\text{rob}} + \mathbf{C}_{\text{rob}}(\mathbf{q}_{\text{rob}}, \dot{q}_{\text{rob}}) + \mathbf{G}_{\text{rob}}(\mathbf{q}_{\text{rob}}) = \boldsymbol{\tau}_{\text{rob}}, \tag{32}$$

where

$$\begin{aligned}
\mathbf{q}_{\text{rob}} &= [q_1, q_2]^T,\\
M_{11} &= (m_1 + m_2)r_1^2 + m_2 r_2^2 + 2m_2 r_1 r_2 \cos(q_2) + J_1,\\
M_{12} &= M_{21} = m_2 r_2^2 + m_2 r_1 r_2 \cos(q_2),\\
M_{22} &= m_2 r_2^2 + J_2,\\
C_1 &= -m_2 r_1 r_2 \sin(q_2)\left(\dot{q}_1^2 + 2\dot{q}_1\dot{q}_2\right),\\
C_2 &= m_2 r_1 r_2 \sin(q_2)\dot{q}_2^2,\\
G_1 &= \left((m_1 + m_2)r_1 \cos(q_2) + m_2 r_2 \cos(q_1 + q_2)\right)g,\\
G_2 &= m_2 r_2 \cos(q_1 + q_2)g,
\end{aligned} \tag{33}$$

where M_{ij} denotes the (i, j) element of the matrix $\mathbf{M}_{\text{rob}}$ and C_i and G_i represent the ith elements of $\mathbf{C}_{\text{rob}}$ and $\mathbf{G}_{\text{rob}}$.

The desired trajectory $\mathbf{q}_{\text{rob},r} = [q_{1,r}, q_{2,r}]^T$ and initial trajectory $\mathbf{q}_{\text{rob},0}$ can be given by

$$\begin{aligned}
q_{1,\text{r}} = {} & a_1 \sin(\omega_1 t) + a_2 \cos(\omega_2 t) + a_3 \sin(\omega_3 t) + a_4 \cos(\omega_4 t)\\
& + a_5 \sin(\omega_5 t) + a_6 \cos(\omega_6 t),
\end{aligned} \tag{34}$$

$$\begin{aligned}
q_{2,r} = {} & b_1 \sin(\omega_1 t) + b_2 \cos(\omega_2 t) + b_3 \sin(\omega_3 t) + b_4 \cos(\omega_4 t)\\
& + b_5 \sin(\omega_5 t) + b_6 \cos(\omega_6 t),
\end{aligned} \tag{35}$$

$$\mathbf{q}_{\text{rob},0} = [1.5, -1.5]^T, \tag{36}$$

where $(a_1 \sim a_6)$, $(b_1 \sim b_6)$, and $(\omega_1 \sim \omega_6)$ are selected as (1, 1, 0.01, 1, 0.01, 0.001), (−1, −1, −0.01, −1, −0.01, −0.001), and (0.1, 0.2, 0.4, 0.8, 1.6, 3.2), respectively.

The estimated values of the dynamic parameters are assumed to be

$$\begin{aligned}
\hat{m}_1 &= 0.4\,\text{kg},\\
\hat{m}_2 &= 1.2\,\text{kg},\\
\hat{J}_1 &= 4\,\text{kg}\cdot\text{m},\\
\hat{J}_2 &= 4\,\text{kg}\cdot\text{m}.
\end{aligned} \tag{37}$$

Therefore, three controllers (NTSMC1, NTSMC2, and ANTSMC) are selected to verify the advantages of the proposed ANTSMC. To fairly compare these controllers, their control parameters except the uncertainty upper bound are chosen as the same.

$$\begin{aligned}
\boldsymbol{\Lambda} &= \begin{bmatrix} 150 & 0 \\ 0 & 150 \end{bmatrix},\\
q &= 5,\\
p &= 9,\\
\xi &= 0.001,\\
\tau_{\max} &= 40,
\end{aligned} \tag{38}$$

where $\tau_{\max}$ denotes the maximum torque of the robot manipulator.

Moreover, the appropriate constant uncertainty upper bound satisfying Assumption 1 is hard to determine in practice, especially for the existing kinds of uncertainties. Two uncertainty upper bound designs of NTSMC are selected: the lower one (NTSMC1) and the higher one (NTSMC2). Additionally, the initial value of the uncertainty upper bound of the ANTSMC is chosen as a low value, and it will adaptively adjust according to the actual tracking errors during the motion period. Therefore, the uncertainty upper bounds of the three controllers are designed as follows.

The uncertainty upper bounds of NTSMC1 are given by

$$\begin{aligned} b_1 &= 1, \\ b_2 &= 8, \\ b_3 &= 3. \end{aligned} \tag{39}$$

The uncertainty upper bounds of NTSMC2 are given by

$$\begin{aligned} b_1 &= 10, \\ b_2 &= 80, \\ b_3 &= 30. \end{aligned} \tag{40}$$

The uncertainty upper bounds of ANTSMC are given by

$$\begin{aligned} \widehat{b}_{1,0} &= 1, \\ \widehat{b}_{2,0} &= 1, \\ \widehat{b}_{3,0} &= 1, \\ d_1 &= 5, \\ d_2 &= 0.1, \\ d_3 &= 1, \end{aligned} \tag{41}$$

where $\widehat{b}_{1,0}$, $\widehat{b}_{2,0}$, and $\widehat{b}_{3,0}$ are the initial values of $\widehat{b}_1$, $\widehat{b}_2$, and $\widehat{b}_3$.

5.1. Fault-Free Conditions. The numerical simulations of the robot manipulator under NTSMC1, NTSMC2, and ANTSMC are achieved in MATLAB 6.5 with the step size of 0.0005 s. The corresponding simulation results are illustrated in Figure 1, where "$q1(*)$," "$q2(*)$," "eq1 $(*)$," "eq2 $(*)$," "u1 $(*)$," and "u2 $(*)$" represent the tracking of joint 1, tracking of joint 2, tracking error of joint 1, tracking error of joint 2, control input of joint 1, and control input of joint 2 under the $(*)$ control scheme, respectively; "q1_desired" and "q2_desired" denote the desired trajectories of joint 1 and joint 2.

The system state errors of the robot manipulator can converge to zero in finite time (2 s) under all of the three controllers, which can be observed in Figures 1(a)–1(d). However, owing to its chosen uncertainty, upper bound is lower than the actual uncertainty, and the tracking condition cannot be maintained under NTSMC1, which can be seen in 2.5~5.8 s of Figures 1(c) and 1(d). Moreover, the tracking performances of NTSMC2 and ANTSMC are satisfactory in all of the simulation time.

In the initial time, there are torque variations under the three controllers, which are always unavoidable for the mechanical systems. However, the torque command under NTSMC2 has serious chattering and saturation problems in the first 1.5 s, and there even exists slight chattering in the stabilization stage (6.7~8.7 s), shown in Figure 1(f). Besides, the torque command under NTSMC1 generates short-time chattering to compensate the tracking error in 4.9~5.2 s, which makes the tracking performance be improved after 6 s. Furthermore, the torque command under ANTSMC is always smooth in 1~20 s. Therefore, ANTSMC is the best control scheme owing to its high-accuracy tracking and smooth input command.

5.2. Faulty Conditions. To further research the influence of the unpredictable faults, the actuator faults are assumed to be

$$\delta_a = \begin{cases} 1, & t < 10, \\ 0.9 - 0.1\cos(0.1(t-10)), & t \geq 10, \end{cases} \tag{42}$$

$$\boldsymbol{\delta}_a = \operatorname{diag}(\delta_a, \delta_a), \tag{43}$$

$$\boldsymbol{\delta}_f = \begin{cases} [0 \;\; 0]^T, & t < 10, \\ [-6 - 0.2\sin(0.2(t-10)) \quad -3 - 0.1\sin(0.2(t-10))]^T, & t \geq 10. \end{cases} \tag{44}$$

Besides, the parameter uncertainty, desired trajectory, and controller parameters of the robot manipulator are assumed as same as the fault-free conditions. Then, the corresponding results are presented in Figure 2.

According to equations (42)–(44), actuator faults occur after 10 s, which will cause the torque mutations under the three controllers (shown in Figures 2(e)–2(g)). Moreover, owing to the simultaneous appearances of actuator faults and disturbances, the torque command is calculated to be saturated in a short time to generate the tracking errors for the robot manipulator. After the torque saturation state, the actual trajectories will well track the desired ones under NTSMC2 and ANTSMC at the cost of short-period torque chattering, but the tracking errors will be still existing under NTSMC1.

In summary, ANTSMC is the best control scheme considering both the tracking errors and torque chattering.

6. Conclusions

In this paper, an adaptive nonsingular terminal sliding mode control (ANTSMC) scheme is proposed for the n-link robot manipulator with parameter uncertainties and actuator faults. The characteristics of the conventional nonsingular terminal sliding mode control (NTSMC) scheme, such as the global nonsingular and finite time reaching, are maintained for the proposed ANTSMC. Moreover, numerical simulations are achieved by comparing the performances of NTSMC and ANTSMC, and the advantages of ANTSMC can be summarized as follows:

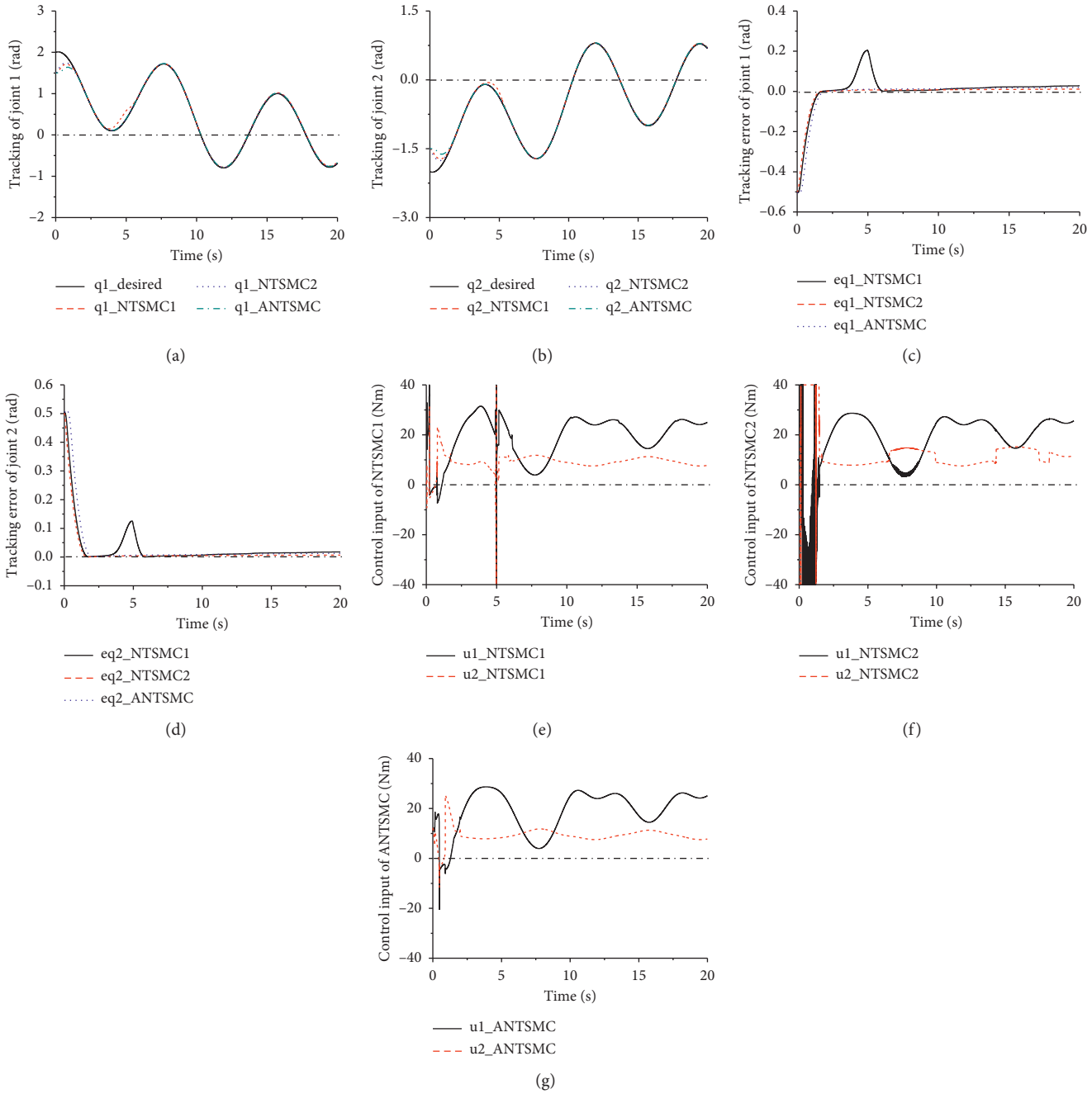

FIGURE 1: Fault-free condition. (a) Tracking of joint 1; (b) tracking of joint 2; (c) tracking error of joint 1; (d) tracking error of joint 2; (e) control input of NTSMC1; (f) control input of NTSMC2; (g) control input of ANTSMC.

(1) *Tracking Performance*. The actual trajectory can track the desired one under ANTSMC and NTSMC2 (higher uncertainty upper bound), even in the conditions of disturbances, faults, and saturation. However, for the trajectory under NTSMC1 (lower uncertainty upper bound), there may exist short-time or long-time errors in the fault-free and faulty conditions, respectively.

(2) *Chattering Phenomenon*. In the initial time, for the torque command under NTSMC2, there exists serious chattering and saturation problem, and the torque commands of NTSMC1 and ANTSMC are satisfactory. In the stabilization period, many factors may cause short-time chattering for the three controllers, such as large tracking error and faults occurrence.

Therefore, according to the results of the simulations, the drawback of existing tracking errors of NTSMC1, the occurrence of serious chattering and saturation for the NTSMC2, and the effectiveness of ANTSMC considering both of the trajectory performance and chattering elimination are observed, respectively.

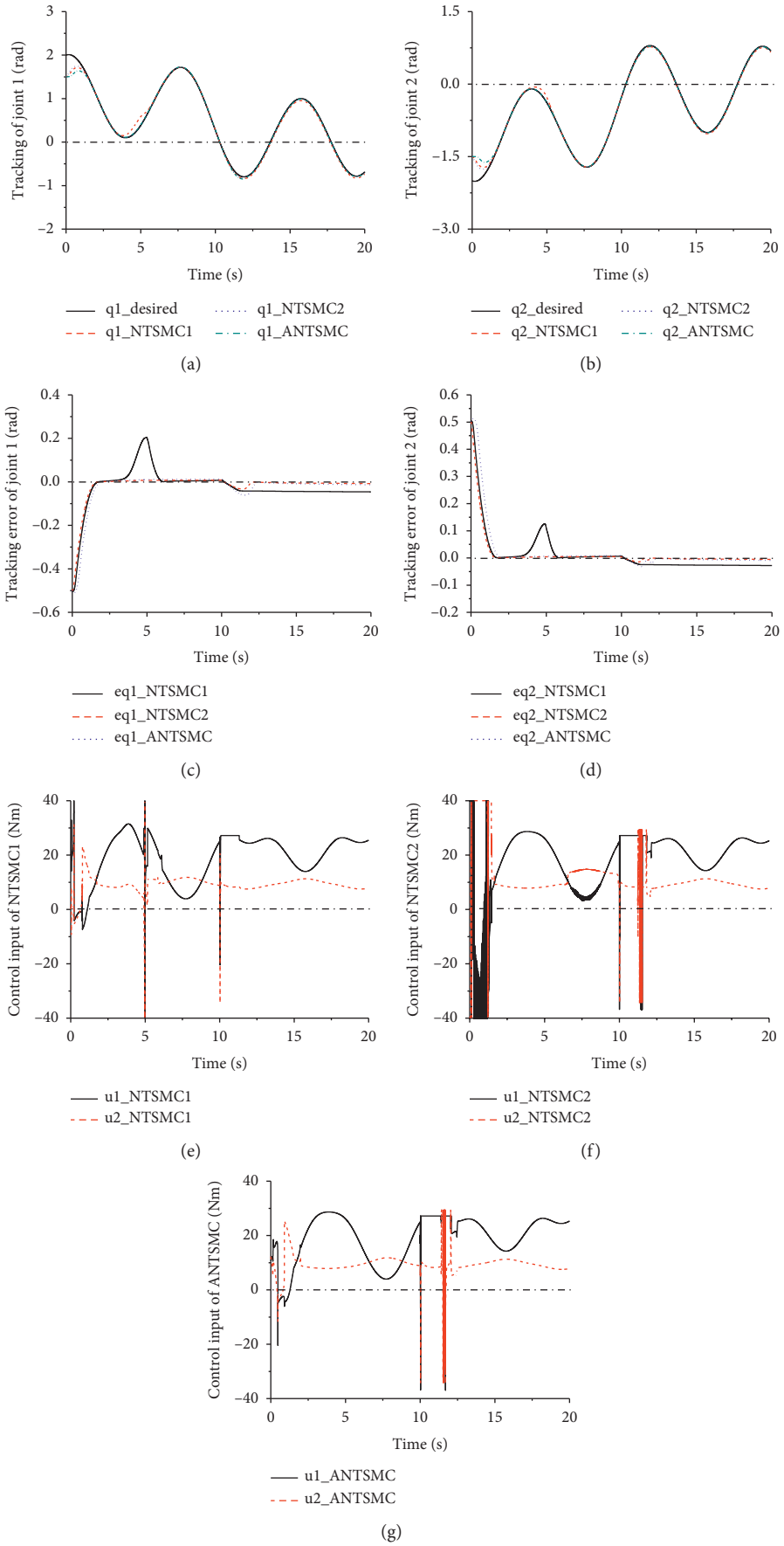

Figure 2: Faulty condition. (a) Tracking of joint 1; (b) tracking of joint 2; (c) tracking error of joint 1; (d) tracking error of joint 2; (e) control input of NTSMC1; (f) control input of NTSMC2; (g) control input of ANTSMC.

7. Future Recommendation

In this paper, we proposed an adaptive nonsingular terminal sliding mode control (ANTSMC) scheme for the general robot manipulator. Further research will be focused on the implementation to the special robot systems in practice.

Data Availability

The data used to support the findings of this study are available from the corresponding author upon request.

Conflicts of Interest

The authors declare that they have no conflicts of interest.

Acknowledgments

The authors are grateful for the financial support of this work by the National Natural Science Foundation of China (no. 51708008).

References

[1] W. E. Dixon, I. D. Walker, and D. M. Dawson, "Fault detection for robot manipulators with parametric uncertainty: a prediction-error-based approach," *IEEE Transactions on Robotics and Automation*, vol. 16, no. 6, pp. 689–699, 2000.

[2] D. Brambilla, L. M. Capisani, and A. Ferrara, "Fault detection for robot manipulators via second-order sliding modes," *IEEE Transactions on Industrial Electronics*, vol. 55, no. 11, pp. 3954–3963, 2008.

[3] M. Van, H. J. Kang, and Y. S. Suh, "A novel neural second-order sliding mode observer for robust fault diagnosis in robot manipulators," *International Journal of Precision Engineering and Manufacturing*, vol. 14, no. 3, pp. 397–406, 2013.

[4] M. L. McIntyre, W. E. Dixon, and D. M. Dawson, "Fault identification for robot manipulators," *IEEE Transactions on Robotics*, vol. 21, no. 5, pp. 1028–1034, 2005.

[5] A. H. Sabry, F. H. Nordin, A. H. Sabry, and M. Z. A. Ab Kadir, "Fault detection and diagnosis of industrial robot based on power consumption modeling," *IEEE Transactions on Industrial Electronics*, vol. 67, no. 9, pp. 7929–7940, 2020.

[6] S. M. H. Moshgani and A. Fakharian, "Fault detection and isolation for manipulator robot using optimal unknown input observer," *Control Engineering and Applied Informatics*, vol. 21, no. 3, pp. 71–79, 2019.

[7] Q. Song, W. J. Hu, L. Yin, and Y. C. Soh, "Robust adaptive dead zone technology for fault-tolerant control of robot manipulators using neural networks," *Journal of Intelligent and Robotic Systems*, vol. 33, no. 2, pp. 113–137, 2002.

[8] A. A. G. Siqueira, M. H. Terra, and C. Buosi, "Fault-tolerant robot manipulators based on output-feedback H-infinity controllers," *Robotics and Autonomous Systems*, vol. 55, no. 10, pp. 785–794, 2007.

[9] A. A. G. Siqueira and M. H. Terra, "A fault-tolerant manipulator robot based on H_2, H_∞, and mixed H_2/H_∞ markovian controls," *IEEE-ASME Transactions on Mechatronics*, vol. 14, no. 2, pp. 257–263, 2009.

[10] L. Z. Liu, L. Y. Zhang, and Y. M. Wang, "A novel robust fixed-time fault-tolerant tracking control of uncertain robot manipulators," *IET Control Theory and Applications*, vol. 15, no. 2, pp. 195–208, 2021.

[11] Y. S. Hagh, R. M. Asl, A. Fekih, H. Wu, and H. Handroos, "Active fault-tolerant control design for actuator fault mitigation in robotic manipulators," *IEEE ACCESS*, vol. 9, pp. 47912–47929, 2021.

[12] L. G. Wu, P. Shi, and H. J. Gao, "State estimation and sliding-mode control of Markovian jump singular systems," *IEEE Transactions on Automatic Control*, vol. 55, no. 5, pp. 1213–1219, 2010.

[13] Q. Meng, T. Zhang, X. Gao, and J.-Y. Song, "Adaptive sliding mode fault-tolerant control of the uncertain Stewart platform based on offline multibody dynamics," *IEEE/ASME Transactions on Mechatronics*, vol. 19, no. 3, pp. 882–894, 2014.

[14] Y. Y. Wang, X. P. Xie, M. Chadli, S. R. Xie, and Y. Peng, "Sliding mode control of fuzzy singularly perturbed descriptor systems," *IEEE Transactions on Fuzzy Systems*, p. 1, 2020.

[15] Y. Y. Wang, B. Jiang, Z. G. Wu, S. R. Xie, and Y. Peng, "Adaptive sliding mode fault-tolerant fuzzy tracking control with application to unmanned marine vehicles," *IEEE Transactions on Systems, Man, and Cybernetics: Systems*, pp. 1–10, 2020.

[16] Y. Wang, Y. Xia, H. Li, and P. Zhou, "A new integral sliding mode design method for nonlinear stochastic systems," *Automatica*, vol. 90, pp. 304–309, 2018.

[17] N. N. Shi, Z. K. Kang, Z Zhao, and Q. Meng, "Adaptive vector nonsingular terminal sliding mode control for a class of *n*-order nonlinear dynamical systems with uncertainty," *Mathematical Problems in Engineering*, vol. 2020, Article ID 7309417, 12 pages, 2020.

[18] Z. Man and X. Yu, "Terminal sliding mode control of MIMO linear systems," *IEEE Transactions on Circuits and Systems I: Fundamental Theory and Applications*, vol. 44, no. 11, pp. 1065–1070, 1997.

[19] Y. Feng, X. H. Yu, and Z. H. Man, "Non-singular terminal sliding mode control of rigid manipulators," *Automatica*, vol. 38, no. 12, pp. 2159–2167, 2002.

[20] C. K. Lin, "Nonsingular terminal sliding mode control of robot manipulators using fuzzy wavelet networks," *IEEE Transactions on Fuzzy Systems*, vol. 14, no. 6, pp. 849–859, 2006.

[21] V. Nekoukar and A. Erfanian, "Adaptive fuzzy terminal sliding mode control for a class of MIMO uncertain nonlinear systems," *Fuzzy Sets and Systems*, vol. 179, no. 1, pp. 34–49, 2011.

[22] D. Z. Xu, B. Jiang, and M. S. Qian, "Terminal sliding mode control using adaptive fuzzy-neural observer," *Mathematical Problems in Engineering*, vol. 2013, Article ID 958958, 8 pages, 2013.

[23] L. Cao, X. Q. Chen, and T. Sheng, "Fault tolerant small satellite attitude control using adaptive non-singular terminal sliding mode," *Advances in Space Research*, vol. 51, no. 12, pp. 2374–2393, 2013.

[24] H. Li, L. Dou, and Z. Su, "Adaptive nonsingular fast terminal sliding mode control for electromechanical actuator," *International Journal of Systems Science*, vol. 44, no. 3, pp. 401–415, 2013.

[25] J. Wang and Z. Sun, "6-DOF robust adaptive terminal sliding mode control for spacecraft formation flying," *ACTA Astronautica*, vol. 73, pp. 76–87, 2012.

[26] W. Q. Tang and Y. L. Cai, "High-order sliding mode control design based on adaptive terminal sliding mode," *International Journal of Robust and Nonlinear Control*, vol. 23, no. 2, pp. 149–166, 2013.

[27] J. Huang, L. N. Sun, and Z. Z. Han, "Adaptive terminal sliding mode control for nonlinear differential inclusion systems with

disturbance," *Nonlinear Dynamics*, vol. 72, no. 1-2, pp. 221–228, 2013.

[28] M. Jin, J. Lee, and P. Chang, "Practical nonsingular terminal sliding-mode control of robot manipulators for high-accuracy tracking control," *IEEE Transactions on Industrial Electronics*, vol. 56, no. 9, pp. 3593–3601, 2009.

[29] Q. Meng, T. Zhang, J.-F. He, J.-Y. Song, and J.-W. Han, "Dynamic modeling of a 6-degree-of-freedom Stewart platform driven by a permanent magnet synchronous motor," *Journal of Zhejiang University Science C*, vol. 11, no. 10, pp. 751–761, 2010.

Hindawi
Mathematical Problems in Engineering
Volume 2021, Article ID 6627495, 17 pages
https://doi.org/10.1155/2021/6627495

Research Article

A Moving Target Tracking Control of Quadrotor UAV Based on Passive Control and Super-Twisting Sliding Mode Control

Wentao Xue, Xunnan Zhu, Xiaofei Yang, Hui Ye, and Xuan Chen

School of Electronic and Information, Jiangsu University of Science and Technology, Zhenjiang 212100, China

Correspondence should be addressed to Xiaofei Yang; yxfei_0809@just.edu.cn

Received 18 December 2020; Accepted 2 May 2021; Published 11 May 2021

Academic Editor: Gang Lei

A novel asymptotic tracking controller for an underactuated quadrotor unmanned aerial vehicle (UAV) is proposed to solve a moving target tracking problem. Firstly, the control system is decoupled into the position control system and the attitude control system. Secondly, a method combined artificial potential field with passivity control (APF&PC) is introduced for the positioning system to achieve high-precision tracking of moving target at a fixed distance. Thirdly, a super-twisting sliding mode (STSM) method with an improved reaching law for the attitude system is applied to ensure that the attitude converges to the desired value. Furthermore, the stabilities of two subsystems are proved, and sufficient stability conditions are derived based on the passive method and Lyapunov method, respectively. Finally, simulation results of the moving target tracking verify the superiority and robustness of the proposed control method in the presence of parameter uncertainties and external disturbances.

1. Introduction

In recent years, quadrotor unmanned aerial vehicles have attracted increasing attention from both industrial and academic communities. With some characteristics of vertical take-off and landing, single or team flight, and low-cost manufacturing, they have wide applications such as military monitoring, traffic information collection, power system detection, and disaster first aid [1–4]. The quadrotor UAV is an underactuated and strongly coupled nonlinear system, which is subject to structural uncertainties and unknown external disturbance. Therefore, it is a great challenge to design an accurate and robust controller for the quadrotor to achieve autonomous flight and target tracking.

Moving target tracking is an essential skill for the quadrotor UAV to perform military and civil tasks, like tracking enemy targets in air combat, tracking vehicles in urban antiterrorism, and timely finding and locking the victims in maritime rescue [5, 6]. Due to the limitation of the observation range and the danger of unfriendly targets, the quadrotor UAV needs to maintain a certain distance in the whole mission, which brings new challenges to target tracking. Currently, many kinds of control methods have been successfully applied in the target tracking of UAVs. Wang et al. [7] proposed an integrated framework for UAV-based target tracking and recognition systems to achieve satisfactory tracking performance. Rabah et al. [8] developed a target tracking algorithm based on a Fuzzy-PI controller to track a moving target under varying speed. Araar et al. [9] proposed a PID method with an EKF filter to track autonomously and land on a moving platform. Chen et al. [10] presented sliding mode control methods based on artificial potential field and RBF neural network for a quadrotor to track the moving target. Based on studies aforesaid, the design of a controller with high precision and strong robustness is the precondition of accurate tracking. Thus, it is the key for the moving target tracking of a quadrotor to realize the position and attitude tracking control of the quadrotor system and improve the robustness of the system.

In order to achieve attitude stabilization and position tracking control of the quadrotor, various advanced control techniques have been developed. Many remarkable achievements have been obtained such as robust PID control [11], active disturbance rejection method [12], feedback linearization control [13], backstepping control [14], model predictive control [15], adaptive control [16], immersion and

invariance control [17], reinforcement learning [18], and composite stability control [19, 20]. Although the above methods can accomplish the autonomous flight of UAVs, some of them still have limited capability to handle uncertainties and external disturbances. Sliding mode control (SMC) is considered an effective method in solving the control problems of uncertain nonlinear systems because of its unique robustness and adaptability to uncertainty and external disturbances [21–23]. Therefore, a wide class of control methods based on SMC has been proposed to solve trajectory tracking of the quadrotor. Chen et al. [24] designed a robust nonlinear controller that combines sliding mode control and backstepping control to achieve trajectory tracking of a quadrotor UAV. Xu et al. [25] presented a quadrotor controller based on the terminal sliding mode control to track the attitude trajectory under input saturation. Castañeda et al. [26] proposed an adaptive second-order sliding mode control method to improve the robustness of the system under different operating conditions and external disturbances. Inspired by the aforementioned papers, we can improve sliding mode control to handle the attitude control problem of quadrotors under uncertainties and external disturbances.

There are some main feasible control methods to realize the position tracking of UAVs. The artificial potential field (APF) is a robust feedback control method based on the virtual force field, which has been widely applied in obstacle avoidance and target tracking [27]. Chen et al. [28] proposed an artificial potential field UAV path planning method to make UAV avoid obstacles efficiently and economically when there are many threats. Hu et al. [29] designed a time-varying sliding surface and a nonlinear adaptive feedback control law based on the APF method for obstacle avoidance control. The passive control (PC) method is to redistribute the energy function of the inverted system by injecting damping into the system so that it conforms to Lyapunov stability law and ensures that the system is asymptotically stable [30]. Ha et al. [31] proposed a unified passivity-based adaptive backstepping control framework for the velocity field following and timed trajectory tracking of a quadrotor on the Internet. Jose and Hugo [32] presented a passivity-based controller for a quadrotor with a cable-suspended load to guarantee asymptotic stability. Based on the aforementioned discussion, we propose a novel double-loop control system based on the position controller and attitude controller, which can achieve high-precision target tracking for the quadrotor. The position controller combines the artificial potential field with passive theory to achieve high-precision position tracking, and the attitude controller uses the super-twisting sliding mode method with an improved reaching law to improve the convergence speed of the attitude.

The main contributions of this study are as follows: firstly, a novel position controller based on artificial potential field and passive control is proposed to improve the precision of fixed distance tracking. The quadrotor can track the moving target at a certain distance by tracking the balance point of the artificial potential field. The passive control can improve the robustness of the system by providing disturbance rejection to uncertainties and disturbances. Besides, a super-twisting sliding mode controller with an improved reaching law is presented for attitude control to ensure fast convergence and strong robustness. The reaching law based on proportional term and exponential term can reduce the chattering and improve the convergence rate, which will guarantee a better tracking performance.

The rest of this paper is organized as follows. In Section 2, the structure of the target tracking system and the dynamic modeling of the quadrotor are presented. In Section 3, a novel quadrotor control method for moving target tracking is studied and its stability is analyzed. In Section 4, numerical simulations are provided to show the feasibility and effectiveness of the proposed approach. Finally, a brief conclusion is drawn in Section 5.

2. Mathematical Model of the Quadrotor

Target tracking is a complex engineering system that involves technical modules in hardware, localization, mapping, planning, and control. The target tracking of UAV is to locate the target according to the distance information of relative observation angle and attitude information of UAV. Then, the future motion state of the target is predicted according to the observation data of sensors. In addition, the target state is filtered and estimated, and motion information of UAV is collected. On the premise that the attitude angle and angular velocity of the quadrotor can be measured, the three-dimensional position and translation velocity of the UAV relative to the moving target are available. Finally, the UAV will be guided to keep track of the moving target through the continuous update of target estimation and prediction state. For the target tracking of the quadrotor, the most critical issues are the control of trajectory tracking. We assume that the relative position of the quadrotor can be obtained from the visual information of the camera, and the state of the tracking target can be estimated by the Kalman filtering method. In this paper, we will focus on the trajectory tracking of the quadrotor control system. By designing the position controller and attitude controller of quadrotor UAV, the moving target can be tracked within a safe distance. The simplified structure of the tracking system is shown in Figure 1.

The dynamical model of the quadrotor is set up by the earth-frame $I(Oxyz)$ and the body-frame $B(Oxyz)$ as illustrated in Figure 2. It is assumed that the moving target is a mobile car, and $\boldsymbol{\rho}$ is the relative distance between the quadrotor and target. In quadrotor systems, f_i ($i = 1, 2, 3, 4$) stands for the thrust force produced by the ith propeller. The vertical motion is created by the collective thrust input of all four propellers. The roll, pitch, and yaw motion can be achieved by changing the speeds of different propellers. The position and attitude of the quadrotor expressed in the inertial frame are defined as $\mathbf{P} = [x, y, z]^{\mathrm{T}}$ and $\boldsymbol{\Theta} = [\phi, \theta, \psi]^{\mathrm{T}}$, where ϕ, θ, and ψ are successively roll, pitch, and yaw angles. These angles are bounded as $\phi \in (-\pi/2 \ \pi/2)$, $\theta \in (-\pi/2 \ \pi/2)$, and $\psi \in (-\pi \ \pi)$.

The dynamic behavior of quadrotor in the inertial coordinate can be described by the dynamic equation based on the Euler–Lagrange method [33] as follows:

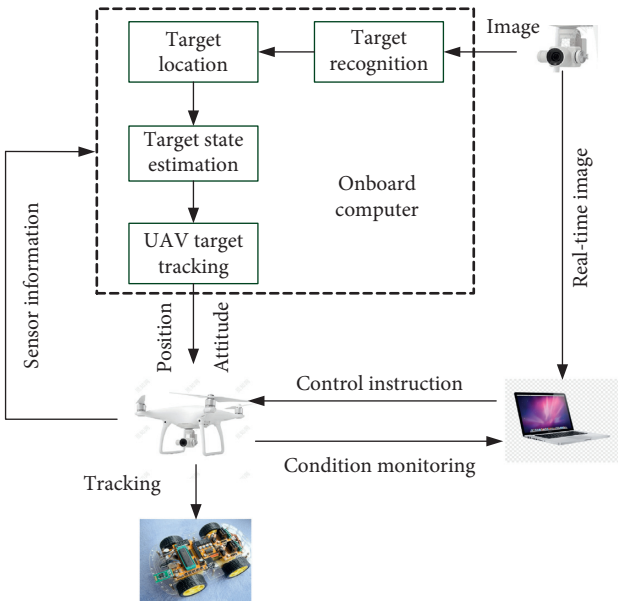

Figure 1: Structure diagram of the tracking system.

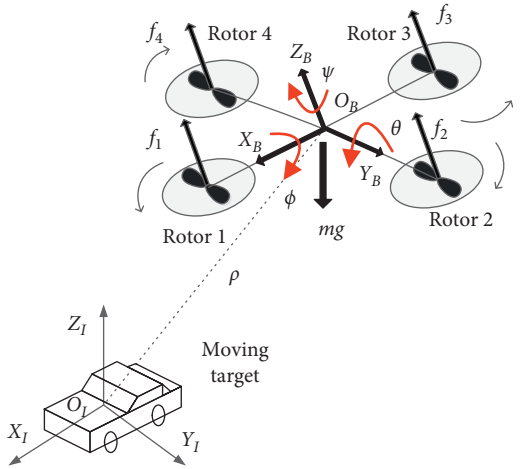

Figure 2: Model diagram of the tracking system.

$$m\ddot{P} = U_1\mathbf{R}e_3 - mge_3 + \mathbf{d}_1, \tag{1}$$

$$\mathbf{J}\ddot{\Theta} = \Gamma - \mathbf{C}\dot{\Theta} + \mathbf{d}_2, \tag{2}$$

where m is the total mass, g is the gravitational acceleration, and $\mathbf{e}_3 = [0\ 0\ 1]^{\mathrm{T}}$ is a unit vector in the vertical direction. The vectors $\mathbf{d}_1$ and $\mathbf{d}_2$ denote, respectively, the norm-bounded uncertainties and disturbances in translational and rotational motions, which are slow time-varying signals.

$\mathbf{R}$ represents an orthonormal rotation matrix, defined by

$$\mathbf{R} = \begin{bmatrix} C_\theta C_\psi & S_\theta S_\phi C_\psi - C_\phi S_\psi & C_\phi S_\theta C_\psi + S_\phi S_\psi \\ C_\theta S_\psi & S_\phi S_\theta S_\psi + C_\phi C_\psi & C_\phi S_\theta S_\psi - S_\phi C_\psi \\ -S_\theta & S_\phi C_\theta & C_\phi C_\theta \end{bmatrix}, \tag{3}$$

where $C_{(\cdot)}$ and $S_{(\cdot)}$, respectively, represent cosine function and sinusoidal function.

The positive definite matrix $\mathbf{J}$ is the moment of inertia, given by

$$\mathbf{J} = \begin{bmatrix} I_{xx} & 0 & -I_{xx}S_\theta \\ 0 & I_{yy}C_\phi^2 + I_{zz}S_\phi^2 & (I_{yy} - I_{zz})S_\phi C_\phi C_\theta \\ -I_{xx}S_\theta & (I_{yy} - I_{zz})S_\phi C_\phi C_\theta & I_{xx}S_\theta^2 + I_{yy}S_\phi^2 C_\theta^2 + I_{zz}C_\phi^2 C_\theta^2 \end{bmatrix}, \tag{4}$$

where $\mathbf{I} = [I_{xx}\ \ I_{yy}\ \ I_{zz}]^{\mathrm{T}}$ represents inertia tensors of the quadrotor.

The vector $\mathbf{C}$ represents a Coriolis and centrifugal force term, which can be calculated by [33]

$$\mathbf{C} = \dot{J} - \frac{1}{2}\frac{\partial}{\partial \Theta}\left(\dot{\Theta}^T \mathbf{J}\right). \tag{5}$$

The control input U_1 denotes total lift force and $\Gamma = [\Gamma_\phi\ \ \Gamma_\theta\ \ \Gamma_\psi]^{\mathrm{T}}$ stand for torques applied on the three axes, which can be calculated by rotor thrusts as follows [34]:

$$U_1 = \sum_{i=1}^{4} f_i = \sum_{i=1}^{4} b_1 \omega_i^2, \tag{6}$$

where b_1 and ω_i represent lift coefficient and angular speed of the relevant propeller, respectively.

Further, the input torque of attitude control for a quadrotor UAV can be obtained as

$$\Gamma = \begin{bmatrix} \Gamma_\phi \\ \Gamma_\theta \\ \Gamma_\psi \end{bmatrix} = \begin{bmatrix} 0 & b_1 l & 0 & -b_1 l \\ -b_1 l & 0 & b_1 l & 0 \\ -c_1 & c_1 & -c_1 & c_1 \end{bmatrix} \begin{bmatrix} \omega_1^2 \\ \omega_2^2 \\ \omega_3^2 \\ \omega_4^2 \end{bmatrix}, \tag{7}$$

where c_1 is an aerodynamic constant, and l is the distance from the motors to the center of gravity.

The control problem considered in this work is to design a control system to guarantee the trajectory tracking of a moving target for the quadrotor system with bounded uncertainties and disturbances.

3. Controller Design

It is assumed that we can gain the trajectory of the moving target by the vision sensor and calculated the velocity and acceleration of the target. The overall control objective for the quadrotor with a desired yaw angle ψ_d is to track the desired trajectory of the target $\mathbf{P}_d = [x_d, y_d, z_d]^{\mathrm{T}}$. The speed and acceleration of the target can be defined as $\mathbf{V}_d$ and $\mathbf{a}_d$, respectively. The distance from the quadrotor to the target can be described by $\rho = \mathbf{P} - \mathbf{P}_d$. For a given expected tracking distance ρ_d, the error of the relative distance is given by $\mathbf{e}_P = \rho - \rho_d$. The purpose of target tracking control is to design a closed-loop controller to make the tracking error approach 0.

In this section, the control system is composed of the position controller and attitude controller. Firstly, a position controller based on the artificial potential field and passive control is designed to obtain the desired position tracking for $\mathbf{P}_d$ and generate the desired roll and pitch references ϕ_d

and θ_d. Besides, an attitude controller based on the super-twisting sliding mode method with an improved reaching law is applied to make the aircraft track the desired attitude vector $\mathbf{\Theta}_d = [\phi_d, \theta_d, \psi_d]^{\mathrm{T}}$. The control structure is depicted in Figure 3.

3.1. Position Controller Design. According to (1), the translational error is obtained by

$$\ddot{e}_P = \frac{\mathbf{U}_P + \mathbf{d}_1}{m} - g\mathbf{e}_3 - \mathbf{a}_d, \tag{8}$$

where $\mathbf{U}_P = U_1\mathbf{R}\mathbf{e}_3$ is the virtual control input.

We use the artificial potential field method to solve the position tracking. Firstly, the repulsion potential J^r is constructed as a generalized Morse function [28]:

$$J^r = \begin{cases} a\dfrac{b}{e^{(\|\boldsymbol{\rho}\|/\mathbf{c})} - e^{(\|\boldsymbol{\rho}\|_{\min}/c)}}, & \|\boldsymbol{\rho}\| \in D, \\ 0, & \|\boldsymbol{\rho}\| \notin D, \end{cases} \tag{9}$$

where b and c are constant, which determine the magnitude and velocity of the repulsion force, respectively. The gain coefficient of the potential field a is a constant. $D = [\|\rho\|_{\min}, \|\rho\|_{\max}$ determines the action area of the artificial potential field. $\|\rho\|_{\min} > 0$ represents the minimum safe distance, and $\|\rho\|_{\max}$ is expressed as the maximum distance.

In order to ensure that the artificial potential field has the correct equilibrium state $\|\rho_d\|$, the gravitational potential J^a is defined as

$$J^a = \begin{cases} \dfrac{1}{2}a \cdot k\|\boldsymbol{\rho}\|^2, & \|\boldsymbol{\rho}\| \in D, \\ 0, & \|\boldsymbol{\rho}\| \notin D, \end{cases} \tag{10}$$

where k indicates a positive constant that can adjust the strength of gravitational potential.

If the quadrotor can keep a certain distance to track the target, the velocity field of the artificial potential field at the equilibrium point is 0. The values of parameters k, b, and c will be satisfied as

$$-k\left(\|\boldsymbol{\rho}_d\|\right) + \frac{b}{c}\frac{1}{\left(e^{(\|\boldsymbol{\rho}_d\|/c)} - e^{(\|\boldsymbol{\rho}\|_{\min}/c)}\right)^2}e^{\|\boldsymbol{\rho}_d\|/c} = 0. \tag{11}$$

When $\|\rho_d\| \le \|\rho\| \le \|\rho\|_{\max}$, the gravitational force has a great effect on the convergence in long distances. When $\|\rho\|_{\min} \le \|\rho\| \le \|\rho_d\|$, the repulsive force plays a leading role in short distances. When $\|\rho\| > \|\rho\|_{\max}$, the potential field no longer works. When $\|\rho\| = \|\rho_d\|$, the two forces are just equal and the potential field reaches equilibrium.

By combining repulsive potential and gravitational potential, the velocity field function between UAV and target for $\|\rho\| \in D$ can be determined as

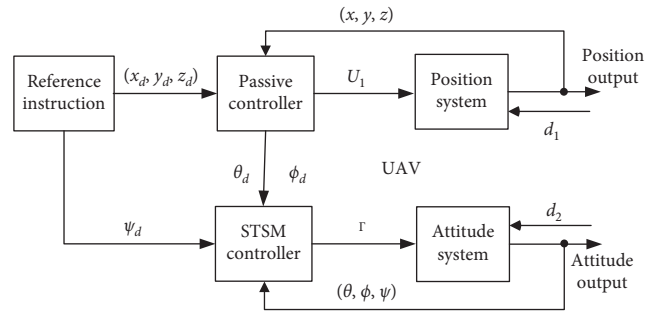

Figure 3: Structure of the quadrotor control system.

$$\begin{aligned} \mathbf{v}_f &= -\nabla J^r - \nabla J^a \\ &= a\left[-k\|\boldsymbol{\rho}\| + \frac{b}{c}\frac{1}{\left(e^{(\|\boldsymbol{\rho}\|/c)} - e^{(\|\boldsymbol{\rho}\|_{\min}/c)}\right)^2}e^{\|\boldsymbol{\rho}\|/c}\right]\frac{\boldsymbol{\rho}}{\|\boldsymbol{\rho}\|}. \end{aligned} \tag{12}$$

Definition 1. Considering nonlinear systems,

$$\begin{cases} \dot{x} = f(x, u), \\ y = h(x). \end{cases} \tag{13}$$

For all $x \in R^n$ and $u \in R^m$, f is a locally Lipschitz function and $f(0, 0) = 0$, and $h(x)$ is continuous and $h(0) = 0$. If a differentiable positive definite function $V(x)$ satisfies

$$u^T y \ge \dot{V} = \frac{\partial V}{\partial x} f(x, u), \tag{14}$$

then, the abovementioned nonlinear system is passive [35].

The velocity error can be set as

$$\dot{e}_P = \dot{P} - \mathbf{v}_d - \dot{\rho}_d = \mathbf{v}_e. \tag{15}$$

The velocity field is used to calculate the relative velocity between UAV and target. The relative velocity is defined as

$$\mathbf{v}_r = \mathbf{v}_e - \mathbf{v}_f + \alpha\mathbf{e}_P, \quad \alpha > 0. \tag{16}$$

Based on (15), the velocity error can be derived as

$$\dot{e}_P = -\alpha\mathbf{e}_P + \mathbf{v}_r + \mathbf{v}_f. \tag{17}$$

The derivative of v_r can be derived as

$$\dot{v}_r = \dot{v}_e - \dot{v}_f + \alpha\dot{e}_p = \frac{\mathbf{U}_p}{m} - g\mathbf{e}_3 + \frac{\mathbf{d}_1}{\mathrm{m}} - \mathbf{a}_t - \dot{v}_f + \alpha\dot{e}_p. \tag{18}$$

To ensure accurate tracking of moving targets, a virtual control input of the position controller is designed as

$$\mathbf{U}_p = mg\mathbf{e}_3 - \hat{d}_1 + m\left(\ddot{P}_d - \lambda_1\mathbf{v}_r + \dot{v}_f + \mathbf{u} - \alpha\dot{e}_p\right), \tag{19}$$

where $\lambda_1 > 0$, $\hat{d}_1$ is the estimate of d_1, and u is the virtual input of the passive system.

Substituting (18) into (17) yields

$$\dot{v}_r = -g\mathbf{e}_3 - \widehat{d}_1 - \lambda_1 \mathbf{v}_r + \dot{v}_f - \alpha \dot{e}_p + g\mathbf{e}_3 - \dot{v}_f + \mathbf{d}_1 + \alpha \dot{e}_p + \mathbf{u} = -\lambda_1 \mathbf{v}_r + \widetilde{d}_1 + \mathbf{u}, \tag{20}$$

where the error $\widetilde{d}_1 = \mathbf{d}_1 - \widehat{d}_1$.

For the tracking system, the structure of the cascaded passive system is shown in Figure 4. The total input of the system is $\widetilde{d}_1 + \mathbf{u}$, and the output is $\mathbf{e}_P$. According to passive theory, the passivity of the system can improve the accuracy of the position tracking and avoid the local minimum of the artificial potential field near the equilibrium point. Thus, the stability of the system will be improved.

Theorem 1. *Consider the quadrotor translational dynamics described in (8). The whole position tracking system acts as a cascade of the drive system (17) and driven system (20). If the relative velocity and the virtual control input are designed according to (16) and (19), the control strategy can guarantee that the position control system is passive and globally stable at the origin.*

Proof. If a candidate storage function is set as

$$\mathbf{V}_3(\mathbf{e}_p, \mathbf{v}_r) = \mathbf{V}_1(\mathbf{e}_p) + \mathbf{V}_2(\mathbf{v}_r), \tag{21}$$

where $\mathbf{V}_1 = (1/2)\mathbf{e}_P^T \mathbf{e}_P$, $\mathbf{V}_2 = (1/2)\mathbf{v}_r^T \mathbf{v}_r$.

According to (11) and (12), we can get

$$\mathbf{e}_P \mathbf{v}_f = a \frac{\boldsymbol{\rho}(\boldsymbol{\rho} - \boldsymbol{\rho}_d)}{\|\boldsymbol{\rho}\|} \left[-k\|\boldsymbol{\rho}\| + \frac{b}{c} \frac{1}{\left(e^{(\|\boldsymbol{\rho}\|/c)} - e^{(\|\boldsymbol{\rho}\|_{\min}/c)}\right)^2} e^{\|\boldsymbol{\rho}\|/c} \right] = T \cdot Q, \tag{22}$$

where $T = a(\rho(\rho - \rho_d)/\|\rho\|)$, $Q = [-k\|\rho\| + b/c(1/(e^{(\|\rho\|/c)} - e^{(\|\rho\|_{\min}/c)})^2)e^{(\|\rho\|/c)}]$.

If $\|\rho\| \geq \|\rho_d\|$, then $T \geq 0$, $Q \leq 0$. If $\|\rho\| < \|\rho_d\|$, then $T < 0$, $Q > 0$. It can be derived as $\mathbf{e}_P^T \mathbf{v}_f \leq 0$.

The derivative of $\mathbf{V}_1$ can be given by

$$\dot{V}_1 = \mathbf{e}_P^T \cdot \dot{e}_P = \mathbf{e}_P^T \mathbf{v}_r - \alpha \mathbf{e}_P^T \mathbf{e}_P + \mathbf{e}_P^T \mathbf{v}_f \leq \mathbf{e}_P^T \mathbf{v}_r. \tag{23}$$

Then, the system is passive to $\mathbf{e}_P$ and $\mathbf{v}_r$.

The derivative of $\mathbf{V}_2$ can be written as

$$\dot{V}_2 = \mathbf{v}_r^T \cdot \dot{v}_r = -\lambda_1 \mathbf{v}_r^T \mathbf{v}_r + \mathbf{v}_r^T(\widetilde{d}_1 + \mathbf{u}) \leq \mathbf{v}_r^T(\widetilde{d}_1 + \mathbf{u}). \tag{24}$$

Thus, the system is passive to $\mathbf{v}_r$ and $\widetilde{d}_1 + \mathbf{u}$.

The derivative of $\mathbf{V}_3$ can be solved as

$$\begin{aligned} \dot{V}_3 &= \mathbf{e}_p \mathbf{v}_r^T + \mathbf{v}_r^T(\widetilde{d}_1 + \mathbf{u}) + \mathbf{e}_P^T \mathbf{v}_f - \alpha \mathbf{e}_P^T \mathbf{e}_p - \lambda_1 \mathbf{v}_r^T \mathbf{v}_r \\ &\leq \mathbf{e}_p \mathbf{v}_r^T + \mathbf{v}_r^T(\widetilde{d}_1 + \mathbf{u}) - \alpha \mathbf{e}_p^T \mathbf{e}_p - \lambda_1 \mathbf{v}_r^T \mathbf{v}_r \\ &\leq \mathbf{e}_p \mathbf{v}_r^T + \mathbf{v}_r^T(\widetilde{d}_1 + \mathbf{u}) = \mathbf{v}_r^T(\mathbf{e}_p + \widetilde{d}_1 + \mathbf{u}). \end{aligned} \tag{25}$$

The feedback control is designed as

$$\mathbf{u} = -\mathbf{e}_p - \beta \mathbf{v}_r, \tag{26}$$

where $\beta > 0$; then,

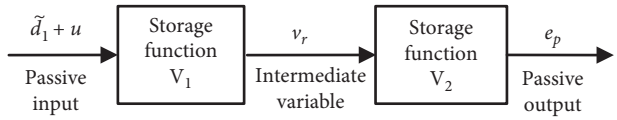

Figure 4: Cascade passive structure of quadrotor.

$$\dot{V}_3 = \mathbf{v}_r^T(\widetilde{d}_1 - \beta \mathbf{v}_r) = \mathbf{v}_r^T \widetilde{d}_1 - \beta \mathbf{v}_r^T \mathbf{v}_r \leq \mathbf{v}_r^T \widetilde{d}_1. \tag{27}$$

Taking into account uncertainties and external disturbances, the storage function $\mathbf{V}$ is chosen as

$$\mathbf{V} = \mathbf{V}_3 + \frac{1}{2}\mathbf{d}_1^T \widetilde{d}_1. \tag{28}$$

The adaptive law is constructed as

$$\dot{\widehat{d}}_1 = -\mathbf{v}_r. \tag{29}$$

Because $\widetilde{d}_1$ is a slow time-varying signal, the derivative of V can be solved as

$$\begin{aligned} \dot{V} &= \mathbf{v}_r \widetilde{d}_1^T - \beta \mathbf{v}_r^T \mathbf{v}_r + \widetilde{d}_1^T \dot{\widetilde{d}}_1 = \mathbf{v}_r \widetilde{d}_1^T - \beta \mathbf{v}_r^T \mathbf{v}_r - \widetilde{d}_1^T \dot{\widehat{d}}_1 \\ &= -\beta \mathbf{v}_r^T \mathbf{v}_r \leq 0. \end{aligned} \tag{30}$$

Therefore, it is shown that the controller can force the states of the system with bounded disturbances and uncertainties to converge asymptotically to origin.

We define the virtual control input $U_P = [U_x, U_y, U_z]^T$, satisfying

$$\begin{bmatrix} U_x \\ U_y \\ U_z \end{bmatrix} = U_1 \begin{bmatrix} C_\theta C_\psi & S_\theta S_\phi C_\psi - C_\phi S_\psi & C_\phi S_\theta C_\psi + S_\phi S_\psi \\ C_\theta S_\psi & S_\phi S_\theta S_\psi + C_\phi C_\psi & C_\phi S_\theta S_\psi - S_\phi C_\psi \\ -S_\theta & S_\phi C_\theta & C_\phi C_\theta \end{bmatrix} \begin{bmatrix} 0 \\ 0 \\ 1 \end{bmatrix}. \tag{31}$$

The above matrix expression can be obtained by

$$\begin{cases} U_x = U_1(C_\phi S_\theta C_\psi + S_\phi S_\psi), \\ U_y = U_1(C_\phi S_\theta S_\psi - S_\phi C_\psi), \\ U_z = U_1 C_\phi C_\theta. \end{cases} \tag{32}$$

According to (32), the actual control input U_1 can be solved as

$$U_1 = \frac{U_z}{C_{\phi_d} C_{\theta_d}}. \tag{33}$$

Substituting U_1 into U_x and U_y, we can get two desired attitude angles from (32); that is,

$$\begin{cases} \theta_d = \arctan\left(\dfrac{U_x C_{\psi_d} + U_y S_{\psi_d}}{U_z}\right), \\ \phi_d = \arctan\left(C_{\theta_d} \dfrac{U_x S_{\psi_d} - U_y C_{\psi_d}}{U_z}\right). \end{cases} \tag{34}$$

□

3.2. Attitude Controller Design. In this section, the attitude controller is designed by using the super-twisting sliding mode control with an improved reaching law. The objective of the controller is to ensure the convergence of the attitude angles to the desired trajectories.

Considering both model uncertainties and external disturbances in the attitude subsystem, (2) can be written as

$$\mathbf{J}_0\ddot{\Theta} = -\mathbf{C}_0\dot{\Theta}_d + \Gamma + \mathbf{d}_2 - \mathbf{J}_\Delta\ddot{\Theta} - \mathbf{C}_\Delta\dot{\Theta}, \tag{35}$$

where $\mathbf{J} = \mathbf{J}_0 + \mathbf{J}_\Delta$, $\mathbf{C} = \mathbf{C}_0 + \mathbf{C}_\Delta$, $\mathbf{C}_0 = 0.9\mathbf{C}$.

$$\mathbf{J}_0 = \begin{bmatrix} I_{xx} & 0 & 0 \\ 0 & I_{xx} + I_{yy} & 0 \\ 0 & 0 & I_{xx} + I_{yy} + I_{zz} \end{bmatrix}. \tag{36}$$

The vector d denote the norm-bounded model uncertainty and external disturbances in rotational motions as

$$\mathbf{d} = \mathbf{d}_2 - \mathbf{J}_\Delta\ddot{\Theta} - \mathbf{C}_\Delta\dot{\Theta}, \tag{37}$$

where $\|\mathbf{d}\| \le D_1$.

The dynamic model of attitude system can be transformed into

$$\mathbf{J}_0\ddot{\Theta} + \mathbf{C}_0\dot{\Theta} = \Gamma + \mathbf{d}. \tag{38}$$

The state-space form of this model can be given by

$$\begin{cases} \dot{\Theta}_1 = \mathbf{\Theta}_2, \\ \dot{\Theta}_2 = f(\mathbf{\Theta}) + g(\mathbf{\Theta})\Gamma + \mathbf{d}, \end{cases} \tag{39}$$

where the vector $f(\Theta) = -\mathbf{J}_0^{-1}\mathbf{C}\dot{\Theta}$ and $g(\Theta) = \mathbf{J}_0^{-1}$.

The tracking error of attitude e_1 is defined as

$$\mathbf{e}_1 = \mathbf{\Theta}_{1\,d} - \mathbf{\Theta}_1. \tag{40}$$

The angular velocity tracking error is given by

$$\mathbf{e}_2 = \dot{e}_1. \tag{41}$$

The sliding mode manifold is designed as

$$s = e_2 + \lambda e_1, \tag{42}$$

where $\mathbf{s} = \begin{bmatrix} s_\phi & s_\theta & s_\psi \end{bmatrix}^{\mathrm{T}}$, $\lambda > 0$.

The reaching law of the sliding mode manifold is chosen as

$$\begin{aligned} \dot{s} = &-k_1\int_0^s \operatorname{sgn}(\mathbf{s}(\tau))\mathrm{d}\tau - k_2|\mathbf{s}|^{(1/2)}\operatorname{sgn}(\mathbf{s}) \\ &- (2k_4 + k_1)\mathbf{s} - k_3\operatorname{sgn}(\mathbf{s}), \end{aligned} \tag{43}$$

where the gain coefficient k_1, k_2, and k_4 are positive constant, $k_3 > D_1 \ge \|\mathbf{d}\|$.

The improved reaching law adds the proportion term and the velocity term. The law provides a power convergence rate in the reaching phase and reduces the approaching time to the sliding surface. In addition, the combined terms can guarantee that the system state reaches the sliding mode surface with a good dynamic performance.

Substituting (42) and (43) into (39) leads to

$$\begin{aligned} \Gamma = g^{-1}(\mathbf{\Theta})\Big\{&-f(\mathbf{\Theta}) + \ddot{\Theta}_{1\,d} + \boldsymbol{\lambda}\dot{e}_1 + (2k_4 + k_1)\mathbf{s} + \mathbf{d} \\ &+ k_1\int_0^s \operatorname{sgn}(\mathbf{s})\mathrm{d}\tau + k_2|\mathbf{s}|^{(1/2)}\operatorname{sgn}(\mathbf{s}) + k_3\operatorname{sgn}(\mathbf{s})\Big\}. \end{aligned} \tag{44}$$

Theorem 2. *Consider the quadrotor rotational dynamics described in (2). If the sliding mode manifold and control input are designed according to (42) and (43), the control strategy can ensure that the attitude tracking error e_1 converges to zero.*

Proof. If a candidate Lyapunov function is selected as

$$W = \frac{1}{2}\mathbf{e}_1^T\mathbf{e}_1 + \frac{1}{2}\mathbf{s}^T\mathbf{s}, \tag{45}$$

the derivative of W is computed as

$$\begin{aligned} \dot{W} &= \mathbf{e}_1^T\mathbf{e}_2 + \mathbf{s}^T\left[-k_1\int_0^t \operatorname{sgn}(\mathbf{s})\mathrm{d}\tau - (2k_4 + k_1)\mathbf{s} - k_2|\mathbf{s}|^{(1/2)}\operatorname{sgn}(\mathbf{s}) - k_3\operatorname{sgn}(\mathbf{s}) + \mathbf{d}\right] \\ &= \mathbf{e}_1^T\mathbf{e}_2 - 2k_4\mathbf{s}^T\mathbf{s} - k_2|\mathbf{s}|^{(3/2)} - k_3|\mathbf{s}| + \mathbf{s}^T\mathbf{d} \le \mathbf{e}_1^T\mathbf{e}_2 - 2k_4\mathbf{s}^T\mathbf{s} - k_2|\mathbf{s}|^{(3/2)} \\ &\le -\left[k_4\lambda^2\mathbf{e}_1^T\mathbf{e}_1 + (2k_4\lambda - 1)\mathbf{e}_1^T\mathbf{e}_2 + k_4\mathbf{e}_2^T\mathbf{e}_2\right] - k_4\mathbf{s}^T\mathbf{s} - k_2|\mathbf{s}|^{(3/2)} \le -\begin{bmatrix}\mathbf{e}_1 & \mathbf{e}_2\end{bmatrix}Q\begin{bmatrix}\mathbf{e}_1 & \mathbf{e}_2\end{bmatrix}^T - k_4\mathbf{s}^T\mathbf{s} - k_2|\mathbf{s}|^{(3/2)}, \end{aligned} \tag{46}$$

where $Q = \begin{bmatrix} k_4\lambda^2 & k_4\lambda - 1/2 \\ k_4\lambda - 1/2 & k_4 \end{bmatrix}$.

The matrix Q can be calculated as $|\mathbf{Q}| = k_4\lambda - (1/4)$. If appropriate values of k_2, k_4, and λ are selected to make $|\mathbf{Q}| > 0$ and $\dot{W} \le 0$, the sliding surface will converge to 0. It can be concluded that the proposed attitude controller can guarantee that the attitude angle asymptotically converges to the desired values. □

4. Simulation and Analysis

Trajectory tracking simulations of the quadrotor have been carried out to verify the validity and efficiency of the proposed control method. Besides, a synthesis controller based on second-order SMC (2-SMC) [36] has been chosen for the comparison.

The parameter values of the quadrotor model are as follows: $m = 0.5$ kg, $b_1 = 5$ Ns^2, $c_1 = 2$ Nms^2, $l = 0.5$ m, $g = 9.8$ m/s^2, $I_{xx} = I_{yy} = 0.004$ kgm^2, $I_{zz} = 0.008$ kgm^2, and the yaw angle $\psi_d = \pi/3$. The external disturbances are considered as $d_1 = [0.1\sin(0.1\pi t),\ 0.1\cos(0.1\pi t),\ 0.1\cos(0.1\pi t)]^T$ and $d_2 = [0.3\sin(0.1\pi t) + 0.1,\ 0.4\cos(0.1\pi t) + 0.1,\ 0.5\sin(0.1\pi t) + 0.2]^T$.

In order to further evaluate the robustness of the proposed control method, another simulation has been executed for the system under external disturbances and parametric uncertainties. The parameter uncertainties are considered as ±30% in the mass m and inertia matrix I_{xx}, I_{yy}, and I_{zz} respectively.

The controller parameters of 2-SMC are given as follows: $c_z = 1$, $c_\psi = 1$, $\varepsilon_1 = 1$, $\varepsilon_2 = 1$, $\varepsilon_3 = 0.5$, $\varepsilon_4 = 0.5$, $\eta_1 = 1$, $\eta_2 = 1$, $\eta_3 = 4$, $\eta_4 = 4$, $c_1 = 10m_s/(u_1\cos\phi\cos\psi)$, $c_2 = 5m_s/(u_1\cos\phi\cos\psi)$, $c_3 = 1$, $c_4 = 5$, $c_5 = -10m_s/(u_1\cos\psi)$, $c_6 = -5m_s/(u_1\cos\psi)$, $c_7 = 1$, and $c_8 = 5$.

The parameters of the control method based on PC and STSM (PC&STSM) are adjusted as $\|\rho\|_{\min} = 1$, $\|\rho_d\| = 2$, $\|\rho\|_{\max} = 5$, $k = 10$, $a = 1$, $b = 16.83$, $c = 2$, $\alpha = 0.8$, $\lambda_1 = 4$, $\beta = 2$, $k_1 = 0.5$, $k_2 = 1$, $k_3 = 3$, $k_4 = 2$, and $\lambda = 10$. According to the tracking target, selecting methods of controller parameters will be given as follows.

(1) First, it is assumed that the expected distance between the aircraft and the moving target $\|\rho_d\| = 2$. The gain coefficient a will be chosen as $a = 1$ to balance the potential field force. When $2 \le \|\rho\| \le 5$, we choose $k = 10$ to get a large gravitational force. When $1 \le \|\rho\| \le 2$, we choose $c = 2$ to get a slightly large repulsive force. According to (11), we can get $b = 16.83$ at the equilibrium point of the artificial potential field

(2) The parameters α and β are in connection with the convergence rate of the relative velocity and position error. The parameter λ_1 is related to the external disturbances in translational motion. Through several simulation attempts, we choose $\alpha = 0.8$, $\beta = 2$, and $\lambda_1 = 4$ in order to improve the convergence rate and accuracy

(3) When $s = 0, \dot{e}_1 = -\lambda e_1$. If any attitude angle error needs to converge to 0.01 in 0.5 s, λ should be chosen as $\lambda = 10$. The parameters k_1, k_2, and k_4 are in connection with the accuracy and convergence speed of attitude angle error. According to (43) and (47), $k_1 > 0$, $k_2 > 0$, and $k_4\lambda > 0.25$. Through several simulation attempts, we choose $k_1 = 0.5$, $k_2 = 1$, and $k_4 = 2$ to obtain fast convergence and small overshoot. Finally, the parameter k_3 is related to the robustness of the system, and k_3 will be adjusted according to $k_3 > \|\mathbf{d}\|$

In order to show the effectiveness of the proposed strategy, we select two tracking scenarios for simulation.

4.1. Ground Moving Target. The initial position and attitude angle values of the quadrotor are [0, 0, 1.5] m and [0.2, 0.2, 0.5] rad. The trajectory of a moving ground target can be described as

$$\mathbf{P}_d = \left[\ 4\mathrm{t}\ \ 4\ \sin\left(\frac{t}{2}\right)\ \ 2\ \right]. \tag{47}$$

Simulation results of trajectory tracking are depicted in Figure 5. Figure 5(a) presents tracking results from the two control methods in 3D space. It can be observed that the PC&STSM method can make the quadrotor track the target accurately at a fixed distance, whereas the 2-SMC approach makes it slightly off the desired track at the beginning. As shown in Figure 5(b), the position tracking from APF&PC achieves null steady-state error for all positions in 1.8 s, while the 2-SMC controller takes 3.8 s to get the steady state. Figure 5(c) shows that the STSM controller has a fast convergence rate than that from 2-SMC. Compared with 2-SMC, the improved reaching law greatly improves the convergence performance. The comparisons of convergence time and overshoot between the two methods are listed in Tables 1 and 2.

As shown in Figure 6, the simulation results of trajectory tracking demonstrate the control quality of the proposed controller in terms of disturbances and uncertainties.

It can be seen from Figure 6(a) that the PC&STSM controller can still track accurately the trajectory of the moving ground target when the mass and inertia matrixes of the quadrotor change by ± 30%. According to Figure 6(b), the position tracking generated by the controller converges to the set position in 2s even if the disturbances and uncertainties are considered. Besides, the figure also shows that parameter uncertainties have few effects on position control. From Figure 6(c), it can be observed that attitude angles converge in a short time and keep the desired values all the time although uncertainties and disturbances cause overshoot. The simulation results have illustrated that the PC&STSM controller has good robustness and tracking performance in the case of external disturbances and parameter uncertainties.

4.2. Aerial Moving Target. The initial position and attitude angle values of the quadrotor are [0, 0, −1] m and [0, 0.2, 0.5] rad. The trajectory of a moving aerial target can be described as

$$\mathbf{P}_d = \left[\ \frac{1}{2}\cos\left(\frac{t}{2}\right)\ \ \frac{1}{2}\sin\left(\frac{t}{2}\right)\ \ 2\ + \frac{t}{10}\right]. \tag{48}$$

According to Figure 7(a), it can be concluded that the aerial target tracking control system can meet the tracking performance, and the PC&STSM has a better tracking effect than 2-SMC. From Figure 7(b), it can be observed that APF&PC is insensitive to disturbances and has a faster convergence speed in position tracking. In contrast, 2-SMC has a longer adjustment time. Figure 7(c) shows that STSM achieves zero steady-state error with a small overshoot between 0 rad and 0.09 rad, while 2-SMC has a bigger amplitude oscillation in attitude tracking. The response speed of STSM is faster than that of 2-SMC, which is helpful

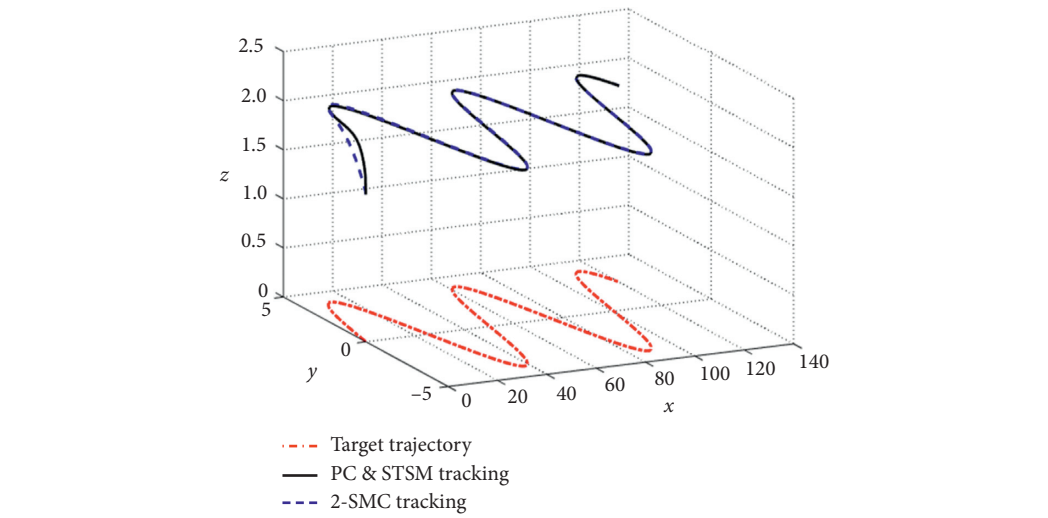

(a)

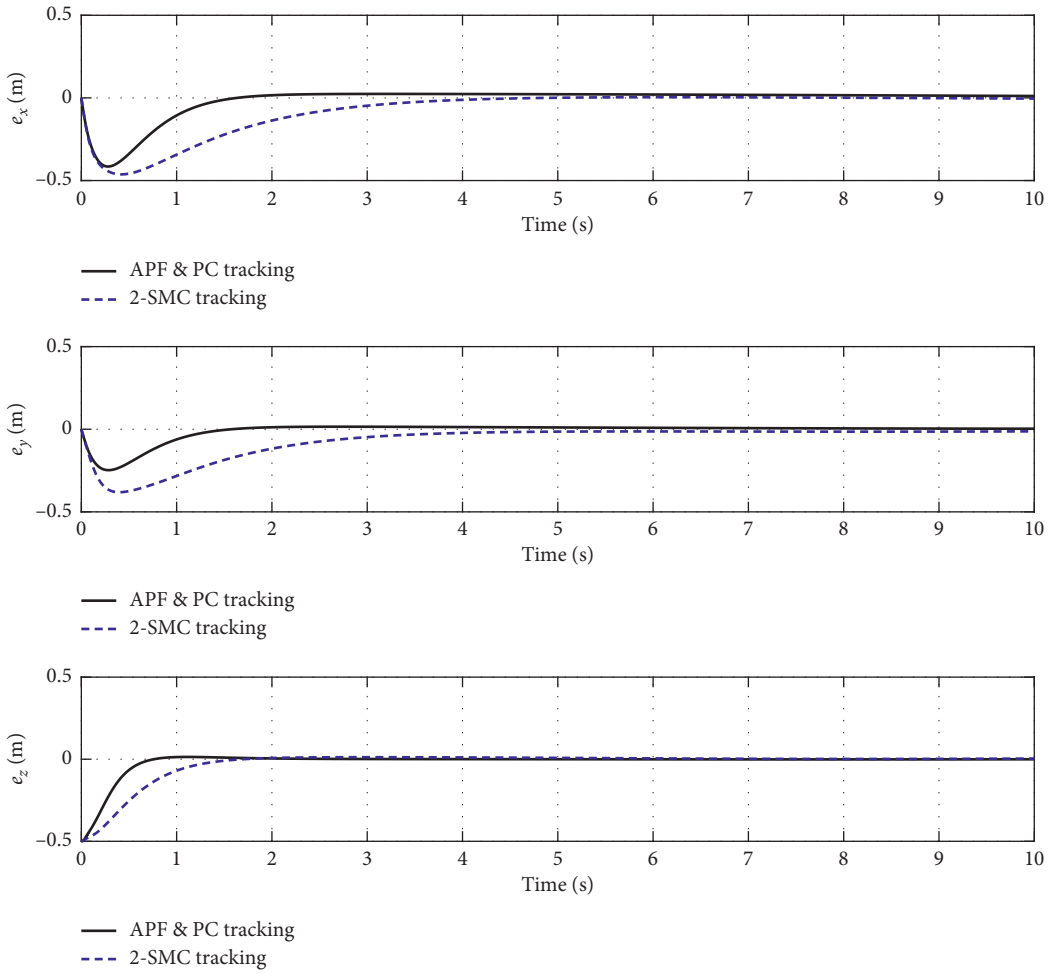

(b)

Figure 5: Continued.

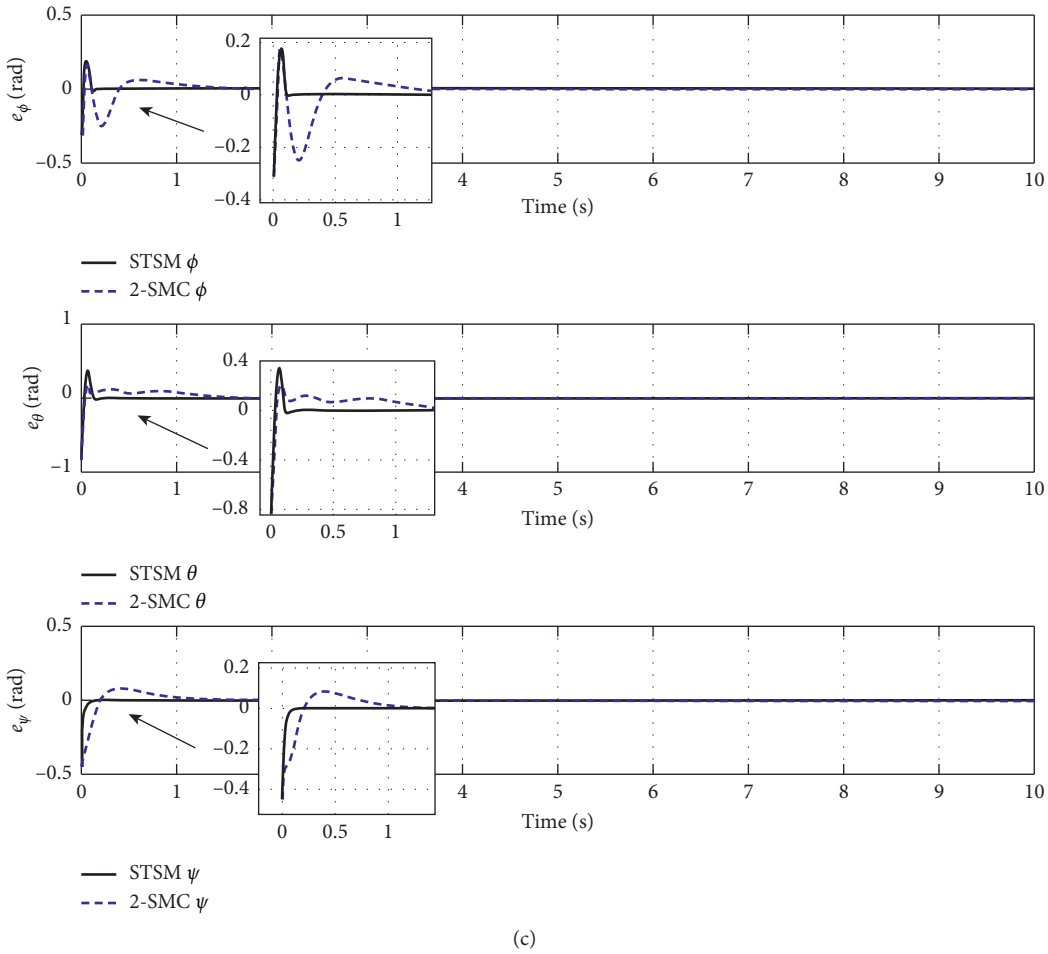

(c)

Figure 5: Ground moving target tracking. (a) Trajectory tracking. (b) Position tracking error. (c) Attitude tracking error.

Table 1: Convergence time of tracking error.

Method	x (s)	y (s)	z (s)	ϕ (s)	θ (s)	ψ (s)
PC&STSM	1.8	1.8	0.9	0.4	0.4	0.25
2-SMC	3.8	3.8	1.8	1.5	1.5	1.2

Table 2: Overshoot of tracking error.

Method	x	y	z	ϕ	θ	ψ
PC&STSM	0	0	0	0.18	0.38	0
2-SMC	0	0	0	0.18	0.24	0.1

to flexibly move in the air. The comparisons of convergence time and overshoot between the two methods are listed in Tables 3 and 4.

As presented in Figures 6 and 8, the convergence of position and attitude state is slightly affected by the variation of system parameters, but the proposed controller can achieve zero steady-state error and compensate for external disturbances and parameter uncertainties. The simulation results verify the robustness of the proposed control scheme.

Numerical simulation indicated that the controller based on PC&STSM can trace the moving target effectively and has a good dynamic performance. Compared with the 2-SMC method, the proposed controller has a better performance in tracking precision and robustness.

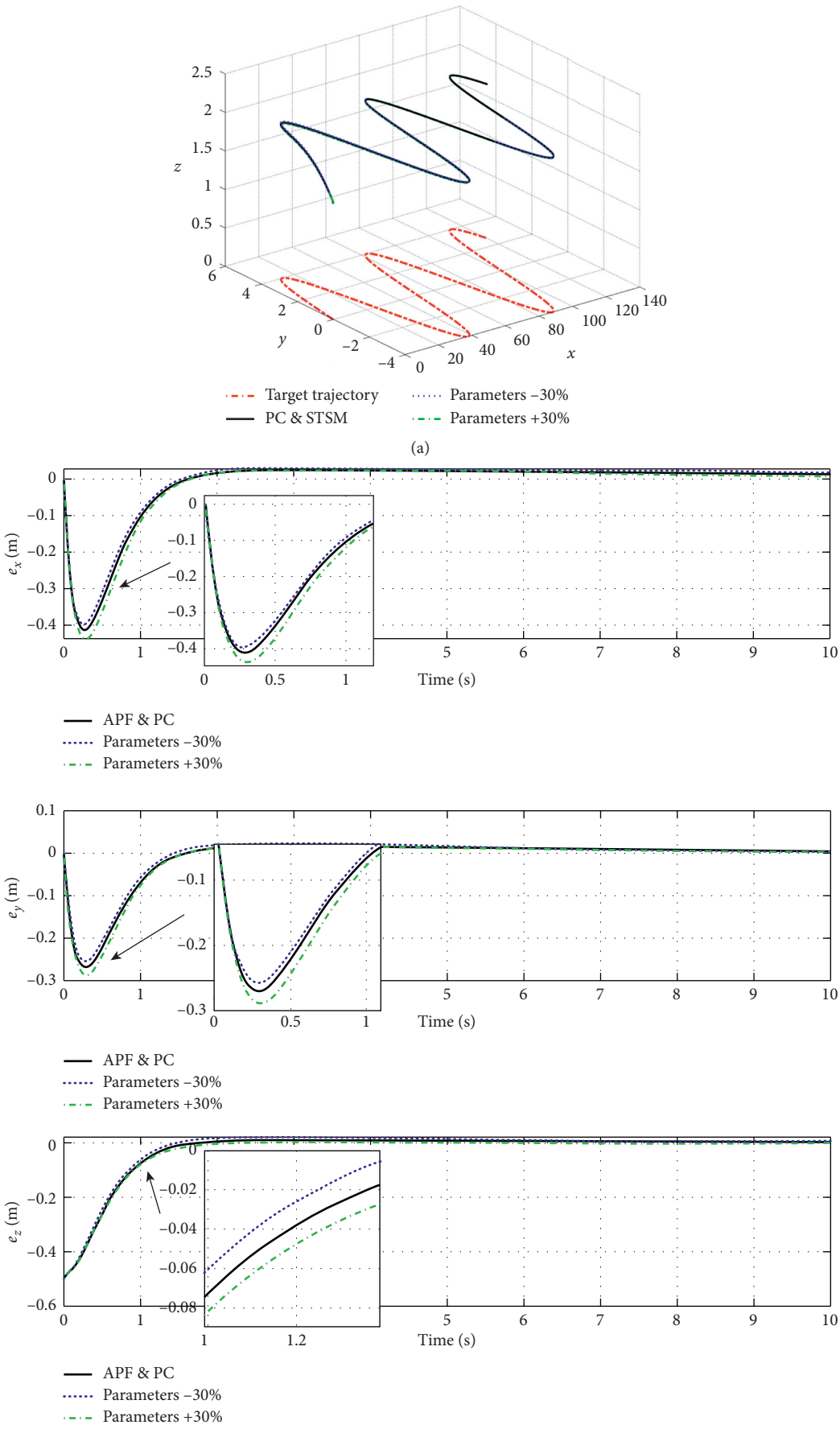

Figure 6: Continued.

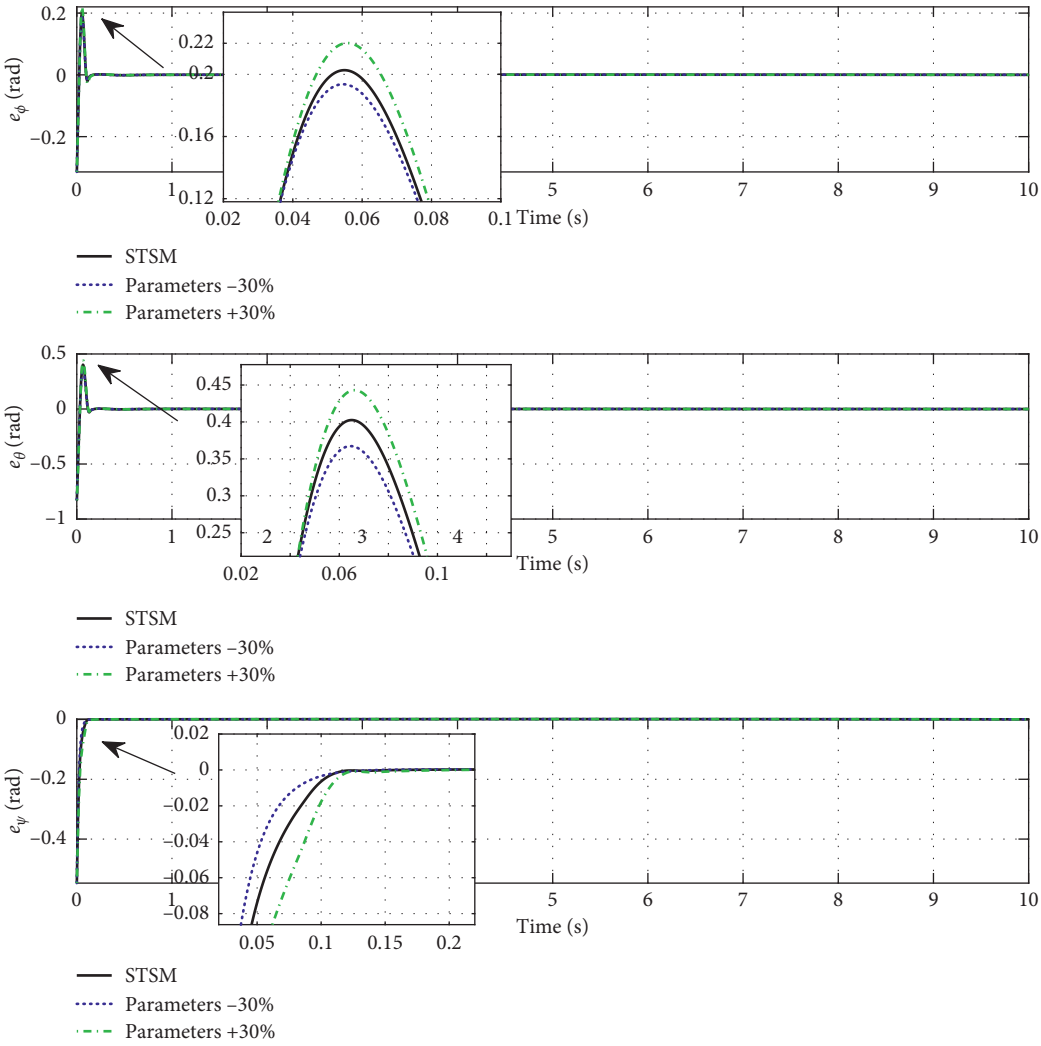

(c)

Figure 6: Target tracking with uncertainties and disturbances. (a) Trajectory tracking. (b) Position tracking error. (c) Attitude tracking error.

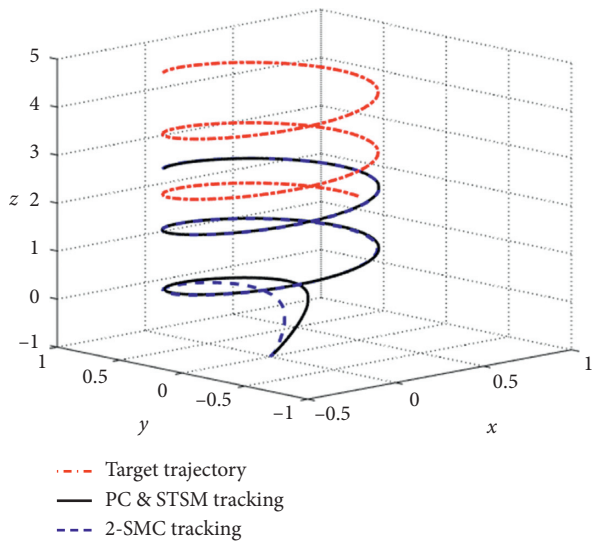

(a)

Figure 7: Continued.

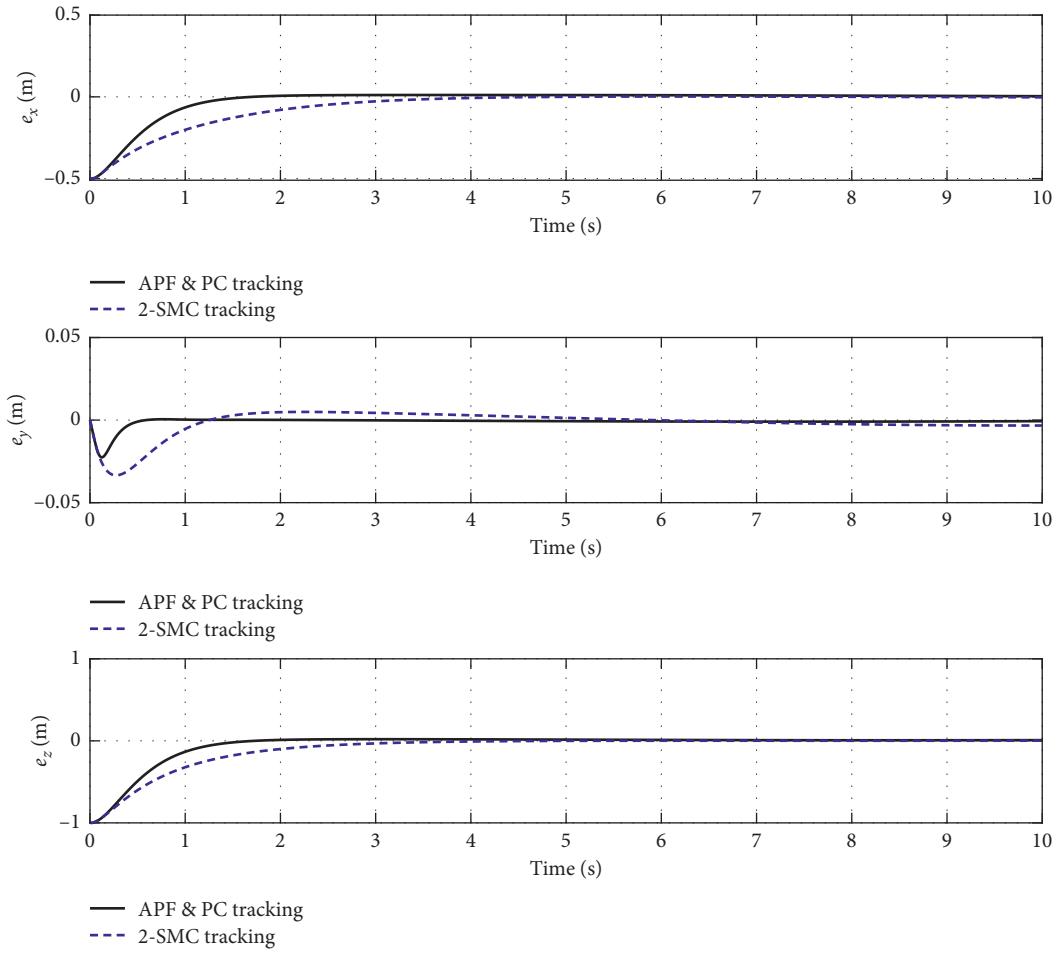

(b)

Figure 7: Continued.

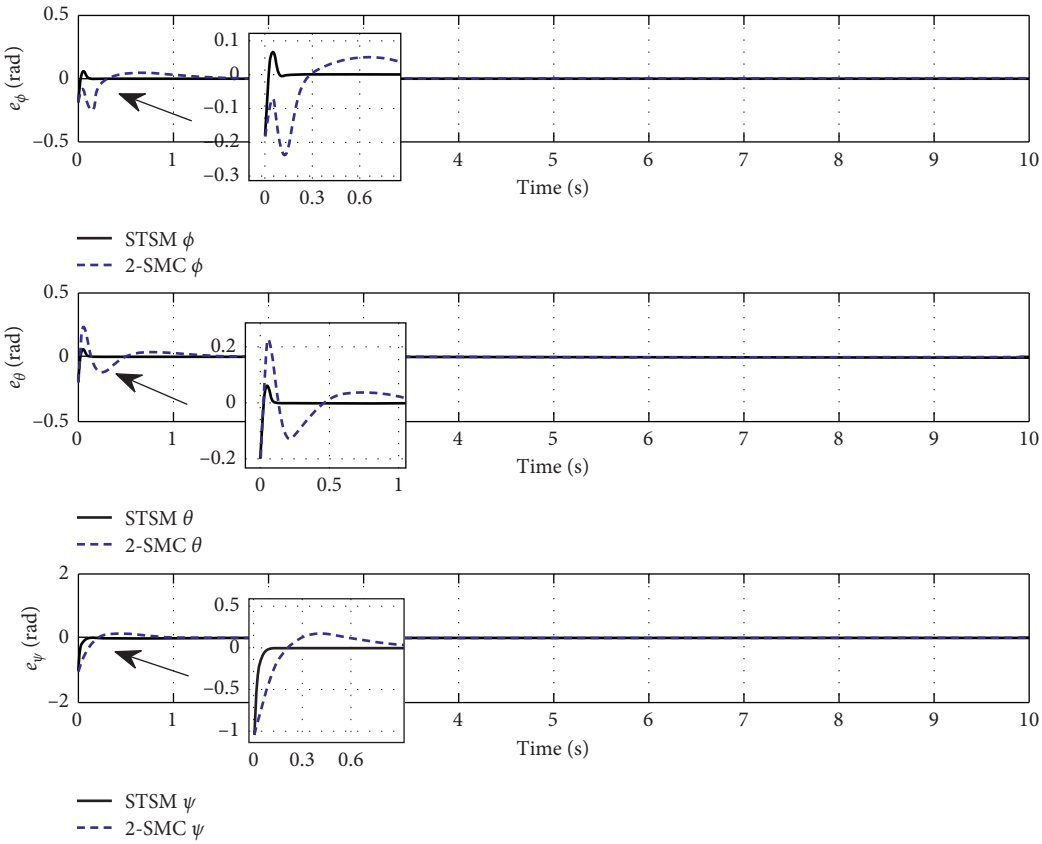

(c)

Figure 7: Aerial moving target tracking. (a) Trajectory tracking. (b) Position tracking error. (c) Attitude tracking error.

Table 3: Convergence time of tracking error.

Method	x (s)	y (s)	z (s)	ϕ (s)	θ (s)	ψ (s)
PC&STSM	1.6	1.4	1.6	0.35	0.35	0.25
2-SMC	3.6	4.2	3.8	1.5	1.4	1.2

Table 4: Overshoot of tracking error.

Method	x	y	z	ϕ	θ	ψ
PC&STSM	0	0	0	0.09	0.08	0
2-SMC	0	0.05	0	0.05	0.24	0.18

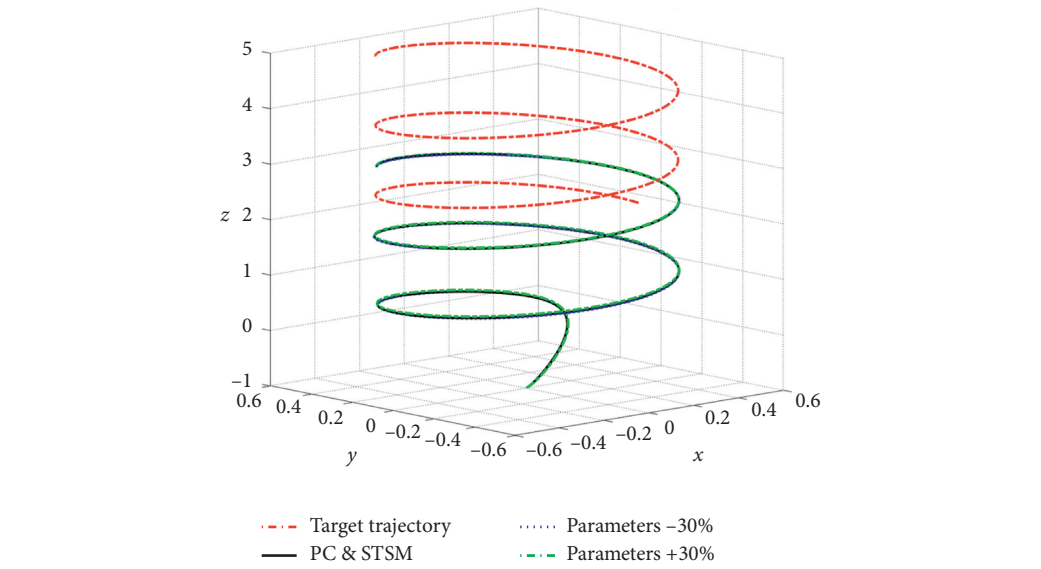

(a)

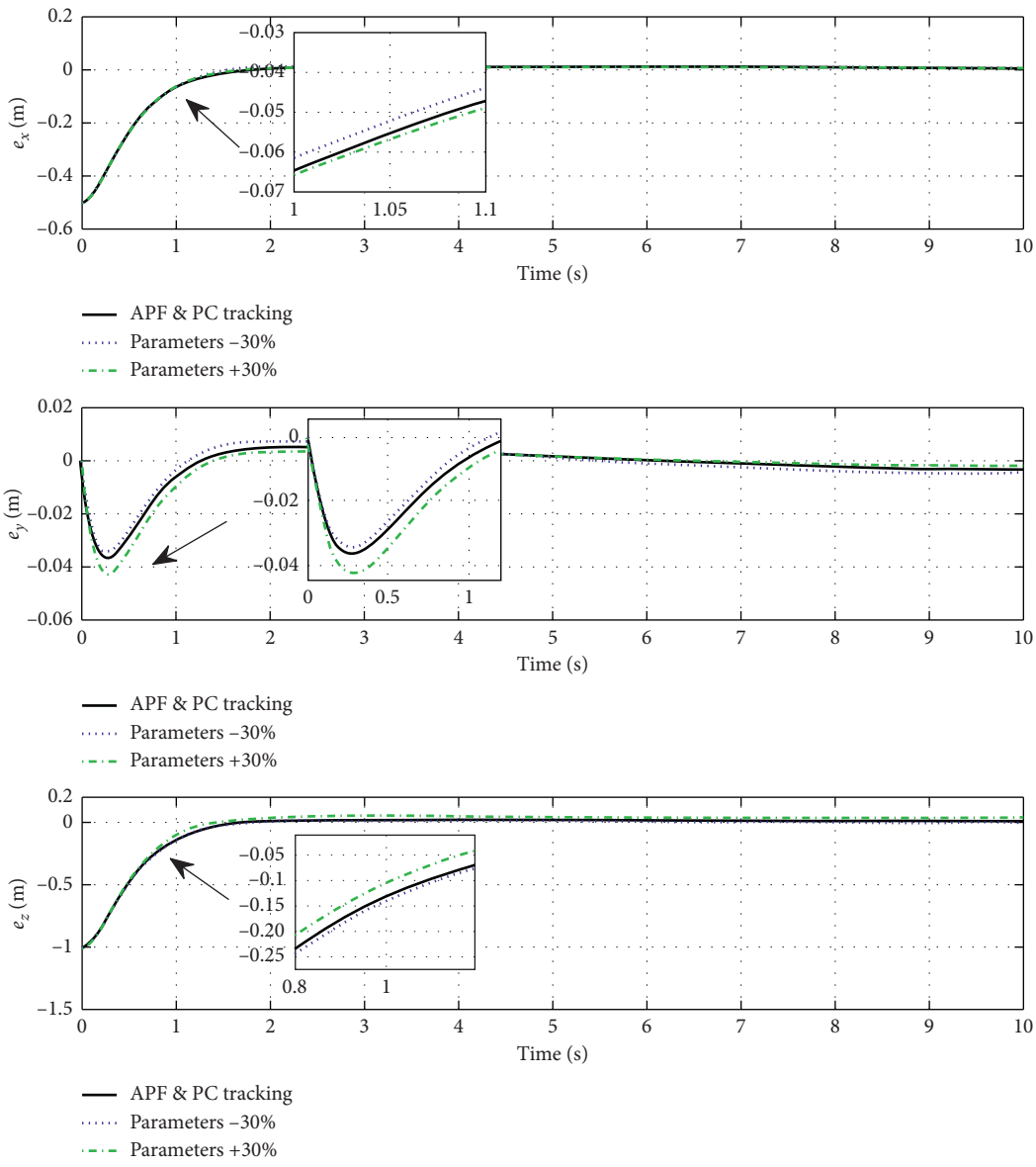

(b)

Figure 8: Continued.

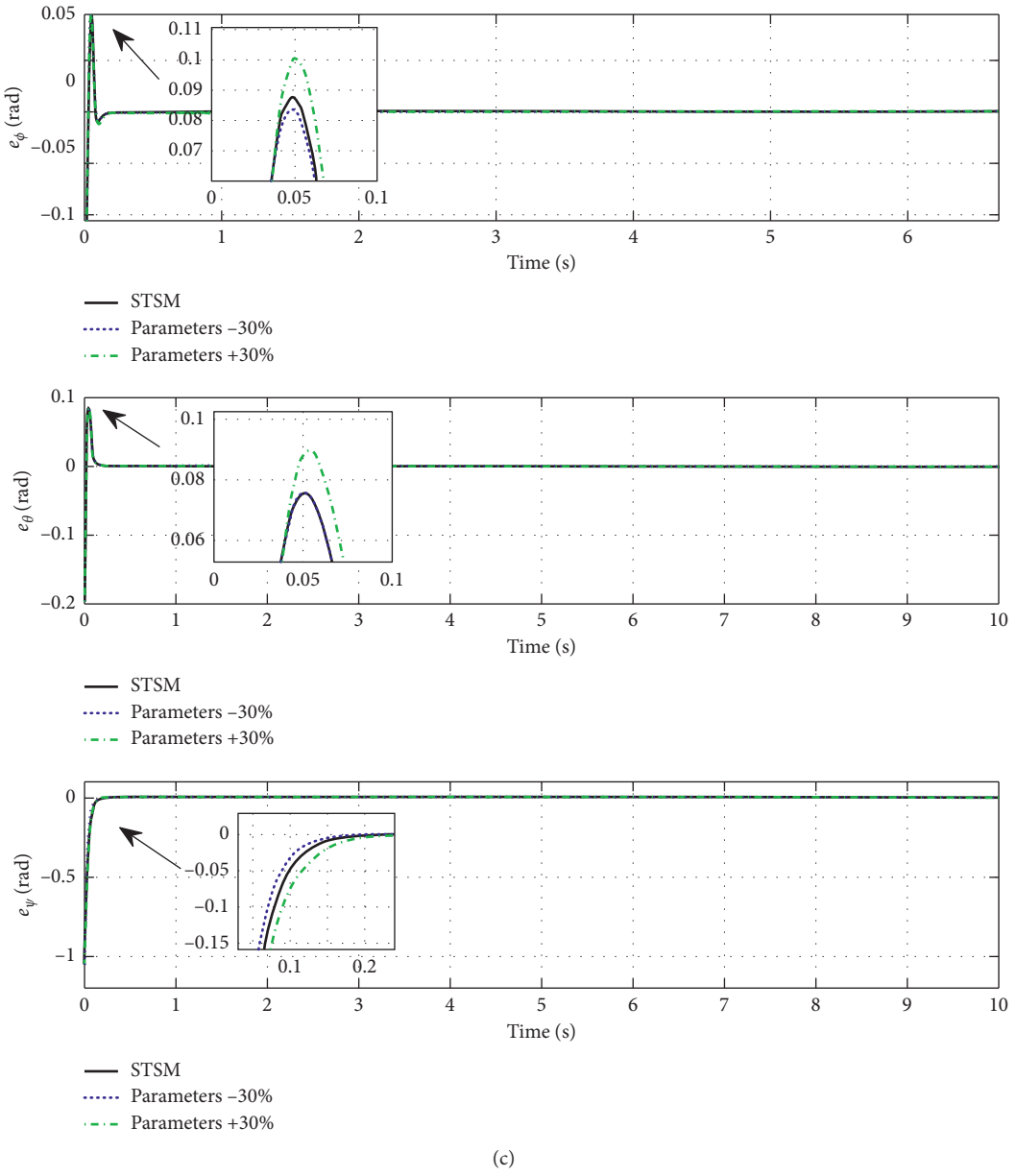

(c)

Figure 8: Target tracking with uncertainties and disturbances. (a) Trajectory tracking. (b) Position tracking error. (c) Attitude tracking error.

5. Conclusion

In this paper, we propose a composite control strategy based on passive control and super-twisting sliding mode control to solve the problem of moving target tracking of quadrotors considering model uncertainties and external disturbances. The control structure is composed of position and an attitude controller. For position control, the artificial potential field method is proposed by combining gravitational potential with repulsion potential to achieve the stable tracking of moving targets at a fixed distance. Meanwhile, the cascade passive control is designed to ensure the stability of the positioning system. Moreover, the super-twisting sliding mode controller with an improved reaching law is introduced to make the attitude angles quickly track the desired trajectory and overcome uncertainties and disturbances. Finally, the simulation results show that the proposed control system can achieve a better tracking performance and robustness compared with 2-SMC in moving target tracking.

Data Availability

No data were used to support this study.

Conflicts of Interest

The authors declare that they have no conflicts of interest.

Acknowledgments

This work was supported in part by the National Natural Science Foundation of China under Grant 61903163, Natural Science Foundation of the Jiangsu Higher Education Institutions of China under Grant 19KJB510023, and Marine Equipment and Technology Institute of JUST under Grant HZ20200007.

References

[1] B. Liu, W. Zhang, W. Chen, H. Huang, and S. Guo, "Online computation offloading and traffic routing for UAV swarms in edge-cloud computing," *IEEE Transactions on Vehicular Technology*, vol. 69, no. 8, pp. 8777–8791, 2020.

[2] S. S. Esfahlan, "Mixed reality and remote sensing application of unmanned aerial vehicle in fire and smoke detection," *Journal of Industrial Information Integration*, vol. 15, pp. 42–49, 2019.

[3] S. Yang, J. Han, L. Xia, and Y.-H. Chen, "Adaptive robust servo constraint tracking control for an underactuated quadrotor UAV with mismatched uncertainties," *ISA Transactions*, vol. 106, pp. 12–30, 2020.

[4] H. Ye, X. Yang, H. Shen, and R. Li, "Standoff tracking of a moving target for quadrotor using Lyapunov potential function," *International Journal of Control, Automation and Systems*, vol. 18, pp. 845–855, 2020.

[5] S. Mario, T. Andrea, E. Zenerino, and M. Chiaberge, "Multipurpose UAV for search and rescue operations in mountain avalanche events," *Geomatics, Natural Hazards and Risk*, vol. 8, pp. 18–33, 2017.

[6] O. Tekinalp, .A. K Ali, D. Kaya et al., "Propulsion system selection and modeling for a quadrotor with search and rescue mission," in *Proceedings of the 54th AIAA Aerospace Sciences Meeting*, San Diego, CA, USA, January 2016.

[7] S. Wang, F. Jiang, B. Zhang, R. Ma, and Q. Hao, "Development of UAV-based target tracking and recognition systems," *IEEE Transactions on Intelligent Transportation Systems*, vol. 21, no. 8, pp. 3409–3422, 2020.

[8] M. Rabah, A. Rohan, S. A. S. Mohamed, and S.-H. Kim, "Autonomous moving target-tracking for a UAV quadcopter based on fuzzy-PI," *IEEE Access*, vol. 7, pp. 38407–38419, 2019.

[9] O. Araar, N. Aouf, and I. Vitanov, "Vision based autonomous landing of multirotor UAV on moving platform," *Journal of Intelligent & Robotic Systems*, vol. 85, no. 2, pp. 369–384, 2017.

[10] X. Chen, W. Xue, H. Qiu, and H. Ye, "A moving target tracking control and obstacle avoidance of quadrotor UAV based on sliding mode control using artificial potential field and RBF neural networks," in *Proceedings of the 39th Chinese Control Conference*, Shenyang China, July 2020.

[11] M. C. Roger and L. T. Aguilar, "Robust PID control of quadrotors with power reduction analysis," *ISA Transactions*, vol. 98, pp. 47–62, 2020.

[12] Y. Zhang, Z. Chen, X. Zhang, Q. Sun, and M. Sun, "A novel control scheme for quadrotor UAV based upon active disturbance rejection control," *Aerospace Science and Technology*, vol. 79, pp. 601–609, 2018.

[13] L. Martins, C. Cardeira, and P. Oliveira, "Feedback linearization with zero dynamics stabilization for quadrotor control," *Journal of Intelligent & Robotic Systems*, vol. 101, no. 7, 2021.

[14] N. Koksal, H. An, and B. Fidan, "Backstepping-based adaptive control of a quadrotor UAV with guaranteed tracking performance," *ISA Transactions*, vol. 105, pp. 98–110, 2020.

[15] A. Eskandarpour and I. Sharf, "A constrained error-based MPC for path following of quadrotor with stability analysis," *Nonlinear Dynamics*, vol. 99, no. 2, pp. 899–918, 2020.

[16] S. Yang and B. Xian, "Energy-based nonlinear adaptive control design for the quadrotor UAV system with a suspended payload," *IEEE Transactions on Industrial Electronics*, vol. 67, no. 3, pp. 2054–2064, 2020.

[17] Y. Zou and Z. Meng, "Immersion and invariance-based adaptive controller for quadrotor systems," *IEEE Transactions on Systems, Man, and Cybernetics: Systems*, vol. 49, no. 11, pp. 2288–2297, 2019.

[18] X. Lin, J. Liu, Y. Yu, and C. Sun, "Event-triggered reinforcement learning control for the quadrotor UAV with actuator saturation," *Neurocomputing*, vol. 415, no. 11, pp. 135–145, 2020.

[19] J. M. Vazquez-Nicolas, E. Zamora, I. González-Hernández, R. Lozano, and H. Sossa, "PD+SMC quadrotor control for altitude and crack Recognition using deep learning," *International Journal of Control, Automation and Systems*, vol. 18, no. 5, pp. 834–844, 2020.

[20] S. Shao, M. Chen, J. Hou, and Q. Zhao, "Event-triggered-based discrete-time neural control for a quadrotor UAV using disturbance observer," *IEEE/ASME Transactions on Mechatronics*, vol. 26, no. 2, pp. 689–699, 2021.

[21] K. Mei, L. Ma, R. He, and S. Ding, "Finite-time controller design of multiple integrator nonlinear systems with input saturation," *Applied Mathematics and Computation*, vol. 372, Article ID 124986, 2020.

[22] L. Liu, W. X. Zheng, and S. Ding, "An adaptive SOSM controller design by using a sliding-mode-based filter and its application to buck converter," *IEEE Transactions on Circuits and Systems I: Regular Papers*, vol. 67, no. 7, pp. 2409–2418, 2020.

[23] S. Ding, W.-H. Chen, K. Mei, and D. J. Murray-Smith, "Disturbance observer design for nonlinear systems represented by input-output models," *IEEE Transactions on Industrial Electronics*, vol. 67, no. 2, pp. 1222–1232, 2020.

[24] F. Chen, R. Jiang, K. Zhang, B. Jiang, and G. Tao, "Robust backstepping sliding-mode control and observer-based fault estimation for a quadrotor UAV," *IEEE Transactions on Industrial Electronics*, vol. 63, no. 8, pp. 5044–5056, 2016.

[25] G. Xu, Y. Xia, D. H. Zhai, and D. Ma, "Adaptive prescribed performance terminal sliding mode attitude control for quadrotor under input saturation," *IET Control Theory & Applications*, vol. 14, no. 17, pp. 2473–2480, 2020.

[26] H. Castañeda, O. S. Salas-Peña, and J. D. León-Morales, "Extended observer based on adaptive second order sliding mode control for a fixed wing UAV," *ISA Transactions*, vol. 66, pp. 226–232, 2017.

[27] Y. Du, X. Zhang, and Z. Nie, "A real-time collision avoidance strategy in dynamic airspace based on dynamic artificial potential field algorithm," *IEEE Access*, vol. 7, pp. 169469–169479, 2019.

[28] Y.-B. Chen, G.-C. Luo, Y.-S. Mei, J.-Q. Yu, and X.-L. Su, "UAV path planning using artificial potential field method updated by optimal control theory," *International Journal of Systems Science*, vol. 47, no. 6, pp. 1407–1420, 2016.

[29] Q. Hu, H. Dong, Y. Zhang, and G. Ma, "Tracking control of spacecraft formation flying with collision avoidance," *Aerospace Science and Technology*, vol. 42, pp. 353–364, 2015.

[30] R. Ortega, A. van der Schaft, F. Castanos, and A. Astolfi, "Control by interconnection and standard passivity-based control of port-hamiltonian systems," *IEEE Transactions on Automatic Control*, vol. 53, no. 11, pp. 2527–2542, 2008.

[31] C. Ha, Z. Zuo, F. B. Choi, and D. Lee, "Passivity-based adaptive backstepping control of quadrotor-type UAVs," *Robotics and Autonomous Systems*, vol. 62, no. 9, pp. 1305–1315, 2014.

[32] G. R. Jose and R. Hugo, "Asymptotic stability for a transformed nonlinear UAV model with a suspended load via energy shaping," *European Journal of Control*, vol. 52, pp. 87–96, 2020.

[33] G. V. Raffo, M. G. Ortega, and F. R. Rubio, "An integral predictive/nonlinear H∞ control structure for a quadrotor helicopter," *Automatica*, vol. 46, no. 1, pp. 29–39, 2010.

[34] A. Das, F. Lewis, and K. Subbarao, "Backstepping approach for controlling a quadrotor using Lagrange form dynamics," *Journal of Intelligent and Robotic Systems*, vol. 56, no. 1-2, pp. 127–151, 2009.

[35] N. Bu, M. Deng, and M. Deng, "Passivity-based tracking control for uncertain nonlinear feedback systems," *Journal of Robotics and Mechatronics*, vol. 28, no. 6, pp. 837–841, 2016.

[36] E.-H. Zheng, J.-J. Xiong, and J.-L. Luo, "Second order sliding mode control for a quadrotor UAV," *ISA Transactions*, vol. 53, no. 4, pp. 1350–1356, 2014.

Hindawi
Mathematical Problems in Engineering
Volume 2021, Article ID 6682160, 14 pages
https://doi.org/10.1155/2021/6682160

Research Article

Design of Standoff Cooperative Target-Tracking Guidance Laws for Autonomous Unmanned Aerial Vehicles

Zhen Li, Xin Chen, and Zhenhua Zhao

College of Automation Engineering, Nanjing University of Aeronautics and Astronautics, Nanjing 211106, China

Correspondence should be addressed to Zhen Li; lizhenbx1503025@nuaa.edu.cn

Received 4 December 2020; Revised 20 March 2021; Accepted 17 April 2021; Published 3 May 2021

Academic Editor: Haibo Du

This paper investigates two guidance laws of standoff cooperative tracking static and moving of multiple autonomous unmanned aerial vehicles for targets from the perspective of the control system design. In the scheme of the proposed guidance laws, one vehicle is chosen as leader and others as followers. The leader only needs the measurement of the target, and the followers only measure the leader and its neighbors in the communication topology network. By using the proposed guidance laws, it is guaranteed that all vehicles can track a static or moving target with an evenly spaced formation of circle. Considering the coupling of tracking and cooperation, the stability analysis is performed by constructing two relatively independent subsystems based on Lyapunov theory, and the corresponding rigorous proofs of stability are given. By comparing with the Lyapunov vector field guidance law, the simulation results verify the effectiveness and superiority of the proposed guidance laws.

1. Introduction

In the past few decades, due to the rapid development of science and technology, the use of unmanned aerial vehicles (UAVs) is from surveillance and reconnaissance to rescue and communication relay [1–3], and its application fields have been greatly expanded. At present, one of the most important applications of UAVs is the use of tracking ground targets; through the UAV guidance system, the target can be always in the field of view, so as to achieve real-time tracking purpose of ground targets [4–6]. Compared with single UAV, multi-UAV cooperative tracking can increase the coverage of the sensor on the ground target and reduce the target state estimation error, and it has a wider range of application prospects [7, 8].

Unlike rotary-wing UAV, fixed-wing UAV must maintain a minimum velocity to produce enough lift. A typical way to accomplish a tracking mission is standoff tracking which means to monitor the ground target by orbiting around it at the desired distance; this tracking mode is called standoff tracking [9, 10]. The guidance problem in cooperative standoff tracking can be divided into two aspects: relative distance control and inter-UAV angle control, which are realized by the lateral and longitudinal guidance law, respectively.

Lawrence proposed a guidance law based on the Lyapunov vector field guidance (LVFG) method [11]. In the study by Frew et al. [12], it is assumed that the target is moving at a constant velocity, and the LVFG has been proposed to improve the guidance accuracy of the relative distance; then, another Lyapunov function is used to solve the flight velocity command as the longitudinal guidance law of the UAV to control the inter-UAV angle. A weighted relative distance and inter-UAV angle error are used as the objective function, and the horizontal and vertical guidance commands for the next optimization step are searched by the method of model predictive control (MPC) [13]. This method not only needs a lot of calculation time but also still has some difficulties to achieve online applications. A cyclic pursuit for coordinated target tracking applications based on sliding mode control and a virtual leader is presented, but the guidance law is too complicated to achieve in practical projects [14]. A variant cycle of standoff tracking applications has also been investigated, while only fixed and uniform moving targets were considered for this method [15]. Cheng proposed a composite impact time control

guidance law considering the problem of simultaneous attack against a ground target [16]. It is also necessary to consider the effect of disturbances, so the robust leader-follower formation guidance laws are derived [17–19].

From the above previous work, we can conclude that the existing research results only study the static target instead of the moving target which limits the practical application of the guidance laws. To the best of the author's knowledge, few research results can consider both scenarios in a unified control framework. The developed results in this paper not only realize the objective of the tracking static target but also can track the moving target in a unified analytical control framework. In this paper, a new leader-follower formation tracking mode is proposed, which is based on the principle that a leader UAV is used to track a ground target in the standoff mode. Besides, when multiple follower UAVs track the leader UAV and are evenly distributed in a circle, the leader UAV and follower UAVs adopt the same tracking distance. As a result, the leader UAV maintains a certain distance from the ground target to avoid being exposed, and the follower UAVs can be closer to monitoring the ground target. The novelty of this paper lays in extending the practical application of standoff cooperative tracking of multi-UAVs not only for static targets but also for moving targets.

This paper is organized as follows. Section 1 describes the mathematical model of a ground target tracking problem. Section 2 provides the new guidance law of the leader UAV and mathematical stability proof. Section 3 provides the new guidance law of the follower UAVs and mathematical stability proof. The results of simulation are discussed in Section 4. The paper ends with some conclusions.

2. Problem Formulation

In order to develop guidance laws for the fixed-wing UAV that tracks a ground target, some assumptions have been stated. Firstly, the UAV is considered at a constant velocity and altitude over the ground. Furthermore, a separate inner loop (stabilization loop) and an outer loop (guidance loop) control approach are designed, similarly as in most applications [20–23].

In Figure 1, let ρ denote the range between the UAV and the target, $\rho \geq 0$ and ρ is bounded. The bearing angle $\chi \in [0, 2\pi)$ is defined as the angle between the UAV forward direction and the direction from the UAV to the target, which is measured counterclockwise. ρ_d denotes the desired radius, and v is the velocity of the UAV.

The system dynamics can be described by the following kinematical model:

$$\begin{cases} \dot{x} = v\cos(\psi), \\ \dot{y} = v\sin(\psi), \\ \dot{\psi} = \omega, \\ \dot{v} = u, \end{cases} \tag{1}$$

where $[x, y]^T$ is the 2D location of the UAV, ψ denotes the heading angle, ω and u are the angular rate and acceleration as the control inputs, respectively, and $[x_t, y_t]^T$ denotes the 2D location of the target; then, the range $\rho = \sqrt{(x - x_t)^2 + (y - y_t)^2}$. The objective is to design control input ω and $u$such that $\rho \longrightarrow \rho_d$ as $t \longrightarrow \infty$.

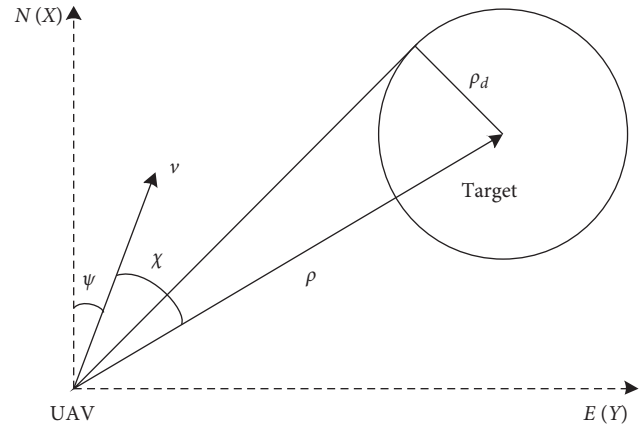

Figure 1: Geometry of tracking a stationary target.

The dynamics (1) can be rewritten as

$$\begin{cases} \dot{\rho} = -v\cos(\chi), \\ \dot{\chi} = \omega + \dfrac{v\sin(\chi)}{\rho}, \\ \dot{v} = u. \end{cases} \tag{2}$$

In dynamics (2), the state variables are changed from $[x, y, \psi]^T$ to $[\rho, \chi, v]^T$. Furthermore, it can be seen that if the velocity of the UAV is constant, $\dot{\rho}$and χ can be determined by eachother. When $\dot{\rho} = 0$, $\chi = (\pi/2)$ or $(3\pi/2)$, which represents the clockwise motion and counterclockwise motion of the UAV, respectively.

3. Leader UAV Guidance Law Design

Firstly, a guidance law of the leader UAV to track a static target is designed, and then, the guidance law is expanded to track a moving target.

3.1. Static Ground Target Tracking. In this paper, the guidance law for the leader UAV tracking a static ground target in the standoff mode is designed as

$$\begin{cases} \omega = kv\cos\chi - \dfrac{v\sin\chi}{\rho} - v(\rho - \rho_d), \\ u = 0. \end{cases} \tag{3}$$

Then, we give the following conclusion.

Theorem 1. *Consider UAV dynamics in (2) subject to the guidance law in (3). If $k > 0$, $(\rho_d, \pi/2)^T$ is the asymptotically stable equilibrium point of the closed-loop system.*

Proof. consider the following candidate Lyapunov function:

$$L_1 = 1 - \sin\chi + \frac{1}{2}(\rho - \rho_d)^2. \tag{4}$$

It can be verified that $L_1 \geq 0$, and $L_1 = 0$ only at $(\rho_d, \pi/2)^T$.

Taking the derivative of L_1 yields that

$$\dot{L}_1 = -\cos\chi \cdot \dot{\chi} + (\rho - \rho_d) \cdot \dot{\rho}. \tag{5}$$

With (2), we have

$$\dot{L}_1 = v\cos\chi \cdot \left(-\frac{\omega}{v} - \frac{\sin\chi}{\rho} - \rho + \rho_d\right). \tag{6}$$

Substituting ω into $\dot{L}_1$, we have

$$\dot{L}_1 = -kv\cos^2\chi. \tag{7}$$

Obviously, when $k > 0$, for any χ, there is $\dot{L}_1 \leq 0$, and it can be concluded that $\dot{L}_1 = 0$ if and only if $\chi = (\pi/2)$. Let $S = \left\{[\rho, \chi]^T \in R \times R | \chi = (\pi/2)\right\}$; when $L_1 = 0$, we can obtain that $\rho = \rho_d$, and no other solution can stay identically in S other than $(\rho_d, \pi/2)^T$. According to LaSalle's invariance principle (Khalil, 2002), $(\rho_d, \pi/2)^T$ is the asymptotically stable equilibrium point of the closed-loop system. □

Remark. this Lyapunov function is well designed as its equilibrium point is $\chi = (\pi/2)$, $\rho = \rho_d$. By designing appropriate guidance laws, we can make $\dot{L}_1 \leq 0$ till $L_1 = 0$, and the control objective can be realized.

3.2. Constant Velocity Ground Target Tracking. When the ground target moves at velocity v_t, the UAV kinematics' model can be written as

$$\begin{cases} \dot{\rho} = -v\cos\chi + v_t\cos(\psi - \psi_t + \chi), \\ \dot{\chi} = \omega + \dfrac{1}{\rho}(v\sin\chi - v_t\sin(\psi - \psi_t + \chi)), \\ \dot{v} = u, \end{cases} \tag{8}$$

where the velocity vector of the UAV can be decomposed into relative velocity, and the target velocity vector (depicted in Figure 2)

$$\vec{v} = \vec{v}_m + \vec{v}_t, \tag{9}$$

where $\vec{v}_m$ is the relative velocity vector. Then, the dynamics in (8) can be rewritten as the relative motion:

$$\begin{cases} \dot{\rho} = -v_m\cos\chi_m, \\ \dot{\chi}_m = \omega_m + \dfrac{1}{\rho}v_m\sin\chi_m, \\ \dot{v}_m = u_m. \end{cases} \tag{10}$$

Velocity vector v_t is constant when the target is in uniformly moving motion. Let $\vec{n}_m$ be the unit tangent vector of $\vec{v}_m$ and $\vec{\omega}$ be the angular velocity vector corresponding to $\vec{v}$; taking the derivative of (9) yields that

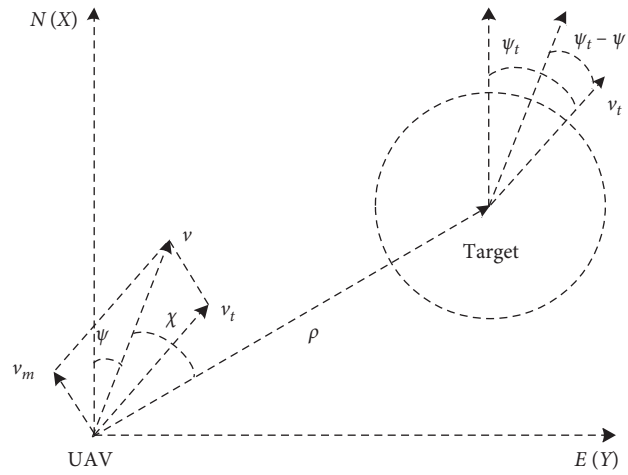

Figure 2: Geometry of tracking a moving target.

$$\vec{\omega} \times \vec{v} = \dot{v}_m \vec{n}_m + \vec{\omega}_m \times \vec{v}_m. \tag{11}$$

The symbol "×" denotes the cross product of vectors. Take the norm of both sides because $\dot{v}_m = (\vec{\omega} \times \vec{v}) \cdot \vec{n}_m$; thus, we can obtain that

$$|\vec{\omega} \times \vec{v}|^2 = \left|(\vec{\omega} \times \vec{v}) \cdot \vec{n}_m\right|^2 + \left|\vec{\omega}_m \times \vec{v}_m\right|^2. \tag{12}$$

Then, we get

$$\begin{aligned} \omega^2 v^2 &= \omega^2 v^2 \sin^2(\psi - \psi_m) + \omega_m^2 v_m^2, \\ \omega_m^2 v_m^4 &= \omega^2\left[v^2 v_m^2 - \left|\vec{v} \times \vec{v}_m\right|^2\right]. \end{aligned} \tag{13}$$

According to the parallelogram law of the vector, the area of the two triangles which are constituted by $\vec{v}$ and $\vec{v}_t$ and $\vec{v}$ and $\vec{v}_m$, respectively, are equal, that is,

$$\left|\vec{v} \times \vec{v}_t\right| = \left|\vec{v} \times \vec{v}_m\right|. \tag{14}$$

Then, we can obtain that

$$\omega_m^2 v_m^4 = \omega^2\left[v^2 v_m^2 - \left|\vec{v} \times \vec{v}_t\right|^2\right]. \tag{15}$$

We have

$$\omega_m = \frac{v\sqrt{v_m^2 - v_t^2\sin(\psi_t - \psi)}}{v_m^2}\omega. \tag{16}$$

Finally, we can obtain the guidance law for tracking the constant velocity ground target:

$$\begin{cases} \omega = \dfrac{v_m^2\left[kv_m\cos\chi_m - (v_m\sin\chi_m/\rho) - v_m(\rho - \rho_d)\right]}{v\sqrt{v_m^2 - v_t^2\sin^2(\psi_t - \psi)}}, \\ u = 0, \end{cases} \tag{17}$$

and the corresponding closed-loop system can be written as

$$\begin{cases} \dot{\rho} = -v_m \cos\chi_m, \\ \dot{\chi} = \dfrac{v_m^2\left[kv_m\cos\chi_m - (v_m\sin\chi_m/\rho) - v_m(\rho-\rho_d)\right]}{v\sqrt{v_m^2 - v_t^2\sin^2(\psi_t-\psi)}} + \dfrac{1}{\rho}v_m\sin\chi_m, \\ \dot{v} = 0. \end{cases} \tag{18}$$

Then, we give the following conclusion.

Theorem 2. *Consider UAV dynamics in (8) subject to the guidance law in (17). If* $k>0$, $(\rho_d, (\pi/2))^T$ *is the asymptotically stable equilibrium* point of the closed-loop system in (18).

Proof. consider the following candidate Lyapunov function:

$$L_2 = 1 - \sin\chi_m + \frac{1}{2}(\rho-\rho_d)^2. \tag{19}$$

Taking the derivative of L_2 yields that

$$\dot{L}_1 = -\cos\chi_m \cdot \dot{\chi}_m + (\rho-\rho_d)\cdot\dot{\rho}. \tag{20}$$

Substitute (10) and (17) into $\dot{L}_2$, then

$$\dot{L}_2 = -kv\cos^2\chi_m. \tag{21}$$

It can be seen that if $k>0$, $\dot{L}_2 \le 0$ always exit and $\dot{L}_2 = 0$ only if $\chi_m(t) = (\pi/2)$. χ_m and $\rho(t)$ are both bounded and $\dot{L}_2(t)$ is also bounded according to Barbalat's lemma [20], when $\dot{L}_2(t) \longrightarrow 0$, $\chi_m(t) \longrightarrow (\pi/2)$. Furthermore, because $\ddot{\chi}_m(t)$ is bounded, still according to Barbalat's lemma, we can conclude that when $\chi_m(t) \longrightarrow 0$, $\rho(t) \longrightarrow \rho_d$, and $(\rho_d, \pi/2)^T$ is the asymptotically stable equilibrium point of the closed-loop system. □

3.3. Variable Velocity Ground Target. When the ground target moves at variable velocity v_t, then v and v_m both are also variable, and equation (9) can be rewritten in the following scalar form:

$$\begin{cases} v\cos\psi = v_m\cos\psi_m + v_t\cos\psi_t, \\ v\sin\psi = v_m\sin\psi_m + v_t\sin\psi_t. \end{cases} \tag{22}$$

Taking the derivative of both sides' yields, one can have

$$\begin{cases} \dot{v}\cos\psi + v\dot{\psi}\cos\psi = \dot{v}_m\cos\psi_m + v_m\dot{\psi}_m\cos\psi_m \\ +\dot{v}_t\cos\psi_t + v_t\dot{\psi}_t\cos\psi_t, \\ \dot{v}\sin\psi + v\dot{\psi}\sin\psi = \dot{v}_m\sin\psi_m + v_m\dot{\psi}_m\sin\psi_m \\ +\dot{v}_t\sin\psi_t + v_t\dot{\psi}_t\sin\psi_t. \end{cases} \tag{23}$$

Solving the quadratic equation and eliminating $\dot{v}_m$, we can obtain the guidance law for tracking the variable velocity ground target:

$$\begin{cases} \omega = \dfrac{1}{v\cos(\psi-\psi_m)}\left(v_m\omega_m + v_t\omega_t\cos(\psi_t-\psi_m)\right), \\ u = \dot{v}_t\dfrac{\sin(\psi_t-\psi_m)}{\sin(\psi-\psi_m)}, \end{cases} \tag{24}$$

where

$$\omega_m = kv_m\cos\chi_m - \frac{v_m\sin\chi_m}{\rho} - v_m(\rho-\rho_d). \tag{25}$$

The corresponding closed-loop system can be written as

$$\begin{cases} \dot{\rho} = -v_m\cos\chi_m, \\ \dot{\chi} = \dfrac{1}{v\cos(\psi-\psi_m)}\left(v_m\omega_m + v_t\omega_t\cos(\psi_t-\psi_m)\right) + \dfrac{1}{\rho}v_m\sin\chi_m, \\ \dot{v} = \dot{v}_t\dfrac{\sin(\psi_t-\psi_m)}{\sin(\psi-\psi_m)}. \end{cases} \tag{26}$$

We can see that equations (26) and (18) are the same, thus still satisfy Theorem 2 for the variable velocity ground target.

4. Follower UAV Guidance Law Design

Consider N follower UAVs in the formation problem, the ith ($i = 1, 2, ..., N$) UAV's Dubins model can be obtained as follows:

$$\begin{cases} \dot{x}_i = v_i\cos(\psi_i) \\ \dot{y}_i = v_i\sin(\psi_i) \\ \dot{\psi}_i = \omega_i \\ \dot{v}_i = u_i \end{cases}, \quad (i = 1, 2, \ldots, N). \tag{27}$$

The geometry between the follower UAVs and the leader UAV is depicted in Figure 3.

In this paper, the follower UAVs are required to maintain a circular formation with the centre at the leader UAV and hold equal angular separation. Meanwhile, the follower UAV's velocity and heading angle should gradually converge to the leader UAV's. The relative motion can be written as

$$\begin{cases} \dot{\rho}_i = v_i\cos(\theta_i-\psi_i) - v_0\cos(\theta_i-\psi_0), \\ \dot{\theta}_i = \dfrac{-v_i\sin(\theta_i-\psi_i) + v_0\sin(\theta_i-\psi_0)}{\rho_i}, \end{cases} \tag{28}$$

where the subscript '0' denotes the leader UAV.

The follower UAV's angular rate control is used to carry out distance and heading angle tracking for the leader UAV, while formation's inter-UAV angle control and velocity tracking are performed by velocity control. We use such a

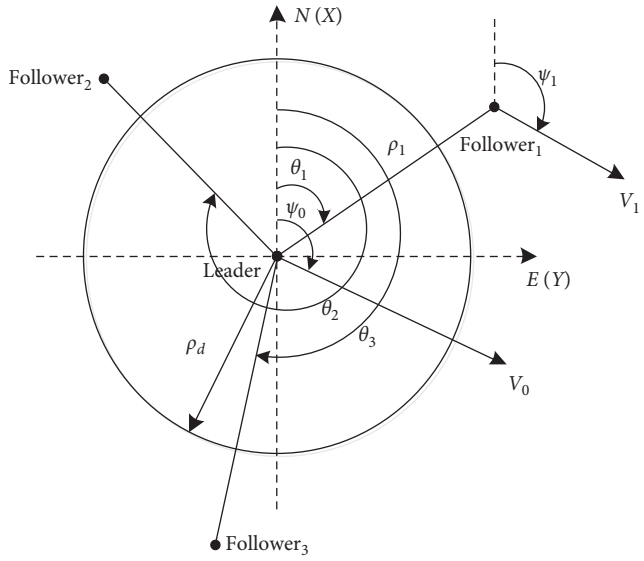

Figure 3: Geometry of follower UAVs to track the leader UAV.

communication topology, that is, the follower UAVs can perceive the state of the leader UAV, and a circular communication structure is implemented among the follower UAVs.

4.1. Angular Rate Guidance Law Design. In this paper, the following angular rate guidance law is designed for the ith follower UAV:

$$\omega_i = \dot{\psi}_0 - \frac{(\rho_i - \rho_d)}{(\psi_i - \psi_0)}\dot{\rho}_i - k_\omega(\psi_i - \psi_0). \tag{29}$$

Then, we give the following conclusion.

Theorem 3. *Consider the UAV formation dynamics in (28) subject to the guidance law in (29). If $k_\omega > 0$, the distance between the follower UAV and the leader UAV will gradually converge to ρ_d, and the heading angle of the follower UAV will also gradually converge to the heading angle of the leader UAV.*

Proof. consider the following candidate Lyapunov function:

$$L_\omega = \frac{1}{2}\sum_{i=1}^{N}\left[(\rho_i - \rho_d)^2 + (\psi_i - \psi_0)^2\right]. \tag{30}$$

Taking the derivative yields that

$$\dot{L}_\omega = \sum_{i=1}^{N}\left[(\rho_i - \rho_d)\cdot\dot{\rho}_i + (\psi_i - \psi_0)\cdot(\dot{\psi}_i - \dot{\psi}_0)\right], \tag{31}$$

where $\dot{\psi}_i = \omega_i$, and

$$\omega_i = \dot{\psi}_0 - \frac{(\rho_i - \rho_d)}{(\psi_i - \psi_0)}\cdot\dot{\rho}_i - k_\omega\cdot(\psi_i - \psi_0), \tag{32}$$

and we get

$$\dot{L}_\omega = \sum_{i=1}^{N}\left(-k_\omega\cdot(\psi_i - \psi_0)^2\right) \le 0. \tag{33}$$

So $\psi_i - \psi_0$ is bounded, as $\dot{L}_\omega$ is uniformly continuous, and $(\psi_i - \psi_0) \longrightarrow 0$ according to Barbalat's lemma. Furthermore, as $\dot{\psi}_i - \dot{\psi}_0$ is uniformly continuous, we have $(\dot{\psi}_i - \dot{\psi}_0) \longrightarrow 0$ according to Barbalat's lemma; then, we can conclude that $\rho_i \longrightarrow \rho_d$. □

4.2. Velocity Guidance Law Design. In this paper, the following velocity guidance law is designed for the ith follower UAV:

$$u_i = \dot{v}_0 - \frac{(\Delta\theta - (2\pi/N))}{(v_i - v_0)}\Delta\dot{\theta} - k_v(v_i - v_0). \tag{34}$$

Then, we give the following conclusion.

Remark. it is easy to find that the Lyapunov function L_ω is bounded, so we can conclude that $(\psi_i - \psi_0) \longrightarrow 0$ and $(\rho_i - \rho_d) \longrightarrow 0$ simultaneously according to Barbalat's lemma. In practice, even if $(\psi_i - \psi_0) = 0$, it is not an attractor which does not affect the convergence of the whole guidance system. It is the same for the case of $(v_i - v_0) \longrightarrow 0$. Hence, we can conclude that there exists no problem of singular values.

Theorem 4. *Consider the UAV formation dynamics in (28) subject to the guidance law in (34); if $k_v > 0$, the inter-UAV angle between follower UAVs will gradually converge to $(2\pi/N)$, and the velocity of the ith follower UAV will gradually converge to the velocity of the leader UAV.*

Proof. consider the following candidate Lyapunov function:

$$L_u = \frac{1}{2}\sum_{i=1}^{N}\left[\left(\Delta\theta_i - \frac{2\pi}{N}\right)^2 + (v_i - v_0)^2\right]. \tag{35}$$

Taking the derivative yields that

$$\dot{L}_u = \sum_{i=1}^{N}\left[\left(\Delta\theta_i - \frac{2\pi}{N}\right)\cdot\Delta\dot{\theta}_i + (v_i - v_0)\cdot(\dot{v}_i - \dot{v}_0)\right], \tag{36}$$

where $\dot{v}_i = u_i$, and

$$u_i = \dot{v}_0 - \frac{(\Delta\theta_i - (2\pi/N))}{(v_i - v_0)}\Delta\dot{\theta}_i - k_v(v_i - v_0), \tag{37}$$

and we get

$$\dot{L}_u = \sum_{i=1}^{N}\left(-k_v\cdot(v_i - v_0)^2\right) \le 0. \tag{38}$$

Similar with Theorem 3, we can also conclude that $\Delta\theta_i \longrightarrow (2\pi/N)$ and $v_i \longrightarrow v_0$. □

5. Simulation Results

In this section, some simulation results are presented in order to demonstrate the effectiveness of the proposed

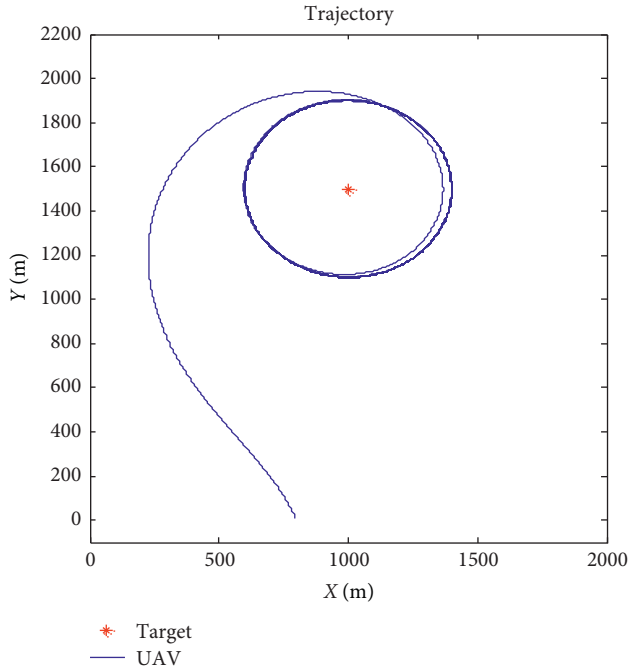

Figure 4: Trajectory of tracking a static target.

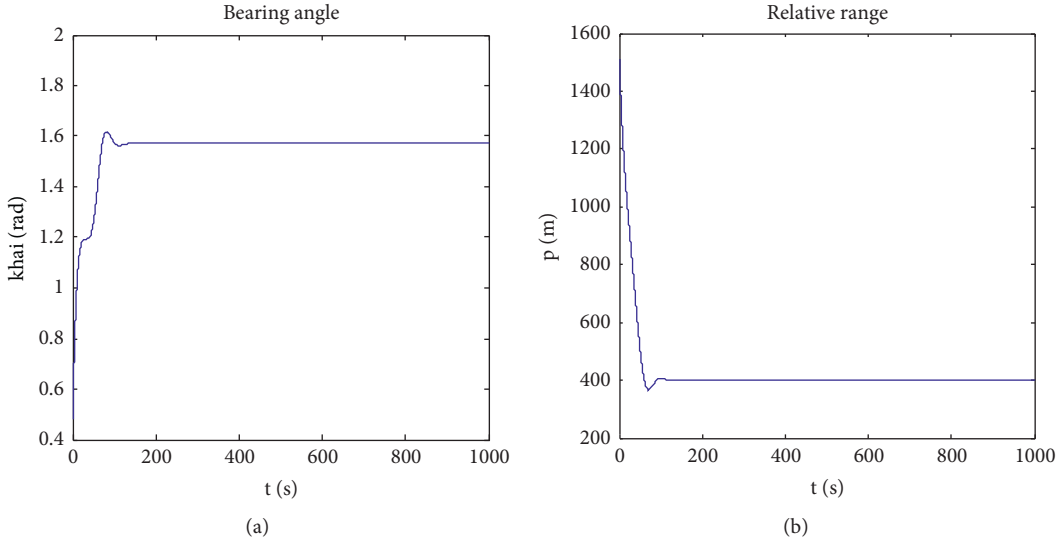

Figure 5: Bearing angle and relative range of tracking a static target. (a) Bearing angle. (b) Relative range.

leader-follower formation guidance laws. In these simulation cases, we consider a 4-UAVs' formation as an example, UAV #0 is the leader UAV and UAV #1–UAV #3 are the follower UAVs. The ground target motion is considered as stationary, linear with constant velocity, and linear with variable velocity.

Firstly, the simulation applies the leader UAV to track a ground target and then the UAV formation to track the ground target in the same way.

5.1. Track a Ground Target Using One UAV. The initial states of the UAV are set as follows:

(i) Position coordinate: (800, 0)

(ii) Heading angle: -60°

(iii) Cruising velocity: 45 m/s

(iv) Maximum heading angular rate: 0.1 rad/s

The initial states of the ground target are set as follows:

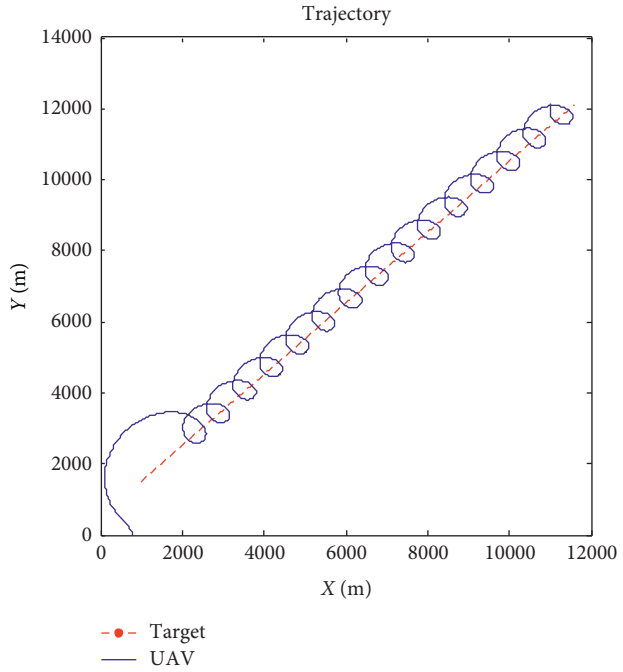

Figure 6: Trajectory of tracking a constant velocity target.

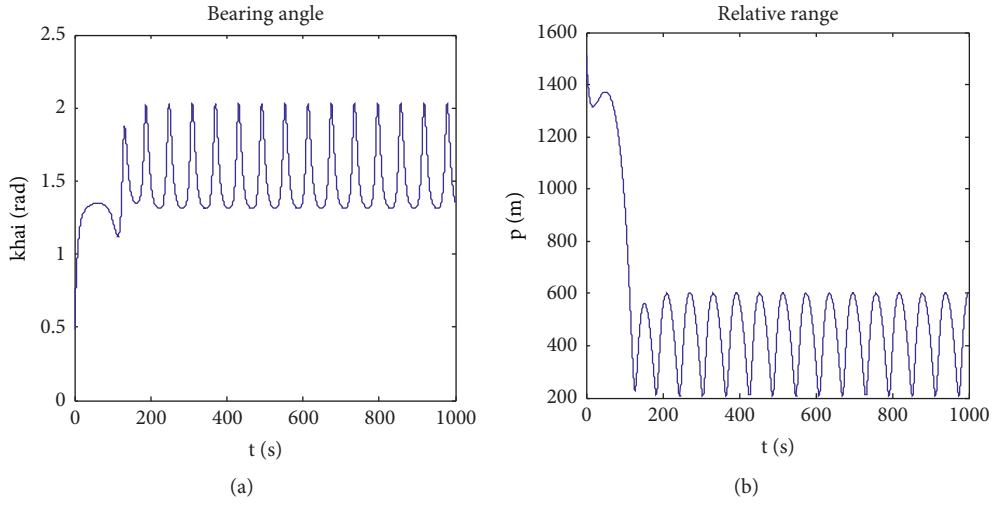

Figure 7: Bearing angle and relative range of tracking a constant velocity target. (a) Bearing angle. (b) Relative range.

(i) Position coordinate: (1000, 1500)

(ii) Heading angle: 30°

(iii) Velocity: 15 m/s

The gain is chosen as $k = 0.0025$.

5.1.1. Static Ground Target. Figure 4 shows that the trajectory of standoff tracking of one UAV around the static target, and it can be seen that the trajectory of the UAV converges to the circle surrounding the target under the proposed guidance law. Figure 5 shows the changes of the bearing angle and relative range.

5.1.2. Constant Velocity Ground Target. Figure 6 shows the standoff tracking trajectory of the UAV when the target moves with constant velocity. It can be seen that the trajectory of the UAV is the combination of circular motion and linear motion. The changes of the bearing angle and relative range during the process of the convergence are shown in Figure 7.

5.1.3. Variable Velocity Ground Target. The velocity of the ground target is chosen as

$$v_t = 12 + 2 \times \sin\left(\frac{t}{10}\right). \tag{39}$$

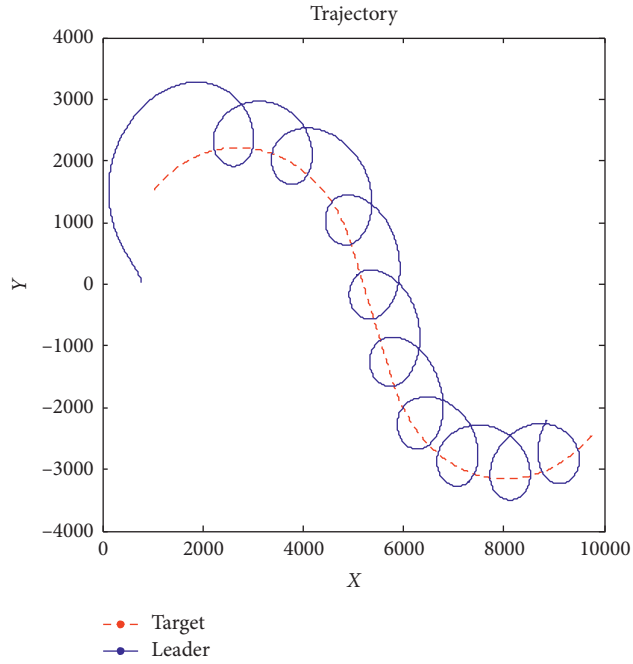

Figure 8: Trajectory of tracking a variable velocity target.

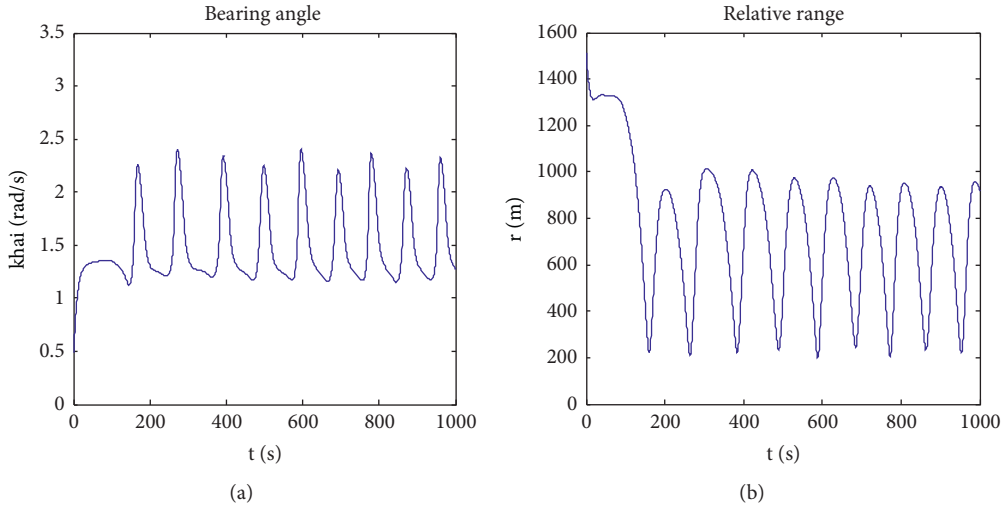

Figure 9: Bearing angle and relative range of tracking a variable velocity target. (a) Bearing angle. (b) Relative range.

The angular velocity of the ground target is set as

$$\dot{\psi}_t(t) = \begin{cases} -0.005, & t < 400, \\ 0, & 400 \le t \le 600, \\ 0.005, & t > 600. \end{cases} \quad (40)$$

In this scenario, the target moves with the sine trajectory. It can be seen that the proposed guidance law can also realize the standoff tracking of the target. The trajectory of the UAV and the ground target are shown in Figure 8, and the convergence curves of the bearing angle and relative range are shown in Figure 9.

From Figures 4 to 9, it can be seen that whether the target is still or moving, and the UAV always can track the ground target well in the standoff mode.

5.2. Track a Ground Target Using Formation UAVs. The initial states of the UAV #1 are set as follows:

(i) Position coordinate: (150, −1000)

(ii) Heading angle: −30°

(iii) Cruising velocity: 40.5 m/s

(iv) Maximum heading angular rate: 0.1 rad/s

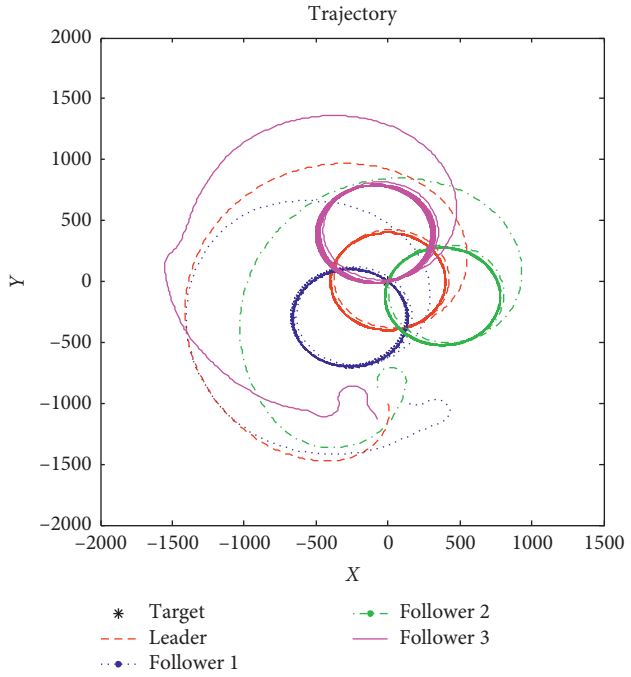

Figure 10: Trajectory of cooperative tracking a static target.

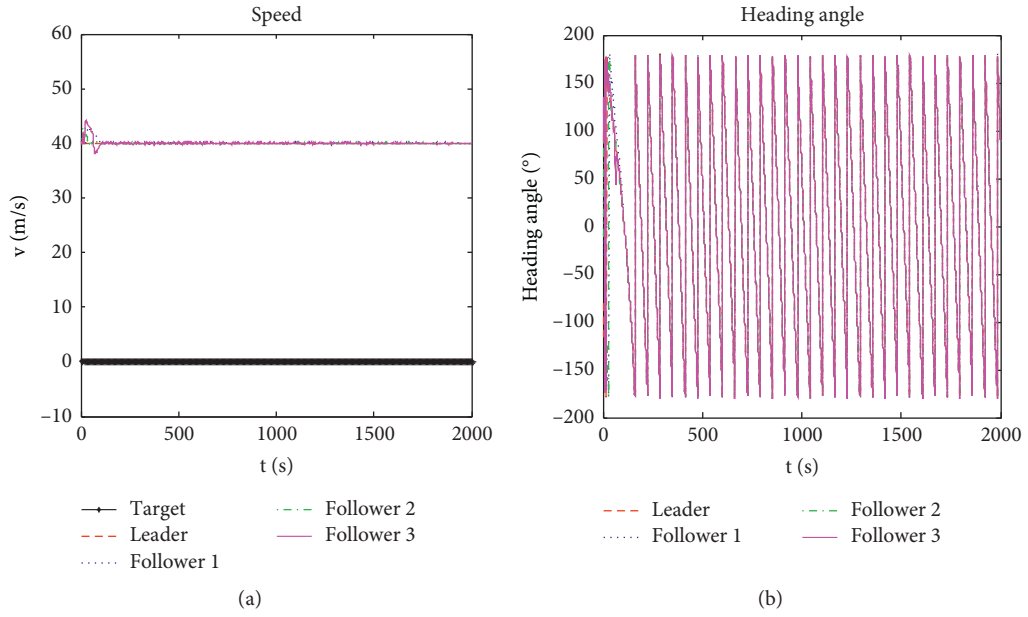

Figure 11: Velocities and heading angles of cooperative tracking a static target. (a) Velocities of target and followers. (b) Heading angles of all UAVs.

The initial states of the UAV #2 are set as follows:

(i) Position coordinate: (−75, −870)
(ii) Heading angle: 80°
(iii) Cruising velocity: 41 m/s
(iv) Maximum heading angular rate: 0.1 rad/s

The initial states of the UAV #3 are set as follows:

(i) Position coordinate: (−75, −1130)
(ii) Heading angle: 100°
(iii) Cruising velocity: 40.5 m/s
(iv) Maximum heading angular rate: 0.1 rad/s

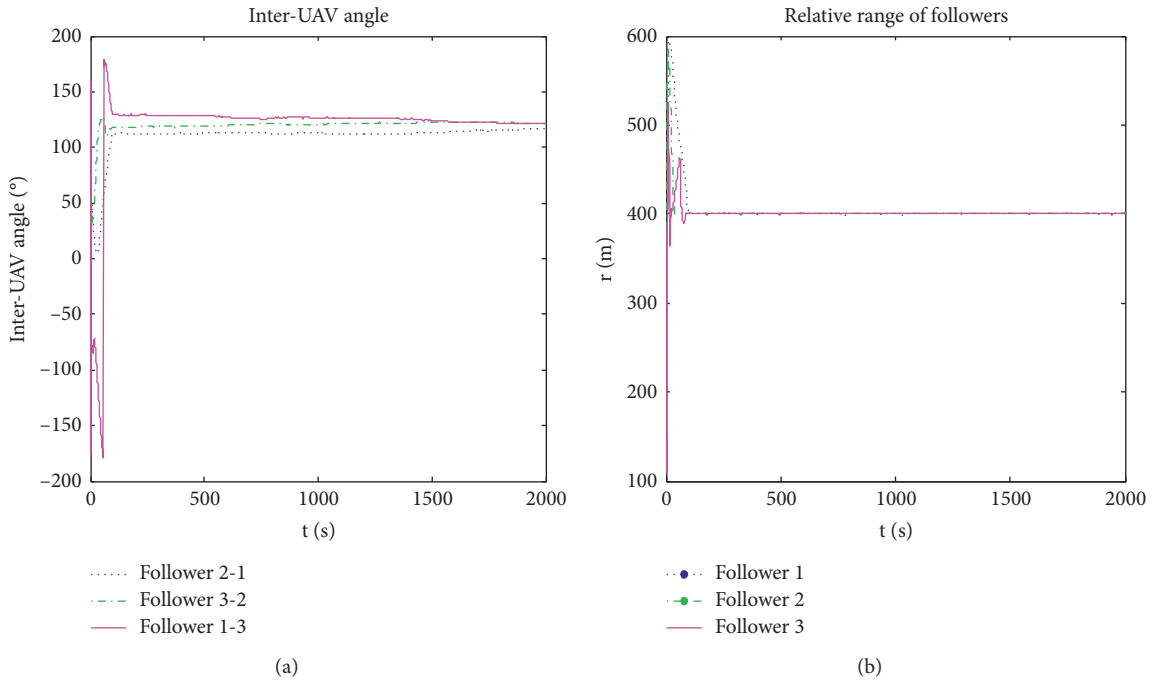

Figure 12: Inter-UAV angles and relative ranges of cooperative tracking a static target. (a) Inter-UAV angles between followers. (b) Relative ranges between leader and follower UAVs.

The gains are chosen as $k_v = 1.28$ and $k_\omega = 1.2$.

5.2.1. Static Ground Target. Under the proposed guidance laws, the multi-UAVs can converge to the desired standoff trajectories when the target is static. The trajectories of the UAVs' formation are shown in Figure 10, the velocities and heading angles of the formation are shown in Figure 11, and the inter-UAV angles and relative range between leader and follower UAVs are shown in Figure 12.

5.2.2. Constant Velocity Ground Target. As shown in Figure 13, the target moves with constant velocity and UAVs can accomplish the objective of standoff tracking, and the changes of the velocities and heading angles are shown in Figure 14, and the inter-UAV angle and relative range between leader and follower UAVs are shown in Figure 15.

5.2.3. Variable Velocity Ground Target. In this scenario, the target moves with the sine trajectory. The proposed guidance laws can also guarantee the convergence of the formation. The trajectories of the UAVs are shown in Figure 16, the changes of the velocities and heading angles are shown in Figure 17, and the inter-UAV angles and relative ranges between the leader and follower UAVs are shown in Figure 18.

From Figures 10 to 18, it can be seen that regardless of the ground target is static or moving, the desired formation always can be achieved, the follower UAVs' velocities and heading angles gradually converge to the leader, and the followers always can track the ground target well.

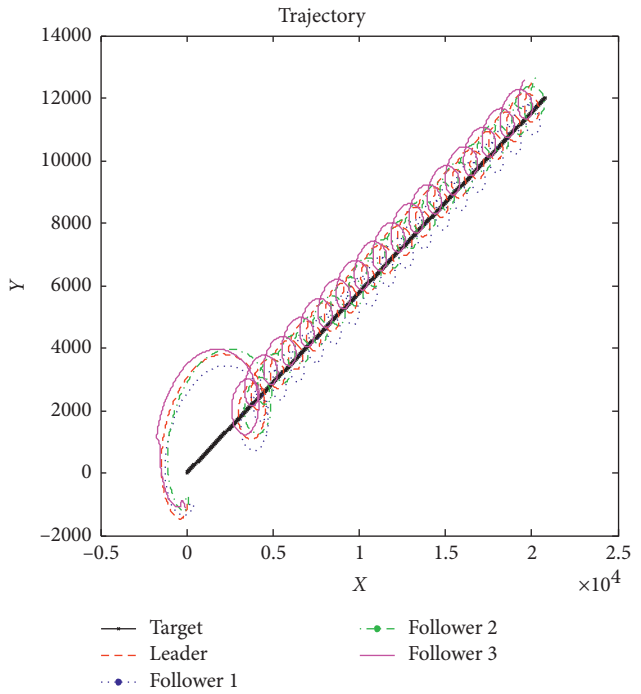

Figure 13: Trajectory of cooperative tracking a constant velocity target.

5.3. Simulation Analysis and Comparison. In order to verify the tracking performance, we adopt the well-known LVFG guidance algorithm proposed in Ref. [12] to run the same simulation case of variable velocity ground target tracking. We choose the tracking performance of UAV #1 as an example.

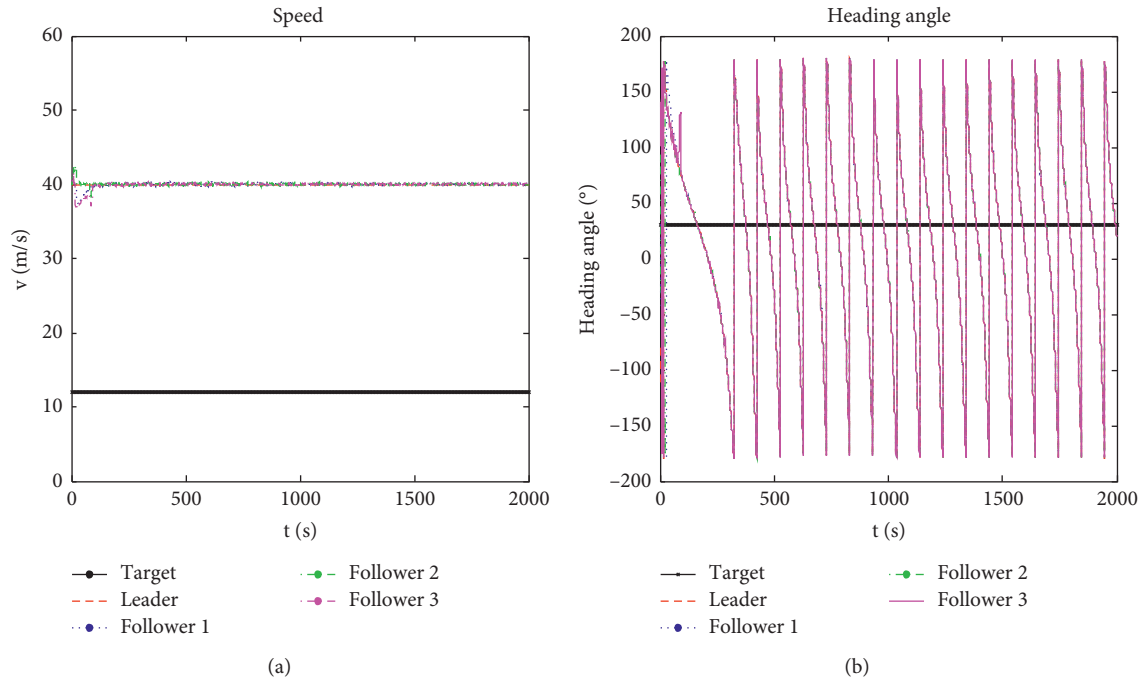

Figure 14: Velocities and heading angle of cooperative tracking a constant velocity target. (a) Velocities of target and followers. (b) Heading angles of all UAVs.

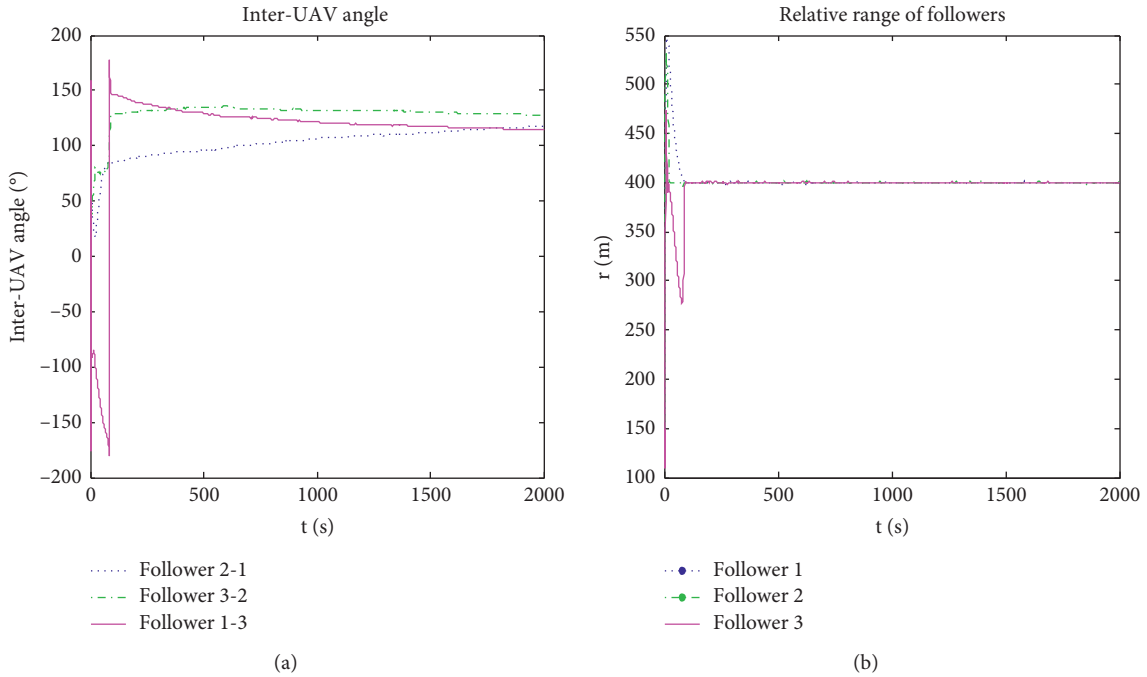

Figure 15: Inter-UAV angle and relative range of cooperative tracking a constant velocity target. (a) Inter-UAV angles between follower UAVs. (b) Relative range between leader and follower UAVs.

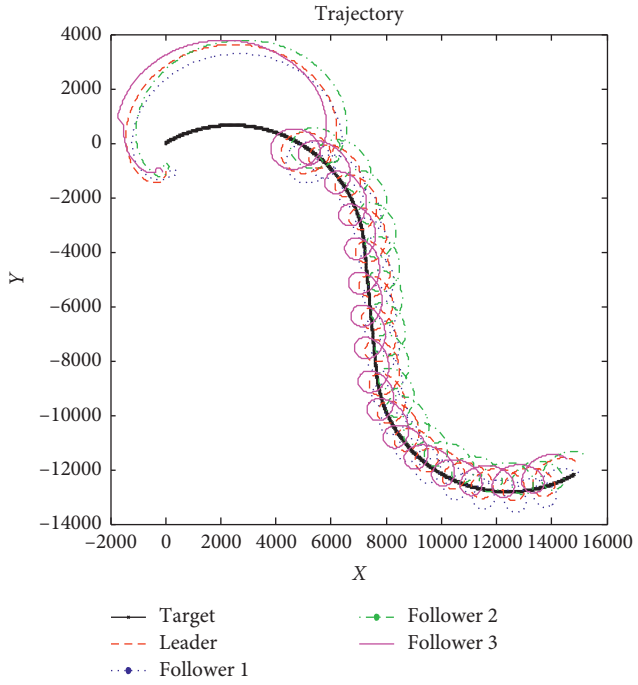

Figure 16: Trajectory of cooperative tracking a variable moving target.

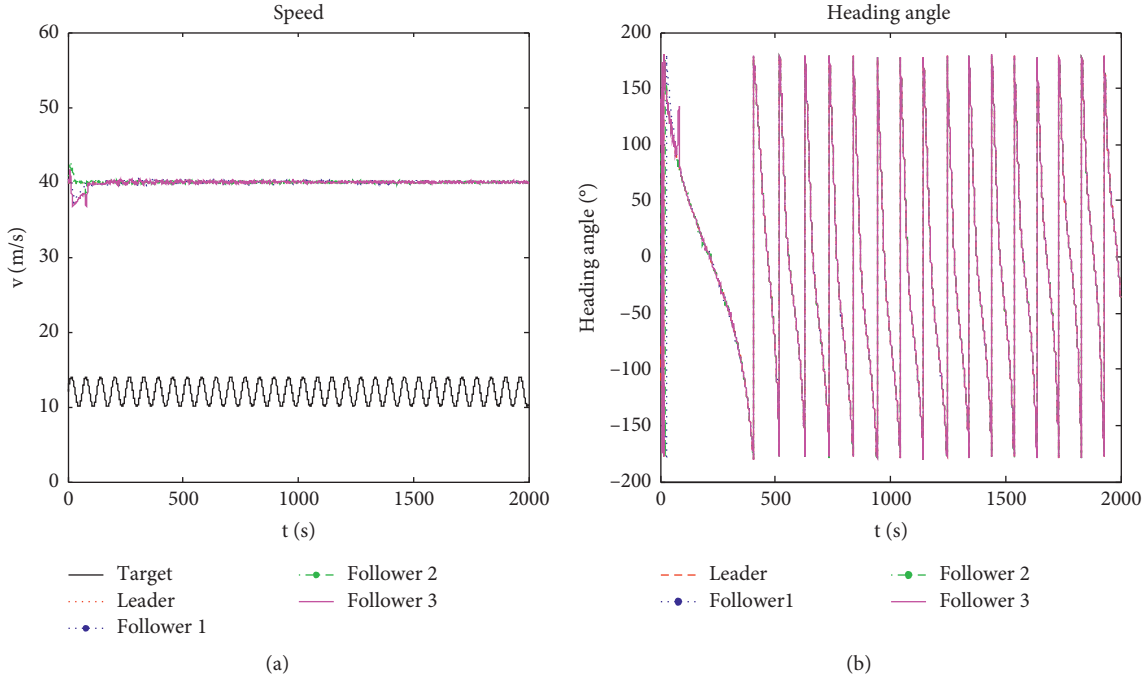

Figure 17: Velocities and heading angles of cooperative tracking a variable velocity target. (a) Velocity of target and followers. (b) Heading angles of all UAVs.

The velocity of UAV #1 and relative range between UAV #1 and the ground target using proposed method in this paper and Ref. [12] are shown in Figure 19.

When other performances are relative equivalent, from Figure 19, the proposed guidance law in this paper makes the velocity and heading angle of the follower UAVs always be

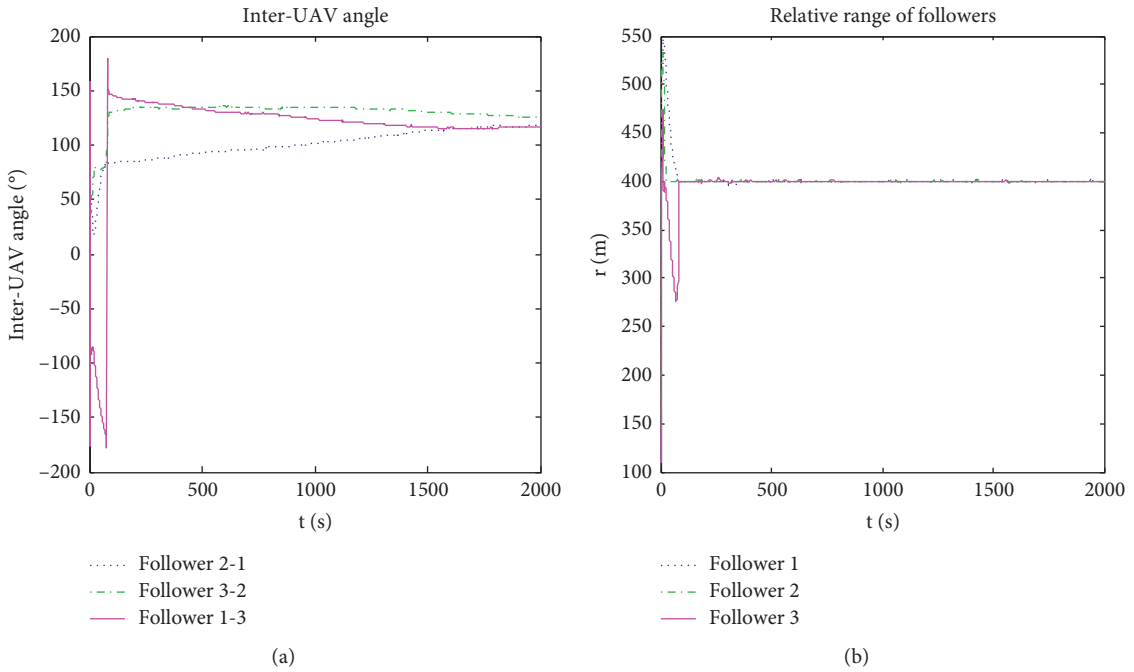

Figure 18: Inter-UAV angles and relative ranges of cooperative tracking a variable velocity target. (a) Inter-UAV angles between follower UAVs. (b) Relative ranges between leader and follower UAVs.

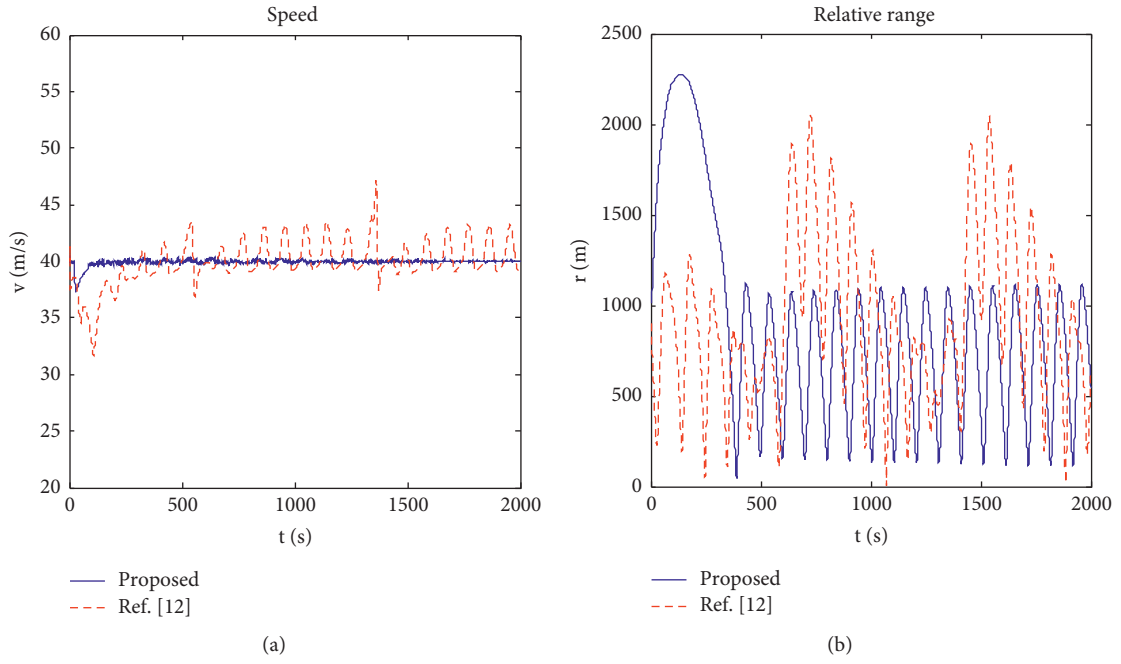

Figure 19: Velocity of UAV #1 and relative range. (a) Velocity of UAV #1. (b) Relative range.

consistent with the leader UAV, thus the convergence characteristics of velocity and relative range of the UAV #1 are better than the results in Ref. [12].

6. Conclusion

In this paper, a new leader-follower formation tracking scheme is proposed, which is based on the principle that a leader UAV is applied to track a ground target in the standoff mode, while multiple follower UAVs to track the leader UAV and are evenly distributed in a circle. As a result, the leader UAV maintains a certain distance to the ground target to avoid being exposed, while the follower UAVs can be closer to monitoring the ground target. The stabilities of the new guidance laws are proved using Lyapunov functions. Numerical simulations of a 4-UAVs' formation show that the new leader-follower

formation can track the static and moving targets well, and its performance is better than the well-known classic LVFG algorithm [24].

Data Availability

The raw/processed data required to reproduce these findings cannot be shared at this time as the data also forms part of an ongoing study.

Conflicts of Interest

The authors declare that there are no conflicts of interest.

Acknowledgments

The work was supported by National Natural Science Foundation of China 61903192 and Natural Science Foundation of Jiangsu Province BK20190402.

References

[1] M. Wu and Y. Fei, *Flight Control System*, pp. 46–64, Beijing University of Aeronautics and Astronautics Press, Beijing, China, 2006.

[2] S. Rathinam, Z. W. Kim, and R. Sengupta, "Vision-based monitoring of locally linear structures using an unmanned aerial vehicle," *Journal of Infrastructure Systems*, vol. 14, no. 1, pp. 52–63, 2008.

[3] Y. Wang, H. Pu, D. Wang, and W. Jiang, "Unmanned aerial vehicles cooperative path planning for ground target tracking via chemical reaction optimization," *Scientia Sinica Technologica*, vol. 45, no. 6, pp. 583–594, 2015.

[4] T. Betts, "Survey of numerical methods for trajectory optimization," *Journal of Guidance, Control, and Dynamics*, vol. 21, no. 2, pp. 193–207, 2008.

[5] V. N. Dobrokhodov, I. I. Kaminer, K. D. Jones, and R. Ghabcheloo, "Vision-based tracking and motion estimation for moving targets using small UAVs," in *Proceedings of the 2006 American Control Conference*, Minneapolis, MN, USA, June 2006.

[6] Z. W. Kim and R. Sengupta, "Target detection and position likelihood using an aerial image sensor," in *Proceedings of the 2008 IEEE International Conference on Robotics and Automation*, Pasadena, CA, USA, May 2008.

[7] T.-H. Kim and T. Sugie, "Cooperative control for target-capturing task based on a cyclic pursuit strategy," *Automatica*, vol. 43, no. 8, pp. 1426–1431, 2007.

[8] S. Daingri and A. Sinha, "nonlinear cyclic pursuit based cooperative target monitoring," in *Proceedings of the International symposium on distributed autonomous robotic systems*, Baltimore, MD, USA, November 2012.

[9] L. F. Bertuccelli and J. P. How, "Search for dynamic targets with uncertain probability maps," in *Proceedings of the 2006 IEEE American Control Conference*, Minneapolis, MN, USA, June 2006.

[10] Z. Li and N. Hovakimyan, "Vision-based target tracking and motion estimation using a small UAV," in *Proceedings of the 2010 IEEE conference on Decision and Control*, Atlanta, GA, USA, December 2010.

[11] D. A. Lawrence and E. W. Frew, "Lyapunov vector fields for autonomous unmanned aircraft flight control," *Journal of Guidance Control and Dynamics*, vol. 31, no. 5, pp. 1220–1229, 2012.

[12] E. W. Frew, D. A. Lawrence, and S. Morris, "Coordinated standoff tracking of moving targets using Lyapunov guidance vector fields," *Journal of Guidance, Control, and Dynamics*, vol. 31, no. 2, pp. 290–306, 2008.

[13] S. Kim, H. Oh, and A. Tsourdos, "Nonlinear model predictive coordinated standoff tracking of a moving ground vehicle," *Journal of Guidance, Control, and Dynamics*, vol. 36, no. 2, pp. 557–566, 2013.

[14] M. Zhang and H. Liu, "Cooperative tracking a moving target using multiple fixed-wing UAVs," *Journal of Intelligent and Robotic Systems*, vol. 81, no. 3, pp. 505–529, 2018.

[15] A. Hashemi, Y. Cao, and D. W. Casbeer, "Unmanned aerial vehicle circumnavigation using noisy range-based measurements without global positioning system information," *Journal of Dynamic Systems Measurement & Control*, vol. 137, no. 3, pp. 1–10, 2015.

[16] Z. Cheng, B. Wang, L. Liu, and Y. Wang, "A composite impact-time-control guidance law and simultaneous arrival," *Aerospace Science and Technology*, vol. 80, pp. 403–412, 2018.

[17] N. Zhang, W. Gai, G. Zhang, and J. Zhang, "An active disturbance rejection control guidance law based collision avoidance for unmanned aerial vehicles," *Aerospace Science and Technology*, vol. 77, pp. 658–669, 2018.

[18] L. He, P. Bai, X. Liang, J. Zhang, and W. Wang, "Feedback formation control of UAV swarm with multiple implicit leaders," *Aerospace Science and Technology*, vol. 72, pp. 327–334, 2018.

[19] X. Ai and J. Yu, "Flatness-based finite-time leader-follower formation control of multiple quadrotors with external disturbances," *Aerospace Science and Technology*, vol. 92, pp. 20–33, 2019.

[20] Y. Cao, "UAV circumnavigating an unknown target under a GPS-denied environment with range-only measurements," *Automatica*, vol. 55, pp. 150–158, 2014.

[21] Y. Cao, "UAV circumnavigating an unknown target using range measurement and estimated range rate," in *Proceedings of the 2014 IEEE American Control Conference*, Portland, OR, USA, June 2014.

[22] M. Varga, J.-C. Zufferey, G. H. M. Heitz, and D. Floreano, "Evaluation of control strategies for fixed-wing drones following slow-moving ground agents," *Robotics and Autonomous Systems*, vol. 72, no. 1, pp. 285–294, 2015.

[23] N. Regina and M. Zanzi, "UAV guidance law for ground-based target trajectory tracking and loitering," in *Proceedings of the 2011 IEEE Aerospace Conference*, Big Sky, MT, USA, March 2011.

[24] H. K. Khalil, *Nonlinear Systems*pp. 139–144, Prentice Hall, Upper Saddle River, NJ, USA, 3rd edition, 2002.

Hindawi
Mathematical Problems in Engineering
Volume 2021, Article ID 6624893, 18 pages
https://doi.org/10.1155/2021/6624893

Research Article

Composite Curve Path following an Underactuated AUV

Ben Li,[1] **Guohua Xu**,[1,2] **Yingkai Xia**,[3] **Wenjin Wang**,[1] **and Zhen Su**[1]

[1]*School of Naval Architecture and Ocean Engineering, Huazhong University of Science and Technology, Wuhan 430074, China*
[2]*Hubei Key Laboratory of Naval Architecture and Ocean Engineering Hydrodynamics, HUST, Wuhan 430074, China*
[3]*College of Engineering, Huazhong Agricultural University, Wuhan 430070, China*

Correspondence should be addressed to Guohua Xu; hustxu@vip.sina.com and Yingkai Xia; ykxia@mail.hzau.edu.cn

Received 16 December 2020; Revised 23 February 2021; Accepted 25 March 2021; Published 8 April 2021

Academic Editor: Chih-Chiang Chen

This paper addresses the problem of composite curve path following for an underactuated autonomous underwater vehicle by utilizing an adaptive integral line-of-sight (AILOS) guidance and nonlinear iterative sliding mode (NISM) controller. First, the composite curve path is parametrized by a common scalar variable in a continuous way. Then, the kinematics error of an underactuated vehicle is described based on the nonprojection Frenet–Serret frame with a virtual point, which can be eliminated by the virtual point control and AILOS guidance. Meanwhile, the subpath switching algorithm is studied to realize the global path following for the composite curve path. Besides, the NISM controller is cascaded with the AILOS guidance law, and the cascade structure proved to be globally κ-exponentially stable under the influence of slow time-varying currents. Finally, simulations are considered to demonstrate the effectiveness of the proposed composite curve path following control scheme.

1. Introduction

In recent years, much research has been done in the field of path following for autonomous underwater vehicles (AUVs). In most of the existing literature, the desired geometric path is a single curve [1, 2]. However, as is known, a single curve cannot represent complex shapes with a high degree; it may result in a very intractable and impractical path due to Runge's phenomenon [3]. Hence, utilizing the composite curve path as the desired path is more practical since it is composed of multiple subpaths and can meet the demands of varied tasks flexibly in a complex and limited marine environment.

It is known that the shape and the properties of the composite curve path have a great influence on the path following control. Generally, the composite curve path is obtained by a path planning algorithm with two steps. Firstly, utilizing a path search algorithm, the given order of waypoints is obtained based on certain optimization objectives. Then, considering the kinematics constraints of the vehicle, multiple curves (such as straight lines, circular arcs, spiral lines, and polynomial curves) can be used to connect all the waypoints to generate a flyable path [4]. In the existing literature, path following of composite curve path such as successive straight lines, straight lines and circles [5,6], and spline interpolation curve [7] has been studied. However, to the best of the authors' knowledge, no general method has been proposed for tracking the composite curve path, which will be studied in this paper.

As the expressions of curve segments vary, and there is no unified parametrization for the composite curve path, they will be inconvenient to calculate and expand. Hence, for better tracking of the composite curve path, it is necessary to choose an appropriate path description method. To solve this problem, all the curve segments are parametrized in a continuous way in this paper. Besides, each curve segment is parametrized by a common scalar variable with the same interval. However, it is usually difficult for the composite curve path to satisfy parametric continuity between the curve segments. Hence, to realize the global path following of the composite curve path, the problem of subpath switching [5, 8] is also discussed.

After the composite curve path has been designed and parametrized, an efficient path following system is proposed. For underactuated AUVs, which have no independent control input in the sway and heaven direction, the line-of-sight (LOS) guidance principle is a very suitable and efficient

solution for path following. When combined with guidance, the position and heading can be controlled simultaneously just by the heading control. Hence, utilizing LOS guidance, this has been no longer an underactuated problem in terms of the variables to be controlled [9]. Proportional LOS guidance is one of the most widely used methods [10]. However, it cannot handle the unknown environmental disturbance such as wind, wave, or currents. To solve this problem, the integral line-of-sight (ILOS) guidance law is proposed for path following of straight-line paths in the presence of constant and irrotational ocean currents [11]. A modified version of the ILOS algorithm based on the adaptive compensation of the sideslip angle is proposed for path following of a parametrized curve under unknown environmental disturbances [6]. Besides, adaptive integral line-of-sight (AILOS) guidance law is designed for marine craft exposed to ocean currents. The expression of the cross-track kinematics error is reformulated using the concept of relative velocity [12].

Generally, the LOS guidance laws are intuitive as they are formulated at a kinematics level without using the vehicle parameters. Through a cascaded system approach [13], the LOS guidance principle can be interconnected with a heading controller to achieve the path following control. In detail, the LOS guidance principle transforms the position error into the desired heading angle, and the heading control system is responsible for eliminating the heading error. For the cascaded system, the heading controller can be designed independently, so more concise control law can be obtained, such as the PID (proportional integral derivative) control, the fuzzy control, the sliding mode control, and the neural network control. Different control algorithms have their own advantages and disadvantages. In [6], to realize the LOS path following for Dubins paths, the PID controller has been used for the heading control, which is easy to implement, but there are the problems of integral saturation and slow convergence speed. Sliding mode control has strong robustness against external environmental disturbances. In [12], the sliding mode control is constructed for the heading control. However, the control law is based on the yaw dynamics model and can be affected by the uncertainty of model parameters. In [14], disturbance observers and modified terminal sliding mode control are combined to design a robust disturbance rejection control law for the dynamics control of a X-rudder AUV. Fuzzy control [1] and neural network control [7,15] are usually combined with other control methods in order to identify the dynamical uncertainty and time-varying ocean disturbances.

In this paper, a new composite curve path following controller is proposed for an underactuated AUV, based on nonlinear iterative sliding mode (NISM) controller [16] and AILOS guidance. The main contributions are summarized as follows:

(1) To eliminate the tracking error, a cascade structure is established based on AILOS guidance law and a NISM controller, which proved to be UGAS (uniformly globally asymptotically stable).

(2) Based on the AILOS guidance law and the subpath switching algorithm, the global path following of the composite curve path in the kinematics layer is realized with the unknown ocean currents.

(3) The NISM control is proposed in the dynamics layer, which has the characteristics of fast convergence and strong antidisturbance ability. In addition, the strictly bounded nonlinear hyperbolic tangent function is used to avoid excessive control input caused by the discontinuity at each connection point between two subpaths. Besides, the incremental feedback control law is designed, which is independent of hydrodynamic parameters.

The remainder of this paper is organized as follows. Section 2 describes the concept and parametrization of the composite curve path, where the continuity characteristics of the composite curve path are analyzed, and parametric forms of common curves are given. Section 3 presents the kinematics and dynamics expressions of REMUS (remote environmental monitoring units) vehicles and problem formulation. Section 4 addresses the design and proof of the path following control system. Section 5 validates the effectiveness of the previous design for the composite curve path following with several simulation cases and discussions. Section 6 demonstrates the conclusion of this work.

2. Preliminaries

The composite curve path can be defined as a set of curves connected in a specific order. Each curve segment is regarded as a subpath. The parametrization and the continuity of the composite curve path are discussed in this section. Besides, the parametric description is proposed for typical curves.

2.1. Path Parametrization. In complex and limited marine environment, the composite paths can meet the demands of varied tasks flexibly by adjusting the type of subpaths. However, as the expressions of subpaths may vary, they will be inconvenient to calculate and hard to expand for the path following of composite curve path.

To handle this problem, the path parametrization method is adopted to describe the composite curve path. Many parametrization methods can be used to describe a path, which may be continuous, discrete, or even hybrid [17]. In this paper, the composite curve path is parametrized in a continuous way, and every curve segment is parametrized by a common scalar variable $s \in [0, n]$ (n is a natural number) with the same interval, which makes it more convenient to calculate considering different kinds of curve segments.

For a continuous parametrization, the composite curve path L with n subpaths can be defined as

$$p_p(s) \coloneqq \begin{cases} L_1(s), & s \in [0,1), \\ L_2(s), & s \in [1,2), \\ \vdots & \\ L_i(s), & s \in [i-1,i), \\ \vdots & \\ L_n(s), & s \in [n-1,n]. \end{cases} \tag{1}$$

The path is then simplified by the set

$$L \coloneqq \left\{ p \in \mathbb{R}^2 \colon \exists s \in [0, n] \text{ s.t. } p = p_p(s) \right\}, \tag{2}$$

where $L_i(s)$ denotes the parametrization of the i th subpath of the composite path L, and p is the set of all the points on L. The coordinates of the point $p_p(s)$ in the inertial frame $\{I\}$ are uniquely determined by a specific value $s \in [0, n]$ with the following form:

$$p_p(s) = \begin{bmatrix} x_p(s) \\ y_p(s) \end{bmatrix}. \tag{3}$$

With a continuous parametrization, for any given parameters of the composite curve path, the position of the corresponding point can be determined uniquely.

Regular curves are desired for the subpaths, which means that such paths never degenerate into a point nor do they have corners. Specifically, these curves include both straight lines and circles [18]. Parametrization for the regular curves satisfies

$$\left| p_p'(s) \right| \triangleq \left| \frac{\mathrm{d} p_p(s)}{\mathrm{d}s} \right|, \tag{4}$$

where $p_p'(s)$ is the first derivative of the point $p_p(s)$ w.r.t. the path parameter$s$. For each subpath, the first and second derivatives w.r.t. s can be described as

$$\begin{cases} x_p'(s) = \dfrac{\mathrm{d}x_p}{\mathrm{d}s} \\ y_p'(s) = \dfrac{\mathrm{d}y_p}{\mathrm{d}s}, \\ x_p''(s) = \dfrac{\mathrm{d}^2 x_p}{\mathrm{d}s^2}, \\ y_p''(s) = \dfrac{\mathrm{d}^2 y_p}{\mathrm{d}s^2}. \end{cases} \tag{5}$$

The first derivative of s w.r.t. time is $\dot{s} = (\mathrm{d}s/\mathrm{d}t)$, and the path-tangential speed is calculated as

$$U_P = \sqrt{\dot{x}_p(s)^2 + \dot{y}_p(s)^2} = \sqrt{x_p'(s)^2 + y_p'(s)^2}\,\dot{s}. \tag{6}$$

The path-tangential angle (or course angle of the path) is computed as

$$\chi_p(s) = a \tan 2 \left(\frac{y_p'(s)}{x_p'(s)} \right). \tag{7}$$

The curvature of the path can be calculated as

$$\kappa = \frac{x_p'(s) y_p''(s) - y_p'(s) x_p''(s)}{\sqrt[3]{x_p'^2(s) + y_p'^2(s)}}. \tag{8}$$

The angular speed of the path can be described as

$$r_p(s) = \dot{\chi}_p(s) = \frac{\partial \chi_p}{\partial s}\dot{s} = \frac{x_p'(s) y_p''(s) - y_p'(s) x_p''(s)}{x_p'^2(s) + y_p'^2(s)}\dot{s}. \tag{9}$$

2.2. Path Smoothness. The smoothness of the desired path has an essential impact on the motion control of the underactuated vehicle. Moreover, two notions can be used to describe the path smoothness, namely, the geometric continuity (GC) and the parametric continuity (PC) [19].

GC is denoted by G^n, with n specifying the degree of smoothness. The brief definition of GC up to the second degree can be given as follows:

(i) G^0: the only requirement is that all subpaths are connected

(ii) G^1: the path-tangential angle in the connection point is continuous

(iii) G^2: the tangential angle and the curvature of the path are continuous

Similarly, PC is denoted by C^n, with n specifying the degree of smoothness. C^n up to the second degree can be defined as follows:

(i) C^0: the definition is the same as that of G^0

(ii) C^1: the velocity vector orientation and magnitude are continuous

(iii) C^2: the acceleration is continuous

Compared with GC, PC is a stricter form of continuity which imposes constraints on how the parameter propagates along the path. Moreover, PC is a measure of smoothness for parametrizations.

From (1), it can be concluded that the composite curve path can satisfy at least the C^0 (or G^0) continuity. However, higher-order PC is usually hard to realize for the composite curve path with different types of curve segments. The derivative of the parameter in the connection point is discontinuous. Relatively, G^1 and G^2 are easy to build and can be used for path following of the composite curve path.

Some common composite curve paths can be used as examples (see Table 1).

2.3. Parametric Description of Typical Curves. Based on [19], the parametric descriptions of straight lines, circular arcs, and Fermat's spiral with a standard scalar variable are given. The parametric description of the line segment is as follows:

$$P_{\text{line}}(s) = \begin{bmatrix} x_0 + Ls\cos(\chi_l) \\ y_0 + Ls\sin(\chi_l) \end{bmatrix}, \tag{10}$$

where (x_0, y_0) is the starting point, L is the length of the line segment, and χ_l is the path-tangential angle of the line segment.

Furthermore, the parametrization of circular arcs can be expressed as

Table 1: Common composite curve paths.

Path	GC	Comments
Piecewise linear path	G^0	Generated directly through waypoints but is not suitable for path following of underactuated AUV
Circular smoothing	G^1	Generated by approximating methods, and curvature between straight and circular segments is discontinuous
Dubins path	G^1	Generated by interpolating methods, and curvature between straight and circular segments is discontinuous
Clothoid smoothing	G^2	Generated by approximating methods, linear varying curvature with an increased computational cost
Fermat's spiral smoothing	G^2	Generated by interpolating methods, curvature-continuous paths with a very low computational cost compared to clothoid smoothing [19]

$$P_{\text{cir}}(s) = \begin{bmatrix} c_{x0} + R\cos(\alpha_0 + s(\alpha_1 - \alpha_0)) \\ c_{y0} + R\sin(\alpha_0 + s(\alpha_1 - \alpha_0)) \end{bmatrix}. \tag{11}$$

Here, (c_{x0}, c_{y0}) is the center of the circle, and R is the radius. Besides, α_0 and α_1 are the heading angles of vectors from the center of the circle to the starting point and the endpoint.

To avoid singularity, the parametrization of Fermat's spiral can be described as

$$P_{\text{FS}}(s) = \begin{bmatrix} x_0 + k\sqrt{\theta_{\text{end}}}\, s\cos\left(\rho\theta_{\text{end}}s^2 + \chi_0\right) \\ y_0 + k\sqrt{\theta_{\text{end}}}\, s\sin\left(\rho\theta_{\text{end}}s^2 + \chi_0\right) \end{bmatrix}, \tag{12}$$

$$s \coloneqq \frac{\sqrt{\theta}}{\sqrt{\theta_{\text{end}}}} \Rightarrow 0 \le s \le 1.$$

For the mirrored curve of Fermat's spiral, the following parametrization is proposed:

$$P_{\overline{\text{FS}}}(s) = \begin{bmatrix} x_{\text{end}} - k\sqrt{\theta_{\text{end}}}\,(1-s)\cos\left(-\rho\theta_{\text{end}}(1-s)^2 + \chi_{\text{end}}\right) \\ y_{\text{end}} + k\sqrt{\theta_{\text{end}}}\,(1-s)\sin\left(-\rho\theta_{\text{end}}(1-s)^2 + \chi_{\text{end}}\right) \end{bmatrix},$$

$$s \coloneqq \frac{\sqrt{\theta_{\text{end}} - \theta}}{\sqrt{\theta_{\text{end}}}} \Rightarrow 0 \le s \le 1 \tag{13}$$

where (x_0, y_0) is the starting point, $(x_{\text{end}}, y_{\text{end}})$ is the endpoint, θ is the polar angle, θ_{end} is the polar angle of the endpoint, χ_0 and χ_{end} are the path-tangential angles of Fermat's spiral at the starting and the endpoint, and ρ determines the direction of spiral rotation.

3. Problem Statement

REMUS vehicles are low-cost AUVs designed by the Woods Hole Oceanographic Institution serving in a range of oceanographic applications, such as surveying and mapping. The vehicles are torpedo-shaped and underactuated without lateral thrust; a propeller and fins are used for steering and diving. Besides, the mathematical model of REMUS vehicles has been well researched, which can be used in motion control simulation of underactuated AUVs [20].

This section describes the kinematics and dynamics expressions of the REMUS vehicles and problem formulation of the composite curve path following.

3.1. AUV Model considering Currents. Considering the influences of currents, the kinematics model in the horizontal plane can be expressed in terms of the relative surge and sway velocities [20,21].

$$\begin{aligned} \dot{x} &= u_r\cos(\psi) - v_r\sin(\psi) + V_x, \\ \dot{y} &= u_r\sin(\psi) + v_r\cos(\psi) + V_y, \\ \dot{\psi} &= r. \end{aligned} \tag{14}$$

As depicted in Figure 1, *(x)* and y are the coordinates of the center of mass of the vehicle expressed in the inertial frame $\{I\}$. ψ and r define its heading angle and yaw velocity. The pair (V_x, V_y) denotes the northeast current velocities in $\{I\}$. Hence, the body-fixed current velocities in surge and sway directions (u_c, v_c) are given by

$$\begin{aligned} u_c &= V_x\cos(\psi) - V_y\sin(\psi), \\ v_c &= V_x\sin(\psi) + V_y\cos(\psi). \end{aligned} \tag{15}$$

The relative surge and sway velocity can be defined as

$$\begin{aligned} u_r &= u - u_c, \\ v_r &= v - v_c, \end{aligned} \tag{16}$$

where u and v are the surge and sway velocity relative to the Earth.

Besides, the relative resultant velocity can be expressed as

$$U_r = \sqrt{u_r^2 + v_r^2}. \tag{17}$$

The REMUS vehicle considered in this paper is based on the following assumptions.

Assumption 1. The vehicle has two axial planes of symmetry, top-bottom and port-starboard symmetry, respectively.

Assumption 2. The vehicle center of gravity is the same as the vehicle center of buoyancy, and the origin of the vehicle body-fixed coordinate system is located at the vehicle center of buoyancy.

Neglecting the motions in heave, roll, and pitch directions, the 3-DOF dynamics model of REMUS vehicle in the horizontal plane can be simplified as

$$\begin{bmatrix} \dot{u}_r \\ \dot{v}_r \\ \dot{r} \end{bmatrix} = \begin{bmatrix} m - X_{\dot{u}} & 0 & 0 \\ 0 & m - Y_{\dot{V}} & -Y_{\dot{r}} \\ 0 & -N_{\dot{v}} & I_{zz} - N_{\dot{r}} \end{bmatrix}^{-1} \begin{bmatrix} \Sigma X \\ \Sigma Y \\ \Sigma N \end{bmatrix}, \tag{18}$$

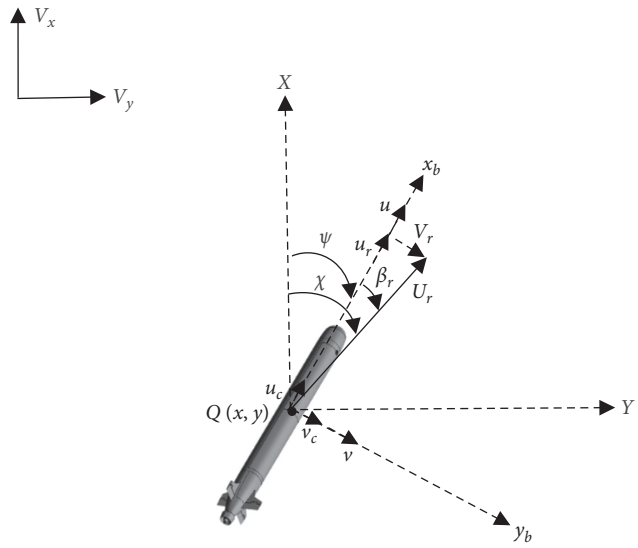

Figure 1: The kinematics description of AUVS in the horizontal plane.

where ΣX and ΣY define the nonacceleration terms along the x-axis and y-axis, and ΣN defines the nonacceleration terms of rotation along the z-axis. The description of ΣX, ΣY, and ΣNcan be shown as

$$\begin{aligned}\Sigma X &= X_{u|u|}u_r|u_r| + X_{vr}v_r r + X_{rr}rr + X_T,\\ \Sigma Y &= Y_{v|v|}v_r|v_r| + Y_{r|r|}r|r| + Y_{ur}u_r r\\ &\quad - mu_r r + Y_{uv}u_r v_r + Y_{uu\delta}u_r^2\delta_r,\\ \Sigma N &= N_{v|v|}v_r|v_r| + N_{r|r|}r|r| + N_{ur}u_r r\\ &\quad + N_{uv}u_r v_r + N_{uu\delta}u_r^2\delta_r,\end{aligned} \tag{19}$$

where u_r, v_r, and r are relative surge, sway, and yaw velocity of the vehicle, which constitute the kinematics status of the vehicle. The thrust X_T and the rudder angle δ_r denote the control input. The symbols similar to $X_{(\cdot)}$, $Y_{(\cdot)}$, and $N_{(\cdot)}$ represent the hydrodynamic parameters of the model, which are used for the calculation of hydrodynamic forces and moments. m represents the mass of the vehicle, and I_{zz} is the moments of inertia. The values of these parameters are presented in Table 2.

3.2. Kinematics Error Description. As depicted in Figure 2, the composite curve path L is composed of two subpaths, L_1 and L_2. Q is the origin of the body-fixed coordinate system of the AUV and P is the virtual point moving along the path. The kinematics error is described in the Frenet–Serret frame $\{F\}$ [22] attached to the point P. However, different from the traditional Frenet–Serret frame $\{F\}$, P is not the closest point on the path to the vehicle, but a point which evolves according to the designed control law. In this way, the singularity caused by parametrization with arc length can also be avoided [23].

The tracking error expressed in $\{F\}$ can be described as

$$\begin{cases} x_e = (x - x_p)\cos(\chi_p) + (y - y_p)\sin(\chi_p),\\ y_e = -(x - x_p)\sin(\chi_p) + (y - y_p)\cos(\chi_p),\end{cases} \tag{20}$$

where x_e is the along-track error and y_e is the cross-track error, (x, y) and (x_p, y_p) are the coordinates of the AUV and the virtual point in the inertial coordinate system, and χ_p is the path-tangential angle of the desired path.

Differentiating (20) yields the error dynamics build in

$$\Sigma_1: \begin{cases} \dot{x}_e = -U_p + U_r\cos(\psi + \beta_r - \chi_p) + r_p y_e + \cos(\chi_p)V_x + \sin(\chi_p)V_y,\\ \dot{y}_e = U_r\sin(\psi + \beta_r - \chi_p) - r_p x_e - \sin(\chi_p)V_x + \cos(\chi_p)V_y,\end{cases} \tag{21}$$

where $r_p = \dot{\chi}_p$ is the angular speed of the path and $\beta_r = a\tan 2(v_r, u_r)$ is the drift angle.

Generally, the problem of the composite curve path following for underactuated AUV can be formulated as follows:

Given a constant thrust X_T and desired composite curve path L, select an appropriate way to parametrize the path (1), design guidance and virtual point control laws to generate the desired heading angle ψ_d and realize the global path following, and then develop an active heading controller to

Table 2: Parameters of the REMUS AUV.

Parameter	Value
m	30.48 kg
$X_{u\|u\|}$	$-1.62\,kg/m$
$X_{\dot{u}}$	−0.93 kg
X_{vr}	35.5 kg/rad
X_{rr}	1.93 kg · m/rad
$Y_{v\|v\|}$	−1310 kg/m
$Y_{\dot{v}}$	−35.5 kg
$Y_{r\|r\|}$	0.632 kg · m/rad^2
$Y_{\dot{r}}$	1.93 kg · m/rad
Y_{ur}	5.22 kg/rad
Y_{uv}	28.6 kg/m
$Y_{uu\delta}$	9.64 kg/ (m · rad)
$N_{r\|r\|}$	−9.4 kg · m^2/rad^2
$N_{v\|v\|}$	−3.18 kg
$N_{\dot{v}}$	1.93 kg/m
$N_{\dot{r}}$	−4.88 kg · m^2/rad
N_{ur}	−2.0 kg · m/rad
N_{uv}	−24 kg
$N_{uu\delta}$	−6.15 kg/rad
I_{zz}	3.45 kg · m^2
$X\Gamma$ max	$6.48N$
δ_r max	35°

achieve the expected heading angle, so that the path tracking error can be eliminated.

4. Path following Control Design

To eliminate the tracking error under the influence of unknown static currents, a new path following controller is proposed with cascade structure, as shown in Figure 3.

First, the designed composite curve path is parametrized by a common scalar variable in a continuous way, and a point (P) is selected as the virtual target to be followed. Then, the kinematics error between the coordinates of the AUV and the virtual target point can be calculated including the along-track error and the cross-track error. To eliminate the along-track error, the speed of the virtual point ($\dot{s}$) is introduced as a control input. Besides, utilizing the adaptive ILOS guidance with a current observer, the desired heading angle is given to eliminate the cross-track error. Next, the heading control system (an improved NISM controller) is designed to realize the desired heading angle ($\psi_e = 0$) by controlling the rudder (δ_r) under constant thrust (X_T). Finally, the cascade structure proved to be globally k-exponentially stable under the influence of static currents.

4.1. The AILOS Guidance. The path-tangential speed of the virtual point can be used as a control input [18,23]:

$$U_p = U_r \cos\left(\psi + \beta - \chi_p\right) + kx_e + \cos\left(\chi_p\right)V_x + \sin\left(\chi_p\right)V_y, \tag{22}$$

where $k > 0$ is a gain parameter; the virtual point will move toward the direct projection of the vehicle onto the x-axis of $\{F\}$, whose purpose is to reduce the along-track error to zero.

Substituting (22) into (21) gives

$$\dot{x}_e = -kx_e + r_p y_e. \tag{23}$$

Simultaneously, adaptive ILOS guidance law is used to derive a desired heading angle to eliminate the cross-track error. As illustrated in Figure 1, the desired heading angle is designed as [3]

$$\psi_d = \chi_p + \chi_r - \beta_r, \tag{24}$$

with

$$\chi_r = \arctan\left(-\frac{1}{\Delta}\left(y_e + \alpha\right)\right), \tag{25}$$

where $\Delta > 0$ is the look-ahead distance along the tangential path in $\{F\}$, which is given in meters and usually takes values between 1.5 and 2.5 times the length of a vehicle. Besides, the parameter α is a virtual control input used to compensate for the disturbance of unknown currents.

As the heading error can be expressed as $\psi_e = \psi - \psi_d$, the expression of $\dot{y}_e$ in (21) can be rewritten as

$$\dot{y}_e = U_r \sin\left(\psi_e + \chi_r\right) - r_p x_e - \sin\left(\chi_p\right)V_x + \cos\left(\chi_p\right)V_y. \tag{26}$$

Substituting (25) into (26) gives

$$\begin{aligned}\dot{y}_e = {} & U_r \sin\left(\psi_e + \arctan\left(-\frac{1}{\Delta}\left(y_e + \alpha\right)\right)\right) - r_p x_e \\ & - \sin\left(\chi_p\right)V_x + \cos\left(\chi_p\right)V_y.\end{aligned} \tag{27}$$

Then, (27) can be rewritten as

$$\begin{aligned}\dot{y}_e = {} & -\frac{U_r\left(y_e + \alpha\right)}{\sqrt{\Delta^2 + \left(y_e + \alpha\right)^2}} - r_p x_e - \sin\left(\chi_p\right)V_x + \cos\left(\chi_p\right)V_y \\ & + U_r \phi_1\left(y_e, \psi_e\right)\psi_e,\end{aligned} \tag{28}$$

where

$$\begin{aligned}\phi_1\left(y_e, \tilde{\psi}\right) = {} & \frac{\sin\left(\psi_e\right)}{\psi_e}\frac{\Delta}{\sqrt{\Delta^2 + \left(y_e + \alpha\right)^2}} \\ & - \frac{\cos\left(\psi_e\right) - 1}{\psi_e}\frac{y_e + \alpha}{\sqrt{\Delta^2 + \left(y_e + \alpha\right)^2}}.\end{aligned} \tag{29}$$

To eliminate the influence of the currents, α can be designed as

$$\alpha = \frac{y_e\theta_n^2 + \theta_n\sqrt{\Delta^2\left(1 - \theta_n^2\right) + y_e^2}}{1 - \theta_n^2}, \tag{30}$$

where

$$\theta_n = \frac{-\sin\left(\chi_p\right)V_x + \cos\left(\chi_p\right)V_y}{U_r}. \tag{31}$$

As the currents considered in this paper are much smaller than the speed of the vehicle, it is easy to conclude

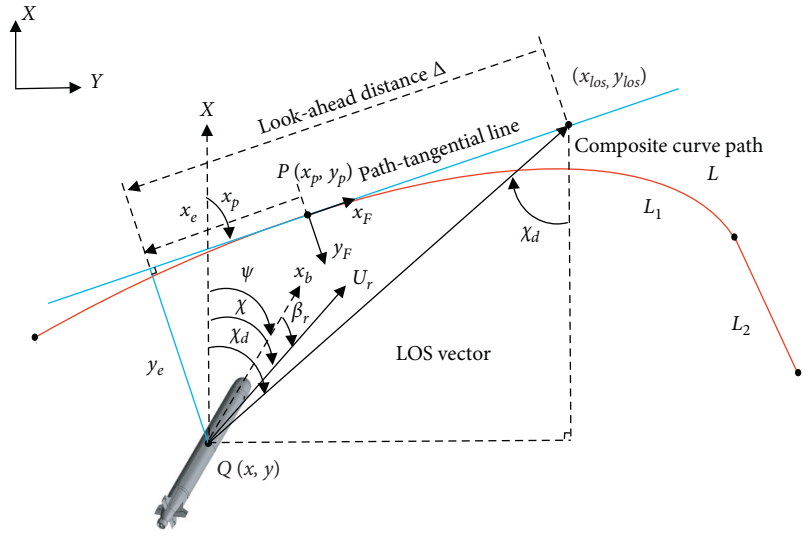

FIGURE 2: The kinematics description of path following in horizontal plane.

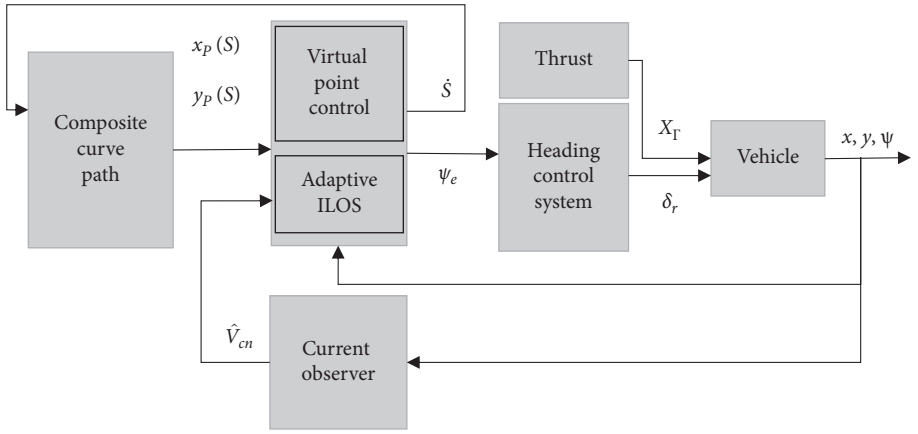

FIGURE 3: The cascade structures with a current observer.

that $|\theta_n| < 1$. Based on this assumption, there is no singularity in (30).

The first derivative of the kinematics error can be described as

$$\begin{cases} \dot{x}_e = -kx_e + r_p y_e, \\ \dot{y}_e = -\dfrac{U_r y_e}{\sqrt{\Delta^2 + (y_e + \alpha)^2}} - r_p x_e + U_r \phi(y_e, \psi_e)\psi_e. \end{cases} \tag{32}$$

Theorem 1. *Assume that $\psi_e = 0$, $U_r > 0$, $\Delta > 0$, and V_x and V_y are known. Furthermore, assume that U_p is computed using (22) and ψ_d is calculated as (24). Then, the equilibrium point $(x_e, y_e) = (0, 0)$ of the system (32) is globally k-exponentially stable.*

Proof. By substituting $\psi_e = 0$ into (32), the Lyapunov Function Candidate (LFC) $V_1 = (1/2)x_e^2 + (1/2)y_e^2$ has the time derivative

$$\begin{aligned} \dot{V}_1 &= x_e \dot{x}_e + y_e \dot{y}_e \\ &= -kx_e^2 - \frac{U_r y_e^2}{\sqrt{\Delta^2 + (y_e + \alpha)^2}}, \end{aligned} \tag{33}$$

which is negative since $k > 0$ and $U_r > 0$. Hence, the equilibrium point $[x_e, y_e]^2 = 0$ is uniformly globally asymptotically stable (UGAS) and uniformly locally exponentially stable (ULES) or globally k-exponentially stable [24].

However, currents are generally difficult to measure. To eliminate the influence of the unknown currents, the current observer is designed to predict the currents. The currents can be described as $V_{cn} = (V_x, V_y)^T$, and $\hat{V}_{cn}$ is the estimated value of V_{cn}. The position of AUV in $\{I\}$ can be express as $\eta_1 = (x, y)^T$, and $\hat{\eta}_1$ is the estimated value of η_1. According to (14), the derivative of η_1 can be expressed as

$$\dot{\eta}_1 = R(\psi)\nu_{1r} + V_{cn}. \tag{34}$$

Here, $\nu_{1r} = (u_r, v_r)$, and $R(\psi) = \begin{bmatrix} \cos(\psi) & -\sin(\psi) \\ \sin(\psi) & \cos(\psi) \end{bmatrix}$.

The current observer can be designed as [25]

$$\begin{cases} \dot{\widehat{V}}_{cn} = k_{ob1} I_2 (\eta_1 - \widehat{\eta}_1), \\ \dot{\widehat{\eta}}_1 = R(\psi)\nu_{1r} + \widehat{V}_{cn} + k_{ob2} I_2 (\eta_1 - \widehat{\eta}_1), \end{cases} \tag{35}$$

where $\widetilde{\eta}_1 = \eta_1 - \widehat{\eta}_1$ and $\widetilde{V}_{cn} = (V_{cn} - \widehat{V}_{cn})$

Assume that the currents are changing slowly relative to time, which means $\dot{V}_{cn} = 0$. Substituting (34) to (35) gives

$$\underbrace{\begin{bmatrix} \dot{\widetilde{V}}_{cn} \\ \dot{\widetilde{\eta}}_1 \end{bmatrix}}_{\dot{X}} = \underbrace{\begin{bmatrix} 0 & -k_{ob1} I_2 \\ I_2 & -k_{ob2} I_2 \end{bmatrix}}_{\mathbf{A}} \underbrace{\begin{bmatrix} \widetilde{V}_{cn} \\ \widetilde{\eta}_1 \end{bmatrix}}_{\mathbf{X}}, \tag{36}$$

where $k_{ob1} > 0$, $k_{ob2} > 0$. □

Theorem 2. *The current observer (36) is globally exponentially stable (GES) for static currents.*

Proof. Consider the following Lyapunov function candidate:

$$V_2 = \mathbf{X}^T \mathbf{P} \mathbf{X}, \tag{37}$$

where $\mathbf{X} = [\widetilde{V}_{cn}, \widetilde{\eta}_1]$; $\mathbf{P} = \mathbf{P}^T > 0$ is given by

$$\mathbf{P}\mathbf{A} + \mathbf{A}^T \mathbf{P} = -q\mathbf{I}_4, \tag{38}$$

where $q > 0$. Substitution of (36) into (38) gives

$$\mathbf{P} = \begin{bmatrix} q\dfrac{k_{ob1} + k_{ob2}^2 + 1}{2k_{ob1}k_{ob2}} I_2 & -\dfrac{1}{2} q I_2 \\ -\dfrac{1}{2} q I_2 & q\dfrac{k_{ob1} + 1}{2k_{ob2}} I_2 \end{bmatrix}. \tag{39}$$

When $k_{ob1} > 0$ and $k_{ob2} > 0$, it can be seen that the leading principal minors of $\mathbf{P}$ are positive. Hence, V_2 is positive definite.

The time derivative of V_2 is

$$\dot{V}_2 = \dot{X}^T \mathbf{P} \mathbf{X} + \mathbf{X}^T \mathbf{P} \dot{X}. \tag{40}$$

Substituting of (36) and (38) into (40) gives

$$\dot{V}_2 = -q\|\mathbf{X}\|^2. \tag{41}$$

Consequently, the equilibrium point $[\widetilde{V}_{cn}, \widetilde{\eta}_1]^T = 0$ is GES, according to Theorem 4.10 in [26]. □

4.2. Subpath Switching Algorithm. The path-tangential speed U_P of the virtual point is used as a control input to stabilize the along-track error. Moreover, according to (6), the first derivative of the parameter s of the virtual point w.r.t. time can be expressed as

$$\dot{s} = \frac{U_P}{\sqrt{x_p'(s)^2 + y_p'(s)^2}}. \tag{42}$$

It can be seen that $\dot{s}$ is singularity-free for all regular paths. Besides, the value of $\dot{s}$ is dependent on U_P and the parametrization of curves. As the composite curve path usually does not satisfy C^1 continuity, and each curve segment is parametrized differently, $\dot{s}$ is discontinuous at the waypoint.

Besides, as each curve segment with different characteristics is parametrized with the same parameter interval, the length of the curve segments will have a significant impact on the value of $\dot{s}$. Relatively, the equal amount of $\dot{s}$ will have a different meaning for different curve segments. Hence, the switching algorithm has to be considered for path following of the composite curve path, especially when the length of subpaths varies a lot.

The parameter s of the virtual point can be obtained from the numerical integration of $\dot{s}$. It can be expressed in Euler's method:

$$s_{k+1} = s_k + \dot{s}_k \Delta t = s_k + \Delta s_k. \tag{43}$$

When $s_k + \Delta s_k >= i$, the reference point will switch to the L_{i+1} subpath from the L_i curve segments. Considering the different effect of $\dot{s}$ for two curve segments, at this time, s_{k+1} cannot be calculated by (43) directly. The problem can be solved by setting $s_{k+1} = i$, which is the parameter of the starting point of L_{i+1} subpath, as the displacement of the reference point in a period is small and has little impact on the path following. Ultimately, the global path following for composite curve path can be achieved.

Besides, an additional path switching mechanism can be introduced to achieve better tracking effect at path switching, especially for the piecewise linear path with G^0 continuity. As shown in Figure 4, it is suggested that a so-called circle of acceptance is associated with each waypoint connecting two subpaths [8]. The switching criterion can be defined as

$$\left(x_{p_k} - x\right)^2 + \left(y_{p_k} - y\right)^2 \le R_k^2, \tag{44}$$

where R_k is the radius of the circle of acceptance. The magnitude of R_k can be determined by considering the turning ability of the AUV. Generally, the parameter R_k can be selected as $R_k \le \Delta$. After the criterion has been satisfied, the next curve segment will be followed.

Generally, for composite curve path following, each subpath switching can be regarded as the beginning of tracking a new path initialized by the current state of the AUV.

4.3. Heading Controller Design. To obtain the desired heading angle given by the guidance law, the heading control system is designed to make the heading error converge to zero.

A non-model-based NISM control algorithm is utilized to realize the heading control. The nonlinear sliding surfaces are designed as

$$\begin{cases} \sigma_1(\psi_e) = k_1 \tanh(k_2 \psi_e) + \dot{\psi}_e, \\ \sigma_2(\sigma_1) = k_3 \tanh(k_4 \sigma_1) + \dot{\sigma}_1, \end{cases} \tag{45}$$

where $k_i > 0 (i = 0, 1, \ldots, 4)$ are the control parameters, $\tanh(x)$ is a strictly bounded nonlinear hyperbolic tangent function, and σ_1 and σ_2 are designed slide mode surfaces.

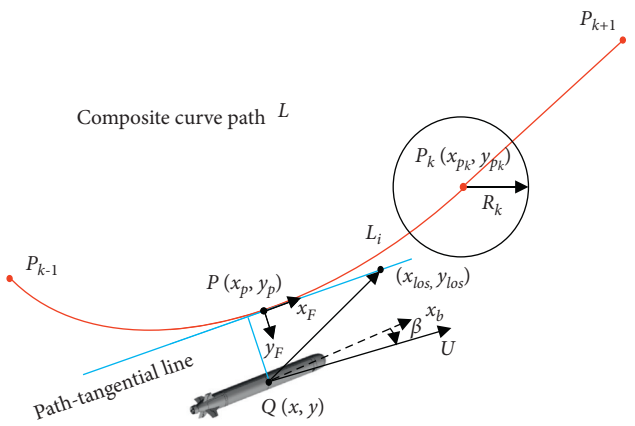

FIGURE 4: The subpath switching algorithm of the composite curve path.

To stabilize σ_1 and σ_2, the incremental feedback control law is designed as

$$\dot{\delta}_r = k_p \tanh(k_5\sigma_2) + k_s \operatorname{sgn}(\sigma_2), \tag{46}$$

where $\dot{\delta}_r$ is the derivative of the rudder angle.

Different from the standard NISM controller [27], $\tanh(x)$ is used for the incremental feedback calculation of $\dot{\delta}_r$. By considering the discontinuity of the connection point between two curve segments, the value of σ_2 may become very large suddenly. This will cause excessive rudder speed which is not practical and may cause damage to the rudder system. Hence, in (46), k_p can be used to limit the maximum rudder speed. When there is time-varying interference, k_s can be set to a smaller value to ensure the stability of the control system. The signs of k_p and k_s are selected relating to the definition of the rudder. For the model of the REMUS vehicle, the rudder angle is defined as positive, when the resulting force causes the vehicle to turn left. Hence, k_p and k_s are selected to be positive. In addition, k_5 is also selected to be positive, which is used to adjust the range of coordinate where $\dot{\delta}_r$ is varying at an exponential rate.

According to (45), when $\sigma_2 = 0$, one can obtain

$$\dot{\sigma}_1 = -k_3 \tanh(k_4\sigma_1). \tag{47}$$

Hence,$\sigma_1 \longrightarrow 0$. Similarly, when $\sigma_1 = 0$, one can obtain

$$\dot{\psi}_e = -k_1 \tanh(k_2\psi_e). \tag{48}$$

Hence, $\psi_e \longrightarrow 0$. This means that the heading error will converge to zero when $\sigma_2 = 0$. According to (47) and (48) and the properties of the hyperbolic function, it can be known that when $k_4\sigma_1$ and $k_2\psi_e$ are large, σ_1 and ψ_e will tend to zero at a fixed rate. Moreover, when $k_4\sigma_1$ and $k_2\psi_e$ are small, σ_1 and ψ_e will exponentially converge to zero. Besides, k_3 and k_1 determine the maximum attenuation rate of σ_1 and ψ_e, and k_4 and k_2 are used to adjust the range of coordinate where σ_1 and ψ_e are decaying at an exponential rate.

Theorem 3. *Assume that the sliding mode surfaces (45) and the incremental feedback control law (46) are used for the heading autopilot system, the definition of the sign of the rudder is known* $((\partial\dot{r}/\partial\delta_r) < 0)$*, and* $k_p > 0$*,* $k_s \geq 0$*; then, the equilibrium point* $\psi_e = 0$ *is globally k-exponentially stable.*

Proof. The Lyapunov Function Candidate (LFC) $V_3 = (1/2)\sigma_2^2$ has the time derivative

$$\dot{V}_3 = \sigma_2 \frac{\partial\sigma_2}{\partial\delta_r}\dot{\delta}_r. \tag{49}$$

According to (45),

$$\sigma_2(\sigma_1) = k_3 \tanh(k_4\sigma_1) + k_1k_2r_e \sec^2(k_2\psi_e) + \dot{r}_e, \tag{50}$$

where $r_e = r - r_d$. According to (18) and (19) and the parameters of the REMUS AUV, ignoring the variables independent of δ_r, one can obtain

$$\frac{\partial\sigma_2}{\partial\delta_r} = \frac{\partial\dot{r}}{\partial\delta_r} < 0. \tag{51}$$

According to (45), it can be known that

$$\sigma_2\dot{\delta}_r = k_p\sigma_2 \tanh(k_5\sigma_2) + k_s|\sigma_2| \geq k_p\sigma_2 \tanh(k_5\sigma_2) \geq 0. \tag{52}$$

Hence, it can be derived that

$$\dot{V}_3 \leq k_p\sigma_2 \tanh(k_5\sigma_2)\frac{\partial\sigma_2}{\partial\delta_r} \leq 0. \tag{53}$$

Depending on the properties of the hyperbolic function and Lyapunov stability theory, it can be concluded that $\sigma_2 = 0$ is UGAS and ULES or globally k-exponentially stable. Similarly, according to (47) and (48), $\psi_e = 0$ is globally k-exponentially stable. □

4.4. Stability of the Cascade System. Consider the following cascade system:

$$\begin{cases} \dot{x}_{pt} = f_1(t, x_{pt}) + g(t, x_{pt}, y_{pt})y_{pt}, \\ \dot{y}_{pt} = f_2(t, y_{pt}). \end{cases} \tag{54}$$

System (54) can be regarded as

$$\sum_{1pt}: \ \dot{x}_{pt} = f_1(t, x_{pt}), \tag{55}$$

which is perturbed by the output of the system

$$\sum_{2pt}: \ \dot{y}_{pt} = f_2(t, y_{pt}). \tag{56}$$

Besides, the theorems proposed by [13] can be used to prove the stability of the cascade system. To be convenient, the theorems are presented here.

Theorem 4. *Cascaded system (54) is GUAS if the following three assumptions hold:*

(i) Assumption on $\sum_{1pt}$: the system $f_1(t, x_{pt})$ is GUAS and there exists a continuously differentiable function $V(t, x_{pt})$: $IR_{\geq 0} \times IR^n \longrightarrow IR$ that satisfies

$$W_x \leq V\left(t, x_{pt}\right),$$
$$\frac{\partial V}{\partial t} + \frac{\partial V}{\partial x_{pt}} \cdot f_1\left(t, x_{pt}\right) \leq 0, \quad \forall \left\| x_{pt} \right\| \geq \eta_{pt}, \tag{57}$$
$$\left\| \frac{\partial V}{\partial x_{pt}} \right\| \cdot \left\| x_{pt} \right\| \leq c_{pt} V\left(t, x_{pt}\right) 0, \quad \forall \left\| x_{pt} \right\| \geq \eta_{pt},$$

where W_x is a positive definite proper function and $c_{pt} > 0$ and $\eta_{pt} > 0$ are constants.

(ii) Assumption on the interconnection: the function $g(t, x_{pt}, y_{pt})$ satisfies for all $t \geq t_0$

$$\left\| g\left(t, x_{pt}, y_{pt}\right) \right\| \leq \theta_1\left(\left\| y_{pt} \right\| \right) + \theta_2\left(\left\| y_{pt} \right\| \right) \left\| x_{pt} \right\|, \tag{58}$$

where θ_1, θ_2: $IR_{\geq 0} \longrightarrow IR_{\geq 0}$ are continuous functions.

(iii) Assumption on $\sum_{2pt}$: the system $\sum_{2pt}$ is GUAS and for all $t_0 \geq 0$

$$\int_{t_0}^{\infty} \left\| y_{pt}\left(t, t_0, y_{pt}\left(t_0\right)\right) \right\| \mathrm{d}t \leq \kappa y_{pt}\left(\left\| t_0 \right\| \right), \tag{59}$$

where the function $\kappa(\cdot)$ is a class κ function [24].

Theorem 5. *In addition to the assumptions in Theorem 4, if both $\sum_{1pt}$ and $\sum_{2pt}$ are globally κ-exponentially stable, then cascaded system (54) is globally κ-exponentially stable.*

For path following under the disturbance of unknown static currents, the stability of cascade system can be proved in two steps. First, without considering the currents, the cascade system described in Theorem 6 can prove to be globally κ-exponentially stable. Then, based on Theorem 6, the cascade system including a current observer can prove to be globally κ-exponentially stable under the influence of unknown static currents.

Theorem 6. *Without considering the currents, the guidance system expressed as (32) and the heading control system described by (45) and (56) can be analyzed as a cascade structure, which is globally κ-exponentially stable at $(x_e, y_e, \psi_e) = (0, 0, 0)$.*

Proof. The cascade can be described as

$$\Sigma_1^1: \begin{cases} \dot{x}_e = -k_1 x_e + r_p y_e, \\ \dot{y}_e = -\dfrac{U_r y_e}{\sqrt{\Delta^2 + \left(y_e + \alpha\right)^2}} - r_p x_e + U_r \phi\left(y_e, \psi_e\right) \psi_e, \end{cases} \tag{60}$$

$$\Sigma_2^1: \dot{\psi}_e = f_1\left(t, \psi_e\right), \tag{61}$$

where $\dot{\psi}_e = f_1(t, \psi_e)$ define the heading error dynamics corresponding to (45).

To prove Theorem 6, the three assumptions in Theorem 4 need to be verified. The nominal system of Σ_1^1 (when $\psi_e = 0$) is

$$\Sigma_{1^*}^1: \begin{cases} \dot{x}_e = -k_1 x_e + r_p y_e, \\ \dot{y}_e = -\dfrac{U_r y_e}{\sqrt{\Delta^2 + \left(y_e + \alpha\right)^2}} - r_p x_e. \end{cases} \tag{62}$$

The LFC is selected as $V_1 = (1/2)x_e^2 + (1/2)y_e^2$, and, according to (33), it is known that $\dot{V}_1 \leq 0$. Hence, the assumption on $\sum_{1*}$ is always satisfied when $c \geq 2$.

Besides, the interconnection term satisfies $|\phi(y_e, \widetilde{\psi})| < = c$, and $c = 1.73$ is the upper bound [12]. Hence, the assumption on the interconnection is also satisfied.

As Σ_2^1 is globally*k*-exponentially stable, the last assumption is also satisfied. Hence, all conditions of Theorem 4 and Theorem 5 are satisfied, and the cascade system is globally *k*-exponentially stable.

Considering the prediction error of observer, the cascade structure can be described as

$$\Sigma_1^2: \begin{cases} \dot{x}_e = -k_1 x_e + r_p y_e + \phi_2\left(\widetilde{V}_{cn}\right), \\ \dot{y}_e = -\dfrac{U_r y_e}{\sqrt{\Delta^2 + \left(y_e + \alpha\right)^2}} - r_p x_e + U_r \phi\left(y_e, \psi_e\right) \psi_e + \phi_3\left(\widetilde{V}_{cn}\right), \\ \dot{\psi}_e = f_1\left(\psi_e\right), \end{cases}$$
$$\Sigma_2^2: \dot{\widetilde{V}}_{cn} = f_2\left(\widetilde{V}_{cn}\right), \tag{63}$$

where

$$\begin{aligned} \phi_2\left(\widetilde{V}_{cn}\right) &= \cos\left(\chi_p\right) \widetilde{V}_x + \sin\left(\chi_p\right) \widetilde{V}_y, \\ \phi_3\left(\widetilde{V}_{cn}\right) &= -\sin\left(\chi_p\right) \widetilde{V}_x + \cos\left(\chi_p\right) \widetilde{V}_y. \end{aligned} \tag{64}$$

□

Theorem 7. *Assume that the currents are changing slowly relative to time and the current observer is designed as (35); by considering the prediction error, the guidance and heading control system expressed as (60) and (61) can be cascaded with the current observer, and the cascade structure is globally k-exponentially stable.*

Proof. The nominal system (Σ_1^2 system with $\widetilde{V}_{cn} = 0$) has proved to be globally k-exponentially stable in Theorem 6. Hence, according to converse Lyapunov theory in [26], there exists Lyapunov function $V_4 = (x_e, y_e, \psi_e)$ that satisfies the assumption on the nominal system. Besides, as the trigonometric functions are strictly bounded and the $\widetilde{V}_{cn}$ is bounded, it can be concluded that $\phi_2(\widetilde{V}_{cn})$ and $\phi_3(\widetilde{V}_{cn})$ are bounded. Moreover, the current observer is GES. Hence, all conditions of Theorem 4 and Theorem 5 are satisfied, and the cascade system is globally k-exponentially stable. □

5. Simulation Results

To verify the effectiveness of the control system for the composite curve path following, three simulation cases are carried out. Case 1 is implemented to verify the performance of the proposed path following controller for the composite curve path without currents. Besides, the PID control and the conventional sliding mode control are introduced as the heading controller to be compared with the improved NISM controller. Based on Case 1, Case 2 is carried out to prove the effectiveness of the additional subpath switching algorithm. In Case 3, unknown static currents are introduced to test the anti-interference ability of the controller based on the current observer.

The composite curve path is designed to contain G0, G1, and G2 continuity at the same time and is composed of seven subpaths, including straight lines, circular arcs, and Fermat's spirals. The parameters of the composite curve path and the controller are shown in Tables 3 and 4. As most parameters of the guidance and heading control system have a clear physical meaning, the parameters are based on hand tuning. The values of the look-ahead distance Δ and the heading control parameter k_p have obvious influence on the control effect and can also be adjusted automatically. Relevant methods can be found in [3, 16].

5.1. Case 1: Path following without Currents. For path following with no currents, $V_x = 0$ and $V_y = 0$. Due to the cascade structure design, the adaptive integral guidance law can be flexibly combined with heading controllers to achieve the desired path tracking. The PID control and conventional sliding mode control [12] are introduced as the heading controller to be compared with the improved NISM controller. The desired composite path and the trajectory of path following are shown in Figure 5. It can be concluded that, by the path parametrization according to (1) and the control of virtual point as (24), the global path planning for composite curve path can be realized.

As shown in Figure 6, compared with the PID control and conventional sliding mode control, the NISM control has faster convergence speed and smaller steady-state error. Besides, the NISM control adopts the incremental feedback control law, which is not based on the model parameters. Hence, it is not easily affected by the uncertainty of the model parameters. In Figure 7, after modifying the value of the hydrodynamic parameter $N_{uu\delta}$ from −6.15 to −4.15, the NISM control can still maintain the heading control, while the conventional sliding mode control produces control error.

Table 3: Parameters of the composite curve path.

No.	Subpath type	Parameter	Value
1	Straight line	(x_0, y_0)	$(-20, 20)$
		L	$200\sqrt{2}$
		χ_l	$\pi/4$
2	Straight line	(x_0, y_0)	$(180, 220)$
		L	200
		χ_l	$\pi/2$
3	Circular arc	(c_{x0}, c_{y0})	$(80, 420)$
		R	100
		α_0	0
		α_1	π
4	Straight line	(x_0, y_0)	$(-20, 420)$
		L	154.9566
		χ_l	$-\pi/2$
5\6	Fermat's spiral	(x_0, y_0)	$(-20, 265.0434)$
		$(x_{\text{end}}, y_{\text{end}})$	$(0, 0)$
		θ_{end}	0.1329
		χ_0	$-\pi/2$
		χ_{end}	$-\pi/4$
		ρ	1
7	Straight line	(x_0, y_0)	$(11.8505, 188.1495)$
		L	237.7993
		χ_l	$-\pi/4$

Table 4: Parameters of the guidance and control system.

Parameter	Value
Δ	6
k	1
k_1	0.8
k_2	1.5
k_3	0.8
k_4	1
k_5	15
k_p	0.1745
k_s	0
X_Γ	$6.48N$
k_{ob1}	1
k_{ob2}	1
R_k	6

The degree of the GC has a high impact on the control of path following. Comparatively, G_1 and G_2 paths have less effect on the path following. However, for G_0 paths, there will be an apparent deviation due to the sudden change of the desired heading angle ψ_d. Hence, G_0 paths are not suitable for path following of underactuated vehicle, and an additional path switching mechanism (44) is required to handle this problem.

The discontinuity of the connection point between two curve segments will cause excessive rudder speed which is not practical and may cause damage to the rudder system. Strictly bounded nonlinear hyperbolic tangent function is used in the NISM control, and the parameter k_p can be used to limit the maximum rudder speed. In Figure 8, the rudder

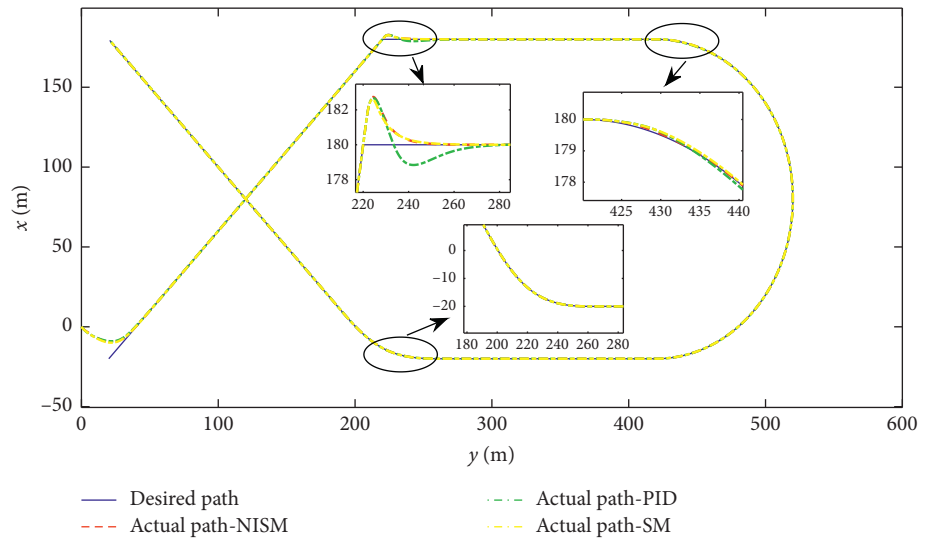

Figure 5: The planned composite curve path and the actual trajectory.

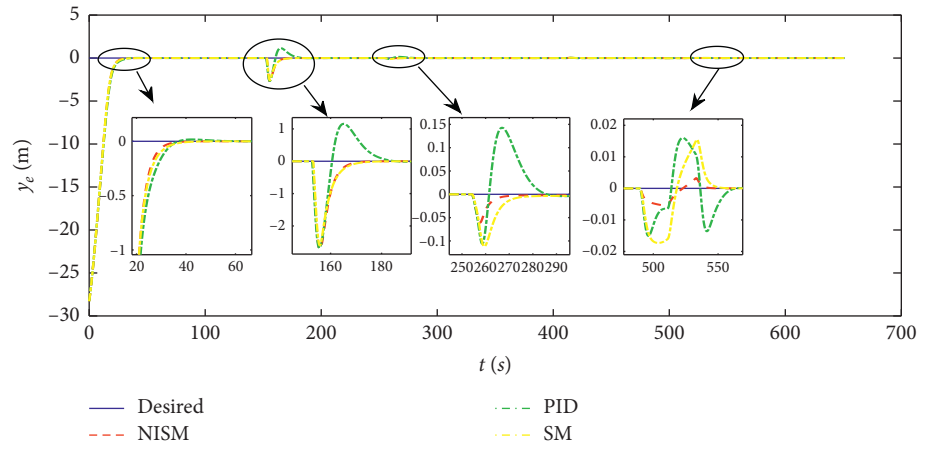

(a)

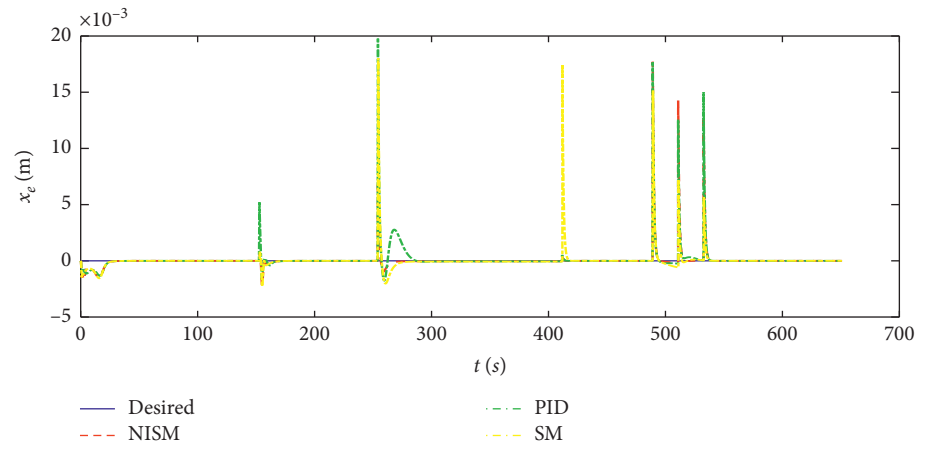

(b)

Figure 6: Continued.

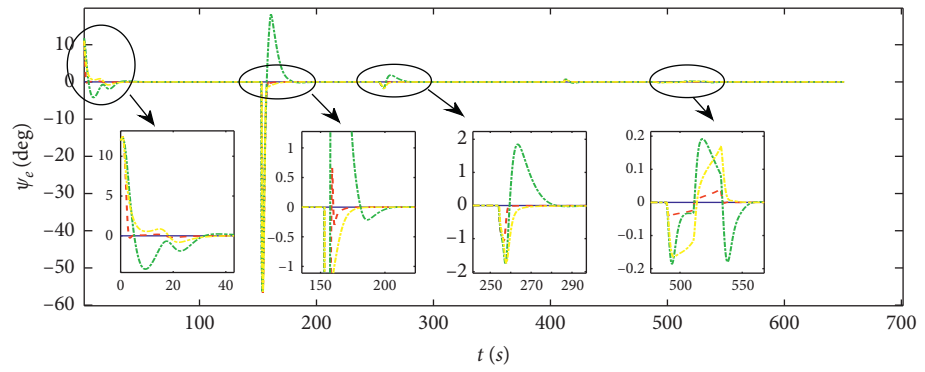

(c)

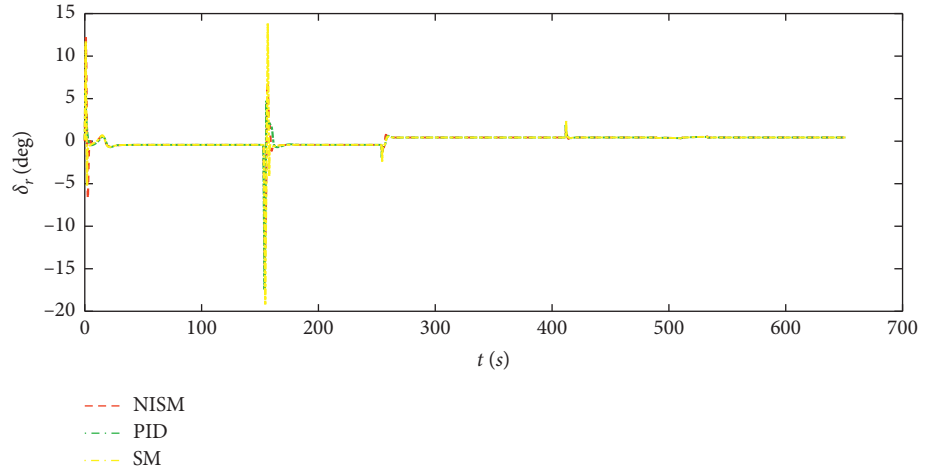

(d)

Figure 6: The tracking error and the heading control error without currents.

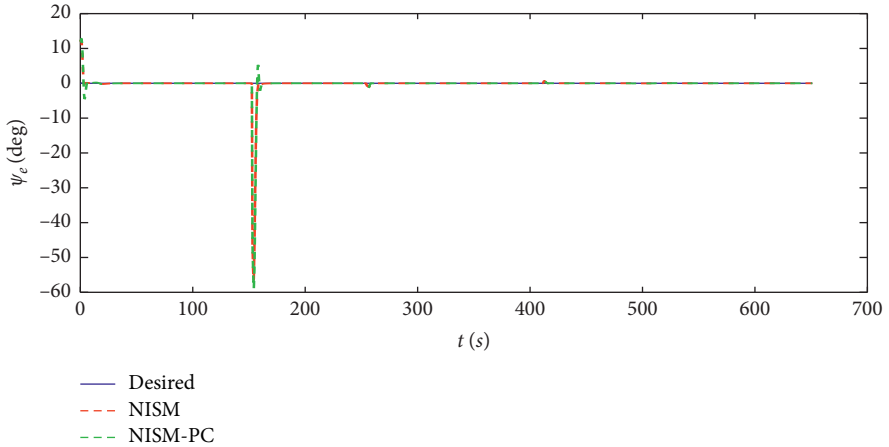

(a)

Figure 7: Continued.

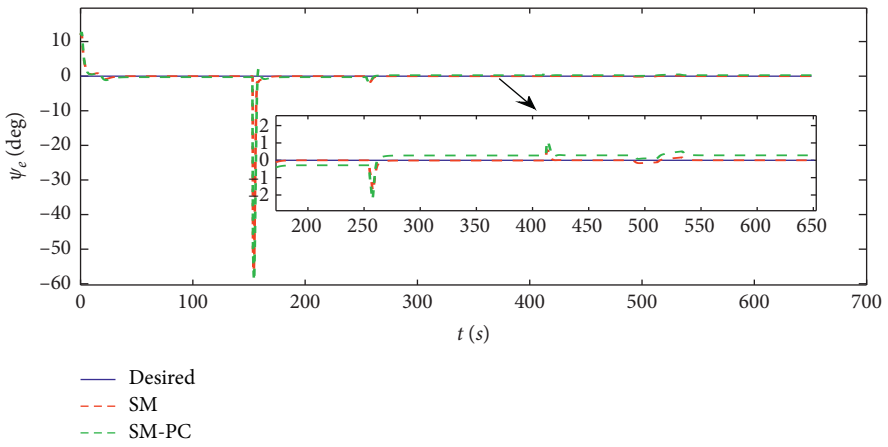

(b)

Figure 7: The comparison of the heading control effect after changing the model parameter.

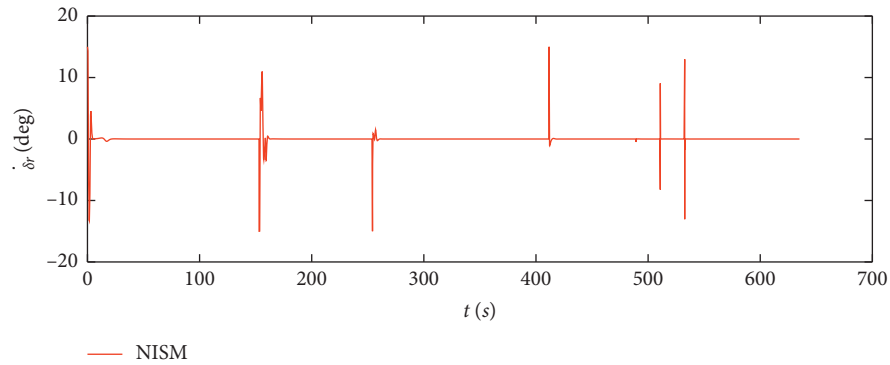

Figure 8: The rudder control of the NISM controller.

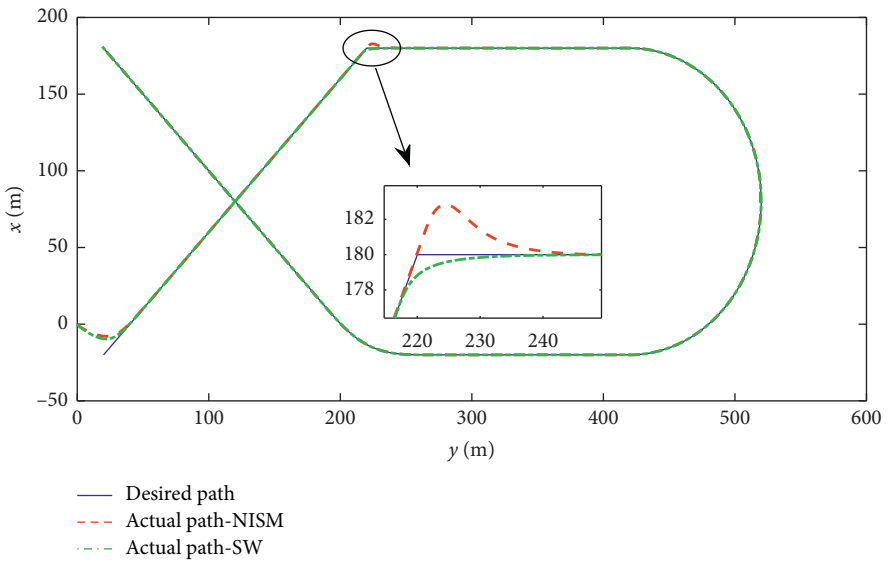

Figure 9: The planned composite curve path and the actual trajectory.

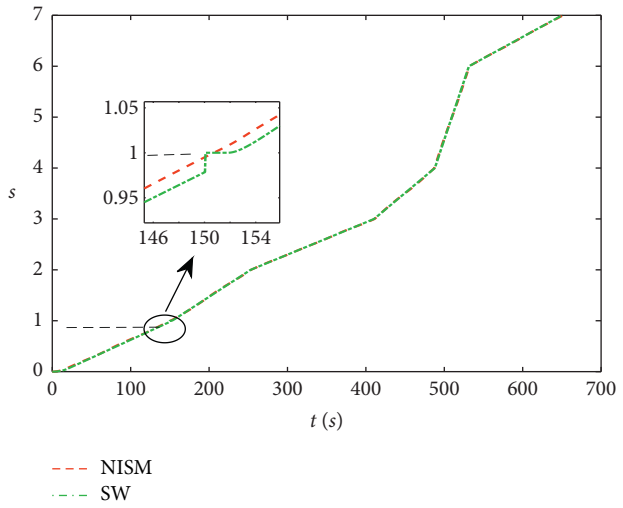

Figure 10: The parameter value of the virtual point.

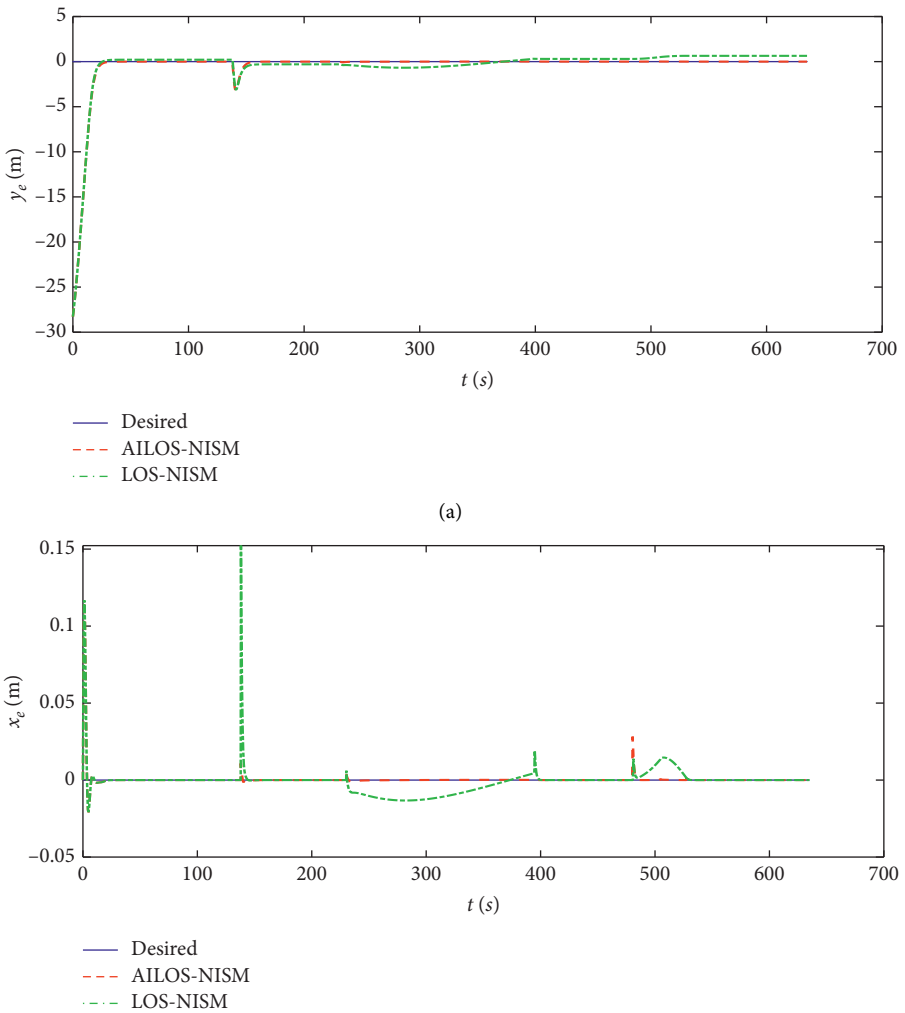

Figure 11: The tracking error under constant currents.

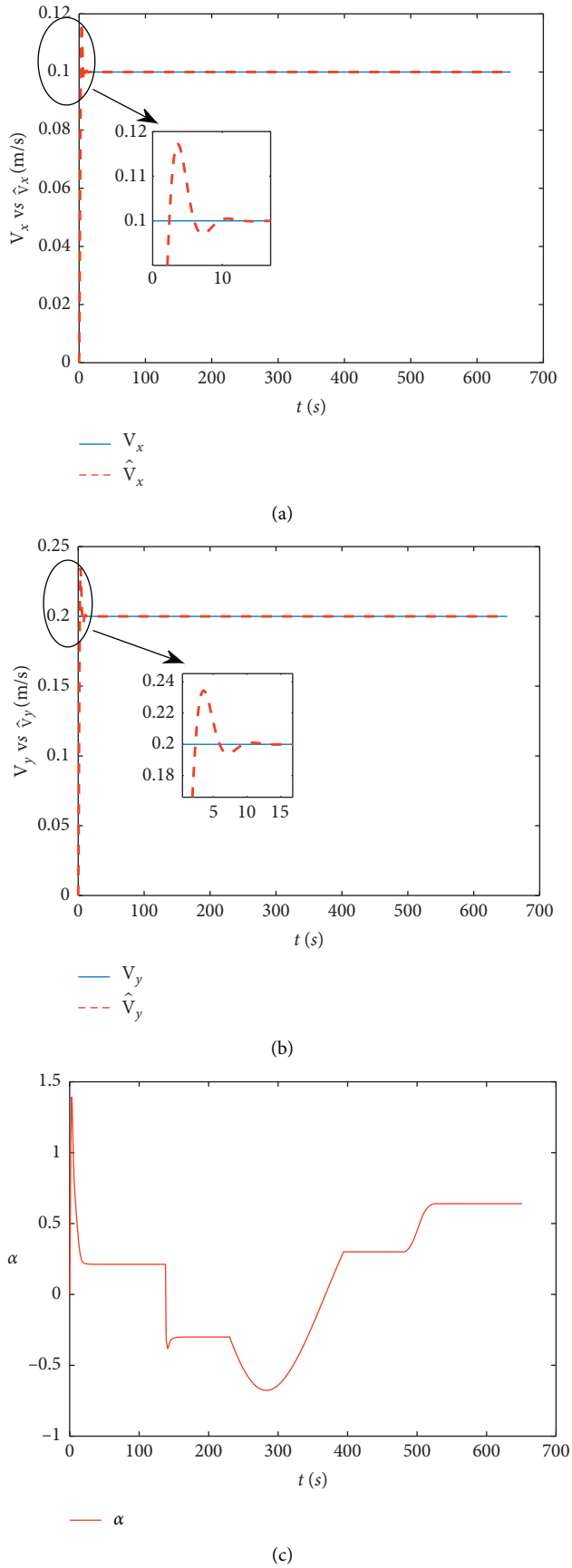

Figure 12: The estimate of constant currents and the compensation coefficient.

speed is limited to 15°/s. Hence, the proposed NISM control is more suitable for the composite curve path following.

5.2. Case 2: Subpath Switching Algorithm. From Case 1, it is known that the tracking trajectory deviates from the desired path obviously at the switching point due to the sudden change of the heading angle for G_0 paths. Hence, in Case 2, an additional path switching mechanism (44) is used to handle this problem.

As shown in Figures 9 and 10, after using the additional path switching algorithm, the vehicle will track the next subpath early near the connection point when the switching criterion is satisfied. In addition, in this way, the tracking error between two subpaths can be reduced obviously.

5.3. Case 3: Path following Unknown Static Currents. For path following with static currents, V_x and V_y are constant values, where V_x is 0.1 (m/s) and V_y is 0.2 (m/s). The simulation results are as follows.

From Figure 11, we can see that, without the current observer, the path following controller will produce certain tracking error under the disturbance of unknown current especially for the curve paths. Besides, from Figure 12, it can be concluded that the currents can be well estimated by the designed observer. Then, the influence of currents can be eliminated at the kinematics level with U_p and α calculated as (22) and (30). Finally, by the cascade structure composed of AILOS guidance and the improved NISM controller, the vehicle can converge to and move along the desired composite curve path.

6. Conclusion

This paper addresses the problems of composite curve path following for an underactuated AUV in the horizontal plane. The global path following of the composite curve path is realized by the virtual point control and the subpath switching algorithm after the parametrization of the composite curve and description of the kinematics error. Besides, the cascade structure composed of AILOS guidance and the improved NISM control proved to be UGAS under the influence of constant currents. Future work will expand the application of the composite curve path following to three-dimensional space.

Data Availability

Partial data used to support the findings of this study are available from the corresponding author upon request.

Conflicts of Interest

The authors declare that there are no conflicts of interest regarding the publication of this paper.

Acknowledgments

This work was supported in part by the National Natural Science Foundation of China (Grant no. 52001132) and Special Funds for Basic Scientific Research in Central Universities of China (Grant no. 2662020GXQD003).

References

[1] C. Yu, C. Liu, L. Lian, X. Xiang, and Z. Zeng, "ELOS-based path following control for underactuated surface vehicles with actuator dynamics," *Ocean Engineering*, vol. 187, p. 106139, 2019.

[2] J. Nie and X. Lin, "Improved adaptive integral line-of-sight guidance law and adaptive fuzzy path following control for underactuated MSV," *ISA Transactions*, vol. 94, pp. 151–163, 2019.

[3] A. M. Lekkas and T. I. Fossen, "Integral LOS path following for curved paths based on a monotone cubic hermite spline parametrization," *IEEE Transactions on Control Systems Technology*, vol. 22, no. 6, pp. 2287–2301, 2014.

[4] Z. Zeng, L. Lian, K. Sammut, F. He, Y. Tang, and A. Lammas, "A survey on path planning for persistent autonomy of autonomous underwater vehicles," *Ocean Engineering*, vol. 110, pp. 303–313, 2015.

[5] Y. A. Kapitanyuk and S. A. Chepinsky, "Control of mobile robot following a piecewise-smooth path," *Gyroscopy and Navigation*, vol. 4, no. 4, pp. 198–203, 2013.

[6] T. I. Fossen, K. Y. Pettersen, and R. Galeazzi, "Line-of-Sight path following for Dubins paths with adaptive sideslip compensation of drift forces," *IEEE Transactions on Control Systems Technology*, vol. 23, no. 2, pp. 820–827, 2015.

[7] L. Liu, D. Wang, and Z. Peng, "Path following of marine surface vehicles with dynamical uncertainty and time-varying ocean disturbances," *Neurocomputing*, vol. 173, pp. 799–808, 2016.

[8] T. I. Fossen, M. Breivik, and R. Skjetne, "Line-of-sight path following of underactuated marine craft," *IFAC Proceedings Volumes*, vol. 36, no. 21, pp. 211–216, 2003.

[9] A. J. Healey and D. B. Marco, "Slow speed flight control of autonomous underwater vehicles: experimental results with NPS AUV II," *Isope*, vol. 11, 1992.

[10] E. Borhaug and K. Y. Pettersen, "Cross-track control for underactuated autonomous vehicles," in *Proceedings of the 44th IEEE Conference on Decision and Control*, pp. 602–608, Seville, Spain, December 2005.

[11] E. Borhaug, A. Pavlov, and K. Y. Pettersen, "Integral LOS control for path following of underactuated marine surface vessels in the presence of constant ocean currents," in *Proceedings of the 2008 47th IEEE Conference on Decision and Control*, pp. 4984–4991, Cancun, Mexico, December 2008.

[12] T. I. Fossen and A. M. Lekkas, "Direct and indirect adaptive integral line-of-sight path-following controllers for marine craft exposed to ocean currents," *International Journal of Adaptive Control and Signal Processing*, vol. 31, no. 4, pp. 445–463, 2017.

[13] E. Panteley, E. Lefeber, A. Loria, and H. Nijmeijer, "Exponential tracking control of a mobile car using a cascaded approach," *IFAC Proceedings Volumes*, vol. 31, no. 27, pp. 201–206, 1998.

[14] Y. Xia, K. Xu, W. Wang, G. Xu, X. Xiang, and Y. Li, "Optimal robust trajectory tracking control of a *X*-rudder AUV with velocity sensor failures and uncertainties," *Ocean Engineering*, vol. 198, p. 106949, 2020.

[15] K. Shojaei and M. Dolatshahi, "Line-of-sight target tracking control of underactuated autonomous underwater vehicles," *Ocean Engineering*, vol. 133, pp. 244–252, 2017.

[16] G. Wang, G. Xu, G. Liu, W. Wang, and B. Li, "Fuzzy iterative sliding mode control applied for path following of an autonomous underwater vehicle with large inertia," *Mathematical Problems in Engineering*, vol. 2019, Article ID 8650243, 14 pages, 2019.

[17] R. Skjetne, *The Maneuvering Problem*, Norwegian University of Science and Technology, Trondheim, Norway, 2005.

[18] M. Breivik and T. I. Fossen, *Guidance Laws for Autonomous Underwater Vehicles*, Springer, Berlin, Germany, 2009.

[19] A. M. Lekkas, *Guidance and Path-Planning Systems for Autonomous Vehicles*, Norwegian University of Science and Technology, Trondheim, Norway, 2014.

[20] T. Timothy and J. Prestero, "Verification of a six-degree of freedom simulation model for the REMUS autonomous underwater vehicle," Thesis, Massachusetts Institute of Technology, Cambridge, MA, USA, 2001.

[21] T. I. Fossen, "How to incorporate wind, waves and ocean currents in the marine craft equations of motion," *IFAC Proceedings Volumes*, vol. 45, no. 27, pp. 126–131, 2012.

[22] X. Xiang, L. Lapierre, and B. Jouvencel, "Smooth transition of AUV motion control: from fully-actuated to under-actuated configuration," *Robotics and Autonomous Systems*, vol. 67, pp. 14–22, 2015.

[23] M. Breivik and T. I. Fossen, "Path following for marine surface vessels," in *Proceedings of the Oceans '04 MTS/IEEE Techno-Ocean '04 (IEEE Cat. No.04CH37600)*, pp. 2282–2289, Kobe, Japan, November2004.

[24] O. J. Sordalen and O. Egeland, "Exponential stabilization of nonholonomic chained systems," *IEEE Transactions on Automatic Control*, vol. 40, no. 1, pp. 35–49, 1995.

[25] F. Alonge, F. D'lppolito, and F. M. Raimondi, "Trajectory tracking of underactuated underwater vehicles," *in Proceedings of the the 40th IEEE Conference on decision and Control*, vol. 6, Orlando, FL, USA, December, 2001.

[26] H. K. Khalil, *Nonlinear Systems*, Prentice-Hall, Upper Saddle River, NJ, USA, 3rd edition, 2002.

[27] C. Dai, N. Zhang, and Z. Shen, "An adaptive nonlinear iterative sliding mode controller based on heuristic critic algorithm," in *Proceedings of the 2016 IEEE International Conference on Information and Automation (ICIA)*, pp. 419–424, Ningbo, China, August 2016.

Hindawi
Mathematical Problems in Engineering
Volume 2021, Article ID 6654193, 14 pages
https://doi.org/10.1155/2021/6654193

Research Article

Fixed-Time Synchronization for Dynamical Complex Networks with Nonidentical Discontinuous Nodes

Xiaoliang Qian,[1] Qian Liu,[1] Qingbo Li,[2] Qi Yang,[1] Yuanyuan Wu ,[3] and Wei Wang [1]

[1]*College of Electric and Information Engineering, Zhengzhou University of Light Industry, Zhengzhou 450002, China*
[2]*College of Mathematics and Information Science, Zhengzhou University of Light Industry, Zhengzhou 450002, China*
[3]*School of Information and Communication Engineering, Hainan University, Haikou 570228, China*

Correspondence should be addressed to Yuanyuan Wu; wyuanyuan82@163.com and Wei Wang; wangwei-zzuli@zzuli.edu.cn

Received 18 December 2020; Revised 3 February 2021; Accepted 27 February 2021; Published 19 March 2021

Academic Editor: Shihong Ding

This article investigates the fixed-time synchronization issue for linearly coupled complex networks with discontinuous nonidentical nodes by employing state-feedback discontinuous controllers. Based on the fixed-time stability theorem and linear matrix inequality techniques, novel conditions are proposed for concerned complex networks, under which the fixed-time synchronization can be realized onto any target node by using a set of newly designed state-feedback discontinuous controllers. To some extent, this article extends and improves some existing results on the synchronization of complex networks. In the final numerical example section, the Chua circuit network is introduced to indicate the effectiveness of our method by showing its fixed-timely synchronization results with the proposed control scheme.

1. Introduction

As we know, in the last few decades, complex networks have been widely presented in our real world, for example, electrical power grids, metabolic pathways, neural networks, food webs, and World Wide Web [1–5]. Synchronization is a well-known crucial collective behavior for complex networks, so the synchronization of complex networks has received more attention due to many crucial applications [6–8] in information processing, secure communication, and biological systems [9–12]. Up to now, there are many research studies on complex network synchronization, most of which focus on asymptotic synchronization, mainly on asymptotic synchronization behavior [13–15] and exponential synchronization results [16], but the two kinds of synchronization belong to the infinite-time category [17–19].

Since it has been found that finite-time control ways will further enhance the rate of convergence greatly and synchronization will be performed in a settling time by designing appropriate finite-time synchronization controllers, the finite-time synchronization research [20–25] in complex networks has been carried out one after another [26–30]. In [20], the issue of the finite-time synchronization is studied between complex networks with nondelay and delay coupling by using pulse control and periodic intermittent control. By use of aperiodically intermittent control, Liu et al. [21] considered the finite-time synchronization problem in dynamic networks with time delay. The global random finite-time synchronization issue is investigated in [22] for discontinuous semi-Markov switched neural networks with time delay and noise interference. The finite-time synchronization analysis of linear coupled complex networks is discussed [23] with discontinuous nonidentical nodes.

The convergence rate of classical finite-time synchronization is relatively fast in contrast to asymptotic synchronization and exponential synchronization. However, it has an obvious disadvantage that the synchronization convergence rate of complex networks depends on the initial states of all nodes. Unfortunately, it is very difficult or even impossible for some chaotic systems to know their state previously. In these results, the finite-time control methods may be ineffective. Taking advantage of the benefits of finite-

time control, a special finite-time synchronization is proposed in [20]. As for the novel fixed-time synchronization, the settling time has no relation with the initial conditions of the network system and only depends on the control parameters of the system controller, see [21, 22]. Thus, synchronization can be accomplished by using the fixed-time controller within a specified time. This remarkable characteristic makes fixed-time synchronization control more desirable than other synchronization controls and improves its practical application range. Therefore, fixed-time synchronization control of complex networks has received more attention [23–25, 31–34].

Moreover, if the dynamics of the nodes are different, then the synchronization issue will be more complex and challenging than the same node condition. By using the free matrix, the equilibrium solution synchronization is concerned on all alone nodes together with the average state trajectory synchronization of different nodes in [35]. The intermittent controller is employed to fix the complex network with different nodes in [36]. In [37], the cluster synchronization problem is investigated for complex dynamic networks with time-delay coupling and nonidentical nodes by the pinning control method. Furthermore, the finite-time synchronization issue is considered for coupled complex networks with discontinuous nonidentical nodes in [23].

Recently, the complex networks with perturbations have attracted more attention for their wide applications [38–43]. In [40], the global exponential synchronization issue is studied for linear coupled neural networks with impulsive disturbance and time-varying delay. The clustering synchronization scheme is deeply concerned with regard to uncertain delayed complex networks in [41]. The adaptive pinning control design is proposed in [42] for the clustering synchronization problem of coupled complex networks with uncertain disturbances.

Until now, there are several research results on the finite-time synchronization of complex networks with different nodes or uncertain disturbances, mostly about the asymptotic or exponential synchronization. However, it has not been fully investigated for the fixed-time synchronization analysis of heterogeneous networks with uncertain disturbances, and the relevant research results are rarely covered. In a word, it is indispensable and significant to consider the fixed-time synchronization problem of complex networks with different nodes and uncertain disturbances, which has profound theoretical and practical significance. From the above analysis, we face two difficulties: (i) what conditions are applicable and easy to verify for general complex networks with different nodes and uncertain disturbances? (ii) How to design the controller to overcome heterogeneity and uncertain disturbance of network nodes? This paper tries to conquer these two difficulties and realize the fixed-time synchronization of a certain kind of complex linear coupled networks with different nodes and uncertain disturbances, and then the theoretical results of network synchronization can be further enriched.

Applying the discontinuous control scheme, the fixed-time synchronization problem is analysed for complex networks with uncertain disturbances and nonidentical nodes. Our main contributions here can be concluded as follows: (1) for a class of heterogeneous networks with uncertain disturbances, a novel state-feedback discontinuous controller is designed to get over the influence on the fixed-time synchronization from heterogeneous nodes and uncertain disturbances simultaneously; (2) several criteria are proposed to deduce the fixed-time synchronization for the considered networks. Unlike most existing results, the obtained fixed-time synchronization conditions are expressed by linear matrix inequality, which is easy to be verified; (3) as special cases, the fixed-time synchronization of complex networks without uncertain disturbances is also considered by employing some existing controllers, respectively, and the corresponding results are given in some corollaries.

The rest of the paper is arranged as follows. A network model is established with uncertain disturbances and nonidentical nodes, and then the problem of the fixed-time synchronization is described; meanwhile, some necessary definitions and assumptions are given in Section 2. The fixed-time synchronization conditions are achieved in Section 3. Several numerical examples are introduced in Section 4 to indicate the effectiveness of the proposed results. Section 5 summarizes the research conclusions of this paper and puts forward the future research directions.

2. Problem Formulation and Preliminaries

A kind of nonlinear system including N nonidentical nodes with diffusion linear coupling is considered, in which each node can be regarded as an n-dimensional dynamic system, as shown in the following:

$$\dot{x}_i(t) = A_i x_i(t) + f_i(t, x_i(t)) + h_i(t, x_i(t)) + c\sum_{j=1}^{N} G_{ij}\Gamma x_j(t), \tag{1}$$

where $x_i(t) = [x_{i1}(t), \ldots, x_{in}(t)]^T \in \mathbb{R}^n$ denotes the state vector of the ith dynamical node; the dynamics of the ith uncoupled node is $\dot{x}_i(t) = A_i x_i(t) + f_i(t, x_i(t)) + h_i(t, x_i(t))$ in which $A_i \in \mathbb{R}^{n\times n}$, and $f_i(t, x_i(t)) = [f_{i1}(t, x_i(t)), f_{i2}(t, x_i(t)), \ldots, f_{in}(t, x_i(t))]^T$: $\mathbb{R}^+ \times \mathbb{R}^n \longrightarrow \mathbb{R}^n$ represents a smooth nonlinear vector showing the node self-dynamics; moreover, $h_i(t, x_i(t)) = [h_{i1}(t, x_i(t)), h_{i2}(t, x_i(t)), \ldots, h_{in}(t, x_i(t))]^T$: $\mathbb{R}^+ \times \mathbb{R}^n \longrightarrow \mathbb{R}^n$ is a uncertain vector and represents the disturbance. The constant $c > 0$ can be considered as the coupling strength of the concerned networks, and $\Gamma = (\gamma_{ij})_{ij} \in \mathbb{R}^{n\times n}$ is a matrix and denotes the inner coupling relation between the network nodes and indicates how the components of each pair of nodes are connected with each other, and $\gamma_{ij} \geq 0$; $G = (G_{ij})_{N\times N}$ is a coupling configuration constant matrix, which describes the topological structure and can be exhibited as the diffusion structure, i.e., $G_{ij} \geq 0$ and $G_{ii} = -\sum_{j=1, j\neq i}^{N} G_{ij}$. In this paper, the driven dynamical node of (1) satisfies

$$\dot{x}_0(t) = A_0 x_0(t) + f_0(t, x_0(t)) + h_0(t, x_0(t)), \tag{2}$$

where $A_0 \in \mathbb{R}^{n\times n}$, $f_0(t, x_0(t)) \in \mathbb{R}^n$, and $h_0(t, x_0(t)) \in \mathbb{R}^n$.

In fact, most of the well-known chaotic systems can be described by the above dynamical equation, such as Sprott circuit, Chua circuit, Rössler's systems, and Chen system [42].

Definition 1 (see [44]). Complex network (1) is said to be synchronized onto (2) in finite time if there exist a designed feedback controller to system (1) and a constant $t^* > 0$ such that

$$\begin{aligned} &\lim_{t\longrightarrow t^*} \left\| x_i(t) - x_0(t) \right\| = 0, \\ &\left\| x_i(t) - x_0(t) \right\| \equiv 0, \quad i = 1, 2 \ldots, N, \end{aligned} \tag{3}$$

where $t^* > 0$ is called the settling time and often depends on the initial state vector value $X(0) = (x_1^T(0), \ldots, x_N^T(0))^T$.

Definition 2 (see [44]). Complex network (1) is said to be synchronized onto (2) in fixed time if there exists a fixed settling time $T^* > 0$ such that

$$\begin{aligned} &\lim_{t\longrightarrow T^*} \left\| x_i(t) - x_0(t) \right\| = 0, \\ &\left\| x_i(t) - x_0(t) \right\| \equiv 0, \quad i = 1, 2 \ldots, N,\ t > T^*, \end{aligned} \tag{4}$$

where $T^* > 0$ is called the settling time and is independent of the initial synchronization error $X(0) = (x_1^T(0), \ldots, x_N^T(0))^T$.

In this paper, the goal is to fixed-timely synchronize the state of network (1) onto the driven one (2) by designing feedback controllers.

Obviously, controlled complex network (1) can be rewritten as follows:

$$\begin{aligned} \dot{x}_i(t) = {} & A_i x_i(t) + f_i(t, x_i(t)) + h_i(t, x_i(t)) \\ & + c \sum_{j=1}^{N} G_{ij} \Gamma x_j(t) + u_i(t). \end{aligned} \tag{5}$$

Introduce the synchronization errors $e_i(t)$, which are defined as $e_i(t) = x_i(t) - x_0(t)$, $i = 1, 2, \ldots, N$, $F_i(t) = f_i(t, x_i) - f_0(t, x_0) + (A_i - A_0)x_i(t)$, and $H_i(t, e_i(t)) = h_i(t, x_i(t)) - h_0(t, x_0(t))$. Subtracting (2) from (5), the error dynamical network model can be given by

$$\begin{aligned} \dot{e}_i(t) = {} & A_0 e_i(t) + F_i(t, e_i(t)) + H_i(t, e_i(t)) \\ & + c \sum_{j=1}^{N} G_{ij} \Gamma e_j + u_i(t), \quad i = 1, \ldots, N. \end{aligned} \tag{6}$$

In order to obtain our main results, some necessary assumptions are listed as follows.

Assumption 1. There exist constant $M_i > 0$ and uniformly symmetric positive definite matrix L_i, $i = 1, 2, \ldots, n$, such that $f_i(t, x)$ satisfies

$$\begin{aligned} (y - x)^T (f_i(t, y) - f_i(t, x)) \le {} & (y - x)^T L_i (y - x) \\ & + M_i \Sigma_{j=1}^{n} \left| y_j - x_j \right|, \quad i = 1, \ldots, n, \end{aligned} \tag{7}$$

for all $t \ge 0$, $x = (x_1, x_2, \ldots, x_n)^T \in \mathbb{R}^n$, and $y = (y_1, y_2, \ldots, y_n)^T \in \mathbb{R}^n$.

Assumption 2. There exist constant $M_0 > 0$ and uniformly symmetric positive definite matrix L_0 such that $f_0(t, x)$ satisfies

$$\begin{aligned} (y - x)^T (f_0(t, y) - f_0(t, x)) \le {} & (y - x)^T L_0 (y - x) \\ & + M_0 \Sigma_{i=1}^{n} \left| y_j - x_j \right|, \end{aligned} \tag{8}$$

for all $t \ge 0$, $x = (x_1, x_2, \ldots, x_n)^T \in \mathbb{R}^n$, and $y = (y_1, y_2, \ldots, y_n)^T \in \mathbb{R}^n$.

Assumption 3 (see [43]). There exists a time-varying function $\mu(t) \ge 0$ such that

$$\left| f_i(t, x) - f_0(t, x) \right| \le \mu(t), \quad i, j = 1, \ldots, N. \tag{9}$$

Assumption 4. For any i, $i == 1, 2, \ldots, n$, the uncertain function vector $h_i(t, x_i(t))$ is assumed to be continuous at $t, x_i(t) \ge 0$ and bounded. Moreover, there is a known nonnegative number $h_{\max}$ such that

$$\left| h_i(t, x_i(t)) \right| \le h_{\max}, \quad i = 0, 1, \ldots, N. \tag{10}$$

Remark 1. Assumptions 1 and 2 are general and satisfied with most of the well-known chaotic systems, for instance, Chua circuit [43], Rössler's systems, and discontinuous Chen system. In fact, the above systems meet the following conditions: there exist some positive constants $k_{ij} > 0, \beta_j$, $i, j = 1, 2, \ldots, n$, satisfying

$$\begin{aligned} \left\| f_i(t, y) - f_i(t, x) \right\| \le \Sigma_{j=1}^{n} k_{ij} \left| y_j(t) - x_j(t) \right| + \beta_i, \\ i = 1, 2, \ldots, n, \end{aligned} \tag{11}$$

for any $t \ge 0$, $x = (x_1, x_2, \ldots, x_n)^T \in \mathbb{R}^n$, and $y = (y_1, y_2, \ldots, y_n)^T \in \mathbb{R}^n$. Using condition (11), we have

$$\begin{aligned}(y(t)-x(t))^T(f_i(t,y)-f_i(t,x)) &\le \Sigma_{i=1}^n\Sigma_{j=1}^n k_{ij}\left|y_i(t)-x_i(t)\right\|y_j(t)-x_j(t)\Big| + \Sigma_{j=1}^n\beta_i\left|y_j(t)-x_j(t)\right| \\ &= \Sigma_{i=1}^n\Sigma_{j=1}^n k_{ij}^{(1/2)}\left|y_i(t)-x_i(t)\right|k_{ij}^{(1/2)}\left|y_j(t)-x_j(t)\right| + \Sigma_{j=1}^n\beta_i\left|y_j(t)-x_j(t)\right| \\ &\le \Sigma_{i=1}^n\Sigma_{j=1}^n\frac{1}{2}\left(k_{ij}+k_{ji}\right)\left|y_i(t)-x_i(t)\right|^2 + \Sigma_{j=1}^n\beta_i\left|y_j(t)-x_j(t)\right| \\ &\le \left(y(t)-x_i(t)\right)L_i(y(t)-x(t)) + M_i\Sigma_{j=1}^n\left|y_j(t)-x_j(t)\right|,\end{aligned} \tag{12}$$

where $L_i = \mathrm{diag}(l_{11}^i, l_{22}^i, \ldots, l_{nn}^i)$, $l_{jj}^i = \Sigma_{j=1}^n (1/2)(k_{ij}+k_{ji})$, and $M_i = \beta_i, 1 \le i \le n$. Clearly, if $\alpha = \max_{1\le i\le n}\left\{l_{jj}^i, j = 1, 2, \ldots, n\right\}$ and $M = \max_{1\le i\le n}\{\beta_i\}$, then Assumptions 1 and 2 involve conditions (H2) and (H3) in [25]. Moreover, the continuous chaotic system is also a special case by setting $M_i = 0$ in Assumption 1 or $M_0 = 0$ in Assumption 2, for instance, the continuous Rössler system, Chua's circuit, Chen system, Lorenz system, and logistic differential system. Hence, Assumptions 1 and 2 are more general, and most popular chaotic systems are applicable. Assumptions 3 and 4 take advantage of conditions on the activation function, and it is seen that they are diffusely imposed in the literature [23, 35–37].

According to Definition 2, it is clear that the fixed-time synchronization of dynamical network (5) onto (2) can be degenerated into the fixed-time stabilization of error dynamic system (6).

3. Fixed-Time Synchronization Analysis

In this part, the controllers are designed for the fixed-time synchronization problem of complex network (1), and concerned complex network (5) can realize the fixed-timely synchronization under the appropriate designed controllers. Firstly, we give the synchronization controller design of complex network (1), and then fixed-time synchronization criteria can be obtained based on error system (6). Several corollaries are also obtained for (5) and (2) with identical nodes. For concerned complex network (1), the control input $u_i(t) \in R^n$, $i = 1, \ldots, N$, is designed as follows:

$$\begin{aligned}u_i(t) = {} & (A_0 - A_i)x_0 - d_i e_i(t) - \eta_i(t)\mathrm{sign}(e_i(t)) \\ & - \overline{\mathrm{sign}}(e_i(t))\left(a\left|e_i(t)\right|^p + b\left|e_i(t)\right|^q\right),\end{aligned} \tag{13}$$

where $d_1, \ldots, d_N$ are positive constants, $\eta_i(t)$ is a function to be determined, a, b are positive constants, $\mathrm{sign}(e_i(t)) = (\mathrm{sign}(e_{i1}(t)), \ldots, \mathrm{sign}(e_{in}(t)))^T$, $|e_i(t)|^p = (|e_{i1}(t)|^p, \ldots, |e_{in}(t)|^p)^T$, $|e_i(t)|^q = (|e_{i1}(t)|^q, \ldots, |e_{in}(t)|^q)^T$, $\overline{\mathrm{sign}}(e_i(t)) = \mathrm{diag}(\mathrm{sign}(e_{i1}(t)), \ldots, \mathrm{sign}(e_{in}(t)))$, and the real numbers p, q follow $0 < q < 1$, $p > 1$.

The following lemmas are necessary and given to derive the subsequent main results.

Lemma 1 (see [2, 45, 46]). *Suppose that function $V(t)$: $\mathbb{R}^n \longrightarrow \mathbb{R}$ is C-regular and $x(t)$: $[0, +\infty) \longrightarrow \mathbb{R}^n$ is absolutely continuous on any compact interval $[0, +\infty)$. Denote $v(t) = V(x(t))$ if there exists a continuous function γ: $[0, +\infty) \longrightarrow \mathbb{R}$ with $\gamma(\sigma) > 0$ for $\sigma \in (0, +\infty)$ such that*

$$\dot{v}(t) \le -\gamma(v), \tag{14}$$

for any $t > 0$ that $v(t) > 0$, and $v(t)$ is differentiable at t and satisfies

$$\int_0^{v(0)} \frac{1}{\gamma(v)} = t_1 < +\infty. \tag{15}$$

Then, we have $v(t) = 0$ for $t \ge t_1$. In particular, if $\gamma(v) = Qv^\mu$, where $\mu \in (0, 1)$ and $Q > 0$, then the setting time is estimated by

$$t_1 = \frac{v^{1-\mu}}{Q(1-\mu)}. \tag{16}$$

Lemma 2 (see [47]). *For matrices A, B, C, and D with appropriate dimensions and a scalar α, the following assertions hold:*

(1) $(\alpha A)\otimes B = A\otimes(\alpha B)$,

(2) $(A+B)\otimes C = A\otimes C + B\otimes C$,

(3) $(A\otimes B)(C\otimes D) = (AC)\otimes(BD)$, *and*

(4) $(A\otimes B)^T = A^T\otimes B^T$,

where $\otimes$ is the Kronecker product.

Lemma 3 (see [48]). *Suppose there exists a continuous, positive-definite function $V(t)$ satisfying*

$$\frac{\mathrm{d}V(t)}{\mathrm{d}t} \le IV(t) - kV^\alpha(t), \quad \forall t \ge t_0,\ V^{1-\alpha}(t_0) \ge \frac{k}{I}, \tag{17}$$

where $k > 0$, $I > 0$, and $0 < \alpha < 1$ are three constants. Then, the following inequality is true:

$$V^{1-\alpha}(t) \ge V^{1-\alpha}(t_0) - k(1-\alpha)(t-t_0), \quad t_0 < t < t_1, \tag{18}$$

$V(t) \equiv 0$, $\forall t > t_1$, and the settling time t_1 is estimated by

$$t_1 = t_0 + \frac{\ln\left(1 - (I/k)V^{1-\alpha}(t_0)\right)}{I(\alpha-1)}. \tag{19}$$

Lemma 4. *Suppose there exists a continuous radially unbounded function $V(e(t))$: $R^{nN} \longrightarrow [0, +\infty)$ satisfying the following two conditions:*

(i) If $e(t) \ne 0$, then $V(e(t)) > 0$ and $V(e(t)) = 0 \Leftrightarrow e(t) = 0$.

(ii) Any solution $e(t)$ of system (6) satisfies

$$\frac{dV(e(t))}{dt} \le -aV^p(e(t)) - bV^q(e(t)), \tag{20}$$

where $a>0$, $b>0$, $p>1$, *and* $0<q<1$ *are all constants. Then,* $V(e(t))$ *satisfies* $V(e(t))\equiv 0$, $\forall t>T^*$, *and the fixed settling time is estimated by*

$$T^* = \frac{1}{a(p-1)} + \frac{1}{b(1-q)}. \tag{21}$$

Lemma 5 (see [48]). *Suppose that* $a_i \ge 0$ $(i=1,\ldots,n)$, $0<p\le 1$, *and* $0<q<2$; *it follows that*

$$\left(\sum_{i=1}^{n} a_i\right)^p \le \sum_{i=1}^{n} (a_i)^p,$$

$$\sum_{i=1}^{n} (a_i)^q \ge \left(\sum_{i=1}^{n} a_i^2\right)^{(q/2)}, \tag{22}$$

$$\left(\frac{1}{n}\sum_{i=1}^{n} (a_i)^q\right) \ge \left(\frac{1}{n}\sum_{i=1}^{n} a_i^2\right)^{(1/2)}.$$

Theorem 1. *For concerned complex network (1) with the control input, if Assumptions 1–4 hold and*

$$\mu(t) + 2h_{\max} + M_i - \eta_i(t) < 0, \quad i=1,2,\ldots,N, \tag{23}$$

$$\mathscr{L} + \mathscr{A} + cG^s \otimes \Gamma - D \otimes I_n < 0, \tag{24}$$

with $D = diag\{d_1,\ldots,d_N\} > 0$, $G^s = ((G+G^T)/2)$, $\mathscr{L} = diag(L_1^s, L_2^s, \ldots L_N^s)$, *and* $\mathscr{A} = diag(A_1^s, A_2^s, \ldots, A_N^s)$, *then driven-response complex networks (1) and (2) can achieve fixed-time synchronization under controller (13), with the settling time*

$$T^* = \frac{1}{2^{(1+p/2)} a (Nn)^{(1-p/2)} (p-1)} + \frac{1}{2^{(1+q/2)} b (1-q)}, \tag{25}$$

where $V(0) = (1/2)\sum_{i=1}^{N} e_i^T(0)e_i(0)$ *and* $e_i(0)$ *is the initial value of* $e_i(t) = x_i(t) - x_0(t)$ *for* $i=1,\ldots,N$. *Proof.*

For error dynamical system (6), a Lyapunov function is listed by

$$V(t) = \frac{1}{2}\sum_{i=1}^{N} e_i^T(t)e_i(t), \tag{26}$$

and the derivative of the above Lyapunov function along the trajectory of system (6) can be computed as

$$\begin{aligned}
\dot{V}(t) &= \sum_{i=1}^{N} e_i^T(t)\dot{e}_i(t) = \sum_{i=1}^{N} e_i^T(t)\left\{A_0 e_i(t) + F_i(t,e_i(t)) + H_i(t,e_i(t)) + c\sum_{j=1}^{N} G_{ij}\Gamma e_j(t) + u_i(t)\right\} \\
&= \sum_{i=1}^{N} e_i^T(t)\left\{-d_i e_i(t) - \eta_i(t)\operatorname{sign}(e_i(t)) - \overline{\operatorname{sign}}(e_i(t))\left(a|e_i(t)|^p + b|e_i(t)|^q\right)\right\} \\
&\quad + I_1(t) + I_2(t) + I_3(t),
\end{aligned} \tag{27}$$

with $I_1(t) = \sum_{i=1}^{N} e_i^T(t)A_0 e_i(t) + c\sum_{i=1}^{N} e_i^T(t)\sum_{j=1}^{N} G_{ij}\Gamma e_j(t)$, $I_2(t) = \sum_{i=1}^{N} e_i^T(t)H_i(t,e_i(t))$, and $I_3(t) = \sum_{i=1}^{N} e_i^T(t)(F_i(t, e_i(t)) - (A_i - A_0)x_0(t))$.

According to Lemma 2, we know the following equation is true:

$$\begin{aligned}
I_1(t) &= e^T(t)(I_N \otimes A_0)e(t) + ce^T(t)(G\otimes\Gamma)e(t) \\
&= e^T(t)(I_N \otimes A_0^s)e(t) + ce^T(t)\frac{G\otimes\Gamma + (G\otimes\Gamma)^T}{2}e(t) \\
&= e^T(t)(I_N \otimes A_0^s + cG^s\otimes\Gamma)e(t).
\end{aligned} \tag{28}$$

For the term $I_2(t)$, using condition (10) in Assumption 4, we get the following inequality:

$$\begin{aligned}
I_2(t) &= \sum_{i=1}^{N} e_i^T(t)(h_i(t,x_1(t)) - h_0(t,x_0(t))) \le \sum_{i=1}^{N} |e_i(t)\| h_i(t,x_1(t)) - h_0(t,x_0(t))| \\
&\le \sum_{i=1}^{N} |e_i(t)|(2h_{\max}) = \sum_{i=1}^{N}\sum_{j=1}^{N} |e_{ij}(t)|(2h_{\max}).
\end{aligned} \tag{29}$$

Also, it can be seen that

$$\begin{aligned} I_3(t) &= \sum_{i=1}^{N} e_i^T(t)\left(\left(f_i(t,x_i(t)) - f_0(t,x_0(t))\right) + (A_i - A_0)x_i(t) - (A_i - A_0)x_0(t)\right) \\ &= \sum_{i=1}^{N} e_i^T(t)\left(\left(f_i(t,x_i(t)) - f_i(t,x_0(t))\right) + \left(f_i(t,x_0(t)) - f_0(t,x_0(t))\right) + (A_i - A_0)e_i(t)\right) \\ &= I_{31}(t) + I_{32}(t) + e(t)^T\left(\mathscr{A} - I_N \otimes A_0^s\right)e(t), \end{aligned} \tag{30}$$

with $I_{31}(t) = \sum_{i=1}^{N} e_i^T(t)(f_i(t,x_i(t)) - f_i(t,x_0(t)))$, $I_{32}(t) = \sum_{i=1}^{N} e_i^T(t)(f_i(t,x_0(t)) - f_0(t,x_0(t)))$, and $\mathscr{A} = \operatorname{diag}(A_1^s, A_2^s, \ldots, A_N^s)$.

From (7) in Assumption 1, it is known that

$$\begin{aligned} I_{31}(t) &\le \sum_{i=1}^{N} e_i^T(t)L_i e_i(t) + \sum_{i=1}^{N}\left(M_i \sum_{j=1}^{N}\left|e_{ij}(t)\right|\right) \\ &= e^T(t)\mathscr{L}e(t) + \sum_{i=1}^{N}\left(M_i \sum_{j=1}^{N}\left|e_{ij}(t)\right|\right), \end{aligned} \tag{31}$$

where $\mathscr{L} = \operatorname{diag}(L_1^s, L_2^s, \ldots, L_N^s)$.

By (9) in Assumption 3, one can get

$$\begin{aligned} I_{32}(t) &\le \sum_{i=1}^{N}\left|e_i(t)\right\| f_i(t,x_0(t)) - f_0(t,x_0(t))\right| \\ &\le \sum_{i=1}^{N}\sum_{j=1}^{N}\left|e_{ij}(t)\right|\mu(t). \end{aligned} \tag{32}$$

Submitting (28)–(32) into (27) yields that

$$\begin{aligned} \dot{V}(t) \le{}& e^T(t)\mathscr{L}e(t) + e^T(t)\left(I_N \otimes A_0^s + cG^s \otimes \Gamma\right)e(t) \\ &+ \mu(t)\sum_{i=1}^{N}\sum_{j=1}^{N}\left|e_{ij}(t)\right| + \sum_{i=1}^{N}\sum_{j=1}^{N}\left|e_{ij}(t)\right|(2h_{\max}) + e(t)^T\left(\mathscr{A} - I_N \otimes (A_0)^s\right)e(t) + \sum_{i=1}^{N}\left(M_i\sum_{j=1}^{N}\left|e_{ij}(t)\right|\right) \\ &+ \sum_{i=1}^{N} e_i^T(t)\left\{-d_i e_i(t) - \eta_i(t)\operatorname{sign}(e_i(t)) - \overline{\operatorname{sign}}(e_i(t))\left(a\left|e_i(t)\right|^p + b\left|e_i(t)\right|^q\right)\right\} \\ ={}& W_1(t) + W_2(t) + W_3(t), \end{aligned} \tag{33}$$

where

$$\begin{aligned} W_1(t) &= e^T(t)\mathscr{L}e(t) + e^T(t)\left(I_N \otimes A_0^s + cG^s \otimes \Gamma\right)e(t) + e(t)^T\left(\mathscr{A} - I_N \otimes A_0^s\right)e(t) \\ &\quad - \sum_{i=1}^{N} e_i^T(t)d_i e_i(t), \\ W_2(t) &= \sum_{i=1}^{N}\sum_{j=1}^{N}\left|e_{ij}(t)\right|\mu(t) + \sum_{i=1}^{N}\sum_{j=1}^{N}\left|e_{ij}(t)\right|(2h_{\max}) + \sum_{i=1}^{N}\left(M_i\sum_{j=1}^{N}\left|e_{ij}(t)\right|\right) \\ &\quad - \sum_{i=1}^{N} e_i^T(t)\left(\eta_i(t)\operatorname{sign}(e_i(t))\right), \end{aligned} \tag{34}$$

$$W_3(t) = -\sum_{i=1}^{N} e_i^T(t)\overline{\operatorname{sign}}(e_i(t))\left(a\left|e_i(t)\right|^p + b\left|e_i(t)\right|^q\right). \tag{35}$$

By use of Lemma 2 and (24), it gives that

$$\begin{aligned} W_1(t) &= e^T(t)\left(\mathscr{L} + I_N \otimes A_0^s + cG^s \otimes \Gamma + \mathscr{A}\right)e_i(t) \\ &\quad - e^T(t)\left(I_N \otimes (A_0)^s\right)e(t) - e^T(t)(D \otimes I_n)e_i(t) \\ &= e^T(t)\left(\mathscr{L} + \mathscr{A} + cG^s \otimes \Gamma - D \otimes I_n\right)e(t) \le 0, \end{aligned} \tag{36}$$

where $D = \mathrm{diag}(d_1, d_2, \ldots, d_N)$.

Obviously, $e_i^T(t)\mathrm{sign}(e_i(t)) = (e_{i1}(t), \ldots, e_{in}(t))(\mathrm{sign}(e_{i1}(t)), \ldots, \mathrm{sign}(e_{in}(t)))^T = \sum_{j=1}^n |e_{ij}(t)|$ and $\|e_i(t)\|_2 - e_i^T(t)\overline{\mathrm{sign}}(e_i(t)) = \left(\sum_{j=1}^n e_{ij}^2(t)\right)^{(1/2)} - \sum_{j=1}^n |e_{ij}(t)| \le 0$, and applying Lemma 5, it gives that

$$\begin{aligned} W_2(t) &= \sum_{i=1}^N \sum_{j=1}^N \left|e_{ij}(t)\right|\mu(t) + \sum_{i=1}^N \sum_{j=1}^N \left|e_{ij}(t)\right|(2h_{\max}) + \sum_{i=1}^N \left(M_i \sum_{j=1}^N \left|e_{ij}(t)\right|\right) \\ &\quad - \sum_{i=1}^N e_i^T(t)\left(\eta_i(t)\overline{\mathrm{sign}}(e_i(t))\right) = \sum_{i=1}^N \left(\mu(t) + 2h_{\max} + M_i - \eta_i(t)\right)\sum_{j=1}^N \left|e_{ij}(t)\right| \le 0. \end{aligned} \tag{37}$$

Considering that $|e_i(t)| = (|e_{i1}(t)|, \ldots, |e_{in}(t)|)^T$ and $|e_i(t)|^\beta = (|e_{i1}(t)|^\beta, \ldots, |e_{in}(t)|^\beta)^T$, we have

$$\begin{aligned} W_3(t) &= -\sum_{i=1}^N e_i^T(t)\overline{\mathrm{sign}}(e_i(t))\left(a\left|e_i(t)\right|^p + b\left|e_i(t)\right|^q\right) - \sum_{i=1}^N e_i^T(t)k\mathrm{sign}(e_i(t))\left|e_i(t)\right|^\beta \\ &= -\left(a\sum_{i=1}^N \left|e_i(t)\right|^T\left|e_i(t)\right|^p + b\sum_{i=1}^N \left|e_i(t)\right|^T\left|e_i(t)\right|^q\right) = -\left(a\sum_{i=1}^N\sum_{j=1}^n \left|e_{ij}(t)\right|^{1+p} + b\sum_{i=1}^N\sum_{j=1}^n \left|e_{ij}(t)\right|^{1+q}\right). \end{aligned} \tag{38}$$

By Lemma 5, it can be obtained that

$$\left(\sum_{i=1}^N\sum_{j=1}^n \left|e_{ij}(t)\right|^{1+q}\right)^{(1/1+q)} \ge \left(\sum_{i=1}^N\sum_{j=1}^n \left|e_{ij}(t)\right|^2\right)^{(1/2)}, \tag{39}$$

and then

$$b\sum_{i=1}^N\sum_{j=1}^n \left|e_{ij}(t)\right|^{1+q} \ge b\left(\sum_{i=1}^N\sum_{j=1}^n \left|e_{ij}(t)\right|^2\right)^{(1+q/2)}. \tag{40}$$

Similarly, using Lemma 5, we have

$$\left(\sum_{i=1}^N\sum_{j=1}^n \left|e_{ij}(t)\right|^{1+p}\right)^{(1/1+p)} \ge (Nn)^{(1/2)-(1/1+p)}\left(\sum_{i=1}^N\sum_{j=1}^n \left|e_{ij}(t)\right|^2\right)^{(1/2)}. \tag{41}$$

Therefore,

$$a\sum_{i=1}^N\sum_{j=1}^n \left|e_{ij}(t)\right|^{1+p} \ge a(Nn)^{(1-p/2)}\left(\sum_{i=1}^N\sum_{j=1}^n \left|e_{ij}(t)\right|^2\right)^{(1+p/2)}, \tag{42}$$

which together with (38)–(42) implies that

$$\begin{aligned} W_3(t) &\le -a(Nn)^{(1-p/2)}\left(\sum_{i=1}^N\sum_{j=1}^n \left|e_{ij}(t)\right|^2\right)^{(1+p/2)} - b\left(\sum_{i=1}^N\sum_{j=1}^n \left|e_{ij}(t)\right|^2\right)^{(1+p/2)} \\ &= -a(Nn)^{(1-p/2)}\left(\sum_{i=1}^N e_i(t)^T e_i(t)\right)^{(1+p/2)} - b\left(\sum_{i=1}^N e_i(t)^T e_i(t)\right)^{(1+p/2)} \\ &= -a(Nn)^{(1-p/2)}2^{(1+p/2)}V(t)^{(1+p/2)} - b2^{(1+p/2)}V(t)^{(1+p/2)}. \end{aligned} \tag{43}$$

Submitting (36), (37), and (43) to (33), we can get

$$\dot{V}(t) \leq -2^{(1+p/2)}(Nn)^{(1-p/2)}aV(t)^{(1+p/2)} - 2^{(1+p/2)}bV(t)^{(1+p/2)}. \tag{44}$$

According to Lemma 4, $V(t)$ converges to zero within a settling time T^*, which is defined in Definition 2, and one can obtain that, by use of controller (13), the considered complex network (1) is fixed-timely synchronized onto driven node (2) within the fixed time T^*, which is given by

$$T^* = \frac{1}{2^{(1+p/2)}a(Nn)^{(1-p/2)}(p-1)} + \frac{1}{2^{(1+p/2)}b(1-q)}. \tag{45}$$

Therefore, it can be concluded that the error vector $e_i(t)$ converges to zero within T^*, and driven-response complex networks (1) and (2) are fixed-timely synchronized under controller (13) within the fixed time T^*. The proof is completed.

Remark 2. In recent years, a lot of extensive research has been conducted on the finite-time synchronization and fixed-time synchronization of complex networks, and many breakthroughs have been made. However, as far as we know, there are few published papers that deal with the fixed-time synchronization of heterogeneous complex networks. Theorem 1 suggests a way to choose the controller to realize the fixed-time synchronization for the heterogeneous complex network. The controller consists of three sections: the first two terms are used to overcome the influence from the linear condition of the nonlinear function, the second one $-\eta_i(t)\text{sign}(e_i(t))$ is introduced to compensate the influence of disturbance $h_i(t, x_i(t))$, and finally, the last section $\overline{\text{sign}}(e_i(t))(a|e_i(t)|^p + b|e_i(t)|^q)$ is employed to force the considered networks achieve the fixed-time synchronization.

Now, if $M = \max_{1\leq i\leq n} M_i$ and $\eta(t) = \max_{1\leq i\leq n}\eta_i(t)$, then the controllers $u_i(t) \in R^n$ can be designed as follows $(i = 1, \ldots, N)$:

$$u_i(t) = -(A_i - A_0)x_0 - d_i e_i(t) - \eta(t)\text{sign}(e_i(t)) - \overline{\text{sign}}(e_i(t))\left(a|e_i(t)|^p + b|e_i(t)|^q\right), \tag{46}$$

where the parameters d_i, a, b, p, and q are defined as the same as in (13).

Therefore, by using the same analysis method in Theorem 1, we can obtain Corollary 1 that is a similar conclusion with [25].

Corollary 1. *For concerned complex networks (1) and (2) under controller (46), if Assumptions 1–4 hold and the control parameters $\eta_i(t)$ and d_i in (46) satisfy the following inequalities,*

$$\mu(t) + 2h_{\max} + M - \eta(t) < 0, \quad \mathscr{L} + \mathscr{A} + cG^s \otimes \Gamma - D \otimes I_n < 0, \tag{47}$$

where $D = diag\{d_1, \ldots, d_N\} > 0$, $G^s = ((G + G^T))/2)$, $\mathscr{L} = diag(L_1^s, L_2^s, \ldots L_N^s)$, and $\mathscr{A} = diag(A_1^s, A_2^s, \ldots, A_N^s)$, then driven-response complex networks (1) and (2) can achieve fixed-time synchronization under controller (46), with the settling time

$$T^* = \frac{1}{2^{(1+p/2)}a(Nn)^{(1-p/2)}(p-1)} + \frac{1}{2^{(1+q/2)}b(1-q)}. \tag{48}$$

If the uncertain disturbance is not considered in the complex network model, i.e., $h_1 = h_2 = \cdots = h_N = 0$, then the following network model is degenerated as

$$\dot{x}_i(t) = A_i x_i(t) + f_i(t, x_i(t)) + c\sum_{j=1}^{N} G_{ij}\Gamma x_j(t), \quad i = 1, \ldots, N. \tag{49}$$

Let $x_0|_{t=0} = x_0(0)$, and then the driven network node is governed by

$$\dot{x}_0(t) = A_0 x_0(t) + f_0(t, x_0(t)). \tag{50}$$

Then, the corresponding error dynamical system can be rewritten as follows:

$$\dot{e}_i(t) = F_i(t, e_i(t)) + c\sum_{j=1}^{N} G_{ij}\Gamma e_j + u_i(t), \tag{51}$$

where $F_i(t) = f_i(t, x_i(t)) - f_0(t, x_0(t)) + (A_i - A_0)x_i(t)$.

The controllers are the same as before, and then a criterion can be obtained on the fixed-time synchronization of the concerned complex networks with nonidentical nodes. By taking $h_{\max} = 0$ in Theorem 1, one can easily get the following corollary, and its proof is omitted here.

Corollary 2. *Consider complex network (49) with drive node (50) under the set of controllers (46). If Assumptions 1–3 hold and the controller parameters satisfy the following matrix inequalities,*

$$\mu(t) + M - \eta(t) < 0, \quad \mathscr{L} + \mathscr{A} + cG^s \otimes \Gamma - D \otimes I_n < 0, \tag{52}$$

where $D = diag(d_1, \ldots, d_N) > 0$, $G^s = ((G + G^T)/2)$, $\mathscr{L} = diag(L_1^s, L_2^s, \ldots L_N^s)$, and $\mathscr{A} = diag(A_1^s, A_2^s, \ldots, A_N^s)$, then (49) can be synchronized to the state of drive node (50) within a fixed time T^* and the settling time

$$T^* = \frac{1}{2^{(1+p/2)}a(Nn)^{(1-p/2)}(p-1)} + \frac{1}{2^{(1+q/2)}b(1-q)}. \tag{53}$$

Furthermore, if $h_i = 0$, $A_i = 0$, and $f_i = f$ for $i = 0, 1, \ldots, N$ in (49), then complex network (1) is further reduced to

$$\dot{x}_i(t) = f(t, x_i(t)) + c\sum_{j=1}^{N} G_{ij}\Gamma x_j(t), \tag{54}$$

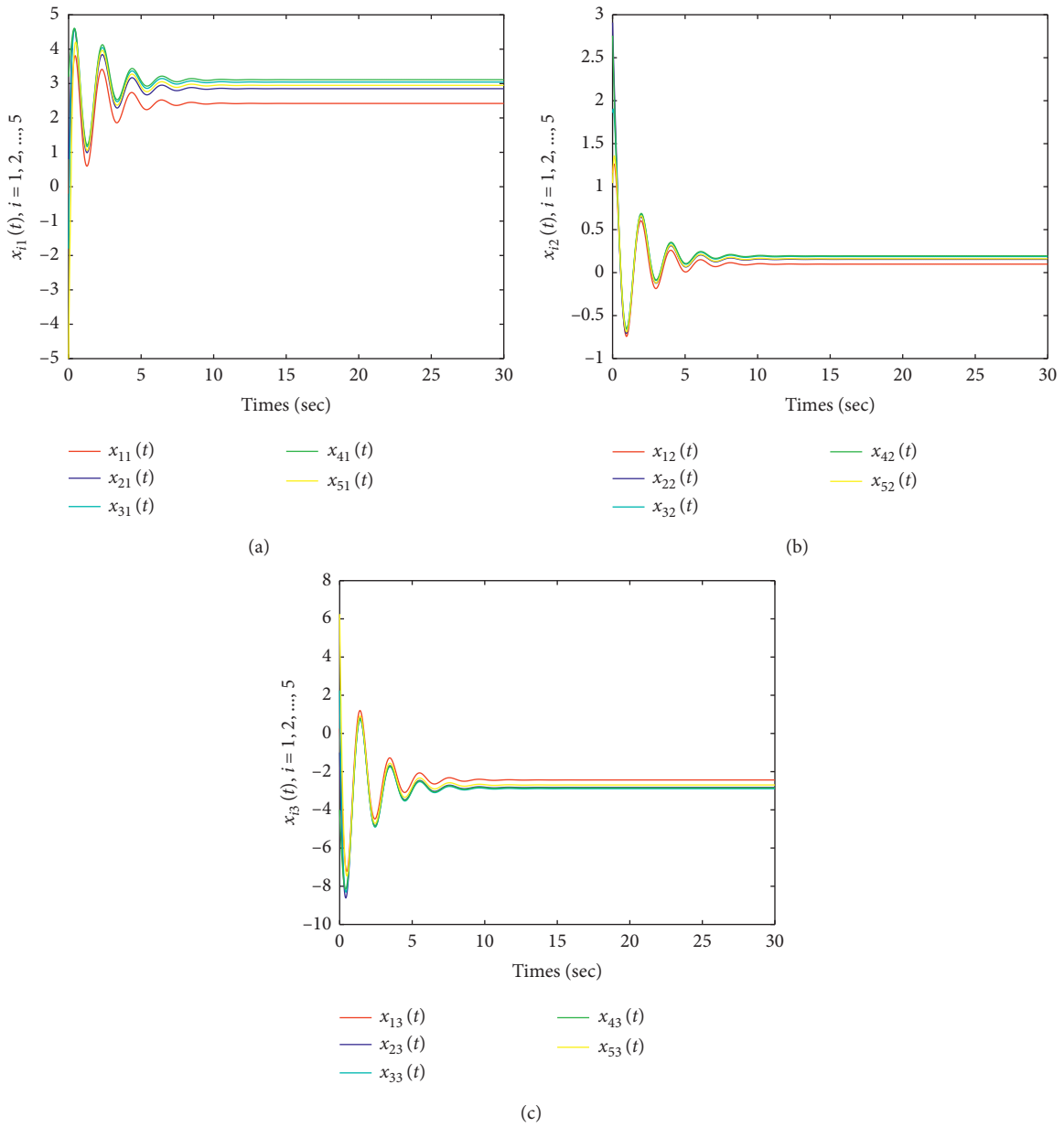

FIGURE 1: State responses without control. (a) State response x_{i1}. (b) State response x_{i2}. (c) State response x_{i3}.

and driven network node (2) is changed correspondingly into the following form:

$$\dot{x_0}\ (t) = f\left(t, x_0(t)\right). \tag{55}$$

In the issue, the proposed fixed-time synchronization scheme can be applied to the corresponding complex networks with identical nodes here, and the criteria are given in the following corollary.

Corollary 3. *For concerned complex networks (54) and (55) under the controllers*

$$u_i(t) = -d_i e_i(t) - \eta(t)\mathrm{sign}\left(e_i(t)\right) - \overline{\mathrm{sign}}\left(e_i(t)\right)\left(a\left|e_i(t)\right|^p + b\left|e_i(t)\right|^q\right), \quad i = 1, \ldots, N, \tag{56}$$

where $d_i \geq 0, i = 1, 2, \ldots, N$, $0 < q < 1, p > 1$, $|e_i(t)|\beta = (|e_{i1}(t)|^\beta, \ldots, |e_{in}(t)|^\beta)^T$, *and* $sign(e_i(t)) = diag(sign(e_{i1}(t))), \ldots, sign(e_{in}(t))$, *if Assumptions 1 and 2 hold and the controller parameters satisfy the following matrix inequalities,*

$$\begin{aligned} &M - \eta(t) < 0, \\ &I_N \otimes L + c\left(G^s \otimes \Gamma\right) - D \otimes I_n < 0, \end{aligned} \tag{57}$$

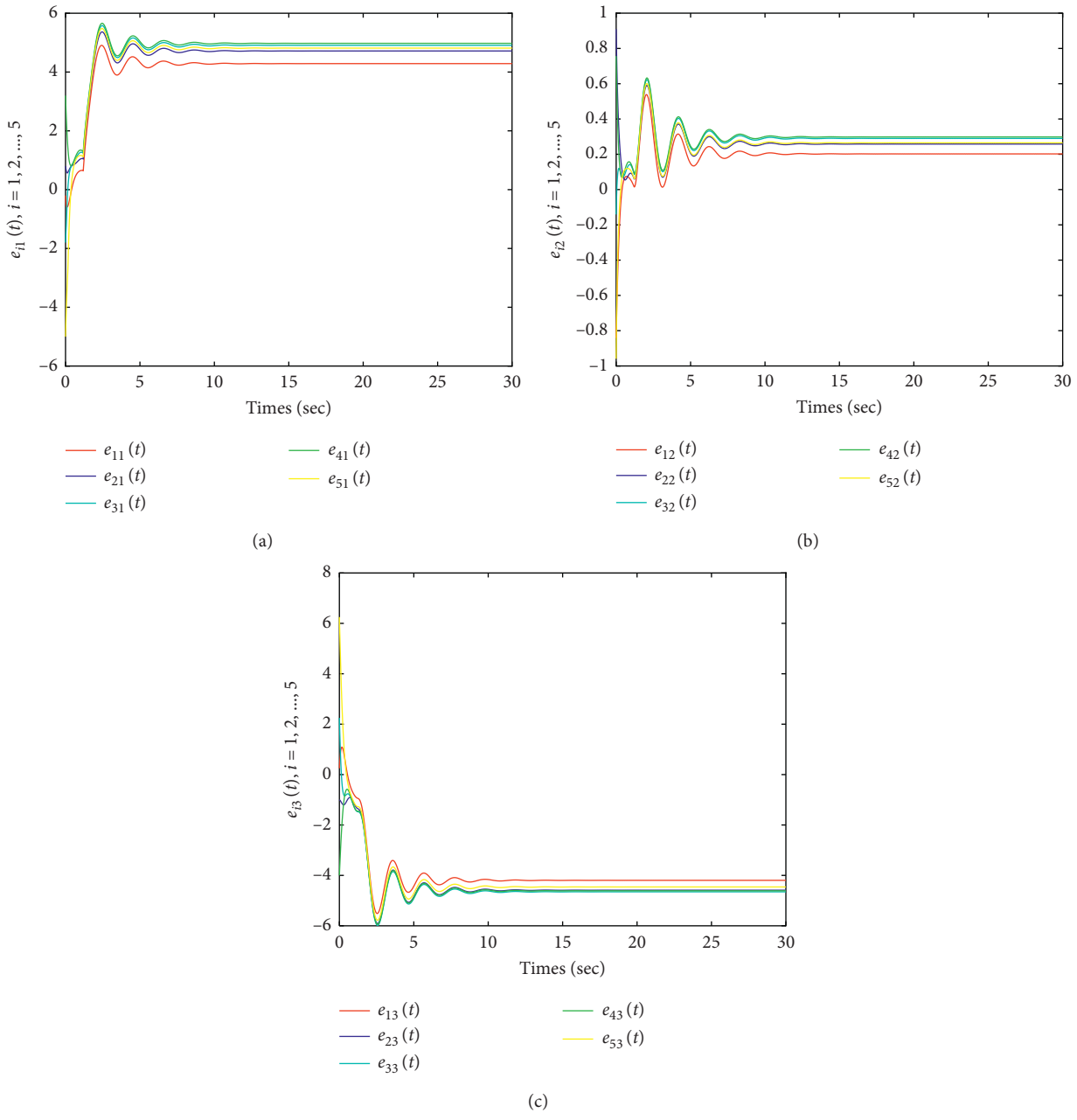

Figure 2: Synchronization error without control. (a) Synchronization error e_{i1}. (b) Synchronization error e_{i2}. (c) Synchronization error e_{i3}.

with $D = diag(d_1, d_2, \ldots, d_N) > 0$ *and* $L_1 = L_2 = \cdots \in = L_N = L$, *then complex network (54) can be synchronized within a fixed time* T^*:

$$T^* = \frac{1}{2^{(1+p/2)} a (Nn)^{(1-p/2)} (p-1)} + \frac{1}{2^{(1+q/2)} b (1-q)}. \quad (58)$$

4. Numerical Example

In this section, numerical simulation results are given to show that the proposed synchronization criterion is feasible. Consider the following discontinuous chaotic Chua circuit with linear and diffusive coupling, where the dynamics of the ith node is described as follows:

$$\dot{x}_i(t) = A_i x_i(t) + f_i(t, x_i) + h_i(t, x_i) + k \sum_{j=1}^{5} G_{ij} \Gamma x_j(t), \quad i = 1, \ldots, 5, \quad (59)$$

with $x_i(t) = (x_{i1}(t), x_{i2}(t), x_{i3}(t))^T$ and initial values $x_i(0)^T = (0, 2, 0)^T + (-1)^i ((i^2/5), |\sin(i)|, -(i^2/4))^T$. The inner coupling matrix Γ, activation matrix A_i, and Laplacian matrix G are defined as

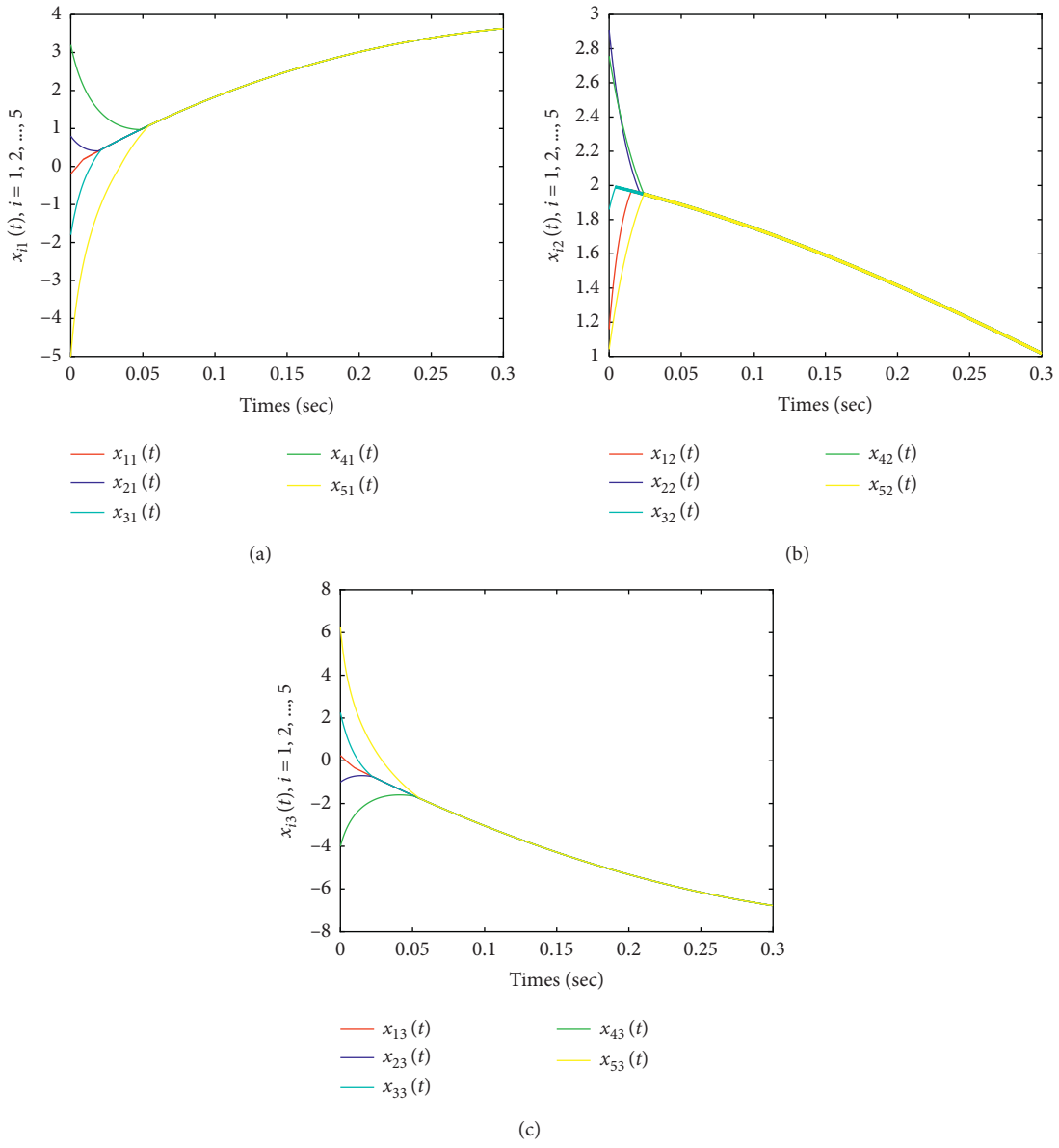

Figure 3: State responses of fixed-time synchronization. (a) State response x_{i1}. (b) State response x_{i2}. (c) State response x_{i3}.

$$\Gamma = \begin{bmatrix} 1 & 0 & 0 \\ 0 & 1 & 0 \\ 0 & 0 & 1 \end{bmatrix},$$

$$A_i = \begin{bmatrix} a_1 + \dfrac{i}{10} & b_1 - \dfrac{i}{10} & 0 \\ 1 & -1 & 1 \\ 0 & c_1 + \dfrac{i}{5} & -1 \end{bmatrix},$$

$$G = \begin{bmatrix} -1 & 1 & 0 & 0 & 0 \\ 0 & -2 & 2 & 0 & 0 \\ 0 & 0 & -2 & 2 & 0 \\ 0 & 0 & 0 & -1 & 1 \\ 1 & 1 & 1 & 0 & -3 \end{bmatrix}. \quad (60)$$

Its activation function $f_i(t, x_i(t)) = ((1 + (i/10))\theta \operatorname{sign}(x_{i1}(t)), 0, 0)^T$, and its uncertain disturbance $h_i(t, x_i) = ((\sin(50t)/100)(\cos(50t)/100)(-\sin(50t)/100))^T$, where $a_1 = -2.75$, $b_1 = 9.0$, $c_1 = -17$, $\theta = 3.86$, and the coupling strength $k = 2.0$. The drive dynamical node is

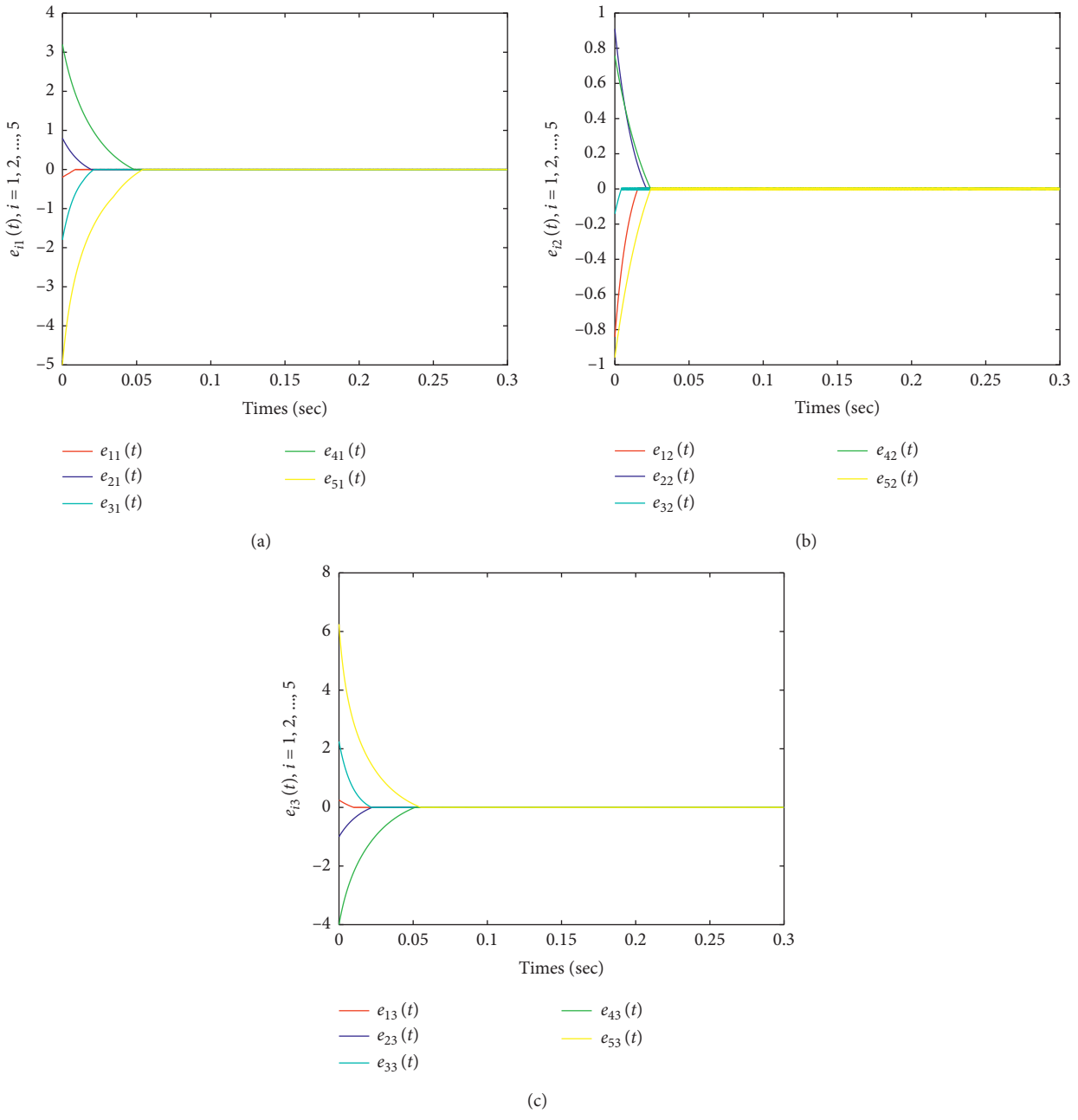

FIGURE 4: Synchronization error of fixed-time synchronization. (a) Synchronization error e_{i1}. (b) Synchronization error e_{i2}. (c) Synchronization error e_{i3}.

$$\dot{x}_0(t) = A_0 x_0(t) + f_0(t, x_0) + h_0(t, x_0), \tag{61}$$

with initial values $x_0(0) = (0, 2, 0)^T$, where $f_0(t, x_0) = (\theta \text{sign}(x_{01}(t)), 0, 0)^T$ and $h_0(t, x_0) = (0, 0, 0)^T$.

By analyzing the state and error response trajectory of uncontrolled heterogeneous complex dynamic network (59) in Figures 1 and 2, we can easily draw the conclusion that the state of the nodes has not been synchronized, and the synchronization errors cannot tend to zero without the control input.

From the analysis of [13], systems (59) and (61) have chaotic behavior, and there exist positive constants $L_i = 0$ and $M_i = 2(1 + (i/10))\theta$ (i = 0, 1, . . ., 5) satisfying Assumptions 1 and 2. Similarly, for $\mu = (2 + (5/10))\ \theta = 2.5\theta = 9.65$, it is easy to verify that systems (59) and (61) satisfy Assumption 3. Let $h_{\max} = (\sqrt[3]{3}/100)$; then, $\|h_i(t, x_i)\| \le h_{\max} = (\sqrt[3]{3}/100)$ is right for $i = 1, 2, \ldots N$. So, systems (59) and (61) satisfy Assumption 4. With $D = \text{diag}(9, 6, 9, 3, 3)$ and $\eta_i(t) = 20 > \mu(t) + 2h_{\max} + \max\{M_i\} = 2.5\theta + 2\ (\sqrt[3]{3}/100) + 2\ (1 + (5/10))\theta = 5.5\theta + 2(\sqrt[3]{3}/100), k = 1, \beta = 0.6$, it is known that $\lambda_{\max}(\mathscr{L} + \mathscr{A} + cG^s \otimes \Gamma - D \otimes I_n) = -3.6480$, which shows that condition (22) can be satisfied. Applying Theorem 1, network (59) under the set of controllers (13) with $a = 2, b = 3, p = 3, q = 0.5$, and $\eta_i(t) = 20$ can realize the synchronization within the fixed time $t^* = 1.3339$. As a matter of fact, the real time of the

synchronization is 0.0609 seconds in the numerical simulation, and the synchronization results of controlled networks are shown in Figures 3 and 4.

5. Conclusions

The fixed-time synchronization problem is studied for a type of dynamic complex networks with nonidentical nodes and uncertain disturbances. By employing the Lyapunov function theory, some novel sufficient conditions are provided and further applied to some special cases, such as the identical node issue. Future work may be centered on synchronous applications of complex networks with nonidentical nodes and uncertain disturbances.

Data Availability

The data used to support the findings of this study are included within the article. No other data are used beyond this article.

Conflicts of Interest

The authors declare that they have no conflicts of interest.

Acknowledgments

This work was supported by the National Key Research and Development Plan of China (Grant no. 2018YFB1404400), National Science Foundation of China (Grant no. 62076223), Key Science and Technology Program of Henan Province (Grant nos. 202102210347 and 202102210143), Key Research Project of Henan Province University (Grant no. 19A413014), and Doctor Fund Project of Zhengzhou University of Light Industry (no. 2019BSJJ014).

References

[1] W. Yu, G. Chen, and J. Lü, "On pinning synchronization of complex dynamical networks," *Automatica*, vol. 45, no. 2, pp. 429–435, 2009.

[2] A. Arenas, A. Díaz-Guilera, J. Kurths, Y. Moreno, and C. Zhou, "Synchronization in complex networks," *Physics Reports*, vol. 469, no. 3, pp. 93–153, 2008.

[3] X. Chen, T. Huang, J. Cao, J. H. Park, and J. Qiu, "Finite-time multi-switching sliding mode synchronisation for multiple uncertain complex chaotic systems with network transmission mode," *IET Control Theory & Applications*, vol. 13, no. 9, pp. 1246–1257, 2019.

[4] Y. Chen, S. Fei, and Y. Li, "Robust stabilization for uncertain saturated time-delay systems: a distributed-delay-dependent polytopic approach," *IEEE Transactions on Automatic Control*, vol. 62, no. 7, pp. 3455–3460, 2017.

[5] W. Sun, S.-F. Su, Y. Wu, J. Xia, and V.-T. Nguyen, "Adaptive fuzzy control with high-order barrier Lyapunov functions for high-order uncertain nonlinear systems with full-state constraints," *IEEE Transactions on Cybernetics*, vol. 50, no. 8, pp. 3424–3432, 2020.

[6] X. Song, J. Man, S. Song, Y. Zhang, and Z. Ning, "Finite/fixed-time synchronization for Markovian complex-valued memristive neural networks with reaction-diffusion terms and its application," *Neurocomputing*, vol. 414, pp. 131–142, 2020.

[7] L. Liu, W. X. Zheng, and S. Ding, "An adaptive SOSM controller design by using a sliding-mode-based filter and its application to buck converter," *IEEE Transactions on Circuits and Systems I: Regular Papers*, vol. 67, no. 7, pp. 2409–2418, 2020.

[8] X. Tang, Q. Zhang, X. Dai, and Y. Zou, "Neural membrane mutual coupling characterisation using entropy-based iterative learning identification," *IEEE Access*, vol. 8, pp. 205231–205243, 2020.

[9] Y. Wu, J. Cao, A. Alofi, A. AL-Mazrooei, and A. Elaiw, "Finite-time boundedness and stabilization of uncertain switched neural networks with time-varying delay," *Neural Networks*, vol. 69, pp. 135–143, 2015.

[10] Z. Ding and Z. Li, "Distributed adaptive consensus control of nonlinear output-feedback systems on directed graphs," *Automatica*, vol. 72, pp. 46–52, 2016.

[11] Y. Wu, J. Cao, Q. Li, A. Alsaedi, and F. E. Alsaadi, "Finite-time synchronization of uncertain coupled switched neural networks under asynchronous switching," *Neural Networks*, vol. 85, pp. 128–139, 2017.

[12] H.-L. Li, C. Hu, H. Jiang, Z. Teng, and Y.-L. Jiang, "Synchronization of fractional-order complex dynamical networks via periodically intermittent pinning control," *Chaos, Solitons & Fractals*, vol. 103, pp. 357–363, 2017.

[13] X. Yang, J. Cao, and J. Lu, "Synchronization of delayed complex dynamical networks with impulsive and stochastic effects," *Nonlinear Analysis: Real World Applications*, vol. 12, no. 4, pp. 2252–2266, 2011.

[14] X. Gong, L. Gan, and Z. Wu, "Adaptive impulsive cluster synchronization in community network with nonidentical nodes," *International Journal of Modern Physics C*, vol. 27, no. 01, p. 1650010, 2016.

[15] W. He, F. Qian, J. Lam, G. Chen, Q.-L. Han, and J. Kurths, "Quasi-synchronization of heterogeneous dynamic networks via distributed impulsive control: error estimation, optimization and design," *Automatica*, vol. 62, pp. 249–262, 2015.

[16] X. Chen, J. H. Park, J. Cao, and J. Qiu, "Sliding mode synchronization of multiple chaotic systems with uncertainties and disturbances," *Applied Mathematics and Computation*, vol. 308, pp. 161–173, 2017.

[17] J. Yuan, S. Ding, and K. Mei, "Fixed-time SOSM controller design with output constraint," *Nonlinear Dynamics*, vol. 102, no. 3, pp. 1567–1583, 2020.

[18] X. Yin, Q. Zhang, H. Wang, and Z. Ding, "Rbfnn-based minimum entropy filtering for a class of stochastic nonlinear systems," *IEEE Transactions on Automatic Control*, vol. 65, no. 1, pp. 376–381, 2020.

[19] X. Chen, J. H. Park, J. Cao, and J. Qiu, "Adaptive synchronization of multiple uncertain coupled chaotic systems via sliding mode control," *Neurocomputing*, vol. 273, pp. 9–21, 2018.

[20] J. Mei, M. Jiang, W. Xu, and B. Wang, "Finite-time synchronization control of complex dynamical networks with time delay," *Communications in Nonlinear Science and Numerical Simulation*, vol. 18, no. 9, pp. 2462–2478, 2013.

[21] M. Liu, H. J. Jiang, and C. Hu, "Finite-time synchronization of delayed dynamical networks via aperiodically intermittent control," *Journal of the Franklin Institute - Engineering and Applied Mathematics*, vol. 354, no. 13, pp. 5373–5397, 2017.

[22] M. Liu and H. Wu, "Stochastic finite-time synchronization for discontinuous semi-Markovian switching neural networks with time delays and noise disturbance," *Neurocomputing*, vol. 310, pp. 246–264, 2018.

[23] X. Yang, Z. Wu, and J. Cao, "Finite-time synchronization of complex networks with nonidentical discontinuous nodes," *Nonlinear Dynamics*, vol. 73, no. 4, pp. 2313–2327, 2013.

[24] A. Polyakov, "Nonlinear feedback design for fixed-time stabilization of linear control systems," *IEEE Transactions on Automatic Control*, vol. 57, no. 8, pp. 2106–2110, 2012.

[25] X. Yang, J. Lam, D. W. C. Ho, and Z. Feng, "Fixed-Time synchronization of complex networks with impulsive effects via nonchattering control," *IEEE Transactions on Automatic Control*, vol. 62, no. 11, pp. 5511–5521, 2017.

[26] Q. Li, J. Guo, Y. Wu, and C.-Y. Sun, "Global asymptotical bounded synchronization for a class of coupled complex networks with nonidentical nodes," *Asian Journal of Control*, vol. 19, no. 4, pp. 1630–1640, 2017.

[27] K. Q. Mei, L. Ma, R. X. He et al., "Finite-time controller design of multiple integrator nonlinear systems with input saturation," *Applied Mathematics and Computation*, vol. 372, 2020.

[28] X. Tang, Q. Zhang, and L. Hu, "An EKF-based performance enhancement scheme for stochastic nonlinear systems by dynamic set-point Adjustment," *IEEE Access*, vol. 8, pp. 62261–62272, 2020.

[29] M. Ren, Q. Zhang, and J. Zhang, "An introductory survey of probability density function control," *Systems Science & Control Engineering*, vol. 7, no. 1, pp. 158–170, 2019.

[30] Q. Li, J. Guo, C. Sun, Y. Wu, and Z. Ding, "Finite-time synchronization for a class of dynamical complex networks with nonidentical nodes and uncertain disturbance," *Journal of Systems Science and Complexity*, vol. 32, no. 3, pp. 818–834, 2019.

[31] W. Zhang, C. Li, T. Huang, and J. Huang, "Fixed-time synchronization of complex networks with nonidentical nodes and stochastic noise perturbations," *Physica A: Statistical Mechanics and Its Applications*, vol. 492, pp. 1531–1542, 2018.

[32] A. Polyakov, D. Efimov, and W. Perruquetti, "Finite-time and fixed-time stabilization: implicit Lyapunov function approach," *Automatica*, vol. 51, pp. 332–340, 2015.

[33] X. Zhu, X. Yang, F. E. Alsaadi, and T. Hayat, "Fixed-time synchronization of coupled discontinuous neural networks with nonidentical perturbations," *Neural Processing Letters*, vol. 48, no. 2, pp. 1161–1174, 2018.

[34] J. D. Cao and R. X. Li, "Fixed-time synchronization of delayed memristor-based recurrent neural networks," *Science China-Information Science*, vol. 60, no. 3, Article ID 032201, 2017.

[35] J. Zhao, D. J. Hill, T. Liu et al., "Stability of dynamical networks with non-identical nodes: a multipleV-Lyapunov function method," *Automatica*, vol. 47, no. 12, pp. 2615–2625, 2011.

[36] Q. Song, J. Cao, and F. Liu, "Synchronization of complex dynamical networks with nonidentical nodes," *Physics Letters A*, vol. 374, no. 4, pp. 544–551, 2010.

[37] S. Wang, H. Yao, S. Zheng, and Y. Xie, "A novel criterion for cluster synchronization of complex dynamical networks with coupling time-varying delays," *Communications in Nonlinear Science and Numerical Simulation*, vol. 17, no. 7, pp. 2997–3004, 2012.

[38] X. Qian, J. Li, J. Cao, Y. Wu, and W. Wang, "Micro-cracks detection of solar cells surface via combining short-term and long-term deep features," *Neural Networks*, vol. 127, pp. 132–140, 2020.

[39] C. Mu and H. He, "Dynamic behavior of terminal sliding mode control," *IEEE Transactions on Industrial Electronics*, vol. 65, no. 4, pp. 3480–3490, 2018.

[40] J. Lu, D. W. C. Ho, J. Cao, and J. Kurths, "Exponential synchronization of linearly coupled neural networks with impulsive disturbances," *IEEE Transactions on Neural Networks*, vol. 22, no. 2, pp. 329–336, 2011.

[41] G. L. Cai, S. Q. Jiang, S. M. Cai et al., "Cluster synchronization of overlapping uncertain complex networks with time-varying impulse disturbances," *Nonlinear Dynamics*, vol. 80, no. 1-2, pp. 503–513, 2015.

[42] S. Jiang, X. Lu, G. Cai, and S. Cai, "Adaptive fixed-time control for cluster synchronisation of coupled complex networks with uncertain disturbances," *International Journal of Systems Science*, vol. 48, no. 16, pp. 3382–3390, 2017.

[43] C. Ma, T. Li, and J. Zhang, "Consensus control for leader-following multi-agent systems with measurement noises," *Journal of Systems Science and Complexity*, vol. 23, no. 1, pp. 35–49, 2010.

[44] X. Yang and J. Cao, "Finite-time stochastic synchronization of complex networks," *Applied Mathematical Modelling*, vol. 34, no. 11, pp. 3631–3641, 2010.

[45] G. Zong, H. Ren, and L. Hou, "Finite-time stability of interconnected impulsive switched systems," *IET Control Theory & Applications*, vol. 10, no. 6, pp. 648–654, 2016.

[46] G. Zong, R. Wang, W. Zheng, and L. Hou, "Finite-time H ∞ control for discrete-time switched nonlinear systems with time delay," *International Journal of Robust and Nonlinear Control*, vol. 25, no. 6, pp. 914–936, 2015.

[47] A. N. Langville and W. J. Stewart, "The Kronecker product and stochastic automata networks," *Journal of Computational and Applied Mathematics*, vol. 167, no. 2, pp. 429–447, 2004.

[48] Y. Wan, J. Cao, G. Wen, and W. Yu, "Robust fixed-time synchronization of delayed Cohen-Grossberg neural networks," *Neural Networks*, vol. 73, pp. 86–94, 2016.

Hindawi
Mathematical Problems in Engineering
Volume 2021, Article ID 6644033, 13 pages
https://doi.org/10.1155/2021/6644033

Research Article

Super-Twisting Sliding Mode Control Law Design for Attitude Tracking Task of a Spacecraft via Reaction Wheels

Yang-Rui Li and Chao-Chung Peng

Department of Aeronautics and Astronautics, National Cheng Kung University, Tainan, Taiwan

Correspondence should be addressed to Chao-Chung Peng; ccpeng@mail.ncku.edu.tw

Received 3 October 2020; Revised 19 November 2020; Accepted 8 December 2020; Published 16 March 2021

Academic Editor: Haibo Du

The attitude control has been recognized as one of the most important research topics for spacecraft. If the desired attitude trajectory cannot be tracked precisely, it may cause mission failures. In the real space mission environment, the unknown external perturbations, for example, atmospheric drag and solar radiation, should be taken into consideration. Such external perturbations could deviate the precision of the spacecraft orientation and thereby lead to a mission failure. Therefore, in this paper, a quaternion-based super-twisting sliding mode robust control law for the spacecraft attitude tracking is developed. The finite time stability based on the formulation of the linear matrix inequality (LMI) is also provided. To avoid losing the control degree of freedom due to the certain actuator fault, a redundant reaction wheels configuration is adopted. The actuators distribution associated force distribution matrix (FDM) is analyzed in detail. Finally, the reference tangent-normal-binormal (TNB) command generation strategy is implemented for simulating the scenario of the space mission. Finally, the simulation results reveal that the spacecraft can achieve the desired attitude trajectory tracking demands in the presence of the time-varying external disturbances.

1. Introduction

Sliding mode control (SMC) techniques have been a popular research topic of the control theory in recent years such as adaptive super-twisting SMC [1–3], fractional-order sliding mode control [4], finite time control [5], robust back-stepping SMC [6–8], and model predictive SMC [9]. The superior robustness to the matched perturbations is one of the features of the SMC. However, the price of the robustness is the chattering effect of the control signal. It causes application difficulty for practical implementations [10]. The ways to attenuate the chattering phenomenon include the following [11–13]: (i) replacing the discontinuous switching function with a saturation function or a sigmoid function, (ii) applying an adaptive law to adjust the switching gain dynamically, and (iii) using the higher-order SMC techniques. Nevertheless, skill (i) results in losing the robustness to the disturbances. Even though approach (ii) can estimate an adequate magnitude of the switching gain with respect to perturbations [14, 15], the estimation of the switch gain could increase monotonically due to the absence of perfect sliding motion in practice. For (iii), the gain/stability determinations are quite challenging.

The high-order SMC approach can drive the sliding variable and its consecutive derivations to zero in the presence of the matched perturbations. However, the main challenge of the high-order SMC is that it uses the information of the high-order time derivatives of the sliding variable [16–18]. Among the higher-order SMC techniques, it is worth remarking that the second-order SMC such as the super-twisting algorithm only needs the feedback information of the sliding variable in control process. The super-twisting algorithm was firstly proposed by Dr. Levant in 1993 [19]. A quadratic Lyapunov function proposed in [20] is considered in the proof of the finite-time convergence property. The successive researches include [21–24]. Owing to the superior properties, the super-twisting algorithm has been applied in several studies, including quadrotor [25, 26], industrial emulator [27], and mobile wheeled inverted pendulum [28]. For this reason, the robust continuous

super-twisting sliding mode algorithm will be adopted for the attitude tracking control design in this paper.

The reaction wheel driven based system is actuated by means of generating the reaction torque from the wheel. The reaction wheel has been widely applied in the most dynamics systems. In literature [29–31], the reaction wheels are used in the attitude tracking control demands. The works in [32, 33] use the reaction wheel to address the balancing control of the inverted pendulum. The main objective of this paper is to apply the super-twisting algorithm for the attitude control of the spacecraft via using four reaction wheels as the actuated source. The attitude representation includes several approaches, eor example, Euler angles, Rodrigues parameters, and quaternion [34]. To avoid singularity, the quaternion-based control is considered. The quaternion-based control has been proposed in several studies [30, 35, 36]. However, it assumes that the scalar component of error quaternion q_{0e} does not equal zero to guarantee that the matrix $0.5(q_{0e}\mathbf{I}_3 + \mathbf{q}_e^{\times})$ is invertible. This assumption leads to the controllers containing a singularity when $q_{0e} = 0$. It should be noted that one of the reasons to use quaternion-based control is to obtain the full attitude tracking task and avoid any singularity limitations. As a result, in this paper, a quaternion-based super-twisting sliding mode algorithm is adopted in the controller design such that the robust performance can be guaranteed. The asymptotic stability proof of the nonlinear reduced-order dynamics by means of an analytic solution will be addressed without imposing assumptions.

Regarding the organization of this article, in Section 2, the governing equations of attitude dynamics based on the quaternion kinematics and the redundant reaction wheels configurations are derived. The configuration is introduced from [30, 37, 38]. To obtain the feasible reaction torques, the FDM is reformulated as a square and invertible matrix, which minimizes the control energy cost [30]. In Section 3, a robust, continuous super-twisting sliding mode algorithm is considered in the controller design so that the spacecraft can handle the external perturbations in the real and complex space environment. The stability problem will be reformulated as a feasibility problem of a LMI and therefore the finite time stability can be achieved in the sense of Lyapunov. In Section 4, the reference TNB command generation strategy is proposed to verify the tracking performance of the spacecraft. In Section 5, the numerical simulation is carried out and the results reveal that the spacecraft can track the desired attitude trajectory in the presence of time-varying disturbances.

The contributions of this paper are summarized as follows: (i) realizes the super-twisting sliding mode algorithm as a robust, continuous quaternion-based attitude controller for the attitude trajectory tracking demands of a spacecraft with the redundant reaction wheels; (ii) proposes a modified version of LMI which has higher degrees of freedom for finding the decision variables and it can satisfy the convergence performance by requirement; (iii) derives the analytic solution of the nonlinear reduced-order dynamics; and (iv) presents a reference TNB command generation strategy so that the feasibility of the controller can be verified.

2. Reaction Wheels Driven Based on Spacecraft Dynamics Modeling

2.1. Geometry Configuration Analysis. From the perspective of practical realization, to avoid losing a degree of freedom of control in space due to certain actuator faults, the redundant reaction wheels configuration is adopted [30, 37, 38]. The dynamic configuration is shown in Figure 1. To formally derive the governing equations of the attitude dynamics, we firstly define the coordinate system as follows: (i) the body frame denoted as xyz, which is fixed in the body of the spacecraft to represent the attitude of the spacecraft, and (ii) the auxiliary rotation frame denoted as $x_iy_iz_i$, which is fixed in the i-th reaction wheel to describe the relative rotation of i-th reaction wheel to spacecraft.

Taking the first reaction wheel as an example, the geometry mapping relation between xyz and $x_1y_1z_1$ is explained in Figures 2 and 3, respectively. Referring to Figure 2, the body frame xyz rotates about the z-axis with an angle β, and the new frame is denoted as $x'y'z'$. From the rotation property, the mapping relation between $x'y'z'$ and xyz can be constructed as

$$\begin{bmatrix} x' \\ y' \\ z' \end{bmatrix} = \begin{bmatrix} \cos\beta & \sin\beta & 0 \\ -\sin\beta & \cos\beta & 0 \\ 0 & 0 & 1 \end{bmatrix} \begin{bmatrix} x \\ y \\ z \end{bmatrix}. \tag{1}$$

Regarding Figure 3, the frame $x'y'z'$ rotates about negative y-axis with an angle α, and then the new frame $x''y''z''$ is obtained. Again, from the rotation property, we have the mapping relation between $x'y'z'$ and $x''y''z''$:

$$\begin{bmatrix} x'' \\ y'' \\ z'' \end{bmatrix} = \begin{bmatrix} \cos(-\alpha) & 0 & -\sin(-\alpha) \\ 0 & 1 & 0 \\ \sin(-\alpha) & 0 & \cos(-\alpha) \end{bmatrix} \begin{bmatrix} x' \\ y' \\ z' \end{bmatrix}. \tag{2}$$

On the basis of previous illustrations, the mapping relation between xyz and $x_1y_1z_1$ can be derived by combining (1) and (2):

$$\begin{aligned} \begin{bmatrix} x_1 \\ y_1 \\ z_1 \end{bmatrix} &= \begin{bmatrix} x'' \\ y'' \\ z'' \end{bmatrix} = \begin{bmatrix} \cos(-\alpha) & 0 & -\sin(-\alpha) \\ 0 & 1 & 0 \\ \sin(-\alpha) & 0 & \cos(-\alpha) \end{bmatrix} \begin{bmatrix} x' \\ y' \\ z' \end{bmatrix} \\ &= \begin{bmatrix} \cos(-\alpha) & 0 & -\sin(-\alpha) \\ 0 & 1 & 0 \\ \sin(-\alpha) & 0 & \cos(-\alpha) \end{bmatrix} \begin{bmatrix} \cos\beta & \sin\beta & 0 \\ -\sin\beta & \cos\beta & 0 \\ 0 & 0 & 1 \end{bmatrix} \begin{bmatrix} x \\ y \\ z \end{bmatrix}. \end{aligned} \tag{3}$$

In general, the mapping relation between xyz and $x_iy_iz_i$ can be formulated as

$$\begin{bmatrix} x_i \\ y_i \\ z_i \end{bmatrix} = \mathbf{R}_i \begin{bmatrix} x \\ y \\ z \end{bmatrix}, \tag{4}$$

where

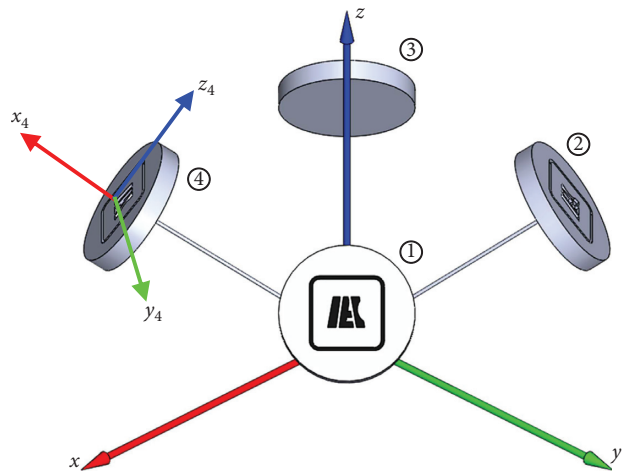

Figure 1: Geometry prototype of the redundant reaction wheels configuration.

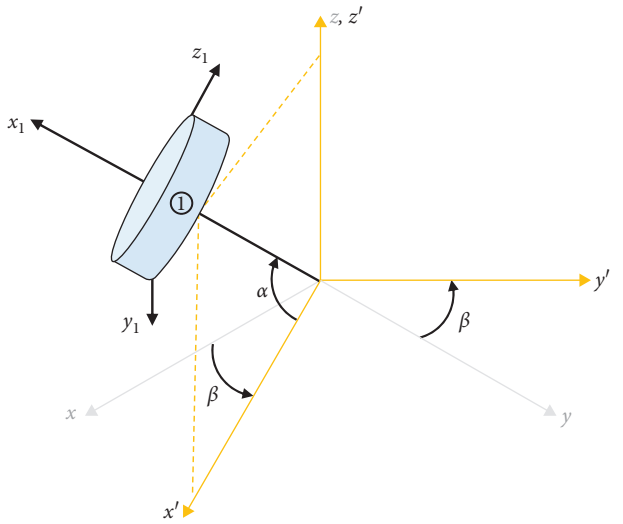

Figure 2: Rotation of body frame xyz to frame $x'y'z'$.

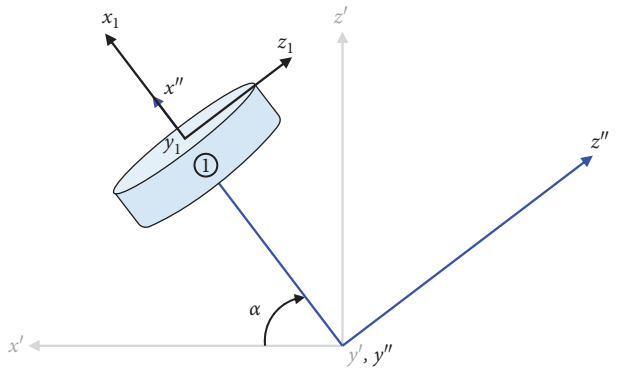

Figure 3: Rotation of frame $x'y'z'$ to frame $x''y''z''$.

$$\mathbf{R}_i = \begin{bmatrix} \cos(-\alpha) & 0 & -\sin(-\alpha) \\ 0 & 1 & 0 \\ \sin(-\alpha) & 0 & \cos(-\alpha) \end{bmatrix} \begin{bmatrix} \cos\beta_i & \sin\beta_i & 0 \\ -\sin\beta_i & \cos\beta_i & 0 \\ 0 & 0 & 1 \end{bmatrix} = \begin{bmatrix} \cos\alpha\cos\beta_i & \cos\alpha\sin\beta_i & \sin\alpha \\ -\sin\beta_i & \cos\beta_i & 0 \\ -\cos\beta_i\sin\alpha & -\sin\alpha\sin\beta_i & \cos\alpha \end{bmatrix}, \tag{5}$$

and $\beta_i = \beta + 0.5(i-1)\pi$, $i = 1, 2, 3, 4$.

2.2. Attitude Dynamics. To avoid the singularity problem in the Euler approaches, the quaternion-based attitude representation is considered. Let $\mathbf{Q} = [q_0, \mathbf{q}^T]^T = [q_0, q_1, q_2, q_3]^T \in \mathbb{R}^4$ be the unit quaternion and let $\boldsymbol{\omega} = [\omega_x, \omega_y, \omega_z]^T \in \mathbb{R}^3$ be the angular velocity of spacecraft; then the quaternion kinematic equations are given by

$$\dot{q}_0 = -\frac{1}{2}\mathbf{q}^T\boldsymbol{\omega}, \tag{6}$$

$$\dot{\mathbf{q}} = \frac{1}{2}(q_0\mathbf{I}_3 + \mathbf{q}^\times)\boldsymbol{\omega}. \tag{7}$$

The above equations can be rewritten in a compact matrix form:

$$\dot{\mathbf{Q}} = \frac{1}{2}\mathbf{E}(\mathbf{Q})\boldsymbol{\omega}, \tag{8}$$

where

$$\mathbf{E}(\mathbf{Q}) = \begin{bmatrix} -\mathbf{q}^T \\ q_0\mathbf{I}_3 + \mathbf{q}^\times \end{bmatrix} = \begin{bmatrix} -q_1 & -q_2 & -q_3 \\ q_0 & -q_3 & q_2 \\ q_3 & q_0 & -q_1 \\ -q_2 & q_1 & q_0 \end{bmatrix}. \tag{9}$$

The symbol $\mathbf{a}^\times$ represents $\mathbf{a}$ cross product matrix of vector $\mathbf{a} = [a_1, a_2, a_3]^T \in \mathbb{R}^3$, which is defined as

$$\mathbf{a}^\times = \begin{bmatrix} 0 & -a_3 & a_2 \\ a_3 & 0 & -a_1 \\ -a_2 & a_1 & 0 \end{bmatrix}. \tag{10}$$

In the following, the kinetic equations based on the redundant reaction wheels configuration will be derived. Let Ω_i, $i = 1, 2, 3, 4$, be the relative rotational speed of each reaction wheel to the spacecraft; then the angular velocity of each reaction wheel with respect to $x_iy_iz_i$ is given by

$$\begin{aligned} \boldsymbol{\omega}_{w,i} &= \mathbf{R}_i\boldsymbol{\omega} + \Omega_i\mathbf{e}_{x_i}, \\ \mathbf{e}_{x_i} &= [\,1 \;\; 0 \;\; 0\,]^T. \end{aligned} \tag{11}$$

The angular momentum of spacecraft relative the body frame xyz is

$$\mathbf{H} = \mathbf{J}\boldsymbol{\omega} = \begin{bmatrix} J_x & -J_{xy} & -J_{xz} \\ -J_{xy} & J_y & -J_{yz} \\ -J_{xz} & -J_{yz} & J_z \end{bmatrix} \begin{bmatrix} \omega_x \\ \omega_y \\ \omega_z \end{bmatrix}. \tag{12}$$

Assume that the reaction wheels are perfect circle plate. Hence, the moment of inertia matrix of i-th reaction wheel with respect to $x_i y_i z_i$ is

$$\mathbf{J}_{w,i} = \begin{bmatrix} J_{m,i} & 0 & 0 \\ 0 & J_i' & 0 \\ 0 & 0 & J_i' \end{bmatrix}. \tag{13}$$

The angular momentum of each reaction wheel relative frame $x_i y_i z_i$ can be constructed:

$$\begin{aligned} \mathbf{H}_{w,i} &= \mathbf{J}_{w,i}\boldsymbol{\omega}_{w,i} \\ &= \mathbf{J}_{w,i}\left(\mathbf{R}_i\boldsymbol{\omega} + \Omega_i \mathbf{e}_{x_i}\right) \\ &= \mathbf{J}_{w,i}\mathbf{R}_i\boldsymbol{\omega} + \mathbf{J}_w\Omega_i\mathbf{e}_{x_i} \\ &= \mathbf{J}_{w,i}\mathbf{R}_i\boldsymbol{\omega} + J_{mi}\Omega_i\mathbf{e}_{x_i}. \end{aligned} \tag{14}$$

Mapping $\mathbf{H}_{w,i}$ onto spacecraft body frame xyz yields

$$\begin{aligned} \mathbf{H}_{w,i}^B &= \mathbf{R}_i^T\boldsymbol{\omega}_{w,i} \\ &= \mathbf{R}_i^T\left(\mathbf{J}_{w,i}\mathbf{R}_i\boldsymbol{\omega} + J_{mi}\Omega_i\mathbf{e}_{x_i}\right) \\ &= \mathbf{R}_i^T\mathbf{J}_{w,i}\mathbf{R}_i\boldsymbol{\omega} + \mathbf{R}_i^T J_{mi}\Omega_i\mathbf{e}_{x_i}. \end{aligned} \tag{15}$$

The total angular momentum of the system (spacecraft and reaction wheels), $\mathbf{H}_T$, is the summation of $\mathbf{H}$ and $\mathbf{H}_{w,i}^B$, which is

$$\begin{aligned} \mathbf{H}_T &= \mathbf{H} + \sum_{i=1}^{4}\mathbf{H}_{w,i}^B \\ &= \mathbf{J}\boldsymbol{\omega} + \sum_{i=1}^{4}\left(\mathbf{R}_i^T\mathbf{J}_{w,i}\mathbf{R}_i\boldsymbol{\omega} + \mathbf{R}_i^T J_{mi}\Omega_i\mathbf{e}_{x_i}\right) \\ &= \left(\mathbf{J} + \sum_{i=1}^{4}\mathbf{R}_i^T\mathbf{J}_{w,i}\mathbf{R}_i\right)\boldsymbol{\omega} + \sum_{i=1}^{4}\mathbf{R}_i^T J_{mi}\Omega_i\mathbf{e}_{x_i}. \end{aligned} \tag{16}$$

The term

$$\begin{aligned} \sum_{i=1}^{4}\mathbf{R}_i^T J_m\Omega_i\mathbf{e}_{x_i} &= \begin{bmatrix} \cos\alpha\cos\beta \\ \cos\alpha\sin\beta \\ \sin\alpha \end{bmatrix} J_{m1}\Omega_1 + \begin{bmatrix} -\cos\alpha\sin\beta \\ \cos\alpha\cos\beta \\ \sin\alpha \end{bmatrix} J_{m2}\Omega_2 + \begin{bmatrix} -\cos\alpha\cos\beta \\ -\cos\alpha\sin\beta \\ \sin\alpha \end{bmatrix} J_{m3}\Omega_3 + \begin{bmatrix} \cos\alpha\cos\beta \\ -\cos\alpha\sin\beta \\ \sin\alpha \end{bmatrix} J_{m4}\Omega_4 \\ &= \begin{bmatrix} \cos\alpha\cos\beta & -\cos\alpha\sin\beta & -\cos\alpha\cos\beta & \cos\alpha\sin\beta \\ \cos\alpha\sin\beta & \cos\alpha\cos\beta & -\cos\alpha\sin\beta & -\cos\alpha\cos\beta \\ \sin\alpha & \sin\alpha & \sin\alpha & \sin\alpha \end{bmatrix} \begin{bmatrix} J_{m1} & 0 & 0 & 0 \\ 0 & J_{m2} & 0 & 0 \\ 0 & 0 & J_{m3} & 0 \\ 0 & 0 & 0 & J_{m4} \end{bmatrix} \begin{bmatrix} \Omega_1 \\ \Omega_2 \\ \Omega_3 \\ \Omega_4 \end{bmatrix}. \end{aligned} \tag{17}$$

Define the following:

(i) Equivalent moment of inertia matrix of the system:

$$\mathbf{J}_{eq} = \mathbf{J} + \sum_{i=1}^{4}\mathbf{R}_i^T\mathbf{J}_{w,i}\mathbf{R}_i. \tag{18}$$

(ii) Force distribution matrix (FDM):

$$\Gamma = \begin{bmatrix} \cos\alpha\cos\beta & -\cos\alpha\sin\beta & -\cos\alpha\cos\beta & \cos\alpha\sin\beta \\ \cos\alpha\sin\beta & \cos\alpha\cos\beta & -\cos\alpha\sin\beta & -\cos\alpha\cos\beta \\ \sin\alpha & \sin\alpha & \sin\alpha & \sin\alpha \end{bmatrix}. \tag{19}$$

(iii) Axial moment of inertia matrix:

$$\mathbf{J}_m = \begin{bmatrix} J_{m1} & 0 & 0 & 0 \\ 0 & J_{m2} & 0 & 0 \\ 0 & 0 & J_{m3} & 0 \\ 0 & 0 & 0 & J_{m4} \end{bmatrix}. \tag{20}$$

Combining (17)–(20), equation (16) can be further simplified to

$$\mathbf{H}_T = \mathbf{J}_{eq}\boldsymbol{\omega} + \Gamma\mathbf{J}_m\boldsymbol{\Omega}, \tag{21}$$

where $\boldsymbol{\Omega} = [\Omega_1, \Omega_2, \Omega_3, \Omega_4]^T$. The Euler equation of motion is given by

$$\mathbf{M}_G = \left(\frac{\mathrm{d}\mathbf{H}_T}{\mathrm{d}t}\right)_B + \boldsymbol{\omega}^{\times}\mathbf{H}_T, \tag{22}$$

in which the total external torque $\mathbf{M}_G$ is equal to the summation of the external control torques $\boldsymbol{\tau}_a$ and the external disturbance torques $\mathbf{d}(t)$. Substituting (21) into (22) yields

$$\boldsymbol{\tau}_a + \mathbf{d} = \mathbf{J}_{eq}\dot{\boldsymbol{\omega}} + \Gamma\mathbf{J}_m\dot{\boldsymbol{\Omega}} + \boldsymbol{\omega}^{\times}\left(\mathbf{J}_{eq}\boldsymbol{\omega} + \Gamma\mathbf{J}_m\boldsymbol{\Omega}\right). \tag{23}$$

Define the control torque τ and the reaction torque τ_w as

$$\begin{aligned} \boldsymbol{\tau}_c &= \Gamma\boldsymbol{\tau}_w \triangleq \begin{bmatrix} \tau_{cx} & \tau_{cy} & \tau_{cz} \end{bmatrix}^T, \\ \boldsymbol{\tau}_w &= -\mathbf{J}_m\dot{\boldsymbol{\Omega}} = -\begin{bmatrix} J_{m1}\dot{\Omega}_1 & J_{m2}\dot{\Omega}_2 & J_{m3}\dot{\Omega}_3 & J_{m4}\dot{\Omega}_4 \end{bmatrix}^T \\ &\triangleq \begin{bmatrix} \tau_{w1} & \tau_{w2} & \tau_{w3} & \tau_{w4} \end{bmatrix}^T. \end{aligned} \tag{24}$$

Hence, (23) can be further simplified as

$$\mathbf{J}_{eq}\dot{\boldsymbol{\omega}} = \boldsymbol{\tau}_a + \boldsymbol{\tau}_c + \mathbf{d} - \boldsymbol{\omega}^{\times}\left(\mathbf{J}_{eq}\boldsymbol{\omega} + \Gamma\mathbf{J}_m\boldsymbol{\Omega}\right). \tag{25}$$

In this paper, $\boldsymbol{\tau}_a = \mathbf{0}$ is considered.

2.3. Actuator Analysis. From (24), we have

$$\begin{bmatrix}\tau_{cx}\\ \tau_{cy}\\ \tau_{cz}\end{bmatrix} = \begin{bmatrix}\cos\alpha\cos\beta & -\cos\alpha\sin\beta & -\cos\alpha\cos\beta & \cos\alpha\sin\beta\\ \cos\alpha\sin\beta & \cos\alpha\cos\beta & -\cos\alpha\sin\beta & -\cos\alpha\cos\beta\\ \sin\alpha & \sin\alpha & \sin\alpha & \sin\alpha\end{bmatrix}\begin{bmatrix}\tau_{w1}\\ \tau_{w2}\\ \tau_{w3}\\ \tau_{w4}\end{bmatrix}. \tag{26}$$

Once $\boldsymbol{\tau}_c$ is designed for the attitude trajectory tracking demands of the system dynamics (6), (7), and (25), it is desired to obtain each reaction torque τ_{wi}. However, FDM (19) is a nonsquare matrix, so the inverse does not exist. To obtain the FDM with a special matrix structure, the two following geometry constraints are imposed [30]:

$$\begin{aligned}\sin\beta &= \cos\beta, \quad 0 \le \beta < \frac{\pi}{2},\\ \cos\alpha\sin\beta &= \sin\alpha, \quad 0 \le \alpha < \frac{\pi}{2},\end{aligned} \tag{27}$$

or, equivalently,

$$\begin{aligned}\beta &= \frac{\pi}{4},\\ \sin\alpha &= \frac{\sqrt{3}}{3}.\end{aligned} \tag{28}$$

From (27), we have the following FDM:

$$\Gamma = \frac{\sqrt{3}}{3}\begin{bmatrix}1 & -1 & -1 & 1\\ 1 & 1 & -1 & -1\\ 1 & 1 & 1 & 1\end{bmatrix}, \tag{29}$$

and then the following static optimization problem is formulated [30]:

$$\min_{\tau_w} \mathscr{T} = \sum_{i=1}^{4}\tau_{wi}^2, \tag{30}$$

subject to

$$\begin{aligned}g_1 &\triangleq \frac{\sqrt{3}}{3}\left(\tau_{w1} - \tau_{w2} - \tau_{w3} + \tau_{w4}\right) - \tau_{cx} = 0,\\ g_2 &\triangleq \frac{\sqrt{3}}{3}\left(\tau_{w1} + \tau_{w2} - \tau_{w3} - \tau_{w4}\right) - \tau_{cy} = 0,\\ g_3 &\triangleq \frac{\sqrt{3}}{3}\left(\tau_{w1} + \tau_{w2} + \tau_{w3} + \tau_{w4}\right) - \tau_{cz} = 0.\end{aligned} \tag{31}$$

To formally address the problem, refer to [39], and define the Lagrangian $\mathscr{L}$ together with the Lagrange multiplier $\boldsymbol{\lambda} = [\boldsymbol{\lambda}_1, \boldsymbol{\lambda}_2, \boldsymbol{\lambda}_3]^T \in \mathbb{R}^3$ as follows:

$$\mathscr{L} = \mathscr{T} + \lambda_1 g_1 + \lambda_2 g_2 + \lambda_3 g_3. \tag{32}$$

Let $\boldsymbol{\tau}_w^*$ and $\boldsymbol{\lambda}^*$ be the optimal solution. The first-order necessary condition to minimize $\mathscr{T}$ is

$$\begin{aligned}\left.\frac{\partial\mathscr{L}}{\partial\tau_{w1}}\right|_{\tau^*,\lambda^*} &= 2\tau_{w1}^* + \frac{\sqrt{3}}{3}\lambda_1^* + \frac{\sqrt{3}}{3}\lambda_2^* + \frac{\sqrt{3}}{3}\lambda_3^* = 0,\\ \left.\frac{\partial\mathscr{L}}{\partial\tau_{w2}}\right|_{\tau^*,\lambda^*} &= 2\tau_{w2}^* - \frac{\sqrt{3}}{3}\lambda_1^* + \frac{\sqrt{3}}{3}\lambda_2^* + \frac{\sqrt{3}}{3}\lambda_3^* = 0,\\ \left.\frac{\partial\mathscr{L}}{\partial\tau_{w3}}\right|_{\tau^*,\lambda^*} &= 2\tau_{w3}^* - \frac{\sqrt{3}}{3}\lambda_1^* - \frac{\sqrt{3}}{3}\lambda_2^* + \frac{\sqrt{3}}{3}\lambda_3^* = 0,\\ \left.\frac{\partial\mathscr{L}}{\partial\tau_{w4}}\right|_{\tau^*,\lambda^*} &= 2\tau_{w4}^* + \frac{\sqrt{3}}{3}\lambda_1^* - \frac{\sqrt{3}}{3}\lambda_2^* + \frac{\sqrt{3}}{3}\lambda_3^* = 0,\end{aligned} \tag{33}$$

and

$$\begin{aligned}\left.\frac{\partial\mathscr{L}}{\partial\lambda_1}\right|_{\tau^*,\lambda^*} &= \frac{\sqrt{3}}{3}\left(\tau_{w1}^* - \tau_{w2}^* - \tau_{w3}^* + \tau_{w4}^*\right) - \tau_{cx} = 0,\\ \left.\frac{\partial\mathscr{L}}{\partial\lambda_2}\right|_{\tau^*,\lambda^*} &= \frac{\sqrt{3}}{3}\left(\tau_{w1}^* + \tau_{w2}^* - \tau_{w3}^* - \tau_{w4}^*\right) - \tau_{cy} = 0,\\ \left.\frac{\partial\mathscr{L}}{\partial\lambda_3}\right|_{\tau^*,\lambda^*} &= \frac{\sqrt{3}}{3}\left(\tau_{w1}^* + \tau_{w2}^* + \tau_{w3}^* + \tau_{w4}^*\right) - \tau_{cz} = 0.\end{aligned} \tag{34}$$

From (33), it is implied that

$$\tau_{w1}^* - \tau_{w2}^* + \tau_{w3}^* - \tau_{w4}^* = 0. \tag{35}$$

Combining (34) and (35), the distribution matrix can be augmented as

$$\begin{bmatrix}\tau_{cx}\\ \tau_{cy}\\ \tau_{cz}\\ 0\end{bmatrix} = \begin{bmatrix}\frac{\sqrt{3}}{3} & -\frac{\sqrt{3}}{3} & -\frac{\sqrt{3}}{3} & \frac{\sqrt{3}}{3}\\ \frac{\sqrt{3}}{3} & \frac{\sqrt{3}}{3} & -\frac{\sqrt{3}}{3} & -\frac{\sqrt{3}}{3}\\ \frac{\sqrt{3}}{3} & \frac{\sqrt{3}}{3} & \frac{\sqrt{3}}{3} & \frac{\sqrt{3}}{3}\\ 1 & -1 & 1 & -1\end{bmatrix}\begin{bmatrix}\tau_{w1}^*\\ \tau_{w2}^*\\ \tau_{w3}^*\\ \tau_{w4}^*\end{bmatrix}. \tag{36}$$

The inverse mapping is

$$\begin{bmatrix}\tau_{w1}^*\\ \tau_{w2}^*\\ \tau_{w3}^*\\ \tau_{w4}^*\end{bmatrix} = \frac{1}{4}\begin{bmatrix}\sqrt{3} & \sqrt{3} & \sqrt{3} & 1\\ -\sqrt{3} & \sqrt{3} & \sqrt{3} & -1\\ -\sqrt{3} & -\sqrt{3} & \sqrt{3} & 1\\ \sqrt{3} & -\sqrt{3} & \sqrt{3} & -1\end{bmatrix}\begin{bmatrix}\tau_{cx}\\ \tau_{cy}\\ \tau_{cz}\\ 0\end{bmatrix}. \tag{37}$$

Hence, when $\boldsymbol{\tau}_c$ is designed for the system dynamics (6), (7), and (25), the reaction torque $\boldsymbol{\tau}_{wi}$ for each reaction wheel can be obtained by inverse mapping (37). Moreover, it can be guaranteed that the reaction torque is an optimal value $\boldsymbol{\tau}_w^*$ to minimize the performance index (30).

Because the reaction wheels are actuated by servo motors, that is, the reaction torques are generated by servo motors, the following linear dynamic equation is considered:

$$J_{mi}\dot{\Omega}_i = -a_i\Omega_i + b_iV_{\text{in},i}, \quad i = 1,2,3,4. \tag{38}$$

From the definition, (24) and (38) become

$$V_{\text{in},i} = \frac{1}{b_i}\left(-\tau_{wi} + a_i\Omega_i\right) \quad i = 1,2,3,4, \tag{39}$$

where the parameters $a_i = 0.02$ and $b_i = 3$ are considered. $V_{\text{in},i}$ is the control input voltage.

Conclusively, $\boldsymbol{\tau}_c$ is first designed for the system dynamics (6), (7), and (25). Secondly, inverse mapping (37) is used to obtain the optimal reaction torque τ_{wi} of each reaction wheel to minimize the energy cost (30). Finally, apply (39) to obtain the corresponding control voltage $V_{\text{in},i}$. In the following, the discussion focuses on how to design $\boldsymbol{\tau}_c$ so that the desired trajectory can be achieved in the presence of time-varying disturbances.

3. Super-Twisting Sliding Mode Controller Design

3.1. Super-Twisting Sliding Mode Algorithm. The design process of sliding mode control includes two steps: (i) A sliding variable s is designed so that the stability of the reduced-order dynamics can be guaranteed. (ii) Seeking the robust, continuous control law to guarantee the sliding mode $s = \dot{s} = 0$ occurs in a finite time in the presence of the time-varying external disturbances. In the following, the super-twisting sliding mode algorithm [19] is introduced.

The super-twisting sliding mode algorithm is one of the outstanding robust control algorithms which handles a system with a relative degree ($u \longrightarrow s$) equal to one. Based on the algorithm, the closed-loop sliding dynamics is designed as

$$\dot{s} = -k_1|s|^{1/2}\text{sign}(s) - k_2\int_0^t \text{sign}(s)\text{d}\tau + \text{d}(t), \tag{40}$$

where $s = s(\text{x},t) \in \mathbb{R}$ is the sliding variable; $\text{x} \in \mathbb{R}^n$ is state vector; $\text{d}(t) \in \mathbb{R}$ is an unknown time-varying perturbation and it is assumed that $|\dot{\text{d}}(t)| \le \delta$; the gain pair (k_1, k_2) is to be designed so that the sliding mode can occur in a finite time.

In fact, the more general representation of (40) is to express it as the following state-space form. Let

$$\begin{aligned} z_1 &= s(x,t). \\ z_2 &= -k_2\int_0^t \text{sign}(s)\text{d}\tau + \text{d}(t), \end{aligned} \tag{41}$$

which implies

$$\begin{aligned} \dot{z}_1 &= -k_1|z_1|^{1/2}\text{sign}(z_1) + z_2, \\ \dot{z}_2 &= -k_2\text{sign}(z_1) + \rho, \end{aligned} \tag{42}$$

where $\rho(t) = \dot{d}(t)$ and $|\rho(t)| = |\dot{d}(t)| \le \delta$. Since (42) is nonlinear, consider the following variable transformation [20]:

$$\begin{aligned} \zeta_1 &= |z_1|^{1/2}\text{sign}(z_1), \\ \zeta_2 &= z_2. \end{aligned} \tag{43}$$

Taking the time derivative yields

$$\begin{aligned} \dot{\zeta}_1 &= \frac{\dot{z}_1|z_1|^{1/2} - z_1\cdot(1/2)|z_1|^{-1/2}\cdot\text{sign}(z_1)\cdot\dot{z}_1}{|z_1|} = \frac{\left[-k_1|z_1|^{1/2}\text{sign}(z_1) + z_2\right]\cdot\left(|z_1|^{1/2} - (1/2)|z_1|^{1/2}\right)}{|z_1|} \\ &= \frac{1}{|z_1|^{1/2}}\left(-\frac{k_1}{2}|z_1|^{1/2}\text{sign}(z_1) + \frac{1}{2}z_2\right) = \frac{1}{|\zeta_1|}\left(-\frac{k_1}{2}\zeta_1 + \frac{1}{2}\zeta_2\right), \\ \dot{\zeta}_2 &= -k_2\text{sign}(z_1) + \rho = \frac{1}{|z_1|^{1/2}}\left(-k_2|z_1|^{1/2}\text{sign}(z_1) + |z_1|^{1/2}\rho\right) = \frac{1}{|\zeta_1|}\left(-k_2\zeta_1 + |\zeta_1|\rho\right), \end{aligned} \tag{44}$$

which can be rewritten in the matrix form as

$$\begin{aligned} \dot{\boldsymbol{\zeta}} &= \frac{1}{|\zeta_1|}\left(\mathbf{A}\boldsymbol{\zeta} + \mathbf{B}\tilde{\rho}\right), \\ \mathbf{A} &= \begin{bmatrix} -0.5k_1 & 0.5 \\ -k_2 & 0 \end{bmatrix}, \\ \mathbf{B} &= \begin{bmatrix} 0 \\ 1 \end{bmatrix}, \end{aligned} \tag{45}$$

where $\boldsymbol{\zeta} = [\zeta_1, \zeta_2]^T$ and $|\zeta_1| = |z_1|^{1/2}$. Disturbance transformation $\tilde{\rho}(t,\zeta_1) = \rho(t)|\zeta_1|$ satisfies

$$|\tilde{\rho}(t,\zeta_1)| \le \delta|\zeta_1|. \tag{46}$$

For system (45), the stability problem is proven in the following. It is shown that the stability issue can be reformulated as a feasibility problem in terms of the LMI.

Theorem 1 (See[21, 22, 25]). *Suppose that there exist symmetric and positive definite matrices* $\mathbf{P} = \mathbf{P}^T > 0$ *and* $\mathbf{Q}_c = \mathbf{Q}_c^T > 0$ *so that the following LMI,*

$$\begin{bmatrix} \mathbf{PA} + \mathbf{A}^T\mathbf{P} + \mathbf{Q}_c + \mathbf{C}^T\mathbf{C} & \mathbf{PB} \\ \mathbf{B}^T\mathbf{P} & -\gamma^2 \end{bmatrix} < 0, \tag{47}$$

is feasible, where $\gamma = 1/\delta$, $\mathbf{C} = [\,1 \;\; 0\,]$, *and* $\mathbf{A}$ *and* $\mathbf{B}$ *are provided in (45). Then the quadratic form,*

$$V = \boldsymbol{\zeta}^T\mathbf{P}\boldsymbol{\zeta}, \tag{48}$$

is a strict Lyapunov function for system (45) and the trajectory reaches the origin in a finite time.

Proof of Theorem 1. Applying the Rayleigh inequality, V is bounded by

$$\lambda_{\min}(\mathbf{P})\|\boldsymbol{\zeta}\|^2 \le V \le \lambda_{\max}(\mathbf{P})\|\boldsymbol{\zeta}\|^2, \tag{49}$$

where $\|\boldsymbol{\zeta}\|^2 = |z_1| + z_2^2$ represents the Euclidean norm of $\boldsymbol{\zeta}$. For (48), taking time derivative gives

$$\dot{V} = \frac{1}{|\zeta_1|}\left[\boldsymbol{\zeta}^T\left(\mathbf{PA} + \mathbf{A}^T\mathbf{P}\right)\boldsymbol{\zeta} + \boldsymbol{\zeta}^T\mathbf{PB}\tilde{\rho} + \tilde{\rho}\mathbf{B}^T\mathbf{P}\boldsymbol{\zeta}\right]. \tag{50}$$

According to (46), the following inequality is satisfied:

$$\left|\tilde{\rho}(t,\zeta_1)\right|^2 \le \delta^2|\zeta_1|^2 \le \delta^2\left(\zeta_1^2 + \zeta_2^2\right), \tag{51}$$

which guarantees

$$\boldsymbol{\zeta}^T\boldsymbol{\zeta} - \frac{1}{\delta^2}\tilde{\rho}(t,\zeta_1)^2 > 0. \tag{52}$$

Hence, (50) can be rewritten as

$$\begin{aligned}
\dot{V} &\le \frac{1}{|\zeta_1|}\left[\boldsymbol{\zeta}^T\left(\mathbf{PA} + \mathbf{A}^T\mathbf{P}\right)\boldsymbol{\zeta} + \boldsymbol{\zeta}^T\mathbf{PB}\tilde{\rho} + \tilde{\rho}\mathbf{B}^T\mathbf{P}\boldsymbol{\zeta} + \boldsymbol{\zeta}^T\boldsymbol{\zeta} - \frac{1}{\delta^2}\tilde{\rho}^2\right] \\
&= \frac{1}{|\zeta_1|}\left[\boldsymbol{\zeta}^T\left(\mathbf{PA} + \mathbf{A}^T\mathbf{P} + \mathbf{C}^T\mathbf{C} + \mathbf{Q}_c - \mathbf{Q}_c\right)\boldsymbol{\zeta} + \boldsymbol{\zeta}^T\mathbf{PB}\tilde{\rho} + \tilde{\rho}\mathbf{B}^T\mathbf{P}\boldsymbol{\zeta} - \frac{1}{\delta^2}\tilde{\rho}^2\right] \\
&= -\frac{1}{|\zeta_1|}\boldsymbol{\zeta}^T\mathbf{Q}_c\boldsymbol{\zeta} + \frac{1}{|\zeta_1|}\begin{bmatrix}\boldsymbol{\zeta} \\ \tilde{\rho}\end{bmatrix}^T\begin{bmatrix}\mathbf{PA} + \mathbf{A}^T\mathbf{P} + \mathbf{Q}_c + \mathbf{C}^T\mathbf{C} & \mathbf{PB} \\ \mathbf{B}^T\mathbf{P} & -\gamma^2\end{bmatrix}\begin{bmatrix}\boldsymbol{\zeta} \\ \tilde{\rho}\end{bmatrix}.
\end{aligned} \tag{53}$$

where $\gamma = 1/\delta$.

Based on (47) and (49), (53) can be further simplified to

$$\dot{V} \le -\frac{1}{|\zeta_1|}\boldsymbol{\zeta}^T\mathbf{Q}_c\boldsymbol{\zeta} \le -\frac{1}{|\zeta_1|}\lambda_{\min}(\mathbf{Q}_c)\|\boldsymbol{\zeta}\|^2 \le -\frac{1}{|\zeta_1|}\lambda_{\min}(\mathbf{Q}_c)\frac{V}{\lambda_{\max}(\mathbf{P})}. \tag{54}$$

Again, from (49), the following inequality can be deduced:

$$-\frac{1}{|\zeta_1|} \le -\frac{1}{\|\boldsymbol{\zeta}\|} \le -\frac{\lambda_{\min}^{1/2}(\mathbf{P})}{V^{1/2}}. \tag{55}$$

Based on (55), it can be concluded that (54) satisfies

$$\dot{V} \le -\alpha V^{1/2}, \quad \alpha = \frac{\lambda_{\min}(\mathbf{Q}_c)\lambda_{\min}^{1/2}(\mathbf{P})}{\lambda_{\max}(\mathbf{P})}. \tag{56}$$

For (56), one has

$$\int_{V(0)}^{V(t)}\frac{\mathrm{d}V}{V^{1/2}} \le -\alpha\int_0^t \mathrm{d}t, \tag{57}$$

which implies

$$V(t) \le \left(V^{1/2}(0) - \frac{\alpha}{2}t\right)^2. \tag{58}$$

Hence, $V(t)$ reaches zero within a finite time described by

$$t_f \le \frac{2V^{1/2}(0)}{\alpha}, \tag{59}$$

where $V(0)$ is the initial condition of $V(t)$ and α is given by (56). Based on the appropriate gain pair (k_1, k_2) selection, the LMI equation (47) can be established. As a result, the finite time stability as shown by (59) can be achieved.

In Theorem 1, we suppose that the LMI (47) is negative definite. Theorem 2 is similar to [21, 22, 25] and is presented for the feasibility of LMI (48) in Theorem 1.

Theorem 2. *Consider the LMI given by (47); there exists a feasible solution* $\mathbf{P}$, $\mathbf{Q}^c$ *so that the LMI (47) can be established if and only if the parameters* k_1 *and* k_2 *in* $\mathbf{A}$ *satisfy*

$$\begin{aligned} k_2 &> \delta, \\ k_1^2 &> 4k_2, \end{aligned} \tag{60}$$

or

$$k_1^2\left(\frac{1}{2}k_2 - \frac{1}{16}k_1^2\right) < \delta^2, \quad 4k_2 > k_1^2. \tag{61}$$

Furthermore, the additional constraints $k_2 \neq 0$ *for (60) and* $k_1 \neq 0$ *and* $k_1^2 \neq 8k_2$ *for (61) must also be satisfied.*

Proof of Theorem 2. If the LMI (45) is feasible, then the $\mathscr{L}_2$-gain of the following system,

$$G(s) = \frac{1/2}{s^2 + (1/2)k_1 s + (1/2)k_2}, \tag{62}$$

must be less than or equal to γ; that is,

$$\max_{\omega} |G(j\omega)| < \gamma = \frac{1}{\delta} \Rightarrow \max_{\omega} |G(j\omega)|^2 < \frac{1}{\delta^2}. \tag{63}$$

The above statement is the so-called bounded-real condition [40]. In order to find proper (k_1, k_2) in (62) so that condition (63) can be satisfied, calculate

$$|G(j\omega)|^2 = \frac{1}{\left(k_2 - 2\omega^2\right)^2 + \left(k_1\omega\right)^2}, \tag{64}$$

and its derivative

$$\frac{\mathrm{d}}{\mathrm{d}\omega}|G(j\omega)|^2 = -\frac{16\omega\left(\omega^2 + (1/8)k_1^2 - (1/2)k_2\right)}{\left[\left(k_2 - 2\omega^2\right)^2 + \left(k_1\omega\right)^2\right]^2}. \tag{65}$$

The extreme point can be obtained by setting (65) equal to zero. Checking for the second-order sufficient condition $\mathrm{d}^2/\mathrm{d}\omega^2|G(j\omega)|^2$, it can be deduced that $\max_\omega|G(j\omega)|$ can be reached, when

$$\omega = \begin{cases} 0, & \text{if } 4k_2 - k_1^2 < 0, \\ \left(\dfrac{4k_2 - k_1^2}{8}\right)^{1/2}, & \text{if } 4k_2 - k_1^2 > 0. \end{cases} \tag{66}$$

Substituting (66) into (64) yields

$$\max_{\omega} |G(j\omega)|^2 = \begin{cases} \dfrac{1}{k_2^2}, & \text{if } 4k_2 - k_1^2 < 0. \\ \dfrac{1}{k_1^2\left((1/2)k_2 - (1/16)k_1^2\right)}, & \text{if } 4k_2 - k_1^2 > 0. \end{cases} \tag{67}$$

Thus, combining (63) and (67) shows that if

$$\begin{aligned} k_2 &> \delta, \\ k_1^2 &> 4k_2, \end{aligned} \tag{68}$$

or

$$k_1^2\left(\frac{1}{2}k_2 - \frac{1}{16}k_1^2\right) > \delta^2, \quad 4k_2 > k_1^2, \tag{69}$$

then the LMI (47) is feasible. Moreover, to avoid the singularity of (67), the constraints $k_2 \neq 0$ for (68) and $k_1 \neq 0$ and $k_1^2 \neq 8k_2$ for (69) are made. □

Remark 1. Notice that system (62) is not a transfer function of system (45); it is the corresponding linear system of LMI (47). More details can be found in [40].

3.2. Controller Design. The control objective is to design a robust control torque τ_c such that the spacecraft can achieve the arbitrary attitude trajectory tracking demands in the presence of time-varying disturbances.

For this reason, let $\mathbf{Q}_d = [q_{0d}, \mathbf{q}_d^T]^T = [q_{0d}, q_{1d}, q_{2d}, q_{3d}]^T \in \mathbb{R}^4$ be the desired quaternion and let $\boldsymbol{\omega}_d = [\omega_{xd}, \omega_{yd}, \omega_{zd}]^T \in \mathbb{R}^3$ be the desired angular velocity. Define the tracking error vectors $\mathcal{Q}_e = [q_{0e}, \mathbf{q}_e^T]^T \in \mathbb{R}^4$ and $\boldsymbol{\omega}_e = [\omega_{xe}, \omega_{ye}, \omega_{ze}]^T \in \mathbb{R}^3$ as follows [36]:

$$\begin{aligned} \mathbf{Q}_e &= \mathbf{Q}_d^{-1} \otimes \mathbf{Q} = \begin{bmatrix} q_{0e} \\ \mathbf{q}_e \end{bmatrix} = \begin{bmatrix} q_{0d}q_0 + \mathbf{q}_d^T\mathbf{q} \\ q_{0d}\mathbf{q} - q_0\mathbf{q}_d - \mathbf{q}_d^\times\mathbf{q} \end{bmatrix}, \\ \boldsymbol{\omega}_e &= \omega - \omega_d = \begin{bmatrix} \omega_{xe} \\ \omega_{ye} \\ \omega_{ze} \end{bmatrix} = \begin{bmatrix} \omega_x - \omega_{xd} \\ \omega_y - \omega_{yd} \\ \omega_z - \omega_{zd} \end{bmatrix}, \end{aligned} \tag{70}$$

where $\otimes$ represents the quaternion multiplication. Based on (70), the quaternion-based error dynamics of (6), (7), and (25) is given by

$$\dot{q}_{0e} = -\frac{1}{2}\mathbf{q}_e^T\omega_e, \tag{71}$$

$$\dot{\mathbf{q}}_e = \frac{1}{2}\left(q_{0e}\mathbf{I}_3 + \mathbf{q}_e^\times\right)\omega_e, \tag{72}$$

$$\dot{\omega}_e = \mathbf{J}_{eq}^{-1}\left[-\boldsymbol{\tau}_c + \mathbf{d} - \omega^\times\left(\mathbf{J}_{eq}\omega + \Gamma\mathbf{J}_m\boldsymbol{\Omega}\right)\right] - \dot{\omega}_d. \tag{73}$$

Select the sliding surface as

$$\mathbf{S} = \boldsymbol{\omega}_e + \lambda\mathbf{q}_e, \tag{74}$$

where $\mathbf{S} = [s_1, s_2, s_3]^T \in \mathbb{R}^3$; $\lambda \in \mathbb{R}^1$ is a positive parameter to be designed.

Suppose that the sliding motion is fulfilled in a finite time $t = t_f$; it gives

$$\mathbf{S} = \dot{\mathbf{S}} = \mathbf{0}, \quad \forall t \geq t_f. \tag{75}$$

From (71), (72), (74), and (75), the nonlinear reduced-order dynamics can be obtained:

$$\begin{aligned} \dot{q}_{0e} &= -\frac{1}{2}\mathbf{q}_e^T\omega_e \\ &= -\frac{1}{2}\mathbf{q}_e^T\left(-\lambda\mathbf{q}_e\right) \\ &= \frac{1}{2}\lambda\mathbf{q}_e^T\mathbf{q}_e, \quad \forall t \geq t_f, \end{aligned} \tag{76}$$

$$\begin{aligned} \dot{\mathbf{q}}_e &= \frac{1}{2}\left(q_{0e}\mathbf{I}_3 + \mathbf{q}_e^\times\right)\left(-\lambda\mathbf{q}_e\right) \\ &= -\frac{1}{2}\lambda q_{0e}\mathbf{q}_e, \quad \forall t \geq t_f. \end{aligned} \tag{77}$$

The term "reduced-order" means that the system error dynamics described by (71)–(73 with order 7 "reduced" to subsystem (76) and (77) with order 4. In order to analyze the stability of the reduced-order dynamics, apply the identity of unit quaternion:

$$q_{0e}^2 + \mathbf{q}_e^T\mathbf{q}_e = 1. \tag{78}$$

Equation (76) can be decoupled as

$$\dot{q}_{0e} = \frac{1}{2}\lambda\left(1 - q_{0e}^2\right), \quad \forall t \geq t_f. \tag{79}$$

Then, consider the following variable transformation:

$$q_{0e}(t) = 1 + \frac{1}{y(t)}, \tag{80}$$

which implies

$$\dot{q}_{0e}(t) = -\frac{\dot{y}(t)}{y^2}. \tag{81}$$

Substituting (79) yields

$$-\frac{\dot{y}(t)}{y^2} = \frac{1}{2}\lambda\left[1 - \left(1 + \frac{1}{y(t)}\right)^2\right] = \frac{1}{2}\lambda\left(-\frac{2}{y} - \frac{1}{y^2}\right), \tag{82}$$

which implies

$$\dot{y} - \lambda y = \frac{1}{2}\lambda. \tag{83}$$

Clearly, equation (83) is a linear ordinary differential equation. Its solution is given by

$$y(t) = Ce^{\lambda t} - \frac{1}{2}, \tag{84}$$

where C is an integration constant. Apply the inverse mapping from (80); we get

$$q_{0e}(t) = 1 + \frac{1}{-(1/2) + Ce^{\lambda t}}. \tag{85}$$

Let $q_{0e}(0)$ be the initial condition; we have

$$C = \frac{1}{2} + \frac{1}{q_{0e}(0) - 1}. \tag{86}$$

Hence, the analytic solution of (79) can be obtained:

$$q_{0e}(t) = 1 + \frac{2\left[q_{0e}\left(t_f\right) - 1\right]}{-q_{0e}\left(t_f\right) + 1 + \left[q_{0e}\left(t_f\right) + 1\right]e^{\lambda\left(t - t_f\right)}}, \quad \forall t \geq t_f. \tag{87}$$

Observing (87), it can be deduced that (i) the singularity occurs as an improper sliding gain λ is chosen such that $-q_{0e}(t_f) + 1 + [q_{0e}(t_f) + 1]e^{\lambda(t - t_f)} = 0$, $\forall t \geq t_f$. Thus, the sliding gain $\lambda > 0$ is designed so that $-q_{0e}(t_f) + 1 + [q_{0e}(t_f) + 1]e^{\lambda(t - t_f)} \neq 0$, $\forall t \geq t_f$. (ii) $q_{0e} \longrightarrow +1$ as $t \longrightarrow \infty$ from (87) and $\mathbf{q}_e \longrightarrow 0$ as $t \longrightarrow \infty$ from the identity of the unit quaternion (78). Observing (70), it can be found that $q_{0e} \longrightarrow 1$ and $\mathbf{q}_e \longrightarrow 0$ imply $\mathbf{q}_0 \longrightarrow \mathbf{q}_{0d}$ and $\vec{\mathbf{q}} \longrightarrow \vec{\mathbf{q}}_d$. That is, the nonlinear reduced-order dynamics (76) and (77) are asymptotically stable. It is different and more outstanding than [30, 35, 36]; the assumption that $q_{0e} \neq 0$ is not made. In the following, how to enter the sliding mode in a finite time in the presence of external disturbances by means of the robust control law will be discussed.

In order to introduce $\boldsymbol{\tau}_c$, taking the time derivative about (74) yields

$$\begin{aligned}\dot{\mathbf{S}} &= \dot{\omega}_e + \lambda\dot{\mathbf{q}}_e \\ &= \mathbf{J}_{eq}^{-1}\left[-\boldsymbol{\tau}_c + \mathbf{d} - \omega^{\times}\left(\mathbf{J}_{eq}\omega + \Gamma\mathbf{J}_m\boldsymbol{\Omega}\right)\right] + \boldsymbol{\xi},\end{aligned} \tag{88}$$

where

$$\boldsymbol{\xi} = -\dot{\boldsymbol{\omega}}_d + 0.5\lambda\left(q_{0e}\mathbf{I}_3 + \mathbf{q}_e^{\times}\right)\boldsymbol{\omega}_e. \tag{89}$$

Based on the super-twisting sliding mode algorithm [21], the following robust control law is designed:

$$\begin{aligned}\boldsymbol{\tau}_{c0} &= \omega^{\times}\left(\mathbf{J}_{eq}\omega + \Gamma\mathbf{J}_m\boldsymbol{\Omega}\right) - \mathbf{J}_{eq}\boldsymbol{\xi}, \\ \boldsymbol{\tau}_{cN} &= -\mathbf{J}_{eq}\left(\mathbf{K}_1\frac{\mathbf{S}}{\|\mathbf{S}\|^{1/2}} + \mathbf{K}_2\int_0^t \operatorname{sign}(\mathbf{S}(\tau))\mathrm{d}\tau\right), \\ \boldsymbol{\tau}_c &= -\left(\boldsymbol{\tau}_{c0} + \boldsymbol{\tau}_{cN}\right),\end{aligned} \tag{90}$$

in which the gain matrices are denoted as

$$\begin{aligned}\mathbf{K}_1 &= \operatorname{diag}\left(\left[\begin{array}{ccc} k_{11} & k_{12} & k_{13}\end{array}\right]\right), \\ \mathbf{K}_2 &= \operatorname{diag}\left(\left[\begin{array}{ccc} k_{21} & k_{22} & k_{23}\end{array}\right]\right).\end{aligned} \tag{91}$$

Substituting (90) into (88) yields the closed-loop sliding dynamics:

$$\dot{\mathbf{S}} = -\mathbf{K}_1\frac{\mathbf{S}}{\|\mathbf{S}\|^{1/2}} - \mathbf{K}_2\int_0^t \operatorname{sign}(\mathbf{S}(\boldsymbol{\tau}))\mathrm{d}\tau + \mathbf{D}, \tag{92}$$

where $\mathbf{D} = \mathbf{J}_{eq}^{-1}\mathbf{d} = [D_1, D_2, D_3]^T \in \mathbb{R}^3$ and $\operatorname{sign}(\mathbf{S}) \in \mathbb{R}^3$ is a sign function defined as follows:

$$\begin{aligned}&\operatorname{sign}(s_i) = \begin{cases} 1, & \text{if } s_i > 0, \\ -1, & \text{if } s_i < 0, \end{cases} \\ &\operatorname{sign}(s_i) \in [-1, 1], \quad \text{if } s_i = 0, \ (i = 1, 2, 3.).\end{aligned} \tag{93}$$

According to the stability criteria derived from Theorems 1 and 2, the following gains are chosen:

$$\begin{aligned}k_{2i} &> \delta_i, \\ k_{1i} &> \sqrt{4k_{2i}},\end{aligned} \tag{94}$$

where $\delta_i = \sup(\dot{D}_i)$, $i = 1, 2, 3$.

4. Spacecraft Reference Command Generation

4.1. Reference Quaternion Generation from TNB Frame. In this section, we are going to illustrate how to obtain the reference quaternion from the TNB frame. The procedures are as follows:

(1) Reference orbital trajectory: Consider the governing equations of the orbital motion [41]:

$$\ddot{\mathbf{r}} = -\frac{\mu}{r^3}\mathbf{r}. \tag{95}$$

where $r = [X, Y, Z]^T \in \mathbb{R}^3$ is the position vector and its magnitude is $r = \|\mathbf{r}\|$; μ is the gravitational parameter. The reference orbital trajectory can be obtained by integrating (95) in a given initial condition.

(2) Construction of the TNB Frame: According to geometry kinematics, the TNB frame can be constructed by the trajectory information. Let $\mathbf{v} = \dot{\mathbf{r}}$ be the velocity vector and let $\mathbf{a} = \ddot{\mathbf{r}}$ be the acceleration vector. The unit tangent vector can be computed by

$$\hat{\mathbf{e}}_t = \frac{\mathbf{v}}{\|\mathbf{v}\|}. \tag{96}$$

The unit normal vector can be obtained by

$$\hat{\mathbf{e}}_n = \frac{\mathbf{a}_n}{\|\mathbf{a}_n\|}. \tag{97}$$

where $\mathbf{a}_n = \mathbf{a} - \mathbf{a}_t$ is the normal acceleration and $\mathbf{a}_t = (\mathbf{a} \cdot \hat{\mathbf{e}}_t)\hat{\mathbf{e}}_t$ is the tangential acceleration. Based on the definition of TNB frame, the binormal vector is

$$\hat{\mathbf{e}}_b = \hat{\mathbf{e}}_t \times \hat{\mathbf{e}}_n. \tag{98}$$

(3) Reference Quaternion: Based on the rotational property, the direction cosine matrix (DCM) can be composed by $\hat{\mathbf{e}}_t$, $\hat{\mathbf{e}}_n$, and $\hat{\mathbf{e}}_b$; that is,

$$\mathbf{C}^v = [\,\hat{\mathbf{e}}_t \vdots \hat{\mathbf{e}}_n \vdots \hat{\mathbf{e}}_b\,]. \tag{99}$$

Applying the quaternion kinematics, the reference quaternion is

$$q_{0d} = \frac{1}{2}\left(1 + \mathbf{C}^v_{11} + \mathbf{C}^v_{22} + \mathbf{C}^v_{33}\right)^{1/2}, q_{1d} = \frac{1}{4q_0}\left(\mathbf{C}^v_{32} - \mathbf{C}^v_{23}\right),$$
$$q_{2d} = \frac{1}{4q_0}\left(\mathbf{C}^v_{13} - \mathbf{C}^v_{31}\right), q_{3d} = \frac{1}{4q_0}\left(\mathbf{C}^v_{21} - \mathbf{C}^v_{12}\right). \tag{100}$$

4.2. Reference Angular Velocity Generation. To generate a feasible command trajectory, the following property is proposed [35].

Property 1. The matrix $\mathbf{E}(\mathbf{Q})$ defined in (9) has the following properties:

$$\mathbf{E}^T(\mathbf{Q})\mathbf{E}(\mathbf{Q}) = \mathbf{I}_3,$$
$$\frac{\mathrm{d}}{\mathrm{d}t}\left[\mathbf{E}^T(\mathbf{Q})\dot{\mathbf{Q}}\right] = \mathbf{E}^T(\mathbf{Q})\ddot{\mathbf{Q}} \tag{101}$$

By using Property 1, from (8), the angular velocity and its time derivative can be expressed as

$$\boldsymbol{\omega} = 2\mathbf{E}^T(\mathbf{Q})\dot{\mathbf{Q}},$$
$$\dot{\boldsymbol{\omega}} = 2\mathbf{E}^T(\mathbf{Q})\ddot{\mathbf{Q}} \tag{102}$$

Hence, the formula of the desired angular velocity ω_d associated with the desired quaternion is

$$\boldsymbol{\omega}_d = 2\mathbf{E}^T(\mathbf{Q}_d)\dot{\mathbf{Q}}_d,$$
$$\dot{\boldsymbol{\omega}}_d = 2\mathbf{E}^T(\mathbf{Q}_d)\ddot{\mathbf{Q}}_d \tag{103}$$

where

$$\mathbf{E}(\mathbf{Q}_d) = \begin{bmatrix} -q_{1d} & -q_{2d} & -q_{3d} \\ q_{0d} & -q_{3d} & q_{2d} \\ q_{3d} & q_{0d} & -q_{1d} \\ -q_{2d} & q_{1d} & q_{0d} \end{bmatrix}. \tag{104}$$

5. Numerical Simulation

According to [42], the numerical data are considered and summarized as follows.

(i) Moment of inertia of the spacecraft and reaction wheels is as follows:

$$\mathbf{J} = \begin{bmatrix} 35 & 3 & -1.5 \\ 3 & 28 & 2 \\ -1.5 & 2 & 30 \end{bmatrix},$$
$$\mathbf{J}_w = \begin{bmatrix} 0.126 & 0 & 0 \\ 0 & 0.063 & 0 \\ 0 & 0 & 0.063 \end{bmatrix} (N\text{-m}). \tag{105}$$

(ii) The external disturbance is chosen as

$$\mathbf{d}(t) = 0.005[\sin 0.8t \quad \cos 0.5t \quad \cos 0.3t]^T (\mathrm{N-m}). \tag{106}$$

(iii) Initial conditions are the following [41]: $\mathbf{r}(0) = [8000, 0, 6000]^T$ (km); $\dot{\mathbf{r}}(0) = [0, 7, 0]^T$ (km/s); $\boldsymbol{\omega}(0) = [7, -8, -7]^T$ (degree/sec); $\mathbf{Q}(0) = [0.999, 0.017, -0.035, -0.026]^T$; and gravitational parameter $\mu = 3.987 \times 10^5$ (N-km^2/kg).

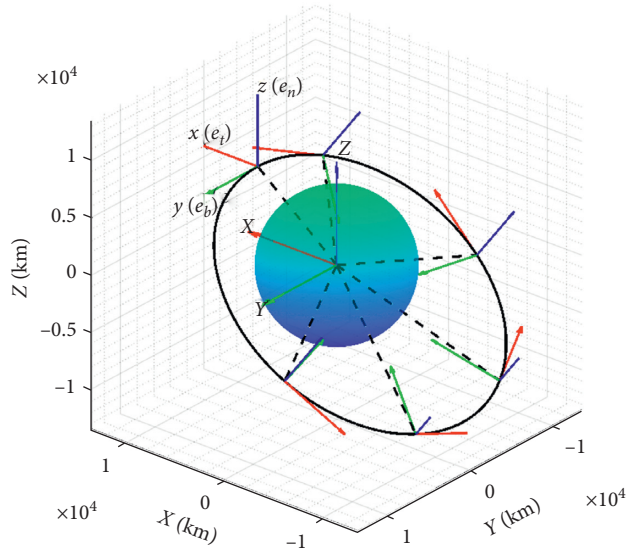

Figure 4: Spacecraft 3D trajectory.

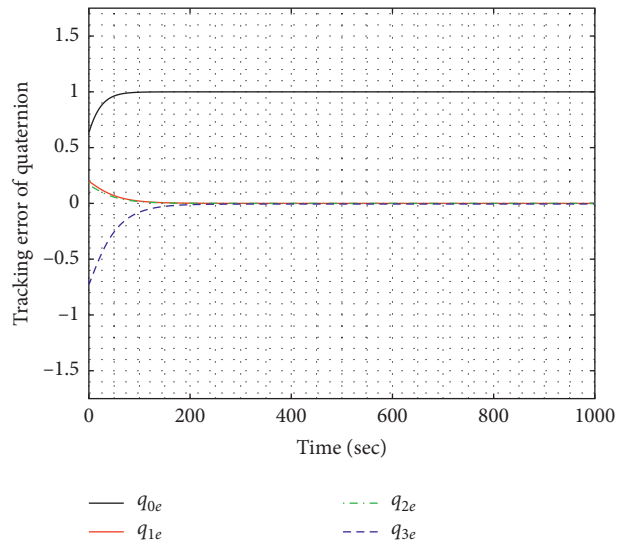

Figure 5: Quaternion tracking error.

(iv) The control gains are

$$\mathbf{K}_1 = \mathrm{diag}([\,0.547 \quad 0.547 \quad 0.547\,]),$$
$$\mathbf{K}_2 = \mathrm{diag}([\,0.05 \quad 0.05 \quad 0.05\,]), \tag{107}$$
$$\lambda = 0.05.$$

The sampling rate is 400 Hz. Total time span is 4.17 hours. The simulation results are shown in Figures 4–7. For convenience, only the transition response is shown.

With regard to Figure 4, it is demonstrated that the spacecraft tracks the reference TNB attitude trajectory successfully. The attitude of the spacecraft with respect to the global frame XYZ is represented as xyz. The response of quaternion tracking errors is shown in Figure 5. It can verify the derivation of analytic solution (87) that the scalar component $q_{0e} \longrightarrow 1$ and the vector component $\mathbf{q}_e \longrightarrow \mathbf{0}$ as $t \longrightarrow \infty$ and they satisfy the constraint $q_{0e} + \mathbf{q}_e^T \mathbf{q}_e = 1$. Figure 6 illustrates the response of the sliding variable. It can be found that the converging speed of the sliding variables is fast even though the spacecraft is under the environment with the time-varying external disturbances. The evolution

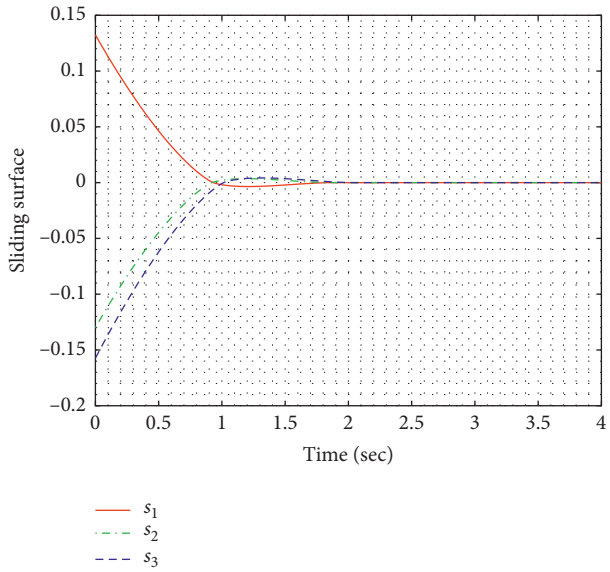

Figure 6: Sliding surface.

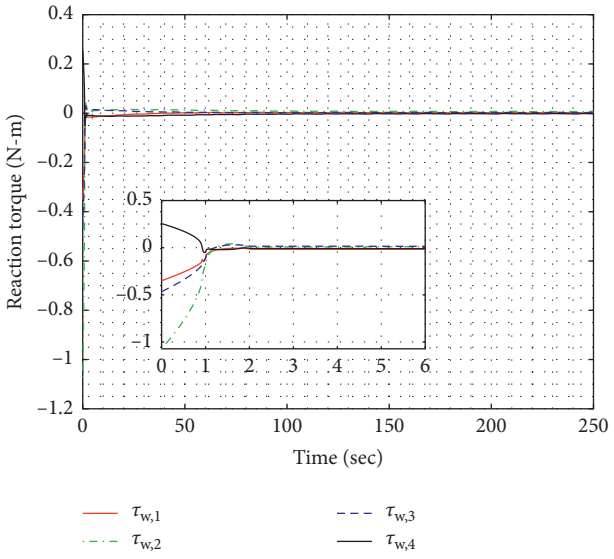

Figure 7: Evolution of reaction torque.

of the reaction torques is shown in Figure 7. It can be seen that the control signal is smooth and there is no chattering phenomenon. We can deduce that the controller based on the super-twisting sliding algorithm can be realized in the spacecraft attitude control problem.

6. Conclusion

In this study, the attitude dynamics based on the redundant reaction wheels configuration of the spacecraft is derived. To achieve full degree of freedom attitude tracking control, the quaternion kinematics is introduced. For practical realization purpose, the nonsquare FDM is reformulated as a square, invertible matrix by means of solving a static optimization problem. The robust, continuous super-twisting sliding mode algorithm is adopted in the attitude controller design to guarantee robust performance in the presence of exogenous disturbances. Furthermore, the corresponding finite time stability based on the LMI is provided in the sense of Lyapunov. Asymptotic stability of the nonlinear reduced-order dynamics is proven by means of an analytic solution without imposing any limitation in quaternion. In a space mission with this scenario, the TNB command generation strategy is presented. Finally, the simulation results verify that the spacecraft can achieve the arbitrary attitude trajectory tracking demands in the presence of the time-varying external disturbances.

Data Availability

No data or software is included in the submission.

Conflicts of Interest

The authors declare no conflicts of interest.

Acknowledgments

This work was supported by the Ministry of Science and Technology under Grant nos. MOST 107-2221-E-006-114-MY3 and MOST 108-2923-E-006-005-MY3.

References

[1] Z. Feng and J. Fei, "Design and analysis of adaptive super-twisting sliding mode control for a microgyroscope," *PloS One*, vol. 13, no. 1, 2018.

[2] Z. Wang, Q. Li, and S. Li, "Adaptive integral-type terminal sliding mode fault tolerant control for spacecraft attitude tracking," *IEEE Access*, vol. 7, pp. 35195–35207, 2019.

[3] Y. Zhao, J. Wang, F. Yan, and Y. Shen, "Adaptive sliding mode fault-tolerant control for type-2 fuzzy systems with distributed delays," *Information Sciences*, vol. 473, pp. 227–238, 2019.

[4] G. Sun, L. Wu, Z. Kuang, Z. Ma, and J. Liu, "Practical tracking control of linear motor via fractional-order sliding mode," *Automatica*, vol. 94, pp. 221–235, 2018.

[5] L. Wang and Z. Song, "Continuous fixed-time sliding mode attitude controller design for rigid-body spacecraft," *IEEE Access*, vol. 8, pp. 105399–105410, 2020.

[6] L. Luque-Vega, B. Castillo-Toledo, and A. G. Loukianov, "Robust block second order sliding mode control for a quadrotor," *Journal of the Franklin Institute*, vol. 349, no. 2, pp. 719–739, 2012.

[7] F. Chen, R. Jiang, K. Zhang, B. Jiang, and G. Tao, "Robust backstepping sliding-mode control and observer-based fault estimation for a quadrotor uav," *IEEE Transactions on Industrial Electronics*, vol. 63, no. 8, pp. 5044–5056, 2016.

[8] D. Almakhles, "Robust backstepping sliding mode control for a quadrotor trajectory tracking application," *IEEE Access*, vol. 63, 2019.

[9] F. Bayat, "Model predictive sliding control for finite-time three-axis spacecraft attitude tracking," *IEEE Transactions on Industrial Electronics*, vol. 66, no. 10, pp. 7986–7996, 2018.

[10] Y. Shtessel, C. Edwards, L. Fridman, and A. Levant, "Sliding mode control and observation," *Springer*, vol. 6, 2014.

[11] Y. B. Shtessel, J. A. Moreno, F. Plestan, L. M. Fridman, and S. Alexander, *Super-twisting adaptive sliding mode control: a lyapunov design*, 2010.

[12] Y. Shtessel, F. Plestan, and M. Taleb, "Lyapunov design of adaptive super-twisting controller applied to a pneumatic actuator," *IFAC Proceedings Volumes*, vol. 44, no. 1, pp. 3051–3056, 2011.

[13] Y. Shtessel, M. Taleb, and F. Plestan, "A novel adaptive-gain supertwisting sliding mode controller: methodology and application," *Automatica*, vol. 48, no. 5, pp. 759–769, 2012.

[14] V. I. Utkin and A. S. Poznyak, "Adaptive sliding mode control with application to super-twist algorithm: equivalent control method," *Automatica*, vol. 49, no. 1, pp. 39–47, 2013.

[15] K. Lu and Y. Xia, "Finite-time attitude control for rigid spacecraft-based on adaptive super-twisting algorithm," *IET Control Theory & Applications*, vol. 8, no. 15, pp. 1465–1477, 2014.

[16] C.-C. Peng and C.-L. Chen, "Robust chaotic control of lorenz system by backstepping design," *Chaos, Solitons & Fractals*, vol. 37, no. 2, pp. 598–608, 2008.

[17] C.-L. Chen, C. C. Peng, and H.-T. Yau, "High-order sliding mode controller with backstepping design for aeroelastic systems," *Communications in Nonlinear Science and Numerical Simulation*, vol. 17, no. 4, pp. 1813–1823, 2012.

[18] L.-H. Chen and C.-C. Peng, "Extended backstepping sliding controller design for chattering attenuation and its application for servo motor control," *Applied Sciences*, vol. 7, no. 3, p. 220, 2017.

[19] A. Levant, "Sliding order and sliding accuracy in sliding mode control," *International Journal of Control*, vol. 58, no. 6, pp. 1247–1263, 1993.

[20] J. A. Moreno and M. Osorio, *A lyapunov approach to second-order sliding mode controllers and observers*, 2008.

[21] A. Dávila, J. A. Moreno, and L. Fridman, "Optimal lyapunov function selection for reaching time estimation of super twisting algorithm," in *Proceedings of the 48h IEEE Conference on Decision and Control (CDC) Held Jointly with 2009 28th Chinese Control Conference*, pp. 8405–8410, IEEE, London, UK, 2009.

[22] J. A. Moreno, "A linear framework for the robust stability analysis of a generalized super-twisting algorithm," in *Proceedings of the 2009 6th International Conference on Electrical Engineering, Computing Science and Automatic Control (CCE)*, IEEE, London, UK, 2009.

[23] J. A. Moreno and M. Osorio, "Strict lyapunov functions for the super-twisting algorithm," *IEEE Transactions on Automatic Control*, vol. 57, no. 4, pp. 1035–1040, 2012.

[24] V. Utkin, "On convergence time and disturbance rejection of super-twisting control," *IEEE Transactions on Automatic Control*, vol. 58, no. 8, 2013.

[25] L. Derafa, A. Benallegue, and L. Fridman, "Super twisting control algorithm for the attitude tracking of a four rotors uav," *Journal of the Franklin Institute*, vol. 349, no. 2, pp. 685–699, 2012.

[26] L. Derafa, "Quadcopter robust adaptive second order sliding mode control based on pid sliding surface," *IEEE Access*, vol. 6, pp. 66850–66860, 2018.

[27] A. Chalanga, S. Kamal, L. M. Fridman, B. Bandyopadhyay , and J. A. Moreno, "Implementation of super-twisting control: super-twisting and higher order sliding-mode observer-based approaches," *IEEE Transactions on Industrial Electronics*, vol. 63, no. 6, pp. 3677–3685, 2016.

[28] M. Zhang, J. Huang, and F. Chen, *Super twisting control algorithm for velocity control of mobile wheeled inverted pendulum systems*, 2018.

[29] S. Nomura, S. Ikari, and S. Nakasuka, "Three-axis attitude maneuver of spacecraft by reaction wheels with rotation speed constraints," *IFAC-PapersOnLine*, vol. 49, no. 17, pp. 130–134, 2016.

[30] M. Navabi and M. R. Hosseini, *Spacecraft quaternion based attitude input-output feedback linearization control using reaction wheels*, 2017.

[31] M. Navabi, "Globally asymptotic three-axis attitude control for a two-wheeled small satellite," *Acta Astronautica*, vol. 157, pp. 17–28, 2019.

[32] M. Muehlebach and R. D'Andrea, "Nonlinear analysis and control of a reaction-wheel-based 3-d inverted pendulum," *IEEE Transactions on Control Systems Technology*, vol. 25, no. 1, pp. 235–246, 2016.

[33] D. Gutiérrez-Oribio, Á. Mercado-Uribe, J. A. Moreno, and L. Fridman, "Reaction wheel pendulum control using fourth-order discontinuous integral algorithm," *International Journal of Robust and Nonlinear Control*, vol. 31, 2020.

[34] N. A. Chaturvedi, K. Amit, and N. H. McClamroch, "Rigid-body attitude control," *IEEE Control Systems Magazine*, vol. 31, no. 3, pp. 30–51, 2011.

[35] S.-C. Lo and Y.-P. Chen, "Smooth sliding-mode control for spacecraft attitude tracking maneuvers," *Journal of Guidance, Control, and Dynamics*, vol. 18, no. 6, pp. 1345–1349, 1995.

[36] S. Wu, G. Radice, Y. Gao, and Z. Sun, "Quaternion-based finite time control for spacecraft attitude tracking," *Acta Astronautica*, vol. 69, no. 1-2, pp. 48–58, 2011.

[37] K. Ibrahim, *Comparison and analysis of attitude control systems of a satellite using reaction wheel actuators*, 2012.

[38] Z. Ismail and R. Varatharajoo, "A study of reaction wheel configurations for a 3-axis satellite attitude control," *Advances in Space Research*, vol. 45, no. 6, pp. 750–759, 2010.

[39] F. L. Lewis, D. Vrabie, and V. L. Syrmos, *Optimal Control*, John Wiley & Sons, New York, NY, USA, 2012.

[40] S. Boyd, L. El Ghaoui, E. Feron, and V. Balakrishnan, *Linear matrix inequalities in system and control theory*, 1994.

[41] H. D. Curtis, *Orbital Mechanics for Engineering Students*, Butterworth-Heinemann, New York, NY, USA, 2013.

[42] A. Zhang, J. Ni, and H. Reza Karimi, "Reaction wheel installation deviation compensation for overactuated spacecraft with finite-time attitude control," *Mathematical Problems in Engineering*, vol. 4, 2013.

Hindawi
Mathematical Problems in Engineering
Volume 2021, Article ID 6642840, 11 pages
https://doi.org/10.1155/2021/6642840

Research Article

Output-Feedback Sliding Mode Control for Permanent Magnet Synchronous Motor Servo System Subject to Unmatched Disturbances

Wei Jiang[1] **and Lu Zhang**[2]

[1]*Department of Electronic Information, Wuxi Vocational Institute of Arts and Technology, Wuxi, China*
[2]*School of Automation, Southeast University, Nanjing, China*

Correspondence should be addressed to Wei Jiang; jiangwei@wxgyxy.cn

Received 14 November 2020; Revised 30 December 2020; Accepted 3 March 2021; Published 15 March 2021

Academic Editor: Richard I. Avery

This paper aims to investigate the speed regulation problem for permanent magnet synchronous motor (PMSM) servo systems subject to unknown load torque disturbances. The proposed method utilizes sliding mode control (SMC), invariant manifold theory, and disturbance observation technique. In the PMSM servo systems, the unknown load torques will affect the control performance to a large extent, which is unmatched. In addition, compared with full-state measurement, the output-feedback framework is easy to implement and reduces the sensor costs. However, it is difficult to handle unmatched disturbance and unmeasured states simultaneously. To this end, this paper specifically combines the sliding mode control theory with the invariant manifold theory and puts forward an output-feedback disturbance rejection control method. The key idea is that the unmatched disturbance in the PMSM servo systems is transformed into matched one by taking advantage of the invariant manifold, which is different from existing results. The transformation maintains most of dynamics of the PMSM system for control design, which improves the accuracy. In addition, an extended state observer is designed to estimate the current and lumped disturbance simultaneously; then, the output-feedback SMC method is proposed by introducing the estimations. Besides, the switching gain in the proposed sliding mode controller can change with estimation errors adaptively, and the chattering reduces. Simulation results on a PMSM system validate the effectiveness of the proposed control strategy.

1. Introduction

Permanent magnet synchronous motor (PMSM) has been widely applied to various practical systems, such as robotics, aerospace, and power generations [1–4], due to the high-efficiency, high air-gap flux density, large torque-to-inertia ratio, and high power density [1]. High-accuracy tracking performance and satisfactory dynamic response are significant in the aforementioned applications. However, it should be noted that the servo control performance is significantly affected by nonlinearities, uncertainties, and disturbances in PMSM systems, and the traditional linear control strategies including the proportional-integral (PI) controller [5] are unable to provide satisfactory control performance [6]. In order to obtain better performance, many advanced nonlinear control methods have been developed for PMSM servo systems in recent years, such as adaptive control [2, 7], robust control [8, 9], linearization control [10], disturbance observer-based control [2, 11], fuzzy-logic based control [6, 12], finite time control [13, 14], fractional order control [15], sliding mode control [16, 17], and neuro-network based control [5, 12]. These control strategies improve control performance for PMSM servo systems from different aspects.

In industrial applications, sliding mode control (SMC) is deemed as one of the most effective control techniques [18, 19] due to its conceptual simplicity and powerful ability to reject matched disturbances/uncertainties [20]. The SMC is able to force the system dynamics to reach a predesigned sliding manifold in a finite time [21], and then the system

trajectory tracking error will converge to zero along the sliding manifold [22, 23]. It is well known that the load torque disturbance in PMSM system is unmatched one if we combine the speed control loop and current control loop together to get fast speed regulation performance [8]. In [24], a disturbance observer-based SMC strategy is developed to handle unmatched disturbances effectively. In [25], an adaptive sliding mode control method is proposed to attenuate the inductance disturbance of the PMSM. In order to estimate the unmeasured mechanical parameters of PMSM, a terminal sliding mode observer is proposed in [26], which can estimate the control performance with a finite-time convergence rate. The work in [27] employs the sliding mode control technique and the extended state observer for PMSM system to improve the robustness against load disturbance and parameter variations. These results are mostly implemented in the condition that all the system states are available. However, in PMSM servo systems, there are measurement noises in current sensors, which will bring adverse effects to the control performance. Toward that end, it is of great importance to investigate output-feedback SMC approaches for PMSM systems, which only require the interested output measurement rather than the full states.

The widely used output-feedback SMC method in PMSM is the observer-based SMC, which develops a state observer [28, 29] to reconstruct all the unmeasured states and then designs a controller by utilizing the estimation values. Most of the existing observer-based SMC methods need large control gains to reject bounded equivalent input disturbances [30], which will cause serious chattering. In recent years, the output-feedback SMC based upon the extended state observer (ESO) [31] provides an intuitive solution for chattering attenuation [32]. In [33], a higher-order ESO-based SMC method is proposed to reject the unknown higher-order lumped disturbances.

It is noticed that the existing ESO-based SMC method for PMSM system requires the second-order derivatives of the angular velocity to obtain a standard form for control design [33]. Under the standard ESO-based framework, the dynamics except for the integral chain are lumped for estimation. The lumped disturbances and uncertainties may change in a wide range due to the variation of operation condition. Therefore, to achieve satisfactory estimation and control performance, it is generally required to assign relatively large observer poles. For a PMSM servo system, the increase of observer poles will result in a drastic increase of observer gains, and the measurement noises will be significantly amplified in practice. Therefore, there will be serious switching action in the control signal, which will bring adverse effects to actuators and even excites the unmodelled dynamics of the system [34]. Besides, the derivatives of the reference signal may be unavailable. The ESO-based methods solve this problem by adding tracking differentiators for online estimation of the unknown information, which will considerably increase the complexity for implementation. Taking all the aforementioned facts into account, it is imperative to investigate some new output-feedback SMC strategies for PMSM system subject to unmatched disturbances to address the above problems and to achieve good disturbance rejection ability and satisfactory control performance.

Actually, the output-feedback SMC for PMSM servo system subject to unknown load torque disturbances is a challenging problem, since it is difficult to estimate both the unmeasured states and the unmatched disturbance at the same time. Reference [35] gives a new idea for output-feedback SMC design, which combines SMC with the basic idea of output regulation theory [36, 37]. Inspired by [35], this paper aims to solve the output-feedback SMC problem for PMSM servo system subject to unmatched disturbances. Under the proposed controller, the angular velocity is driven to track the reference signal asymptotically. The main contributions and benefits of the proposed method are summarized as follows: (1) full dynamics of the PMSM system are thoroughly exploited in the invariant manifold based output-feedback SMC design process, which admits higher bandwidth without higher observer gains, attenuating measurement noises to a large extent; (2) the switching gain changes with estimation errors adaptively, and thus the chattering will be reduced; (3) the proposed output-feedback SMC method can compensate the influences caused by unknown derivatives of the desired reference signal without resorting to tracking differentiators, which results in a simpler control structure and saves the implementation burden of the algorithm. To further demonstrate the effectiveness of the output-feedback SMC method proposed in this paper, simulations on a PMSM system are carried out by utilizing MATLAB/Simulink.

The paper is organized as follows. Section 2 shows the mathematical model of the PMSM system and formulates the problem. In Section 3, the output-feedback sliding mode controller is developed and stability analysis is shown in detail. Then, Section 4 gives the simulation results and the conclusion is shown in Section 5.

2. System Model and Problem Formulation

2.1. Mathematical Model of PMSM. The magnetic circuit is assumed to be unsaturated, the eddy current loss and hysteresis are ignored, and the distribution of the magnetic field is supposed to be in sine space. A three-phase surface-mounted PMSM system can be modeled in $d-q$ coordinate, and the mathematical model is given by [2]

$$\begin{aligned}
\frac{\mathrm{d}i_d}{\mathrm{d}t} &= -\frac{R}{L}i_d + n_p\omega i_q + \frac{1}{L}u_d,\\
\frac{\mathrm{d}i_q}{\mathrm{d}t} &= -n_p\omega i_d - \frac{R}{L}i_q - \frac{1}{L}n_p\omega\psi_f + \frac{1}{L}u_q,\\
\frac{\mathrm{d}\omega}{\mathrm{d}t} &= \frac{3n_p\psi_f}{2J}i_q - \frac{B}{J}\omega - \frac{T_L}{J},
\end{aligned} \tag{1}$$

where i_q and i_d are the q–axis and d–axis stator currents, respectively; u_q and u_d are the q–axis and d–axis stator voltages, respectively; ψ_f is the rotor flux linkage; n_p is the number of pole pairs; J is the rotor inertia; L is the stator inductance; R is the stator resistance; B is the viscous friction

coefficient; ω is the angular velocity; and T_L is the unknown load torque.

The field-oriented control is one of the widely used control frameworks in PMSM, and Figure 1 shows the schematic diagram. Under this framework, the flux-producing and torque-producing components of the stator current are decoupled such that flux controls and the independent torque are possible as those in DC motors. In PMSM, the controllers take advantage of the cascade control loop, which includes two current loops and a speed loop. In the two current loops, two PI controllers are used. Here, we pay our attention to developing a controller for speed loop to reject the unknown load torque disturbance.

In a PMSM servo system, it is always expected to obtain maximum torque; thus, there should be $i_d = 0$. Therefore, the mathematical model (1) can be decoupled as the following form:

$$\begin{aligned}\frac{\mathrm{d}i_q}{\mathrm{d}t} &= -\frac{R}{L}i_q - \frac{1}{L}n_p\omega\psi_f + \frac{1}{L}u_q,\\ \frac{\mathrm{d}\omega}{\mathrm{d}t} &= \frac{3n_p\psi_f}{2J}i_q - \frac{B}{J}\omega - \frac{T_L}{J},\end{aligned} \tag{2}$$

where u_q is the control signal and T_L is the unknown unmatched disturbance. This paper mainly explores the control strategy for the decoupled system given by (2).

2.1.1. Control Objective. This paper attempts to utilize the sliding mode control theory to address speed regulation problem for PMSM servo systems subject to unmatched disturbances. For system (2), an output-feedback sliding mode controller combining invariant manifold with disturbance observer is designed to drive the angular velocity ω to track the reference signal ω^* asymptotically.

2.2. Traditional Output-Feedback SMC Design. Define the system output tracking error as $y = \omega - \omega^*$. Taking the second-order derivative of y, one obtains [33]

$$\begin{aligned}\dot{y} &= \dot{\omega} - \dot{\omega}^* = \frac{3n_p\psi_f}{2J}i_q - \frac{B}{J}\omega - \frac{T_L}{J} - \dot{\omega}^*,\\ y &= \frac{3n_p\psi_f}{2J}\dot{i}_q - \frac{B}{J}\dot{\omega} - \frac{\dot{T}_L}{J} - \ddot{\omega}^*\\ &= -\left(\frac{3n_p\psi_f R}{2JL} + \frac{3n_p\psi_f B}{2J^2}\right)i_q - \left(\frac{3n_p^2\psi_f^2}{2JL} - \frac{B^2}{J^2}\right)\omega\\ &\quad + \frac{BT_L}{J} - \frac{\dot{T}_L}{J} + \frac{3n_p\psi_f}{2JL}u_q.\end{aligned} \tag{3}$$

Denoting $D = -((3n_p\psi_f R/2JL) + (3n_p\psi_f B/2J^2))i_q - ((3n_p^2\psi_f^2/2JL) - (B^2/J^2))\omega + (BT_L/J) - (\dot{T}_L/J) - \ddot{\omega}^*$ as the lumped disturbances and $\kappa = (3n_p\psi_f/2JL)$ as the control coefficient, one has the following input-output formulation:

$$\ddot{y} = D + \kappa u_q. \tag{4}$$

Denote $\nu_1 = y$, $\nu_2 = \dot{y}$, and $\nu_3 = D$. Then we have the following controllable state-space model:

$$\begin{bmatrix}\dot{\nu}_1\\ \dot{\nu}_2\\ \dot{\nu}_3\end{bmatrix} = \begin{bmatrix}0 & 1 & 0\\ 0 & 0 & 1\\ 0 & 0 & 0\end{bmatrix}\begin{bmatrix}\nu_1\\ \nu_2\\ \nu_3\end{bmatrix} + \begin{bmatrix}0\\ \kappa\\ 0\end{bmatrix} + \begin{bmatrix}0\\ 0\\ \varpi\end{bmatrix}. \tag{5}$$

It is assumed that the lumped disturbance D and its derivative ϖ are bounded and satisfy $\lim_{t\longrightarrow\infty}\varpi = 0$. On the basis of (5), the observer is constructed as

$$\begin{aligned}\dot{\widehat{\nu}}_1 &= \widehat{\nu}_2 + l_1(\nu_1 - \widehat{\nu}_1),\\ \dot{\widehat{\nu}}_2 &= \widehat{\nu}_3 + l_2(\nu_1 - \widehat{\nu}_1) + \kappa u_q,\\ \dot{\widehat{\nu}}_3 &= l_3(\nu_1 - \widehat{\nu}_1),\end{aligned} \tag{6}$$

where l_1, l_2, and l_3 are observer gains. Introducing the estimations, the sliding manifold is developed as

$$s = \widehat{\nu}_2 + \beta\widehat{\nu}_1, \tag{7}$$

where $\beta > 0$. The output-feedback controller is

$$u_q = -\frac{1}{\kappa}[\widehat{\nu}_3 + \beta\widehat{\nu}_2 + k_1\mathrm{sgn}(s) + k_2 s], \tag{8}$$

where $k_1 = \rho + |(\beta l_1 + l_2)(\nu_1 - \widehat{\nu}_1)|$, $\rho > 0$, $k_2 > 0$.

2.3. Motivations. For the PMSM system (2) subject to unmatched disturbance, the effects caused by unmatched disturbance can be removed by the traditional output-feedback sliding mode controller effectively. Nevertheless, it is seen from coordinate transformation given by (3) and (4) that all unmeasured states are lumped into D, which includes q-axis current and load torques. In order to obtain satisfactory performance, we have to choose large observer poles; thus, large observer gains are required. As a result, measurement noises are amplified, and high-frequency fluctuations will be brought in control signal, which may excite the unmodelled dynamics of PMSM system, cause adverse effects on actuator, and even destabilize the system.

3. Main Results

3.1. Output-Feedback Sliding Mode Controller Design. Motivated by the basic idea of output regulation theory [36, 38], the steady states of the PMSM system (2) are calculated from regulator equations, which are shown as follows:

$$\begin{aligned}\frac{\mathrm{d}\pi_{i_q}}{\mathrm{d}t} &= -\frac{R}{L}\pi_{i_q} - \frac{1}{L}n_p\psi_f\pi_\omega + \frac{1}{L}\pi_{u_q},\\ \frac{\mathrm{d}\pi_\omega}{\mathrm{d}t} &= \frac{3n_p\psi_f}{2J}\pi_{i_q} - \frac{B}{J}\pi_\omega - \frac{T_L}{J},\\ 0 &= \pi_\omega - \omega^*,\end{aligned} \tag{9}$$

where π_{i_q}, π_ω, and π_{u_q} represent the steady states of the PMSM system states i_q, ω, and the control input u_q, respectively. It is obvious that the solutions of (9) are

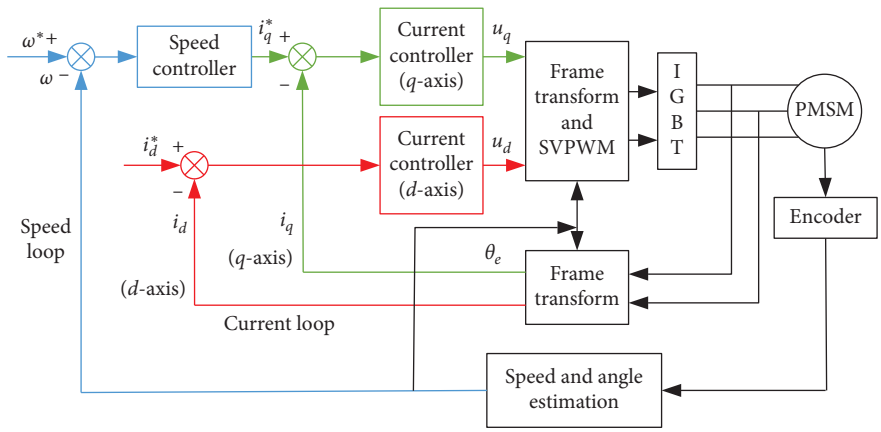

Figure 1: Schematic diagram of field-oriented control for PMSM.

impossible to be obtained due to the presence of unknown load torque disturbance T_L. This section will take advantage of the observation technique and sliding mode control to develop an output-feedback controller to solve this problem, which will only need the computable $\pi_\omega = \omega^*$.

Denote $\varepsilon_1 = i_q - \pi_{i_q}$ and $\varepsilon_2 = \omega - \pi_\omega$. Combining the PMSM system model (2) with the regulator equations given in (9), the invariant manifold is introduced as $\overline{E} = \left\{\varepsilon_1, \varepsilon_2 | [\varepsilon_1, \varepsilon_2]^T = [0,0]^T\right\}$. On the basis of the invariant manifold, the PMSM system (2) is transformed into

$$\begin{aligned}\dot{\varepsilon}_1 &= -\frac{R}{L}\varepsilon_1 - \frac{1}{L}n_p\psi_f\varepsilon_2 + \frac{1}{L}\left(u_q - \pi_{u_q}\right),\\ \dot{\varepsilon}_2 &= \frac{3n_p\psi_f}{2J}\varepsilon_1 - \frac{B}{J}\varepsilon_2.\end{aligned} \tag{10}$$

From (10), it is seen that the unmatched disturbance in (2) is lumped into the matched disturbance π_{u_q}, which needs to be compensated.

Denote $\varepsilon_3 = \pi_{u_q}$ as an extended state. Then an augmented system is

$$\begin{aligned}\dot{\varepsilon}_1 &= -\frac{R}{L}\varepsilon_1 - \frac{1}{L}n_p\psi_f\varepsilon_2 + \frac{1}{L}u_q - \frac{1}{L}\varepsilon_3,\\ \dot{\varepsilon}_2 &= \frac{3n_p\psi_f}{2J}\varepsilon_1 - \frac{B}{J}\varepsilon_2,\\ \dot{\varepsilon}_3 &= \varsigma,\\ e &= \varepsilon_2,\end{aligned} \tag{11}$$

where $\varsigma = \dot{\pi}_{u_q}$.

Assumption 1. The lumped disturbance π_{u_q} in system (10) and its derivative $\dot{\pi}_{u_q}$ are assumed to be bounded and satisfy the condition that $\lim_{t\longrightarrow\infty}\dot{\pi}_{u_q} = 0$.

An extended state observer for augmented system (11) is designed as

$$\begin{aligned}\dot{\hat{\varepsilon}}_1 &= -\frac{R}{L}\hat{\varepsilon}_1 - \frac{1}{L}n_p\psi_f\hat{\varepsilon}_2 + \frac{1}{L}u_q - \frac{1}{L}\hat{\varepsilon}_3 + l_1(e-\hat{e}),\\ \dot{\hat{\varepsilon}}_2 &= \frac{3n_p\psi_f}{2J}\hat{\varepsilon}_1 - \frac{B}{J}\hat{\varepsilon}_2 + l_2(e-\hat{e}),\\ \dot{\hat{\varepsilon}}_3 &= l_3(e-\hat{e}),\\ \hat{e} &= \hat{\varepsilon}_2,\end{aligned} \tag{12}$$

where l_1, l_2, l_3 are observer gains to be determined and $\hat{\varepsilon}_1, \hat{\varepsilon}_2, \hat{\varepsilon}_3$ are estimations of $\varepsilon_1, \varepsilon_2, \varepsilon_3$ in (11). Introducing the estimations, the sliding manifold is designed as

$$s = \hat{\varepsilon}_1 + \beta\hat{\varepsilon}_2, \tag{13}$$

where $\beta > 0$ is the parameter to be determined. The output-feedback sliding mode controller is constructed as

$$\begin{aligned}u_q = L\Bigg[&\left(\frac{R}{L} - \frac{3n_p\psi_f\beta}{2J}\right)\hat{\varepsilon}_1 + \left(\frac{n_p\psi_f}{L} + \frac{B\beta}{J}\right)\hat{\varepsilon}_2 + \frac{1}{L}\hat{\varepsilon}_3\\ &- k_1\mathrm{sgn}(s) - k_2 s\Bigg],\end{aligned} \tag{14}$$

where $k_1 = \rho + |(l_1 + \beta l_2)(\varepsilon_2 - \hat{\varepsilon}_2)|$, $k_2 > 0$, and $\rho > 0$.

3.2. Stability Analysis. To begin with, we give a lemma as follows, which will play an essential role in analysis.

Lemma 1 (see [39]). *If the matrix $A \in \mathbb{R}^{n\times n}$ is Hurwitz, then there is a scalar $c > 0$ such that $\|e^{At}\| \le ce^{(\lambda_{\max}(A)/2)t}$, where $\lambda_{\max}(A) = \max\{\mathrm{Re}(\lambda_i(A))\}$.*

Taking the time derivative of the designed sliding manifold s along (13) and substituting the extended state observer (12) and the output-feedback controller (14), we have

$$\begin{aligned}\dot{s} &= \dot{\widehat{\varepsilon}}_1 + \beta\dot{\widehat{\varepsilon}}_2 \\ &= -\frac{R}{L}\widehat{\varepsilon}_1 - \frac{1}{L}n_p\psi_f\widehat{\varepsilon}_2 - \frac{1}{L}\widehat{\varepsilon}_3 + \frac{1}{L}u_q \\ &\quad + l_1(e-\widehat{e}) + \beta\left(\frac{3n_p\psi_f}{2J}\widehat{\varepsilon}_1 - \frac{B}{J}\widehat{\varepsilon}_2 + l_2(e-\widehat{e})\right) \\ &= -k_1\operatorname{sgn}(s) - k_2 s + (\beta l_2 + l_1)(e-\widehat{e}).\end{aligned} \tag{15}$$

Define the candidate Lyapunov function as $V = (1/2)s^2$. Taking the derivative of V and considering (15), one obtains

$$\begin{aligned}\dot{V} = s\dot{s} &\le -k_1|s| - k_2 s^2 + |s|\left|(\beta l_2 + l_1)(e-\widehat{e})\right| \\ &< -\rho|s| - k_2 s^2 = -\sqrt{2}\rho V^{1/2} - 2k_2 V.\end{aligned} \tag{16}$$

As a result, the system trajectories will reach the sliding manifold in a finite time T_r with [18]

$$T_r \le \frac{1}{k_2}\ln\left(1 + \frac{\sqrt{2}\,k_2}{\rho}V^{1/2}(s(0))\right). \tag{17}$$

Denote the estimation errors as $\widetilde{e}_1 = \varepsilon_1 - \widehat{\varepsilon}_1$ and $\widetilde{e}_2 = \varepsilon_2 - \widehat{\varepsilon}_2$. On sliding motion, there is

$$s = \widehat{\varepsilon}_1 + \beta\widehat{\varepsilon}_2 = 0 \Longrightarrow \widehat{\varepsilon}_1 = -\beta\widehat{\varepsilon}_2. \tag{18}$$

Then, we have

$$\varepsilon_1 = \widetilde{e}_1 + \widehat{\varepsilon}_1 = \widetilde{e}_1 - \beta\widehat{\varepsilon}_2 = \widetilde{e}_1 - \beta(\varepsilon_2 - \widetilde{e}_2). \tag{19}$$

Define $\xi = [\,\varepsilon_2, \widetilde{e}_1, \widetilde{e}_2, \widetilde{e}_3\,]^T$. On sliding motion, the reduced-order closed-loop system can be written in a compact form, which is shown as

$$\dot{\xi} = \Theta\xi + \Psi\varsigma, \tag{20}$$

where $\Psi = [\,0, 0, 0, 1\,]^T$, and

$$\Theta = \begin{bmatrix} -\left(\frac{B}{J} + \frac{3n_p\psi_f\beta}{2J}\right) & \frac{3n_p\psi_f}{2J} & \frac{3n_p\psi_f\beta}{2J} & 0 \\ 0 & -\frac{R}{L} & -\left(\frac{n_p\varphi_f}{L} + l_1\right) & -\frac{1}{L} \\ 0 & \frac{3n_p\psi_f\beta}{2J} & -\left(\frac{B}{J} + l_2\right) & 0 \\ 0 & 0 & -l_3 & 0 \end{bmatrix}. \tag{21}$$

The main theorem of this paper is summarized as follows.

Theorem 1. *Under Assumption 1, if the observer gains l_1, l_2, and l_3 in (12) are selected such that the matrix,*

$$\mathbf{M} = \begin{bmatrix} -\frac{R}{L} & -\left(\frac{n_p\varphi_f}{L} + l_1\right) & -\frac{1}{L} \\ \frac{3n_p\psi_f}{2J} & -\left(\frac{B}{J} + l_2\right) & 0 \\ 0 & -l_3 & 0 \end{bmatrix}, \tag{22}$$

is Hurwitz and the controller parameter β in (13) and (14) is chosen such that $-((B/J) + ((3n_p\psi_f\beta)/2J)) < 0$, then the estimation errors and the output tracking error of the PMSM system (2) will converge to a bounded neighbourhood of the origin, and the ultimate bound can be made arbitrarily small. Furthermore, if $\dot{\pi}_{u_q}$ tends to zero as $t \longrightarrow \infty$, then the closed-loop system (20) is globally asymptotically stable.

For better understanding of the main design idea of the proposed control strategy, the detailed proof for Theorem 1 is given in the Appendix. Figure 2 shows the schematic diagram of the proposed output-feedback SMC strategy in implementation.

Remark 1. In parameter tuning, there are usually a number of conflicts/constraints, such as tracking versus disturbance rejection and nominal performance versus robustness. There are three parameters l_1, l_2, and l_3 to be determined in the extended state observer given in (12). For tuning the observer gains, we usually choose the observer poles ω_o and calculated the values of l_1, l_2, and l_3 based on the observer expressions (12). If the observer poles are larger, the settling time will be shorter, but the overshoot will be larger, and the measurement noise will be amplified more seriously. In the controller given in (13) and (14), there are three parameters to be assigned, which are β, k_1, and k_2. The detailed expression of k_1 is given by $k_1 = \rho + |(l_1 + \beta l_2)(\varepsilon_2 - \widehat{\varepsilon}_2)|$, and ρ should be positive. The larger ρ means that system states will reach the sliding manifold in a shorter time, but the chattering will be more seriously. The parameters of β and k_2 should be positive. Large values of control gains will reduce the settling time, but the overshoot and the control efforts will be large. Generally, when choosing the parameters, one needs to balance the overshoot, the settling time, and the control efforts.

4. Simulations

Simulations, using MATLAB/Simulink, are carried out to validate the control performance of the proposed output-feedback sliding mode control method, especially in rejecting unmatched disturbances. Table 1 lists the nominal values of the PMSM parameters.

In simulations, to demonstrate the superiority of the proposed output-feedback sliding mode controller, the traditional output-feedback SMC given by (6)–(8) is compared as benchmark method. The observer poles of the proposed method and the traditional method are chosen as

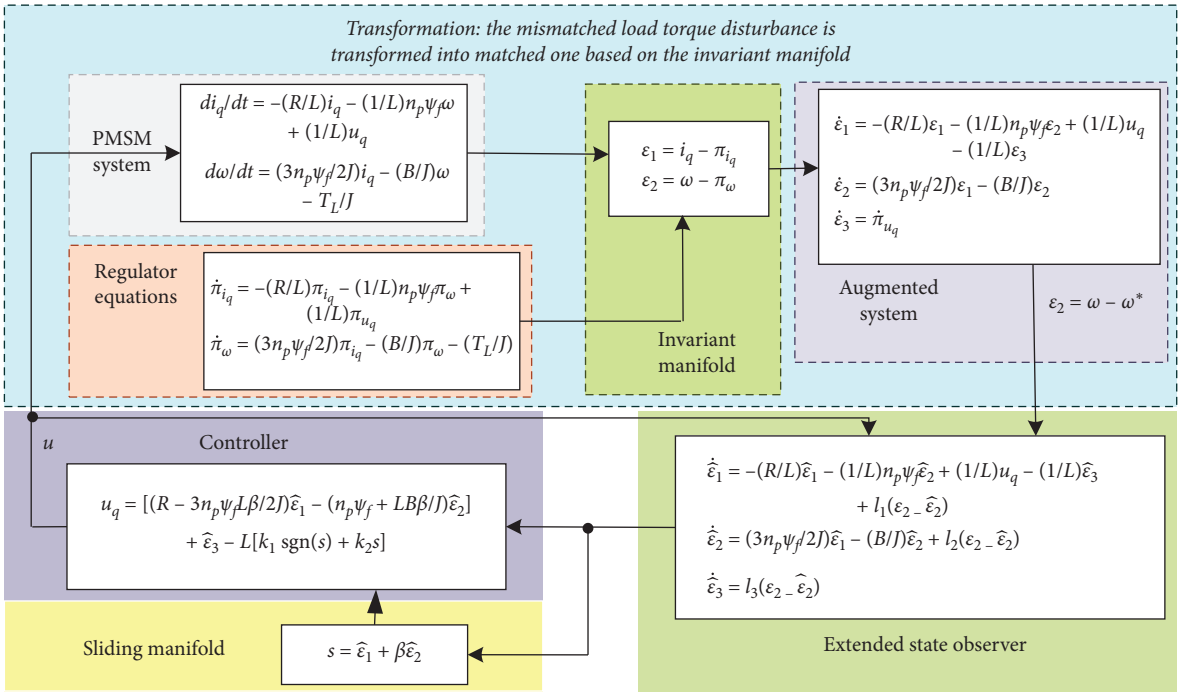

Figure 2: Schematic diagram of the proposed output-feedback SMC strategy for PMSM system.

Table 1: Parameters of PMSM system in simulations.

Meanings	Parameters	Nominal value
Pole pairs	n_p	4
Rotor flux linkage	φ_f	0.402 wb
Stator inductance	L	4 mH
Rotor inertia	J	1.78×10^{-4} kg · m^2
Viscous friction coefficient	B	7.4×10^{-5} $N \cdot m \cdot s$/rad
Stator resistance	R	1.74 Ω

Table 2: Control parameters of two methods.

Methods	Controller parameters		Observer parameters	
	Symbols	Values	Symbols	Values
Proposed	β	1	l_1	7116.5
Output-feedback	ρ	1	l_2	1964.6
SMC	k_2	5	l_3	−151.1376
Traditional	β	80	l_1	3000
Output-feedback	ρ	1	l_2	3×10^6
SMC	k_2	5	l_3	1×10^9

$\omega_o = -800$ and $\omega_o = -1000$, respectively (the reason why we choose different poles for the two observers will be discussed in the following Case 1). The parameters of the two controllers are shown in Table 2.

In this section, we will present three simulation scenarios, which are listed in Table 3.

Table 3: Simulation scenarios.

Cases	Scenarios	Details
I	Constant reference Speed tracking	$\omega^* = 150$ rad/s
II	Sudden load Torque disturbance	$\omega^* = 150$ rad/s $T_L = 0 \longrightarrow 1N \cdot m$
III	Time-varying load Torque disturbance	$\omega^* = 150$ rad/s $T_L = 0 \longrightarrow 2 + \sin(2\pi t)N \cdot m$

Case 1. Constant Reference Speed Tracking. In this case, the reference angular velocity is set as $\omega^* = 150$ rad/s. The response curves of the angular velocity ω, the q-axis current i_q, and the q-axis stator voltage u_q are shown in Figure 3. It is observed that larger observer poles are needed in the traditional output-feedback SMC method to achieve similar control performance with the output-feedback sliding mode controller proposed in this paper. This is the main reason why we choose different poles for the two observers. Moreover, the changes of the switching gains in the two controllers are shown in Figure 4, from which it can be seen that the switching gain k_1 in the proposed controller is much smaller than that in the traditional one during the transient period.

Case 2. Sudden Load Torque Disturbance. When unknown load torques are suddenly imposed, the simulation results are shown by Figure 5. It can be observed from Figure 5(a) that the angular velocity fluctuations of the PMSM are much smaller under the proposed controller than in the traditional method, although the observer poles of the traditional method are larger than those of the proposed one.

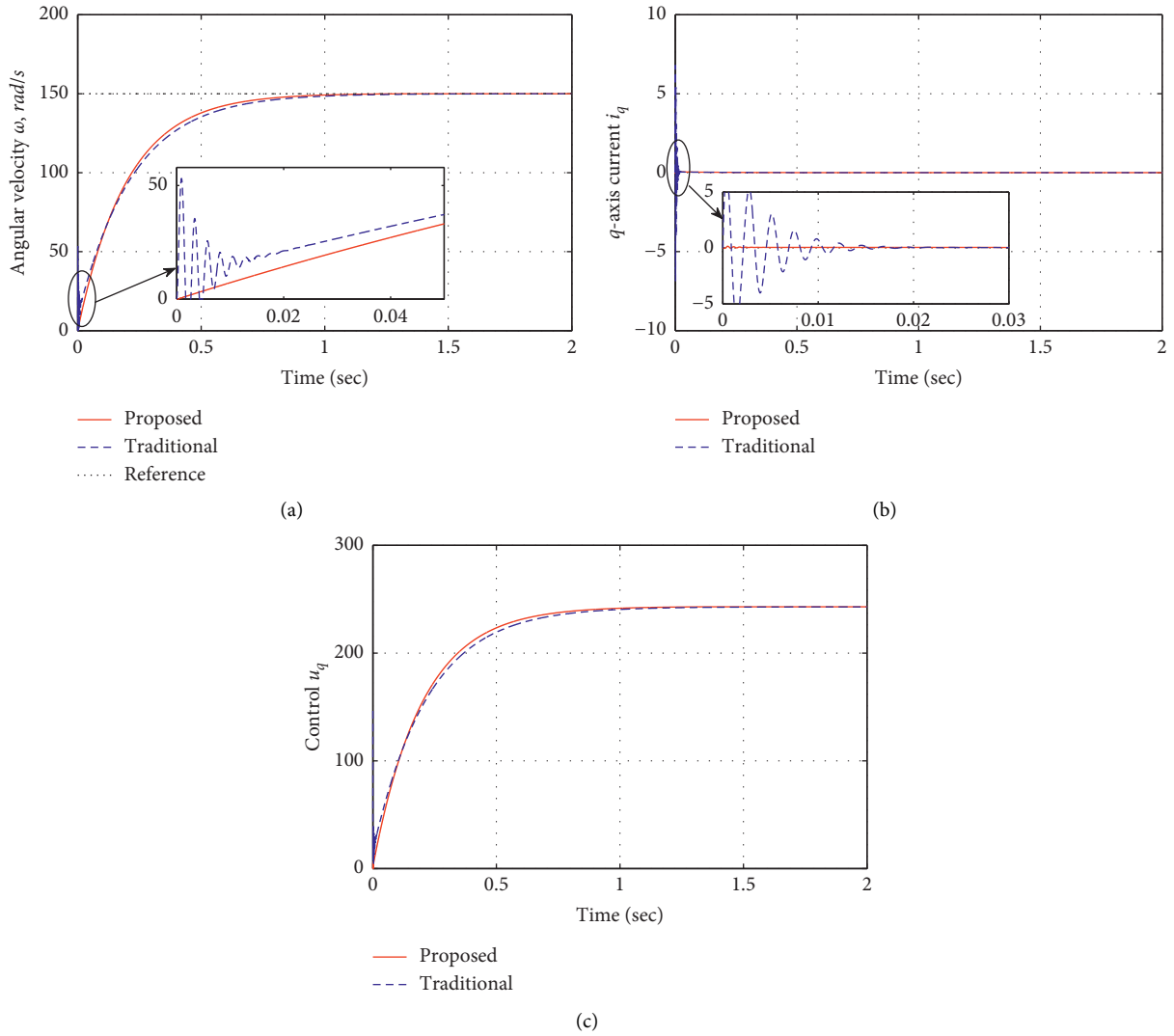

Figure 3: Response curve of the proposed output-feedback SMC and traditional SMC (Case 1): (a) angular velocity ω; (b) q-axis current i_q; (c) control input u_q.

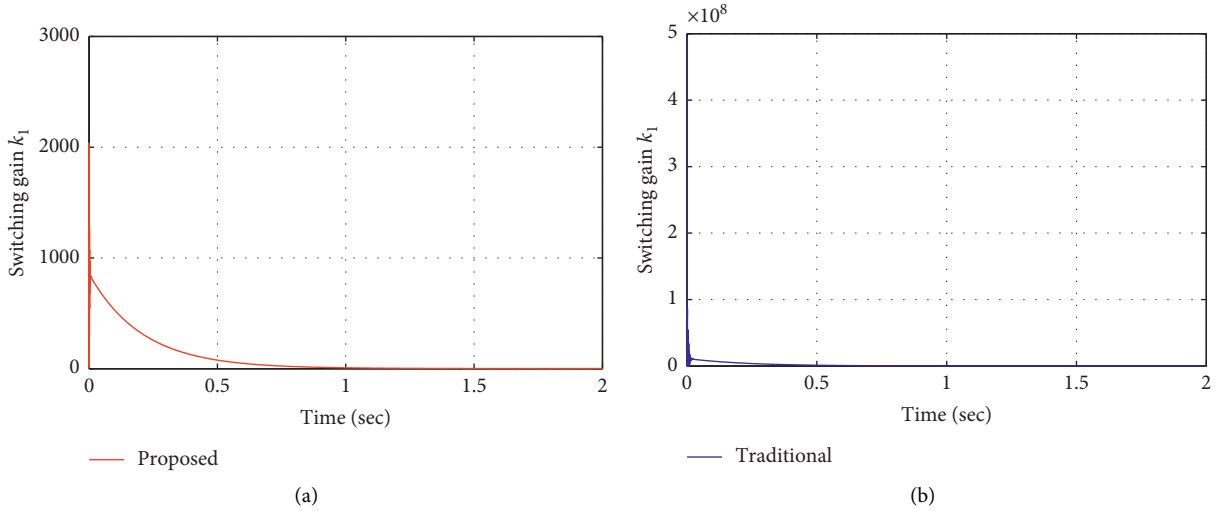

Figure 4: Switching gain of the two controllers: (a) proposed output-feedback SMC; (b) traditional output-feedback SMC.

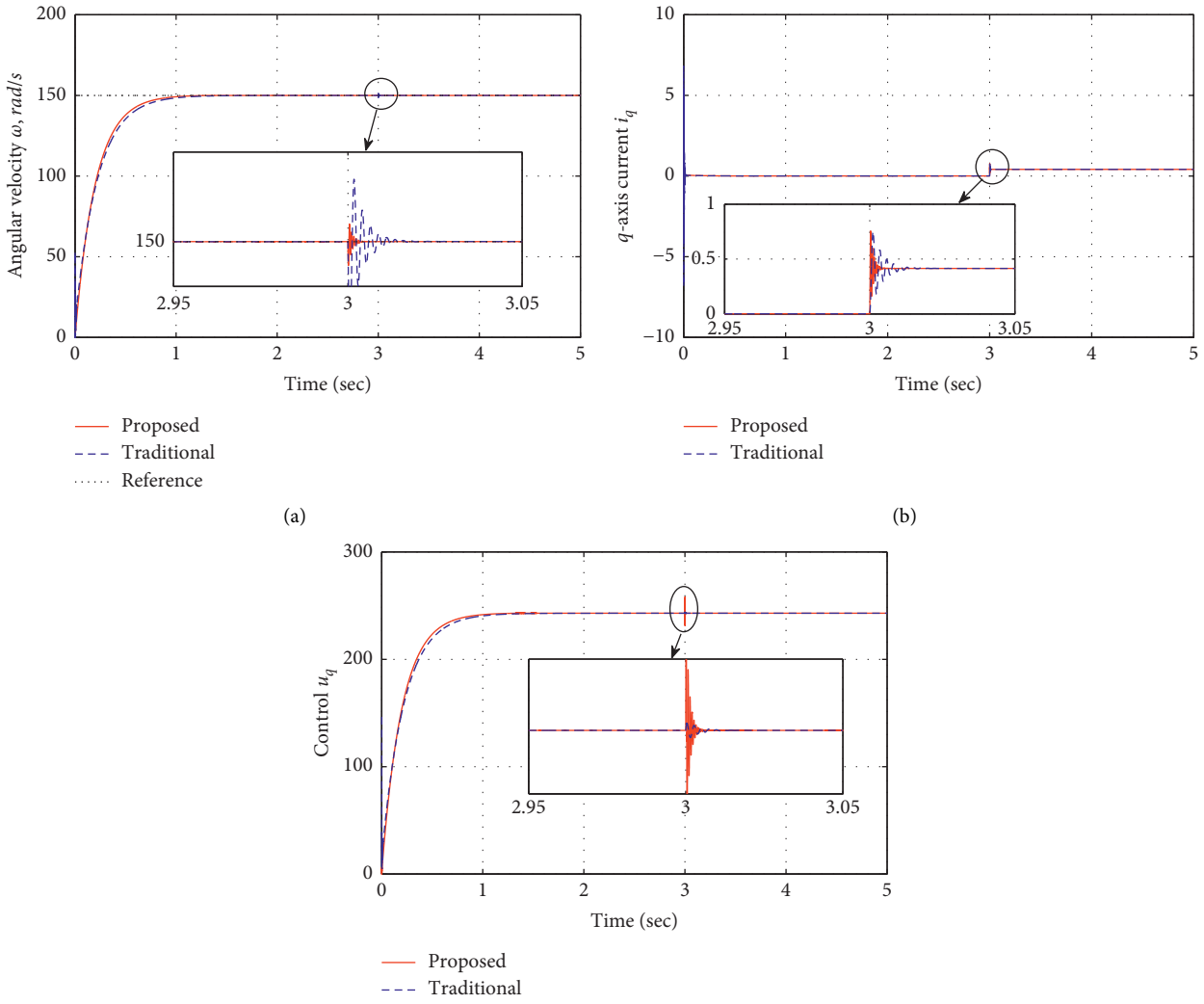

Figure 5: Response curve of the proposed output-feedback SMC and traditional SMC in the presence step load torque disturbance (Case 2): (a) angular velocity ω; (b) q-axis current i_q; (c) control input u_q.

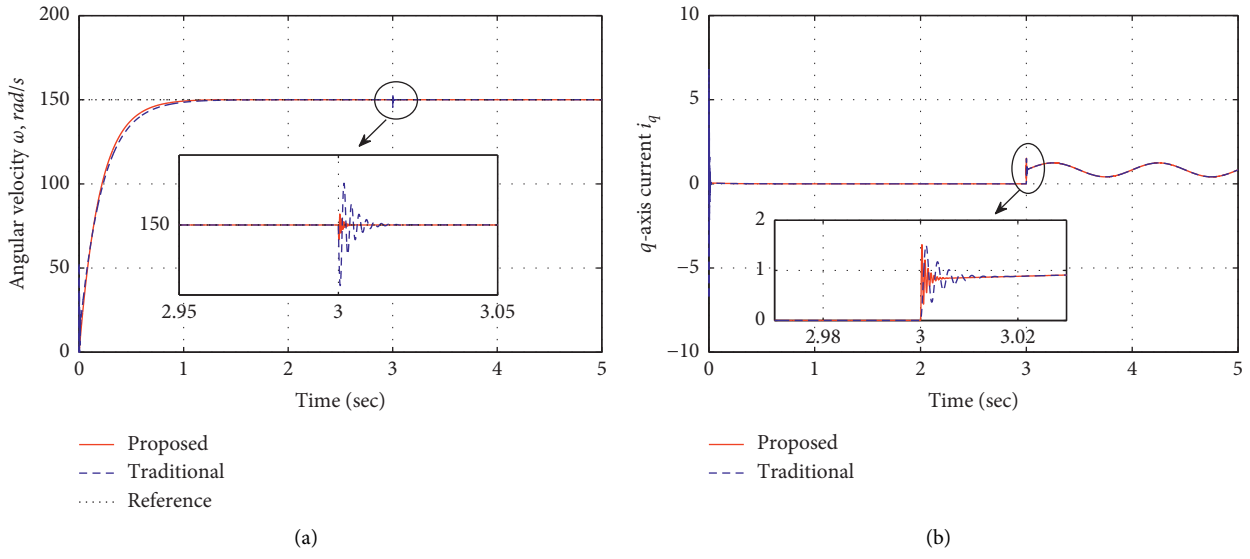

Figure 6: Continued.

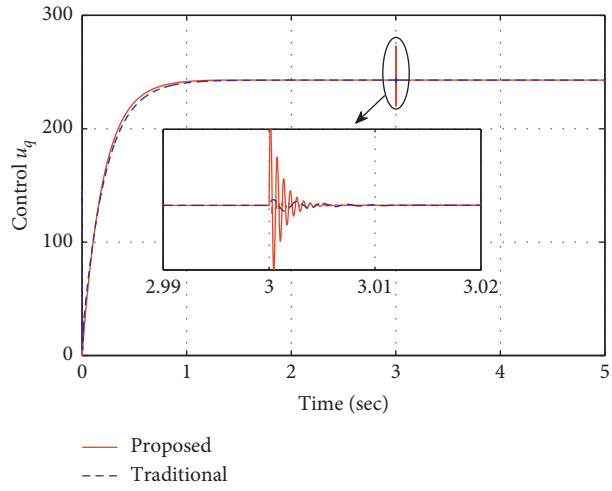

(c)

FIGURE 6: Response curve of the proposed output-feedback SMC and traditional SMC in the presence sinusoidal load torque disturbance (Case 3): (a) angular velocity ω; (b) q-axis current i_q; (c) control input u_q.

Case 3. Sinusoidal Load Torque Disturbance. Different from Case 3, where constant load torque disturbance is considered; in this case, we aim to evaluate the influences of period time-varying external disturbances on the steady-state performance. Response curves of the angular velocity, the q-axis current, and the q-axis voltage are shown in Figure 6. It can be seen from Figure 6 that the proposed control method shows better disturbance rejection ability than the traditional output-feedback SMC method.

5. Conclusion

This paper has investigated the speed regulation problem for PMSM system subject to unmatched disturbance. Taking advantage of the invariant manifold, the unmatched disturbance has been transformed into matched one and an augmented system has been obtained. An extended state observer has been developed for the augmented system to reconstruct unmeasured states. An output-feedback sliding mode controller, based on invariant manifold, has been proposed to achieve asymptotic tracking. Under the proposed control method, the angular velocity of the PMSM system can track the desired signal asymptotically even in the presence of the unmatched disturbance. Simulations have been carried out to validate the superiority of the controller proposed in this paper.

Appendix

A. Proof of Theorem 1

Proof □

Step 1. According to the input-to-state stability given in [40], there is a class of $\mathcal{K}$ functions α and a class of $\mathcal{KL}$ functions η such that, for any bounded $\varsigma(t)$ and initial state $\xi(0)$, the solutions of the compact system (20) satisfy $\|\xi(t)\| \le \eta(\|\xi(0)\|, t) + \alpha(\sup_{0\le\tau\le t}|\varsigma(\tau)|)$ and $\|\xi(\infty)\| \le \alpha(\delta) \le \infty$ with $|\dot{\pi}_{u_q}(t)| \le \delta$, where δ is a positive constant. Therefore, the estimation errors and the output tracking error are bounded.

Step 2. Denote $\tilde{e} = [\tilde{e}_1, \tilde{e}_2, \tilde{e}_3]^T$. Combining the augmented system (11), the extended state observer (12), and the reduced-order closed-loop system (20), the subsystem of observer estimation error is given as

$$\dot{\tilde{\mathbf{e}}} = \mathbf{M}\tilde{\mathbf{e}} + \mathbf{N}\varsigma, \tag{A.1}$$

where $\mathbf{N} = [0, 0, 1]^T$. Based on the comparison lemma [40], there is

$$\tilde{\mathbf{e}}(t) = e^{\mathbf{M}t}\tilde{\mathbf{e}}(0) + \int_0^t e^{\mathbf{M}(t-s)}\mathbf{N}\varsigma(s)\mathrm{d}s. \tag{A.2}$$

In general, if the observer poles are chosen as $\omega_o < 0$, then, combining with Lemma 1, we have

$$\begin{aligned}\|\tilde{\mathbf{e}}(t)\| &\le \int_0^t \left\| e^{(\bar{\mathbf{A}}-\mathbf{L}\bar{\mathbf{C}})(t-s)} \right\| \|\mathbf{N}\| |\varsigma(s)| \mathrm{d}s \\ &\quad + \left\| e^{(\bar{\mathbf{A}}-\mathbf{L}\bar{\mathbf{C}})t} \right\| \|\tilde{\mathbf{e}}(0)\| \\ &\le \delta \int_0^t c_2 e^{(\omega_o/2)(t-s)}\mathrm{d}s + c_1 e^{(\omega_o/2)t}\|\tilde{\mathbf{e}}(0)\| \\ &\le \frac{2\delta c_2\left(1 - e^{(\omega_o/2)t}\right)}{-\omega_o} + c_1 e^{(\omega_o/2)t}\|\tilde{\mathbf{e}}(0)\|,\end{aligned} \tag{A.3}$$

where $c_1 > 0$ and $c_2 > 0$ are constants. As time goes by, there is $\lim_{t\to\infty}\|\tilde{\mathbf{e}}(t)\| = (2\delta c_2/-\omega_o)$. If the observer gains in (12) are selected such that the matrix $\mathbf{M}$ is Hurwitz, then the estimation errors are bounded and can be arbitrarily small by increasing observer poles.

It can be obtained from (20) that the state subsystem is

$$\dot{\varepsilon}_2 = -\left(\frac{B}{J} + \frac{3n_p\varphi_f\beta}{2J}\right)\varepsilon_2 + \frac{3n_p\varphi_f}{2J}\tilde{e}_1 + \frac{3n_p\psi_f\beta}{2J}\tilde{e}_2. \quad (A.4)$$

Based on the comparison lemma given in [40], we have the following inequality:

$$\begin{aligned}\varepsilon_2(t) = {} & e^{-\left((B/J)+\left(3n_p\varphi_f\beta/2J\right)\right)t}\varepsilon_2(0) \\ & + \int_0^t e^{-\left((B/J)+\left(3n_p\varphi_f\beta/2J\right)\right)(t-s)}\left(\frac{3n_p\varphi_f}{2J}\tilde{e}_1(\tau)\right. \\ & \left. + \frac{3n_p\psi_f\beta}{2J}\tilde{e}_2(\tau)\right)\mathrm{d}\tau.\end{aligned} \quad (A.5)$$

Denote a positive constant

$$\hbar = \left|\frac{3n_p\varphi_f}{2J}\tilde{e}_1(t) + \frac{3n_p\psi_f\beta}{2J}\tilde{e}_2(t)\right|. \quad (A.6)$$

Since the parameter β is chosen such that $-((B/J) + (3n_p\psi_f\beta/2J)) < 0$, similar to (A.3), one obtains

$$\begin{aligned}\left|\varepsilon_2(t)\right| \le {} & m_1 e^{-\left((B/J)+\left(3n_p\psi_f\beta/2J\right)\right)t}\left|\varepsilon_2(0)\right| \\ & + \frac{2m_2\hbar}{(B/J) + \left(3n_p\psi_f\beta/2J\right)} \\ & \cdot \left(1 - e^{-\left(\left((B/J)+\left(3n_p\psi_f\beta/2J\right)\right)/2\right)t}\right),\end{aligned} \quad (A.7)$$

where $m_1, m_2 > 0$. As a result, we have

$$\lim_{t\longrightarrow\infty}\varepsilon_2(t) = \frac{2m_2\hbar}{\left((B/J) + \left(3n_p\psi_f\beta/2J\right)\right)}. \quad (A.8)$$

It is noted that the ultimate bound of estimation errors can be made arbitrarily small; therefore, the ultimate bound of the tracking error $\varepsilon_2(t)$ can be arbitrarily small.

Step 3. Furthermore, if the assumption that $\lim_{t\longrightarrow\infty}\dot{\pi}_{u_q} = 0$ is satisfied, following the method given in [41], one obtains

$$\begin{aligned}\lim_{t\longrightarrow\infty}\tilde{\mathbf{e}}(t) &= \lim_{s\longrightarrow 0}\tilde{\mathbf{E}}(s) = \lim_{s\longrightarrow 0}[s\mathbf{I} - \mathbf{M}]^{-1}\mathbf{N}\mathscr{L}(\varsigma(t)) \\ &= \lim_{s\longrightarrow 0}[s\mathbf{I} - \mathbf{M}]^{-1}\mathbf{N}\cdot\lim_{t\longrightarrow\infty}\varsigma(t) = \mathbf{0}.\end{aligned} \quad (A.9)$$

Based on the above analysis, we have

$$\begin{aligned}\lim_{t\longrightarrow\infty}\varepsilon_2(t) &= \lim_{s\longrightarrow 0}\left(s + \left(\frac{B}{J} + \frac{3n_p\psi_f\beta}{2J}\right)\right)^{-1} \\ &\quad \cdot \mathscr{L}\left(\frac{3n_p\psi_f}{2J}\tilde{e}_1(t) + \frac{3n_p\psi_f\beta}{2J}\tilde{e}_2(t)\right) \\ &= \lim_{s\longrightarrow 0}\left(s + \left(\frac{B}{J} + \frac{3n_p\psi_f\beta}{2J}\right)\right)^{-1} \\ &\quad \cdot \lim_{t\longrightarrow\infty}\left(\frac{3n_p\psi_f}{2J}\tilde{e}_1(t) + \frac{3n_p\psi_f\beta}{2J}\tilde{e}_2(t)\right).\end{aligned} \quad (A.10)$$

Taking (19) in mind, one obtains

$$\lim_{t\longrightarrow\infty}\varepsilon_1(t) = \lim_{t\longrightarrow\infty}\tilde{e}_1 - \beta\tilde{\varepsilon}_2 = \tilde{e}_1 - \beta(\varepsilon_2 - \tilde{e}_2) = 0. \quad (A.11)$$

Since $\varepsilon_2 = \omega - \omega^*$, we have $\lim_{t\longrightarrow\infty}\omega = \omega^*$. As a result, the angular velocity of the PMSM system can track the desired reference signal asymptotically. This completes the proof.

Data Availability

The mathematical model of PMSM system data used to support the findings of this study have been deposited in the Web of Science repository (DOI: 10.1109/TIE.2009.2024655).

Conflicts of Interest

The authors declare that they have no conflicts of interest.

Acknowledgments

This work was supported in part by the National Natural Science Foundation of China under Grant 61973080.

References

[1] P. Krause, O. Wasynczuk, S. Sudhoff, and S. Pekarek, *Analysis of Electric Machinery and Drive Systems*, Wiley, Hoboken, NJ, USA, 2013.

[2] S. Li and Z. Liu, "Adaptive speed control for permanent-magnet synchronous motor system with variations of load inertia," *IEEE Transactions on Industrial Electronics*, vol. 56, no. 8, pp. 3050–3059, 2009.

[3] R. He and Q. Han, "Dynamics and stability of permanent-magnet synchronous motor," *Mathematical Problems in Engineering*, vol. 2017, Article ID 4923987, 8 pages, 2017.

[4] W.-C. Gan and L. Qiu, "Torque and velocity ripple elimination of AC permanent magnet motor control systems using the internal model principle," *IEEE/ASME Transactions on Mechatronics*, vol. 9, no. 2, pp. 436–447, 2004.

[5] G. J. Wang, C. T. Fong, and K. J. Chang, "Neural-network-based self-tuning PI controller for precise motion control of PMAC motors," *IEEE Transactions on Industrial Electronics*, vol. 48, no. 2, pp. 408–415, 2001.

[6] A. V. Sant and K. R. Rajagopal, "PM synchronous motor speed control using hybrid fuzzy-PI with novel switching functions," *IEEE Transactions on Magnetics*, vol. 45, no. 10, pp. 4672–4675, 2009.

[7] T.-B. T. Nguyen, T.-L. Liao, H.-H. Kuo, and J.-J. Yan, "An improved adaptive tracking controller of permanent magnet synchronous motor," *Abstract and Applied Analysis*, vol. 2014, Article ID 987308, 12 pages, 2014.

[8] Y. Yan, J. Yang, Z. Sun, C. Zhang, S. Li, and H. Yu, "Robust speed regulation for PMSM servo system with multiple sources of disturbances via an augmented disturbance observer," *IEEE/ASME Transactions on Mechatronics*, vol. 23, no. 2, pp. 769–780, 2018.

[9] F. F. M. El-Sousy, "Hybrid ${\rm H}^{\infty}$-Based wavelet-neural-network tracking control for permanent-magnet synchronous motor servo drives," *IEEE Transactions on Industrial Electronics*, vol. 57, no. 9, pp. 3157–3166, 2010.

[10] H. A. Zarchi, G. R. A. Markadeh, and J. Soltani, "Direct torque and flux regulation of synchronous reluctance motor drives based on input-output feedback linearization," *Energy Conversion and Management*, vol. 51, no. 1, pp. 71–80, 2010.

[11] Y.-H. Lan and L. Lei-Zhou, "Backstepping control with disturbance observer for permanent magnet synchronous motor," *Journal of Control Science and Engineering*, vol. 2018, Article ID 4938389, 8 pages, 2018.

[12] R. J. Wai, "Hybrid fuzzy neural-network control for nonlinear motor toggle servomechanism," *IEEE Transactions on Control Systems Technology*, vol. 10, no. 4, pp. 519–532, 2002.

[13] S. Li, H. Liu, and S. Ding, "A speed control for a PMSM using finite-time feedback control and disturbance compensation," *Transactions of the Institute of Measurement and Control*, vol. 32, no. 2, pp. 170–187, 2010.

[14] K. Mei, L. Ma, R. He, and S. Ding, "Finite-time controller design of multiple integrator nonlinear systems with input saturation," *Applied Mathematics and Computation*, vol. 372, Article ID 124986, 2020.

[15] Y. Luo, Y. Chen, H.-S. Ahn, and Y. Pi, "Fractional order robust control for cogging effect compensation in PMSM position servo systems: stability analysis and experiments," *Control Engineering Practice*, vol. 18, no. 9, pp. 1022–1036, 2010.

[16] L. Liu, W. X. Zheng, and S. Ding, "An adaptive SOSM controller design by using a sliding-mode-based filter and its application to buck converter," *IEEE Transactions on Circuits and Systems I: Regular Papers*, vol. 67, no. 7, pp. 2409–2418, 2020.

[17] C.-F. Huang, J.-S. Lin, T.-L. Liao, C.-Y. Chen, and J.-J. Yan, "Quasi-sliding mode control of chaos in permanent magnet synchronous motor," *Mathematical Problems in Engineering*, vol. 2011, Article ID 964240, 10 pages, 2011.

[18] S. Yu, X. Yu, B. Shirinzadeh, and Z. Man, "Continuous finite-time control for robotic manipulators with terminal sliding mode," *Automatica*, vol. 41, no. 11, pp. 1957–1964, 2005.

[19] J. Yuan, S. Ding, and K. Mei, "Fixed-time SOSM controller design with output constraint," *Nonlinear Dynamics*, vol. 102, no. 3, pp. 1567–1583, 2020.

[20] V. Utkin, "Variable structure systems with sliding modes," *IEEE Transactions on Automatic Control*, vol. 22, no. 2, pp. 212–222, 1977.

[21] V. Utkin, A. Poznyak, Y. Orlov, and A. Polyakov, "Conventional and high order sliding mode control," *Journal of the Franklin Institute*, vol. 357, no. 15, pp. 10244–10261.

[22] V. Utkin, *Sliding Modes in Control Optimisation*, Springer-Verlag, Berlin, Germany, 1992.

[23] A. Levant, "Higher-order sliding modes, differentiation and output-feedback control," *International Journal of Control*, vol. 76, pp. 9-10, 2003.

[24] J. Yang, S. Li, and X. Yu, "Sliding-mode control for systems with mismatched uncertainties via a disturbance observer," *IEEE Transactions on Industrial Electronics*, vol. 60, no. 1, pp. 160–169, 2013.

[25] M. Zhang, F. Xiao, R. Shao, and Z. Deng, "Robust fault detection for permanent-magnet synchronous motor via adaptive sliding-mode observer," *Mathematical Problems in Engineering*, vol. 2020, Article ID 6405923, 6 pages, 2020.

[26] Y. Feng, X. Yu, and F. Han, "High-order terminal sliding-mode observer for parameter estimation of a permanent-magnet synchronous motor," *IEEE Transactions on Industrial Electronics*, vol. 60, no. 10, pp. 4272–4280, 2013.

[27] P. Xia, Y. Deng, Z. Wang, and H. Li, "Speed adaptive sliding mode control with an extended state observer for permanent magnet synchronous motor," *Mathematical Problems in Engineering*, vol. 2018, Article ID 6405923, 13 pages, 2018.

[28] J. M. Daly and D. W. L. Wang, "Output feedback sliding mode control in the presence of unknown disturbances," *Systems & Control Letters*, vol. 58, no. 3, pp. 188–193, 2009.

[29] M. V. Basin, C. B. Panathula, Y. B. Shtessel, and P. C. R. Ramirez, "Continuous finite-time higher order output regulators for systems with unmatched unbounded disturbances," *IEEE Transactions on Industrial Electronics*, vol. 63, no. 8, pp. 5036–5043, 2016.

[30] J. P. V. S. Cunha, R. R. Costa, F. Lizarralde, and L. Hsu, "Peaking free variable structure control of uncertain linear systems based on a high-gain observer," *Automatica*, vol. 45, no. 5, pp. 1156–1164, 2009.

[31] J. Han, "From PID to active disturbance rejection control," *IEEE Transactions on Industrial Electronics*, vol. 56, no. 3, pp. 900–906, 2009.

[32] Y. Xia, F. Pu, M. Fu, and L. Ye, "Modeling and compound control for unmanned turret system with coupling," *IEEE Transactions on Industrial Electronics*, vol. 63, no. 9, pp. 5794–5803, 2016.

[33] J. Mao, J. Yang, S. Li, Y. Yan, and Q. Li, "Output feedback-based sliding mode control for disturbed motion control systems via a higher-order ESO approach," *IET Control Theory & Applications*, vol. 12, no. 15, pp. 2118–2126, 2018.

[34] J. A. Moreno, "Discontinuous integral control for mechanical systems," in *Proceedings of 14th International Workshop on Variable Structure Systems*, pp. 142–147, IEEE, Nanjing, China, June 2016.

[35] L. Zhang, J. Yang, S. Li, and X. Yu, "Invariant manifold based output-feedback sliding mode control for systems with mismatched disturbances," *IEEE Transactions on Circuits and Systems II: Express Briefs*, vol. 68, no. 3, pp. 933–937.

[36] A. Isidori and C. I. Byrnes, "Output regulation of nonlinear systems," *IEEE Transactions on Automatic Control*, vol. 35, no. 2, pp. 131–140, 1990.

[37] M. Hosseini-Pishrobat, J. Keighobadi, A. Oveisi, and T. Nestorović, "Robust linear output regulation using extended state observer," *Mathematical Problems in Engineering*, vol. 2018, Article ID 4095473, 12 pages, 2018.

[38] A. Mesbahi and J. Mohammadpour Velni, "Cooperative output regulation of multiagent linear parameter-varying systems," *Mathematical Problems in Engineering*, vol. 2017, Article ID 8489308, 10 pages, 2017.

[39] W. Zhang, "Stability of networked control systems," Ph. D. Thesis, Case Western Reserve University, Department of Electrical Engineering and Computer Science, Cleveland, OH, USA, 2001.

[40] H. Khalil, *Nonlinear Systems*, Prentice-Hall, Upper Saddle River, NJ, USA, 3rd edition, 2002.

[41] S. Li, J. Yang, W.-H. Chen, and X. Chen, "Generalized extended state observer based control for systems with mismatched uncertainties," *IEEE Transactions on Industrial Electronics*, vol. 59, no. 12, pp. 4792–4802, 2012.

Hindawi
Mathematical Problems in Engineering
Volume 2021, Article ID 6652342, 25 pages
https://doi.org/10.1155/2021/6652342

Research Article

Event-Triggered Adaptive Sliding Mode Attitude Containment Control for Microsatellite Cluster under Directed Graph

Fengzhi Guo,[1] **Shijie Zhang**,[1] **Tingting Zhang**,[1] **and Anhui Zhang**[2]

[1]*Research Center of Satellite Technology, Harbin Institute of Technology, Harbin 150080, China*
[2]*School of Astronautics, Harbin Institute of Technology, Harbin 150001, China*

Correspondence should be addressed to Shijie Zhang; sjzhang@hit.edu.cn

Received 13 December 2020; Revised 27 January 2021; Accepted 9 February 2021; Published 2 March 2021

Academic Editor: Chih-Chiang Chen

In order to investigate the attitude containment control problem for a microsatellite cluster, an event-triggered adaptive sliding mode attitude containment control algorithm is proposed for the satellite cluster flight system under directed topology, so that attitude of followers asymptotically converges to the convex hull formed by the leaders' orientations. At first, the event-triggered control strategy is introduced into the attitude containment control problem for the microsatellite cluster. The triggering condition consisting of state-dependent and time-dependent function is designed to adjust control period and avoid the Zeno behaviour. When the function value meets the triggering condition, the event is triggered, state information is sampled, control law is computed, and actuators are updated, while the control action performed in nontriggering time is the same as the previous triggering instant. Then, in the presence of model uncertainties and external disturbances, an event-triggered adaptive sliding mode attitude containment control algorithm is presented under directed topology, and sufficient and necessary conditions for the followers to enter into the target area formed by the leaders are given. Furthermore, cell partitions from graph theory are employed to investigate the influence of information topology on steady states of followers, which provides theoretical basis for orientation design of cluster satellites. Finally, simulation results show that the proposed control strategy could reduce control execution frequency, as well as ensure the similar control performance with the time-triggered one, and followers belonging to the same cell have the same steady states.

1. Introduction

Satellite cluster has received growing attention in the recent years [1, 2] for its advantages of greater flexibility, faster response, higher reliability, lower cost, and better reconfigurability [3]. Contrary to satellite formation flight, cluster flight does not impose strict limits on the geometry of the cluster [4] and is hence more suitable for implementation by multiple microsatellite systems. Satellite cluster has been deployed by many institutes, such as ANTS [5], Breakthrough Starshot project [6], and so on.

Several technical barriers need to be broken down to pave the way for cluster satellites to come into being. Coordinated attitude control of cluster satellites has been identified as one of the enabling technologies. Although there has been lots of results on coordinated control problem for multiple satellites systems, we note that most of the existing research studies consider leaderless [7, 8] or one leader case [9, 10], where there exists no group objective or only a single group objective.

However, the presence of multiple leaders is more attractive for the satellite cluster system, owing to the fact that such strategies provide attractive solutions to cluster problems, both in terms of complexity and computational load. As a kind of extended consensus problem, the case with multiple leaders is what we call containment control [11]. The objective of containment control is to guarantee that all the followers asymptotically converge into the convex hull formed by the leaders through information interaction and coordinated control. The containment control problem received significant research interest due to its various applications, such as mobile robots [12], unmanned aerial vehicles (UAVs) [13], underwater vehicles [14], and satellite formation systems [15, 16].

By now, there has been lots of research studies on distributed containment control, and research studies could be divided into several types from different perspectives. According to the dynamics, the research studies include first-order systems [12, 17, 18], second-order systems [19–21], linear systems [12, 17, 18], nonlinear systems [15, 22–24], homogeneous and heterogeneous multiagent systems [25], etc. In view of information topology, fixed topology [15, 19, 22, 23], and switching topology [18], undirected graph [20] and directed graph [17, 23] are, respectively, considered. In many research studies, containment control is combined with other novel control strategies, such as finite-time control [14, 15, 22], adaptive control [14, 16], neural network [16], event-triggered control [26], and so on. For the design of leaders, there exists the case of stationary leaders [20, 24], dynamic leaders (constant velocity or time-varying velocity) [17], leaders formation [25, 27], and so on. In addition, other problems such as time delay [11, 21], model uncertainties [15, 16, 23], external disturbances [15, 16], collision avoidance [27], and unmeasured relative velocity [28] are also discussed.

Recently, distributed attitude containment control strategies have gained increased attention in satellite coordinated control community. In [22], the distributed finite-time attitude containment control problem for multiple rigid bodies was addressed. For multiple stationary leaders, a model-independent control law was proposed to guarantee the attitudes of followers converge to the stationary convex hull formed by leaders in finite time by using both the one-hop and two-hop neighbours' information. Then, for dynamic leaders, a distributed sliding mode estimator and a nonsingular sliding surface were given to guarantee the attitudes and angular velocities of followers converge, respectively, to the dynamic convex hull formed by those of the leaders in finite time. Under undirected fixed connected graph, Weng et al. [29] investigated distributed robust finite-time attitude containment control for multiple rigid bodies with uncertainties including parametric uncertainties, external disturbances, and actuator failures. In [30], a distributed control strategy combined with finite-time command filtered backstepping (FTCFB) and an adaptive technique was established to solve the attitude containment control problem of spacecraft formation flying (SFF) with unknown external disturbances. The proposed novel distributed adaptive FTCFB approach could guarantee the containment errors of attitudes between leader spacecraft and follower spacecraft reach the desired neighbourhood in finite time under undirected topology. However, the information topology of cluster satellites may be directional in actual space missions. Because only a fraction of satellites was equipped with necessary sensors or communication equipment to measure relative state in cluster system, obviously, the directional information topology is more general. Ma et al. [31] studied the distributed finite-time attitude containment control problem for multiple rigid body systems with multiple stationary and dynamic leaders under directed graph. Based on sliding mode observer, adaptive attitude control algorithms were given, and the necessary and sufficient conditions were achieved which rendered all the followers converge to the convex hull spanned by the static and dynamic leaders in finite time. In [24], an attitude containment control algorithm was proposed in the case of undirected angle information topology and directed angular velocity information topology, and the case of unavailable relative angle velocity was also investigated.

Continuous or periodic sampled control scheme is usually applied to the aforementioned attitude containment control problem of satellite formation, whose results belong to time-triggered control. The state information of cluster satellites is usually sampled with a fixed and high sampling frequency, and the actuators are updated at each sampling instant, which increase the pressure of the whole network communication and lead to the wear of actuators and unnecessary energy consumption, thus seriously shortening the in-orbit operation life of cluster satellites. Moreover, in time-triggered control schemes, control action updates periodically even when the system has reached the desired state with satisfactory accuracy. Computation and communication pressure will be greatly increased, while resource and network bandwidth of the microsatellite cluster are extremely limited.

Efforts to overcome these problems have led to the proposal of event-triggered control strategy. Information interaction and controller updates are not determined by time, but by the triggering condition (event). Event-triggered mechanism consists of two types: state-dependent events [32] and time-dependent events [33]. In the event-triggered control strategy, the control tasks, consisting of sampling state information of satellites, computing control law, and updating actuators, are executed when the well-designed triggering condition is satisfied. Thus, communication and computation resources are utilized only when "needed" to preserve desired control performance [34]. It makes event-triggered control favourable, especially for satellite cluster missions with limited bandwidth and resources.

So far, event-triggered control has been investigated in the multi-rigid body system model with nonlinear characteristics. In [35], an event-triggered distributed adaptive controller was proposed to study the leader-follower consensus problem for a directed network of Euler–Lagrange agents. For the attitude control problem of spacecraft, Wu et al. [36] investigated the problem of spacecraft attitude stabilization control system with limited communication and external disturbances based on an event-triggered control scheme. Sun et al. [37] introduced an event-triggered control (ETC) strategy for the spacecraft attitude stabilization problem from the view of cyber-physical systems (CPSs); a new quaternion-based nonlinear control algorithm was proposed to ensure attitude dynamics systems' exponential stability, and parameter selection of event function and controllers was discussed in this paper. There are also research studies combining event-triggered schemes with containment control. In [38], distributed event-triggered cooperative attitude control of multiple rigid bodies with leader-follower architecture was

investigated; under the designed controllers with the event-triggered strategies, the orientations of followers converge to the convex hull formed by the desired leaders' orientations with zero angular velocities. Xu et al. [26] studied the distributed event-triggered adaptive containment control problem for multiple Euler–Lagrange systems with stationary/dynamic leaders over directed communication networks.

Although various novel control strategies have been investigated for the attitude containment control problem of a satellite cluster, which enables cluster members to converge to the convex hull formed by leaders with a faster convergence rate, little attention has been paid to the relationship between system performance and information topology design of the satellite cluster system. Note that the interaction between satellites need not be bidirectional in practice due to communication bandwidth or sensor capability. Constrained by intersatellite distance and performance of sensors, only parts of followers can receive information from leaders directly. To the best of the authors' knowledge, the event-triggered attitude containment control for the microsatellite cluster system under directed topology is worth studying and awaits a breakthrough. However, the existence of system uncertainties and unavoidable external disturbances of cluster system results in an unsatisfactory performance [39, 40]. Thus, the sliding mode control (SMC) strategy, which is robust to external disturbances and model uncertainties, is employed. The adaptive control method is also combined to realize the online estimation of uncertain parameters in real time, and it would not destroy the robustness properties of SMC [41].

In this paper, the attitude containment control problem and information topology structure design for the microsatellite cluster are investigated. First, the triggering condition consisting of the relative state error is given to adjust controller update period. If and only if the triggering condition is satisfied, state information is sampled, control law is computed, and actuators are updated. Then, an event-triggered adaptive sliding mode attitude containment control algorithm is proposed in the pressure of inertia uncertainties and external disturbances, which makes attitude of cluster members to enter asymptotically into the convex hull formed by leaders' orientations. Furthermore, cell partitions in the view of graph theory are employed to investigate the influence of information topology on orientation of followers, which provides theoretical basis for information topology design of satellite cluster missions. Finally, simulation results show that the proposed event-triggered adaptive sliding mode attitude containment controller could drive the followers to enter into the convex hull formed by the leaders' orientations in the presence of inertia uncertainties and external disturbances, and followers belonging to the same cell have the same orientation. Compared with the existing results, the proposed results in this paper have the following advantages.

(1) In the framework of the Euler–Lagrange system, this paper presents an event-triggered adaptive sliding mode attitude containment control algorithm for the microsatellite cluster system under directed topology, so that the followers asymptotically converge to the target area formed by the leaders' orientation in the presence of inertia uncertainties and external disturbances. The controller is updated only when the triggering condition is satisfied, and the state information of the triggering instant is utilized at the nontriggering time. Therefore, the control input is a piecewise function and the controller update for each satellite is asynchronous. Compared with the time-triggered method, the event-triggered adaptive sliding mode attitude containment control algorithm not only ensures the similar control performance of cluster satellites but also effectively reduces information transmission and actuator update frequency of the satellite cluster system. Event-triggered attitude containment control is superior in microsatellite cluster missions with limited resource and lower precision.

(2) The triggering condition of time-varying threshold is given in this paper. Most researches only study state-dependent or time-dependent triggering condition. However, the triggering condition in this paper is the combination of state-dependent and time-dependent. The time-dependent function is introduced to avoid the Zeno behaviour, i.e., the controller does not update infinitely in finite time, nor does it update in a periodical manner. When the triggering condition is satisfied, state information is sampled, control law is computed, and actuator is updated, which can effectively reduce the computation and actuator update frequency while ensuring the control performance of cluster system.

(3) From the perspective of graph theory, the control algorithm is fully distributed in the sense that each satellite can select their control gains according to only local information. Then, the influence of information topology design on orientation of the microsatellite cluster is analysed. It is shown that in an ideal environment, the stable state of each follower is a convex combination of all leaders' states it can access. Two kinds of cell partition of cluster information topology are given, and it is proved that satellites belonging to the same cell partition have the same stable state. It provides a theoretical basis for information topology design of microsatellite cluster missions with performance requirements such as full coverage of the target area.

The remainder of this paper is organized as follows. Mission scenarios, relative attitude dynamics of satellite cluster, basic knowledge of graph theory, and attitude containment control problem are briefly given in Section 2. In Section 3, the event-triggered adaptive sliding mode attitude containment control algorithm is proposed for the satellite cluster in the presence of inertia uncertainties and external disturbances. Then, sufficient and necessary conditions for asymptotical convergence of the cluster system and the absence of the Zeno behaviour are derived. Orientation of cluster satellites based on information topology design is given in Section 4, providing theoretical basis for information topology design of the microsatellite cluster. Numerical simulations to verify the effectiveness of the proposed control algorithm and information topology structure design are completed in Section 5, and concluding comments are given Section 6.

2. Preliminaries and Problem Formulation

In this section, some problem descriptions about mission scenarios are introduced, and then preliminary knowledge about containment control strategies is given.

2.1. Mission Scenarios. Traditional single leader consensus is a group of satellites aiming to achieve an agreement through information interaction and coordinated control, where leader's trajectory will be tracked by followers of the cluster system. In contrast, containment control can drive the followers to enter into the target area formed by the multiple leaders. Containment control is more robust in the case of leader failure and more practical in microsatellite cluster missions with limited resource and lower precision. Two typical microsatellite cluster flying scenarios which are closely related to attitude containment control are firstly given and analysed as follows.

2.1.1. Earth Observation or Deep Space Exploration of Microsatellite Cluster. Microsatellite cluster has been employed in many observation missions, such as the Earth observation or deep space exploration. It is necessary for satellites to obtain and maintain a certain relative attitude [32]. In the observation missions, such as expanding observation view or searching observation target, members are not required to converge to the same orientation, but to enter into a target area formed by the leaders' orientations, which is called attitude containment control. One of the basic objectives is that a subset of the satellite set (leaders) stabilizes to a specific relative attitude, and the orientation of the rest members (followers) enters into and remains within the specific attitude, determined by a convex hull formed by the leaders' orientation. Meanwhile, each satellite is only allowed to communicate (attitude or angular velocity) with a specific member of the set, and these constraints limit the information interaction between satellites.

2.1.2. Coordinated Attitude Control for Fractionated Spacecraft. Fractionated spacecraft distributes the functional capabilities of a monolithic spacecraft into multiple free-flying, wirelessly linking modules (service modules and different payloads) [42]. One of the main challenges of this architecture is cluster flight, keeping the various modules within bounded configurations. The fractionated spacecraft generally does not require precise relative orbit and attitude control, as long as the relative distance is within the range of communication and the relative attitude control enables power transmission links [43]. In this case, some (virtual) module spacecraft form an orientation area for the cluster members' attitude, which makes modules to maintain communication and power transmission.

There is no precise requirement for the final attitude of cluster members in the aforementioned attitude control missions of the microsatellite cluster. The attitude of followers only needs to reach an area instead of the consensus state. It is necessary to form the target area using (virtual) leaders' orientation and then control the followers to enter into the target area through intersatellite information interaction and properly designed coordinated attitude control protocol.

Constrained by unidirectional measurement characteristics of sensors or GPS-like radio frequency communication, as well as relative distance limitation between satellites, information topology of microsatellite cluster is unidirectional, asymmetric, and sparse. And the information topology structure generally remains fixed in a short time if there does not exist large disturbance. In the following, we will study the attitude containment control problem of the microsatellite cluster under fixed directed topology.

2.2. Relative Dynamics Model of Satellite Cluster. In this paper, the modified Rodriguez parameters (MRPs) are used to describe attitude motion of the satellite cluster. MRP is a kind of attitude description method without redundancy and singularity. Attitude vector $\sigma \in \mathbb{R}^3$ of MRPs is expressed by Euler axis $\mathbf{e}$ and Euler angle Φ as follows:

$$\boldsymbol{\sigma} = \mathbf{e} \tan \frac{\Phi}{4}, \quad -2\pi < \Phi < 2\pi. \tag{1}$$

The kinematic equation of follower i is

$$\dot{\sigma}_i = \mathbf{G}(\boldsymbol{\sigma}_i)\boldsymbol{\omega}_i, \tag{2}$$

where $\sigma_i \in \mathbb{R}^3$ and $\omega_i \in \mathbb{R}^3$, respectively, are MRPs and attitude angular velocity of the fixed-body coordinate system of satellite i relative to the inertia coordinate system, $\mathbf{G}(\sigma_i) = (1/4)\{(1 - \sigma_i^T\sigma_i)\mathbf{I}_3 + 2[\sigma_i^\times] + 2\sigma_i\sigma_i^T\}$, $\mathbf{I}_3$ is the 3×3 identity matrix, and $\sigma^\times$ is the skew-symmetric matrix of σ_i and is expressed as

$$\boldsymbol{\sigma}^\times = \begin{bmatrix} 0 & -(\boldsymbol{\sigma})_3 & (\boldsymbol{\sigma})_2 \\ (\boldsymbol{\sigma})_3 & 0 & -(\boldsymbol{\sigma})_1 \\ -(\boldsymbol{\sigma})_2 & (\boldsymbol{\sigma})_1 & 0 \end{bmatrix}, \tag{3}$$

where $(\mathbf{v})_k$ represents the kth component of vector $\mathbf{v}$.

Attitude dynamics equation of satellite i is expressed as

$$\mathbf{J}_i\dot{\omega}_i = -\boldsymbol{\omega}_i^{\times}\mathbf{J}_i\boldsymbol{\omega}_i + \boldsymbol{\tau}_i + \boldsymbol{\tau}_{\mathrm{d}i}, \tag{4}$$

where $\mathbf{J}_i = \mathbf{J}_i^T \in \mathbb{R}^3$ is the positive inertia matrix, $\tau_i \in \mathbb{R}^3$ represents the control torques, and $\tau_{\mathrm{d}i} \in \mathbb{R}^3$ represents the external disturbance torques.

Attitude kinematic equation using MRPs as the attitude parameter can be converted into an unified Euler–Lagrange form by appropriate transformation [44]. The Euler–Lagrange equation can effectively introduce the linear relative attitude expression between different satellites, which plays a beneficial role in coordinated attitude control design of satellite cluster. Taking the derivative of (2) and substituting (3) into (2), the Euler–Lagrange form of attitude dynamics equation for satellite i could be obtained as follows:

$$\mathbf{M}_i(\boldsymbol{\sigma}_i)\ddot{\sigma}_i + \mathbf{C}_i(\boldsymbol{\sigma}_i, \dot{\sigma}_i)\dot{\sigma}_i + \mathbf{g}_i(\boldsymbol{\sigma}_i) = \mathbf{u}_i + \mathbf{d}_i, \tag{5}$$

where $\sigma_i = [\sigma_i^{(1)}, \sigma_i^{(2)}, \sigma_i^{(3)}]^T$, $\mathbf{M}_i(\sigma_i) = \mathbf{G}^{-T}(\sigma_i)\mathbf{J}_{0i}\mathbf{G}^{-1}(\sigma_i)$ is symmetric positive-definite inertia matrix of satellite i, $\mathbf{C}_i(\sigma_i, \dot{\sigma}_i) = -\mathbf{G}^{-T}(\sigma_i)\mathbf{J}_{0i}\mathbf{G}^{-1}(\sigma_i)\dot{\mathbf{G}}(\sigma_i)\mathbf{G}^{-1}(\sigma_i) - \mathbf{G}^{-T}(\sigma_i)[\mathbf{J}_{0i}\mathbf{G}^{-1}(\sigma_i)\dot{\sigma}_i]^{\times}\mathbf{G}^{-1}(\sigma_i)$ is Coriolis and centrifugal torques matrix, $\mathbf{J}_i = \mathbf{J}_{0i} + \Delta\mathbf{J}_i$, $\mathbf{J}_{0i}$ is nominal inertia of follower i, $\Delta\mathbf{J}_i$ is uncertainties part, $\mathbf{g}_i(\sigma_i)$ is uncertainties causing by model uncertainties, $\mathbf{u}_i = \mathbf{G}^{-T}(\sigma_i)\tau_i$ is control torques, and $\mathbf{d}_i = \mathbf{G}^{-T}(\sigma_i)\tau_{\mathrm{d}i}$ is disturbance torques. According to Reference [45], the Euler–Lagrange equation has the following properties: (a) $\mathbf{M}_i(\sigma_i) \in \mathbb{R}^{3\times3}$ is a symmetric positive-definite matrix; (b) here we assume that there exist positive $k_{\underline{m}}, k_{\overline{m}}, k_C, k_g$ satisfying $0 < k_{\underline{m}}\mathbf{I}_n \le \mathbf{M}_i(\sigma_i) \le k_{\overline{m}}\mathbf{I}_n$, $\|\mathbf{C}_i(\sigma_i, \dot{\sigma}_i)\| < k_C\|\dot{\sigma}_i\|$, $\mathbf{g}_i(\sigma_i) \le k_g$; (c) for any $\sigma_i, \dot{\sigma}_i \in \mathbb{R}^3$, $(1/2)\dot{\mathbf{M}}_i(\sigma_i, \dot{\sigma}_i) - \mathbf{C}_i(\sigma_i, \dot{\sigma}_i)$ is a skew-symmetric matrix, and there exist $\mathbf{x} \in \mathbb{R}^3$, $\mathbf{x}^T((1/2)\dot{\mathbf{M}}_i(\sigma_i) - \mathbf{C}_i(\sigma_i, \dot{\sigma}_i))\mathbf{x} = 0$; (d) we assume that the left-hand side of (5) can be parameterized in linear expression as $\mathbf{M}_i(\sigma_i)x + \mathbf{C}_i(\sigma_i, \dot{\sigma}_i)y + g_i = \mathbf{Y}_i(\sigma_i, \dot{\sigma}_i, x, y)\Theta_i.g_i$, for any $x, y \in \mathbb{R}^3$, where $\mathbf{Y}_i(\sigma_i, \dot{\sigma}_i, x, y)$ is the regression function matrix and Θ_i is the unknown constant parameter vector.

Assumption 1. All leaders' states and state derivatives are bounded, that is, there exist constants σ_{LM} and $\dot{\sigma}_{\mathrm{LM}}$ such that $\|\sigma_L(t)\| \le \sigma_{\mathrm{LM}}, \|\dot{\sigma}_L(t)\| \le \dot{\sigma}_{\mathrm{LM}}$. In this paper, we add an additional assumption that $\lim_{t\longrightarrow\infty}\|\dot{\sigma}_L\| \longrightarrow 0$.

Assumption 2. The external disturbance torque $\mathbf{d}_i$ is bounded, that is, there exists a positive constant d_M such that $\|\mathbf{d}_i\| \le d_M$, where d_M is bounded and unknown.

2.3. Graph Theory. Graph theory is introduced as an useful mathematical tool to describe intersatellite information interaction, providing theoretical basis for control performance analysis of the cluster system.

Suppose there are $N+M$ satellites in the cluster, consisting of N followers (denoted by 1, 2, . . ., N) and M leaders (denoted by $N+1, \ldots, N+M$). We assume that the (virtual) satellites belong to either one of the two subsets, namely, the subset of followers $F = \{1, 2, \ldots, N\}$ or the subset of leaders $L = \{N+1, \ldots, N+M\}$.

Information interaction topology of the cluster system can be modelled by a digraph $G = (V, E)$ with node set $V(G) = \{1, \ldots, N+M\}$ denoting satellite with dynamics or kinematic characteristics and edge set $E(G) = V(G) \times V(G)$ denoting intersatellite information interaction. Each edge $(i, j) \in E(G)$ means satellite j can access state information from satellite i, and satellite i is called a neighbour of satellite j. The neighbour set $N_i = \{j \in V(G) | (j, i) \in E(G)\}$ of satellite i is a collection of all the satellites from which satellite i can access state information. If $(i, j) \in E(G) \Leftrightarrow (j, i) \in E(G)$, bidirectional edge (i, j) indicates that satellites i and j can access state information from each other. A directed path from node i to node j is a sequence of edges of the form (i, i_1), (i_1, i_2), . . ., (i_n, j), in a directed graph. A directed tree is a directed graph, where every node has exactly one parent except for one node, called the root, and the root has directed paths to every other node. A directed spanning tree of a directed graph is a direct tree that contains all nodes of the directed graph. A directed graph has or contains a directed spanning tree, if there exists a directed spanning tree as a subset of the directed graph.

Two matrices are frequently used to represent interaction topology: one is adjacency matrix $\mathbf{A} = [a_{ij}]$ with $a_{ij} \ge 0$, $a_{ij} > 0$ if $(i, j) \in E(G)$. In this paper, we assume that self-edges are not allowed, i.e., $a_{ii} = 0$. And the other is Laplacian matrix $\mathbf{L} = [l_{ij}]$ with $l_{ii} = \sum_{j=1, j\neq i}^{N} a_{ij}$, $l_{ij} = -a_{ij}$, $(i \neq j)$.

The system Laplacian matrix $\mathbf{L}$ can also be written as block matrix:

$$\mathbf{L} = \begin{bmatrix} \mathbf{L}_F & \mathbf{L}_{\mathrm{FL}} \\ 0 & 0 \end{bmatrix}, \tag{6}$$

where $\mathbf{L}_F$ is the $N \times N$ submatrix composed by rows and columns in which the followers of $\mathbf{L}$ are located, and it represents information interaction relationship among followers. $\mathbf{L}_{FL}$ is the $N \times M$ submatrix composed by rows and columns in which the followers and leaders of $\mathbf{L}$ are, respectively, located, and it represents the information flow from leaders to followers. G_F denotes followers and information interaction between followers.

Several graph theory tools are given to provide theoretical basis for information topology design of the cluster system.

Definition 1 (see [46]). For directed graph G, a k partition π of $V(G)$ is composed of k cells $C_1, \ldots, C_k$ with $C_i \cap C_j = \Phi$, $(i, j = 1, \ldots, k, i \neq j)$ and $\cup_{i=1}^{k} C_i = V(G)$. C_j is a neighbour of C_i $(i, j = 1, \ldots, k, i \neq j)$ if there exist $i' = c_i$ and $j' = c_j$ such that j' is a neighbour of i'.

Definition 2 (see [47]). Suppose that $\pi = \{C_1, \cdots, C_k\}$ is a k partition of $V(G)$; if any two distinct vertices in C_i have the same number of neighbours in C_j for all $j \neq i$, then π is called a π^1 partition. In particular, $\pi^1 = \{H_1, \ldots, H_m\}$ denotes the π^1 cell partition containing H_i $(i = 1, \ldots, m)$ as m cells of π^1.

Definition 3 (see [46]). Suppose $\pi = \{C_1, \ldots, C_k\}$ is a k partition of $V(G)$; if for each vertex in C_i, it has the same

number of neighbours in all neighbour cells of $C_i\,(i = 1, \ldots, m)$, then π is called a π^2 partition.

2.4. Containment Control Model. The following definitions, assumptions, and lemmas related to containment control strategy are needed to derive the main results of this paper.

2.4.1. Convex Hull. There may exist multiple leaders in microsatellite cluster missions, and all followers are required to enter into the target area formed by the leaders' state instead of reaching a consensus state. Several vertices on the boundary of the target area are selected so that the target area can be approximately replaced by convex polygons which are formed by these vertices [48]. Generally, the more the vertices are selected, the higher the approximate accuracy is.

Suppose that the target area (moving or stationary) can be approximated by a convex hull formed by M vertices.

The definition of convex hull is given as follows.

Definition 4 (see [23]). Let C be a set in a real vector space $V \subseteq \mathbf{R}^p$. The set C is convex if, for any x and y in C, the point $(1-t)x + ty \in C$ for any $t \in [0, 1]$. The convex hull for a set of points $X = \{x_1, \ldots, x_M\}$ in V is the minimal convex set containing all points in X. We use $\mathrm{CO}(X)$ to denote the convex hull of X, that is, $\mathrm{CO}(X) = \left\{\sum_{i=1}^{M} \alpha_i x_i | x_i \in X, \alpha_i \in \mathbf{R}, \alpha_i \geq 0, \sum_{i=1}^{M} \alpha_i = 1\right\}$.

Vertex information of the target area could be provided by the Earth station or could be autonomously generated by cluster members which have strong sense, communication, and information processing capability.

Once the convex hull which approximates the target area is selected, vertex information of the convex hull can be seen as (virtual) leaders of the cluster system, while cluster members are regarded as followers.

2.4.2. Distributed Attitude Containment Control Formulation. Followers need to generate control decisions based on absolute state of itself and relative state information of its neighbours, which makes attitude of followers to converge to the convex hull formed by the leaders' orientation.

Containment control protocol for followers could be written in the following form:

$$\mathbf{u}_i = h_i\left(\boldsymbol{\sigma}_F, \boldsymbol{\omega}_F, \boldsymbol{\sigma}_L, \boldsymbol{\omega}_L\right), \quad i \in F, \tag{7}$$

where $\sigma_F = [\sigma_1^T, \ldots, \sigma_N^T]^T$, $\omega_F = [\omega_1^T, \ldots, \omega_N^T]^T$, $\sigma_L = [\sigma_{N+1}^T, \ldots, \sigma_{N+M}^T]^T$, and $\omega_L = [\omega_{N+1}^T, \ldots, \omega_{N+M}^T]^T$, respectively, are the attitudes and angular velocities of followers and leaders.

We assume that there is no information interaction between leaders. The trajectories of leaders are not affected by other members, while followers need to generate control instructions with neighbours' information [49]. To drive all the states of followers to enter into the convex hull formed by the leaders' orientation, it must be ensured that each follower can receive information from leaders directly or indirectly. Otherwise, there will exist followers whose motion is not affected by any leader, nor will converge to the convex hull formed by the leaders' orientation. Thus, the information topology of the cluster system needs to meet the following assumption.

Assumption 3 (see [20]). Suppose that for each follower i, there exists at least one leader j that has a path to the follower i.

Lemma 1 (see [20]). *If Assumption 3 holds, then $\mathbf{L}_F$ is invertible; each entry of $-L_F^{-1}L_{FL}$ is nonnegative and each row sum of $-\mathbf{L}_F^{-1}\mathbf{L}_{\mathrm{FL}}$ is equal to one.*

Lemma 2 (see [23]). *Let $\mathbf{L}$ be the Laplacian matrix associated with a directed graph G. Then, $\mathbf{L}$ has a single zero eigenvalue and all other eigenvalues have positive real parts if and only if G has a directed spanning tree.*

Lemma 3 (see [50]). *Consider the system $\dot{x} = f(t, x, u)$, where $f(t, x, u)$ is continuously differentiable and globally uniform Lipschitz in (x, u) for all t. If the unforced system $\dot{x} = f(t, x, 0)$ has a globally exponentially stable equilibrium point at the origin $x = 0$, then the system $\dot{x} = f(t, x, u)$ is input-to-state stable.*

According to Definition 4 and Lemma 1, the desired state is convex weighted average of the leaders' attitude and angular velocity, which can be written as

$$\begin{aligned} \boldsymbol{\sigma}_d &= -\mathbf{L}_F^{-1}\mathbf{L}_{\mathrm{FL}}\boldsymbol{\sigma}_L, \\ \boldsymbol{\omega}_d &= -\mathbf{L}_F^{-1}\mathbf{L}_{\mathrm{FL}}\boldsymbol{\omega}_L, \end{aligned} \tag{8}$$

where σ_d and ω_d, respectively, are the desired attitude and desired angular velocity.

Our aim in this paper is to propose appropriate distributed attitude control algorithm for the followers (i.e., those indexed from 1 to N), so that in an asymptotic manner, they can travel into the convex hull formed by the leaders (i.e., those satellites indexed from $N+1$ to $N+M$). We will also analyse under what conditions the containment behaviours can be guaranteed and perform rigorous convergence with less sampled information and control action, that is, $\lim_{t\longrightarrow\infty}\sigma_F(t) \longrightarrow -(\mathbf{L}_F^{-1}\mathbf{L}_{\mathrm{FL}} \otimes \mathbf{I}_3)\sigma_L$, $\lim_{t\longrightarrow\infty}\omega_F(t) \longrightarrow 0$, $\forall i \in F$. On this basis, the influence of information topology design on orientation of followers is analysed, which provides a theoretical reference for orientation design of cluster members.

3. Distributed Attitude Containment Control for Microsatellite Cluster

For attitude containment control problem of leader-follower satellite cluster, an event-triggered adaptive sliding mode control algorithm is proposed in the presence of inertia uncertainties and external disturbances. The triggering condition based on relative attitude error is set for each follower, that is, the entire system is triggered asynchronously and triggering time of each follower is different. State information is sampled, control law is computed, and actuators are updated if and only if triggering conditions are

met. At nontriggering time, controller of followers uses the state information of triggering instant.

The event-triggered adaptive sliding mode controller and triggering condition are designed to make attitude of followers asymptotically enter into the convex hull formed by the leaders and attitude angular velocity converge to 0; meanwhile, the update frequency of control tasks is reduced.

3.1. Event-Triggered Formulation for Attitude Containment Control. The traditional time-triggered control scheme is usually updated periodically, and periodic sampling may be a better control scheme in the view of control scheme design and problem analysis. However, when the system is working normally, periodic control will cause unnecessary energy consumption and actuator update.

To reduce the pressure of computation, communication, and actuators and meet the constraints of mass, volume, and power on the microsatellites, the event-triggered mechanism is introduced to solve coordinated attitude control of the microsatellite cluster, while to ensure the control performance of the microsatellite cluster, the triggering condition is used to adjust update period of controller and reduce the amount of computation and communication pressure. The design of the event-triggered coordinated attitude controller could be divided into two main steps. First is the setting of triggering condition. The triggering function with relative attitude error is designed to adjust update period of controller, state information is sampled, control law is computed, and actuator is updated if and only if the event is triggered. Second, the event-triggered distributed attitude controller is designed in the presence of model uncertainties and external disturbances, which makes followers to converge to the convex hull formed by the leaders' orientation. And the Zeno behaviour is excluded. Triggering frequency is reduced and resource is saved as well as control performance of cluster system is ensured. The triggering condition is given in this section, and distributed attitude containment control protocol will be proposed in the next section.

First, to rewrite the dynamics equation of the satellite cluster into the form which is convenient for stability analysis, auxiliary variable $\dot{\sigma}_{ri}$ is introduced:

$$\dot{\sigma}_{ri} = -\alpha \sum_{j=1}^{N+M} a_{ij}\left(\boldsymbol{\sigma}_i(t) - \boldsymbol{\sigma}_j(t)\right), \quad i \in F, j \in F \cup L. \tag{9}$$

Design the sliding variable $\mathbf{s}_i$:

$$\mathbf{s}_i = \dot{\sigma}_i(t) - \dot{\sigma}_{ri}(t) = \dot{\sigma}_i(t) + \alpha \sum_{j=1}^{N+M} a_{ij}\left(\boldsymbol{\sigma}_i(t) - \boldsymbol{\sigma}_j(t)\right), \tag{10}$$

where α is a positive constant and a_{ij} is the weight of adjacency matrix $\mathbf{A}$ of directed graph G.

According to the properties of equations (5) and (9), the dynamics system could be rewritten as

$$\begin{aligned}\mathbf{M}_i(\boldsymbol{\sigma}_i)\ddot{\sigma}_{ri} + \mathbf{C}_i\left(\boldsymbol{\sigma}_i, \dot{\sigma}_i\right)\dot{\sigma}_{ri} + \mathbf{g}_i \\ = \mathbf{Y}_i\left(\boldsymbol{\sigma}_i, \dot{\sigma}_i, \ddot{\sigma}_{ri}, \dot{\sigma}_{ri}\right)\Theta_i + \boldsymbol{\varepsilon}_i, \quad i = 1, \ldots, N.\end{aligned} \tag{11}$$

In coordinated attitude control of the satellite cluster, Θ_i is the inertia matrix with unknown parameters, $\Theta_i = [J_{11}, J_{22}, J_{33}, J_{12}, J_{13}, J_{23}]^T$. For any $\mathbf{x} \in \mathbb{R}^3$, there exists $\mathbf{J}_i\mathbf{x} = \mathbf{L}(\mathbf{x})\Theta_i$. ε_i is the approximation error for the ith follower, $\|\varepsilon_i\| \le \varepsilon_M$. Linear operator $\mathbf{L}(x)$ is shown as follows:

$$\mathbf{L}(\mathbf{x}) = \begin{bmatrix} x_1 & 0 & 0 & x_2 & x_3 & 0 \\ 0 & x_2 & 0 & x_1 & 0 & x_3 \\ 0 & 0 & x_3 & 0 & x_1 & x_2 \end{bmatrix}. \tag{12}$$

Regression function matrix:

$$\begin{aligned}\mathbf{Y}_i\left(\boldsymbol{\sigma}_i, \dot{\sigma}_i, \dot{\sigma}_{ri}, \ddot{\sigma}_{ri}\right) = \mathbf{G}^{-T}(\boldsymbol{\sigma}_i)\mathbf{L}\left(\mathbf{G}^{-1}(\boldsymbol{\sigma}_i)\ddot{\sigma}_{ri}\right) \\ - \mathbf{G}^{-T}(\boldsymbol{\sigma}_i)\mathbf{L}\left(\mathbf{G}^{-1}(\boldsymbol{\sigma}_i)\dot{G}(\boldsymbol{\sigma}_i)\mathbf{G}^{-1}(\boldsymbol{\sigma}_i)\dot{\sigma}_{ri}\right) \\ + \mathbf{G}^{-T}(\boldsymbol{\sigma}_i)\left(\mathbf{G}^{-1}(\boldsymbol{\sigma}_i)\dot{\sigma}_{ri}\right)^{\times}\mathbf{L}\left(\mathbf{G}^{-1}(\boldsymbol{\sigma}_i)\dot{\sigma}_i\right).\end{aligned} \tag{13}$$

Let the triggering time sequence of follower i be $t_0^i, t_1^i, \ldots, t_k^i, \ldots$, where $k = 0, 1, \ldots$, and $t_0^i = 0$. t_k^i denotes the kth event time of the ith satellite.

Two types of state errors are defined to facilitate the design of the triggering condition:

$$\begin{aligned}\mathbf{e}_{si}\left(t^i\right) &= \mathbf{s}_i\left(t_k^i\right) - \mathbf{s}_i\left(t^i\right); t^i \in \left[t_k^i, t_{k+1}^i\right), \\ \mathbf{e}_{Ji}\left(t^i\right) &= \mathbf{Y}_i\left(t_k^i\right)\widehat{\Theta}_i\left(t_k^i\right) - \mathbf{Y}_i\left(t^i\right)\widehat{\Theta}_i\left(t^i\right),\end{aligned} \tag{14}$$

where $\widehat{\Theta}_i(t^i)$ is the estimation of Θ_i at time t^i.

According to Reference [35], the triggering condition can be defined as follows:

$$\left\|\mathbf{e}_{Ji}\left(t^i\right)\right\| + \lambda_{\max}(\mathbf{K}_i)\left\|\mathbf{e}_{\mathrm{si}}\left(t^i\right)\right\| - \frac{\gamma_i}{2}\lambda_{\min}(\mathbf{K}_i)\left\|\mathbf{s}_i\left(t^i\right)\right\| - \mu_i\left(t^i\right) \ge 0, \tag{15}$$

where $\mathbf{K}_i$ is the symmetric positive-definite matrix, $0 < \gamma_i < 1$, $\mu_i(t^i) = \rho_i\sqrt{\lambda_{\min}(\mathbf{K}_i)}\exp(-\nu_i t^i)$, $\rho_i > 0$, and $0 < \nu_i < 1$.

Remark 1. $\mu_i(t^i)$ is a time-dependent function. The introduction of $\mu_i(t^i)$ can completely avoid the Zeno behaviour. The initial attitude and angular velocity $\sigma_i(t_0^i)$, $\omega_i(t_0^i)$, $i \in F$ of followers and attitude and angular velocity $\sigma_i(t_0^i)$, $\omega_i(t_0^i)$, $i \in L$ of leaders are given at initial time t_0^i. The system continuously monitors the auxiliary state $\mathbf{s}_i(t^i)$ and uncertain parameter $\widehat{\Theta}_i(t^i)$ of each follower. Once the triggering condition of satellite i is satisfied, that is, $f_i(\mathbf{e}_{\mathrm{si}}(t^i), \mathbf{e}_{\mathrm{Ji}}(t^i)) \ge 0$, the event of satellite i is triggered immediately, triggering time is $t^i = t_k^i$, state information is sampled, control law is computed, and actuators are updated. The state errors $\mathbf{e}_{\mathrm{Ji}}(t^i)$ and $\mathbf{e}_{si}(t^i)$ are reset to 0. In nontriggering time, the controller uses state information of the last triggering instant, i.e., for $t^i \in [t_k^i, t_{k+1}^i)$, $\mathbf{u}_i(t^i) = \mathbf{u}_i(t_k^i)$. Control law is not computed until the next event is triggered, and thus the control input is piecewise constant. Under the action of the event-triggered attitude

containment controller, the attitude of followers asymptotically converges to the convex hull formed by the leaders' orientation.

In this paper, the event-triggered distributed attitude control algorithm could be written in the following form:

$$\begin{cases} \mathbf{u}_i\left(t_k^i\right) = h_i\left(\mathbf{s}_i\left(t_k^i\right), \mathbf{Y}_i\left(t_k^i\right)\widehat{\Theta}_i\left(t_k^i\right)\right), \\ \mathbf{u}_i\left(t^i\right) = \mathbf{u}\left(t_k^i\right), \quad t^i \in \left[t_k^i, t_{k+1}^i\right). \end{cases} \tag{16}$$

It is noteworthy that the control law does not need be computed until the next event.

Attitude dynamics equation of followers could be rewritten in the following form:

$$\mathbf{M}_i(\boldsymbol{\sigma}_i)\dot{s}_i + \mathbf{C}_i(\boldsymbol{\sigma}_i, \dot{\sigma}_i)\mathbf{s}_i = \mathbf{u}_i + \mathbf{d}_i - \mathbf{Y}_i(\boldsymbol{\sigma}_i, \dot{\sigma}_i, \ddot{\sigma}_r, \dot{\sigma}_r)\Theta_i - \boldsymbol{\varepsilon}_i, \quad i = 1, \ldots, N. \tag{17}$$

Correspondingly, triggering time is defined as

$$t_{k+1}^i = \inf\left\{t^i > t_k^i \mid f_i\left(\mathbf{e}_{\mathrm{si}}\left(t^i\right), \mathbf{e}_{\mathrm{Ji}}\left(t^i\right)\right) \geq 0\right\}. \tag{18}$$

Once $t^i = t_k^i$, the event is triggered, state information is sampled, control law is computed and actuators are updated for satellite i, and the corresponding triggering function is less than 0 again.

The event-triggered control scheme is shown in Figure 1. The scenarios we consider include sampling time and triggering time; the sampling time is determined by the fixed clock frequency of the sensor, and the latter is controlled by the triggering condition based on the state. It is noteworthy that the time interval between two consecutive events is usually variable and can be equal to the minimum interval (that is, the sampling period). When the interval between two consecutive events is a fixed sampling period, the system degenerates into a traditional periodic sampling control. For the triggering conditions in this paper, continuous detection is necessary, which may require additional equipment and is a waste of communication and computing resources.

3.2. Event-Triggered Adaptive Sliding Mode Attitude Containment Control. For each follower i, the event-triggered adaptive sliding mode control protocol is designed as

$$\mathbf{u}_i\left(t^i\right) = -\mathbf{K}_i\mathbf{s}_i\left(t_k^i\right) + \mathbf{Y}_i\left(t_k^i\right)\widehat{\Theta}_i\left(t_k^i\right) - \widehat{k}_i\left(t_k^i\right)\mathrm{sgn}\left(\mathbf{s}_i\left(t_k^i\right)\right), \quad i \in F, t^i \in \left[t_k^i, t_{k+1}^i\right). \tag{19}$$

Adaptation law of $\widehat{\Theta}_i(t^i)$ and $\widehat{k}_i$ is defined as follows:

$$\dot{\widehat{\Theta}}_i(t) = -\boldsymbol{\Lambda}_i\mathbf{Y}_i^T\left(t^i\right)\mathbf{s}_i\left(t^i\right), \tag{20}$$

$$\dot{\widehat{k}}_i\left(t^i\right) = \Gamma_i\left\|\mathbf{s}_i\left(t^i\right)\right\|_1, \tag{21}$$

where Λ_i is a symmetric positive-definite matrix and Γ_i is a positive constant.

According to (9) and (10), system (17) can be rewritten as

$$\mathbf{M}_i(\boldsymbol{\sigma}_i)\dot{s}_i\left(t^i\right) + \mathbf{C}_i(\boldsymbol{\sigma}_i, \dot{\sigma}_i)\mathbf{s}_i\left(t^i\right) = -\mathbf{K}_i\mathbf{s}_i\left(t_k^i\right) + \mathbf{Y}_i\left(t_k^i\right)\widehat{\Theta}_i\left(t_k^i\right) - \widehat{k}_i\mathrm{sgn}\left(\mathbf{s}_i\left(t_k^i\right)\right) + \mathbf{d}_i - \mathbf{Y}_i\left(t^i\right)\Theta_i - \boldsymbol{\varepsilon}_i, i \in F, \quad t^i \in \left[t_k^i, t_{k+1}^i\right). \tag{22}$$

The following conclusion shows that event-triggered adaptive sliding mode attitude control protocol (19), adaption laws (20) and (21), and triggering condition (15) can realize attitude containment control of microsatellite cluster system (5) under directed information topology. When $t \longrightarrow \infty$, the attitude and angular velocity of followers asymptotically enter into the convex hull formed by leaders, that is, $\lim_{t\longrightarrow\infty}\sigma_F(t) \longrightarrow -(\mathbf{L}_F^{-1}\mathbf{L}_{FL} \otimes \mathbf{I}_3)\sigma_L$ and $\lim_{t\longrightarrow\infty}\omega_F(t) \longrightarrow 0$. Moreover, it can be further proved that the Zeno behaviour will not occur in the microsatellite cluster system under the action of the proposed event-triggered attitude control strategy.

Theorem 1. *If Assumptions 1 and 2 hold, under the action of triggering condition (15), event-triggered adaptive sliding mode attitude control protocol (19), and adaption laws (20) and (21), the attitude of followers asymptotically enters into the convex hull formed by leaders' orientation, that is,* $\lim_{t\longrightarrow\infty}\sigma_F(t) \longrightarrow -(\mathbf{L}_F^{-1}\mathbf{L}_{FL} \otimes \mathbf{I}_3)\sigma_L$ *and* $\lim_{t\longrightarrow\infty}\omega_F(t) \longrightarrow 0$*, and then the sufficient and necessary condition is that Assumption 3 holds.*

(1) Proof. Sufficiency: The proof includes the following two consecutive steps. (i) State trajectory asymptotically converges to the sliding surface, that is, $\lim_{t^i\longrightarrow\infty}\mathbf{s}_i = 0$. (ii) In the case of $\mathbf{s}_i = 0$, the state of followers will reach $\lim_{t\longrightarrow\infty}\sigma_F(t) \longrightarrow -(\mathbf{L}_F^{-1}\mathbf{L}_{\mathrm{FL}} \otimes \mathbf{I}_3)\sigma_L$, $\lim_{t\longrightarrow\infty}\omega_F(t) \longrightarrow 0$ asymptotically.

First, consider the following Lyapunov candidate:

$$V_1 = \frac{1}{2}\sum_{i=1}^{N}\mathbf{s}_i^T\mathbf{M}_i(\boldsymbol{\sigma}_i)\mathbf{s}_i + \frac{1}{2}\sum_{i=1}^{N}\widetilde{\Theta}_i^T\boldsymbol{\Lambda}_i^{-1}\widetilde{\Theta}_i + \frac{1}{2}\sum_{i=1}^{N}\left(k_i - \widehat{k}_i\right)^2\Gamma_i^{-1}, \tag{23}$$

where $k_i \geq \varepsilon_M + d_M$ and the estimation error is

$$\widetilde{\Theta}_i = \Theta_i - \widehat{\Theta}_i. \tag{24}$$

Taking the derivative of V_1, we can obtain

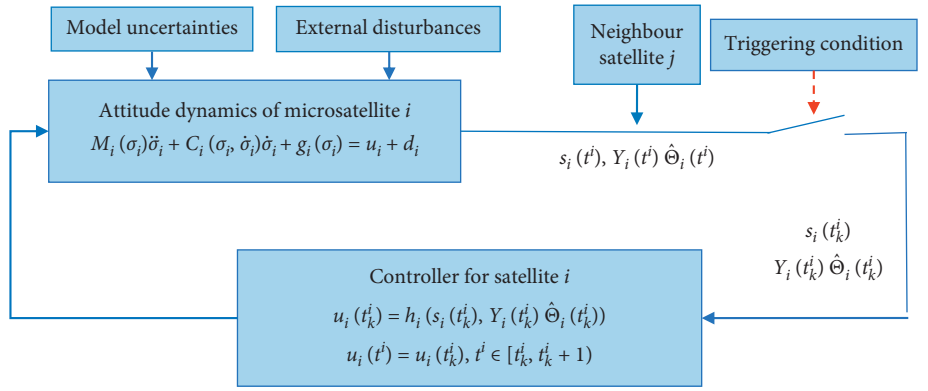

Figure 1: Control scheme of the event-triggered strategy.

$$\begin{aligned}\dot{V}_1 &= \frac{1}{2}\sum_{i=1}^{N}\mathbf{s}_i^T\dot{M}_i(\boldsymbol{\sigma}_i)\mathbf{s}_i + \sum_{i=1}^{N}\mathbf{s}_i^T\mathbf{M}_i(\boldsymbol{\sigma}_i)\dot{s}_i + \sum_{i=1}^{N}\tilde{\Theta}_i^T\boldsymbol{\Lambda}_i^{-1}\dot{\tilde{\Theta}}_i - \sum_{i=1}^{N}\left(k_i - \hat{k}_i\right)\Gamma_i^{-1}\dot{\hat{k}}_i \\ &= \sum_{i=1}^{N}\mathbf{s}_i^T\left(\frac{1}{2}\dot{M}_i(\boldsymbol{\sigma}_i) - \mathbf{C}_i(\boldsymbol{\sigma}_i, \dot{\sigma}_i)\right)\mathbf{s}_i - \sum_{i=1}^{N}\mathbf{s}_i^T\mathbf{K}_i\mathbf{s}_i\left(t_k^i\right) + \sum_{i=1}^{N}\mathbf{s}_i^T\mathbf{Y}_i\left(t_k^i\right)\widehat{\Theta}_i\left(t_k^i\right) \\ &\quad - \sum_{i=1}^{N}\mathbf{s}_i^T\hat{k}_i\mathrm{sgn}\left(\mathbf{s}_i\left(t_k^i\right)\right) - \sum_{i=1}^{N}\mathbf{s}_i^T\mathbf{Y}_i\Theta_i - \sum_{i=1}^{N}\mathbf{s}_i^T\boldsymbol{\varepsilon}_i + \sum_{i=1}^{N}\mathbf{s}_i^T\mathbf{d}_i + \sum_{i=1}^{N}\tilde{\Theta}_i^T\mathbf{Y}_i^T\mathbf{s}_i - \sum_{i=1}^{N}\left(k_i - \hat{k}_i\right)|\mathbf{s}_i|.\end{aligned} \tag{25}$$

According to property (c) of the Euler–Lagrange equation, $(1/2)\dot{M}_i(\sigma_i) - \mathbf{C}_i(\sigma_i)$ is a skew-symmetric matrix; substituting (24) into (25), we can obtain that

$$\begin{aligned}\dot{V}_1 &= -\sum_{i=1}^{N}\mathbf{s}_i^T\mathbf{K}_i\mathbf{s}_i\left(t_k^i\right) + \sum_{i=1}^{N}\mathbf{s}_i^T\mathbf{Y}_i\left(t_k^i\right)\widehat{\Theta}_i\left(t_k^i\right) - \sum_{i=1}^{N}\mathbf{s}_i^T\hat{k}_i\mathrm{sgn}\left(\mathbf{s}_i\left(t_k^i\right)\right) \\ &\quad - \sum_{i=1}^{N}\mathbf{s}_i^T\mathbf{Y}_i\left(\tilde{\Theta}_i + \widehat{\Theta}_i\right) + \sum_{i=1}^{N}\tilde{\Theta}_i^T\mathbf{Y}_i^T\mathbf{s}_i - \sum_{i=1}^{N}k_i|\mathbf{s}_i| + \sum_{i=1}^{N}\hat{k}_i|\mathbf{s}_i| + \sum_{i=1}^{N}\mathbf{s}_i^T\left(\mathbf{d}_i - \boldsymbol{\varepsilon}_i\right) \\ &= -\sum_{i=1}^{N}\mathbf{s}_i^T\mathbf{K}_i\mathbf{s}_i\left(t_k^i\right) + \sum_{i=1}^{N}\mathbf{s}_i^T\left(\mathbf{Y}_i\left(t_k^i\right)\widehat{\Theta}_i\left(t_k^i\right) - \mathbf{Y}_i\widehat{\Theta}_i\right) - \sum_{i=1}^{N}\mathbf{s}_i^T\mathbf{Y}_i\tilde{\Theta}_i + \sum_{i=1}^{N}\tilde{\Theta}_i^T\mathbf{Y}_i^T\mathbf{s}_i \\ &\quad - \sum_{i=1}^{N}\mathbf{s}_i^T\hat{k}_i\mathrm{sgn}\left(\mathbf{s}_i\left(t_k^i\right)\right) + \sum_{i=1}^{N}\hat{k}_i|\mathbf{s}_i| - \sum_{i=1}^{N}k_i|\mathbf{s}_i| + \sum_{i=1}^{N}\mathbf{s}_i^T\left(\mathbf{d}_i - \boldsymbol{\varepsilon}_i\right).\end{aligned} \tag{26}$$

Substituting definitions of state errors (14) into (26), it can be obtained that

$$\begin{aligned}\dot{V}_1 &= -\sum_{i=1}^{N}\mathbf{s}_i^T\mathbf{K}_i\mathbf{s}_i - \sum_{i=1}^{N}\mathbf{s}_i^T\mathbf{K}_i\mathbf{e}_{\mathrm{si}} + \sum_{i=1}^{N}\mathbf{s}_i^T\mathbf{e}_{Ji} \\ &\quad - \sum_{i=1}^{N}\mathbf{s}_i^T\hat{k}_i\mathrm{sgn}\left(\mathbf{s}_i\left(t_k^i\right)\right) + \sum_{i=1}^{N}\hat{k}_i|\mathbf{s}_i| - \sum_{i=1}^{N}k_i|\mathbf{s}_i| + \sum_{i=1}^{N}\mathbf{s}_i^T\left(\mathbf{d}_i - \boldsymbol{\varepsilon}_i\right).\end{aligned} \tag{27}$$

According to Assumption 2, we can get $\mathbf{s}_i^T\left(\mathbf{d}_i - \varepsilon_i\right) \le |\mathbf{s}_i||\mathbf{d}_i| + |\mathbf{s}_i||\varepsilon_i| \le k_i|\mathbf{s}_i|$. Thus,

$$\begin{aligned}\dot{V}_1 \le &-\sum_{i=1}^{N}\mathbf{s}_i^T\mathbf{K}_i\mathbf{s}_i - \sum_{i=1}^{N}\mathbf{s}_i^T\mathbf{K}_i\mathbf{e}_{\mathrm{si}} + \sum_{i=1}^{N}\mathbf{s}_i^T\mathbf{e}_{Ji} \\ &- \sum_{i=1}^{N}\mathbf{s}_i^T\hat{k}_i\mathrm{sgn}\left(\mathbf{s}_i\left(t_k^i\right)\right) + \sum_{i=1}^{N}\hat{k}_i|\mathbf{s}_i|.\end{aligned} \tag{28}$$

In the time interval $t^i \in [t_k^i, t_{k+1}^i)$, we can know that the system trajectories start from a region where $\mathrm{sgn}(\mathbf{s}_i(t_k^i)) = \mathrm{sgn}(\mathbf{s}_i(t^i))$. And $\mathbf{K}_i$ is a symmetric positive-definite matrix; then, the upper bound for $\dot{V}_1$ can be expressed as

$$\dot{V}_1 \le -\sum_{i=1}^{N} \mathbf{s}_i^T \mathbf{K}_i \mathbf{s}_i - \sum_{i=1}^{N} \mathbf{s}_i^T \mathbf{K}_i \mathbf{e}_{\mathrm{si}} + \sum_{i=1}^{N} \mathbf{s}_i^T \mathbf{e}_{\mathrm{Ji}}$$
$$\le -\sum_{i=1}^{N} \lambda_{\min}(\mathbf{K}_i)\|\mathbf{s}_i\|^2 + \sum_{i=1}^{N} \lambda_{\max}(\mathbf{K}_i)\|\mathbf{s}_i\|\|\mathbf{e}_{\mathrm{si}}\| + \sum_{i=1}^{N} \|\mathbf{s}_i\|\|\mathbf{e}_{\mathrm{Ji}}\|. \tag{29}$$

It is worth noting that triggering condition (15) guarantees $\|\mathbf{e}_{\mathrm{Ji}}\| + \lambda_{\max}(\mathbf{K}_i)\|\mathbf{e}_{\mathrm{si}}\| \le (\gamma_i/2)\lambda_{\min}(\mathbf{K}_i)\|\mathbf{s}_i\| + \mu_i(t)$ holds throughout the evolution of cluster system (5). Thus, we can get

$$\dot{V}_1 \le -\sum_{i=1}^{N} \lambda_{\min}(\mathbf{K}_i)\|\mathbf{s}_i\|^2 + \sum_{i=1}^{N} \frac{\gamma_i}{2}\lambda_{\min}(\mathbf{K}_i)\|\mathbf{s}_i\|^2 + \sum_{i=1}^{N} \sqrt{\lambda_{\min}(\mathbf{K}_i)}\rho_i e^{-\gamma_i t}\|\mathbf{s}_i\|. \tag{30}$$

Because $\forall x, y \in \mathbb{R}$, $|xy| \le (\gamma_i/2)x^2 + (1/2\gamma_i)y^2$ holds. For $0 < \gamma_i < 1$, analysing the right-hand side of (24), the upper bound of $\dot{V}_1$ can be expressed as

$$\dot{V}_1 \le -\sum_{i=1}^{N} (1-\gamma_i)\lambda_{\min}(\mathbf{K}_i)\|\mathbf{s}_i\|^2 + \sum_{i=1}^{N} \frac{\rho_i^2}{2\gamma_i} e^{-2\gamma_i t}. \tag{31}$$

Integrating both sides of (25), for any $t^i > 0$, we can get

$$V_1(t) + \sum_{i=1}^{N} (1-\gamma_i)\lambda_{\min}(\mathbf{K}_i)\int_0^{t^i} \|\mathbf{s}_i(\tau)\|^2 \mathrm{d}\tau \le V_1(0) + \sum_{i=1}^{N} \frac{\rho_i^2}{4\gamma_i\nu_i}. \tag{32}$$

Because $0 < \gamma_i < 1$, $\sum_{i=1}^{N}(1-\gamma_i)\lambda_{\min}(\mathbf{K}_i)\int_0^{t^i}\|\mathbf{s}_i(\tau)\|^2\mathrm{d}\tau > 0$, we obtain that $V_1(t) \le V_1(0) + \sum_{i=1}^{N}(\rho_i^2/4\gamma_i\nu_i)$, and thus V_1 is bounded. According to (23), $\mathbf{s}_i$ and $\widetilde{\Theta}_i(t)$ are bounded for every $i = 1, \ldots, N$. When Assumption 3holds, we can know $\mathbf{L}_F^{-1}$ exists according to Lemma 1. Then, (10) can be rewritten as follows:

$$\dot{\sigma}_F = -\alpha(\mathbf{L}_F \otimes \mathbf{I}_3)\boldsymbol{\sigma}_F - \alpha(\mathbf{L}_{\mathrm{FL}} \otimes \mathbf{I}_3)\boldsymbol{\sigma}_L + \mathbf{s}_F. \tag{33}$$

Let $\overline{\sigma}_F = \sigma_F + (\mathbf{L}_F^{-1}\mathbf{L}_{\mathrm{FL}} \otimes \mathbf{I}_3)\sigma_L$, and equation (33) can be written as

$$\dot{\overline{\sigma}}_F = -\alpha(\mathbf{L}_F \otimes \mathbf{I}_3)\overline{\sigma}_F + (\mathbf{L}_F^{-1}\mathbf{L}_{\mathrm{FL}} \otimes \mathbf{I}_3)\dot{\sigma}_L + \mathbf{s}_F. \tag{34}$$

According to Lemma 2, all eigenvalues of $\mathbf{L}_F$ have positive real parts. According to Assumption 1, $\dot{\sigma}_L$ is bounded and $\lim_{t\longrightarrow\infty}\dot{\sigma}_L \longrightarrow 0$. It thus follows that when $\mathbf{s}_F = 0$, (34) is globally exponentially stable at the origin $\overline{\sigma}_F = 0$. We can conclude from Lemma 3 that cluster system (34) is input-to-state stable with respect to the input $\mathbf{s}_F$ and the state $\overline{\sigma}_F$. According to Lemma 3, because input $\mathbf{s}_F$ is bounded, state $\overline{\sigma}_F$ is bounded. Thus, we can obtain that $\dot{\overline{\sigma}}_F$ is bounded from (34). Equation (9) can be written as $\dot{\sigma}_r = -\alpha(\mathbf{L}_F \otimes \mathbf{I}_3)\overline{\sigma}_F$, and thus $\dot{\sigma}_r$ is bounded. It also follows from (10) that $\dot{\sigma}_F$ is bounded. Differentiating (9), we can get that $\ddot{\sigma}_r$ is bounded.

According to property (b) of the Euler–Lagrange equation, $\mathbf{M}_i(\sigma_i)$, $\mathbf{C}_i(\sigma_i, \dot{\sigma}_i)\dot{\sigma}_r$, $\mathbf{g}_i(\sigma_i)\dot{\sigma}_r$, $\ddot{\sigma}_r$, and ε_i, $i \in F$ are all bounded. Then, according to equation (11), we can obtain that $\mathbf{Y}_i(\sigma_i, \dot{\sigma}_i, \dot{\sigma}_{ri}, \ddot{\sigma}_{ri})$ is bounded. Because $\|\mathbf{C}_i(\sigma_i, \dot{\sigma}_i)\mathbf{s}_i\| < k_C\|\dot{\sigma}_i\|\|\mathbf{s}_i\|$, we can obtain from (17) that $\dot{s}_F$ is bounded.

Because $V_1(t) \ge 0$, and $\mathbf{s}_i, \dot{s}_i \in L_\infty$, then it can be derived from (32) that

$$\sum_{i=1}^{N} (1-\gamma_i)\lambda_{\min}(\mathbf{K}_i)\int_0^t \|\mathbf{s}_i(\tau)\|^2 \mathrm{d}\tau \le V_1(0) + \sum_{i=1}^{N} \frac{\rho_i^2}{4\gamma_i\nu_i}, \tag{35}$$

which implies that $\int_0^t \|\mathbf{s}_i(\tau)\|^2 \mathrm{d}\tau$ is bounded, that is, $\mathbf{s}_i \in L_2$.

$\mathbf{s}_i, \dot{s}_i \in L_\infty$, $\mathbf{s}_i \in L_2$, and thus $\mathbf{s}_i(t)$ is uniformly continuous. According to Barbalat's lemma [51], $\lim_{t\longrightarrow\infty}\mathbf{s}_F \longrightarrow 0$. Because (34) is input-to-state stable with respect to the input $\mathbf{s}_F$ and state $\overline{\sigma}_F(t)$, it can be concluded that $\lim_{t\longrightarrow\infty}\overline{\sigma}_F(t) \longrightarrow 0$. As a result, it follows that $\lim_{t\longrightarrow\infty}\sigma_F(t) \longrightarrow -(\mathbf{L}_F^{-1}\mathbf{L}_{\mathrm{FL}} \otimes \mathbf{I}_3)\sigma_L$, so similarly $\lim_{t\longrightarrow\infty}\dot{\sigma}_F \longrightarrow -(\mathbf{L}_F^{-1}\mathbf{L}_{\mathrm{FL}} \otimes \mathbf{I}_3)\dot{\sigma}_L$; according to Assumption 1, $\lim_{t\longrightarrow\infty}\dot{\sigma}_L \longrightarrow 0$, and thus $\lim_{t\longrightarrow\infty}\dot{\sigma}_F \longrightarrow 0$. According to $\dot{\sigma}_i = \mathbf{G}(\sigma_i)\omega_i$, we can obtain that $\lim_{t\longrightarrow\infty}\omega_F \longrightarrow 0$. The attitude of followers asymptotically converges to the convex hull formed by leaders' orientation.

According to Reference [52], we see that the system trajectories are attracted towards the sliding manifold as long as $\mathrm{sgn}(\mathbf{s}_i(t_k^i)) = \mathrm{sgn}(\mathbf{s}_i(t^i))$. This holds for all triggering instants whenever $\mathrm{sgn}(\mathbf{s}_i(t_k^i)) = \mathrm{sgn}(\mathbf{s}_i(t^i))$. As a result, the trajectories reach the neighbourhood of the sliding manifold due to $\lim_{t\longrightarrow\infty}\mathbf{s}_F \longrightarrow 0$ and enter the region where the sign of $\mathbf{s}_i$ changes before next triggering occurs. So, in the time interval, the decrement of V_1 cannot be guaranteed because zero crossing of $\mathbf{s}_i$ occurs, and hence the trajectory increases. However, the sliding trajectories are ultimately bounded within this region. Therefore, the ultimate band is the region where $\mathrm{sgn}(\mathbf{s}_i(t_k^i)) \ne \mathrm{sgn}(\mathbf{s}_i(t^i))$. The size of this band can be calculated by finding the maximum deviation of sliding trajectory with zero crossing.

This ultimate region can now be derived as follows. We know that for any $t^i \in [t_k^i, t_{k+1}^i)$,

$$\left\|\mathbf{s}_i(t_k^i) - \mathbf{s}_i(t^i)\right\| = \left\|\mathbf{e}_{\mathrm{si}}(t^i)\right\| \le \frac{1}{\lambda_{\max}(\mathbf{K}_i)}\left(\frac{\gamma_i}{2}\lambda_{\min}(\mathbf{K}_i)\|\mathbf{s}_i(t)\| + \mu_i(t) - \|\mathbf{e}_{Ji}(t)\|\right). \tag{36}$$

This gives the maximum deviation of sliding variable from its immediate sampled value. Then, the maximum value of band can be obtained for the case $\mathbf{s}_i(t_k^i) = 0$ and is given in (15).

According to (32), $V_1(t) \le V_1(0) + \sum_{i=1}^{N} (\rho_i^2/4\gamma_i\nu_i)$; then, substituting (23) into it, we can obtain

$$\sum_{i=1}^{N} \mathbf{s}_i^T \mathbf{M}_i \mathbf{s}_i + \sum_{i=1}^{N} \widetilde{\Theta}_i^T \Lambda_i^{-1} \widetilde{\Theta}_i + \sum_{i=1}^{N} \widetilde{k}_i^2 \Gamma_i^{-1} \le \sum_{i=1}^{N} \mathbf{s}_i^T(0) \mathbf{M}_i(0) \mathbf{s}_i(0) + \sum_{i=1}^{N} \widetilde{\Theta}_i^T(0) \mathbf{\Lambda}_i^{-1} \widetilde{\Theta}_i(0) + \sum_{i=1}^{N} \widetilde{k}_i^2(0) \Gamma_i^{-1} + \sum_{i=1}^{N} \frac{\rho_i^2}{2\gamma_i\nu_i}. \tag{37}$$

Because $\sum_{i=1}^{N} \widetilde{\Theta}_i^T \Lambda_i^{-1} \widetilde{\Theta}_i + \sum_{i=1}^{N} \widetilde{k}_i^2 \Gamma_i^{-1} \ge 0$, we can obtain that

$$\left\| \sum_{i=1}^{N} \mathbf{s}_i^T \mathbf{M}_i \mathbf{s}_i \right\| \le \left\| \sum_{i=1}^{N} \mathbf{s}_i^T(0) \mathbf{M}_i(0) \mathbf{s}_i(0) + \sum_{i=1}^{N} \widetilde{\Theta}_i^T(0) \mathbf{\Lambda}_i^{-1} \widetilde{\Theta}_i(0) + \sum_{i=1}^{N} \widetilde{k}_i^2(0) \Gamma_i^{-1} + \sum_{i=1}^{N} \frac{\rho_i^2}{2\gamma_i\nu_i} \right\|. \tag{38}$$

Further,

$$\left\| \sum_{i=1}^{N} \mathbf{s}_i^T \mathbf{s}_i \right\| \le \left(\lambda_{\min}(\mathbf{M}_i) \right)^{-1} \left\| \sum_{i=1}^{N} \mathbf{s}_i^T(0) \mathbf{M}_i(0) \mathbf{s}_i(0) + \sum_{i=1}^{N} \widetilde{\Theta}_i^T(0) \mathbf{\Lambda}_i^{-1} \widetilde{\Theta}_i(0) + \sum_{i=1}^{N} \widetilde{k}_i^2(0) \Gamma_i^{-1} + \sum_{i=1}^{N} \frac{\rho_i^2}{2\gamma_i\nu_i} \right\|. \tag{39}$$

That is,

$$\begin{aligned} \|\mathbf{s}_F\| &\le \sqrt{\left(\lambda_{\min}(\mathbf{M}_i) \right)^{-1} \left\| \sum_{i=1}^{N} \mathbf{s}_i^T(0) \mathbf{M}_i(0) \mathbf{s}_i(0) + \sum_{i=1}^{N} \widetilde{\Theta}_i^T(0) \mathbf{\Lambda}_i^{-1} \widetilde{\Theta}_i(0) + \sum_{i=1}^{N} \widetilde{k}_i^2(0) \Gamma_i^{-1} + \sum_{i=1}^{N} \frac{\rho_i^2}{2\gamma_i\nu_i} \right\|} \\ &= s_M. \end{aligned} \tag{40}$$

Second, consider the following Lyapunov function candidate:

$$V_2 = \overline{\sigma}_F^T (\mathbf{D} \otimes \mathbf{I}_3) \overline{\sigma}_F. \tag{41}$$

Taking the derivative of V_2 along (34) gives

$$\begin{aligned} \dot{V}_2 &= \dot{\overline{\sigma}}_F^T (\mathbf{D} \otimes \mathbf{I}_3) \overline{\sigma}_F + \overline{\sigma}_F^T (\mathbf{D} \otimes \mathbf{I}_3) \dot{\overline{\sigma}}_F \\ &= 2\left(\left(\mathbf{L}_F^{-1} \mathbf{L}_{\mathrm{FL}} \otimes \mathbf{I}_3 \right) \dot{\sigma}_L + \mathbf{s}_F \right) (\mathbf{D} \otimes \mathbf{I}_3) \overline{\sigma}_F - \alpha \overline{\sigma}_F^T \left(\mathbf{D}\mathbf{L}_F + \mathbf{L}_F^T \mathbf{D} \right) \overline{\sigma}_F \\ &\le \frac{2 \max(d_i) \left\| \left(\mathbf{L}_F^{-1} \mathbf{L}_{\mathrm{FL}} \otimes \mathbf{I}_3 \right) \dot{\sigma}_L + \mathbf{s}_F \right\|}{\sqrt{\min(d_i)}} \sqrt{V_2} - \frac{\alpha \lambda_{\min}(Q)}{\max(d_i)} V_2. \end{aligned} \tag{42}$$

There exists a diagonal matrix $D = \mathrm{diag}(d_1, \ldots, d_N)$ with $d_i > 0$, $\forall i = 1, \cdots, N$, such that $\mathbf{Q} = \mathbf{D}\mathbf{L}_F + \mathbf{L}_F^T \mathbf{D}$ is symmetric positive definite. Because $\forall x, y \in \mathbb{R}$, $|2xy| \le \gamma_i x^2 + (1/\gamma_i) y^2$ holds. Then, (42) can be written as

$$\begin{aligned} \dot{V}_2 &\le 2 \sqrt{\frac{\alpha \lambda_{\min}(Q)}{2 \max(d_i)} V_2} \cdot \sqrt{\frac{2 \max(d_i)}{\alpha \lambda_{\min}(Q)}} \cdot \frac{\max(d_i) \left\| \left(\mathbf{L}_F^{-1} \mathbf{L}_{FL} \otimes \mathbf{I}_3 \right) \dot{\sigma}_L + \mathbf{s}_F \right\|}{\sqrt{\min(d_i)}} - \frac{\alpha \lambda_{\min}(Q)}{\max(d_i)} V_2 \\ &\le \frac{2 \max(d_i)^3 \left\| \left(\mathbf{L}_F^{-1} \mathbf{L}_{FL} \otimes \mathbf{I}_3 \right) \dot{\sigma}_L + \mathbf{s}_F \right\|^2}{\alpha \lambda_{\min}(Q) \min(d_i)} - \frac{\alpha \lambda_{\min}(Q)}{2 \max(d_i)} V_2. \end{aligned} \tag{43}$$

Furthermore,

$$\dot{V}_2 + \frac{\alpha\lambda_{\min}(Q)}{2\max(d_i)}V_2 \le \frac{\max(d_i)^3\left\|\left(\mathbf{L}_F^{-1}\mathbf{L}_{\mathrm{FL}}\otimes\mathbf{I}_3\right)\dot{\sigma}_L + \mathbf{s}_F\right\|^2}{\alpha\lambda_{\min}(Q)\min(d_i)}. \tag{44}$$

It can be obtained that

$$V_2(t) \le V_2(0)e^{-(\alpha\lambda_{\min}(Q)/2\max(d_i))t} + \frac{4\left(\max(d_i)\right)^4\left\|\left(\mathbf{L}_F^{-1}\mathbf{L}_{FL}\otimes\mathbf{I}_3\right)\dot{\sigma}_L + \mathbf{s}_F\right\|^2\left(1 - e^{-(\alpha\lambda_{\min}(Q)/2\max(d_i))t}\right)}{\alpha^2\left(\lambda_{\min}(Q)\right)^2\min(d_i)}. \tag{45}$$

Let $c_M = 2(\max(d_i))^2/(\alpha\lambda_{\min}(Q)\min(d_i))$. Because $\lim_{t\longrightarrow\infty}e^{-(\alpha\lambda_{\min}(Q)/2\max(d_i))t} \longrightarrow 0$, then according to (41), we can get

$$\begin{aligned}\limsup_{t\longrightarrow\infty}\left\|\overline{\sigma}_F\right\| &\le c_M\limsup_{t\longrightarrow\infty}\left\|\left(\mathbf{L}_F^{-1}\mathbf{L}_{FL}\otimes\mathbf{I}_3\right)\dot{\sigma}_L + \mathbf{s}_F\right\| \\ &\le c_M\limsup_{t\longrightarrow\infty}\left\|\mathbf{s}_F\right\| + c_M\limsup_{t\longrightarrow\infty}\left\|-\left(\mathbf{L}_F^{-1}\mathbf{L}_{FL}\otimes\mathbf{I}_3\right)\dot{\sigma}_L\right\|.\end{aligned} \tag{46}$$

According to the aforementioned analysis, $\lim_{t\longrightarrow\infty}\|\mathbf{s}_F\| \longrightarrow 0$. According to Assumption 1, $\dot{\sigma}_L$ is bounded, and thus $\limsup_{t\longrightarrow\infty}\|-(\mathbf{L}_F^{-1}\mathbf{L}_{FL}\otimes\mathbf{I}_3)\dot{\sigma}_L\|$ is bounded. Moreover, we assume that $\lim_{t\longrightarrow\infty}\|\dot{\sigma}_L\| \longrightarrow 0$, and thus we can obtain that $\lim_{t\longrightarrow\infty}\|\overline{\sigma}_F\| \longrightarrow 0$.

Substituting (41) into equation (45), we can get

$$\begin{aligned}\left\|\overline{\sigma}_F(t)\right\| &\le \sqrt{\frac{V_2(0)}{\min(d_i)} + c_M^2\left\|\left(\mathbf{L}_F^{-1}\mathbf{L}_{FL}\otimes\mathbf{I}_3\right)\dot{\sigma}_L + \mathbf{s}_F\right\|^2} \\ &\le \sqrt{\frac{\max(d_i)\overline{\sigma}_F^2(0)}{\min(d_i)} + c_M^2\left\|\lambda_{\max}\left(\mathbf{L}_F^{-1}\mathbf{L}_{\mathrm{FL}}\right)\dot{\sigma}_{\mathrm{LM}} + s_M\right\|^2} \\ &= \overline{\sigma}_{\mathrm{FM}}.\end{aligned} \tag{47}$$

From definitions of σ_F and $\dot{\sigma}_F$, we can also obtain

$$\begin{aligned}\left\|\boldsymbol{\sigma}_F\right\| &\le \left\|\overline{\sigma}_F\right\| + \left\|\left(\mathbf{L}_F^{-1}\mathbf{L}_{\mathrm{FL}}\otimes\mathbf{I}_3\right)\boldsymbol{\sigma}_L\right\| \\ &\le \overline{\sigma}_{\mathrm{FM}} + \lambda_{\max}\left(\mathbf{L}_F^{-1}\mathbf{L}_{\mathrm{FL}}\right)\sigma_{\mathrm{LM}} \\ &= \sigma_{\mathrm{FM}}, \\ \left\|\dot{\sigma}_F\right\| &\le \left\|\alpha\left(\mathbf{L}_F\otimes\mathbf{I}_3\right)\boldsymbol{\sigma}_F\right\| + \left\|\alpha\left(\mathbf{L}_{\mathrm{FL}}\otimes\mathbf{I}_3\right)\boldsymbol{\sigma}_L\right\| + \left\|\mathbf{s}_F\right\| \\ &\le \alpha\lambda_{\max}\left(\mathbf{L}_F\right)\sigma_{\mathrm{FM}} + \alpha\lambda_{\max}\left(\mathbf{L}_{\mathrm{FL}}\right)\sigma_{\mathrm{LM}} + s_M \\ &= \dot{\sigma}_{\mathrm{FM}}.\end{aligned} \tag{48}$$

Therefore, for any bounded initial states and $t \ge 0$, the states of (5) using equations (15) and (19)–(21) will always lie in the compact set $\{(\sigma_i(t), \dot{\sigma}_i(t)) | \|\sigma_F(t)\| \le \sigma_{\mathrm{FM}}, \|\dot{\sigma}_F(t)\| \le \dot{\sigma}_{\mathrm{FM}}\}$.

(2) Proof. Necessity: Necessity is proven by contradiction. If Assumption 3 does not hold, then there must exist parts of followers which cannot receive information from any leader directly or indirectly (through other followers). According to Reference [53], the followers can be divided into two subsets, namely, one set with the followers that can receive the information from the leaders directly or indirectly, denoted by F_1, and the follower set, which cannot receive information from leaders denoted by F_2. The system Laplacian matrix $\mathbf{L}$ can also be in the following form:

$$\mathbf{L} = \begin{bmatrix}\mathbf{L}_{F_1F_1} & \mathbf{L}_{F_1F_2} & \mathbf{L}_{F_1L} \\ 0 & \mathbf{L}_{F_2F_2} & 0 \\ 0 & 0 & 0\end{bmatrix}. \tag{49}$$

Let the attitude of F_1 and F_2 be σ_{F_1} and σ_{F_2}. Auxiliary variables $\mathbf{s}_{F_1}$,$\mathbf{s}_{F_2}$ are given with respect to σ_{F_1} and σ_{F_2}. Then, we can obtain

$$\begin{aligned}\dot{\sigma}_{F_1} &= -\alpha\left(\mathbf{L}_{F_1F_1}\otimes\mathbf{I}_3\right)\boldsymbol{\sigma}_{F_1} - \alpha\left(\mathbf{L}_{F_1F_2}\otimes\mathbf{I}_3\right)\boldsymbol{\sigma}_{F_2} \\ &\quad - \alpha\left(\mathbf{L}_{F_1L}\otimes\mathbf{I}_3\right)\boldsymbol{\sigma}_L + \mathbf{s}_{F_1}, \\ \dot{\sigma}_{F_2} &= -\alpha\left(\mathbf{L}_{F_2F_2}\otimes\mathbf{I}_3\right)\boldsymbol{\sigma}_{F_2} + \mathbf{s}_{F_2}.\end{aligned} \tag{50}$$

Because $\mathbf{s}_{F_1}$ and $\mathbf{s}_{F_2}$ are proved to converge to zero, the final states of σ_{F_1} and σ_{F_2} will depend on the equilibrium points. We can get from equation (50) that the trajectories of the followers in F_2 are independent of the leaders, and thus these followers cannot always converge to the convex hull formed by the leaders from any initial state. For the followers in F_1, Assumption 3 holds. From the analysis of the sufficiency in this proof, the motion of followers in F_1 may also be affected by its neighbours including leaders and followers in F_2, and thus there might exist some followers in F_1 that cannot converge to the convex hull formed by the leaders.

The proof is completed.

Remark 2. In order to avoid the chattering problem caused by the sign function, controller (19) can be substituted by saturation function

$$\mathrm{sat}(x,\delta) = \begin{cases}1, & x > \delta, \\ \dfrac{x}{\delta}, & |x| \le \delta, \\ -1, & x < -\delta,\end{cases} \tag{51}$$

where δ is a small positive constant.

Remark 3. The attitude containment control problem with multiple leaders has been studied in the context. Obviously, if there exists one leader in control protocol (19), the multiple leader-follower coordinated attitude containment control problem becomes the coordinated attitude tracking problem with single leader.

3.3. The Absence of Zeno Behaviour. Zeno behaviour means the minimum time interval between two consecutive events is 0 and the event triggers infinite times in a finite time, which is forbidden in control tasks. Let T denote interevent time interval of event-triggered attitude control protocol (19)–(21) and triggering condition (15). T needs to be strictly positive to exclude the Zeno behaviour.

$\lim_{t^i \longrightarrow \infty} \mathbf{s}_i \longrightarrow 0$ is satisfied in the context. But at t^i_{k+1}, there may exist the case of $\mathbf{s}_i(t^i) = 0, \dot{s}_i(t^i) \neq 0$. The attitude containment control is not reached at this moment. Therefore, the event is triggered in the following two cases:

(1) If $\|\mathbf{s}_i(t^i_{k+1})\| \neq 0$, the interevent time interval of this case is denoted as T_1 and triggering condition is $\|\mathbf{e}_{\mathrm{Ji}}(t^i_{k+1})\| + \lambda_{\max}(\mathbf{K}_i)\|\mathbf{e}_{\mathrm{si}}(t^i_{k+1})\| \geq (\gamma_i/2)\,\lambda_{\min}(\mathbf{K}_i)\|\mathbf{s}_i(t^i_{k+1})\| + \mu_i(t^i_{k+1})$.

(2) If $\|\mathbf{s}_i(t^i_{k+1})\| = 0$, the interevent time interval of this case is denoted as T_2 and triggering condition is $\|\mathbf{e}_{Ji}(t^i_{k+1})\| + \lambda_{\max}(\mathbf{K}_i)\|\mathbf{e}_{si}(t^i_{k+1})\| \geq \mu_i(t^i_{k+1})$.

Comparing the aforementioned two cases, we can know that for any $\|\mathbf{s}_i(t^i_{k+1})\| \neq 0$, there exists $\|\mathbf{s}_i(t^i_{k+1})\| > 0$, so it can be concluded that case (1) takes longer time, which implies $T_2 < T_1$. We just need to prove that there exists strictly positive T_2 to exclude the Zeno behaviour.

Theorem 2. *If conditions of Theorem 1 hold, then the interevent time interval T of triggering condition (15) has positive lower bound.*

Proof. According to Reference [35], for any $k \geq 0$ and $t^i \in [t^i_k, t^i_{k+1})$, $i = 1, \ldots, N$, the derivative of $\|\mathbf{e}_{\mathrm{si}}(t^i)\|$ with respect to time satisfies

$$\frac{\mathrm{d}}{\mathrm{d}t}\left\|\mathbf{e}_{\mathrm{si}}\left(t^i\right)\right\| \leq \left\|\dot{s}_i\left(t^i\right)\right\|, \tag{52}$$

where $\dot{s}_i(t^i)$ has been proved to be bounded. Let positive constant B_s denote the maximum of $\|\dot{s}_i(t^i)\|$, and we obtain $(\mathrm{d}/\mathrm{d}t)\|\mathbf{e}_{\mathrm{si}}(t^i)\| \leq B_s$.

Similar to equation (42), the derivative of $\|\mathbf{e}_{Ji}(t^i)\|$ satisfies

$$\frac{\mathrm{d}}{\mathrm{d}t}\left\|\mathbf{e}_{\mathrm{Ji}}\left(t^i\right)\right\| \leq \left\|\frac{\mathrm{d}}{\mathrm{d}t}\left(\mathbf{Y}_i\left(t^i\right)\widehat{\Theta}_i\left(t^i\right)\right)\right\| = \left\|\dot{Y}_i\left(t^i\right)\widehat{\Theta}_i\left(t^i\right) + \mathbf{Y}_i\left(t^i\right)\dot{\widehat{\Theta}}_i\left(t^i\right)\right\|. \tag{53}$$

It can be seen from the Section 3.1 that $\mathbf{Y}_i(t^i)$ and $\widehat{\Theta}_i(t^i)$ are both bounded; according to Assumption 1 in Reference [35], we know that $\dot{Y}_i$ is bounded. Then, because $\mathbf{Y}_i(t^i)$ and $\mathbf{s}_i(t^i)$ are bounded, $\dot{\widehat{\Theta}}_i(t^i)$ is bounded according to adaption update law. Let positive constant B_J denote the upper bound of $\|(\mathrm{d}/\mathrm{d}t)(\mathbf{Y}_i(t^i)\widehat{\Theta}_i(t^i))\|$, and $(\mathrm{d}/\mathrm{d}t)\|\mathbf{e}_{\mathrm{Ji}}(t^i)\| \leq B_J$ can be obtained.

Let $B = \max\{B_J, \lambda_{\max}(\mathbf{K}_i)B_s\}$; it follows that

$$\left\|\mathbf{e}_{\mathrm{Ji}}\left(t^i\right)\right\| + \lambda_{\max}(\mathbf{K}_i)\left\|\mathbf{e}_{\mathrm{si}}\left(t^i\right)\right\| \leq 2\int_{t^i_k}^{t^i} B\mathrm{d}t = 2B\left(t^i - t^i_k\right), \quad t^i \in \left[t^i_k, t^i_{k+1}\right). \tag{54}$$

According to case (2), the lower bound of interevent time interval T_2 can be derived:

$$2BT_2 \geq \rho_i\sqrt{\lambda_{\min}(\mathbf{K}_i)}\exp(-\gamma_i T_2), \tag{55}$$

where $B > 0$. T_2 can get positive solution from equation (55). Thus, there exists time interval between two consecutive events, and the system avoids continuous control. It means that the interevent time interval of triggering condition (15) has positive lower bound.

4. The Influence of Information Topology Design on Followers' Orientation

Compared with single leader/leaderless case, containment control has lower accuracy requirement for the final state of cluster members. However, in practical space missions, the orientation of satellites in the target area needs to meet certain constraints, such as multiple satellites observing the same orientation simultaneously, the observation field covering the entire target area, and so on.

It indicates in [46] that the steady state of each follower is a convex combination of all leaders' states it can access, and the combination coefficient is a quantity related to the system Laplacian matrix. It can be concluded that the orientation of followers in the target area is determined by system information topology (including the weights that are assigned to edges).

In this section, approaches from graph theory to investigate influence of information topology on the distributions of followers are presented to provide a reference for orientation design of the microsatellite cluster.

4.1. The Constraints of Leader Reachable Set on Followers' Orientation. Denote $\mathbf{C} = -\mathbf{L}_F^{-1}\mathbf{L}_{\mathrm{FL}}$ as the coefficient matrix of steady state of followers with respect to the state of leaders, where $0 \leq c_{\mathrm{ij}} \leq 1$, $\sum_{j=1}^{M} c_{ij} = 1$. It reflects the relationship between system information topology and steady state of followers. According to the definition of reachable set [46], (1) if follower i is reachable from multiple leaders including $N + j$, $0 < c_{\mathrm{ij}} < 1$, the motion of i is affected by multiple leaders, and its stable state is correspondingly determined by the states of these leaders. (2) If follower i is only reachable from leader $N + j$, $c_{ij} = 1$, there exists a directed path from $N + j$ to i, that is, the motion of follower i will be only affected directly or indirectly by leader $N + j$. (3) If follower i is not reachable from leader $N + j$, $c_{ij} = 0$, the motion of i will not be affected by leader $N + j$, and thus the steady state of follower i is not related to $N + j$.

$R_j\,(j = 1, 2, \ldots, m)$ is denoted as the reachable set of leader $N + j$. $H_j = (R_j/\cup_{j\neq i}R_i)$ is a set of all followers which is only reachable from leader $N + j$. $Y_j = (F/R_j)$ represents the unreachable set from leader $N + j$. $P_j = (R_j/H_j)$

represents other follower set in R_j without H_j, and $\widetilde{H}_j = (H_j/\{N+j\})$ represents the subset without $N+j$ in H_j.

Then, $\mathbf{L}_F$ and $\mathbf{L}_{\mathrm{FL}}$ can be written in the following block matrix forms:

$$\mathbf{L}_F = \begin{bmatrix} \mathbf{L}_{\widetilde{H}_j} & 0 & 0 \\ \mathbf{L}_{P_j\widetilde{H}_j} & \mathbf{L}_{P_j} & \mathbf{L}_{P_jY_j} \\ 0 & 0 & \mathbf{L}_{Y_j} \end{bmatrix}, \qquad \mathbf{L}_{FL} = [\delta_1, \ldots, \delta_N], \tag{56}$$

where $\delta_j = \begin{bmatrix} \mathbf{L}^T_{\widetilde{H}_j,N+j} & \mathbf{L}^T_{P_j,N+j} & 0 \end{bmatrix}^T$.

Theorem 3. *Assume all leaders have converged to the steady states $\sigma^e_{N+1}, \sigma^e_{N+2}, \ldots, \sigma^e_{N+M}$. Then, under the action of triggering condition (15), adaptive sliding mode attitude containment control algorithm (19), and adaption laws (20) and (21), all followers of cluster system (5) will asymptotically converge to the steady state $\sigma^e_i = \sum_{j=1}^{M} c_{ij}\sigma^e_{N+j}, i \in F, j \in L$.*

Proof. Since

$$\mathbf{L}_{\widetilde{H}_j} 1_{\widetilde{H}_j} + \mathbf{L}_{\widetilde{H},N+j} = 0, \tag{57}$$

we have

$$\mathbf{L}^{-1}_{\widetilde{H}_j}\mathbf{L}_{\widetilde{H},N+j} = -1_{\widetilde{H}_j}, \tag{58}$$

and we can obtain that

$$\begin{aligned} -\mathbf{L}_F^{-1}\boldsymbol{\delta}_j &= -\begin{bmatrix} \mathbf{L}^{-1}_{\widetilde{H}_j}\mathbf{L}_{\widetilde{H}_{j,N+j}} \\ -\mathbf{L}^{-1}_{P_j}\mathbf{L}_{P_j\widetilde{H}_{j,N+j}} + \mathbf{L}^{-1}_{P_j}\mathbf{L}_{P_{j,N+j}} \\ 0 \end{bmatrix} \\ &= \begin{bmatrix} 1_{\widetilde{H}_j} \\ \mathbf{L}^{-1}_{P_j}\left(\mathbf{L}_{P_j\widetilde{H}_j}1_{\widetilde{H}_j} + \mathbf{L}_{P_{j,N+j}}\right) \\ 0 \end{bmatrix}. \end{aligned} \tag{59}$$

Further, each entry of $\mathbf{L}^{-1}_{P_j}(\mathbf{L}_{P_j\widetilde{H}_j}1_{\widetilde{H}_j} + \mathbf{L}_{P_{j,N+j}})$ is positive. Otherwise, $\mathbf{L}_{P_j\widetilde{H}_j}1_{\widetilde{H}_j} + \mathbf{L}_{P_{j,N+j}} = 0$, which means $\mathbf{P}_j$ does not have neighbours in $\mathbf{H}_j$, which contradicts the definition of $\mathbf{P}_j$.

Now Theorem 3 has been proved.

4.2. The Constraints of Graph Differentiation on Followers' Orientation. In microsatellite cluster flying missions, each member obtains the information from its neighbours through communication or relative state measurement. Due to the performance difference of sensors and communication equipment, as well as relative distance between members, neighbour satellite sets of each satellite are different. However, there may exist some commonalities among cluster members in information interaction, according to which cluster members can be divided into several subsets, and dynamic behaviour of cluster members belonging to the same subset may also have commonalities.

Although steady orientation of followers can be roughly estimated based on leader reachable sets, in some observation missions, there exist more constraints on followers' orientation. The steady state of followers can be described using π^1 partition and π^2 partition of cluster information topology. These two graph theory tools can divide the cluster member into several subsets, and the number of neighbours in other subsets of cluster members belonging to the same subset has a certain commonality, which provides theoretical basis for information topology design of the microsatellite cluster.

At first, we prove that the satellites in the same cell partition belonging to $\pi^1_{\{H_1,\ldots,H_m\}}$ partition have same steady state.

Theorem 4. *For event-triggered adaptive sliding mode attitude containment control protocol (19), triggering condition (15), and adaption laws (20) and (21) of the microsatellite cluster system which satisfies $\sigma^e_F = -\mathbf{L}_F^{-1}\mathbf{L}_{FL}\sigma_L$, if system information topology G has a cell partition $\pi^1_{\{H_1,\ldots,H_m\}} = \{C_1, \cdots, C_k\}$, then all the followers that belong to the same cell $C_i (i = 1, \cdots k)$ have the same steady state.*

Proof. According to Reference [46], suppose $\pi^1_{\{H_1,\ldots,H_m\}} = \{C_1, \ldots, C_k\}$ is a cell partition of $V(G)$ with $C_1 = H_1, \ldots, C_m = H_m$; then, according to the cell partition of $V(G)$, by ordering the vertices appropriately, the graph Laplacian can be written in the following form:

$$L = \begin{bmatrix} L_{C_1C_1} & \cdots & 0 & 0 & \cdots & 0 \\ \vdots & \ddots & \vdots & \vdots & \ddots & \vdots \\ 0 & \cdots & L_{C_mC_m} & 0 & \cdots & 0 \\ L_{C_{m+1}C_1} & \cdots & L_{C_{m+1}C_m} & L_{C_{m+1}C_{m+1}} & \cdots & L_{C_{m+1}C_k} \\ \vdots & \ddots & \vdots & \vdots & \ddots & \vdots \\ L_{C_kC_1} & \cdots & L_{C_kC_m} & L_{C_kC_{m+1}} & \cdots & L_{C_kC_k} \end{bmatrix}. \tag{60}$$

The block matrix at the lower left corner and the lower right corner is denoted by $\mathbf{A}$, $\mathbf{B}$, respectively. Since $\mathbf{L}\sigma^e_F = 0$, $\mathbf{A}\sigma^e_H + \mathbf{B}\sigma^e_{\overline{F}} = 0$ is obtained. Then, by Lemma 2 in [46], $\sigma^e_{\overline{F}} = -\mathbf{B}^{-1}\mathbf{A}\sigma^e_H$. Assuming that each vertex in C_i has s_{ij} number of neighbours in $C_j (i, j = 1, \ldots, k, i \neq k)$, then, according to the definition of π^1 partition, each row sum of the submatrix $L_{C_iC_j} (i, j = 1, \ldots, k, i \neq j)$ equals s_{ij}. Combining with Corollary 1 in [46], it is given that

$$\mathbf{A}\boldsymbol{\sigma}^e_H = \begin{bmatrix} -s_{m+1,1}1_{rm+1} \\ \vdots \\ -s_{k,1}1_{rk} \end{bmatrix}\boldsymbol{\sigma}^e_{N+1} + \cdots + \begin{bmatrix} -s_{m+1,m}1_{rm+1} \\ \vdots \\ -s_{k,m}1_{rk} \end{bmatrix}\boldsymbol{\sigma}^e_{N+M}, \tag{61}$$

where r_i is the cardinality of $C_i (i = m+1, \ldots, k)$.

It follows that

$$\boldsymbol{\sigma}_{\overline{F}}^{e} = \mathbf{B}^{-1}\begin{bmatrix} s_{m+1,1}1_{rm+1} \\ \vdots \\ s_{k,1}1_{rk} \end{bmatrix}\boldsymbol{\sigma}_{N+1}^{e} + \cdots + \mathbf{B}^{-1}\begin{bmatrix} s_{m+1,m}1_{rm+1} \\ \vdots \\ s_{k,m}1_{rk} \end{bmatrix}\boldsymbol{\sigma}_{N+M}^{e}. \tag{62}$$

By using Lemma 3 in [46], it can be concluded that all the followers that belong to the same cell $C_i (i = 1, \ldots, k)$ have the same steady state.

Now Theorem 4 has been proved.

Then, another cell partition, $\pi^2_{\{H_1,\ldots,H_m\}}$ partition, is provided to prove that satellites in the same cell partition belonging to $\pi^2_{\{H_1,\ldots,H_m\}}$ partition have the same steady state.

Theorem 5. *For event-triggered adaptive sliding mode containment control protocol (19)–(21) of microsatellite cluster which satisfies $\sigma_F^e = -\mathbf{L}_F^{-1}\mathbf{L}_{FL}\sigma_L$, if the system information topology G has a cell partition $\pi^2 = \{C_1, \ldots, C_k\}$ with $C_i \subseteq H_j$ or $C_i \subseteq F$, $i = 1, \ldots, k$, $j = 1, \ldots, m$, then all the followers that belong to the same cell C_i $(i = 1, \ldots, k)$ have the same steady state.*

Proof. According to Reference [46], construct the deduced unweighted graph $\overline{G}^2$ of G as follows: use a follower $\overline{i}$ to represent cell C_i and draw an edge from $\overline{j}$ to $\overline{i}$ is a neighbour cell of C_i. Then, $\overline{G}^2$ has m reaches according to Assumption 3. Let $\overline{L}^2$ be the Laplacian matrix of the deduced graph $\overline{G}^2$; it can be derived that $\overline{L}^2\overline{\sigma}_F = 0$ with $\overline{\sigma}_i = \sigma^e_{N+j}$ if $C_i \subseteq H_j$ has unique solution. Finally, it can be verified that $\sigma^e_{FC_i} = \overline{\sigma}_i 1_{C_i}$ is the solution of $\overline{L}\overline{\sigma}^e_F = 0$.

Now Theorem 5 has been proved.

5. Simulation Results

5.1. Simulation Results and Analysis of Attitude Containment Control. In this section, simulations for multiple leader-follower satellite cluster are presented to illustrate the effectiveness of the proposed control protocol and information topology design. Suppose that in microsatellite cluster observation mission, six satellites, denoted by $F = \{1, 2, \ldots, 6\}$, are needed to obtain observation information from three different directions. Suppose the target area is defined by three attitude orientations, and the leaders $L = \{7, 8, 9\}$ are stationary relative to the reference frame. The attitude of leaders, respectively, is

$$\begin{aligned} \boldsymbol{\sigma}_7 &= \begin{bmatrix} 0.09 & 0.06 & -0.08 \end{bmatrix}^T \text{rad}, \\ \boldsymbol{\sigma}_8 &= \begin{bmatrix} 0.06 & -0.1 & 0.05 \end{bmatrix}^T \text{rad}, \\ \boldsymbol{\sigma}_9 &= \begin{bmatrix} -0.08 & 0.1 & 0.09 \end{bmatrix}^T \text{rad}. \end{aligned} \tag{63}$$

The nominal inertia of six followers, respectively, is

$$\begin{aligned} \mathbf{J}_1 &= \begin{bmatrix} 20 & 0 & 2 \\ 0 & 25 & 0 \\ 2 & 0 & 29 \end{bmatrix}\text{kgm}^2, \\ \mathbf{J}_2 &= \begin{bmatrix} 22 & 1 & 0.5 \\ 1 & 24 & 3 \\ 0.5 & 3 & 22 \end{bmatrix}\text{kgm}^2, \\ \mathbf{J}_3 &= \begin{bmatrix} 25 & 0.8 & 2 \\ 0.8 & 29 & 1 \\ 2 & 1 & 21 \end{bmatrix}\text{kgm}^2, \\ \mathbf{J}_4 &= \begin{bmatrix} 23 & 0.4 & 0 \\ 0.4 & 26 & 0.8 \\ 0 & 0.8 & 28 \end{bmatrix}\text{kgm}^2, \\ \mathbf{J}_5 &= \begin{bmatrix} 22 & 0.2 & 0 \\ 0.2 & 26 & 0.6 \\ 0 & 0.6 & 24 \end{bmatrix}\text{kgm}^2, \\ \mathbf{J}_6 &= \begin{bmatrix} 23 & 0.4 & 0 \\ 0.4 & 24 & 0.8 \\ 0 & 0.8 & 28 \end{bmatrix}\text{kgm}^2. \end{aligned} \tag{64}$$

The initial estimation parameter is $\widehat{\Theta}_i(0) = [22, 26, 25, 0, 0, 0]^T$.

The initial state of followers is, respectively, shown in Table 1.

System information topology is shown in Figure 2.

Control gain coefficients and adaptive parameters are

$$\begin{aligned} \alpha_i &= 0.02, \\ \mathbf{K}_i &= \begin{bmatrix} 1 & 1 & 1 \end{bmatrix}^T, \\ \boldsymbol{\Lambda}_i &= \text{diag}\left(\begin{bmatrix} 2 & 2 & 2 \end{bmatrix}\right), \\ \Gamma_i &= 0.001. \end{aligned} \tag{65}$$

Triggering parameters are $\gamma_i = 0.6, \rho_i = 2, \nu_i = 0.5$.

A microsatellite cluster in LEO is mainly affected by the gravity gradient torque, while the disturbances such as the solar radiation pressure torque will be dominant for a cluster in high-Earth orbits such as the geostationary orbit. All these torques are slowly varying and can be treated as signals composed of constants and periodic trigonometric functions. Taking into account these factors, the disturbances are chosen as

$$\mathbf{d}_i = \mathbf{d}_{\text{li}} + \mathbf{d}_{\text{uni}}, \tag{66}$$

where

Table 1: The initial attitude information of followers.

Followers	Attitude σ_i(rad)	Angular velocity ω_i(rad/s)
1	$[0.1\ \ 0.4\ \ -0.3]^T$	$[0.01\ \ 0\ \ 0]^T$
2	$[0.3\ \ 0.2\ \ 0.3]^T$	$[0\ \ 0.01\ \ 0]^T$
3	$[-0.2\ \ 0.1\ \ -0.1]^T$	$[0\ \ 0\ \ 0.01]^T$
4	$[-0.4\ \ 0.2\ \ -0.1]^T$	$[0\ \ 0\ \ -0.01]^T$
5	$[0.3\ \ -0.5\ \ 0.1]^T$	$[0\ \ -0.015\ \ 0]^T$
6	$[0.2\ \ 0.2\ \ -0.3]^T$	$[0\ \ 0\ \ 0.015]^T$

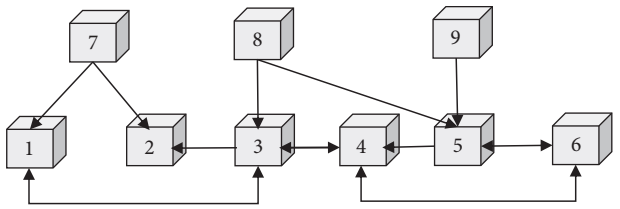

Figure 2: Topology structure of satellite cluster.

$$\begin{aligned}
\mathbf{d}_{l1} &= [\,0.0012\ \ -0.0018\ \ 0.0012\,]^T\text{N.m},\\
\mathbf{d}_{l2} &= [\,0.001\ \ 0.0014\ \ -0.0017\,]^T\text{N.m},\\
\mathbf{d}_{l3} &= [\,-0.0013\ \ 0.0016\ \ -0.001\,]^T\text{N.m},\\
\mathbf{d}_{l4} &= [\,0.0015\ \ -0.0014\ \ -0.0013\,]^T\text{N.m},\\
\mathbf{d}_{l5} &= [\,-0.001\ \ -0.001\ \ 0.0015\,]^T\text{N.m},\\
\mathbf{d}_{l6} &= [\,-0.0012\ \ 0.0013\ \ 0.0014\,]^T\text{N.m}
\end{aligned} \tag{67}$$

denote the constant disturbing torques and

$$\mathbf{d}_{\text{uni}} = \frac{1}{5}\begin{pmatrix} d_{li(1)}\sin\left(\dfrac{t}{12}\right) \\ d_{li(2)}\cos\left(\dfrac{t}{15}\right) \\ d_{\text{li}(3)}\sin\left(\dfrac{t}{10}\right)\cos\left(\dfrac{t}{15}\right) \end{pmatrix} \tag{68}$$

is used to simulate the residual disturbances including aerodynamic torques, solar radiation torques, and similar effects.

5.1.1. Event-Triggered Attitude Containment Control. Simulation results of satellite cluster are shown in Figure 3. Figures 3(a) and 3(b) are the curves of relative attitude and relative angular velocity over time, respectively. It can be seen that the relative attitude converges to the convex hull formed by the leaders at about 600 s, and relative angular velocity converges to 0 within 700 s. The followers can converge to the convex hull even though there exists large disturbance torque. The interevent time of each follower is shown in Figures 3(c) and 3(d). At the initial stage, the state of cluster members is far from the desired state, then the event is triggered frequently, and the update of control input is relatively frequent, but when the system asymptotically converges to the desired state, fewer events are triggered, and interevent time increases and tends to be stable finally. We can find that if satellites are influenced by periodic disturbance, the interevent time also changes periodically. The control torques acting on each satellite are shown in Figure 3(e). It can be seen that control torques acting on the followers are piecewise function, and the control input is only updated at the next triggering instant. The control torques are limited within the range of $[-1, 1]$ N · m. Attitude trajectories of followers are shown in Figure 3(f), from which we can see that followers asymptotically converge to the convex hull formed by the leaders. Figures 3(g) and 3(h) show the event error and triggering threshold for each follower in 200 s. It can be seen that if event error exceeds threshold, the event is triggered and the state is sampled.

In a word, under the action of the event-triggered adaptive sliding mode attitude controller, the attitude of each satellite asymptotically converges to the convex hull formed by the leaders, and angular velocity asymptotically converges to 0.

5.1.2. Traditional Time-Triggered Attitude Containment Control. According to Reference [53], the time-triggered adaptive sliding mode attitude containment control algorithm is

$$\begin{aligned}
\mathbf{u}_i(t) &= -\mathbf{K}_i\mathbf{s}_i + \mathbf{Y}_i\widehat{\Theta}_i - \widehat{k}_i\text{sgn}(\mathbf{s}_i), \quad i \in F,\\
\dot{\widehat{\Theta}}_i(t) &= -\mathbf{\Lambda}_i\mathbf{Y}_i^T(t)\mathbf{s}_i(t),\\
\dot{\widehat{k}}_i(t) &= \Gamma_i\|\mathbf{s}_i(t)\|_1.
\end{aligned} \tag{69}$$

The simulation results of time-triggered distributed attitude adaptive sliding mode controller are shown in Figure 4. The attitude of the cluster system converges to the convex hull formed by the leaders at about 600 s, and attitude angular velocity converges to 0 within 700 s. The controller is continuously updated while the convergence rate and control accuracy are not better than the event-triggered one.

It can be clearly seen from Figures 3 and 4 that both time-triggered and event-triggered control strategies can realize attitude containment. In addition, it is noteworthy that event-triggered containment control is updated in an aperiodic manner, while time-triggered control is updated at a fixed interval of 0.01 s. Within 1200 s, the sampling and control input update times of the time-triggered control method are 120,000, while the event of each follower, respectively, is 391, 445, 405, 354, 402, and 480, from which the update frequency of control action is greatly reduced by the event-triggered control strategy. Compared with time-triggered attitude containment control protocol, event-triggered one can effectively reduce the control input update frequency while ensuring the similar control performance. Through the reasonable selection of control parameters and triggering function, event-triggered control can guarantee the convergence rate and control accuracy and reduce the amount of computation and communication, as well as the update frequency of actuators.

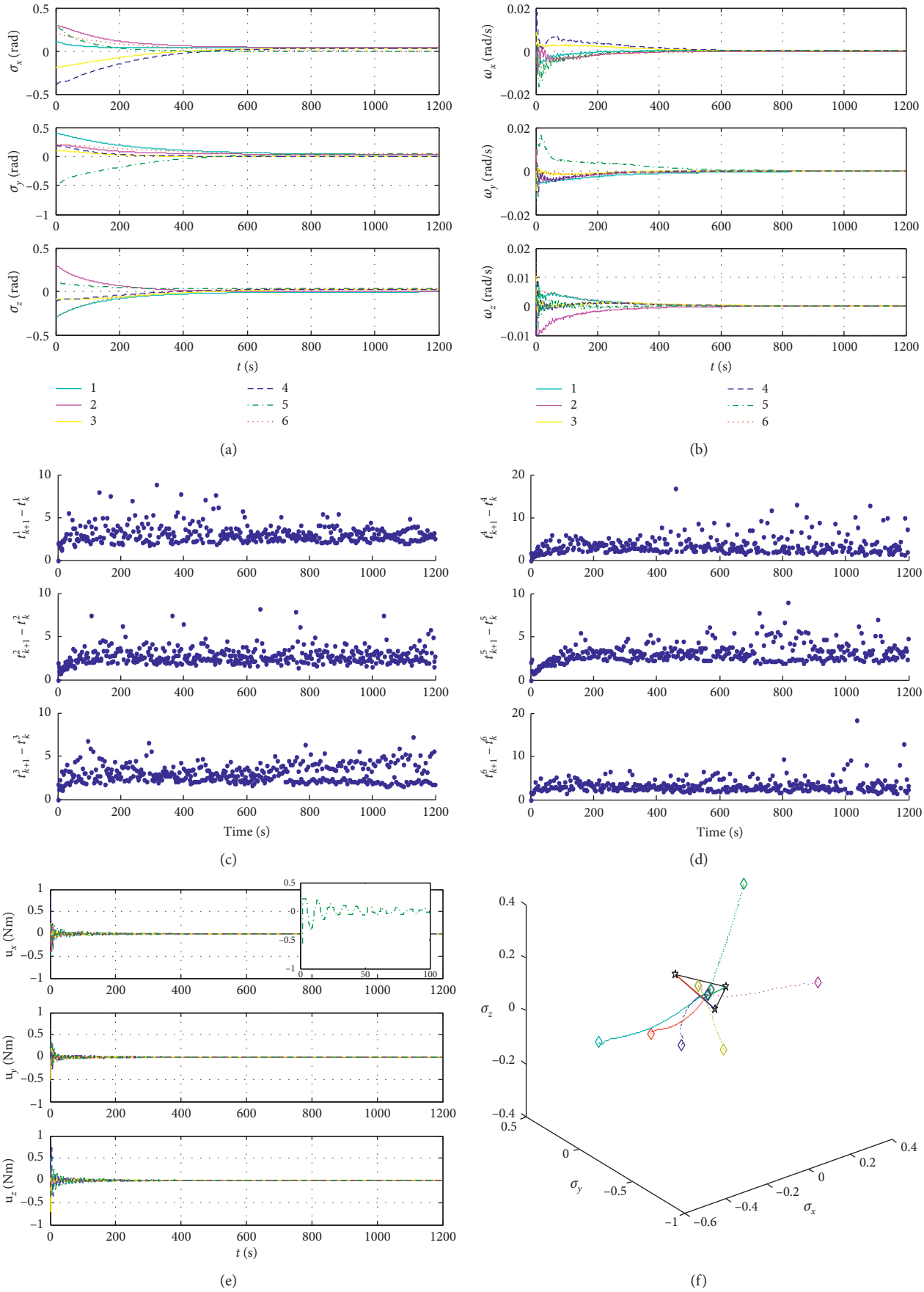

Figure 3: Continued.

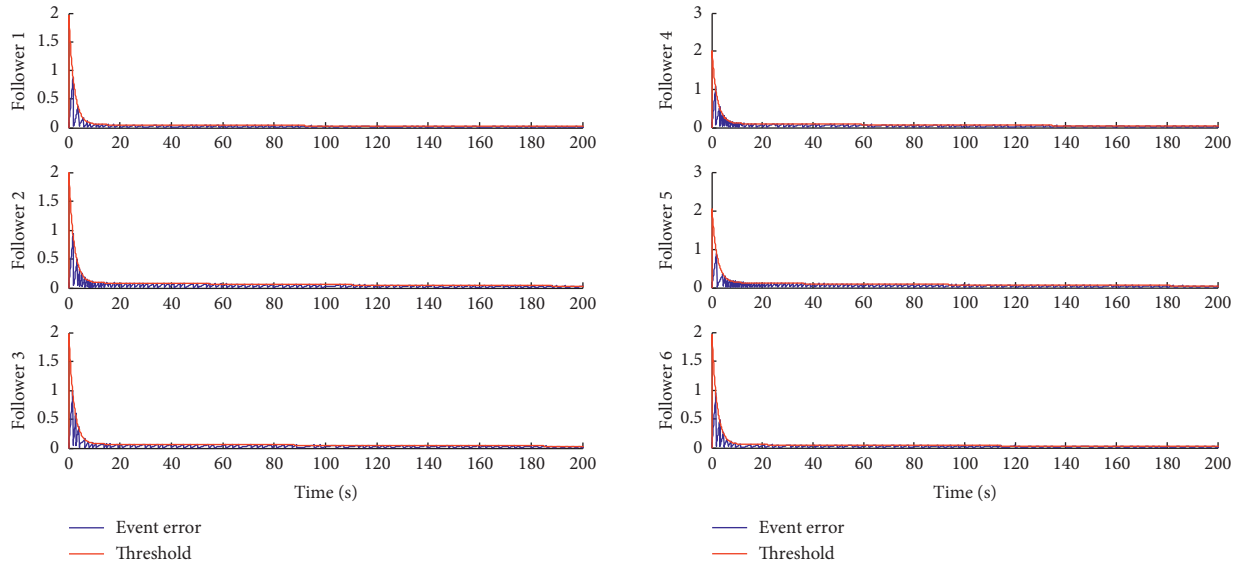

(g) (h)

Figure 3: Simulation results of controller (19) and Figure 2. (a) Attitude of follower satellites. (b) Attitude angular velocity of follower satellites. (c) Interevent time of follower satellites 1–3. (d) Interevent time of follower satellites 4–6. (e) Control torques acting on followers. (f) Attitude trajectories of follower satellites. (g) Triggering condition of follower satellites 1–3 in 200 s. (h) Triggering condition of follower satellites 4–6 in 200 s.

5.2. The Influence of Information Topology on Follower's Orientation. Suppose in the Earth observation mission of the microsatellite cluster, twelve satellites are used to obtain the observation information of three different orientations. In order to meet the accuracy requirement, two satellites can be used to observe the same azimuth at the same time. Suppose the target area is formed by three attitude orientations. The initial state of leaders, respectively, is

$$\begin{aligned}\boldsymbol{\sigma}_{10} &= \left[\, 0.09 \;\; 0.06 \;\; -0.08 \,\right]^T \text{rad},\\ \boldsymbol{\sigma}_{11} &= \left[\, 0.06 \;\; -0.1 \;\; 0.05 \,\right]^T \text{rad},\\ \boldsymbol{\sigma}_{12} &= \left[\, -0.08 \;\; 0.1 \;\; 0.09 \,\right]^T \text{rad}.\end{aligned} \tag{70}$$

Nominal inertia of followers, respectively, is

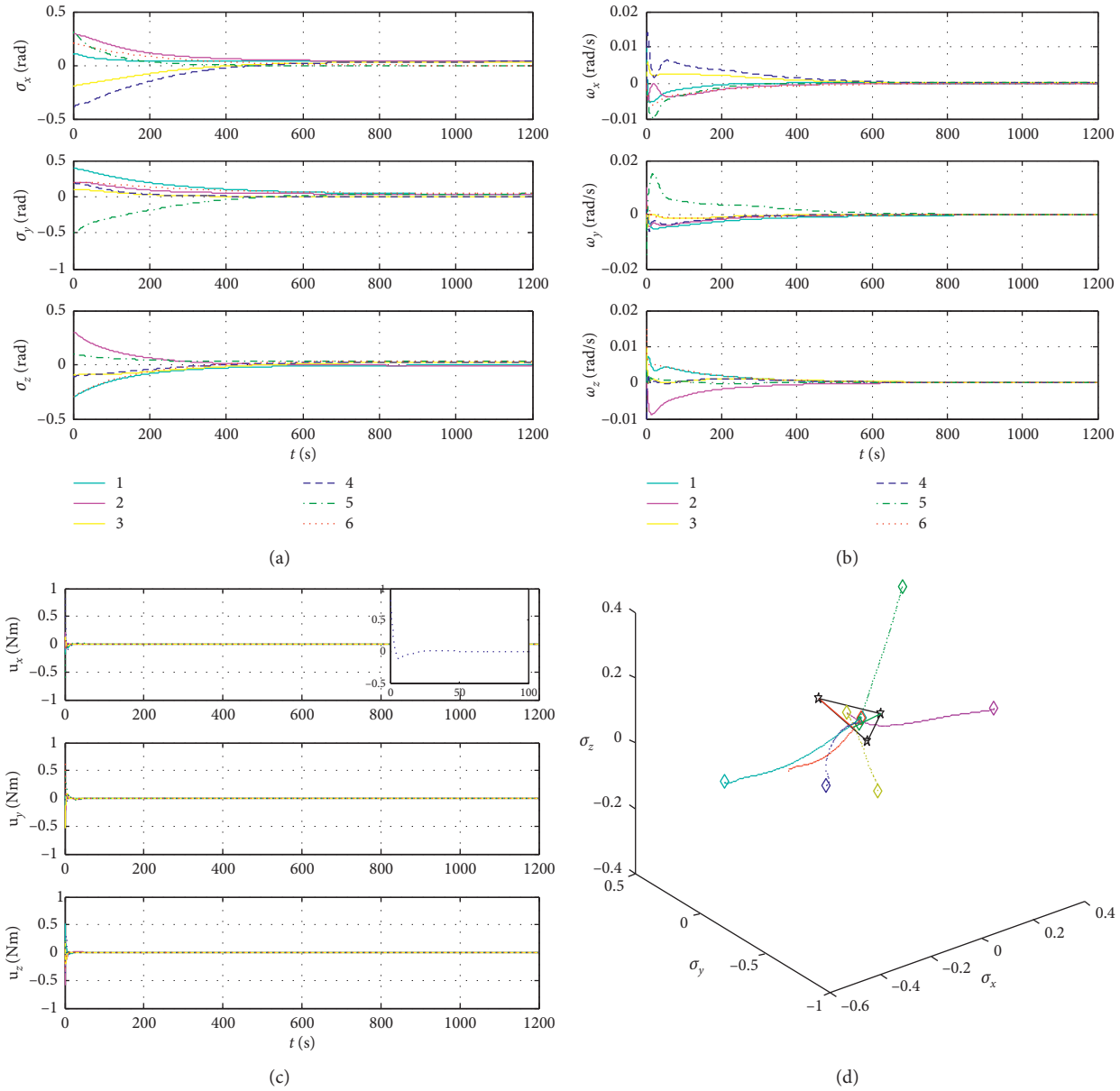

Figure 4: Simulation results of controller (69). (a) Attitude of follower satellites. (b) Attitude angular velocity of follower satellites. (c) Control torques acting on followers. (d) Attitude trajectories of follower satellites.

$$\mathbf{J}_1 = \begin{bmatrix} 20 & 0 & 2 \\ 0 & 25 & 0 \\ 2 & 0 & 29 \end{bmatrix} \text{kgm}^2,$$

$$\mathbf{J}_2 = \begin{bmatrix} 22 & 1 & 0.5 \\ 1 & 24 & 3 \\ 0.5 & 3 & 22 \end{bmatrix} \text{kgm}^2,$$

$$\mathbf{J}_3 = \begin{bmatrix} 25 & 0.8 & 2 \\ 0.8 & 29 & 1 \\ 2 & 1 & 21 \end{bmatrix} \text{kgm}^2,$$

$$\mathbf{J}_4 = \begin{bmatrix} 23 & 0.4 & 0 \\ 0.4 & 26 & 0.8 \\ 0 & 0.8 & 28 \end{bmatrix} \text{kgm}^2,$$

$$\mathbf{J}_5 = \begin{bmatrix} 22 & 0.2 & 0 \\ 0.2 & 26 & 0.6 \\ 0 & 0.6 & 24 \end{bmatrix} \text{kgm}^2, \quad (71)$$

$$\mathbf{J}_6 = \begin{bmatrix} 23 & 0.4 & 0 \\ 0.4 & 24 & 0.8 \\ 0 & 0.8 & 28 \end{bmatrix} \text{kgm}^2,$$

$$\mathbf{J}_7 = \begin{bmatrix} 22 & 0.2 & 0.3 \\ 0.2 & 29 & 0 \\ 0 & 0.3 & 25 \end{bmatrix} \text{kgm}^2,$$

$$\mathbf{J}_8 = \begin{bmatrix} 21 & 0.2 & 1 \\ 0.2 & 26 & 0.2 \\ 1 & 0.2 & 24 \end{bmatrix} \text{kgm}^2,$$

$$\mathbf{J}_9 = \begin{bmatrix} 24 & 0.6 & 0.3 \\ 0.6 & 25 & 0 \\ 0 & 0.3 & 27 \end{bmatrix} \text{kgm}^2.$$

Table 2: The initial attitude information of followers.

Followers	Attitude σ_i(rad)	Angular velocity ω_i(rad/s)
1	$[0.1 \ 0.4 \ -0.3]^T$	$[0.01 \ 0 \ 0]^T$
2	$[0.3 \ 0.2 \ 0.3]^T$	$[0 \ 0.01 \ 0]^T$
3	$[-0.2 \ 0.1 \ -0.1]^T$	$[0 \ 0 \ 0.01]^T$
4	$[-0.4 \ 0.2 \ -0.1]^T$	$[0 \ 0 \ -0.01]^T$
5	$[0.3 \ -0.5 \ 0.1]^T$	$[0 \ -0.015 \ 0]^T$
6	$[0.2 \ 0.2 \ -0.3]^T$	$[0 \ 0 \ 0.015]^T$
7	$[0.2 \ -0.1 \ -0.4]^T$	$[0.01 \ -0.01 \ 0]^T$
8	$[-0.4 \ -0.3 \ 0.1]^T$	$[0 \ 0.015 \ -0.01]^T$
9	$[-0.2 \ -0.3 \ 0.2]^T$	$[0.01 \ 0 \ -0.015]^T$

The initial estimation parameter of followers is $\Theta(0) = [22, 26, 25, 0, 0, 0]^T$.

The constant disturbance acting on the followers 1–6 and periodic disturbances are the same as Section 5.1, while constant disturbance acting on followers 7–9 is

$$\mathbf{d}_{l7} = [-0.0016 \ 0.001 \ 0.0012]^T \text{N} \cdot \text{m},$$
$$\mathbf{d}_{l8} = [-0.0018 \ 0.001 \ -0.0012]^T \text{N} \cdot \text{m}, \quad (72)$$
$$\mathbf{d}_{l9} = [0.0011 \ -0.0015 \ -0.0014]^T \text{N} \cdot \text{m}.$$

The initial state of followers is, respectively, shown in Table 2.

Information topology of the cluster system is shown in Figure 5.

The information topology structure of the microsatellite cluster system is shown in Figure 5. It can be seen that Figure 5 belongs to π^1 partition. Satellites 1, 2, 7, and 8 belong to the same cell, 3 and 4 belong to the same cell, and 5 and 6 belong to the same cell. According to Theorem 4, satellites belonging to the same cell converge to the same azimuth under the action of control torques in the presence of model uncertainties and external disturbances. This property can be used to observe the same azimuth. Simulation results are shown in Figure 6. The attitude of follower converges to the convex hull formed

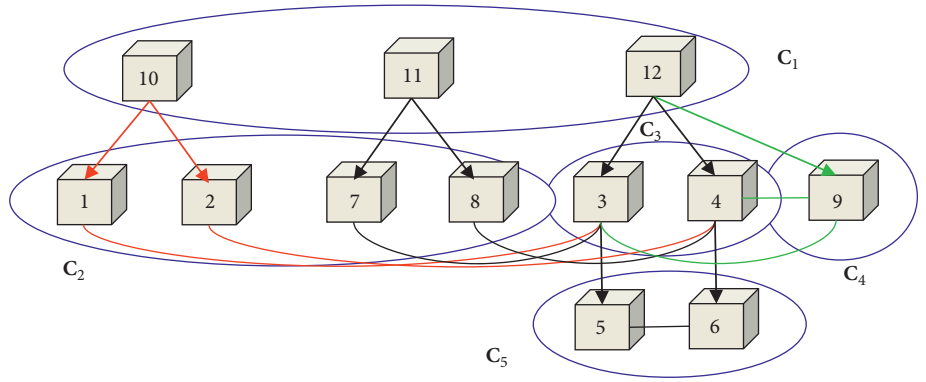

Figure 5: Topology structure of satellite cluster satisfying π^1 cell partition.

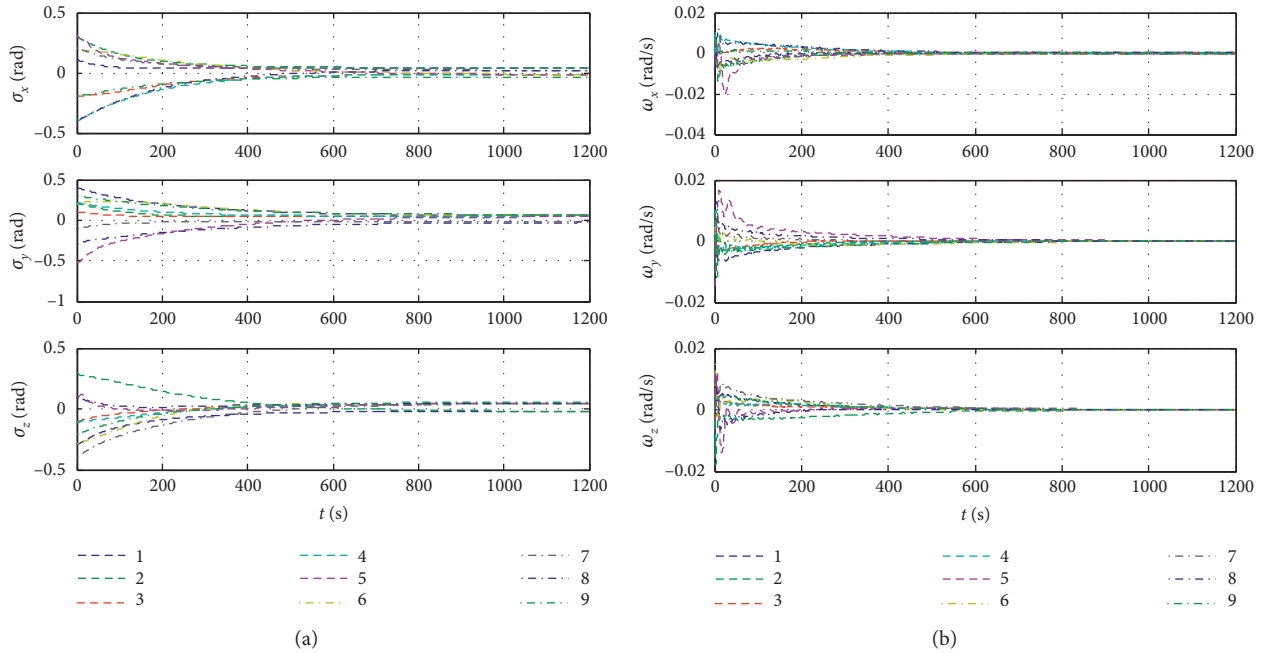

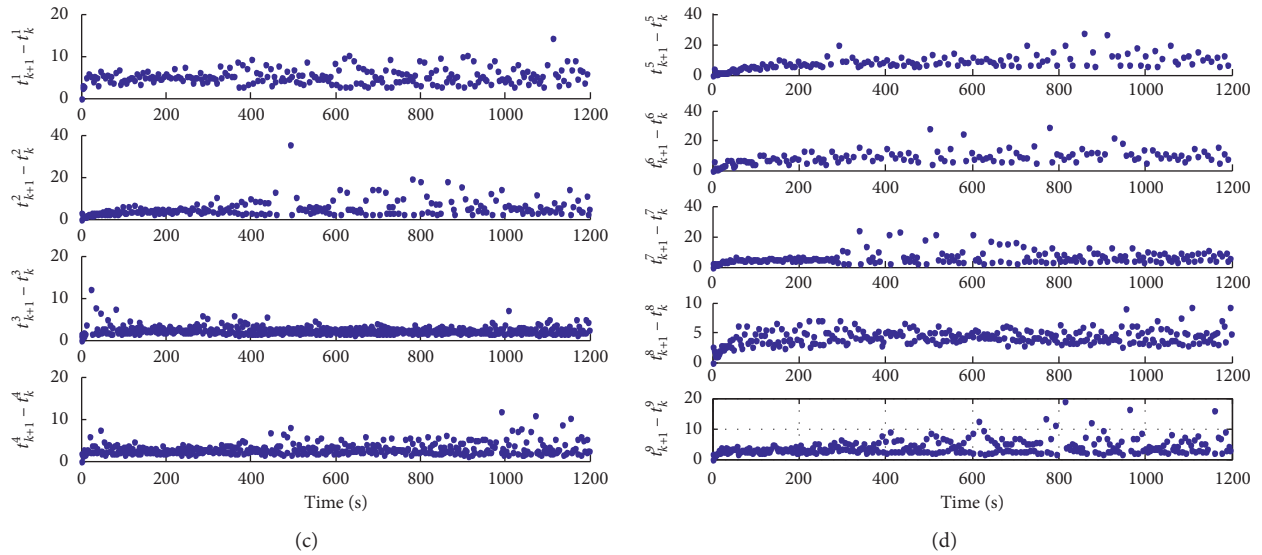

Figure 6: Continued.

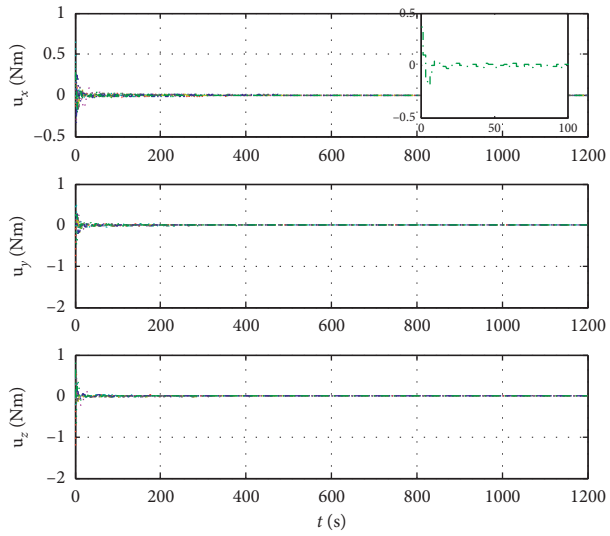

(e)

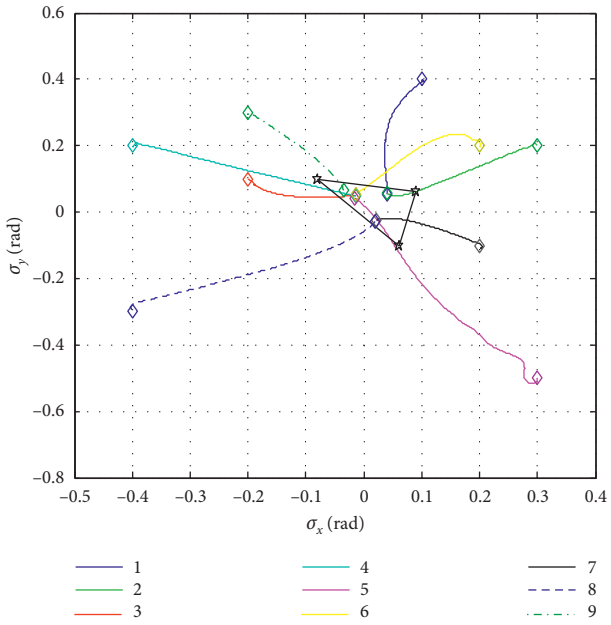

(f)

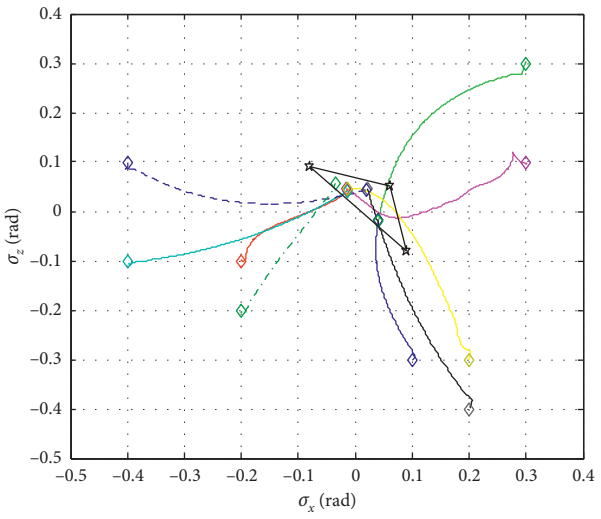

(g)

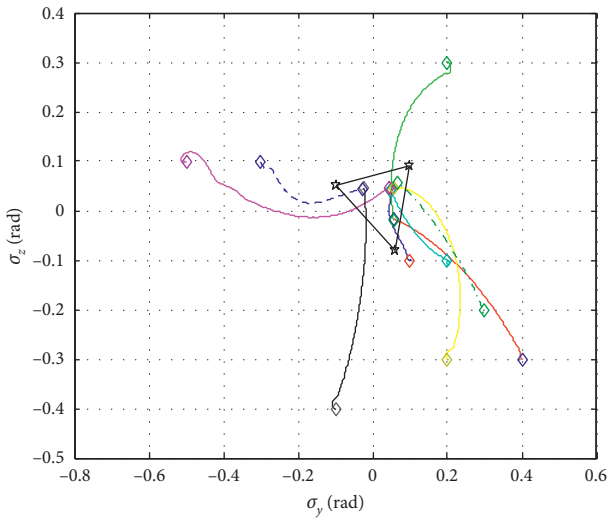

(h)

Figure 6: Continued.

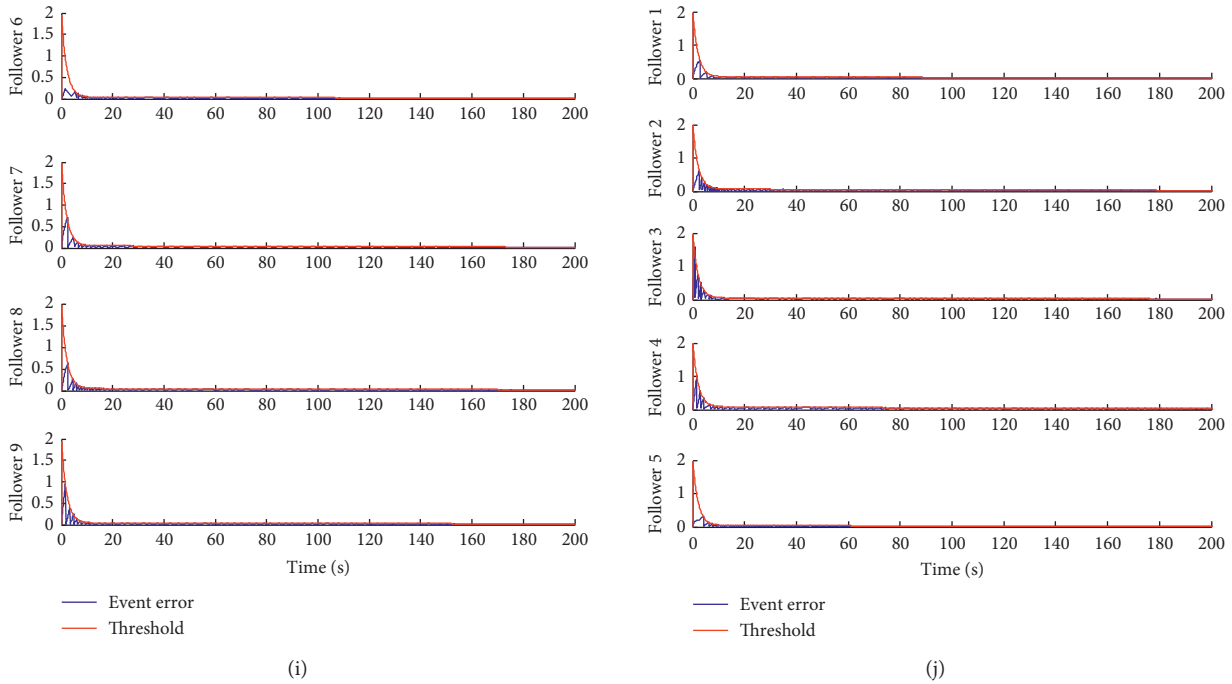

Figure 6: Simulation results of controller (19) and Figure 5. (a) Attitude of follower satellites. (b) Attitude angular velocity of follower satellites. (c) Interevent time of follower satellites 1–4. (d) Interevent time of follower satellites 5–9. (e) Control torques acting on followers. (f) Attitude trajectory of followers projected on σ_x-σ_y axis. (g) Attitude trajectory of followers on σ_x-σ_z axis. (h) Attitude trajectory of followers on σ_y-σ_z axis. (i) Triggering condition of follower satellites 1–3 within 200 s. (j) Triggering condition of follower satellites 4–6 within 200 s.

by the leaders within 600 s, and attitude angular velocity converges to 0 within 700 s. The control torques are piecewise constant. Satellites 1 and 2 converge to the same azimuth, and 7 and 8 converge to same azimuth, respectively. Because satellites in $\mathbf{C}_5$ only receive information from $\mathbf{C}_3$, 3, 4, 5, and 6 converge to the same azimuth. Within 1200 s, the sampling and control input update times of each follower, respectively, are 232, 247, 522, 420, 162, 142, 196, 288, and 315.

6. Conclusion

In this paper, an event-triggered adaptive sliding mode attitude containment control protocol is proposed in the framework of the Euler–Lagrange model for the attitude containment control problem of the microsatellite cluster system. Considering the constraints of resource and power on the microsatellite cluster system, the event-triggered control strategy is introduced into the attitude containment control problem of the microsatellite cluster. The triggering condition consisting of state-dependent function and the time-dependent function is given to adjust controller update period and exclude the Zeno behaviour. If and only if the triggering condition is satisfied, state information is sampled, control law is computed, and actuators are updated. Then, under directed topology, the event-triggered adaptive sliding mode attitude containment control algorithm is proposed, which makes attitude of followers asymptotically enter into the convex hull formed by leaders' orientation in the presence of inertia uncertainties and external disturbances. Numerical simulation is carried out to verify the effectiveness of the proposed event-triggered distributed attitude containment control algorithm. Then, compared with the time-triggered one, it can be seen that while ensuring the control performance of the cluster system, the designed event-triggered attitude containment controller only updates control law in the triggering instant, which effectively reduces the amount of computation and communication and update frequency of actuators and saves resources on board.

Furthermore, the influence of cluster information topology structure design on the stable state of containment control algorithm is also studied. An appropriate information topology is designed to meet the attitude orientation requirements of containment control. It is shown that the steady state of each follower is a convex combination of all leaders' states it can access. The cell partition of cluster information topology is given based on the number of satellite's neighbours, and it is proved that the cluster members belonging to the same cell have the same stable state. However, there is no requirement for the information interaction between satellites inside the cell, and the information links inside the cell will not affect the stable state of cluster members. It provides a theoretical basis for the design of information topology of the microsatellite cluster system. Numerical simulation is conducted to verify the influence of information topology on steady state of the microsatellite cluster system.

Data Availability

No data were used to support this study.

Conflicts of Interest

The authors declare that they have no conflicts of interest.

References

[1] O. Ben-Yaacov, A. Ivantsov, and P. Gurfil, "Covariance analysis of differential drag-based satellite cluster flight," *Acta Astronautica*, vol. 123, pp. 387–396, 2016.

[2] J. Luo, L. Zhou, and B. Zhang, "Consensus of satellite cluster flight using an energy-matching optimal control method," *Advances in Space Research*, vol. 60, no. 9, pp. 2047–2059, 2017.

[3] W. Zhong, *Research on the orbit navigation and control of the satellite cluster*, Ph.D. dissertation, HIT, Harbin, China, 2014.

[4] H. Zhang and P. Gurfil, "Satellite cluster flight using on-off cyclic control," *Acta Astronautica*, vol. 106, no. 3, pp. 1–12, 2015.

[5] E. Vassev and M. Hinchey, "Self-awareness in autonomous nano-technology swarm missions," in *Proceedings of the 2011 Fifth IEEE Conference on Self-Adaptive and Self-Organizing Systems Workshops*, pp. 133–136, Ann Arbor, MI, USA, October 2011.

[6] Z. Li, L. Guo, J. Huang et al., "Study on development status of light sail spacecraft and key technologies of breakthrough starshot project," *Spacecraft Engineering*, vol. 25, no. 5, pp. 111–118, 2016.

[7] J. R. Lawton and R. W. Beard, "Synchronized multiple spacecraft rotations," *Automatica*, vol. 38, no. 8, pp. 1359–1364, 2002.

[8] H. Liang, Z. Sun, and J. Wang, "Robust decentralized attitude control of spacecraft formations under time-varying topologies, model uncertainties and disturbances," *Acta Astronautica*, vol. 81, no. 2, pp. 445–455, 2012.

[9] H. Du, M. Z. Q. Chen, and G. Wen, "Leader-following attitude consensus for spacecraft formation with rigid and flexible spacecraft," *Journal of Guidance, Control, and Dynamics*, vol. 39, no. 4, pp. 1–8, 2016.

[10] H. Cai and J. Huang, "Leader-following attitude consensus of multiple rigid body systems by attitude feedback control," *Automatica*, vol. 69, pp. 87–92, 2016.

[11] L. Shi, J. Shao, W. X. Zheng, and T.-Z. Huang, "Asynchronous containment control for discrete-time second-order multi-agent systems with time-varying delays," *Journal of the Franklin Institute*, vol. 354, no. 18, pp. 8552–8569, 2017.

[12] M. Ji, G. Ferrari-Trecate, M. Egerstedt, and A. Buffa, "Containment control in mobile networks," *IEEE Transactions on Automatic Control*, vol. 53, no. 8, pp. 1972–1975, 2008.

[13] X. Dong, Y. Hua, Y. Zhou et al., "Theory and experiment on formation-containment control of multiple multirotor unmanned aerial vehicle systems," *IEEE Transactions on Automation Science and Engineering*, vol. 16, no. 1, 2019.

[14] H. Qin, H. Chen, Y. Sun, and Z. Wu, "The distributed adaptive finite-time chattering reduction containment control for multiple ocean bottom flying nodes," *International Journal of Fuzzy Systems*, vol. 21, no. 2, pp. 607–619, 2019.

[15] Y. Sun, G. Ma, M. Liu, and L. Chen, "Distributed finite-time configuration containment control for satellite formation," *Proceedings of the Institution of Mechanical Engineers, Part G: Journal of Aerospace Engineering*, vol. 231, no. 9, pp. 1609–1620, 2016.

[16] Y. Sun, G. Ma, L. Chen, and P. Wang, "Neural network-based distributed adaptive configuration containment control for satellite formations," *Proceedings of the Institution of Mechanical Engineers, Part G: Journal of Aerospace Engineering*, vol. 232, no. 12, pp. 2349–2363, 2018.

[17] Y. C. Cao and W. Ren, "Containment control with multiple stationary or dynamic leaders under a directed interaction graph," in *Proceedings of the 48th IEEE Conference on Decision and Control*, pp. 3014–3019, Piscataway, NJ, USA, December 2009.

[18] G. Notrastefano, M. Egerstedt, and M. Haque, "Containment in leader-follower networks with switching communication topologies," *Automatica*, vol. 47, no. 5, pp. 1035–1040, 2011.

[19] Y. Cao, D. Stuart, W. Ren, and Z. Meng, "Distributed containment control for multiple autonomous vehicles with double-integrator dynamics: algorithms and experiments," *IEEE Transactions on Control Systems Technology*, vol. 19, no. 4, pp. 929–938, 2011.

[20] A. Zhang, J. Chen, X. Kong et al., "Containment control protocol and its convergence speed analysis for double-integrator dynamics systems," *Journal of Harbin Institute of Technology*, vol. 46, no. 9, pp. 1–8, 2014.

[21] K. Liu, G. Xie, and L. Wang, "Containment control for second-order multi-agent systems with time-varying delays," *Systems & Control Letters*, vol. 67, no. 7, pp. 24–31, 2014.

[22] Z. Meng, W. Ren, and Z. You, "Distributed finite-time attitude containment control for multiple rigid bodies," *Automatica*, vol. 46, no. 12, pp. 2092–2099, 2010.

[23] J. Mei, W. Ren, and G. Ma, "Distributed containment control for Lagrangian networks with parametric uncertainties under a directed graph," *Automatica*, vol. 48, no. 4, pp. 653–659, 2012.

[24] A. Zhang, X. Kong, S. Zhang et al., "Distributed attitude cooperative control with multiple leaders," *Journal of Harbin Institute of Technology*, vol. 45, no. 3, pp. 1–6, 2013.

[25] S. Zuo, Y. Song, F. L. Lewis, and A. Davoudi, "Time-varying output formation containment of general linear homogeneous and heterogeneous multiagent systems," *IEEE Transactions on Control of Network Systems*, vol. 6, no. 2, pp. 537–548, 2019.

[26] T. Xu, Y. Hao, and Z. Duan, "Fully distributed containment control for multiple euler-Lagrange systems over directed graphs: an event-triggered approach," *IEEE Transactions on Circuits and Systems I: Regular Papers*, vol. 67, no. 6, pp. 2078–2090, 2020.

[27] L. Chen, Y. Guo, C. Li et al., "Clarification: satellite formation-containment flying control with collision avoidance," *Journal of Aerospace Information Systems*, vol. 17, no. 11, p. 647, 2018.

[28] Y. Sun, C. Li, J. Yao et al., "Adaptive neural-network containment control of multiple Euler-Lagrange systems without using relative velocity information," *Control and Decision*, vol. 31, no. 4, pp. 693–700, 2016.

[29] S. Weng, D. Yue, Z. Sun, and L. Xiao, "Distributed robust finite-time attitude containment control for multiple rigid bodies with uncertainties," *International Journal of Robust and Nonlinear Control*, vol. 25, no. 15, pp. 2561–2581, 2015.

[30] L. Zhao, J. Yu, and P. Shi, "Command filtered backstepping-based attitude containment control for spacecraft formation," *IEEE Transactions on Systems, Man, and Cybernetics: Systems*, vol. 51, no. 2, pp. 1278–1287, 2019.

[31] L. Ma, S. Wang, H. Min, S. Liao, and Y. Liu, "Distributed finite-time attitude containment control of multi-rigid-body

systems," *Journal of the Franklin Institute*, vol. 352, no. 5, pp. 2187–2203, 2015.
[32] D. V. Dimarogonas, E. Frazzoli, and K. H. Johansson, "Distributed event-triggered control for multi-agent systems," *IEEE Transactions on Automatic Control*, vol. 57, no. 5, pp. 1291–1297, 2012.
[33] G. S. Seyboth, D. V. Dimarogonas, and K. H. Johansson, "Event-based broadcasting for multi-agent average consensus," *Automatica*, vol. 49, no. 1, pp. 245–252, 2013.
[34] F. Guo and S. Zhang, "Event-triggered coordinated attitude method for chip satellite cluster," *Acta Astronautica*, vol. 160, pp. 451–460, 2019.
[35] Q. Liu, M. Ye, J. Qin et al., "Event-based leader-follower consensus for multiple Euler-Lagrange systems with parametric uncertainties," in *Proceedings of the 2016 IEEE 55th Conference on Decision and Control (CDC)*, pp. 2240–2246, IEEE, Las Vegas, NV, USA, December 2016.
[36] B. Wu, Q. Shen, and X. Cao, "Event-triggered attitude control of spacecraft," *Advances in Space Research*, vol. 61, no. 3, pp. 927–934, 2017.
[37] S. Sun, M. Yang, and L. Wang, "Event-triggered nonlinear attitude control for a rigid spacecraft," in *Proceedings of the 2017 36th Chinese Control Conference (CCC)*, pp. 7582–7586, Da lian, China, July 2017.
[38] S. Weng and D. Yue, "Distributed event-triggered cooperative attitude control of multiple rigid bodies with leader-follower architecture," *International Journal of Systems Science*, vol. 47, no. 3, pp. 631–643, 2015.
[39] Q. Hou, S. Ding, and X. Yu, "Composite super-twisting sliding mode control design for PMSM speed regulation problem based on a novel disturbance observer," *IEEE Transactions on Energy Conversion*, vol. 99, pp. 1–9. In press, 2020.
[40] Q. Hou and S. Ding, "GPIO based super-twisting sliding mode control for PMSM," *IEEE Transactions on Circuits and Systems II: Express Briefs*, vol. 68, no. 2, p. 747, 2021.
[41] L. Liu, W. X. Zheng, and S. Ding, "An adaptive SOSM controller design by using a sliding-mode-based filter and its application to buck converter," *IEEE Transactions on Circuits and Systems I: Regular Papers*, vol. 67, no. 7, pp. 2409–2418, 2020.
[42] B. Owen, "Fractionated spacecraft workshop: vision and objectives," in *Proceedings of the DARPA Fractionated Spacecraft Workshop*, Colorado Spring, CO, USA, August 2006.
[43] M. Hu, H. Chen, and G. Zeng, "Cyclic pursuit control for fractionated spacecraft formation reconfiguration using local information only," in *Proceedings of the 2012 24th Chinese Control and Decision Conference (CCDC)*, May 2012.
[44] L. Cao, B. Xiao, and M. Golestani, "Robust fixed-time attitude stabilization control of flexible spacecraft with actuator uncertainty," *Nonlinear Dynamics*, vol. 100, no. 3, pp. 2505–2519, 2020.
[45] B. Xiao, L. Cao, S. Xu, and L. Liu, "Robust tracking control of robot manipulators with actuator faults and joint velocity measurement uncertainty," *IEEE/ASME Transactions on Mechatronics*, vol. 25, no. 3, pp. 1354–1365, 2020.
[46] A. Zhang, J. Chen, S. Zhang, X. Kong, and F. Wang, "Graph-theoretic characterisations of the steady states for containment control," *International Journal of Control*, vol. 85, no. 10, pp. 1574–1580, 2012.
[47] S. Martini, M. Egerstedt, and A. Bicchi, "Controllability analysis of multi-agent systems using relaxed equitable partitions," *International Journal of Systems, Control and Communications*, vol. 2, no. 1–3, pp. 100–121, 2010.
[48] A. Aggarwal, J. S. Chang, and C. K. Yap, "Minimum area circumscribing polygons," *The Visual Computer*, vol. 1, no. 2, pp. 112–117, 1985.
[49] S. Zhang, F. Guo, A. Zhang et al., "Orbital containment control algorithm and complex information topology design for large-scale cluster of spacecraft," *IEEE Access*, vol. 8, no. 99, pp. 1–24, 2020.
[50] H. K. Khalil, *Nonlinear Systems*, Prentice Hall, Upper Saddle River, NJ, USA, 3rd edition, 2002.
[51] S. Sastry, *Nonlinear Systems Analysis, Stability, and Control*, Springer-Verlag, New York, NY, USA, 1999.
[52] A. K. Behera and B. Bandyopadhyay, "Robust sliding mode control: an event-triggering approach," *IEEE Transactions on Circuits and Systems II: Express Briefs*, vol. 64, no. 2, pp. 146–150, 2017.
[53] J. Mei, W. Ren, B. Li, and G. Ma, "Distributed containment control for multiple unknown second-order nonlinear systems with application to networked Lagrangian systems," *IEEE Transactions on Neural Networks and Learning Systems*, vol. 26, no. 9, pp. 1885–1899, 2015.

Hindawi
Mathematical Problems in Engineering
Volume 2021, Article ID 6635975, 10 pages
https://doi.org/10.1155/2021/6635975

Research Article

A Random Access Protocol Approach to Stochastic Jumping Systems with Singular Perturbations

Saijiang Kai

State Grid Xinjiang Electric Power Co., Ltd., Wulumuqi, China

Correspondence should be addressed to Saijiang Kai; ksj_xj@163.com

Received 18 December 2020; Revised 24 January 2021; Accepted 9 February 2021; Published 25 February 2021

Academic Editor: Shihong Ding

This paper focuses on the stochastic jumping systems with singular perturbation subject to a random access protocol. The key challenge with controller design issue of stochastic jumping systems is how to assess the coordination of communication orders. In this study, a joint Markov process is established, and a novel control law is proposed. In contrast with the existing methods, the developed controller is more general. Finally, a practical example is exhibited to show the effectiveness of the achieved theories.

1. Introduction

In practical, random faults, random communication failures, and so on are commonly encountered. In these systems, the effect of unpredictable random abrupt events can be modeled as a Markov chain model. Markov jumping systems (MJSs) consist of a series of submodels, in which the switching is determined by the Markov process. In recent years, MJSs have been successfully applied in various areas such as biological systems, networked control systems, hybrid systems, and economic systems [1–3]. Due to the great advantage of MJSs, up to now, many valuable results on the issues of MJSs have been published [4–8], including state estimation [5] and robust control [7, 8].

On the contrary, there exists a set of practical systems, whose dynamic behavior is characterized by the multiple time scales (MTSs) property. Especially, in the MTS-based systems, the small parameters lead to difficulty in system performance analysis. Therefore, it is unsolvable by means of the conventional single time-scale technique. It is well known that MTS-based systems can be described by singularly perturbed systems (SPSs). In light of its unique characteristic, a singularly perturbed parameter (SPP) is employed, where the MTS-based systems can be divided into fast and slow dynamic states [9–11]. Recently, quantities of excellent results on SPSs have been exhibited [12]. However, when it comes to Markov jumping SPSs (MJSPSs), the investigation of relevant problems is far away from maturity. How to tackle the sophisticated systems with both SPP and transition probabilities partly is the motive of this study.

Note that the information exchange in the networked control systems may result in the heavy communication burden. These limited bandwidths may result in network-induced phenomena, such as data collisions, packet losses, and network-induced delay [13]. Recently, the protocol-based networked systems have attracted increasing interest, for instance, try-once-discard protocol [14] and round-robin protocol (RRP) [15]. Note that the RRP is a static transmission mechanism, which limits the practical application. Compared with the RRP, the random access protocol (RAP) is a dynamic case, in which the sensor node will get access to transmit data in a randomly way [16, 17]. However, to the best of our knowledge, the RAP has not been applied in MJSPSs yet, which partly motives us to fill this gap.

Inspired by the above discussion, it is imperative to study the problem of MJSPSs with RAP. To avoid data collisions, the RAP is introduced to regulate the data transmission order. With respect to the dynamic behavior of the MJSPS and the RAP, a joint Markov process is proposed. Therefore, a novel control design technique is presented, which covers the conventional case. Finally, a practical simulation is given to show the effectiveness of the

obtained theories.*Notations*. The notations are fairly standard. $\mathbb{R}^m$ refers to the m-dimensional Euclidean space. $\lambda_{\min}(L)$ denotes the minimum eigenvalue of L. diag$\{\ldots\}$ represents a block diagonal matrix. mod(y_1, y_2) stands for the nonnegative remainder on division of y_1 by y_2.

2. Problem Formulations

Consider the following MSSPS described as follows:

$$\begin{cases} \alpha_1(k+1) = A^{11}_{\mu(k)}\alpha_1(k) + \varepsilon A^{12}_{\mu(k)}\alpha_2(k) + B^1_{\mu(k)}u(k) + C^1_{\mu(k)}v(k), \\ \alpha_2(k+1) = A^{21}_{\mu(k)}\alpha_1(k) + \varepsilon A^{22}_{\mu(k)}\alpha_2(k) + B^2_{\mu(k)}u(k) + C^2_{\mu(k)}v(k), \\ z(k) = D^1_{\mu(k)}\alpha_1(k) + \varepsilon D^2_{\mu(k)}\alpha_2(k) + F_{\mu(k)}u(k) + H_{\mu(k)}v(k), \end{cases} \tag{1}$$

where $\alpha_1(k) \in \mathbb{R}^{n_s}$ means the fast vector and $\alpha_2(k) \in \mathbb{R}^{n_f}$ stands for the slow vector, respectively. $u(k) \in \mathbb{R}^{n_u}$ symbolizes the control input, $z(k) \in \mathbb{R}^{n_z}$ signifies the output state, $\varepsilon > 0$ symbolizes a singular perturbation parameter, and $v(k) \in l_2[0, \infty)$ renders the disturbance signal. The stochastic variable $\{\mu(k), k \geq 0\}$ indicates a discrete-time Markov chain (DTMC) obeying a finite set $\mathcal{N} = \{1, 2, \ldots, N\}$. Clearly, the transition probability matrix (TPM) of $\mu(k)$ is defined by $\Pi = [\varphi_{pq}]_{\mathcal{N}\times\mathcal{N}}$, where

$$\varphi_{pq} = \Pr\{\mu(k+1) = q \mid \mu(k) = p\}, \tag{2}$$

where $\varphi_{pq} \geq 0$ and $\sum_{q\in\mathcal{N}}\varphi_{pq} = 1, \forall p, q \in \mathcal{N}$. Therefore, it is easy to derive that $\forall p \in \mathcal{N}$, and $A^{11}_{\mu(k)}$, $A^{12}_{\mu(k)}$, $A^{21}_{\mu(k)}$, $A^{22}_{\mu(k)}$, $B^1_{\mu(k)}$, $B^2_{\mu(k)}$, $C^1_{\mu(k)}$, $C^2_{\mu(k)}$, $D^1_{\mu(k)}$, $D^2_{\mu(k)}$, $F_{\mu(k)}$, and $H_{\mu(k)}$ can be represented by A^{11}_p, A^{12}_p, A^{21}_p, A^{22}_p, B^1_p, B^2_p, C^1_p, C^2_p, D^1_p, D^2_p, M_p, and G_p, respectively.

Let $\alpha(k) = [\alpha_1^\top(k)\alpha_2^\top(k)]^\top$, and the MSSPS (1) can be rewritten as

$$\begin{cases} \alpha(k+1) = A_pE_\varepsilon\alpha(k) + B_pu(k) + C_pv(k), \\ z(k) = D_pE_\varepsilon\alpha(k) + M_pu(k) + G_pv(k), \end{cases} \tag{3}$$

where

$$\begin{aligned} E_\varepsilon &= \operatorname{diag}\left\{I_{n_s}, \varepsilon I_{n_f}\right\}, \\ A_p &= \begin{bmatrix} A^{11}_p & A^{12}_p \\ A^{21}_p & A^{22}_p \end{bmatrix}, \\ B_p &= \begin{bmatrix} B^1_p \\ B^2_p \end{bmatrix}, \\ C_p &= \begin{bmatrix} C^1_p \\ C^2_p \end{bmatrix}, \\ D_p &= \begin{bmatrix} D^1_p & D^2_p \end{bmatrix}. \end{aligned} \tag{4}$$

The signal transmission between the plant and the controller via a shared communication networks, which may result in many network-induced phenomena, for example, data collisions. To regulate the data transmission, the RAP is applied between the sensors and the actuators. When the RAP is triggered, only one node can access network at each time instant. Note that the RAP is a dynamic scheduling agreement. Employ a stochastic variable $\nu(k) \in \{1, 2, \ldots, M\}$ to schedule network resources. Here, $\nu(k)$ is known as a homogeneous DTMC obeying a set $\mathcal{N}_c = \{1, 2, \ldots, M\}$, and the TPM $\Phi = [\psi_{fg}]_{M\times M}$ is inferred as

$$\psi_{fg} = \Pr\{\nu(k+1) = g \mid \nu(k) = f\}, \tag{5}$$

where $\forall f, g \in \mathcal{M}$, $\psi_{fg} \in [0, 1]$, and $\sum_{g\in\mathcal{M}}\psi_{fg} = 1$.

Denoting $v(k) = \left[\, v_1^\top(k) \;\; v_2^\top(k) \;\; \ldots \;\; v_{n_u}^\top(k) \,\right]$ and $u(k) = \left[\, u_1^\top(k) \;\; u_2^\top(k) \;\; \ldots \;\; u_{n_u}^\top(k) \,\right]$, where $v_m(k)$ signifies the f^{th} control input state and u_n indicates the n^{th} actuator. By considering the zero-order hold technique, the f^{th} actuator $u_f(k)$ can be updated as

$$u_f(k) = \begin{cases} v_f(k), & \text{if } \nu(k) = f, \\ u_f(k-1), & \text{otherwise.} \end{cases} \tag{6}$$

In what follows, a Kronecker sign function is given by

$$\delta(F - \beth) = \begin{cases} 1, & \text{if } F = \beth, \\ 0, & \text{otherwise.} \end{cases} \tag{7}$$

Therefore, by the updated rule (6), for $\forall f \in \mathcal{M}$, the actuator $u(k)$ is formulated as

$$u(k) = \Phi_{\nu(k)}\nu(k) + \left(I - \Phi_{\nu(k)}\right)u(k-1), \tag{8}$$

where $\Phi_f \triangleq \operatorname{diag}\left\{\delta^1_f, \delta^2_f, \ldots, \delta^{n_u}_f\right\}$ $(f = 1, 2, \ldots, n_u)$ and $\delta^{\beth}_{\mathsf{F}} = \delta(F - \beth)$. Clearly, it can be devised from (8) that $u(k) = \left[\, u_1(k-1) \;\; u_2(k-1) \;\; \ldots \;\; u_{f-1}(k) \;\; v_f(k) \;\; u_{f+1}(k) \;\; \ldots \;\; u_{n_u}(k) \,\right]^\top$.

It can be observed from (3) and (8) that two Markov processes $\mu(k)$ and $\nu(k)$ are involved in this paper. To reveal the relationship between the Markov processes (MPs) $\mu(k)$ and $\nu(k)$, the merging strategy is absorbed in Lemma 1.

Lemma 1 (see [4]). *The MPs $\mu(k)$ and $\nu(k)$ can be mapped to a novel MP $r(k) \in \{1, 2, \ldots, S\}$, which can be described as follows:*

$$r(k) = R(\mu(k), \nu(k)) = \mu(k) + (\nu(k) - 1)N, \tag{9}$$

where $S = NM$.

In virtue of $\xi(k)$, the values of $\mu(k)$ and $\nu(k)$ could be acquired by $\zeta_1(r(k))$ and $\zeta_2(r(k))$:

$$\mu(k) = \zeta_1(r(k)) = \mathrm{mod}(r(k) - 1, N) + 1,$$
$$\nu(k) = \zeta_2(r(k)) = \lfloor \frac{r(k) - 1}{N} \rfloor + 1. \tag{10}$$

Obviously, the values of $r(k)$ can be determined by the pair $(\mu(k), \nu(k))$. The joint TPM of the MP $r(k)$ is expressed as

$$\begin{aligned}\theta_{hl} &= \Pr\{r(k+1) = l | r(k) = h\} \\ &= \Pr\{\varphi(k+1) = \zeta_1(l) | \varphi(k) = \zeta_1(h)\} \\ &\quad \times \Pr\{\psi(k+1) = \zeta_2(l) | \psi(k) = \zeta_2(h)\} \\ &= \pi_{\zeta_1(h)\zeta_1(l)} \tau_{\zeta_2(h)\zeta_2(l)},\end{aligned} \tag{11}$$

where $\pi_{\zeta_1(h)\zeta_1(l)}$ and $\tau_{\zeta_2(h)\zeta_2(l)}$ are in (2) and (4).

By resorting to the joint MP, the control law $\nu(k)$ is designed as

$$\nu(k) = K_{r(k)} E_\varepsilon x(k), \tag{12}$$

where $K_{r(k)}$ are matrices being solved.

Remark 1. The matrix $K_{r(k)}$ in (12) is assumed to be dependent on the joint Markov process $r(k)$, which implies that $K_{r(k)}$ is characterized by both the corresponding mode $\mu(k)$ and the RAP case $\nu(k)$. Otherwise, the controller gain is reduced to $K_{\mu(k),\nu(k)}$, which will rise the difficulty in the MSSPS analysis.

According to (3), (8), and (12), the augmented MSPS (13) is established:

$$\begin{cases} x(k+1) = \mathscr{A}_h E_\varepsilon x(k) + B_i(I - \Psi_m)u(k-1) + C_i v(k), \\ z(k) = \mathscr{D}_h E_\varepsilon x(k) + F_i(I - \Psi_m)u(k-1) + H_i v(k), \end{cases} \tag{13}$$

where

$$\mathscr{A}_h = \mathscr{A}_{im} = A_i + B_i \Psi_m K_h, \mathscr{D}_h = \mathscr{D}_{im} = D_i + F_i \Psi_m K_h. \tag{14}$$

Definition 1 (see [18]). The MSSPS (13) with $v(k) = 0$ is said to be stochastic stable (SS), if for any (δ_0, ϑ_0), such that

$$\mathscr{E}\left\{ \sum_{k=0}^{\infty} \|\delta(k)\|^2 | \delta_0, \vartheta_0 \right\} < \infty. \tag{15}$$

Definition 2 (see [18]). The MSSPS (13) with is called SS with a $\mathscr{H}_\infty$ performance level γ, if the MSSPS (11) is SS, and under zero initial condition, one gets

$$\sum_{k=0}^{\infty} \mathscr{E}\{\|\delta(k)\|^2\} < \gamma^2 \sum_{k=0}^{\infty} \mathscr{E}\{\|\varrho(k)\|^2\}. \tag{16}$$

Lemma 2 (see [11]). *For symmetric matrices $\mathscr{Z}_t (t = 1, 2, 3, 4)$ and matrix $\mathscr{Z}_5$ satisfies*

$$\begin{aligned} &\mathscr{Z}_1 > 0, \\ &\begin{bmatrix} \mathscr{Z}_1 + \overline{\epsilon}\mathscr{Z}_3 & \overline{\epsilon}\mathscr{Z}_5^\top \\ * & \overline{\epsilon}\mathscr{Z}_2 \end{bmatrix} > 0, \\ &\begin{bmatrix} \mathscr{Z}_1 + \overline{\epsilon}\mathscr{Z}_3 & \overline{\epsilon}\mathscr{Z}_5^\top \\ * & \overline{\epsilon}\mathscr{Z}_2 + \overline{\epsilon}^2\mathscr{Z}_4 \end{bmatrix} > 0, \end{aligned} \tag{17}$$

such that $E_\epsilon \mathscr{Z}_\epsilon = \mathscr{Z}_\epsilon^\top E_\epsilon > 0$ for all $\epsilon \in (0, \overline{\epsilon}]$, where

$$\mathscr{Z}_\epsilon = \begin{bmatrix} \mathscr{Z}_1 + \epsilon\mathscr{Z}_3 & \epsilon\mathscr{Z}_5^\top \\ * & \epsilon\mathscr{Z}_2 + \epsilon^2\mathscr{Z}_4 \end{bmatrix}. \tag{18}$$

Lemma 3 (see [11]). *For given a scalar $\overline{\epsilon} > 0$, $\mathscr{W}_1$, $\mathscr{W}_2$, and $\mathscr{W}_3$ are with suitable dimensions. For all $\epsilon \in (0, \overline{\epsilon}]$, if $\mathscr{W}_1 + \epsilon\mathscr{W}_1 + \epsilon^2\mathscr{W}_1 > 0$, one gets*

$$\begin{aligned} &\mathscr{W}_1 > 0, \\ &\mathscr{W}_1 + \overline{\epsilon}\mathscr{W}_1 > 0, \\ &\mathscr{W}_1 + \overline{\epsilon}\mathscr{W}_2 + \overline{\epsilon}^2\mathscr{W}_3 > 0. \end{aligned} \tag{19}$$

3. Main Results

Theorem 1. *The augmented MSSPS (13) is said to be SS with a given $\mathscr{H}_\infty$ performance, if there exists symmetric matrices $\overline{P}_h > 0$, $\overline{Q}_h > 0$, $\mathscr{Z}_1$, $\mathscr{Z}_2$, $\mathscr{Z}_3$, $\mathscr{Z}_4$, and $\mathscr{Z}_5$, $\overline{K}_{\epsilon f}$, one has*

$$\mathscr{Z}_1 > 0, \tag{20}$$

$$\begin{bmatrix} \mathscr{Z}_1 + \overline{\epsilon}\mathscr{Z}_3 & \overline{\epsilon}\mathscr{Z}_5^\top \\ \overline{\epsilon}\mathscr{Z}_5 & \overline{\epsilon}\mathscr{Z}_2 \end{bmatrix} > 0, \tag{21}$$

$$\begin{bmatrix} \mathscr{Z}_1 + \overline{\epsilon}\mathscr{Z}_3 & \overline{\epsilon}\mathscr{Z}_5^\top \\ \overline{\epsilon}\mathscr{Z}_5 & \overline{\epsilon}\mathscr{Z}_2 + \overline{\epsilon}^2\mathscr{Z}_4 \end{bmatrix} > 0, \tag{22}$$

$$\begin{bmatrix} \Theta_h^{1(t)} & \Theta_h^{2(t)\top}\mathscr{T}_h & \Theta_h^{3(t)\top}\mathscr{T}_h & \Theta_h^{4(t)\top} \\ * & \Theta_h^5 & 0 & 0 \\ * & * & \Theta_h^6 & 0 \\ * & * & * & -I \end{bmatrix} < 0, \quad (t = \ell, \imath, \jmath). \tag{23}$$

Meanwhile, the controller gains can be achieved:

$$K_h = \overline{K}_{\varepsilon h}(\mathscr{Y}_1^\top + \epsilon\mathscr{Y}_1^\top)^{-1}, \quad (h \in \mathcal{S}), \tag{24}$$

where

$$
\begin{aligned}
\Theta_h^{1(\ell)} &= \operatorname{diag}\left\{\overline{P}_h - (\mathscr{V}_1 + \mathscr{V}_1^\top), \overline{Q}_h - (Y_h + Y_h^\top), -\gamma^2 I\right\},\\
\Theta_h^{1(1)} &= \operatorname{diag}\left\{\overline{P}_h - (\mathscr{Z}_{\overline{\epsilon}} + \mathscr{Z}_{\overline{\epsilon}}^\top), \overline{Q}_h - (Y_h + Y_h^\top), -\gamma^2 I\right\},\\
\Theta_h^{1(j)} &= \operatorname{diag}\left\{\overline{P}_h - (\mathscr{Z}_{\overline{\epsilon}} + \mathscr{Z}_{\overline{\epsilon}}^\top), \overline{Q}_h - (Y_h + Y_h^\top), -\gamma^2 I\right\},\\
\Theta_h^{2(\ell)} &= \left[\begin{array}{ccc} A_i\mathscr{Y}_1 + B_i\Psi_h\overline{K}_{\varepsilon f}E_0 & B_i(I-\Psi_h)Y_h & C_i \end{array}\right],\\
\Theta_h^{2(1)} &= \left[\begin{array}{ccc} A_i\mathscr{Y}_2 + B_i\Psi_h\overline{K}_{\varepsilon f}E_{\overline{\epsilon}} & B_i(I-\Psi_h)Y_h & C_i \end{array}\right],\\
\Theta_h^{2(j)} &= \left[\begin{array}{ccc} A_i\mathscr{Y}_3 + B_i\Psi_h\overline{K}_{\varepsilon f}E_{\overline{\epsilon}} & B_i(I-\Psi_h)Y_h & C_i \end{array}\right],\\
\Theta_h^{3(\ell)} &= \left[\begin{array}{ccc} \Psi_h\overline{K}_{\varepsilon f}E_0 & (I-\Psi_h)Y_h & 0 \end{array}\right],\\
\Theta_h^{3(1)} &= \Theta_h^{3(j)}\\
\Theta_h^{4(\ell)} &= \left[\begin{array}{ccc} D_i\mathscr{Y}_1 + F_i\Psi_h\overline{K}_{\varepsilon f}E_0 & F_i(I-\Psi_h)Y_h & H_i \end{array}\right],\\
\Theta_h^{4(1)} &= \left[\begin{array}{ccc} D_i\mathscr{Y}_2 + F_i\Psi_h\overline{K}_{\varepsilon f}E_{\overline{\epsilon}} & F_i(I-\Psi_h)Y_h & H_i \end{array}\right],\\
\Theta_h^{4(j)} &= \left[\begin{array}{ccc} D_i\mathscr{Y}_3 + F_i\Psi_h\overline{K}_{\varepsilon f}E_{\overline{\epsilon}} & F_i(I-\Psi_h)\mathscr{Z}_{\overline{\epsilon}} & H_i \end{array}\right],\\
\Theta_h^5 &= \operatorname{diag}\{-\overline{P}_1, -\overline{P}_2, \ldots, -\overline{P}_S\},\\
\Theta_h^6 &= \operatorname{diag}\{-\overline{Q}_1, -\overline{Q}_2, \ldots, -\overline{Q}_S\},\\
\mathscr{T}_h &= \left[\begin{array}{cccc} \sqrt{\theta_{f1}}I & \sqrt{\theta_{f2}}I & \ldots & \sqrt{\theta_{fN_r}}I \end{array}\right],\\
\mathscr{Z}_{\overline{\epsilon}} &= \mathscr{V}_1 + \overline{\epsilon}\mathscr{V}_2,\\
\mathscr{Y}_1 &= \mathscr{W}_1,\\
\mathscr{Y}_2 &= \mathscr{W}_1 + \overline{\epsilon}\mathscr{W}_2,\\
\mathscr{Y}_3 &= \mathscr{W}_1 + \overline{\epsilon}\mathscr{W}_2 + \overline{\epsilon}^2\mathscr{W}_3,\\
\mathscr{V}_1 &= \left[\begin{array}{cc} \mathscr{Z}_1 & 0 \\ \mathscr{Z}_5 & \mathscr{Z}_2 \end{array}\right],\\
\mathscr{V}_2 &= \left[\begin{array}{cc} \mathscr{Z}_3 & \mathscr{Z}_5^\top \\ 0 & \mathscr{Z}_4 \end{array}\right],\\
\mathscr{W}_1 &= \left[\begin{array}{cc} \mathscr{Z}_1 & 0 \\ 0 & 0 \end{array}\right],\\
\mathscr{W}_2 &= \left[\begin{array}{cc} \mathscr{Z}_3 & \mathscr{Z}_5^\top \\ \mathscr{Z}_5 & \mathscr{Z}_2 \end{array}\right],\\
\mathscr{W}_3 &= \left[\begin{array}{cc} 0 & 0 \\ 0 & \mathscr{Z}_4 \end{array}\right],\\
E_0 &= \left[\begin{array}{cc} I_{n_s} & 0 \\ 0 & 0 \end{array}\right],\\
E_{\overline{\epsilon}} &= \left[\begin{array}{cc} I_{n_s} & 0 \\ 0 & \overline{\epsilon}I_{n_h} \end{array}\right].
\end{aligned}
\tag{25}
$$

Proof. Recalling the LMIs (20)–(22) and by means of Lemma 2, for all $\epsilon \in (0, \overline{\epsilon}]$, we have

$$
\left[\begin{array}{cccc} \widetilde{\Theta}_h^1 & \widetilde{\Theta}_h^{2\top}\mathscr{T}_h & \widetilde{\Theta}_h^{3\top}\mathscr{T}_h & \widetilde{\Theta}_h^{4\top} \\ * & \Theta_h^5 & 0 & 0 \\ * & * & \Theta_h^6 & 0 \\ * & * & * & -I \end{array}\right] < 0, \tag{26}
$$

where

$$
\begin{aligned}
\widetilde{\Theta}_h^1 &= \operatorname{diag}\left\{\overline{P}_h - (\mathscr{Z}_\epsilon + \mathscr{Z}_\epsilon^\top), \overline{Q}_h - (\mathscr{Z}_\epsilon + \mathscr{Z}_\epsilon^\top), -\gamma^2 I\right\},\\
\widetilde{\Theta}_h^2 &= \left[\begin{array}{ccc} A_iE_\epsilon\mathscr{Z}_\epsilon + B_i\Psi_hK_h\mathscr{Z}_\epsilon^\top E_\epsilon & B_i(I-\Psi_h)\mathscr{Z}_\epsilon & C_i \end{array}\right],\\
\widetilde{\Theta}_h^3 &= \left[\begin{array}{ccc} \Psi_hK_h\mathscr{Z}_\epsilon^\top E_\epsilon & (I-\Psi_h)\mathscr{Z}_\epsilon & 0 \end{array}\right],\\
\widetilde{\Theta}_h^4 &= \left[\begin{array}{ccc} D_iE_\epsilon\mathscr{Z}_\epsilon + F_i\Psi_hK_h\mathscr{Z}_\epsilon^\top E_\epsilon & F_i(I-\Psi_h)\mathscr{Z}_\epsilon & H_i \end{array}\right].
\end{aligned}
\tag{27}
$$

By virtue of Lemma 3 and the LMIs (13)–(21), for all $\epsilon \in (0, \overline{\epsilon}]$, one derives the fact that $E_\epsilon\mathscr{Z}_\epsilon = \mathscr{Z}_\epsilon^\top E_\epsilon > 0$. Furthermore, it is well recognized that the following inequalities $(\mathscr{Z}_\epsilon^\top - \overline{P}_h)P_h(\mathscr{Z}_\epsilon - \overline{P}_h) \geq 0$ and $(\mathscr{Z}_\epsilon^\top - \overline{Q}_h)Q_h(\mathscr{Z}_\epsilon - \overline{Q}_h) \geq 0$ hold. Denote $\overline{P}_h = P_h^{-1}$ and $\overline{Q}_h = Q_h^{-1}$, and we obtain

$$
\left[\begin{array}{cccc} \widehat{\Theta}_h^1 & \widehat{\Theta}_h^{2\top}\mathscr{T}_h & \widehat{\Theta}_h^{3\top}\mathscr{T}_h & \widehat{\Theta}_h^{4\top} \\ * & \Theta_h^5 & 0 & 0 \\ * & * & \Theta_h^6 & 0 \\ * & * & * & -I \end{array}\right] < 0, \tag{28}
$$

where

$$
\begin{aligned}
\widehat{\Theta}_h^1 &= \operatorname{diag}\left\{-\mathscr{Z}_\epsilon^\top P_h\mathscr{Z}_\epsilon, -\mathscr{Z}_\epsilon^\top Q_h\mathscr{Z}_\epsilon, -\gamma^2 I\right\},\\
\widehat{\Theta}_h^2 &= \left[\begin{array}{ccc} \mathscr{A}_hE_\epsilon\mathscr{Z}_\epsilon & B_i(I-\Psi_h)\mathscr{Z}_\epsilon & C_i \end{array}\right],\\
\widehat{\Theta}_h^3 &= \left[\begin{array}{ccc} \Psi_hK_hE_\epsilon\mathscr{Z}_\epsilon & (I-\Psi_h)\mathscr{Z}_\epsilon & 0 \end{array}\right],\\
\widehat{\Theta}_h^4 &= \left[\begin{array}{ccc} \mathscr{D}_hE_\epsilon\mathscr{Z}_\epsilon & F_i(I-\Psi_h)\mathscr{Z}_\epsilon & H_i \end{array}\right],\\
\widehat{\Theta}_h^5 &= \operatorname{diag}\left\{-P_1^{-1}, -P_2^{-1}, \ldots, -P_S^{-1}\right\},\\
\widehat{\Theta}_h^6 &= \operatorname{diag}\left\{-Q_1^{-1}, -Q_2^{-1}, \ldots, -Q_S^{-1}\right\}.
\end{aligned}
\tag{29}
$$

Recalling (28), with the help of term, $\operatorname{diag}\{\mathscr{Z}_\epsilon^{-\top}, \mathscr{Z}_\epsilon^{-\top}, I, \ldots, I\}$ and its transpose, for any $\mathscr{Z}_\epsilon = \mathscr{Y}_1 + \epsilon\mathscr{Y}_2$, the following inequality holds:

$$
\left[\begin{array}{cccc} \overline{\Theta}_h^1 & \overline{\Theta}_h^{2\top}\mathscr{T}_h & \overline{\Theta}_h^{3\top}\mathscr{T}_h & \overline{\Theta}_h^{4\top} \\ * & \Theta_h^5 & 0 & 0 \\ * & * & \Theta_h^6 & 0 \\ * & * & * & -I \end{array}\right] < 0, \tag{30}
$$

where

$$\begin{aligned}
\overline{\Theta}_h^1 &= \operatorname{diag}\{-P_h, -Q_h, -\gamma^2 I\},\\
\overline{\Theta}_h^2 &= [\ \mathscr{A}_h E_\epsilon \quad B_i(I-\Psi_h) \quad C_i\ ],\\
\overline{\Theta}_h^3 &= [\ \Psi_h K_h E_\epsilon \quad (I-\Psi_h) \quad 0\ ],\\
\overline{\Theta}_h^4 &= [\ \mathscr{D}_h E_\epsilon \quad F_i(I-\Psi_h) \quad H_i\ ].
\end{aligned} \tag{31}$$

Next, choose a Lyapunov functional candidate as

$$V(k, x(k), u(k), r(k)) = x^\top(k) P(r(k)) x(k) + u^\top(k-1) Q(r(k)) u(k-1). \tag{32}$$

Calculating the time derivative of (32), one gets $V(k, x(k), u(k), r(k))$, and one has

$$\begin{aligned}
&\mathscr{E}\{V(k+1, x(k+1), u(k+1), r(k+1) = g | k, x(k), u(k), f)\},\\
&\quad - V(k, x(k), u(k), r(k)),\\
&x^\top(k+1)\mathscr{P}_h x(k+1) - x^\top(k) P_h x(k) + u^\top(k)\mathscr{Q}_h u(k),\\
&\quad - u^\top(k-1) Q_h u(k-1),\\
&x^\top(k)\left(P_h + E_\varepsilon \mathscr{A}_h^\top \mathscr{P}_h \mathscr{A}_h E_\varepsilon\right) x(k) + x^\top(k) E_\varepsilon \mathscr{A}_h^\top \mathscr{P}_h B_i (I-\Psi_h) u(k-1),\\
&\quad + u^\top(k-1)(I-\Psi_h) B_i^\top \mathscr{P}_h \mathscr{A}_h E_\varepsilon x(k),\\
&\quad + x^\top(k) E_\varepsilon \mathscr{A}_h^\top \mathscr{P}_h C_i v(k) + v^\top(k) C_i^\top \mathscr{P}_h \mathscr{A}_h E_\varepsilon x(k),\\
&\quad + u^\top(k-1)(I-\Psi_h)^\top B_i^\top \mathscr{P}_h B_i (I-\Psi_h) u(k-1),\\
&\quad + u^\top(k-1)(I-\Psi_h) B_i^\top \mathscr{P}_h C_i v(k),\\
&\quad + v^\top(k) C_i^\top \mathscr{P}_h B_i (I-\Psi_h) u(k-1) + v^\top(k) C_i^\top \mathscr{P}_h C_i v(k),\\
&\quad + \left[\Psi_h K_h E_\varepsilon x(k) + (I-\Psi_h) u(k-1)\right]^\top \mathscr{Q}_h,\\
&\quad \times \left[\Psi_h K_h E_\varepsilon x(k) + (I-\Psi_h) u(k-1)\right],\\
&\quad + x^\top(k) E_\varepsilon K_h^\top \Psi_h^\top \mathscr{Q}_h \Psi_h K_h E_\varepsilon x(k),\\
&\quad + x^\top(k) E_\varepsilon K_h^\top \Psi_h^\top \mathscr{Q}_h (I-\Psi_h) u(k-1),\\
&\quad + u^\top(k-1)(I-\Psi_h) \mathscr{Q}_h \Psi_h K_h E_\varepsilon x(k),\\
&\quad + u^\top(k-1)(I-\Psi_h) \mathscr{Q}_h (I-\Psi_h) u(k-1).
\end{aligned} \tag{33}$$

where $\mathscr{P}_h = \sum_{g\in\mathscr{N}_r} \theta_{hl} P_g$, $\mathscr{Q}_h = \sum_{g\in\mathscr{N}_r} \theta_{hl} Q_g$.

Note that inequality (33) can be rewritten as

$$\mathscr{E}\{\Delta V(k)\} = \vartheta^\top(k) \overrightarrow{\Theta}_h \vartheta(k), \tag{34}$$

where

$$\begin{aligned}
\vartheta(k) &= \left[\ x^\top(k) \quad u^\top(k-1) \quad v^\top(k)\ \right],\\
\overrightarrow{\Theta}_h^1 &= \operatorname{diag}\{-P_h, -Q_h, 0\},\\
\overrightarrow{\Theta}_h &= \overrightarrow{\Theta}_h^1 + \overline{\Theta}_h^{2\top} \mathscr{P}_h \overline{\Theta}_h^2 + \overline{\Theta}_h^{3\top} \mathscr{Q}_h \overline{\Theta}_h^3.
\end{aligned} \tag{35}$$

In case of $v(k) = 0$, by resorting to (34), it is clear that

$$\mathscr{E}\{\Delta V(k)\} \le \underline{\vartheta}^\top(k) \underline{\Theta}_h \underline{\vartheta}(k) \le -\chi \mathscr{E}\left\{\|x(k)\|^2\right\}, \tag{36}$$

where $\underline{\vartheta}(k) = \left[\ x^\top(k) \quad u^\top(k-1)\ \right]$, $\underline{\Theta}_h = \underline{\Theta}_h^1 + \underline{\Theta}_h^{2\top} \mathscr{P}_h \underline{\Theta}_h^2 + \underline{\Theta}_h^{3\top} \mathscr{Q}_h \underline{\Theta}_h^3$, $\underline{\Theta}_h^1 = \operatorname{diag}\{-P_h, -Q_h\}$, $\underline{\Theta}_h^2 = [\ \mathscr{A}_h E_\epsilon \quad B_i(I-\Psi_h)\ ]$, $\underline{\Theta}_h^3 = [\ \mathscr{D}_h E_\epsilon \quad F_i(I-\Psi_h)\ ]$, and $\varpi = \min_{f\in\mathscr{S}, p, q\in\{1,2,\ldots,r\}} \{\lambda_{\min}(\underline{\Theta}_h)\}$. Apparently, condition (30) implies $\varpi > 0$. Therefore, we have

$$\begin{aligned}
&\mathscr{E}\left\{\sum_{k=0}^{\infty} \|x(k)\|^2\right\} < -\frac{1}{\varpi} \mathscr{E}\left\{\sum_{k=0}^{\infty} \Delta V(k)\right\},\\
&\le \frac{1}{\varpi} \mathscr{E}\{V(0, x(0), u(0), r(0))\} < \infty.
\end{aligned} \tag{37}$$

By Definition 1, in case of $v(k) = 0$, one concludes that the MSSPS (13) is SS.

In the following, when $v(k) \neq 0$, we first denoting the H_∞ performance as

$$\mathcal{J}(T) = \mathcal{E}\left\{\sum_{k=0}^{T} z^{\top}(k)z(k) - \gamma^2 v^{\top}(k)v(k)\right\}. \tag{38}$$

Taking (34) and (38) into consideration, $J(T)$ is shown as follows:

$$\mathcal{J}(T) \le \mathcal{E}\left\{\sum_{k=0}^{T}\left[z^{\top}(k)z(k) - \gamma^2 v^{\top}(k)v(k) + \Delta V(k)\right]\right\} \le \vartheta^{\top}(k)\Theta_h^{'}\vartheta(k), \tag{39}$$

where

$$\begin{aligned}\Theta_h^{'} &= \overrightarrow{\Theta}_h + \Theta_h^{4\top}\Theta_h^4,\\ \Theta_h^4 &= \left[\begin{array}{ccc}\mathscr{D}_h E_\epsilon & F_i(I-\Psi_h) & H_i\end{array}\right].\end{aligned} \tag{40}$$

Clearly, it is easy to derive the following condition from (30) and (39) that

$$\mathcal{J}(T) < 0. \tag{41}$$

Letting $T \longrightarrow \infty$, it can be derived from (41) that

$$\sum_{k=0}^{\infty}\mathcal{E}\left\{\|z(k)\|^2\right\} \le \gamma^2\sum_{k=0}^{\infty}\mathcal{E}\left\{\|v(k)\|^2\right\}. \tag{42}$$

Therefore, recalling the Definition 2, we can conclude that the MSSPS (13) is SS with $\mathscr{H}_\infty$ performance. This ends our proof. □

Remark 2. Remarkably, in updated actuator $u(k)$, the compensation strategy is applied to schedule the information exchange. By omitting the compensation scheme, $\forall m = 1, 2, \ldots, n_u$, the received measurement signal (RMS) can be debased into

$$u_f(k) = \begin{cases} v_f(k), & \text{if } \nu(k) = m,\\ 0, & \text{otherwise.}\end{cases} \tag{43}$$

Consequently, the RMS is degraded as

$$u(k) = \Psi_{\nu(k)}v(k). \tag{44}$$

Accordingly, the closed-loop FMSSPS (13) will be reformulated as

$$\begin{cases} x(k+1) = A_i E_\epsilon x(k) + B_i\Psi_h K_h E_\epsilon x(k) + C_i v(k),\\ z(k) = D_i E_\epsilon x(k) + F_i\Psi_h K_h E_\epsilon x(k) + H_i v(k).\end{cases} \tag{45}$$

To exploit the dynamic behavior of the augmented MSSPS (45), the sufficient condition is forwarded in Corollary 1.

Corollary 1. *The augmented MSSPS (45) is called SS with a prescribed $\mathscr{H}_\infty$ performance level γ, if there exists symmetric matrices $\overline{P}_h > 0$, $\overline{Q}_h > 0$, $\mathscr{Z}_1$, $\mathscr{Z}_2$, $\mathscr{Z}_3$, $\mathscr{Z}_4$, and matrices $\mathscr{Z}_5$, $\overline{K}_{\epsilon f}$, such that (20)–(22) hold and*

$$\begin{bmatrix}\Theta_h^{1(t)} & \underline{\Theta}_h^{2(t)\top}\mathscr{T}_h & \underline{\Theta}_h^{4(t)\top}\\ * & \Theta_h^5 & 0\\ * & * & -I\end{bmatrix} < 0, \quad (t = \ell, \imath, \jmath). \tag{46}$$

Meanwhile, the ϵ-dependent controller gains are achieved as

$$K_h = \overline{K}_{\varepsilon f}\left(\mathscr{Y}_1^{\top} + \varepsilon\mathscr{Y}_1^{\top}\right)^{-1}, \tag{47}$$

where

$$\begin{aligned}\Theta_h^{2(\ell)} &= \left[\begin{array}{cc}A_i\mathscr{Y}_1 + B_i\Psi_h\overline{K}_{\varepsilon f}E_0 & C_i\end{array}\right],\\ \Theta_h^{2(\imath)} &= \left[\begin{array}{cc}A_i\mathscr{Y}_2 + B_i\Psi_h\overline{K}_{\varepsilon f}E_{\bar{\epsilon}} & C_i\end{array}\right],\\ \Theta_h^{2(\jmath)} &= \left[\begin{array}{cc}A_i\mathscr{Y}_3 + B_i\Psi_h\overline{K}_{\varepsilon f}E_{\bar{\epsilon}} & C_i\end{array}\right],\\ \Theta_h^{4(\ell)} &= \left[\begin{array}{cc}D_i\mathscr{Y}_1 + F_i\Psi_h\overline{K}_{\epsilon f}\mathscr{Z}_\epsilon^{\top}E_0 & H_i\end{array}\right],\\ \Theta_h^{4(\imath)} &= \left[\begin{array}{cc}D_i\mathscr{Y}_2 + F_i\Psi_h\overline{K}_{\epsilon f}\mathscr{Z}_\epsilon^{\top}E_{\bar{\epsilon}} & H_i\end{array}\right],\\ \Theta_h^{4(\jmath)} &= \left[\begin{array}{cc}D_i\mathscr{Y}_3 + F_i\Psi_h\overline{K}_{\epsilon f}\mathscr{Z}_\epsilon^{\top}E_{\bar{\epsilon}} & H_i\end{array}\right].\end{aligned} \tag{48}$$

4. Numerical Examples

Example 1. (a dc motor via gear train model (DMGTM)).

To explain the validity of the attained scheme, a practical DMGTM is borrowed from [19]. The dynamic equation is governed by

$$\begin{cases}\dot{\theta}_p(t) = x_2(t),\\ \ddot{\theta}_p(t) = \dfrac{g}{l}\sin\left(\theta_p(t)\right) + \dfrac{NK_h}{ml^2}I_a(t),\\ L_a\dot{I}_a(t) = -K_b N\dot{\theta} - R_i I_a(t) + u_1(t) + u_2(t) + \omega(t),\end{cases} \tag{49}$$

where the physical meaning of (49) is expressed in Table 1. The parameters are elicited as $g = 9.8\text{h/s}^2$, $K_h = 0.1\text{Nm/s}$, $K_b = 0.1\text{Vs/rad}$, $N_r = 10$, $l = 1\text{h}$, and $L_a = 50\text{mH}$. For any $i = 1, 2$, letting $x_1(t) = \theta_p(t)$, $x_2(t) = \dot{\theta}_p(t)$, and $x_3(t) = I_a(t)$, $x(t) = \left[\begin{array}{ccc}x_1^{\top}(t) & x_2^{\top}(t) & x_3^{\top}(t)\end{array}\right]^{\top}$ and $\epsilon = L_a$, and one gets

$$E_\epsilon \dot{x}(t) = A_i x(t) + B_i u(t) + C_i \omega(t), \tag{50}$$

where

$$A_1 = \begin{bmatrix} 0 & 1 & 0 \\ \dfrac{g}{l} & 0 & \dfrac{NK_h}{ml^2} \\ 0 & -K_b N_r & -R_i \end{bmatrix},$$

$$B_i = \begin{bmatrix} 0 & 0 \\ 0 & 0 \\ 1 & 1 \end{bmatrix}, \tag{51}$$

$$C_i = \begin{bmatrix} 0 & 0 & 1 \end{bmatrix}^\top, \quad (i = 1, 2),$$

$$E_\epsilon = \text{diag}\{1, 1, \epsilon\}.$$

By means of a zero-order and sampling period $T = 0.05$s, (49) can be discretized into the following model:

$$x(k+1) = A_i E_\varepsilon x(k) + B_i u(k) + C_i v(k), \tag{52}$$

where

$$A_1 = \begin{bmatrix} 1.0122 & 0.0499 & 0.0184 \\ 0.4888 & 0.9939 & 0.6302 \\ -0.1800 & -0.6302 & 7.0938 \end{bmatrix},$$

$$A_2 = \begin{bmatrix} 1.0122 & 0.0499 & 0.0142 \\ 0.4894 & 0.9981 & 0.4316 \\ -0.1389 & -0.4316 & 2.5584 \end{bmatrix},$$

$$B_1 = \begin{bmatrix} 0.0003 & 0.0003 \\ 0.0184 & 0.0184 \\ 0.6269 & 0.6269 \end{bmatrix},$$

$$B_2 = \begin{bmatrix} 0.0003 & 0.0003 \\ 0.0142 & 0.0142 \\ 0.4290 & 0.4290 \end{bmatrix},$$

$$C_1 = \begin{bmatrix} 0.0003 \\ 0.0184 \\ 0.6269 \end{bmatrix}, \tag{53}$$

$$C_2 = \begin{bmatrix} 0.0003 \\ 0.0184 \\ 0.6269 \end{bmatrix},$$

$$D_1 = \begin{bmatrix} 1 & 1 & 1 \end{bmatrix},$$

$$D_2 = \begin{bmatrix} 1 & 1 & 1 \end{bmatrix},$$

$$F_1 = \begin{bmatrix} 0.2 & 0.3 \end{bmatrix},$$

$$F_2 = \begin{bmatrix} 0.3 & 0.7 \end{bmatrix},$$

$$H_1 = 0.5,$$

$$H_2 = 0.4.$$

Table 1: The meaning of parameters.

$\theta_p(t)$	Angle of the pendulum
$I_a(t)$	Current of the motor
K_m	Motor torque constant
l	Length of shaft
$R_i\,(i = 1, 2)$	Resistance
$\dot{\theta}_p(t)$	Angular velocity
g	Gravitational constant
K_b	Back emf constant
N_r	Gear ratio
L_a	Inductance

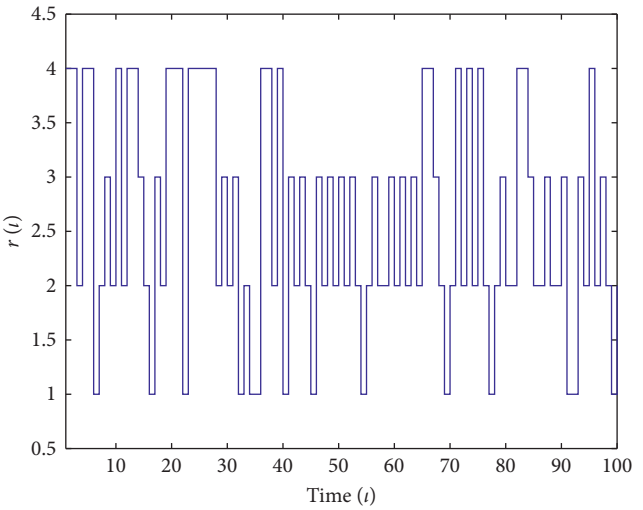

Figure 1: The possible mode switching of MP $r(k)$.

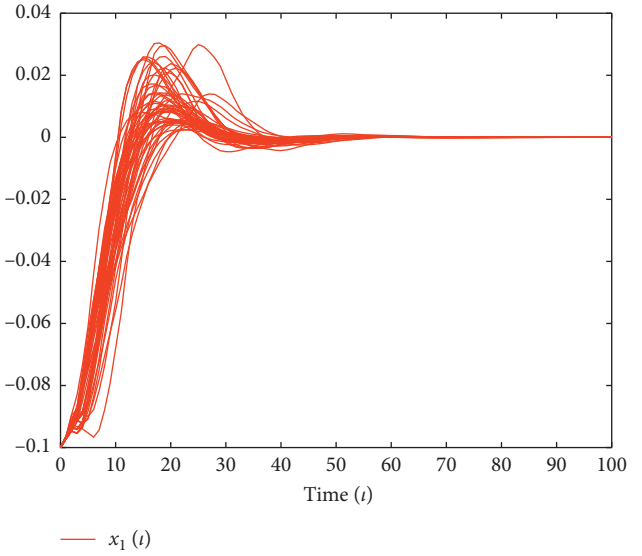

Figure 2: The evolution of states $x_1(k)$.

The TPM of the corresponding FMSSPS (1) is selected as $\Pi = \begin{bmatrix} 0.25 & 0.75 \\ 0.65 & 0.35 \end{bmatrix}$. For another MP Φ in the RAP (6), the

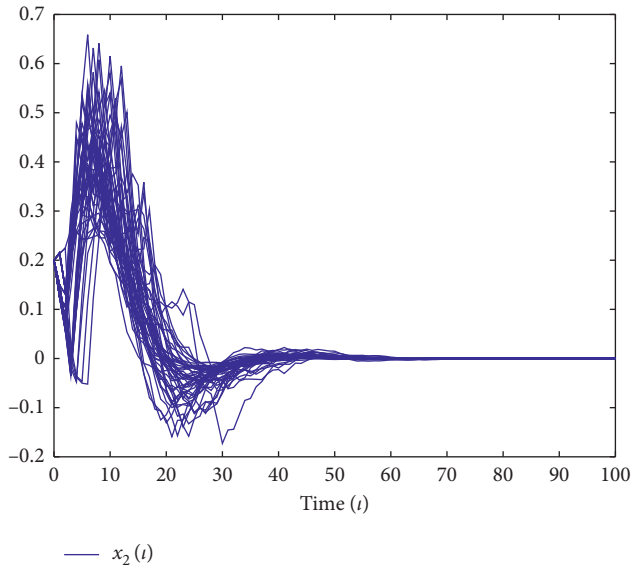

Figure 3: The evolution of states $x_2(k)$ over 50 realizations.

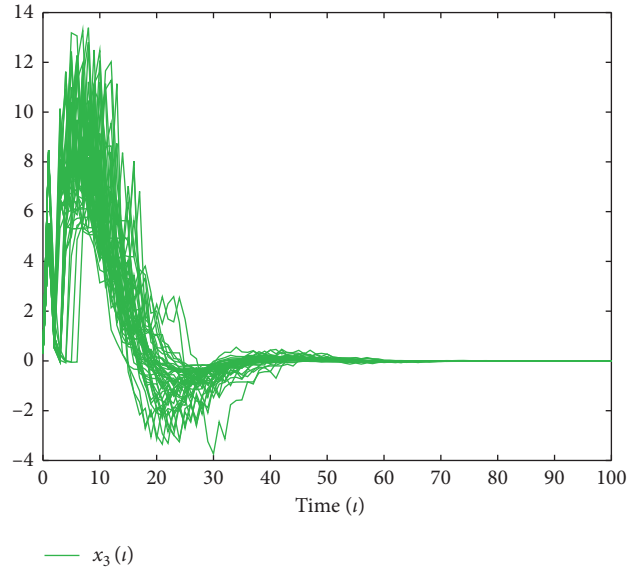

Figure 4: The evolution of states $x_3(k)$ over 50 realizations.

TPM is chosen as $\Phi = \begin{bmatrix} 0.4 & 0.6 \\ 0.5 & 0.5 \end{bmatrix}$. Consequently, by virtue of Lemma 1, the joint TPM can be inferred as

$$\Theta = \begin{bmatrix} 0.1 & 0.3 & 0.15 & 0.45 \\ 0.26 & 0.14 & 0.39 & 0.21 \\ 0.125 & 0.375 & 0.125 & 0.375 \\ 0.325 & 0.175 & 0.325 & 0.175 \end{bmatrix}. \tag{54}$$

Letting $\epsilon = 0.05$ and $\gamma = 5$. In view of LMIs of Theorem 1, the controller gains K_h can be listed as follows:

$$\begin{aligned} K_1 &= \begin{bmatrix} -143.2309 & 30.8397 & 9.2890 \\ 0 & 0 & 0 \end{bmatrix}, \\ K_2 &= \begin{bmatrix} -149.0814 & 27.7277 & 7.4494 \\ 0 & 0 & 0 \end{bmatrix}, \\ K_3 &= \begin{bmatrix} 0 & 0 & 0 \\ -151.4691 & 35.2964 & 9.9320 \end{bmatrix}, \\ K_4 &= \begin{bmatrix} 0 & 0 & 0 \\ -154.4086 & 28.5113 & 7.4207 \end{bmatrix}. \end{aligned} \tag{55}$$

In this section, according to the TPMs of corresponding plant and RAP, Figure 1 depicts the possible mode switching of Markov process $r(k)$. The evolution of states $x_1(k)$, $x_2(k)$, and $x_3(k)$ over 50 realizations is depicted in Figures 2–4,

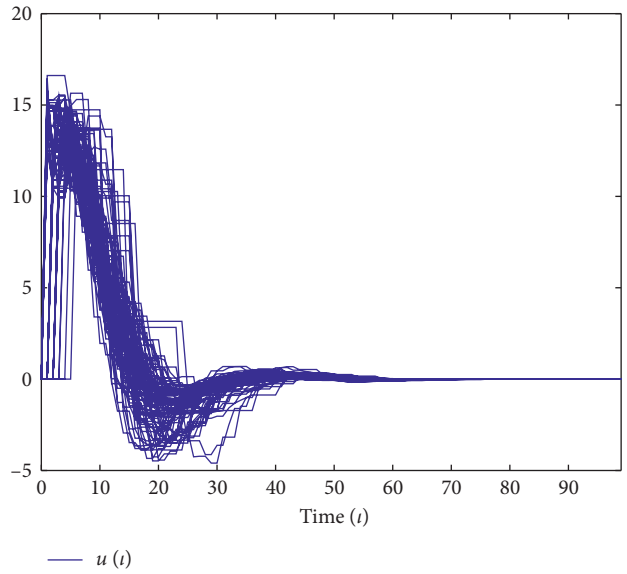

Figure 5: The control input $u(k)$ over 50 realizations.

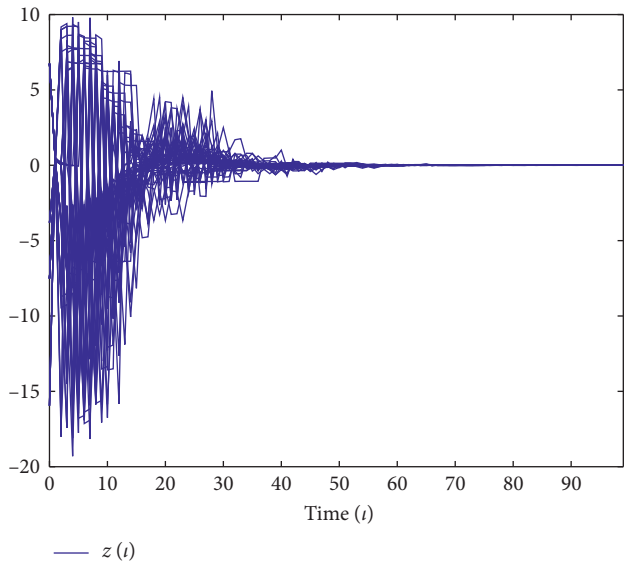

Figure 6: The output $z(k)$ over 50 realizations.

respectively. With the designed control law, the control input over 50 realizations is shown in Figure 5. Meanwhile, the evolution of the output $z(k)$ over 50 realizations is shown in Figure 6. From the above results, it is obvious that the RAP is effective in regulating the data transmission.

5. Conclusions

This paper has studied a type of MJSPS with RAP. A dynamic RAP was adopted to regulate the data transmission, in which only one sensor node has gained the access to transmit data each time. Furthermore, a joint Markov process is established, and sufficient conditions are achieved. Finally, a practical example has been exhibited to show the effectiveness of the achieved theories. Besides, to extend the achieved results to sliding mode-based filter/controller is an issue [20, 21], and we will devote ourselves to tacking in near future.

Data Availability

No data were used to support this study.

Conflicts of Interest

The author declares that there are no conflicts of interest.

References

[1] N. H. A. Nguyen, S. H. Kim, and J. Choi, "Stabilization of semi-Markovian jump systems with uncertain probability intensities and its extension to quantized control," *Mathematical Problems in Engineering*, vol. 2016, Article ID 8417475, 12 pages, 2016.

[2] Y. Wu, J. Cheng, X. Zhou, J. Cao, and M. Luo, "Asynchronous filtering for nonhomogeneous markov jumping systems with deception attacks," *Applied Mathematics and Computation*, vol. 394, Article ID 125790, 2021.

[3] J. Cheng, J. H. Park, J. Cao, and W. Qi, "A hidden mode observation approach to finite-time SOFC of Markovian switching systems with quantization," *Nonlinear Dynamics*, vol. 100, no. 1, pp. 509–521, 2020.

[4] L. Zou, Z. Wang, and H. Gao, "Observer-based H_∞ control of networked systems with stochastic communication protocol: the finite-horizon case," *Automatica*, vol. 63, pp. 366–373, 2016.

[5] J. Cheng, J. H. Park, J. Cao, and W. Qi, "Hidden Markov model-based nonfragile state estimation of switched neural network with probabilistic quantized outputs," *IEEE Transactions on Cybernetics*, vol. 50, no. 5, pp. 1900–1909, 2020.

[6] J. Cheng, D. Zhang, W. Qi, J. Cao, and K. Shi, "Finite-time stabilization of T-S fuzzy semi-Markov switching systems: a coupling memory sampled-data control approach," *Journal of The Franklin Institute*, vol. 357, no. 16, pp. 11256–11280, 2020.

[7] B. Wang, J. Cheng, and X. Zhou, "A multiple hierarchical structure strategy to quantized control of Markovian switching systems," *Applied Mathematics and Computation*, vol. 373, Article ID 125037, 2020.

[8] Z. Cao, Y. Niu, and H. Reza Karimi, "Dynamic output feedback sliding mode control for Markovian jump systems under stochastic communication protocol and its application," *International Journal of Robust and Nonlinear Control*, vol. 30, no. 17, pp. 7307–7325, 2020.

[9] W. Assawinchaichote and S. K. Nguang, "Fuzzy H_∞ output feedback control design for singularly perturbed systems with pole placement constraints: an LMI approach," *IEEE Transactions on Fuzzy Systems*, vol. 14, no. 3, pp. 361–371, 2006.

[10] J. Dong and G. H. Yang, "Control design for fuzzy discrete-time singularly perturbed systems via slow state variables feedback: an LMI based approach," *Journal of Information Science*, vol. 179, no. 17, pp. 3041–3058, 2009.

[11] Y. Wang, P. Shi, and H. Yan, "Reliable control of fuzzy singularly perturbed systems and its application to electronic circuits," *IEEE Transactions on Circuits and Systems I: Regular Papers*, vol. 65, no. 10, pp. 3519–3528, 2018.

[12] J. Wang, S. Ma, C. Zhang, and M. Fu, "Finite-time $\mathscr{H}_\infty$ filtering for nonlinear singular systems with nonhomogeneous Markov jumps," *IEEE Transactions on Cybernetics*, vol. 49, no. 6, pp. 2133–2143, 2019.

[13] K. Mei, L. Ma, R. He, and S. Ding, "Finite-time controller design of multiple integrator nonlinear systems with input saturation," *Applied Mathematics and Computation*, vol. 372, Article ID 124986, 2020.

[14] Y. Shen, Z. Wang, B. Shen, and F. E. Alsaadi, "Fusion estimation for multi-rate linear repetitive processes under weighted try-once-discard protocol," *Information Fusion*, vol. 55, pp. 281–291, 2020.

[15] Y. Xu, H. Su, Y.-J. Pan, Z.-G. Wu, and W. Xu, "Stability analysis of networked control systems with round-robin scheduling and packet dropouts," *Journal of the Franklin Institute*, vol. 350, no. 8, pp. 2013–2027, 2013.

[16] K. Liu, E. Fridman, and K. H. Johansson, "Networked control with stochastic scheduling," *IEEE Transactions on Automatic Control*, vol. 60, no. 11, pp. 3071–3076, 2015.

[17] J. Song, Z. Wang, and Y. Niu, "On H_∞sliding mode control under stochastic communication protocol," *IEEE Transactions on Automatic Control*, vol. 64, no. 5, pp. 2174–2181, 2019.

[18] J. Cheng, J. H. Park, X. Zhao, H. R. Karimi, and J. Cao, "Quantized nonstationary filtering of networked markov switching RSNSs: a multiple hierarchical structure strategy," *IEEE Transactions on Automatic Control*, vol. 65, no. 11, pp. 4816–4823, 2020.

[19] G. Wang, C. Huang, Q. Zhang, and C. Yang, "Stabilisation bound of stochastic singularly perturbed systems with Markovian switching by noise control," *IET Control Theory & Applications*, vol. 8, no. 5, pp. 367–374, 2014.

[20] L. Liu, W. X. Zheng, and S. Ding, "An adaptive SOSM controller design by using a sliding-mode-based filter and its application to buck converter," *IEEE Transactions on Circuits and Systems I: Regular Papers*, vol. 67, no. 7, pp. 2409–2418, 2020.

[21] K. Mei and S. Ding, "Second-order sliding mode controller design subject to an upper-triangular structure," *IEEE Transactions on Systems, Man, and Cybernetics: Systems*, vol. 51, no. 1, pp. 497–507, 2021.

Hindawi
Mathematical Problems in Engineering
Volume 2021, Article ID 6690729, 10 pages
https://doi.org/10.1155/2021/6690729

Research Article

Fuzzy-Model-Based Control for Markov Switching Singularly Perturbed Systems with the Stochastic Communication Protocol

Zhiguo An,[1,2] Qijuan Chen,[1] Junxiang Liu,[2] Le Luan,[2] Yong Wang,[2] Kai Zhou,[2] Wenxiong Mo,[2] and Huihong Huang[2]

[1]*School of Power and Mechanical Engineering, Wuhan University, Wuhan, China*
[2]*Guangzhou Power Supply Bureau, Guangdong Power Grid Co., Ltd., Guangzhou, China*

Correspondence should be addressed to Qijuan Chen; qjchen@whu.edu.cn

Received 16 December 2020; Revised 21 January 2021; Accepted 1 February 2021; Published 18 February 2021

Academic Editor: Shihong Ding

This work is concerned with the H_∞ control for Markov switching singularly perturbed systems with the stochastic communication protocol. To coordinate the data transmission and save the bandwidth usage, the stochastic communication protocol with a compensator is applied to schedule the information exchange. The goal of this work is to design a joint-Markov-process-based controller such that the resulting system is stochastically stable with prescribed performance. Based on the Lyapunov functional technique, a sufficient condition is derived to ensure the existence of the achieved controller. Finally, the effectiveness and correctness of the developed results are verified by the simulation example.

1. Introduction

As a significant component of hybrid systems, Markov switching systems (MSSs) have gained extensive interest due to their capability in modeling subsystems [1–4]. Note that MSSs consist of a finite number of subsystems, and some abrupt variations can be depicted by a Markov process, which is recognized as a key feature of MSSs. Nowadays, owing to their potential practical application, much effort has been devoted, and wonderful fruitful achievements have been gained for both continuous-time MSSs and discrete-time cases [5–8]. Nevertheless, as pointed out in [5, 6], the most existing results are concerned with Markov switching linear systems. Due to the widespread of nonlinear characteristics, it is natural to investigate the Markov switching nonlinear systems. Compared with the standard MSSs, the Markov switching nonlinear systems are more general as they contain high nonlinearity. Lately, the T-S fuzzy model has been tendered to deal with the system's nonlinearities [9, 10]. Benefit from the T-S fuzzy model, many Markov switching nonlinear systems can be approximated as T-S fuzzy MSSs (FMSSs). Following this excellent result, quantities of valuable results have been forwarded on T-S FMSSs [11–13]. For instance, in [11], a dropout compensation approach has been studied for T-S FMSSs. With respect to the network-induced phenomena, the cyber attack has been considered in FMSSs [13].

In many dynamic systems, the system behaviors are involved in multiple-time-scale property. The parasitic parameters, for instance, small-time constants and inductances, may result in the numerical ill-conditioned issues of physical systems. In this regard, the singular perturbation strategy has been employed to tackle the above obstacles. Thanks to singularly perturbed systems (SPSs), the multiple-time-scale-based systems can be transformed into a framework model. Note that the examples of SPSs can be widely found in power systems, airplane systems, etc. Recently, many scholars have drawn their attention to both continuous-time SPSs and discrete-time cases [14–16]. When investigating the SPSs, an extra phenomenon can be encountered, for example, the sudden changes of parameters. To tackle this occurrence, Markov switching SPSs have been studied in [17, 18]. However, the aforementioned results are concerned with linear systems, little attention has been devoted to T-S fuzzy Markov switching SPSs (FMSSPS) except for [19, 20], and this issue remains open and a challenge, which deserves further research.

In the networked control systems (NCSs), massive signals are communicated through a shared wireless network. As an unavoidable phenomenon, the NCSs always experience data collisions, fading channels, and input saturation [21]. To prevent the above shortage and mitigate the side effects, many communication protocols have been addressed to govern which sensors can obtain access to send signals such as the popular communication schedule called round-robin protocol [22, 23], try-once-discard protocol [24], and stochastic communication protocol (SCP) [25, 26]. Among them, the SCP is known as an effective method to schedule the signal exchange via a shared channel, in which only one sensor is activated to transmit data. Nevertheless, to our knowledge, no one carries out the exploration of FMSSPSs with the SCP mechanism, which motivates us to this work.

Inspired by the aforementioned discussions, our attention focuses on the control issue for FMSSPSs with the communication protocol. The main contributions are outlined as follows: in light of discrete-time FMSSPSs, to coordinate the data transmission and save the bandwidth usage, the SCP is applied to schedule the information exchange. Benefit from the novel Markov process, a mode-dependent Lyapunov functional is formulated such that the resulting system is stochastically stable, and the controller is designed.

2. Problem Formulations

Consider the ith discrete-time Markov switching system modeled by the T-S fuzzy model.

Plant Rule p: IF $\xi_1(k)$ is M_{p1}, and $\xi_2(k)$ is M_{p2}, and $\cdots$, and $\xi_g(k)$ is M_{pg}, THEN

$$\begin{cases} x_1(\iota+1) = A^{11}_{p,\varphi(\iota)}x_1(\iota) + \varepsilon A^{12}_{p,\varphi(\iota)}x_2(\iota) + B^1_{p,\varphi(\iota)}u(\iota) + C^1_{p,\varphi(\iota)}\omega(\iota), \\ x_2(\iota+1) = A^{21}_{p,\varphi(\iota)}x_1(\iota) + \varepsilon A^{22}_{p,\varphi(\iota)}x_2(\iota) + B^2_{p,\varphi(\iota)}u(\iota) + C^2_{p,\varphi(\iota)}\omega(\iota), \\ z(\iota) = D^1_{p,\varphi(\iota)}x_1(\iota) + \varepsilon D^2_{p,\varphi(\iota)}x_2(\iota) + M_{p,\varphi(\iota)}u(\iota) + G_{p,\varphi(\iota)}\omega(\iota), \end{cases} \tag{1}$$

where $x_1(\iota) \in \mathbb{R}^{n_s}$ and $x_2(\iota) \in \mathbb{R}^{n_f}$ are the fast state and the slow state, respectively. $z(k) \in \mathbb{R}^{n_z}$ and $u(\iota) \in \mathbb{R}^{n_u}$ are the output vector and control input, respectively. $\omega(\iota) \in l_2[0,\infty)$ means the disturbance signal. The sequence $\{\varphi(\iota), \iota \geq 0\}$ renders a discrete-time Markov chain (DTMC) subject to a finite set $\mathcal{N}_s = \{1, 2, \ldots, N_s\}$. Here, $\varphi(\iota)$ describes a homogeneous DTMC with the transition probability matrix of FMSSPS (1) inferred as

$$\pi_{ij} = \Pr\{\varphi(\iota+1) = j | \varphi(\iota) = i\}, \tag{2}$$

where $\pi_{ij} \geq 0$, $\sum_{j\in\mathcal{N}_s}\pi_{ij} = 1$, $\forall i, j \in \mathcal{N}_s$, and TPM $\Pi = [\pi_{ij}]_{\mathcal{N}_s\times\mathcal{N}_s}$.

For technique analysis, $\forall i \in \mathcal{N}_s$, $A^{11}_{p,\varphi(\iota)}$, $A^{12}_{p,\varphi(\iota)}$, $A^{21}_{p,\varphi(\iota)}$, $A^{22}_{p,\varphi(\iota)}$, $B^1_{p,\varphi(\iota)}$, $B^2_{p,\varphi(\iota)}$, $C^1_{p,\varphi(\iota)}$, $C^2_{p,\varphi(\iota)}$, $D^1_{p,\varphi(\iota)}$, $D^2_{p,\varphi(\iota)}$, $M_{p,\varphi(\iota)}$, and $G_{p,\varphi(\iota)}$ are denoted by A^{11}_{pi}, A^{12}_{pi}, A^{21}_{pi}, A^{22}_{pi}, B^1_{pi}, B^2_{pi}, C^1_{pi}, C^2_{pi}, D^1_{pi}, D^2_{pi}, M_{pi}, and G_{pi}, respectively.

Recall the fuzzy weighting function $\hbar_p(\xi(\iota)) = (\prod_{s=1}^{t} M_{ps}(\xi_s(\iota)))/(\sum_{p=1}^{r}\prod_{s=1}^{t} M_{ps}(\xi_s(\iota)))$, where $M_{ps}(\xi_s(\iota))$ refers to the grade of the membership degree of $\xi_s(\iota)$ in M_{ps}. In general, assume $\sum_{p=1}^{r}\hbar_p(\xi(\iota)) = 1$ and $\hbar_p(\xi(\iota)) \geq 0$.

Let $x(\iota) = \left[\, x_1^\top(\iota) \;\; x_2^\top(\iota) \,\right]^\top$; by virtue of T-S fuzzy technique, FMSSPS (1) is derived as

$$\begin{cases} x(\iota+1) = \sum_{p=1}^{r}\hbar_p(\xi(\iota))\left[A_{pi}E_\varepsilon x(\iota) + B_{pi}u(\iota) + C_{pi}\omega(\iota)\right], \\ z(\iota) = \sum_{p=1}^{r}\hbar_p(\xi(\iota))\left[D_{pi}E_\varepsilon x(\iota) + M_{pi}u(\iota) + G_{pi}\omega(\iota)\right], \end{cases} \tag{3}$$

where $E_\epsilon = \operatorname{diag}\left\{I_{n_s}, \epsilon I_{n_f}\right\}$, $A_{pi} = \begin{bmatrix} A^{11}_{pi} & A^{12}_{pi} \\ A^{21}_{pi} & A^{22}_{pi} \end{bmatrix}$, $B_{pi} = \begin{bmatrix} B^1_{pi} \\ B^2_{pi} \end{bmatrix}$, $C_{pi} = \begin{bmatrix} C^1_{pi} \\ C^2_{pi} \end{bmatrix}$, and $D_{pi} = \begin{bmatrix} D^1_{pi} & D^2_{pi} \end{bmatrix}$.

In the NCSs, some redundant signals are communicated in the conventional data transmission manner, which may result in unfavorite phenomena, for instance, data collisions. The control signal $v(k)$ and the actuators $u(k)$ share the same communication network (CN). To prevent such unfavorite factors, the SCP scheduling is used to regulate the node order in transmitting data. Note that only one sensor is borrowed to release the signal each time, and the sensors are chosen in a stochastic way. In general, letting $\psi(\iota) \in \{1, 2, \ldots, N_c\}$ signifies the chosen actuator which gains the permission to access the CN at the time interval ι. Notably, $\psi(\iota)$ can be recognized as a stochastic process regulated by another DTMC obeying a set $\mathcal{N}_c = \{1, 2, \ldots, N_c\}$, and TPM $\Psi = [\tau_{mn}]_{N_c\times N_c}$ is determined by

$$\tau_{mn} = \Pr\{\psi(\iota+1) = n | \psi(\iota) = m\}, \tag{4}$$

where $\forall m, n \in \mathcal{N}_c$, $\tau_{mn} \in [0, 1]$, and $\sum_{n\in\mathcal{N}_c}\tau_{mn} = 1$.

Let $v(\iota) = \left[v_1^\top(\iota) \;\; v_2^\top(\iota) \;\; \cdots \;\; v_{n_u}^\top(\iota) \right]$ and $u(\iota) = \left[u_1^\top(\iota) \;\; u_2^\top(\iota) \;\; \cdots \;\; u_{n_u}^\top(\iota) \right]$, where $v_m(\iota)$ denotes the mth control input vector and u_n signifies the nth actuator. Firstly, assume that a set of zero-order hold is employed in the signal transmission. Accordingly, the mth actuator $u_m(\iota)$ is updated by the following principle:

$$u_m(\iota) = \begin{cases} v_m(\iota), & \text{if } \psi(\iota) = m, \\ u_m(\iota - 1), & \text{otherwise.} \end{cases} \tag{5}$$

Aiming at describing the data transmission strategy of actuators mathematically, a Kronecker sign function is inferred as

$$\delta(x - y) = \begin{cases} 1, & \text{if } x = y, \\ 0, & \text{otherwise.} \end{cases} \tag{6}$$

As indicated from the updating principle (5), the mth actuator $u_m(\iota)$ is updated when $\psi(\iota) = m$. Consequently, for $\forall \iota$, the updated actuator $u(\iota)$ can be devised as

$$u(\iota) = \Psi_{\psi(\iota)} v(\iota) + \left(I - \Psi_{\psi(\iota)}\right) u(\iota - 1), \tag{7}$$

where $\Psi_m \triangleq \operatorname{diag}\left\{\delta_m^1, \delta_m^2, \ldots, \delta_m^{n_u}\right\}$ $(m = 1, 2, \ldots, n_u)$ and $\delta_x^y = \delta(x - y)$.

The control law $v(k)$ in this work is constructed as follows:

$$v(\iota) = \sum_{q=1}^{r} \hbar_q(\xi(\iota)) K_{q,\varphi(\iota)} E_\varepsilon x(\iota), \tag{8}$$

where $K_{q,\varphi(\iota)}$ are matrices to be designed.

Substituting (8) into (3), the closed-loop FMSPS (9) is formulated as

$$\begin{cases} x(\iota + 1) = \sum_{p=1}^{r} \hbar_p(\xi(\iota)) \sum_{q=1}^{r} \hbar_q(\xi(\iota)) \left[\mathscr{A}_{pqim} E_\varepsilon x(\iota) + B_{pi}\left(I - \Psi_m\right) u(\iota - 1) + C_{pi} \omega(\iota) \right], \\ z(\iota) = \sum_{p=1}^{r} \hbar_p(\xi(\iota)) \sum_{q=1}^{r} \hbar_q(\xi(\iota)) \left[\mathscr{D}_{pqim} E_\varepsilon x(\iota) + M_{pi}\left(I - \Psi_m\right) u(\iota - 1) + G_{pi} \omega(\iota) \right], \end{cases} \tag{9}$$

where

$$\begin{aligned} \mathscr{A}_{pqim} &= A_{pi} + B_{pi} \Psi_m K_{qi}, \\ \mathscr{D}_{pqim} &= D_{pi} + M_{pi} \Psi_m K_{qi}. \end{aligned} \tag{10}$$

Before proceeding further, some lemmas and definitions are provided.

Definition 1 (see [27]). The FMSSPS (9) with $\omega(k) = 0$ is named stochastic stable (SS) if for any (δ_0, ϑ_0), one has

$$\mathrm{E}\left\{ \sum_{k=0}^{\infty} \|\delta(k)\|^2 | \delta_0, \vartheta_0 \right\} < \infty. \tag{11}$$

Definition 2 (see [27]). The FMSSPS (9) is named SS with a prescribed $\mathscr{H}_\infty$ performance level γ if the FMSSPS (18) is SS and under zero initial condition such that

$$\sum_{k=0}^{\infty} \mathrm{E}\left\{ \|\delta(k)\|^2 \right\} < \gamma^2 \sum_{k=0}^{\infty} \mathrm{E}\left\{ \|\varrho(k)\|^2 \right\}. \tag{12}$$

Lemma 1 (see [18]). *For given a scalar $\overline{\epsilon} > 0$, $\mathscr{W}_1$, $\mathscr{W}_2$, and $\mathscr{W}_3$ are matrices with suitable dimensions. For any $\epsilon \in (0, \overline{\epsilon}]$, $\mathscr{W}_1 + \epsilon \mathscr{W}_1 + \epsilon^2 \mathscr{W}_1 > 0$ such that*

$$\begin{aligned} \mathscr{W}_1 &> 0, \\ \mathscr{W}_1 + \overline{\epsilon} \mathscr{W}_1 &> 0, \\ \mathscr{W}_1 + \overline{\epsilon} \mathscr{W}_2 + \overline{\epsilon}^2 \mathscr{W}_3 &> 0. \end{aligned} \tag{13}$$

Lemma 2 (see [18]). *For any symmetric matrices $\mathscr{R}_t$ $(t = 1, 2, 3, 4)$ and matrix $\mathscr{R}_5$ which meets*

$$\begin{aligned} \mathscr{R}_1 &> 0, \\ \begin{bmatrix} \mathscr{R}_1 + \overline{\epsilon} \mathscr{R}_3 & \overline{\epsilon} \mathscr{R}_5^\top \\ * & \overline{\epsilon} \mathscr{R}_2 \end{bmatrix} &> 0, \\ \begin{bmatrix} \mathscr{R}_1 + \overline{\epsilon} \mathscr{R}_3 & \overline{\epsilon} \mathscr{R}_5^\top \\ * & \overline{\epsilon} \mathscr{R}_2 + \overline{\epsilon}^2 \mathscr{R}_4 \end{bmatrix} &> 0, \end{aligned} \tag{14}$$

one has $E_\epsilon \mathscr{R}_\epsilon = \mathscr{R}_\epsilon^\top E_\epsilon > 0$ for any $\epsilon \in (0, \overline{\epsilon}]$, where

$$\mathscr{R}_\varepsilon = \begin{bmatrix} \mathscr{R}_1 + \epsilon \mathscr{R}_3 & \epsilon \mathscr{R}_5^\top \\ * & \epsilon \mathscr{R}_2 + \epsilon^2 \mathscr{R}_4 \end{bmatrix}. \tag{15}$$

3. Main Results

In this section, sufficient conditions are elicited to ensure the SS and a prescribed $\mathscr{H}_\infty$ performance level of the FMSSPS (9).

Theorem 1. *The closed FMSSPS (9) is called SS with a prescribed $\mathscr{H}_\infty$ performance level γ if there exist symmetric matrices $\overline{P}_i > 0$, $\overline{Q}_i > 0$, $\mathscr{R}_1$, $\mathscr{R}_2$, $\mathscr{R}_3$, and $\mathscr{R}_4$ and matrices $\mathscr{R}_5$, $\overline{K}_{\epsilon qi}$, $\mathscr{U}_1$, and $\mathscr{U}_2$ such that*

$$\mathscr{R}_1 > 0, \tag{16}$$

$$\begin{bmatrix} \mathscr{R}_1 + \overline{\epsilon} \mathscr{R}_3 & \overline{\epsilon} \mathscr{R}_5^\top \\ \overline{\epsilon} \mathscr{R}_5 & \overline{\epsilon} \mathscr{R}_2 \end{bmatrix} > 0, \tag{17}$$

$$\begin{bmatrix} \mathscr{R}_1 + \overline{\epsilon}\mathscr{R}_3 & \overline{\epsilon}\mathscr{R}_5^\top \\ \overline{\epsilon}\mathscr{R}_5 & \overline{\epsilon}\mathscr{R}_2 + \overline{\epsilon}^2\mathscr{R}_4 \end{bmatrix} > 0, \tag{18}$$

$$\Gamma_{ppim}(t) < 0, \quad (1 \le p \le r, t = \ell, \imath, \jmath), \tag{19}$$

$$\Gamma_{pqim}(t) + \Gamma_{qpim}(t) < 0, \quad (1 \le p < q \le r, t = \ell, \imath, \jmath). \tag{20}$$

Meanwhile, the ϵ-dependent controller gains are achieved as

$$K_{qi} = \overline{K}_{\epsilon qi}\left(\mathscr{U}_1^\top + \epsilon\mathscr{U}_2^\top\right)^{-1}, \quad (q = 1, 2, \ldots, r, i \in \mathscr{N}_s), \tag{21}$$

where

$$\Gamma_{pqim}(t) = \begin{bmatrix} \Gamma_{pqi}^{1(t)} & \Gamma_{pqim}^{2(t)\top}\mathscr{T}_f & \Gamma_{pqim}^{3(t)\top}\mathscr{T}_f & \Gamma_{pqim}^{4(t)\top} \\ * & \Gamma_{pqi}^5 & 0 & 0 \\ * & * & \Gamma_{pqi}^6 & 0 \\ * & * & * & -I \end{bmatrix}, \quad (t = \ell, \imath, \jmath),$$

$$\begin{aligned}
&\Gamma_{pqi}^{1(\ell)} = \operatorname{diag}\left\{\overline{P}_i - \left(\mathscr{V}_1 + \mathscr{V}_1^\top\right), \overline{Q}_i - \left(Y_i + Y_i^\top\right), -\gamma^2 I\right\}, \Gamma_{pqi}^{1(\imath)} = \operatorname{diag}\left\{\overline{P}_i - \left(\mathscr{R}_{\overline{\epsilon}} + \mathscr{R}_{\overline{\epsilon}}^\top\right), \overline{Qm}_i - \left(Y_i + Y_i^\top\right), -\gamma^2 I\right\}, \\
&\Gamma_{pqi}^{1(\jmath)} = \operatorname{diag}\left\{\overline{P}_i - \left(\mathscr{R}_{\overline{\epsilon}} + \mathscr{R}_{\overline{\epsilon}}^\top\right), \overline{Q}_i - \left(Y_i + Y_i^\top\right), -\gamma^2 I\right\}, \Gamma_{pqim}^{2(\ell)} = \begin{bmatrix} A_{pi}\mathscr{U}_1 + B_{pi}\Psi_m\overline{K}_{\epsilon qi}E_0 & B_{pi}(I - \Psi_m)Y_i & C_{pi} \end{bmatrix}, \\
&\Gamma_{pqim}^{2(\imath)} = \begin{bmatrix} A_{pi}\mathscr{U}_2 + B_{pi}\Psi_m\overline{K}_{\epsilon qi}E_{\overline{\epsilon}} & B_{pi}(I - \Psi_m)Y_i & C_{pi} \end{bmatrix}, \Gamma_{pqim}^{2(\jmath)} = \begin{bmatrix} A_{pi}\mathscr{U}_3 + B_{pi}\Psi_m\overline{K}_{\epsilon qi}E_{\overline{\epsilon}} & B_{pi}(I - \Psi_m)Y_i & C_{pi} \end{bmatrix}, \\
&\Gamma_{pqim}^{3(\ell)} = \begin{bmatrix} \Psi_m\overline{K}_{\epsilon qi}E_0 & (I - \Psi_m)Y_i & 0 \end{bmatrix}, \Gamma_{pqim}^{3(\imath)} = \Gamma_{pqi}^{3(\jmath)} = \begin{bmatrix} \Psi_m\overline{K}_{\epsilon qi}E_{\overline{\epsilon}} & (I - \Psi_m)Y_i & 0 \end{bmatrix}, \\
&\Gamma_{pqim}^{4(\ell)} = \begin{bmatrix} D_{pi}\mathscr{U}_1 + M_{pi}\Psi_m\overline{K}_{\epsilon qi}E_0 & M_{pi}(I - \Psi_m)Y_i & G_{pi} \end{bmatrix}, \Gamma_{pqim}^{4(\imath)} = \begin{bmatrix} D_{pi}\mathscr{U}_2 + M_{pi}\Psi_m\overline{K}_{\epsilon qi}E_{\overline{\epsilon}} & M_{pi}(I - \Psi_m)Y_i & G_{pi} \end{bmatrix}, \\
&\Gamma_{pqim}^{4(\jmath)} = \begin{bmatrix} D_{pi}\mathscr{U}_3 + M_{pi}\Psi_m\overline{K}_{\epsilon qi}E_{\overline{\epsilon}} & M_{pi}(I - \Psi_m)\mathscr{R}_{\overline{\epsilon}} & G_{pi} \end{bmatrix}, \Gamma_{pqi}^5 = \operatorname{diag}\left\{-\overline{P}_1, -\overline{P}_2, \ldots, -\overline{P}_{N_r}\right\}, \\
&\Gamma_{pqi}^6 = \operatorname{diag}\left\{-\overline{Q}_1, -\overline{Q}_2, \ldots, -\overline{Q}_{N_r}\right\}, \mathscr{T}_i = \begin{bmatrix} \sqrt{\theta_{f1}}I & \sqrt{\theta_{f2}}I & \cdots & \sqrt{\theta_{fN_r}}I \end{bmatrix}, \mathscr{R}_{\overline{\epsilon}} = \mathscr{V}_1 + \overline{\epsilon}\mathscr{V}_2, \mathscr{U}_1 = \mathscr{W}_1, \\
&\mathscr{U}_2 = \mathscr{W}_1 + \overline{\epsilon}\mathscr{W}_2, \mathscr{U}_3 = \mathscr{W}_1 + \overline{\epsilon}\mathscr{W}_2 + \overline{\epsilon}^2\mathscr{W}_3, \mathscr{V}_1 = \begin{bmatrix} \mathscr{R}_1 & 0 \\ \mathscr{R}_5 & \mathscr{R}_2 \end{bmatrix}, \mathscr{V}_2 = \begin{bmatrix} \mathscr{R}_3 & \mathscr{R}_5^\top \\ 0 & \mathscr{R}_4 \end{bmatrix}, \\
&\mathscr{W}_1 = \begin{bmatrix} \mathscr{R}_1 & 0 \\ 0 & 0 \end{bmatrix}, \mathscr{W}_2 = \begin{bmatrix} \mathscr{R}_3 & \mathscr{R}_5^\top \\ \mathscr{R}_5 & \mathscr{R}_2 \end{bmatrix}, \mathscr{W}_3 = \begin{bmatrix} 0 & 0 \\ 0 & \mathscr{R}_4 \end{bmatrix}, E_0 = \begin{bmatrix} I_{n_s} & 0 \\ 0 & 0 \end{bmatrix}, E_{\overline{\epsilon}} = \begin{bmatrix} I_{n_s} & 0 \\ 0 & \overline{\epsilon}I_{n_i} \end{bmatrix}.
\end{aligned} \tag{22}$$

Proof. Combining with the linear matrix inequalities (LMIs) (17)–(19) and Lemma 2, for any $\epsilon \in (0, \overline{\epsilon}]$, it yields that

$$\begin{bmatrix} \widetilde{\Gamma}_{pqi}^1 & \widetilde{\Gamma}_{pqim}^{2\top}\mathscr{T}_i & \widetilde{\Gamma}_{pqim}^{3\top}\mathscr{T}_i & \widetilde{\Gamma}_{pqim}^{4\top} \\ * & \Gamma_{pqi}^5 & 0 & 0 \\ * & * & \Gamma_{pqi}^6 & 0 \\ * & * & * & -I \end{bmatrix} < 0, \tag{23}$$

where

$$\begin{aligned}
&\widetilde{\Gamma}_{pqi}^1 = \operatorname{diag}\left\{\overline{P}_i - \left(\mathscr{R}_\epsilon + \mathscr{R}_\epsilon^\top\right), \overline{Q}_i - \left(\mathscr{R}_\epsilon + \mathscr{R}_\epsilon^\top\right), -\gamma^2 I\right\}, \\
&\widetilde{\Gamma}_{pqim}^2 = \begin{bmatrix} A_{pi}E_\epsilon\mathscr{R}_\epsilon + B_{pi}\Psi_m K_{qi}\mathscr{R}_\epsilon^\top E_\epsilon & B_{pi}(I - \Psi_m)\mathscr{R}_\epsilon & C_{pi} \end{bmatrix}, \\
&\widetilde{\Gamma}_{pqim}^3 = \begin{bmatrix} \Psi_m K_{qi}\mathscr{R}_\epsilon^\top E_\epsilon & (I - \Psi_m)\mathscr{R}_\epsilon & 0 \end{bmatrix}, \\
&\widetilde{\Gamma}_{pqim}^4 = \begin{bmatrix} D_{pi}E_\epsilon\mathscr{R}_\epsilon + M_{pi}\Psi_m K_{qi}\mathscr{R}_\epsilon^\top E_\epsilon & M_{pi}(I - \Psi_m)\mathscr{R}_\epsilon & G_{pi} \end{bmatrix}.
\end{aligned} \tag{24}$$

Recalling Lemma 2 and LMIs (17)–(19), for any $\epsilon \in (0, \overline{\epsilon}]$, it is clear that $E_\epsilon\mathscr{R}_\epsilon = \mathscr{R}_\epsilon^\top E_\epsilon > 0$. On the contrary, with respect to the fact that inequality $(\mathscr{R}_\epsilon^\top - \overline{P}_i)P_i(\mathscr{R}_\epsilon - \overline{P}_i) \ge 0$, $(\mathscr{R}_\epsilon^\top - \overline{Q}_i)Q_i(\mathscr{R}_\epsilon - \overline{Q}_i) \ge 0$, $\overline{P}_i = P_i^{-1}$, and $\overline{Q}_i = Q_i^{-1}$, which yields

$$\begin{bmatrix} \widehat{\Gamma}^1_{pqi} & \widehat{\Gamma}^{2\top}_{pqim}\mathscr{T}_i & \widehat{\Gamma}^{3\top}_{pqim}\mathscr{T}_i & \widehat{\Gamma}^{4\top}_{pqim} \\ * & \Gamma^5_{pqi} & 0 & 0 \\ * & * & \Gamma^6_{pqi} & 0 \\ * & * & * & -I \end{bmatrix} < 0, \tag{25}$$

where

$$\begin{aligned} \widehat{\Gamma}^1_{pqi} &= \operatorname{diag}\left\{-\mathscr{R}_\epsilon^\top P_i \mathscr{R}_\epsilon, -\mathscr{R}_\epsilon^\top Q_i \mathscr{R}_\epsilon, -\gamma^2 I\right\}, \\ \widehat{\Gamma}^2_{pqim} &= \left[\begin{array}{ccc} \mathscr{A}_{pqi}E_\epsilon\mathscr{R}_\epsilon & B_{pi}(I-\Psi_m)\mathscr{R}_\epsilon & C_{pi} \end{array}\right], \\ \widehat{\Gamma}^3_{pqim} &= \left[\begin{array}{ccc} \Psi_m K_{qi}E_\epsilon\mathscr{R}_\epsilon & (I-\Psi_m)\mathscr{R}_\epsilon & 0 \end{array}\right], \\ \widehat{\Gamma}^4_{pqim} &= \left[\begin{array}{ccc} \mathscr{D}_{pqi}E_\epsilon\mathscr{R}_\epsilon & M_{pi}(I-\Psi_m)\mathscr{R}_\epsilon & G_{pi} \end{array}\right], \\ \widehat{\Gamma}^5_{pqi} &= \operatorname{diag}\left\{-P_1^{-1}, -P_2^{-1}, \ldots, -P_{N_s}^{-1}\right\}, \\ \widehat{\Gamma}^6_{pqi} &= \operatorname{diag}\left\{-Q_1^{-1}, -Q_2^{-1}, \ldots, -Q_{N_s}^{-1}\right\}. \end{aligned} \tag{26}$$

Premultiplying and postmultiplying (25) with $\operatorname{diag}\{\mathscr{R}_\epsilon^{-\top}, \mathscr{R}_\epsilon^{-\top}, I, \ldots, I\}$ and its transpose, where $\mathscr{R}_\epsilon = \mathscr{U}_1 + \epsilon\mathscr{U}_2$, yield

$$\begin{bmatrix} \overline{\Gamma}^1_{pqi} & \overline{\Gamma}^{2\top}_{pqim}\mathscr{T}_i & \overline{\Gamma}^{3\top}_{pqim}\mathscr{T}_i & \overline{\Gamma}^{4\top}_{pqim} \\ * & \Gamma^5_{pqi} & 0 & 0 \\ * & * & \Gamma^6_{pqi} & 0 \\ * & * & * & -I \end{bmatrix} < 0, \tag{27}$$

where

$$\begin{aligned} \overline{\Gamma}^1_{pqi} &= \operatorname{diag}\left\{-P_i, -Q_i, -\gamma^2 I\right\}, \\ \overline{\Gamma}^2_{pqim} &= \left[\begin{array}{ccc} \mathscr{A}_{pqi}E_\epsilon & B_{pi}(I-\Psi_m) & C_{pi} \end{array}\right], \\ \overline{\Gamma}^3_{pqim} &= \left[\begin{array}{ccc} \Psi_m K_{qi}E_\epsilon & (I-\Psi_m) & 0 \end{array}\right], \\ \overline{\Gamma}^4_{pqim} &= \left[\begin{array}{ccc} \mathscr{D}_{pqi}E_\epsilon & M_{pi}(I-\Psi_m) & G_{pi} \end{array}\right]. \end{aligned} \tag{28}$$

In the following, a Lyapunov functional for FMSSPS (9) is established:

$$\begin{aligned} V(\iota, x(\iota), u(\iota), \varphi(\iota)) &= x^\top(\iota)P(\varphi(\iota))x(\iota) \\ &\quad + u^\top(k-1)Q(\varphi(\iota))u(k-1). \end{aligned} \tag{29}$$

By calculating the difference of $V(\iota, x(\iota), u(\iota), \varphi(\iota))$, one has

$$\begin{aligned} \mathscr{E}\{\Delta V(\iota)\} &= \mathscr{E}\{V(\iota+1, x(\iota+1), u(\iota+1), \\ \varphi(\iota+1) &= g|\iota, x(\iota), u(\iota), f)\} \\ &\quad - V(\iota, x(\iota), u(\iota), \varphi(\iota)). \end{aligned} \tag{30}$$

Recalling FMSSPS (9), $\mathscr{E}\{\Delta V(\iota)\}$ can be derived as

$$\begin{aligned} \mathscr{E}\{\Delta V(\iota)\} &= x^\top(\iota+1)\mathscr{P}_i x(\iota+1) \\ &\quad - x^\top(\iota)P_i x(\iota) + u^\top(\iota)\mathscr{Q}_i u(\iota) \\ &\quad - u^\top(k-1)Q_i u(k-1), \end{aligned} \tag{31}$$

where

$$\begin{aligned} \mathscr{P}_i &= \sum_{j\in\mathscr{N}_s} \pi_{ij}P_j, \\ \mathscr{Q}_i &= \sum_{j\in\mathscr{N}_s} \theta_{ij}Q_j. \end{aligned} \tag{32}$$

In (31), the first term can be further devised as

$$\begin{aligned} & x^\top(\iota+1)\mathscr{P}_i x(\iota+1) \\ &= \sum_{p=1}^{r} \hbar_p(\xi(\iota)) \sum_{q=1}^{r} \hbar_q(\xi(\iota)) \\ &\quad \cdot \begin{bmatrix} x^\top(\iota)\left(P_i + E_\epsilon\mathscr{A}^\top_{pqim}\mathscr{P}_i\mathscr{A}_{pqim}E_\epsilon\right)x(\iota) \\ + x^\top(\iota)E_\epsilon\mathscr{A}^\top_{pqim}\mathscr{P}_i B_{pi}(I-\Psi_m)u(\iota-1) + u^\top(\iota-1)(I-\Psi_m)B^\top_{pi}\mathscr{P}_i\mathscr{A}_{pqim}E_\epsilon x(\iota) \\ + x^\top(\iota)E_\epsilon\mathscr{A}^\top_{pqim}\mathscr{P}_i C_{pi}\omega(k) + \omega^\top(k)C^\top_{pi}\mathscr{P}_i\mathscr{A}_{pqim}E_\epsilon x(\iota) \\ + u^\top(\iota-1)(I-\Psi_m)^\top B^\top_{pi}\mathscr{P}_i B_{pi}(I-\Psi_m)u(\iota-1) \\ + u^\top(\iota-1)(I-\Psi_m)B^\top_{pi}\mathscr{P}_i C_{pi}\omega(k) \\ + \omega^\top(k)C^\top_{pi}\mathscr{P}_i B_{pi}(I-\Psi_m)u(\iota-1) + \omega^\top(k)C^\top_{pi}\mathscr{P}_i C_{pi}\omega(k) \end{bmatrix}. \end{aligned} \tag{33}$$

Besides, the third term in (31) can be rewritten as

$$\begin{aligned} u^{\top}(\iota)\mathcal{Q}_i u(\iota) &= \sum_{q=1}^{r} \hbar_q(\xi(\iota))\left[\Psi_m K_{qi} E_\epsilon x(\iota) + (I-\Psi_m)u(\iota-1)\right]^{\top}\mathcal{Q}_i \\ &\quad \times \left[\Psi_m K_{qi} E_\epsilon x(\iota) + (I-\Psi_m)u(\iota-1)\right] \\ &= \sum_{q=1}^{r} \hbar_q(\xi(\iota))\begin{bmatrix} x^{\top}(\iota)E_\epsilon K_{qi}^{\top}\Psi_m^{\top}\mathcal{Q}_i\Psi_m K_{qi}E_\epsilon x(\iota) \\ + x^{\top}(\iota)E_\epsilon K_{qi}^{\top}\Psi_m^{\top}\mathcal{Q}_i(I-\Psi_m)u(\iota-1) \\ + u^{\top}(\iota-1)(I-\Psi_m)\mathcal{Q}_i\Psi_m K_{qi}E_\epsilon x(\iota) \\ + u^{\top}(\iota-1)(I-\Psi_m)\mathcal{Q}_i(I-\Psi_m)u(\iota-1) \end{bmatrix}. \end{aligned} \tag{34}$$

Combining (29)–(34) yields

$$\mathscr{E}\{\Delta V(\iota)\} = \vartheta^{\top}(k)\sum_{p=1}^{r}\hbar_p(\xi(\iota))\sum_{q=1}^{r}\hbar_q(\xi(\iota))\overrightarrow{\Gamma}_{pqim}\vartheta(k), \tag{35}$$

where

$$\begin{aligned} \vartheta(k) &= \left[\, x^{\top}(\iota) \;\; u^{\top}(\iota-1) \;\; \omega^{\top}(k)\,\right], \\ \overrightarrow{\Gamma}^{1}_{pqi} &= \mathrm{diag}\{-P_i, -Q_i, 0\}, \\ \overrightarrow{\Gamma}_{pqim} &= \overrightarrow{\Gamma}^{1}_{pqi} + \overline{\Gamma}^{2\top}_{pqim}\mathscr{P}_i\overline{\Gamma}^{2}_{pqim} + \overline{\Gamma}^{3\top}_{pqim}\mathcal{Q}_i\overline{\Gamma}^{3}_{pqim}. \end{aligned} \tag{36}$$

When $\omega(k) = 0$, it follows from inequality (35) that

$$\begin{aligned} \mathscr{E}\{\Delta V(\iota)\} &\le \overleftarrow{\vartheta}^{\top}(\iota)\sum_{p=1}^{r}\hbar_p(\xi(\iota))\sum_{q=1}^{r}\hbar_q(\xi(\iota))\overleftarrow{\Gamma}_{pqim}\overleftarrow{\vartheta}(\iota) \\ &\le -\chi\mathscr{E}\left\{\|x(\iota)\|^2\right\}, \end{aligned} \tag{37}$$

where $\overleftarrow{\vartheta}(k) = \left[\, x^{\top}(\iota)\, u^{\top}(\iota-1)\,\right]$, $\overleftarrow{\Gamma}_{pqim} = \overleftarrow{\Gamma}^{1}_{pqi} + \overleftarrow{\Gamma}^{2\top}_{pqim}\mathscr{P}_i \overleftarrow{\Gamma}^{2}_{pqim} + \overleftarrow{\Gamma}^{3\top}_{pqim}\mathcal{Q}_i\overleftarrow{\Gamma}^{3}_{pqim}$, $\overleftarrow{\Gamma}^{1}_{pqi} = \mathrm{diag}\{-P_i, -Q_i\}$, $\overleftarrow{\Gamma}^{2}_{pqim} = \left[\mathscr{A}_{pqim}\; E\mathscr{B}_{pi}(I-\Psi_m)\right]$, $\overleftarrow{\Gamma}^{3}_{pqim} = \left[\mathscr{D}_{pqim}E_\epsilon M_{pi}(I-\Psi_m)\right]$, and $\chi = \min_{f\in\mathcal{N}_s, p,q\in\{1,2,\ldots,r\}}\left\{\lambda_{\min}(\overleftarrow{\Gamma}_{pqim})\right\}$. Clearly, recalling (27), one gets $\chi > 0$. Consequently, one concludes that

$$\begin{aligned} \mathscr{E}\left\{\sum_{\iota=0}^{\infty}\|x(\iota)\|^2\right\} &< -\frac{1}{\chi}\mathscr{E}\left\{\sum_{\iota=0}^{\infty}\Delta V(\iota)\right\} \\ &\le \frac{1}{\chi}\mathscr{E}\{V(0,x(0),u(0),r(0))\} < \infty. \end{aligned} \tag{38}$$

Recalling Definition 1, when $\omega(k) = 0$, FMSSPS (16) is SS.

Next, in the case of $\omega(k) \neq 0$, we will provide the analysis of H_∞ performance for FMSSPS (16). Define the H_∞ performance index:

$$\mathscr{J}(T) = \mathscr{E}\left\{\sum_{k=0}^{T} z^{\top}(\iota)z(\iota) - \gamma^2\omega^{\top}(\iota)\omega(\iota)\right\}. \tag{39}$$

Substituting (35) into (39), $\mathscr{J}(T)$ can be formulated as

$$\begin{aligned} \mathscr{J}(T) &\le \mathscr{E}\left\{\sum_{k=0}^{T}\left[z^{\top}(\iota)z(\iota) - \gamma^2\omega^{\top}(\iota)\omega(\iota) + \Delta V(\iota)\right]\right\} \\ &\le \vartheta^{\top}(\iota)\sum_{p=1}^{r}\hbar_p(\xi(\iota))\sum_{q=1}^{r}\hbar_q(\xi(\iota))\Gamma'_{pqim}\vartheta(\iota), \end{aligned} \tag{40}$$

where

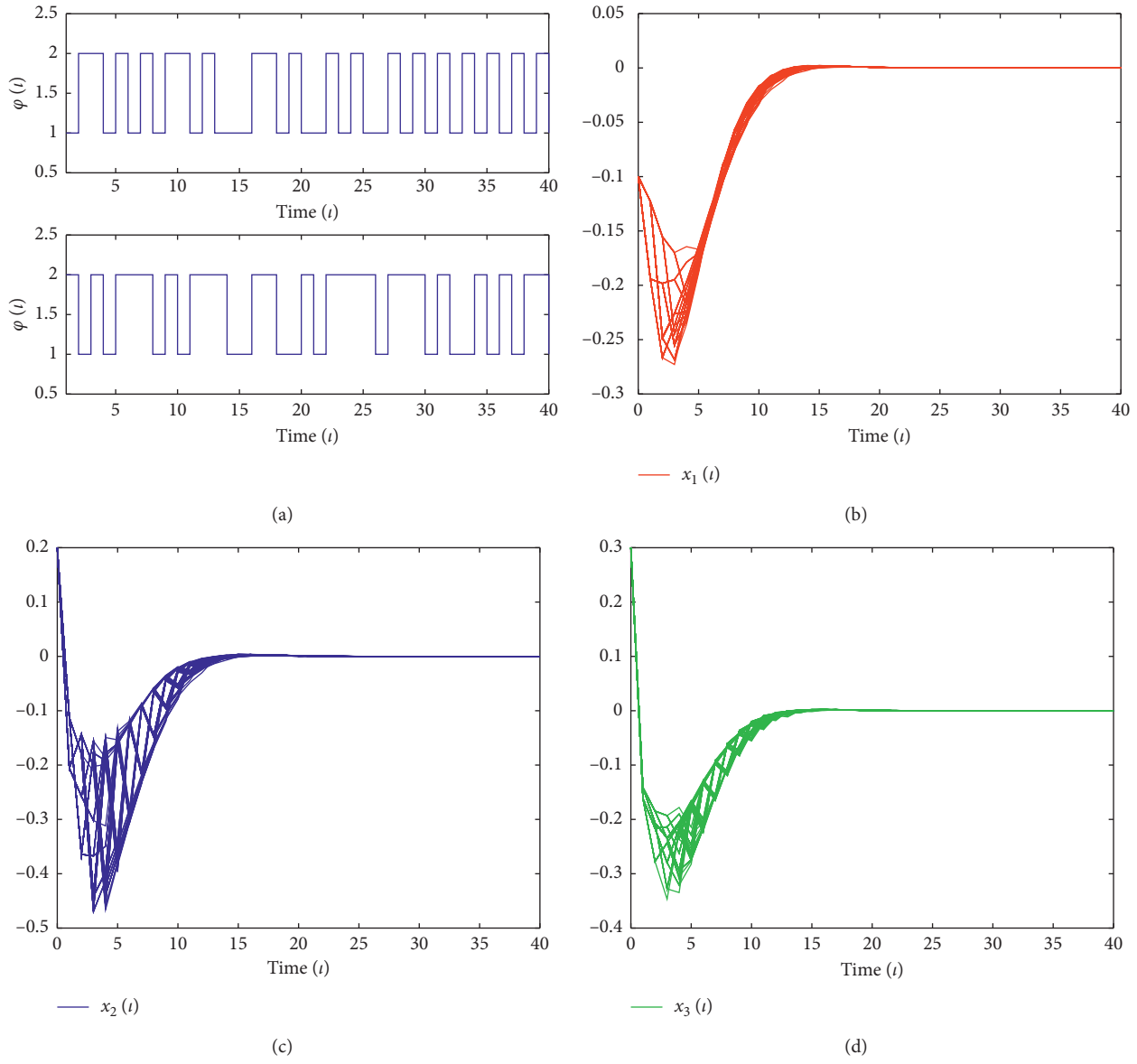

FIGURE 1: The dynamics of FMSSPS (18) in Example 1. (a) The possible mode switching of MP $'\varphi(\iota)$. (b) The evolution of state $x_1(\iota)$. (c) The evolution of state $x_2(\iota)$. (d) The evolution of state $x_3(\iota)$.

$$\begin{aligned}\Gamma'_{pqim} &= \overrightarrow{\Gamma}_{pqim} + \Gamma^{4\top}_{pqim}\Gamma^{4}_{pqim}, \Gamma^{4}_{pqim} \\ &= \left[\mathscr{D}_{pqim}E_{\epsilon} \;\; M_{pi}(I-\Psi_m) \;\; G_{pi}\right].\end{aligned} \tag{41}$$

Additionally, by applying the Schur complement to (27) and (40), one gets

$$\mathscr{J}(T) < 0. \tag{42}$$

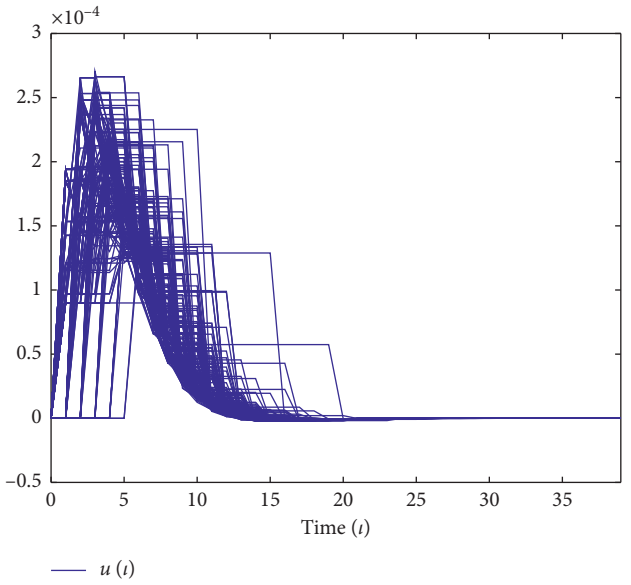

Figure 2: The control input $u(\iota)$ over 100 realizations in Example 1.

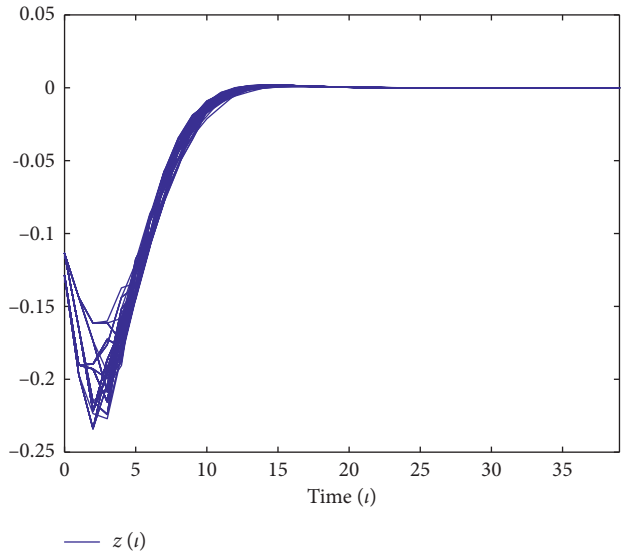

Figure 3: The output $z(\iota)$ over 100 realizations in Example 1.

Letting $T \longrightarrow \infty$, it is directly attained from (42) that

$$\sum_{\iota=0}^{\infty} \mathscr{E}\left\{\|z(\iota)\|^2\right\} \leq \gamma^2 \sum_{\iota=0}^{\infty} \mathscr{E}\left\{\|\omega(\iota)\|^2\right\}. \tag{43}$$

Accordingly, by means of Definition 2, one concludes that FMSSPS (16) is SS with $\mathscr{H}_\infty$ performance index γ. This completes the proof. □

4. Simulation Examples

Example 1. Consider FMSSPS (16) with the following parameters:

$$\begin{aligned}
A_{11} &= \begin{bmatrix} 0.3 & 1.7 & 0.3 \\ 0.8 & 0.1 & 0.3 \\ 1.4 & 0.2 & 0.9 \end{bmatrix}, \\
B_{11} &= \begin{bmatrix} 0.5 & 0.4 \\ 1.2 & 0.2 \\ 0.2 & 0.3 \end{bmatrix}, \\
C_{11} &= \begin{bmatrix} 0.6 & 0.2 & 0.7 \end{bmatrix}^\top, \\
D_{11} &= \begin{bmatrix} 0.3 & 0.4 & 0.9 \end{bmatrix}, \\
M_{11} &= \begin{bmatrix} 0.5 & 0.8 \end{bmatrix}, \\
G_{11} &= 0.7, \\
A_{12} &= \begin{bmatrix} 0.1 & 0.4 & 1.1 \\ 1.5 & 0.2 & 0.1 \\ 0.8 & 1.1 & 0.6 \end{bmatrix}, \\
B_{12} &= \begin{bmatrix} 1.4 & 0.6 \\ 0.7 & 0.1 \\ 0.5 & 0.8 \end{bmatrix}, \\
C_{12} &= \begin{bmatrix} 0.3 & 0.5 & 1 \end{bmatrix}^\top, \\
D_{12} &= \begin{bmatrix} 0.6 & 0.2 & 0.3 \end{bmatrix}, \\
M_{12} &= \begin{bmatrix} 1.5 & 0.5 \end{bmatrix}, \\
G_{12} &= 0.4, \\
A_{21} &= \begin{bmatrix} 0.2 & 1.1 & 0.1 \\ 0.2 & 1.1 & 1.2 \\ 0.6 & 0.9 & 1.1 \end{bmatrix}, \\
B_{21} &= \begin{bmatrix} 0.3 & 0.2 \\ 0.4 & 0.5 \\ 0.2 & 0.3 \end{bmatrix}, \\
C_{21} &= \begin{bmatrix} 1.8 & 0.7 & 0.2 \end{bmatrix}^\top, \\
D_{21} &= \begin{bmatrix} 0.6 & 0.9 & 0.1 \end{bmatrix}, \\
M_{21} &= \begin{bmatrix} 0.3 & 0.5 \end{bmatrix}, \\
G_{21} &= 0.5, \\
A_{22} &= \begin{bmatrix} 1.1 & 1.5 & 2.4 \\ 1.5 & 0.7 & 0.6 \\ 0.1 & 1.1 & 0.8 \end{bmatrix}, \\
B_{22} &= \begin{bmatrix} 0.6 & 0.2 \\ 0.5 & 0.3 \\ 0.7 & 0.5 \end{bmatrix}, \\
C_{22} &= \begin{bmatrix} 0.6 & 0.3 & 0.4 \end{bmatrix}^\top, \\
D_{22} &= \begin{bmatrix} 0.7 & 0.6 & 0.7 \end{bmatrix}, \\
M_{22} &= \begin{bmatrix} 0.5 & 0.6 \end{bmatrix}, \\
G_{22} &= 0.3.
\end{aligned} \tag{44}$$

The TPM of the corresponding FMSSPS (1) is selected as $\Pi = \begin{bmatrix} 0.25 & 0.75 \\ 0.65 & 0.35 \end{bmatrix}$. For another MP Φ in SCP (7), the TPM is chosen as $\Phi = \begin{bmatrix} 0.4 & 0.6 \\ 0.5 & 0.5 \end{bmatrix}$.

Let $\gamma = 5$, $\epsilon = 0.002$, $\hbar_1(\xi(\iota)) = (15 - x_2(\iota))/30$, and $\hbar_2(\xi(\iota)) = 1 - \hbar_1(\xi(\iota))$. In view of the LMIs of Theorem 1,

the controller gains K_{qi} $(q = 1, 2; f = 1, 2, 3, 4)$ can be derived as follows:

$$K_{1,1} = \begin{bmatrix} -0.0008 & -0.0016 & -0.0001 \\ -0.0010 & -0.0011 & 0.0005 \end{bmatrix},$$
$$K_{1,2} = \begin{bmatrix} -0.0011 & -0.0063 & -0.0088 \\ -0.0010 & -0.0061 & -0.0085 \end{bmatrix},$$
$$K_{2,1} = \begin{bmatrix} -0.0007 & 0.0032 & 0.0022 \\ -0.0006 & 0.0017 & 0.0015 \end{bmatrix}, \quad (45)$$
$$K_{2,2} = \begin{bmatrix} -0.0009 & 0.0146 & 0.0249 \\ -0.0010 & 0.0148 & 0.0244 \end{bmatrix}.$$

To carry on the simulation study, the external disturbance and the initial condition are selected as $\omega(k) = 0.9 \exp(-0.4\iota)\sin(50\iota)$ and $x(0) = \begin{bmatrix} -0.1 & 0.2 & 0.3 \end{bmatrix}^{\top}$, respectively. The possible mode switching of Markov process $\varphi(\iota)$ and the evolution of states $x_1(\iota)$, $x_2(\iota)$, and $x_3(\iota)$ over 100 realizations are depicted in Figure 1, respectively. The control input over 100 realizations is plotted in Figure 2. Furthermore, the evolution of the output $z(\iota)$ over 100 realizations is shown in Figure 3.

5. Conclusions

In this work, the H_∞ control problem has been discussed for FMSSPSs with the SCP. In order to coordinate the data transmission and save the bandwidth usage, the SCP with a compensator is applied to schedule the information exchange. Furthermore, some sufficient criteria have been forwarded such that the resulting system is SS. Finally, one example is exhibited to show the effectiveness and correctness of the developed results. In addition, some advanced techniques including the sliding mode-based filter will be researched in our following work [28, 29].

Data Availability

No data were utilized to support this work.

Conflicts of Interest

The authors declare that they have no conflicts of interest.

Acknowledgments

This work was supported by the Science and Technology Project of China Southern Power Grid Company Ltd. (nos. 080037KK52190037 and GZHKJXM20190108).

References

[1] L. Kang, Y. Wang, and T. Hou, "Robust control for nonlinear Markov jump systems with partially unknown transition probabilities," *Mathematical Problems in Engineerin*, vol. 2020, Article ID 1940676, 2020.

[2] B. Wang, J. Cheng, and X. Zhou, "A multiple hierarchical structure strategy to quantized control of Markovian switching systems," *Applied Mathematics and Computation*, vol. 373, Article ID 125037, 2020.

[3] Y. Wu, J. Cheng, X. Zhou, J. Cao, and M. Luo, "Asynchronous filtering for nonhomogeneous Markov jumping systems with deception attacks," *Applied Mathematics and Computation*, vol. 394, Article ID 125790, 2021.

[4] J. Cheng, Y. Wu, L. Xiong, J. Cao, and J. H. Park, "Resilient asynchronous state estimation of Markov switching neural networks: a hierarchical structure approach," *Neural Networks*, vol. 135, pp. 29–37, 2021.

[5] J. Cheng, J. H. Park, J. Cao, and W. Qi, "A hidden mode observation approach to finite-time SOFC of Markovian switching systems with quantization," *Nonlinear Dynamics*, vol. 100, no. 1, pp. 509–521, 2020.

[6] J. Cheng, Y. Shan, J. Cao, and J. H. Park, "Nonstationary control for T-S fuzzy Markovian switching systems with variable quantization density," *IEEE Transactions on Fuzzy Systems*, p. 1, 2020.

[7] J. Xiao, J. Cao, J. Cheng, S. Zhong, and S. Wen, "Novel methods to finite-times Mittag-Leffler synchronization problem of fractional-order quaternion-valued neural networks," *Information Sciences*, vol. 526, pp. 221–244, 2020.

[8] J. Cheng, D. Zhang, W. Qi, J. Cao, and K. Shi, "Finite-time stabilization of T-S fuzzy semi-Markov switching systems: a coupling memory sampled-data control approach," *Journal of The Franklin Institute*, vol. 357, no. 16, pp. 11256–11280, 2020.

[9] L. Fang, S. Ding, J. H. Park, and L. Ma, "Adaptive fuzzy control for nontriangular stochastic high-order nonlinear systems subject to asymmetric output constraints," *IEEE Transactions on Cybernetics*, p. 1, 2020.

[10] M.-J. Hu, J. H. Park, and Y.-W. Wang, "Stabilization of positive systems with time delay via the Takagi-Sugeno fuzzy impulsive control," *IEEE Transactions on Cybernetics*, p. 1, 2020.

[11] J. Cheng, W. Huang, H.-K. Lam, J. Cao, and Y. Zhang, "Fuzzy-model-based control for singularly perturbed systems with nonhomogeneous Markov switching: a dropout compensation strategy," *IEEE Transactions on Fuzzy Systems*, p. 1, 2020.

[12] Y. Shan, X. Liu, K. She, S. Zhong, J. Cheng, and X. Zhang, "Extended dissipative asynchronous filtering for T-S fuzzy switched systems with partial transition descriptions and incomplete measurements," *Nonlinear Analysis: Hybrid Systems*, vol. 37, Article ID 100906, 2020.

[13] J. Cheng, W. Huang, J. H. Park, and J. Cao, "A hierarchical structure approach to finite-time filter design for fuzzy Markov switching systems with deception attacks," *IEEE Transactions on Cybernetics*, p. 1, 2021.

[14] W. Assawinchaichote and S. K. Sing Kiong Nguang, "Fuzzy H/sub/spl infin//output feedback control design for singularly perturbed systems with pole placement constraints: an LMI approach," *IEEE Transactions on Fuzzy Systems*, vol. 14, no. 3, pp. 361–371, 2006.

[15] J. Dong and G.-H. Yang, "control design for fuzzy discrete-time singularly perturbed systems via slow state variables feedback: an LMI-based approach," *Information Sciences*, vol. 179, no. 17, pp. 3041–3058, 2009.

[16] G. Wang, C. Huang, Q. Zhang, and C. Yang, "Stabilisation bound of stochastic singularly perturbed systems with Markovian switching by noise control," *IET Control Theory Appl*, vol. 8, no. 5, pp. 367–374, 2014.

[17] H. Shen, F. Li, S. Xu, and V. Sreeram, "Slow state variables feedback stabilization for semi-markov jump systems with singular perturbations," *IEEE Transactions on Automatic Control*, vol. 63, no. 8, pp. 2709–2714, 2018.

[18] J. Wang, S. Ma, C. Zhang, and M. Fu, "Finite-time," *IEEE Trans. Cybern.*vol. 49, no. 6, pp. 2133–2143, 2019.

[19] H. Shen, F. Li, Z. G. Wu, J. H. Park, and V. Sreeram, "Fuzzy-model based nonfragile control for nonlinear singularly perturbed systems with semi-Markov jump parameters," *IEEE Trans. Fuzzy Syst.*vol. 26, no. 6, pp. 3428–3439, 2018.

[20] J. Cheng, Y. Wang, J. H. Park, J. Cao, and K. Shi, "Static output feedback quantized control for fuzzy Markovian switching singularly perturbed systems with deception attacks," *IEEE Transactions on Fuzzy Systems, Early Access*, 2021.

[21] K. Mei, L. Ma, R. He, and S. Ding, "Finite-time controller design of multiple integrator nonlinear systems with input saturation," *Applied Mathematics and Computation*, vol. 372, Article ID 124986, 2020.

[22] Y. Xu, H. Su, Y. J. Pan, Z. G. Wu, and W. Xu, "Stability analysis of networked control systems with round-robin scheduling and packet dropouts," *J Frankl Inst*, vol. 350, no. 8, pp. 2013–2027, 2013.

[23] Y. Chen, Q. Gao, J. Cheng, K. Shi, and W. Qi, "Static output feedback control for fuzzy systems with stochastic fading channel and actuator faults," *IEEE Access*, vol. 8, pp. 200714–200723, 2020.

[24] G. Walsh, H. Ye, and L. Bushnell, "Stability analysis of networked control systems," *IEEE Trans. Control Syst. Technol.*vol. 10, no. 3, pp. 438–446, 2002.

[25] J. Song, Z. Wang, and Y. Niu, "On H∞ sliding mode control under stochastic communication protocol," *IEEE Transactions on Automatic Control*, vol. 64, no. 5, pp. 2174–2181, 2019.

[26] Z. Cao, Y. Niu, and H. R. Karimi, "Dynamic output feedback sliding mode control for Markovian jump systems under stochastic communication protocol and its application," *Int J Robust Nonlinear Control*, vol. 30, pp. 7307–7325, 2020.

[27] J. Cheng, J. H. Park, X. Zhao, H. R. Karimi, and J. Cao, "Quantized nonstationary filtering of network-based Markov switching RSNSs: a multiple hierarchical structure strategy," *IEEE Transactions on Automatic Control*, vol. 65, no. 11, pp. 4816–4823, 2020.

[28] L. Liu, W. X. Zheng, and S. Ding, "An adaptive SOSM controller design by using a sliding-mode-based filter and its application to buck converter," *IEEE Transactions on Circuits and Systems-I: Regular Papers*, vol. 67, no. 7, pp. 2409–2418, 2020.

[29] K. Mei and S. Ding, "Second-order sliding mode controller design subject to an upper-triangular structure," *IEEE Transactions on Systems, Man and Cybernetics: Systems*, vol. 51, no. 1, pp. 497–507, 2021.

Hindawi
Mathematical Problems in Engineering
Volume 2021, Article ID 6637641, 9 pages
https://doi.org/10.1155/2021/6637641

Research Article

SMC-Based Synchronization of Multiple Inertial Measurement Units with Application to Attitude Tracking Control

Yuping He and Shijie Zhang

Research Center of Satellite Technology, Harbin Institute of Technology, Harbin 150080, China

Correspondence should be addressed to Yuping He; 13b918053@hit.edu.cn

Received 26 October 2020; Revised 30 December 2020; Accepted 25 January 2021; Published 17 February 2021

Academic Editor: Shihong Ding

In this paper, the attitude control of aircraft with multiple inertial measurement units under the influence of unknown gyro zero drift and external disturbance is studied. First of all, the observers are designed to estimate the zero drift biases based on the consensus algorithm. The angular velocity used for aircraft control is obtained by compensating the biases. Then, considering the external disturbance in the aircraft motion, this paper introduces a super-twisting sliding-mode algorithm to design the observer in order to compensate the disturbance. In addition, based on the proposed observers, a controller is designed to realize attitude control of the aircraft with the gyro zero drift and the external disturbance. Finally, the simulation results are given to verify the effectiveness of the proposed control law.

1. Introduction

The aircraft is the unmanned robot operated by radio remote control equipment or self-contained program control device. It is widely used in transportation, reconnaissance, photography, and other fields [1]. In recent years, the research on the aircraft is hot at home and abroad because of many advantages of the aircraft, such as the easy maintenance, high maneuverability, and high reliability [2]. In this paper, the hot spot field of aircraft-attitude control is studied. It is worth mentioning that there are two main factors that interfere with the attitude control of the aircraft: external disturbance of the aircraft and measurement deviation of the inertial measurement unit (IMU). The external disturbance of the aircraft, such as the disturbance of air flow, will lead to the unstable movement of the aircraft and lead to the failure of control. Measurement deviations, such as zero drift biases, can lead to inaccurate angular velocity of the aircraft, resulting in aircraft control failure. In addition, the attitude information obtained by a single IMU cannot meet the requirements of attitude control.

For the external disturbance, most of the current research results use the observer to estimate the disturbance and compensate the controller. As a class of nonlinear observers, sliding mode observers can work under less conservative conditions [3, 4]. Mofid et al. [5] proposed an adaptive sliding mode disturbance observer for synchronization of a fractional-order Dadras–Momeni chaotic system with time-varying disturbances is presented. Hou et al. [6] proposed a novel disturbance observer with the super-twisting sliding mode technique in order to improve the performance of the permanent magnet synchronous motor speed regulation system. To deal with the effect of the angular velocity biases caused by the zero drift, there are two main solutions in the current literature: (1) through the physical calibration of the gyro to solve the effect of zero drift bias on the measurement results [7–10] and (2) the zero drift biases can be estimated and compensated by attitude estimation [11–13], which is like the idea of disturbance estimation and compensation [14]. The authors in [15] proposed a novel analytic calibration of gyro biases with arbitrary double position based on the transformation model of gyro biases. According to the analytic-coarse-alignment principle, the sensitivities of Euler angles with respect to inertial sensor biases are analyzed uniquely. The authors in [16] proposed a bias compensation and parameter

calibration method based on Gauss–Newton algorithm. The method can effectively suppress zero drift, but its operation is cumbersome. Unscented Kalman filters (UKF) [17], extended Kalman filters (EKF) [18], and nonlinear complementary filters [19] are the popular methods of attitude estimation in the literature. However, small aircrafts are often equipped with low-precision gyros, which often carry non-Gaussian noise during the measurement process. This will cause the Kalman estimation algorithm to fail. The authors in [20] proposed a solution by constructing an observer. This work designed an observer for estimating the constant biases caused by the zero drift and proposed a coupled nonlinear spacecraft attitude controller. The authors in [21] presented a nonlinear attitude estimator based on an alternate error function, and this estimator can be implemented using a low-cost inertial measurement unit.

The conventional IMU consists of an accelerometer and a gyro for aircraft attitude control. IMU has also been widely used in smart wearable devices [22], navigation of unmanned systems [23, 24], guidance of military equipment [25], and so forth. Due to the increasing demand for inertial measurement devices in various fields, higher requirements have been placed on the measurement accuracy of inertial devices. In recent years, researchers have also proposed the configuration design of multiple accelerometers and gyro arrays. The authors in [26] analyzed the performance of the IMU and its various sensor configurations. The measurement accuracy is effectively improved by selecting the appropriate geometric configuration and the combination of multiple inertial navigation sensors. The authors in [27] used a single-axis gyro and multiple spatially distributed accelerometers to achieve the correction of the attitude measurement value. The authors in [28] designed three two-axis accelerometer inertial measurement units to measure the angular velocity of six degrees of freedom and compensated the measurement error through data fusion. The authors in [29] studied 12 accelerometers and gyros assigned IMU and proposed an EKF program to estimate the direction and amplitude of angular velocity. Research shows that attitude measurement systems that use multiple sensors have advantages over single sensor. The main difficulty in attitude control of multiple IMUs is how to design the multiple observers to synchronize [30–32]. Also, there some results have been reported about the synchronization of multiple observers/controllers [33–35].

So far, most of the research results on attitude control adopt single IMU. For the large aircraft, a single IMU can no longer meet its technical requirements [36]. Since the measurement range of a single gyro is easily saturated in high dynamic motion, its application is also limited. In addition, the attitude control of the aircraft will be unstable due to the zero drift and external disturbance. Therefore, considering the above problems, it is necessary to study the anti-interference control of aircraft attitude under multiple IMUs.

Motivated by the above discussions, this paper studies the attitude tracking control law of the aircraft with zero drift and external disturbance based on multiple inertial measurement units. As in the work [37], this paper assumes that the biases caused by the zero drift are constant in this paper. In order to solve this problem, this article will make full use of the data measured by each IMU to design the nonlinear observer, estimate the zero drift biases, and compensate for it. Then, a super-twisting sliding mode observer will be designed to compensate the disturbance. In addition, a tracking controller will be proposed. By constructing a suitable Lyapunov function, the asymptotic stability of the attitude system will be strictly proven. The asymptotic stability of the combined system of the observer and controller will be proved by the theory of cascade system. Finally, a simulation will be given to verify the effectiveness of the proposed control law. The main innovation points/contributions of the method proposed in this paper are as follows. (1) In this paper, multiple IMUs are used for measurement and observers are designed based on consensus algorithm. The observer designed in this paper can estimate the zero drift biases. (2) In this paper, a super-twisting sliding mode observer is used to estimate and eliminate external disturbances. Combined with the proposed attitude observer, the internal disturbance and external disturbance can be eliminated. (3) The aircraft model has highly nonlinear and strong coupling, the design of the control system is very difficult. In this paper, by analyzing the aircraft attitude system, the attitude observer and controller are proposed. By compensating for the zero drift, the attitude tracking control of the aircraft is realized.

2. Preliminaries

2.1. Problem Description. The attitude model is mainly composed of kinematics and dynamics equations. In this article, the Euler angles will be used to describe the attitude with respect to the inertial frame. The Euler vector is given by

$$\Phi = [\phi, \theta, \psi]^T \in \mathbb{R}^3, \tag{1}$$

where ϕ is the angle of pitch, θ is the angle of roll, and ψ is the yaw angle.

Based on the Euler angles, the attitude kinematics equation of the aircraft is

$$\dot{\Phi} = W(\Phi)w, \tag{2}$$

where $w \in \mathbb{R}^3$ is the angular velocity which can be measured by gyro, and the matrix $W(\Phi)$ is given by

$$W(\Phi) = \begin{bmatrix} 1 & \sin\phi\tan\theta & \cos\phi\tan\theta \\ 0 & \cos\phi & -\sin\phi \\ 0 & \sin\phi\sec\theta & \cos\phi\sec\theta \end{bmatrix}. \tag{3}$$

In fact, the inertial measurement unit composed of a single gyro and a single accelerometer cannot meet the measurement accuracy requirements of the aircraft. To this end, this paper will adopt multiple IMUs to attitude control.

In this paper, n sets of IMUs are considered for measurement and let $\Gamma = \{1, 2, \ldots, n\}$. Each IMU is independent, and its measurement results include the angular velocity and the attitude, i.e., $m_i = [w_{gi}, \Phi_i]^T$. In addition, due to the inherent shortcomings of the device, the gyro will produce

zero drift, which leads to the measurement of angular velocity with unknown bias, as shown in [20]. The measured angular velocity of ith IMU can be written as follows:

$$w_{gi} = \left[w_{g,1}, w_{g,2}, w_{g,3}\right]^T = w + b_i, \tag{4}$$

where b_i is the unknown gyro bias of ith IMU's gyro.

The control objective of this paper is to obtain accurate attitude data through multisensor measurement data. On this basis, the attitude tracking control of the aircraft is carried out.

Assumption 1 (see [37]). This paper assumes that the zero drift bias b_i of ith IMU's gyro is a constant value, and the zero drift bias of each gyro is different.

2.2. Related Definition and Lemma

Definition 1. For any $\beta > 0$, the nonlinear function $\mathrm{sig}^{\beta}(x)$ is defined as

$$\mathrm{sig}^{\beta}(x) = \mathrm{sign}(x)|x|^{\beta}. \tag{5}$$

Lemma 1 (super-twisting sliding-mode algorithm, see [38]). Consider the system

$$\begin{aligned} \dot{\tilde{x}}_1 &= -\iota_1 \mathrm{sig}^{1/2}(\tilde{x}_1) + \iota_2 \tilde{x}_2, \\ \dot{\tilde{x}}_2 &= -\iota_3 \mathrm{sign}(\tilde{x}_1) + \nu(\tilde{x}_1, \tilde{x}_2, t), \end{aligned} \tag{6}$$

where $\iota_i > 0$ are the gains to be designed and $\nu(\tilde{x}_1, \tilde{x}_2, t)$ are the perturbation terms; it satisfies

$$\left|\nu(\tilde{x}_1, \tilde{x}_2, t)\right| \le \delta, \tag{7}$$

where $\delta > 0$. Under some conditions on $\iota_1, \iota_2, \iota_3$, the equilibrium point of system (6) will converge to the origin in a finite time T.

2.3. Graph Theory.

In this paper, the multiple IMU will be considered. Each IMU can be seen as a node. The information interaction among n nodes can be represented by the directed graph $G(A) = \{V, E, A\}$. $V = \{v_i, i = 1, \ldots, n\}$ is the set of nodes, $E \subseteq V \times V$ is the set of edges, and $A = [a_{ij}] \in R^{n \times n}$ is the weighted adjacency matrix of the graph $G(A)$ with nonnegative adjacency elements a_{ij}. If there is an edge from node j to node i, i.e., $(v_j, v_i) \in E$, then $a_{ij} > 0$, which means there exists an available information channel from node j to node i. The set of neighbors of node i is denoted by $N_i = \{j: (v_j, v_i) \in E\}$. The out-degree of node v_i is defined as $\deg_{\mathrm{out}}(v_i) = d_i = \sum_{j=1}^{n} a_{ij} = \sum_{j \in N_i} a_{ij}$. Then, the degree matrix of digraph G is $D = \mathrm{diag}\{d_1, \ldots, d_n\}$ and the Laplacian matrix of digraph G is $L = D - A$.

A path in graph G from v_{i_1} to v_{i_k} is a sequence of $v_{i_1}, v_{i_2}, \ldots, v_{i_k}$ of finite nodes starting with v_{i_1} and ending with v_{i_k} such that $(v_{i_l}, v_{i_{l+1}}) \in E$ for $l = 1, 2, \ldots, k-1$. The graph G is connected if there is a path between any two distinct vertices.

3. Main Results

To solve the attitude tracking maneuver in the presence of unknown gyro bias, the main design procedure is divided into two steps:

The observer for each IMU to estimate the gyro bias is designed based on the consensus algorithm

An attitude controller based on the observer is designed to realize asymptotically stable attitude tracking

3.1. Design of Nonlinear Observers Based on Consensus Algorithm.

Because of the nonlinear structure of attitude system (2), it is difficult to design an observer under multiple IMUs. In this paper, let $\hat{b}_i = [\hat{b}_{i,1}, \hat{b}_{i,2}, \hat{b}_{i,3}]^T$ denote the estimation of the gyro unknown bias for the ith IMU's gyro and $\hat{\Phi}_i$ denote the estimated value of the real-time attitude of the aircraft for the ith IMU's accelerometer. Based on models (2) and (4), we can design the following observer.

Theorem 1. *Considering the attitude system (2) and Assumption 1, if the observers are designed as*

$$\begin{aligned} \dot{\hat{\Phi}}_i &= W(\Phi_i)\left(w_{gi} - \hat{b}_i\right) - k_1 e_i - \sum_{j \in N_i} a_{ij}\left(e_i - e_j\right), \\ \dot{\hat{b}}_i &= k_2 W^T(\Phi_i) e_i, \quad i \in \Gamma, \end{aligned} \tag{8}$$

where $k_1 > 0, k_2 > 0$, and $e_i = [e_{i,1}, e_{i,2}, e_{i,3}]^T = \hat{\Phi}_i - \Phi_i$, then the estimation value $(\hat{\Phi}_i, \hat{b}_i)$ will globally asymptotically converge to true value (Φ_i, b_i).

Proof. First of all, let the estimation error for gyro bias be $f_i = \hat{b}_i - b$. Then, the error dynamical equation can be obtained:

$$\begin{aligned} \dot{e}_i &= -W(\Phi_i) f_i - k_1 e_i - \sum_{j \in N_i} a_{ij}\left(e_i - e_j\right), \\ \dot{f}_i &= k_2 W^T(\Phi_i) e_i, \quad i \in \Gamma. \end{aligned} \tag{9}$$

Choose the Lyapunov function for the error system (9) as

$$V = \sum_{i=1}^{n}\left[\frac{k_2}{2}\sum_{k=1}^{3} e_{i,k}^2 + \frac{1}{2} f_i^T f_i\right], \tag{10}$$

whose derivative is

$$\begin{aligned}\dot{V} &= \sum_{i=1}^{n}\left[k_2\sum_{k=1}^{3}\dot{e}_{i,k}e_{i,k} + \dot{f}_i^T f_i\right]\\ &= \sum_{i=1}^{n}\left[k_2 e_i^T\left[-W(\Phi_i)f_i - k_1 e_i - \sum_{j=1}^{n}a_{ij}(e_i - e_j)\right] + k_2\left[W^T(\Phi_i)e_i\right]^T f_i\right]\\ &= -k_1k_2\sum_{i=1}^{n}e_i^T e_i - k_2\sum_{i=1}^{n}e_i^T\sum_{j=1}^{n}a_{ij}(e_i - e_j)\\ &= -k_1k_2\sum_{i=1}^{n}e_i^T e_i - \frac{k_2}{2}\sum_{i=1}^{n}\sum_{j=1}^{n}a_{ij}(e_i - e_j)^T(e_i - e_j)\\ &= -k_1k_2\sum_{i=1}^{n}\sum_{k=3}^{n}e_{i,k}^2 - \frac{k_2}{2}\sum_{i=1}^{n}\sum_{j=1}^{n}a_{ij}\sum_{k=1}^{3}\left(e_{i,k} - e_{j,k}\right)^2 \le 0.\end{aligned} \tag{11}$$

Based on LaSalle's invariant principle, it is easy to get the conclusion that (e_i, f_i) will globally asymptotically converge to the origin, i.e., $(\widehat{\Phi}_i, \widehat{b}_i)$ will globally asymptotically converge to true value (Φ_i, b_i). The proof is completed. □

Remark 1. With observer (8), the gyro of ith IMU can estimate the true value of the gyro zero drift $\widehat{b}_i$. By compensating the bias, the angular velocity of the ith IMU can be obtained, i.e., $\overline{w}_i = w_{gi} - \widehat{b}_i$. The angular velocity used to control the attitude of the aircraft in this paper is given by

$$\overline{w} = \frac{1}{n}\sum_{i=1}^{n}\left(w_{gi} - \widehat{b}_i\right). \tag{12}$$

3.2. Design of a Nonlinear Controller Based on a Super-Twist Observer. The dynamic equation of the aircraft is as follows:

$$J\dot{w} = -w^{\times}Jw + \tau + d, \tag{13}$$

where $J \in \mathbb{R}^3$ and $\tau \in \mathbb{R}^3$ are, respectively, the positive definite inertia matrix, and the control torque of spacecraft, d denotes the external disturbance satisfies $d \le d^*$ with a positive constant d^*, and the symbol $(\cdot)^{\times}$ denotes the skew symmetry matrix, i.e.,

$$x^{\times} = \begin{bmatrix} 0 & -x_3 & x_2 \\ x_3 & 0 & -x_1 \\ -x_2 & x_1 & 0 \end{bmatrix}, \quad \forall x \in \mathbb{R}^3. \tag{14}$$

The desired attitude is described as $\Phi_d = [\phi_d, \theta_d, \psi_d]^T$, and it is constant in this paper. Define the attitude error between the true value and the desired value as $\Phi_e = [\Phi_{e1}, \Phi_{e2}, \Phi_{e3}]^T = \Phi - \Phi_d$. To sum up, the attitude error system of the aircraft is

$$\begin{aligned}\dot{\Phi}_e &= \dot{\Phi} - \dot{\Phi}_d = W(\Phi)w,\\ J\dot{w} &= -w^{\times}Jw + \tau + d.\end{aligned} \tag{15}$$

Theorem 2. *For the attitude error system (15), if the controller is designed as*

$$\begin{aligned}\tau &= -k_3\overline{w} - k_4W^T(\Phi)\Phi_e - \widehat{d},\\ \dot{\widehat{w}} &= J^{-1}\left(-\overline{w}^{\times}J\overline{w} - k_3\overline{w} - k_4W^T(\Phi)\Phi_e\right) - k_5\mathrm{sig}^{1/2}(\widehat{w} - \overline{w}),\\ \dot{\widehat{d}} &= -k_6\mathrm{sign}(\widehat{w} - \overline{w}),\end{aligned} \tag{16}$$

where $k_3, k_4, k_5, k_6 > 0$, $\widehat{w}$ represents the estimate of the angular velocity, and $\widehat{d}$ denotes the estimate of the external disturbance; then, the asymptotic tracking of attitude can be implemented.

Proof. It can be known from Theorem 1 that $\overline{w}$ will eventually converge to w. The observation errors e_1 and e_2 are defined as

$$\begin{aligned}e_1 &= \widehat{w} - \overline{w},\\ e_2 &= \widehat{d} - d,\end{aligned} \tag{17}$$

whose derivative is

$$\begin{aligned}\dot{e}_1 &= -k_5\mathrm{sig}^{1/2}(e_1) + J^{-1}e_2,\\ \dot{e}_2 &= -k_6\mathrm{sign}(e_1).\end{aligned} \tag{18}$$

From Lemma 1, we know that e_1 and e_2 will converge to 0 in a finite time. In other words, the estimated disturbance value $\widehat{d}$ will converge to the true value d in a finite time T_1. After T_1, it follows (15) and (16) that

$$\begin{aligned}\dot{\Phi}_e &= W(\Phi)w,\\ J\dot{w} &= -w^{\times}Jw - k_3\overline{w} - k_4W^T(\Phi)\Phi_e.\end{aligned} \tag{19}$$

It follows (9), (15), and (19) that

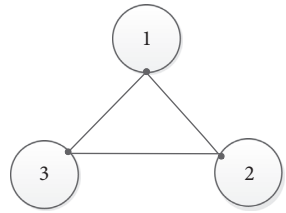

Figure 1: The information exchange of three IMUs.

$$\begin{aligned}
\dot{\Phi}_e &= W(\Phi)w,\\
J\dot{w} &= -w^{\times}Jw + u_1 + (u_2 - u_1),\\
\dot{e}_i &= -W(\Phi_i)f_i - k_1 e_i - \sum_{j\in N_i} a_{ij}(e_i - e_j),\\
\dot{f}_i &= k_2 W^T(\Phi_i)e_i, \quad i \in \Gamma,
\end{aligned} \tag{20}$$

where $u_1 = -k_3 w - k_4 W^T(\Phi)\Phi_e$ and $u_2 = -k_3\overline{w} - k_4 W^T(\Phi)\Phi_e$. Obviously, system (20) can be regarded as a cascaded system with the cascaded term $(u_1 - u_2)$. Next, we will use cascaded systems' theory [39] to analyze the stability of system (20). The proof includes two steps:

Step 1: proof of global asymptotic stability of subsystems.

Consider the following system:

$$\begin{aligned}
\dot{\Phi}_e &= W(\Phi)w,\\
J\dot{w} &= -w^{\times}Jw + u_1.
\end{aligned} \tag{21}$$

Choose the following Lyapunov function for the attitude error system (21):

$$H = \frac{k_4}{2}\sum_{j=1}^{3}\Phi_{ej}^2 + \frac{1}{2}w^T Jw. \tag{22}$$

Based on the matrix $w^T w^{\times} Jw$ which is skew symmetric, the derivative of H along system (21) is

$$\begin{aligned}
\dot{H} &= k_4\sum_{j=1}^{3}\Phi_{ej}\dot{\Phi}_{ej} + w^T J\dot{w}\\
&= k_4 w^T W^T(\Phi)\Phi_e + w^T(-w^{\times}Jw + u_1)\\
&= k_4 w^T W^T(\Phi)\Phi_e + w^T\left(-k_3 w - k_4 W^T(\Phi)\Phi_e\right)\\
&= -k_3 w^2 \le 0.
\end{aligned} \tag{23}$$

Based on LaSalle's invariant principle, it can be concluded that $\dot{H}(t) \longrightarrow 0$ as $t \longrightarrow \infty$, which implies that system (21) is globally asymptotically stable. It is easy to get the conclusion that $(\Phi_e, w) \longrightarrow 0$ as $t \longrightarrow \infty$.

Clearly, system (9) and system (21) are globally asymptotically stable with equilibrium $(w, \Phi_e, e_i, f_i) = (0, 0, 0, 0)$.

Step 2: proof of global state bounded of cascaded system.

According to the cascaded systems' theory [39], cascades of the globally asymptotically stable systems remain globally asymptotically stable if and only if solutions are globally bounded. With these facts in mind, to prove the stability of system (20), we only need to prove that the state of system (20) is globally bounded. To achieve this objective, choose the Lyapunov function:

$$U = V + H. \tag{24}$$

According to (11) and (23), it obtains

$$\begin{aligned}
\dot{U} = &-k_1 k_2\sum_{i=1}^{n} e_i^2 - \frac{k_2}{2}\sum_{i=1}^{n}\sum_{j=1}^{n} a_{ij}(e_i - e_j)^2 - k_3 w^2\\
&+ w^T(u_1 - u_2).
\end{aligned} \tag{25}$$

Since systems (9) and (21) are globally asymptotically stable, f_i and w are globally bounded. There is a constant $0 < d < +\infty$ such that $\|u_1 - u_2\| \le d$. We have

$$\dot{U} \le -k_1 k_2\sum_{i=1}^{n} e_i^2 - \frac{k_2}{2}\sum_{i=1}^{n}\sum_{j=1}^{n} a_{ij}(e_i - e_j)^2 - k_3 w^2 + \sum_{j=1}^{3} w_i d. \tag{26}$$

Clearly, when $k_1 k_2 \sum_{i=1}^{n} e_i^2 + (k_2/2)\sum_{i=1}^{n}\sum_{j=1}^{n} a_{ij}(e_i - e_j)^2 + k_3 w^2 > \sum_{j=1}^{3} w_i d$, then $\dot{U} < 0$. Thus, the state (w, Φ_e, e_i, f_i) is globally bounded.

With this fact in mind, it can be concluded that the state of system (20) is globally bounded, which implies that this system is asymptotically stable. That is to say the attitude tracking is achieved asymptotically. □

Remark 2. According to the previous proof, when the observer gains meet $k_1, k_2 > 0$ and the controller gains meet $k_3, k_4, k_5, k_6 > 0$, the attitude asymptotic stability tracking can be realized. In practical applications, the observer gain and controller gain can be selected step by step to obtain better performance.

4. Simulation Example

A simulation example is given to verify the effectiveness of the proposed method. In this paper, three inertial measurement units are selected for simulation. Next, the initial values, parameters, and real values required for simulation in this paper are given. The information exchange topology among IMU is shown in Figure 1. The initial values of the observer part are selected as $\widehat{b}_i(0) = [0.1, 0.1, 0.1]^T$ rad/sec and $\widehat{\Phi}_i(0) = [0.3, 0.3, 0.3]^T$ deg, $i = 1, 2, 3$. The observer parameters are

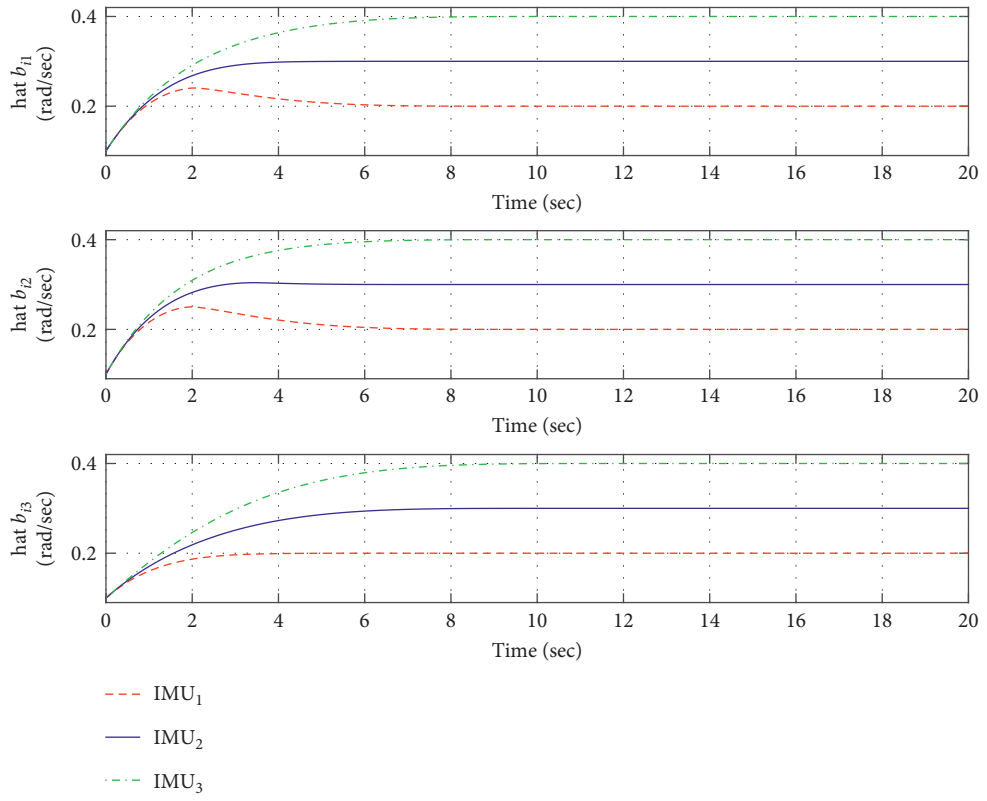

FIGURE 2: The bias estimation $\widehat{b}_i$ of ith IMU by using the proposed observer.

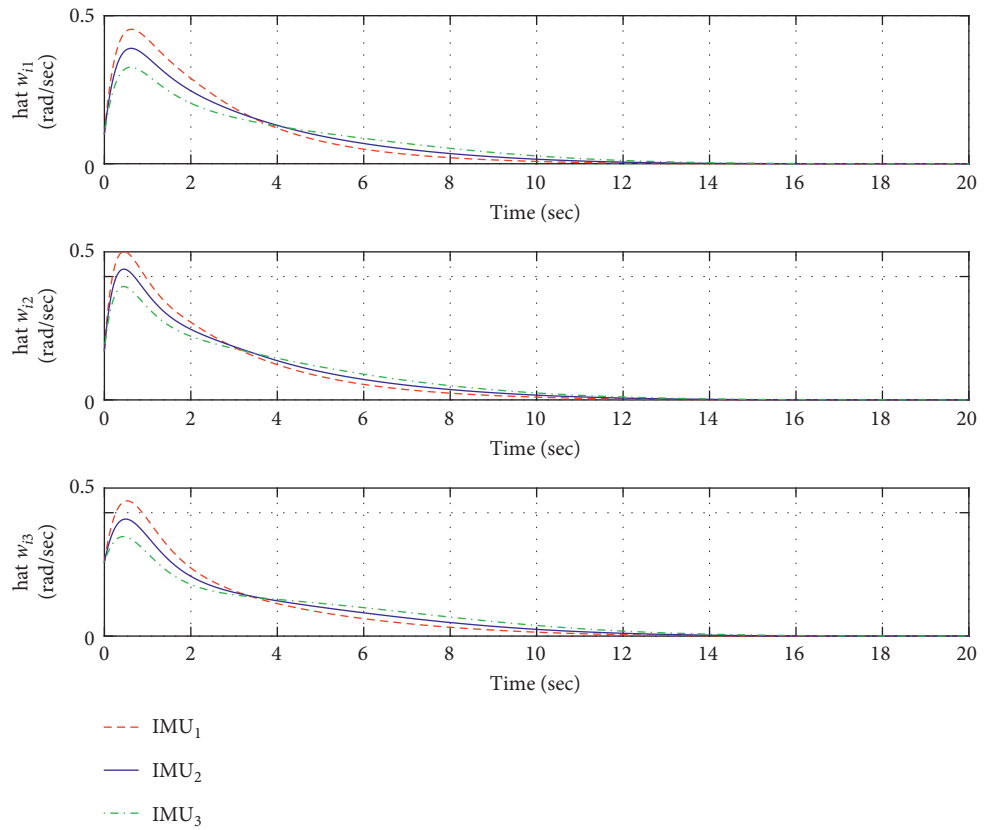

FIGURE 3: The angular velocity $\widehat{w}_i$ of ith by using the proposed observer.

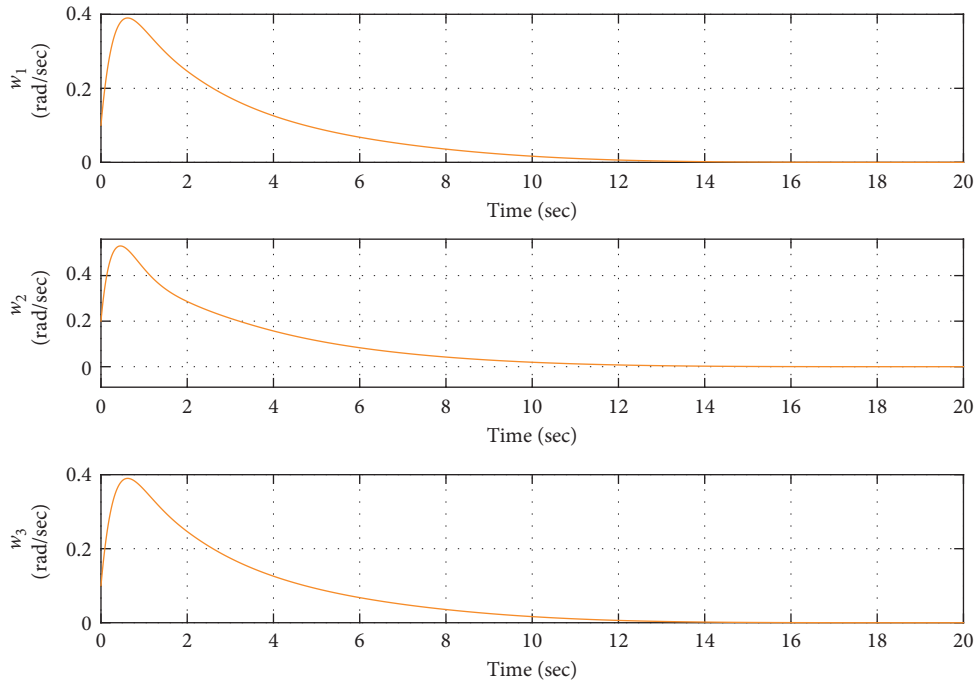

Figure 4: The response curve of aircraft's angular velocity.

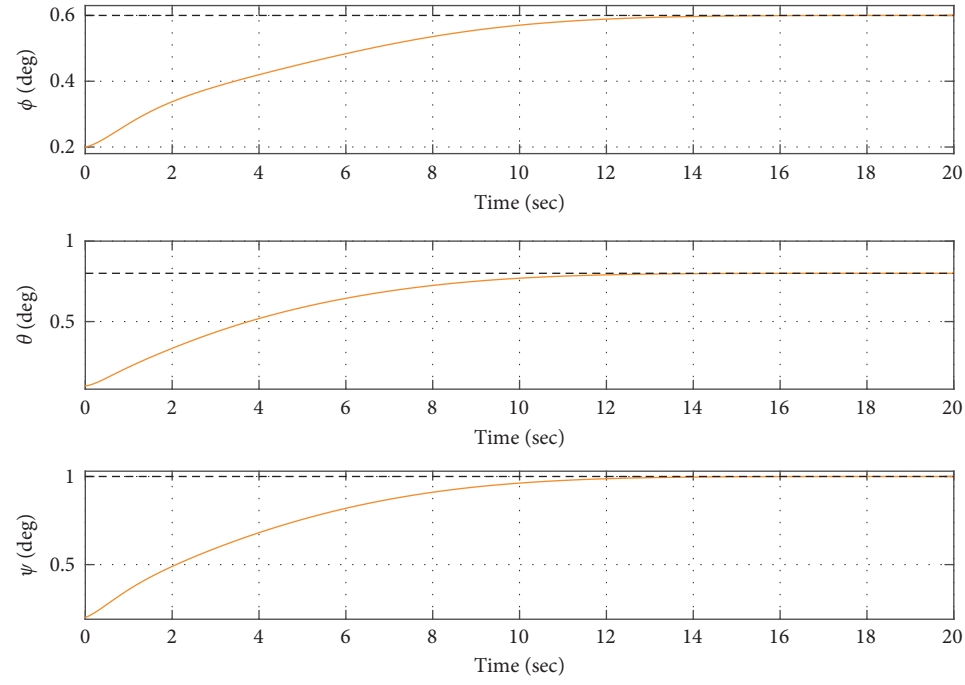

Figure 5: The response curve of aircraft's attitude.

$k_1 = 13$ and $k_2 = 2.36$. The initial values of the controller are selected as $\Phi(0) = [0.2, 0.1, 0.2]^T$ deg and $w(0) = [0.1, 0.2, 0.3]^T$ rad/sec. The controller parameters are $k_3 = 9.754$, $k_4 = 3.21$, $k_5 = 2.3$, and $k_6 = 1.4$. The desired attitude of the aircraft is set as $\Phi_d = [0.6, 0.8, 1]^T$ deg. The true biases of the IMUs' gyro are selected as $b_{\text{ture1}} = [0.2, 0.2, 0.2]^T$ rad/sec, $b_{\text{ture2}} = [0.3, 0.3, 0.3]^T$ rad/sec, and $b_{\text{ture3}} = [0.4, 0.4, 0.4]^T$ rad/sec. The external disturbance is set as $d(t) = [0.2 + \sin(t), 0.3 + \sin(3t), 0.1 + \sin(t)]^T$. The inertia matrix of the aircraft is chosen as that in [40]:

$$J = \begin{bmatrix} 1 & 0 & 0 \\ 0 & 0.63 & 0 \\ 0 & 0 & 0.85 \end{bmatrix}. \quad (27)$$

The simulation results are shown in Figures 2–5. First, the bias estimation $\widehat{b}_i$ of the ith IMU is given in Figure 2, from which it can be found that the proposed nonlinear observer is effective. The angular velocity of the ith IMU is given in Figure 3.

In addition, the response curve of aircraft's angular velocity is given in Figure 4 and the response curve of aircraft's attitude is given in Figure 5.

5. Conclusions and Future Directions

5.1. Conclusions. The aircraft adopts a single IMU as the attitude measurement sensor, which can no longer meets the requirements of measurement accuracy. And, due to the shortage of sensors and noise, gyro will produce zero drift, which will lead to constant biases of measured angular velocity. Measurements of angular velocity with constant biases and external disturbance will make the attitude control system unstable. Therefore, the attitude anti-interference control under multiple IMUs is studied in this paper. Firstly, aiming at the zero drift, this paper adopts multiple IMUs for measurement, and the consensus observer is designed to ensure that each IMU converges to the true value of angular velocity. Aiming at the instability of aircraft control caused by external disturbances, this paper introduces a super-twisting sliding mode observer, which compensates for the external disturbances. In addition, a controller is proposed in this paper, and the actual attitude can globally asymptotically converge to the desired attitude based on the observer. Simulation results also demonstrate the effectiveness of the proposed method.

5.2. Future Directions. Future work will focus on designing observers that the zero drift biases of gyros are time-varying conditions and that the attitude information is unknown.

Data Availability

Some or all data, models, or code generated or used during the study are available from the corresponding author upon request.

Conflicts of Interest

The authors declare that there are no conflicts of interest regarding the publication of this paper.

Acknowledgments

This work was supported by the National Natural Science Foundation of China under Grant no. 52075118.

References

[1] A. Abdessameud and A. Tayebi, *Motion Coordination for VTOL Unmanned Aerial Vchicles Advances in Industrial Control*, Springer-Verlag, New York, NY, USA, 2013.

[2] P. Castillo, R. Lozano, and A. Dzul, *Modelling and Control of Mini-Flying Machines*, Springer-Verlag, New York, NY, USA, 2005.

[3] L. Wang, H. Du, W. Zhang, D. Wu, and W. Zhu, "Implementation of integral fixed-time sliding mode controller for speed regulation of PMSM servo system," *Nonlinear Dynamics*, vol. 102, no. 1, pp. 185–196, 2020.

[4] K. Mei and S. Ding, "Second-order sliding mode controller design subject to an upper-triangular structure," *IEEE Transactions on Systems, Man, and Cybernetics: Systems*, vol. 51, no. 1, p. 497, 2021.

[5] O. Mofid, S. Mobayen, and M. Khooban, "Sliding mode disturbance observer control based on adaptive synchronization in a class of fractional-order chaotic systems," *International Journal of Adaptive Control and Signal Processing*, vol. 33, no. 3, pp. 462–474, 2019.

[6] Q. Hou, S. Ding, and X. Yu, "Composite super-twisting sliding mode control design for PMSM speed regulation problem based on a novel disturbance observer," *IEEE Transactions on Energy Conversion*, p. 1, 2020.

[7] A. Norouzpour-Shirazi and F. Ayazi, "A dual-mode actuation and sensing scheme for in-run calibration of bias and scale factor errors in axisymmetric resonant gyroscopes," *IEEE Sensors Journal*, vol. 18, no. 5, pp. 1993–2005, 2017.

[8] M. Dai, C. Zhang, and J. Lu, "In-field calibration method for DTG IMU including g-sensitivity biases," *IEEE Sensors Journal*, vol. 19, no. 13, pp. 4972–4981, 2019.

[9] S. Bonnet, C. Bassompierre, C. Godin, S. Lesecq, and A. Barraud, "Calibration methods for inertial and magnetic sensors," *Sensors and Actuators A: Physical*, vol. 156, no. 2, pp. 302–311, 2009.

[10] R. Fontanella, D. Accardo, R. S. Lo Moriello, L. Angrisani, and D. De Simone, "MEMS gyros temperature calibration through artificial neural networks," *Sensors and Actuators A: Physical*, vol. 279, pp. 553–565, 2018.

[11] L. Chang, B. Hu, and K. Li, "Iterated multiplicative extended Kalman filter for attitude estimation using vector observations," *IEEE Transactions on Aerospace and Electronic Systems*, vol. 52, no. 4, pp. 2053–2060, 2016.

[12] P. Tsiotras, "Stabilization and optimality results for the attitude control problem," *Journal of Guidance, Control, and Dynamics*, vol. 19, no. 4, pp. 772–779, 1996.

[13] B. N. Stovner, T. A. Johansen, T. I. Fossen, and I. Schjølberg, "Attitude estimation by multiplicative exogenous Kalman filter," *Automatica*, vol. 95, pp. 347–355, 2018.

[14] H. Du, G. Wen, Y. Cheng, and J. Lu, "Design and implementation of bounded finite-time control algorithm for speed regulation of permanent magnet synchronous motor," *IEEE Transactions on Industrial Electronics*, vol. 68, no. 3, pp. 2417–2426, 2021.

[15] J. Li, J. Fang, and M. Du, "Error analysis and gyro-bias calibration of analytic coarse alignment for airborne POS," *IEEE Transactions on Instrumentation and Measurement*, vol. 61, no. 11, pp. 3058–3064, 2012.

[16] Z. Yang, D. Bi, Q. Meng, and J. Wang, "Error compensation and calibration for attitude heading reference system with four-rotor aircraft," *Computer Measurement and Control*, vol. 24, no. 02, pp. 267–270, 2016.

[17] M. S. Challa, J. G. Moore, and D. J. Rogers, "A simple attitude unscented kalman filter: theory and evaluation in a magnetometer-only spacecraft scenario," *IEEE Access*, vol. 4, pp. 1845–1858, 2016.

[18] T. Zhang and Y. Liao, "Attitude measure system based on extended Kalman filter for multi-rotors," *Computers and Electronics in Agriculture*, vol. 134, pp. 19–26, 2017.

[19] R. Mahony, T. Hamel, and J.-M. Pflimlin, "Nonlinear complementary filters on the special orthogonal group," *IEEE Transactions on Automatic Control*, vol. 53, no. 5, pp. 1203–1218, 2008.

[20] J. Thienel and R. M. Sanner, "A coupled nonlinear spacecraft attitude controller and observer with an unknown constant gyro bias and gyro noise," *IEEE Transactions on Automatic Control*, vol. 48, no. 11, pp. 2011–2015, 2003.

[21] D. E. Zlotnik and J. R. Forbes, "Exponential convergence of a nonlinear attitude estimator," *Automatica*, vol. 72, pp. 11–18, 2016.

[22] G. Baldini, G. Steri, F. Dimc, R. Giuliani, and R. Kamnik, "Experimental identification of smartphones using fingerprints of built-in micro-electro mechanical systems (MEMS)," *Sensors*, vol. 16, no. 6, p. 818, 2016.

[23] Y. Al-Rawashdeh, M. Elshafei, and M. Al-Malki, "In-flight estimation of center of gravity position using all-accelerometers," *Sensors*, vol. 14, no. 9, pp. 17567–17585, 2014.

[24] H. Sheng and T. Zhang, "MEMS-based low-cost strap-down AHRS research," *Measurement*, vol. 59, pp. 63–72, 2015.

[25] M. Trkov, K. Chen, J. Yi, and T. Liu, "Inertial sensor-based slip detection in human walking," *IEEE Transactions on Automation Science and Engineering*, vol. 16, no. 3, pp. 1399–1411, 2019.

[26] M. Jafari, "Optimal redundant sensor configuration for accuracy increasing in space inertial navigation system," *Aerospace Science and Technology*, vol. 47, pp. 467–472, 2015.

[27] I. M. Brooks, "Spatially distributed measurements of platform motion for the correction of ship-based turbulent fluxes," *Journal of Atmospheric and Oceanic Technology*, vol. 25, no. 11, pp. 2007–2017, 2008.

[28] H. Naseri and M. R. Homaeinezhad, "Improving measurement quality of a MEMS-based gyro-free inertial navigation system," *Sensors and Actuators A: Physical*, vol. 207, pp. 10–19, 2014.

[29] S. Park and S. K. Hong, "Angular rate estimation using a distributed set of accelerometers," *Sensors*, vol. 11, no. 11, pp. 10444–10457, 2011.

[30] H. Du, C. Jiang, G. Wen, W. Zhu, and Y. Cheng, "Current sharing control for parallel DC-DC buck converters based on finite-time control technique," *IEEE Transactions on Industrial Informatics*, vol. 15, no. 4, pp. 2186–2198, 2019.

[31] B. Vaseghi, M. A. Pourmina, and S. Mobayen, "Finite-time chaos synchronization and its application in wireless sensor networks," *Transactions of the Institute of Measurement and Control*, vol. 40, no. 13, pp. 3788–3799, 2018.

[32] S. Mobayen and J. Ma, "Robust finite-time composite nonlinear feedback control for synchronization of uncertain chaotic systems with nonlinearity and time-delay," *Chaos, Solitons & Fractals*, vol. 114, pp. 46–54, 2018.

[33] H. Du, G. Wen, D. Wu, Y. Cheng, and J. La, "Distributed fixed-time consensus for nonlinear heterogeneous multi-agent systems," *Automatica*, vol. 113, pp. 1–11, 2020.

[34] J. Yuan, S. Ding, and K. Mei, "Fixed-time SOSM controller design with output constraint," *Nonlinear Dynamics*, vol. 102, no. 3, pp. 1567–1583, 2020.

[35] K. Mei, L. Ma, R. He, and S. Ding, "Finite-time controller design of multiple integrator nonlinear systems with input saturation," *Applied Mathematics and Computation*, vol. 372, Article ID 124986, 2020.

[36] F. Liu, Z. Su, H. Zhao, Q. Li, and C. Li, "Attitude measurement for high-spinning projectile with a hollow mems imu consisting of multiple accelerometers and gyros," *Sensors*, vol. 19, no. 8, p. 1799, 2019.

[37] L. Wang, H. Du, and D. Wu, "A coupled finite-time attitude controller and finite-time observer with an unknown constant drift bias," in *Proceedings of 39th Chinese Control Conference (CCC)*, pp. 526–531, Kunming, China, July 2020.

[38] J. A. Moreno and M. Osorio, "Strict Lyapunov functions for the super-twisting algorithm," *IEEE Transactions on Automatic Control*, vol. 57, no. 4, pp. 1035–1040, 2012.

[39] R. Sepulchre, M. Jankovic, and P. Kokotovic, *Constructive Nonlinear Control*, Springer, London, UK, 2007.

[40] J. T.-Y. Wen and K. Kreutz-Delgado, "The attitude control problem," *IEEE Transactions on Automatic Control*, vol. 36, no. 10, pp. 1148–1162, 1991.

Hindawi
Mathematical Problems in Engineering
Volume 2021, Article ID 6664215, 10 pages
https://doi.org/10.1155/2021/6664215

Research Article

The Impact of Urban Rail Transit on Industrial Agglomeration Based on the Intermediary Effects of Factor Agglomeration

Zhonghui Li,[1,2] Tongshui Xia,[1] Zhiqing Xia,[3] and Xinjun Wang[4]

[1]*Shandong Normal University, Business School, Jinan 250358, Shandong, China*
[2]*Jinan Rail Transit Group Co.,Ltd., Jinan 250101, Shandong, China*
[3]*Qilu University of Technology, School of Finance, Jinan 250353, Shandong, China*
[4]*Shandong Normal University, School of Information Science and Engineering, Jinan 250358, Shandong, China*

Correspondence should be addressed to Tongshui Xia; tsxia@sina.com and Xinjun Wang; wangxinjun1991@gmail.com

Received 1 December 2020; Revised 4 January 2021; Accepted 18 January 2021; Published 1 February 2021

Academic Editor: Shihong Ding

Urban rail transit is an important form of infrastructure for a city or even a country. This paper uses location entropy to measure the industrial agglomeration level of cities at the prefecture level or above in China from 2006 to 2018 and empirically tests the mechanisms of urban rail transit construction, factor agglomeration, and industrial agglomeration. The empirical results show the following: (1) the construction of urban rail transit infrastructure has a significant positive effect on the agglomeration of the labor force, capital, and technological innovation; (2) urban rail transit construction effectively induces agglomeration in the urban manufacturing industry and consumer service industry; and (3) the impact of urban rail transit construction on agglomeration in the urban manufacturing industry and consumer services industry is primarily due to the intermediary effects of factor agglomeration. The results show that gradually improving the urban rail transit network, strengthening the construction of comprehensive rail transit hubs, and optimizing capital allocation within urban rail transit allow for the full utilization of urban rail transit construction in promoting industrial agglomeration.

1. Introduction

Urban rail transit is the main artery of a country's economic and social development as well as an important emerging strategic industry and has profound socioeconomic impacts in many areas. Urban rail transit can enhance a city's regional advantages, and the continual agglomeration of capital, population, and technology could cause more factors of production to flow into cities with a higher rate of return, which could in turn expand production, increase aggregate demand, and improve the cities' industrial structure and industrial agglomeration. As of the end of 2019, a total of 40 cities in Mainland China had opened urban rail transit systems, and these systems had a collective total of 6,736.2 km of urban rail mileage, setting a historic record. The construction of urban rail transit makes the city's location advantage more important. The continuous agglomeration of industry, population, and technology makes more capital tend to flow to these cities with higher return rate, which brings a lot of investment, expands production, and improves the urban infrastructure and investment environment. Urban rail transit is an important transportation foundation of urban integration, regional coordination, and economic intensification, which plays a great role in industrial agglomeration.

Under the real-world background of the rapid development of urban rail transit in China, what effect could urban rail transit have on industrial agglomeration? Are any mediating variables involved in this effect? Answering these questions could help improve the development of urban rail transit in China and provide governments with a reference for the more precise positioning of cities' features and functions.

2. Research Overview

Research on the topic of urban rail transit and economic benefit began during the 1960s with the research of Liszt

(1961) [1] on the relationship between transportation and regional economics, which incorporated transportation as a major constituent factor and found that Britain's economic growth benefited to a large extent from increases in transportation capacity. Starting from the state of urban rail transit development in the United States and referring to relationships between the rail transit construction, the economy, and the population, Cervero (1996) [2] pointed out that the construction and development of rail transit promoted the development of whole countries and regions and that rail transit had a significant impact on the population, industry, and overall economic development under its radiation scope. Prasertsubpakij and Nitivattananon (2012) [3] pointed out that metro systems served as fast and efficient transit systems in numerous modern cities, and the traditional research methods of metro rail accessibility had not fully considered the equal right of users to enjoy the metro system. Therefore, they suggested that it was necessary to use multidimensional criteria to assess the accessibility of the Bangkok Metro system to users and the equal right of users to the metro. They found that the development of metro lines had not fully satisfied the travel needs of different types of users and had not promoted population concentration.

The price of land in urban centers has increased rapidly with steadily growing populations, so growing numbers of people working in city centers have been forced to live in outlying areas, which has resulted in home-work separation. Cervero (1994) [4] found that the implementation of rail transit projects brought about a significant increase in peripheral real estate prices. McMillen and McDonald (2004) [5] showed that housing markets can predict the development of transport lines, and this development can cause home prices to rise. The study of Kim and Zhang (2005) [6] discovered that rail transit projects had a greater impact on real estate prices in city centers than in other areas. Lee and Hong (2013) [7] analyzed the relationship between Seoul Metro passenger traffic and land uses around metro stations, with the goal of testing the hypothesis that the passenger volume of bus stations at both ends of the city under the influence of density is conducive to land-use diversity. They found that land-use diversity had a major impact on passenger traffic between stations, and metro passenger traffic in both Seoul's central business district and fringe areas was chiefly affected by population density, while central areas were uniformly influenced by intermodal bus transit. The studies of Liu, Li, and Deng (2015) [8] and Wang and Chen (2017) [9] verified this rule and discovered that rail transit projects had different impacts on the increases in the price of land in areas along transit lines during the construction and development stages, with transit projects bringing about a greater increase in land prices during construction than during the development or operation period.

Several studies have examined the capitalization effect of rail transit on home prices and land prices. For instance, in a study of the effect of metro systems on housing and commercial real estate, Mohammad et al. (2017) [10] found that metro systems had a significant promoting effect on the prices of both housing and commercial real estate, and this promoting effect was significantly greater in the case of commercial real estate than in the case of housing. In a study of the Sydney's Inner West Light Rail line, Mulley and Tsai (2018) [11] found that light rail service increased the value of peripheral land by improving accessibility. In their analysis of the spatial and temporal effect of metro availability on apartment prices, Trojanek and Gluszak (2018) [12] discovered that metro systems raised apartment prices before they opened, and this effect also gradually but significantly increased with the passage of time. Luo Jia and Mo Shuang Ning (2019) [13] analyzed the influence mechanism of subway station on the price of surrounding houses. Subway station can increase the use value and utility of surrounding houses by improving the travel convenience of surrounding residents, thus driving the rise of house prices. This paper empirically tests the "premium effect" by using the panel data of 964 second-hand commercial houses in Shanghai from 2013 to 2018 The closer to the subway station, the higher the price of second-hand commercial housing; in addition, the existence of affordable housing nearby can weaken the premium effect of subway station on commercial housing, but the weakening effect is very weak.

Based on the "center-periphery" theory, Wang Wei and Ma Hui (2019) [14] analyzed the industrial agglomeration effect of rapid transit network from the perspective of labor transfer. The research shows that the opening of high-speed railway significantly reduces the industrial agglomeration level of regional noncentral cities and strengthens the industrial agglomeration level of central cities through labor transfer channels. Iordanka Stateva (2019) [15] believes that after the UK decided to leave the EU, with the decentralization of financial services, the financial capital of London financial center is attracted by the network of smaller financial centers such as Frankfurt and Paris. The overall competitiveness of the emerging capital network depends on the degree of financial capital concentration and technological innovation.

After performing a careful review of existing research, we saw that while there has been much research employing traditional theories addressing the relationships between the transport industry and industrial agglomeration and between industrial agglomeration and economic growth, there has been little research on the effect of urban rail transit on urban industrial agglomeration. Also, refer to the studies of Gu and Chen(2020) [16], Yuan and Ding et al.(2020) [17], Y. Shu et al.(2020) [18], Chen et al.(2014) [19], Li et al.(2018) [20], and Ji Wei et al. (2019) [21]. This paper therefore analyzes the relationship between urban rail transit and industrial agglomeration from the new perspective of factor agglomeration, while incorporating a mediating effect model. Most previous studies have employed qualitative research methods to investigate the effect of urban rail development on economic growth or industrial agglomeration and have failed to quantify this effect. To provide empirical support for the effect of urban rail development on industrial agglomeration, this study employs the data of Chinese cities at the prefecture level and above during 2006–2018 and consequently constructs fixed-effects panel-data models and dynamic generalized methods of moments

(GMM) models to analyze the mechanism by which urban rail transit affects industrial agglomeration via factor agglomeration.

3. Empirical Design

3.1. Model Construction. Adopting the principles of the mediating effect testing method proposed by Preacher and Hayes (2008) [22], this study takes urban industrial agglomeration as the explained variable, factor agglomeration as a mediating variable, and urban rail transit as the core explanatory variable. This study aims to test whether the transmission mechanism of urban rail transit to industrial agglomeration is mainly realized by factor agglomeration. If true, this would imply that factor agglomeration is the model's mediating variable. Specifically, a mediating effect is tested via a three-step quantitative model.

In this model, the first step is to test the effect of urban rail transit on industrial agglomeration:

$$LQ1_{it} = \alpha + \beta_1 TRAN_{it} + \beta_2 GDP_{it} + \beta_3 INS_{it} + \beta_4 GOV_{it} + \beta_5 WAGE_{it} + \beta_6 HUM_{\mathrm{it}} + v_i + u_t + \varepsilon_{it}, \quad (1)$$

$$LQ2_{it} = \alpha + \beta_1 TRAN_{it} + \beta_2 GDP_{it} + \beta_3 INS_{it} + \beta_4 GOV_{it} + \beta_5 WAGE_{it} + \beta_6 HUM_{\mathrm{it}} + v_i + u_t + \varepsilon_{it}, \quad (2)$$

where $LQ1$ is the industrial agglomeration of manufacturing industries, $LQ2$ is the industrial agglomeration of consumer service industries, and $TRAN$ is urban rail development. At the same time, to maximally lessen the effect of endogenous issues caused by omissions, this study also controls for other major variables affecting urban economic growth. After taking theory and the availability of data into consideration, this study adopts economic growth (GDP), upgrading of the industrial structure (INS), government expenditures (GOV), wage level ($WAGE$), and human capital (HUM) as the control variables; α is a constant term; β is the estimated coefficient of the explanatory variable; i is the entity; t is the year; v_i and u_t indicate the individual effect and time effect, respectively; and ε_{it} is a random error term.

When testing coefficient β_1 in equations (1 and 2), if β_1 is not significant, this indicates that no mediating effect exists, and testing stops; but if β_1 is significant, this is still not sufficient to indicate that a mediating effect exists. At that time, it is necessary to perform the second testing step, which involves the city's factor agglomeration:

$$LA_{it} = \alpha + \beta_1 TRAN_{it} + \beta_2 GDP_{it} + \beta_3 INS_{it} + \beta_4 GOV_{it} + \beta_5 WAGE_{it} + \beta_6 HUM_{it} + v_i + u_t + \varepsilon_{it}, \quad (3)$$

$$CA_{it} = \alpha + \beta_1 TRAN_{it} + \beta_2 GDP_{it} + \beta_3 INS_{it} + \beta_4 GOV_{it} + \beta_5 WAGE_{it} + \beta_6 HUM_{it} + v_i + u_t + \varepsilon_{it}, \quad (4)$$

$$TA_{it} = \alpha + \beta_1 TRAN_{it} + \beta_2 GDP_{it} + \beta_3 INS_{it} + \beta_4 GOV_{it} + \beta_5 WAGE_{it} + \beta_6 HUM_{it} + v_i + u_t + \varepsilon_{it}. \quad (5)$$

In equations (3)–(5), LA, CA, and TA are, respectively, labor agglomeration, capital agglomeration, and technical innovation agglomeration and $TRAN$ is urban rail development. If coefficient β_1 is significant, this indicates that urban rail development can indeed affect factor agglomeration in the city, but this is not sufficient to show that a mediating effect exists.

It is therefore necessary to proceed to the third step, which consists of testing of the relationships between urban rail development, factor agglomeration, and industrial agglomeration:

$$LQ1_{it}/LQ2_{it} = \alpha + \beta_1 TRAN_{it} + \beta_2 LA_{it} + \beta_3 GDP_{it} + \beta_4 INS_{it} + \beta_5 GOV_{it} + \beta_5 WAGE_{it} + \beta_6 HUM_{it} + v_i + u_t + \varepsilon_{it}, \quad (6)$$

$$LQ1_{it}/LQ2_{it} = \alpha + \beta_1 TRAN_{it} + \beta_2 CA_{it} + \beta_3 GDP_{it} + \beta_4 INS_{it} + \beta_5 GOV_{it} + \beta_5 WAGE_{it} + \beta_6 HUM_{it} + v_i + u_t + \varepsilon_{it}, \quad (7)$$

$$LQ1_{it}/LQ2_{it} = \alpha + \beta_1 TRAN_{it} + \beta_2 TA_{it} + \beta_3 GDP_{it} + \beta_4 INS_{it} + \beta_5 GOV_{it} + \beta_5 WAGE_{it} + \beta_6 HUM_{it} + v_i + u_t + \varepsilon_{it}. \quad (8)$$

Equations (6)–(8) chiefly serve to test the effect of factor agglomeration on industrial agglomeration. If, for instance, both β_1 and β_2 are significant, this verifies that a mediating effect exists; if either β_1 or β_2 is significant, but it is not known whether the other is significant, then the Sobel test must be performed. If the result of the Sobel test is significant, the existence of a mediating effect can be confirmed.

3.2. Explanation of Variables

3.2.1. Explained Variable. As industrial agglomeration theory has developed, scholars have come up with a number of methods for measuring industrial agglomeration. These methods, which include the industry share and industry concentration indicators (the simple ones) and the dynamic agglomeration indicator method, have been used to assess the level of industrial agglomeration, and all have their individual advantages and disadvantages. At present, many scholars choose to use the location quotient to assess the level of industrial agglomeration. Because the location quotient can eliminate factors associated with the differences in size between areas, it can truly express the spatial distribution of geographical factors. For instance, Liu and Xu (2010) [23], Chen et al.(2012) [24], Sun et al. (2012) [25], Yang and Liu (2019) [26], Mei and Ma et al.(2020) [27], Xia et al. (2020) [28] all employed the location quotient as their chief indicator for assessing industrial agglomeration. At the same time, when performing economic analysis of the agglomeration of an individual industry, the number of people working in a particular industry relates to the level of industrial agglomeration and can effectively reveal the specialized agglomeration effect in that industry. Accordingly, this study uses the location quotient to assess the level of industrial agglomeration:

$$LQ_{ij} = \left(Q_{ij} / \sum Q_{ij}\right) / \left(\sum Q_{ij} / \sum Q_i \sum Q_j\right). \tag{9}$$

In equation (9), LQ_{ij} indicates the level of industrial agglomeration and Q_{ij} indicates the number of persons employed in industry j in city i. When $LQ_{ij} > 1$, this indicates that industry j in city i has a relative advantage over industry j in other cities. This study adopted the location quotient to quantify the level of the industrial agglomeration of cities' manufacturing industries and consumer service industries.

3.2.2. Core Explanatory Variable. Urban rail development: this study's core explanatory variable is the urban rail transit line length, where the greater a city's urban rail transit line length, the greater the city's urban rail transit development.

3.2.3. Mediating Variables. This study's mediating variables consist of factor agglomeration variables. In accordance with the general Cobb–Douglas production function model, mediating variables chiefly include labor agglomeration, capital agglomeration, and technical innovation agglomeration.

First, to broadly compare the labor agglomeration characteristics of Chinese cities, this study chiefly relies on the concept of labor density to measure the level of labor agglomeration in cities. Labor density is obtained by dividing the population in each city's area of jurisdiction at the end of each year by the area of the city's administrative area:

$$\text{labor agglomeration} = \frac{\text{population in each city's area of jurisdiction at year} - \text{end}}{\text{area of the city's jurisdiction}} \times 100\%. \tag{10}$$

Second, regarding capital agglomeration, this study constructs a comprehensive capital agglomeration assessment indicator system and uses the factor analysis method to assess this indicator:

As shown in Table 1, the primary indicator of foreign capital agglomeration is the amount of foreign capital actually used in a city at the end of the year (RMB 10,000), which is denoted K1. The primary indicator of fixed capital agglomeration is the state of all social fixed asset investments in a city at year-end (RMB 10,000), which is denoted K2. The primary indicator of financial capital agglomeration is the balance of all RMB deposits in a city at year-end (RMB 10,000) and the balance of all RMB loans in a city at year-end (RMB 10,000), which are denoted K3 and K4, respectively.

Lastly, the indicator of technical innovation agglomeration consists of a city's level of technical innovation agglomeration, which is calculated by the patent updating model of Kou and Liu (2020) [29]. The first step is to estimate the value of all expired utility patents that were applied for in 1987–1997. The parameter obtained by this estimation process is used to model the distribution of patent value. This allows the calculation of the average values of patents of different ages, and these values serve as weighting coefficients for the values of relevant patents. Taking the end of each year (December 31) as the observation time for that year, utility patents that are still valid at that point in time (approved and still within the period of validity) are selected, and a patent value inventory is obtained after adding up the values of patents in different cities (or industries). Normalizing the country's aggregate patent value in 2001 to 100, each cities' technical innovation agglomeration indicators for the period of 2006–2018 are calculated.

3.2.4. Control Variables. Economic growth: China has already entered a key period of slowing economic growth and economic structural adjustment. Since conventional aggregate indicators of economic growth are inadequate to accurately portray the state of economic activities, this study employs the actual GDP per capital of city residents as an indicator of cities' levels of economic growth.

Table 1: Comprehensive capital agglomeration indicator system.

Primary indicator	Secondary indicator	Unit	Code
Foreign capital agglomeration	Amount of foreign capital actually used in a city at the end of the year	RMB 10, 000	K1
Fixed capital agglomeration	State of all social fixed asset investment in city at the end of the year	RMB 10, 000	K2
Financial capital agglomeration	Balance of all RMB deposits in city at the end of the year	RMB 10, 000	K3
	Balance of all RMB loans in city at the end of the year	RMB 10, 000	K4

Note: data are chiefly obtained from the China City Statistical Yearbook.

Upgrading of the industrial structure: upgrading of the industrial structure is an important step in the promotion of rapid economic development. This study chiefly employs the ratio of the sum of the value added by secondary and tertiary industries to GDP as the indicator of industrial structure upgrade.

Government expenditures: because local governments in China usually pursue local economic growth as their paramount goal, these governments use a portion of their fiscal revenue for public expenditures to promote economic growth. A series of fiscal policies adopted by governments to participate in economic activities could inevitably have an impact on their cities' economic growth. This study therefore chiefly employs the ratio of government expenditures to GDP as a proxy variable for government expenditures.

Wage level: the wage level constitutes the labor remuneration paid to employees by enterprises during a certain period. Generally, the higher the wage level in a city, the greater the city's appeal to workers, and the more it can attract high-end talent. Since this agglomeration of talent can promote the city's economic growth, wage level is an important indicator of local development and developmental ability. This study consequently adopts the average wage level of in-service employees as a proxy variable for a city's wage level.

Human capital: human capital has an extremely important promoting effect on the level of factor agglomeration. Some scholars have used average years of education to assess human capital, while others employ the share of persons at each educational level to assess this metric. Since the *China City Statistical Yearbook* published by the National Bureau of Statistics does not contain detailed data on the level of education of city residents, this study takes the number of in-school university students per 10,000 persons in each city as a proxy variable for human capital.

3.3. Data Sources. To maintain consistency in the statistical caliber, this study employs data for cities at the prefecture level and above in the period of 2006–2018. All data are obtained from the *China Statistical Yearbook*, *China City Statistical Yearbook*, and *China Urban Construction Statistical Yearbook* for the period of 2006–2018.

4. Empirical Results

4.1. Empirical Results and Analysis. In accordance with the theoretical principles of mediating effect testing, SPSS 22.0 software and the mediating effect model testing procedures proposed by Preacher and Hayes (2008) [16] are used to perform empirical analysis. The obtained empirical results are shown in Tables 2–4. The analysis of urban rail line length in Table 2 yields the following empirical results concerning the effect of urban rail line length on the industrial agglomeration of manufacturing and consumer service via labor agglomeration.

First, from the empirical results on urban rail line length, labor agglomeration, and manufacturing industry agglomeration, after controlling for the upgrading of the industrial structure, government expenditures, wage level, and human capital, model (1) indicates that urban rail line length has a significant promoting effect on manufacturing industry agglomeration; model (2) indicates that urban rail line length also has a significant promoting effect on labor agglomeration; and model (3) indicates that urban rail line length and labor agglomeration have a significant promoting effect on manufacturing industry agglomeration. These findings suggest that urban rail line length can promote manufacturing industry agglomeration via labor agglomeration.

Second, from the empirical results on urban rail line length, labor agglomeration, and consumer service industry agglomeration, model (4) indicates that urban rail line length has a significant promoting effect on consumer service industry agglomeration; model (5) indicates that urban rail line length also has a significant promoting effect on labor agglomeration; and model (6) indicates that urban rail line length and labor agglomeration have a significant promoting effect on consumer service industry agglomeration. These results suggest that urban rail line length can promote consumer service industry agglomeration via labor agglomeration.

Thirdly, from the empirical results of control variables, GDP, wage level, and human capital can promote the manufacturing industry agglomeration, consumer service industry agglomeration, and labor agglomeration; industrial technology upgrading can inhibit the manufacturing industry agglomeration; government expenditure can promote the consumer service industry agglomeration and labor agglomeration.

The analysis of urban rail line length in Table 3 yields the following empirical results concerning the effect of capital agglomeration on the industrial agglomeration of manufacturing and customer services.

First, from the empirical results on urban rail line length, capital agglomeration, and manufacturing industry agglomeration, model (7) indicates that urban rail line length has a significant promoting effect on manufacturing industry agglomeration; model (8) indicates that urban rail line length has a significant promoting effect on capital

Table 2: Empirical analysis results 1.

	Model (1) LQ_{1it}	Model (2) $LnLA_{it}$	Model (3) LQ_{1it}	Model (4) LQ_{2it}	Model (5) $LnLA_{it}$	Model (6) LQ_{2it}
$LnTRAN_{it}$	0.1628**	0.2781***	0.1398**	0.2318***	0.2331***	0.2205***
	(2.23)	(3.31)	(2.26)	(5.56)	(3.41)	(4.75)
$LnLA_{it}$			0.0723**			0.0681***
			(2.41)			(2.92)
$LnGDP_{it}$	0.6590***	0.6397***	0.6431***	0.6019**	0.5747***	0.5746***
	(4.19)	(3.28)	(3.66)	(2.35)	(2.80)	(2.55)
$LnINS_{it}$	−0.3142***	−0.0302	−0.3292***	0.0735	0.0634	0.0655
	(−6.38)	(−1.38)	(−6.28)	(1.06)	(0.86)	(0.92)
$LnGOV_{it}$	−0.0748	0.0165	−0.0736	0.8668***	0.7040***	0.1169
	(−1.03)	(0.19)	(−1.01)	(3.02)	(2.91)	(0.46)
$LnWAGE_{it}$	0.0577	0.1121***	0.1073***	0.0340	0.0648	0.7722***
	(1.11)	(4.61)	(4.41)	(0.44)	(0.73)	(3.09)
$LnHUM_{it}$	0.3005***	0.5137***	0.2852***	0.2726**	0.2959**	0.3044**
	(4.56)	(2.62)	(4.25)	(2.02)	(2.09)	(2.11)
$CONSTANT_{it}$	5.2378***	3.8542***	4.9153***	6.0183***	5. 0818**	0.0534
	(15.91)	(4.42)	(11.21)	(4.54)	(2.08)	(0.68)
R-squared	0.36	0.48	0.33	0.31	0.46	0.34
Obs.	230	230	230	230	230	230

Note: *, **, and *** indicate 10%, 5%, and 1% levels of significance; t values are in parentheses.

Table 3: Empirical analysis results 2.

	Model (7) LQ_{1it}	Model (8) $LnCA_{it}$	Model (9) LQ_{1it}	Model (10) LQ_{2it}	Model (11) $LnCA_{it}$	Model (12) LQ_{2it}
$LnTRAN_{it}$	0.0091**	0.1324**	0.1142*	0.2519***	0.0091**	0.2551***
	(2.19)	(2.34)	(1.85)	(6.57)	(2.19)	(6.82)
$LnCA_{it}$			0.2033*			0.3471**
			(1.72)			(2.34)
$LnGDP_{it}$	0.0384***	0.2505**	0.3274***	−0.1994***	1.1264***	−0.3071***
	(5.67)	(2.45)	(2.91)	(−3.14)	(9.10)	(−4.23)
$LnINS_{it}$	0.0264***	−0.3057***	−0.2528**	0.1421	0.5137***	0.0930
	(3.02)	(−2.54)	(−2.16)	(1.53)	(2.62)	(1.01)
$LnGOV_{it}$	0.0055	−0.0748	−0.0638	0.0204	0.0165	0.0189
	(0.47)	(−1.03)	(−1.10)	(0.34)	(0.19)	(0.32)
$LnWAGE_{it}$	0.0071	0.0577	0.0720	0.0246	0.1023	0.0148
	(1.49)	(1.11)	(1.26)	(0.48)	(0.85)	(0.30)
$LnHUM_{it}$	−0.0012	−0.1931***	−0.1955***	0.1148**	−0.1357	0.1278**
	(−0.22)	(−2.85)	(−2.92)	(2.03)	(−1.17)	(2.26)
$CONSTANT_{it}$	1.8061***	1.1578	4.7759	0.6563	−11.2270***	1.7299**
	(17.87)	(0.88)	(1.57)	(0.89)	(−6.63)	(2.22)
R-squared	0.37	0.39	0.38	0.31	0.47	0.33
Obs.	230	230	230	230	230	230

Note: *, **, and *** indicate 10%, 5%, and 1% levels of significance; t values are in parentheses.

agglomeration; and model (9) indicates that urban rail line length and capital agglomeration have a significant promoting effect on manufacturing industry agglomeration. These results suggest that urban rail line length can promote manufacturing industry agglomeration via capital agglomeration.

Second, from the empirical results on urban rail line length, capital agglomeration, and consumer service industry agglomeration, model (10) indicates that urban rail line length has a significant promoting effect on consumer service industry agglomeration; model (11) indicates that urban rail line length has a significant promoting effect on capital agglomeration; and model (12) indicates that urban rail line length and capital agglomeration have a significant promoting effect on consumer service industry agglomeration. These results suggest that urban rail line length can promote consumer service industry agglomeration via capital agglomeration.

Third, from the empirical results of the control variables, only GDP can promote capital agglomeration and manufacturing agglomeration, and the effect of other variables cannot be judged.

The analysis of the effect of urban rail line length on industrial agglomeration via technical innovation agglomeration in Table 4 yields the following empirical results.

First, from the empirical results on urban rail line length, technical innovation agglomeration, and manufacturing

Table 4: Empirical analysis results 3.

	Model (13) LQ_{1it}	Model (14) $LnTA_{it}$	Model (15) LQ_{1it}	Model (16) LQ_{2it}	Model (17) $LnTA_{it}$	Model (18) LQ_{2it}
$LnTRAN_{it}$	0.1324***	0.1870***	0.1096*	0.0382**	0.1870***	0.0346*
	(2.34)	(3.32)	(1.77)	(2.11)	(3.32)	(1.84)
$LnTA_{it}$			0.1218*			0.0193***
			(1.67)			(2.66)
$LnGDP_{it}$	0.2505**	1.2624***	0.4042***	0.2579*	0.2801**	0.2810**
	(2.45)	(11.72)	(3.21)	(1.93)	(2.02)	(1.98)
$LnINS_{it}$	−0.3057***	1.1247***	−0.1687	−0.1602**	−0.1901**	−0.1945**
	(−2.54)	(6.26)	(−1.24)	(−2.24)	(−2.40)	(−2.42)
$LnGOV_{it}$	−0.0748	0.2214	−0.0478	0.0445	0.0413	0.0438
	(−1.03)	(1.08)	(−0.81)	(1.30)	(1.19)	(1.24)
$LnWAGE_{it}$	0.0577	0.1096**	0.0710	0.1068***	0.1065***	0.1070***
	(1.11)	(2.04)	(1.27)	(6.94)	(6.99)	(7.21)
$LnHUM_{it}$	−0.1931***	−0.0860	−0.2036***	0.0503	0.0475	0.0497
	(−2.85)	(−0.77)	(−2.92)	(1.52)	(1.44)	(1.47)
$CONSTANT_{it}$	1.1578*	−17.6493***	−0.9911	7.2990***	3.1011***	8.0390***
	(1.88)	(−10.12)	(−0.63)	(7.63)	(2.52)	(8.17)
R-squared	0.38	0.66	0.30	0.43	0.56	0.57
Obs.	230	230	230	230	230	230

Note: *, **, and *** indicate 10%, 5%, and 1% levels of significance; t values are in parentheses.

Table 5: Empirical analysis results 4.

	Model (19) LQ_{1it}	Model (20) $LnLA_{it}$	Model (21) LQ_{1it}	Model (22) LQ_{2it}	Model (23) $LnLA_{it}$	Model (24) LQ_{2it}
$LQ_{it\text{-}1}$	0.3437**	0.0853***	0.3281***	0.2323**	0.0715**	0.1590***
	(2.13)	(2.79)	(2.58)	(1.97)	(2.28)	(7.15)
$LnTRAN_{it}$			0.1227***			0.0379***
			(3.15)			(3.69)
$LnLA_{it}$			0.6261***			0.1121**
			(5.85)			(2.32)
$LnGDP_{it}$	0.2451	−0.2708*	−0.0617	−0.2075	−0.0414*	0.0258***
	(1.62)	(−1.75)	(−0.95)	(−1.60)	(−1.76)	(3.72)
$LnINS_{it}$	−0.1903	0.0839	0.2145∗	0.3127	0.0842	0.0029
	(−1.03)	(0.30)	(1.75)	(1.63)	(1.22)	(0.25)
$LnGOV_{it}$	−0.0131	0.0915***	0.0118	−0.0203	−0.0143	0.0108
	(−0.26)	(2.68)	(0.83)	(−0.57)	(−1.26)	(0.79)
$LnWAGE_{it}$	0.0263	−0.0275	−0.0477	−0.1675**	0.0316	0.0026
	(0.75)	(−0.41)	(−0.82)	(−2.24)	(1.63)	(0.74)
$LnHUM_{it}$	−0.0421	−0.0389	0.0133	−0.0487	0.0197	−0.0009
	(−0.42)	(−0.32)	(0.28)	(−0.60)	(0.57)	(−0.16)
$CONSTANT_{it}$	0.0482	4.3551*	0.2280	2.9495**	0.7388*	2.0719***
	(0.03)	(1.89)	(0.25)	(2.29)	(1.67)	(19.70)
Dum_Individual	YES	YES	YES	YES	YES	YES
Dum_Year	YES	YES	YES	YES	YES	YES
Wald value	16.47***	33.96***	15.10***	40.95***	44.52***	48.98***
Obs.	196	196	196	196	196	196

Note: *, **, and *** indicate 10%, 5%, and 1% levels of significance; z values are in parentheses.

industry agglomeration, model (13) indicates that urban rail line length has a significant promoting effect on manufacturing industry agglomeration; model (14) indicates that urban rail line length has a significant promoting effect on technical innovation agglomeration; and model (15) indicates that urban rail line length and technical innovation agglomeration have a significant promoting effect on manufacturing industry agglomeration. These findings suggest that urban rail line length can promote manufacturing industry agglomeration via technical innovation agglomeration.

Second, from the empirical results on urban rail line length, technical innovation agglomeration, and consumer service industry agglomeration, model (16) indicates that urban rail line length has a significant promoting effect on consumer service industry agglomeration; model (17) indicates that urban rail line length has a significant promoting effect on technical innovation agglomeration; and model

Table 6: Empirical analysis results 5.

	Model (25) LQ_{1it}	Model (26) $LnCA_{it}$	Model (27) LQ_{1it}	Model (28) LQ_{2it}	Model (29) $LnCA_{it}$	Model (30) LQ_{2it}
$LQ_{it\text{-}1}$	−0.3528**	−0.2643*	0.2710**	0.2891**	−0.1052	0.0527*
	(−2.12)	(−1.78)	(2.21)	(2.31)	(−0.94)	(1.79)
$LnTRAN_{it}$	0.0740*	0.0464*	0.0925***	0.1367***	0.0467***	0.0646***
	(1.68)	(1.66)	(3.56)	(3.62)	(3.40)	(4.47)
$LnCA_{it}$			0.0781*			0.0190*
			(1.72)			(1.85)
$LnGDP_{it}$	0.3712***	−0.4654***	−0.1012**	−0.3096*	−0.0977***	0.1538***
	(3.23)	(−3.35)	(−2.20)	(−1.90)	(−2.92)	(5.81)
$LnINS_{it}$	−0.0048	−0.0741	0.1396	0.2624	−0.0204	−0.0902***
	(−0.02)	(−0.21)	(1.38)	(1.04)	(−0.37)	(−8.01)
$LnGOV_{it}$	0.0254	0.0952	−0.0076	−0.0879	−0.0161*	0.0637***
	(0.59)	(1.64)	(−0.29)	(−0.45)	(−1.69)	(8.60)
$LnWAGE_{it}$	0.0209	0.0157	−0.0319	−0.1190***	0.0405*	0.0534***
	(0.56)	(0.19)	(−0.83)	(−2.72)	(1.65)	(8.04)
$LnHUM_{it}$	−0.1886**	0.0995	0.0288	0.0974	0.0710***	0.0820***
	(−2.34)	(0.73)	(0.61)	(1.01)	(2.68)	(8.06)
$CONSTANT_{it}$	−1.2483	5.9138***	0.8837	3.2508	1.3719***	8.9015***
	(−0.93)	(3.67)	(1.45)	(1.48)	(2.67)	(62.07)
Dum_Individual	YES	YES	YES	YES	YES	YES
Dum_Year	YES	YES	YES	YES	YES	YES
Wald value	27.98***	76.38***	51.08***	125.42***	88.39***	190.23***
Obs.	196	196	196	196	196	196

Note: *, **, and *** indicate 10%, 5%, and 1% levels of significance; z values are in parentheses.

Table 7: Empirical analysis results 6.

	Model (31) LQ_{1it}	Model (32) $LnTA_{it}$	Model (33) LQ_{1it}	Model (34) LQ_{5it}	Model (35) $LnTA_{it}$	Model (36) LQ_{5it}
$LQ_{it\text{-}1}$	−0.6618**	−0.2513	0.4776***	0.2664***	0.0339	0.2103***
	(−2.28)	(−1.57)	(3.05)	(2.62)	(0.19)	(7.14)
$LnTRAN_{it}$	0.1620***	0.2184**	0.1684***	0.0366**	0.2184***	0.0342***
	(6.92)	(1.95)	(7.43)	(1.97)	(3.85)	(3.39)
$LnTA_{it}$			0.0297*			0.0107***
			(1.80)			(2.61)
$LnGDP_{it}$	0.5332***	−0.4726**	−0.0832	0.9308***	−0.3422***	−0.1923***
	(2.83)	(−2.11)	(−1.01)	(7.59)	(−3.35)	(−4.14)
$LnINS_{it}$	0.0368	0.1408	0.1295	0.5930**	−0.2642*	0.3554***
	(0.17)	(0.32)	(0.96)	(2.12)	(−1.78)	(5.71)
$LnGOV_{it}$	0.0069	0. 1282**	−0.0084	0.2506	0.2331**	−0.0217
	(0.13)	(2.42)	(−0.39)	(1.21)	(2.39)	(−0.99)
$LnWAGE_{it}$	0.0311	0.0110	0.0239	0.0420	−0.0008	−0.0080
	(0.36)	(0.08)	(0.41)	(1.09)	(−0.04)	(−1.33)
$LnHUM_{it}$	−0.0666	0.0525	−0.0020	0.0695	0.2393***	0.0421
	(−0.57)	(0.43)	(−0.04)	(0.56)	(2.52)	(1.25)
$CONSTANT_{it}$	−4.0070**	5.1434*	−0.1086	−12.0428***	4.0413***	1.0548**
	(−2.06)	(1.87)	(−0.09)	(−6.03)	(3.08)	(1.95)
Dum_Individual	YES	YES	YES	YES	YES	YES
Dum_Year	YES	YES	YES	YES	YES	YES
Wald value	14.25***	60.54***	31.86***	106.34***	106.23***	118.98***
Obs.	196	196	196	196	196	196

Note: *, **, and *** indicate 10%, 5%, and 1% levels of significance; z values are in parentheses.

(18) indicates that urban rail line length and technical innovation agglomeration have a significant promoting effect on consumer service industry agglomeration. These findings suggest that urban rail line length can promote consumer service industry agglomeration via technical innovation agglomeration.

Thirdly, from the empirical results of control variables, GDP can promote the agglomeration of technological innovation, manufacturing, and consumer services; wage level can promote the agglomeration of technological innovation and consumer services; human capital can inhibit the agglomeration of manufacturing.

4.2. Robustness Test. The foregoing section describes the use of empirical models to analyze the effect of urban rail development on industrial agglomeration. To further test the rigor and scientific validity of the conclusions drawn above, this study uses the two-step method GMM to perform empirical estimates of the above dynamic models with panel data. Tables 5–7 provide quantitative empirical results for the dynamic panel data models, which take urban rail line length as the explanatory variable.

First, the regression results for urban rail development, labor agglomeration, and industrial agglomeration in Table 5 show that after controlling for the upgrading of the industrial structure, government expenditures, wage level, and human capital, urban rail line length can still exert a significant promoting effect on manufacturing industry agglomeration and consumer service industry agglomeration via labor agglomeration. This is consistent with the results shown in Table 2 and indicates that increases in urban rail line length can effectively induce manufacturing industry agglomeration and consumer service industry agglomeration in a city through labor agglomeration.

Second, the regression results for urban rail development, capital agglomeration, and industrial agglomeration in Table 6 show that urban rail line length still exerts a significant promoting effect on manufacturing industry agglomeration and consumer service industry agglomeration in a city. This is consistent with the results shown in Table 3 and indicates that urban rail line length can effectively induce manufacturing industry agglomeration and consumer service industry agglomeration in a city through capital agglomeration.

Third, the regression results for urban rail development, technical innovation agglomeration, and industrial agglomeration in Table 7 show that urban rail line length exerts a significant positive promoting effect on manufacturing industry agglomeration and consumer service industry agglomeration in a city. This is consistent with the results shown in Table 4 and indicates that increases in urban rail line length can effectively induce manufacturing industry agglomeration and consumer service industry agglomeration in a city through technical innovation agglomeration.

In summary, this study uses GMM-based dynamic panel models to convincingly verify that urban rail development affects industrial agglomeration via factor agglomeration, and this study's conclusions possess a certain degree of scientific validity and robustness.

5. Conclusions and Recommendations

This study uses location quotients to calculate levels of industrial agglomeration in Chinese cities of the prefecture level and above during 2006–2018 and conducts empirical analysis of the effect of urban rail line length on industrial agglomeration. This study draws the following conclusions: (1) urban rail development has a significant promoting effect on labor agglomeration, capital agglomeration, and technical innovation agglomeration; (2) urban rail development can effectively induce manufacturing industry agglomeration and consumer service industry agglomeration in cities; (3) the influence of urban rail development on urban manufacturing industry agglomeration and consumer service industry agglomeration is chiefly attributable to the mediating effect of factor agglomeration (labor agglomeration, capital agglomeration, and technical innovation agglomeration). This study therefore makes the following recommendations:

(1) Progressively completing urban rail transit networks and promoting the coordinated development of urban rail transit: to achieve a strong economic stimulating effect from urban rail transit, urban centers should engage in coordinated rail transit planning and batchwise development and establish dedicated departments to manage and design rail transit systems.

(2) Strengthening the development of integrated rail transit hubs and the coordination of urban rail transit with other modes of transportation: the connection and convenience of rail transit systems and other modes of transportation should be constantly strengthened so that various modes of transportation can be organically combined to maximize network effects and provide more convenient services for urban agglomerations.

(3) Optimizing the allocation of capital to urban rail transit and improving the investment performance of rail transit capital: more functional, broader-coverage total factor markets should be established to promote the robust development of capital factor markets. This could allow capital to move more freely between different cities and between cities and their suburban districts, so that the radiating role of central cities could be fully promoted to increase the effectiveness of capital investment in rail transit.

Data Availability

The data used to support the findings of this study are included within the article.

Conflicts of Interest

The authors declare that there are no conflicts of interest.

Acknowledgments

This work was supported in part by the Taishan Scholar Project of Shandong Province of China, under Grant no. tsqn20190-9078.

References

[1] F. Liszt, *The National System of Political Economy*, Foreign Language Teaching and Research Press, 1961.

[2] R. Cervero, "Mixed land use and commuting evidence from the American hosing survey," *Transportation Reseach*, vol. 30, no. 5, pp. 120–156, 1996.

[3] D. Prasertsubpakij and V. Nitivattananon, "Evaluating accessibility to Bangkok Metro Systems using multi-

dimensional criteria across user groups," *IATSS Research*, vol. 36, no. 1, pp. 56–65, 2012.

[4] R. Cervero, "Rail transit and joint development: land market impacts in Washington, D.C. and atlanta," *Journal of the American Planning Association*, vol. 60, no. 1, pp. 83–94, 1994.

[5] D. P. Mc Millen and J. McDonald, "Reaction of house prices to a new rapid transit line: Chicago's midway line, 1983—1999," *Real Estate Economics*, vol. 32, no. 3, pp. 463–486, 2004.

[6] J. Kim and M. Zhang, "Determining transit's impact on Seoul commercial land values: an application of spatial econometrics," *International Real Estate Review*, vol. 8, no. 1, pp. 1–26, 2005.

[7] S. Lee, C. Yi, and S.-P. Hong, "Urban structural hierarchy and the relationship between the ridership of the Seoul metropolitan subway and the land-use pattern of the station areas," *Cities*, vol. 35, pp. 69–77, 2013.

[8] H. P. Liu, J. F. Li, and H. Q. Deng, "Analyze of submarket effect of the influence of rail transit on nearby housing prices: the case study of No.1 line in Wuhan," *Journal of South China Normal University(Natural Science Edition)*, vol. 47, no. 42, pp. 128–134, 2015, in Chinese.

[9] Y. N. Wang and J. Chen, "Research on the incremental effect of urban rapid rail transit on real estate value," *CONSTRUCTION ECONOMY*, vol. 38, no. 2, pp. 68–71, 2017, in Chinese.

[10] S. I. Mohammad, D. J. Graham, and P. C. Melo, "The effect of the dubai metro on the value of residential and commercial properties," *Journal of Transport and Land Use*, vol. 10, no. 1, pp. 263–290, 2017.

[11] C. Mulley, C. H. P. Tsai, and L. Ma, "Does residential property price benefit from light rail in Sydney?" *Research in Transportation Economics*, pp. 3–10, 2018.

[12] R. Trojanek and M. Gluszak, "Spatial and time effect of subway on property prices," *Journal of Housing and the Built Environment*, vol. 33, no. 2, pp. 359–384, 2018.

[13] J. Luo and S. N. Mo, "Subway opening, "affordable housing and commercial housing prices," *Shanghai Journal of Economics*, vol. 11, pp. 84–93, 2019, in Chinese.

[14] W. Wang and H. Ma, *High-speed Railway Network, Labor Transfer and Industrial Space Agglomeration*, vol. vol22, pp. 38–48, Contemporary Economy & Management, 2019, in Chinese.

[15] I. Stateva and Financial Centers, "Europe -what is the perspective?" *Ikonomiceski I Sotsialni Alternativi*, vol. 1, pp. 36–43, 2019.

[16] H. L. Gu and Y. Chen, "Using the grey model to analyze the impact of the primary, secondary, and tertiary industries on the public's attention to air pollution in three cities," *Mathematical Problems in Engineering*, vol. 2020, 15 pages, 2020.

[17] J. Yuan, S. Ding, and K. Mei, "Fixed-time SOSM controller design with output constraint," *Nonlinear Dynamics*, vol. 102, no. no3, pp. pp1567–1583, 2020.

[18] Y. Shu, L. Lin, and Y. Hu, "A study on the health output effect of Chinese medical service industry agglomeration based on big data analysis," *Mathematical Problems in Engineering*, vol. 2020, 9 pages, 2020.

[19] W. Chen, H. Zeng, and Y. Liu, "Analysis on the spatial-temporal dynamics of financial agglomeration with Markov chain approach in China," *Mathematical Problems in Engineering*, vol. 2014, 6 pages, 2014.

[20] T. Li, L. Liang, and D. Han, "Research on the efficiency of green technology innovation in China's provincial high-end manufacturing industry based on the RAGA-PP-SFA model," *Mathematical Problems in Engineering*, vol. 2018, 13 pages, 2018.

[21] W. JiG. Chen et al., "Recognition method of green pepper in greenhouse based on least-squares support vector machine optimized by the improved particle swarm optimization," *IEEE Access*, vol. 7, pp. 119742–119754, 2019.

[22] K. J. Xu and A. F Hayes, "Asymptotic and resampling strategies for assessing and comparing indirect effects in multiple mediator models," *Behavior Research Methods*, vol. 40, pp. 879–891, 2008.

[23] J. Liu and K. N. Xu, "Industrial agglomeration, industrialization level and regional disparity: an empirical study based on provincial panel data in China," *Finance & Economics*, vol. 10, pp. 65–72, 2010, in Chinese.

[24] G. L. Chen and J. J. Chen, *Industrial Association, spatial geography and co agglomeration of secondary and tertiary industries*, vol. 4, pp. 82–100, Management World, 2012, in Chinese.

[25] P. Y. Sun, S. Han, and S. J. Jin, "An analysis of the impact of industrial agglomeration on foreign direct investment," *Journal of Quantitative & Technical Economics*, vol. 29, no. 9, pp. 40–57, 2012, in Chinese.

[26] R. F. Yang and Q. W. Liu, "Productive service input and manufacturing global value chain status: impact mechanism and empirical test," *Word Economy Studies*, vol. 4, pp. 71–82, 2019, in Chinese.

[27] K. Mei, Li Ma, R. He, and S. Ding, "Finite-time controller design of multiple integrator nonlinear systems with input saturation," *Applied Mathematics and Computation*, vol. 372, p. 124986, 2020.

[28] Z. Q. Xiaothers et al., "Trilemma among energy, economic and environmental efficiency: can dilemma of EEE address simultaneously in era of COP 21?" *Journal of Environmental Management*, vol. 276, 2020.

[29] Z. L. Kou and X. Y. Liu, "On patenting behavior of Chinese firms: stylized facts and effects of innovation policy," *Economic Research Journal*, vol. 55, no. 03, pp. 83–99, 2020, in Chinese.

Hindawi
Mathematical Problems in Engineering
Volume 2021, Article ID 8887479, 15 pages
https://doi.org/10.1155/2021/8887479

Research Article

Relative Position Model Predictive Control of Double Cube Test-Masses Drag-Free Satellite with Extended Sliding Mode Observer

Enyou Wang,[1] **Jinxiu Zhang**,[1,2] **Huayi Li**,[1] **and Ming Liu**[1]

[1]*School of Astronautics, Harbin Institute of Technology, Harbin 150001, China*
[2]*School of Aeronautics and Astronautics, Sun Yat-sen University, Guangzhou 511436, China*

Correspondence should be addressed to Enyou Wang; enyou.w@gmail.com

Received 11 September 2020; Revised 26 November 2020; Accepted 13 December 2020; Published 23 January 2021

Academic Editor: Shihong Ding

The drag-free satellites, being space-borne ultrahigh precise measurement platforms, have played irreplaceable roles in a great number of space science missions such as navigation, earth science, fundamental physics, and astrophysics. Most of these missions have to be performed based on the satellites placed with double cube test-masses, which makes the satellite layout and control strategy be more complex. This paper investigates the orbit keeping control problem of a class of low Earth orbit drag-free satellites with double cube test masses. A disturbance observer-based composite control method is proposed, which consists of an extended sliding mode observer and the tube-based robust model predictive control approach. In this design, the observer is proposed to estimate the relative position and velocity of the satellite and the external space disturbance force. A tube-based robust model predictive control scheme is then developed to stabilize the satellite orbit control systems in the presence of actuator saturation, state constraints, and additive stochastic noises. Finally, a simulation example is presented to demonstrate the efficacy and superiority of the proposed orbit control method.

1. Introduction

In recent years, the drag-free satellites [1], being space-borne ultrahigh precise measurement platforms, have played irreplaceable roles in many space science missions, such as the test of equivalence principle [2], the measurement of the Earth gravity field [3], and the detection of gravitational waves [4]. The drag-free satellites possess many advantages; for example, they can provide autonomous precision orbit determination, map the static and time-varying components of the Earth's mass distribution more accurately, deepen the understanding of the fundamental force of gravity, eventually open up a new window to the universe through the detection and observation of gravitational waves, and so forth.

The key technology of the drag-free satellite is the gravitational reference sensor (GRS), which insulates an internal free-floating test mass (TM, also called proof mass) from both external disturbances and disturbances caused by the spacecraft itself [5]. The drag-free satellites can be divided into two types [6]. The first one is the "accelerometer" drag-free mode, where an electrostatic accelerometer is used as the primary sensor and an electrostatic suspension actuator is paired to maintain the TM to be centred in its cage; therefore it can counter the disturbance forces acting on the spacecraft [7–11]. The second one is free-falling TM mode, in which the satellite provides indirect drag-free behaviour by tracking the movement of the free-falling TM in the cage [12–15]. In particular, the structure of a satellite with two cube TMs is always regarded as the primary layout in these missions, which makes the GRS be more complex and the control system design work be more challenging. For example, as shown in Figure 1, the drag-free satellite containing two cube TMs will enter a low Earth orbit (LEO), which decays more rapidly due to the decelerating effects of the Earth's atmosphere.

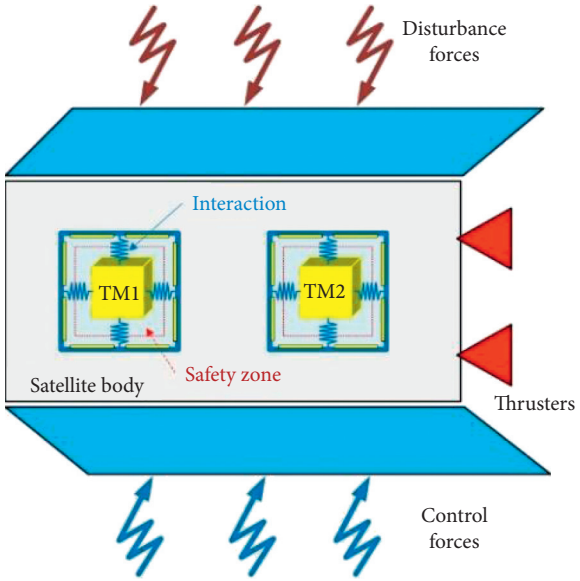

Figure 1: A kind of drag-free satellite structure with double test-masses.

In the research area of control for drag-free satellites, a trade-off should be considered among system complexity, fuel conservation, cost of components, operations, performance, and so forth [16]. In fact, it is always difficult for the drag-free satellite to obtain control satisfactory performance due to the existence of external time-varying environmental disturbances and the unmodelled internal uncertainties. To solve this problem, various types of robust control algorithms have been proposed, such as model predictive control (MPC) [17], H_∞ control [18, 19], μ-synthesis control [20], embedded model control (EMC) technique [21], and quantitative feedback theory [22]. However, these design results can only realize disturbance attenuation but not disturbance rejection. In order to improve closed-loop control performance, the disturbance observer-based control [23–31] and active disturbance rejection control [32–39] have been developed for drag-free satellite to pursue more ideal control system performance [25, 40–50]. However, how to design a suitable observer to estimate the disturbances more precisely is still an open and attractive problem [51].

This paper investigates the orbit control problem for a class of LEO drag-free satellites with double cube TMs based on the relative position dynamics with state constraints, actuator saturation, and the additive stochastic disturbances. In this design, an extended sliding mode observer method is developed to estimate the system states. Then, a tube-based robust model predictive control (TRMPC) approach is presented [52] to stabilize the resulting orbit control systems. In particular, the TRMPC design approach is divided into the following two steps: (i) an offline evaluation of the constraints to ensure the uncertain future trajectories to lie in sequence of sets, which is called tubes, and (ii) an online MPC scheme designed for the nominal trajectories. As a result, the orbit control issue for the drag-free satellite is solved.

The remaining of this paper is organized as follows. Section 2 formulates the design problem under investigation; the design of disturbance observation-based composite control strategy is presented in Section 3. A demonstrated simulation example is provided in Section 4, and the paper is concluded in Section 5.

2. Problem Formulation

According to [22, 53], for a LEO satellite containing two TMs, as shown in Figure 2, the drag-free control strategy is defined as follows: TM1 is chosen as the gravitational reference, which flies freely in a pure gravitational orbit, and the satellite and TM2 are controlled to follow TM1; then the linearized relative position dynamics between the TMs and the satellite are given as follows:

$$\ddot{\rho}_{1i}(t) + M_t\dot{\rho}_{1i}(t) + N_t\rho_{1i}(t) = \frac{1}{m_i}\left[F_{c,1i}(t) + F'_{d,1i}(t)\right], \quad i = 0 \text{ or } 2, \tag{1}$$

where $i = 0$ means the satellite and $i = 2$ means the TM2; $\rho_{1i}(t)$, m_i, and $F_{c,1i}(t)$ represent the relative position variables, the mass of the satellite or the TM2, and the control forces; $F'_{d,1i}(t)$ is the sum of all kinds of disturbances, which for the satellite, the air drag, the solar radiation pressure, and the thruster quantization error and other stochastic noises is considered primarily, and, for the TM2, it mainly consists of electrostatic interference signals, actuator quantization error, and other stochastic noises [9, 40].

$$M_t = \begin{bmatrix} 0 & -2\omega_0 & 0 \\ 2\omega_0 & 0 & 0 \\ 0 & 0 & 0 \end{bmatrix} - K_t,$$
$$N_t = \begin{bmatrix} -3\omega_0 & 0 & 0 \\ 0 & 0 & 0 \\ 0 & 0 & \omega_0^2 \end{bmatrix} - D_t, \tag{2}$$

where ω_0 is orbit angular velocity of the TM1 and K_t and D_t are the damping factors between the TM and its condenser cage [54].

The desired positions and velocities of the satellite and TM2 are denoted as $\rho_{10}^d(t)$, $\dot{\rho}_{10}^d(t)$, $\rho_{12}^d(t)$, and $\dot{\rho}_{12}^d(t)$, respectively. The desired positions $\rho_{10}^d(t)$ and $\rho_{12}^d(t)$ are some constants dependent on the layout of the satellite. The relative velocities are defined as follows: $\dot{\rho}_{10}^d(t) = 0$ and $\dot{\rho}_{12}^d(t) = 0$. Define the following error variables for case of presentation:

$$\begin{aligned} \tilde{\rho}_{1i}(t) &= \rho_{1i}(t) - \rho_{1i}^d(t), \\ \dot{\tilde{\rho}}_{1i}(t) &= \dot{\rho}_{1i}(t) - \dot{\rho}_{1i}^d(t), \\ i &= 0 \text{ or } 2. \end{aligned} \tag{3}$$

By substituting (3) into (1), one can obtain

$$\ddot{\tilde{\rho}}_{1i}(t) + M_t\dot{\tilde{\rho}}_{1i}(t) + N_t\tilde{\rho}_{1i}(t) = \frac{1}{m_i}\left[F_{c,1i}(t) + F_{d,1i}(t)\right], \quad i = 0 \text{ or } 2. \tag{4}$$

Due to the limit volume of the capacitor cage, the relative error variables should satisfy $\tilde{\rho}_{1i}(t) \le \tilde{\rho}_{\max}$ and $\dot{\tilde{\rho}}_{1i}(t) \le \dot{\tilde{\rho}}_{\max}$, which are the state constraints. For convenience, formations (4) should be translated into a state space model. By

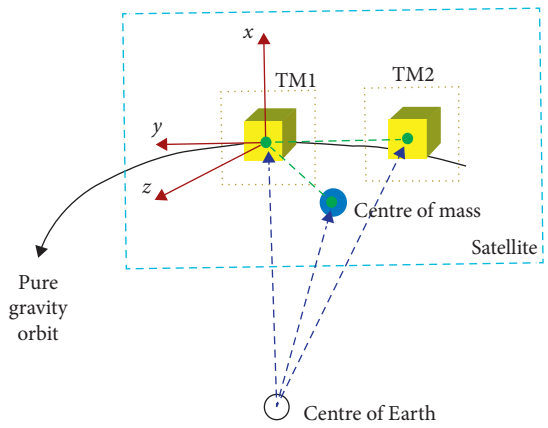

FIGURE 2: The relative position dynamics between the TMs and the satellite, with respect to TM1 Hill reference system.

choosing $x_1(t) = [\tilde{\rho}_{10}^T(t), \dot{\tilde{\rho}}_{10}^T(t)]^T$ and $x_2(t) = [\tilde{\rho}_{12}^T(t), \dot{\tilde{\rho}}_{12}^T(t)]^T$, $u_1(t) = F_{c,10}(t)$, $u_2(t) = F_{c,12}(t)$, $F_{d,10}(t) = \omega_1(t) + \xi_1(t)$, and $F_{d,12}(t) = \omega_2(t) + \xi_2(t)$, where $\omega_i(t)$ and $\xi_i(t)$ $(i = 1, 2)$ denote the unknown stochastic noises and unknown estimable disturbances, respectively. Then, the state space model is given as follows:

$$\begin{cases} \dot{x}_i(t) = A_i x_i(t) + B_i u_i(t) + B_{\omega,i}(\omega_i(t) + \xi_i(t)), \\ y_i(t) = C_i x_i(t), \end{cases} \tag{5}$$

where

$$A_i = \begin{bmatrix} 0_3 & I_3 \\ N_t & M_t \end{bmatrix},$$

$$B_1 = B_{\omega,1} = \begin{bmatrix} 0_3 \\ \frac{1}{m_0} I_3 \end{bmatrix},$$

$$B_2 = B_{\omega,2} = \begin{bmatrix} 0_3 \\ \frac{1}{m_2} I_3 \end{bmatrix}, \tag{6}$$

$$C_i = [\, I_3 \;\; 0_3 \,],$$

$$i = 1, 2.$$

Before designing the disturbance observer-based composite control strategy, the following assumptions are given about ω_i(t) and $\xi_i(t)$ $(i = 1, 2)$.

Assumption 1. The unknown external disturbance $\xi_i(t)$ $(i = 1, 2)$ satisfies the following: $\|\xi_i(t)\| < \varrho_i$ and $\|\dot{\xi}_i(t)\| < \varsigma_i$, where ϱ_i and ς_i are known real constants.

Assumption 2. The unknown stochastic noise $\omega_i(t)$ $(i = 1, 2)$ is assumed to be discontinuous but bounded subject to $\|\omega_i(t)\| \le \varpi_i$ and belongs to a bounded and convex subset $\mathbb{W} \subset \mathbb{R}^n$ containing the origin in its interior.

3. Design of Disturbance Observer-Based Composite Control

The control system composition of a LEO satellite with two cube TMs is shown in Figure 3. To achieve the "drag-free" goal and eliminate the effects of external disturbances (the environment disturbances may contain the atmosphere and the solar radiation pressure, the thruster quantization error, the electrostatic noises, the actuator quantization error, etc.), a disturbance observer-based composite control approach is proposed, which consists of an extended sliding mode observer and a tube-based robust model predictive control. The detailed design process is as follows. First, for system (5), the observer is proposed to estimate states x_i for state feedback control and $\xi_i(t)$ for active disturbance rejection control $u_{ffc,i}$. Second, a tube-based robust model predictive control $u_i = u_{fbc,i} + u_{ffc,i}$ is adopted, which can cope with state constraints and actuator saturation and attenuate the effects of additive stochastic noises. For convenience, in the following discussion, the subscript i in (5) is omitted.

3.1. Design of Extended Sliding Mode Observers. Motivated by the augmented strategy method in [34, 36, 55], we define the following extended vectors and matrices:

$$\begin{aligned} \overline{x}(t) &= \left[x^T(t), \xi^T(t)\right]^T, \\ \overline{A} &= \begin{bmatrix} A & B_\omega \\ 0 & 0 \end{bmatrix}, \\ \overline{B} &= \begin{bmatrix} B \\ 0 \end{bmatrix}, \\ \overline{D} &= \begin{bmatrix} 0 \\ I_p \end{bmatrix}, \\ \overline{B}_w &= \begin{bmatrix} B_w \\ 0 \end{bmatrix}, \\ \overline{C} &= [\, C \;\; 0 \,]. \end{aligned} \tag{7}$$

For system (7), consider the following continuous-time extended SMO [55]:

$$\dot{\hat{\overline{x}}}(t) = \overline{A}\hat{\overline{x}}(t) + \overline{B}u(t) + L\tilde{y}(t) + \overline{D}F\nu_2(t), \tag{8}$$

where $\tilde{y}(t) = y(t) - \overline{C}\hat{\overline{x}}(t)$ and $\nu_2(t)$ is the discontinuous term designed as follows:

$$\nu_2(t) = \begin{cases} \eta \dfrac{\tilde{y}(t)}{\|\tilde{y}(t)\|}, & \text{if } \|\tilde{y}(t)\| > \dfrac{\varepsilon}{\eta}, \\ \eta^2 \dfrac{\tilde{y}(t)}{\varepsilon}, & \text{if } \|\tilde{y}(t)\| \le \dfrac{\varepsilon}{\eta}, \end{cases} \tag{9}$$

where $\eta > (\overline{\lambda}_F / \underline{\lambda}_F^2)$ and $\overline{\lambda}_F = \sqrt{\lambda_{\max}(F^T F)}$, $\underline{\lambda}_F = \sqrt{\lambda_{\min}(F^T F)}$, and $\lambda_{\max}(F^T F)$ and $\lambda_{\min}(F^T F)$ are the maximal and minimal nonzero eigenvalues of matrix $F^T F$, respectively.

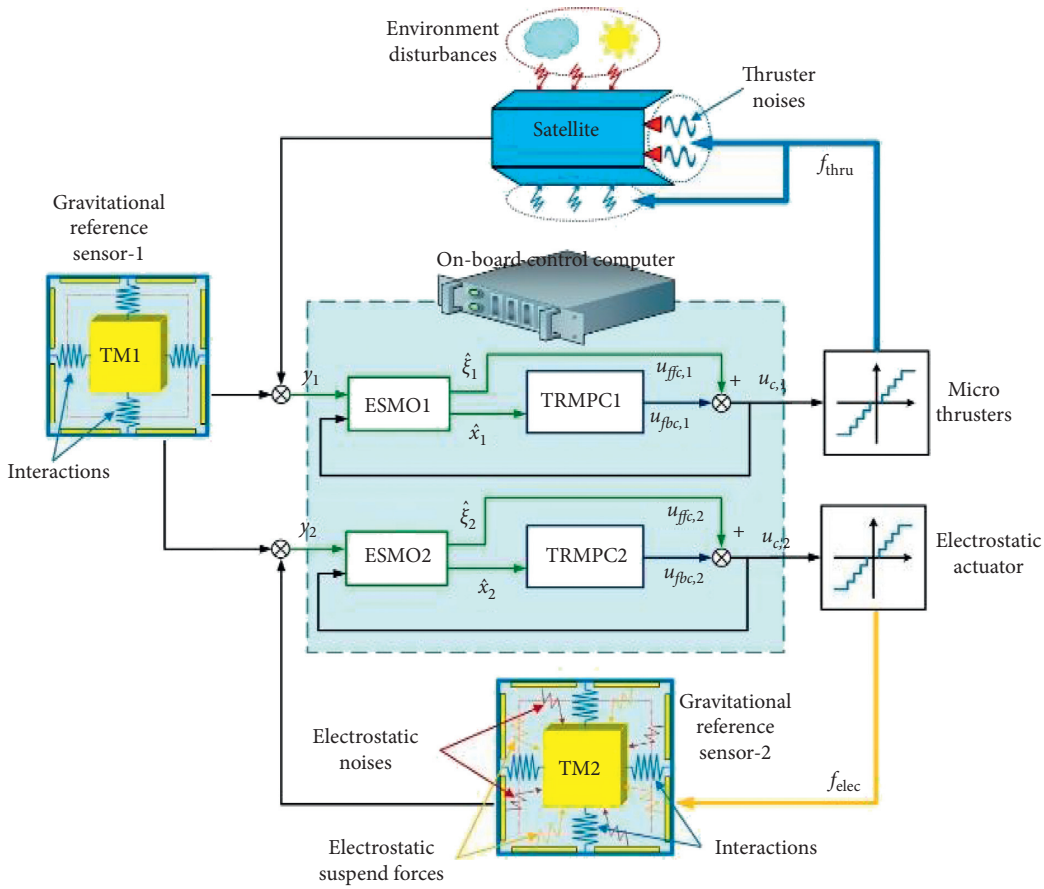

FIGURE 3: The control system schematic diagram of a LEO satellite with two cube TMs; the satellite and TM2 are controlled, respectively.

Remark 1. It is worth mentioning that the main function of the proposed extended SMO is to estimate the state and disturbances vectors simultaneously, which is a design basis of the subsequent composite control law.

Define $\tilde{\bar{x}}(t) = \bar{x}(t) - \hat{\bar{x}}(t)$; then the error system is derived as follows:

$$\dot{\tilde{\bar{x}}}(t) = (\bar{A} - L\bar{C})\tilde{\bar{x}}(t) + \bar{D}\left(\dot{\xi}(t) - Fv_2(t)\right) + \bar{B}_w\omega(t). \quad (10)$$

Lemma 1 (see [56]). *System (5) has the relative degree n with respect to the unknown input $\xi(t)$ (i.e., the system is strongly observable).*

Lemma 2. *If the matrix pair (A, C) is detectable and the condition*

$$\operatorname{rank}\left(\begin{bmatrix} A & B_\omega \\ C & 0 \end{bmatrix}\right) = n + p, \quad (11)$$

holds, then the pair $(\bar{A}, \bar{C})$ is detectable; that is, there exists an observer gain matrix L such that $\bar{A} - L\bar{C}$ is Hurwitz.

Proof. It can be derived that

$$\operatorname{rank}\left(\begin{bmatrix} \bar{A} - \lambda I_{n+p} \\ \bar{C} \end{bmatrix}\right) = \operatorname{rank}\left(\begin{bmatrix} A - \lambda I_n & B_w \\ 0_{p\times n} & -\lambda I_p \\ C & 0_{q\times p} \end{bmatrix}\right). \quad (12)$$

□

Case 1. When $\lambda \neq 0$, for the matrix in right side of equation (12), we have

$$\begin{bmatrix} I_n & \lambda^{-1}B_w & 0 \\ 0 & I_p & 0 \\ 0 & 0 & I_q \end{bmatrix}\begin{bmatrix} A - \lambda I_n & B_w \\ 0_{p\times n} & -\lambda I_p \\ C & 0_{q\times p} \end{bmatrix} = \begin{bmatrix} A - \lambda I_n & 0_{p\times n} \\ 0_{p\times n} & -\lambda I_p \\ C & 0_{q\times p} \end{bmatrix}, \quad (13)$$

which means that

$$\begin{aligned}\operatorname{rank}\left(\begin{bmatrix} A-\lambda I_n & B_w \\ 0_{p\times n} & -\lambda I_p \\ C & 0_{q\times p}\end{bmatrix}\right) &= \operatorname{rank}\left(\begin{bmatrix} I_n & \lambda^{-1}B_w & 0 \\ 0 & I_p & 0 \\ 0 & 0 & I_q\end{bmatrix}\begin{bmatrix} A-\lambda I_n & B_w \\ 0_{p\times n} & -\lambda I_p \\ C & 0_{q\times p}\end{bmatrix}\right) \\ &= \operatorname{rank}\left(\begin{bmatrix} A-\lambda I_n & 0_{n\times p} \\ 0_{p\times n} & -\lambda I_p \\ C & 0_{q\times p}\end{bmatrix}\right) \\ &= \operatorname{rank}\left(\begin{bmatrix} A-\lambda I_n \\ \overline{C}\end{bmatrix}\right)+p.\end{aligned} \tag{14}$$

That means

$$\operatorname{rank}\left(\begin{bmatrix} \overline{A}-\lambda I_{n+p} \\ \overline{C}\end{bmatrix}\right) = \operatorname{rank}\left(\begin{bmatrix} A-\lambda I_n \\ \overline{C}\end{bmatrix}\right)+p. \tag{15}$$

Hence, if the pair (A, C) is detectable, we have

$$\operatorname{rank}\left(\begin{bmatrix} A-\lambda I_n \\ \overline{C}\end{bmatrix}\right) = n. \tag{16}$$

Then, the following rank condition holds:

$$\operatorname{rank}\left(\begin{bmatrix} A-\lambda I_{n+p} \\ \overline{C}\end{bmatrix}\right) = n+p. \tag{17}$$

Case 2. When $\lambda = 0$, if rank condition (11) holds, we have

$$\operatorname{rank}\left(\begin{bmatrix} \overline{A} \\ \overline{C}\end{bmatrix}\right) = \operatorname{rank}\left(\begin{bmatrix} A & B_w \\ C & 0\end{bmatrix}\right) = n+p. \tag{18}$$

Finally, for both cases, we can always imply $\operatorname{rank}\left(\begin{bmatrix} A-\lambda I_{n+p} \\ \overline{C}\end{bmatrix}\right) = n+p$, $\lambda \in \mathbb{C}$, $\operatorname{Re}[\lambda] \geq 0$, which implies that the pair $(\overline{A}, \overline{C})$ is detectable.

To attenuate the influence of $\omega(t)$ for error system (10), we define the prescribed H_∞ performance index as follows:

$$\|H\|_\infty = \sup_{\|\omega(t)\|_{L_2}\neq 0} \frac{\|\psi\tilde{\overline{x}}(t)\|_{L_2}}{\|\omega(t)\|_{L_2}} \leq \sqrt{\gamma_1}, \tag{19}$$

where $\psi\tilde{\overline{x}}(t)$ is the weighted estimation error and ψ is the weight matrix. The following main theorem provides the existence condition of the proposed observer (8).

Theorem 1. *The solution of observer error system (10) is asymptotically stable with the prescribed H_∞ performance index if there exist positive and definite matrix $Q > 0$ and matrix F with appropriate dimensions, in minimizing $\gamma_1 > 0$, such that the following matrix constraints hold:*

$$\begin{aligned}&\overline{Q} = \begin{bmatrix} \bar{A}^T Q + Q\bar{A} - \bar{C}^T\bar{C} + \psi^T\psi & Q\bar{B}_w \\ \bar{B}_w^T Q & -\gamma_1 I\end{bmatrix} < 0, \\ &Q\overline{D} = \bar{C}^T F^T.\end{aligned} \tag{20}$$

Moreover, the observer gain is designed as $L = (1/2)Q^{-1}\bar{C}^T$.

Proof. For system (10), select the Lyapunov function as $V(t) = \tilde{\overline{x}}^T(t)Q\tilde{\overline{x}}(t)$ with $Q > 0$ being designed; it is easy to obtain that

$$\begin{aligned}\dot{V}(t) &= \dot{\tilde{\overline{x}}}^T(t)Q\tilde{\overline{x}}(t) + \tilde{\overline{x}}^T(t)Q\dot{\tilde{\overline{x}}}(t) \\ &= 2\tilde{\overline{x}}^T(t)Q\left[(\overline{A}-L\overline{C})\tilde{\overline{x}}(t) + \overline{D}\left(\dot{\xi}(t) - Fv_2(t)\right) + \overline{B}_w\omega(t)\right] \\ &= \tilde{\overline{x}}^T(t)\left[\overline{A}^T Q + Q\overline{A} - \overline{C}^T\overline{C}\right]\tilde{\overline{x}}(t) + 2\tilde{\overline{x}}(t)\overline{C}^T F^T\left(\dot{\xi}(t) - Fv_2(t)\right) + \tilde{\overline{x}}^T(t)Q\overline{B}_w\omega(t) + \omega^T(t)\overline{B}_w^T Q\tilde{\overline{x}}(t) \\ &= \tilde{\overline{x}}^T(t)\left[\overline{A}^T Q + Q\overline{A} - \overline{C}^T\overline{C}\right]\tilde{\overline{x}}(t) + 2\tilde{y}F^T\left(\dot{\xi}(t) - Fv_2(t)\right) + 2\tilde{\overline{x}}^T(t)Q\overline{B}_w\omega(t).\end{aligned} \tag{21}$$

In the following analysis, let $Y(t) = 2\tilde{y}F^T(\dot{\xi}(t) - Fv_2(t))$; we consider two cases separately. □

Case 3. $\|\tilde{y}\| > (\varepsilon/\eta)$; in this case, we have

$$\begin{aligned} Y(t) &= 2\tilde{y}F^T\left(\dot{\xi}(t) - F\eta\frac{\tilde{y}(t)}{\|\tilde{y}(t)\|}\right) \\ &\le 2\|\tilde{y}\|\left(\|F\|\rho - \|F\|^2\eta\right) \\ &\le 2\|\tilde{y}\|\left(\overline{\lambda}_F\rho - \underline{\lambda}_F^2\eta\right) \le 0, \end{aligned} \tag{22}$$

where η can be chosen such that $\eta > (\overline{\lambda}_F/\underline{\lambda}_F^2)\rho$.

Case 4. $\|\tilde{y}\| \le (\varepsilon/\eta)$; in this case, it can be derived that

$$\begin{aligned} Y(t) &= 2\tilde{y}F^T\left(\dot{\xi}(t) - F\eta^2\frac{\tilde{y}(t)}{\varepsilon}\right) \\ &\le 2\rho\overline{\lambda}_F\|\tilde{y}\| - 2\eta^2\underline{\lambda}_F^2\frac{\|\tilde{y}\|^2}{\varepsilon} \le 2\eta\underline{\lambda}_F^2\|\tilde{y}\| - 2\eta^2\underline{\lambda}_F^2\frac{\|\tilde{y}\|^2}{\varepsilon} \le -2\underline{\lambda}_F^2\left(\frac{\eta\|\tilde{y}\|}{\sqrt{\varepsilon}} - \frac{\sqrt{\varepsilon}}{2}\right)^2 + \frac{\underline{\lambda}_F^2\varepsilon}{2} \le 2\underline{\lambda}_F^2\left(\frac{\eta(\varepsilon/\eta)}{\sqrt{\varepsilon}} - \frac{\sqrt{\varepsilon}}{2}\right)^2 + \frac{\underline{\lambda}_F^2\varepsilon}{2} \le 0. \end{aligned} \tag{23}$$

Based on Cases 3 and 4, we can conclude that

$$\begin{aligned} \dot{V}(t) &= Y(t) + \dot{\tilde{x}}^T(t)\left[\overline{A}^TQ + Q\overline{A} - \overline{C}^T\overline{C}\right]\tilde{\tilde{x}}(t) + 2\dot{\tilde{x}}^T(t)Q\overline{B}_\omega\omega(t) \\ &\le \dot{\tilde{x}}^T(t)\left[\overline{A}^TQ + Q\overline{A} - \overline{C}^T\overline{C}\right]\tilde{\tilde{x}}(t) + 2\dot{\tilde{x}}^T(t)Q\overline{B}_\omega\omega(t). \end{aligned} \tag{24}$$

To minimize the effect of the disturbance on the estimation error in the sense of L_2 norm, we consider the following constraint:

$$W(t) = \dot{V}(t) + \dot{\tilde{x}}^T(t)\psi^T\psi\tilde{\tilde{x}}(t) - \gamma_1\omega^T(t)\omega(t) \le 0. \tag{25}$$

In light of Schur complement, it is easy to derive that

$$\begin{aligned} W(t) &\le \dot{\tilde{x}}^T(t)\left[\overline{A}^TQ + Q\overline{A} - \overline{C}^T\overline{C}\right]\tilde{\tilde{x}}(t) + \dot{\tilde{x}}^T(t)Q\overline{B}_\omega\omega(t) + \omega^T(t)\overline{B}_\omega^TQ\dot{\tilde{x}}(t) + \dot{\tilde{x}}^T(t)\psi^T\psi\dot{\tilde{x}}^T(t) - \gamma_1\omega^T(t)\omega(t) \\ &\le \begin{bmatrix}\dot{\tilde{x}}^T(t) & \omega^T(t)\end{bmatrix}\overline{Q}\begin{bmatrix}\tilde{\tilde{x}}(t) \\ \omega(t)\end{bmatrix} < 0. \end{aligned} \tag{26}$$

Accordingly, it can be seen that $W(t) \le 0$ is ensured provided that $\overline{Q} < 0$ holds. Therefore, the solution of error system (10) is asymptotically stable with the prescribed H_∞ performance index as $t \longrightarrow \infty$.

Remark 2. It should be pointed out that, in Theorem 1, the equality constraint $Q\overline{D} = \overline{C}^TF^T$ can be rewritten as

$$\mathrm{Trace}\left(\left(Q\overline{D} - \overline{C}^TF^T\right)^T\left(Q\overline{D} - \overline{C}^TF^T\right)\right) = 0. \tag{27}$$

Hence, we can introduce the following condition:

$$\left(Q\overline{D} - \overline{C}^TF^T\right)^T\left(Q\overline{D} - \overline{C}^TF^T\right) < \gamma_2 I, \tag{28}$$

where $\gamma_2 > 0$ is a parameter to be designed. Then the design problem of observer gains L can be converted into the following minimization problem:

$$\begin{aligned} &\min \gamma_1, \gamma_2 \\ &\text{subject to} \quad (20) \text{ and } (28). \end{aligned} \tag{29}$$

3.2. Design of Tube-Based Robust Model Predictive Control. For equations (5), $\xi_i(t)$ is estimated and eliminated through the extended sliding mode observer; thus we have to compensate it by disturbance compensation feed-forward control. Translate formulations (5) without $\xi_i(t)$ into the discrete model of the form in (30) as follows:

$$x_{k+1} = A_dx_k + B_du_k + B_{\omega_d}(\xi_k + \omega_k). \tag{30}$$

As mentioned before, the controller is designed as $u_k = u_{k,ffc} + u_{k,fbc}$, where

$$u_{k,ffc} = -\hat{\xi}_k, \tag{31}$$

is the feed-forward control part to compensate ξ_k and $u_{k,fbc}$ is the model predictive control law to be designed. Define the estimation error as

$$\widetilde{\xi}_k = \widehat{\xi}_k - \xi_k. \tag{32}$$

Then, system (30) becomes

$$x_{k+1} = A_d x_k + B_d u_{k,fbc} + B_{\omega_d}\left(\omega_k - \widetilde{\xi}_k\right). \tag{33}$$

As proved in the observer design results in Theorem 1, we have $\|\widetilde{\xi}_k\| \longrightarrow 0$ with $k \longrightarrow \infty$; thus $\|\omega_k - \widetilde{\xi}_k\| \leq \|\omega_k\| + \|\widetilde{\xi}_k\| = (1+\beta)\|\omega_k\|$ holds, where $\beta > 0$ is a small constant and $\beta \longrightarrow 0$ when $k \longrightarrow \infty$.

Define $d_k = \omega_k - \widetilde{\xi}_k$; it satisfies $\|d_k\| \leq (1+\beta)\varpi$, which belongs to the bounded and convex subset $\mathbb{W}$. Hence, system (30) can be written in the following form:

$$x_{k+1} = A_d x_k + B_d u_{k,fbc} + B_{\omega_d} d_k. \tag{34}$$

The investigated system (30) is subject to hard constraints on both state and input vectors with the following form:

$$\begin{aligned} x &\in \mathbb{X}, \\ u &\in \mathbb{U}, \end{aligned} \tag{35}$$

where $\mathbb{X}$ and $\mathbb{U}$ are polytopes.

To solve this control problem, a robust MPC algorithm is considered [57] by repeatedly solving an optimal control problem, where the finite horizon quadratic cost $J_N(x,u)$ to be minimized at the current time k is

$$J_N(x_k, u_k) = \sum_{i=0}^{N-1}\left(x_{i|k}^T \mathcal{Q} x_{i|k} + u_{i|k}^T \mathcal{R} u_{i|k}\right) + x_{N|k}^T P x_{N|k}. \tag{36}$$

In (36), $N \in \mathbb{R}^+$ is the MPC prediction horizon, $\mathcal{Q} \in \mathbb{R}^{n\times n}$, $\mathcal{Q} > 0$, $\mathcal{R} \in \mathbb{R}^{m\times m}$, $\mathcal{R} > 0$ and P is the solution of the algebraic Riccati equation [57].

$$\left(A_d + B_d K\right)^T P \left(A_d + B_d K\right) + \mathcal{Q} + K^T \mathcal{R} K = P. \tag{37}$$

Due to the presence of the unknown disturbance d_k, we rewrite the state vector $x_{i|k}$ of the system as the sum of a nominal part $z_{i|k}$ and an error part $e_{i|k}$ in the following form:

$$x_{i|k} = z_{i|k} + e_{i|k}, \tag{38}$$

where $e_{i|k}$ denotes the deviation of the real state $e_{i|k}$ with respect to the nominal one.

Design the following feedback policy (39) for system (30):

$$u_{i|k} = v_{i|k} + K\left(x_{i|k} - z_{i|k}\right), \tag{39}$$

where $v_{i|k}$ denotes the nominal input vector and the gain matrix K should be selected such that $A_K = A_d + B_d K$ is Schur-stable; then the corresponding nominal and error dynamics can be described, respectively, as follows:

$$\begin{aligned} z_{i+1|k} &= A_d z_{i|k} + B_d v_{i|k}, \\ z_{0|k} &= x_{0|k}, \end{aligned} \tag{40}$$

$$\begin{aligned} e_{i+1|k} &= A_K e_{i|k} + B_{\omega_d} d_{i|k}, \\ e_{0|k} &= 0. \end{aligned} \tag{41}$$

Hence, the finite horizon optimal quadratic cost (36) can be redefined in terms of nominal state z_k and control input v_k as

$$J_N(z_k, v_k) = \sum_{i=0}^{N-1}\left(z_{i|k}^T \mathcal{Q} z_{i|k} + v_{i|k}^T \mathcal{R} v_{i|k}\right) + z_{N|k}^T P z_{N|k}, \tag{42}$$

and the finite horizon optimal control problem can be reformulated as follows.

Definition 1. Given the nominal system dynamics (40), cost (42), and nominal constraints set $\mathbb{Z}, \mathbb{V}, \mathbb{Z}_f$, the nominal robust MPC finite horizon optimization problem can be described as

$$\begin{aligned} &\min_{v} J_N(z_k, v_k) \\ &\text{s.t.} \quad z_{i+1|k} = A_d z_{i|k} + B_d v_{i|k}, z_{0|k} = x_k \\ &z_{i|k} \in \mathbb{Z}, \quad i \in [1, N] \\ &v_{i|k} \in \mathbb{V}, \quad i \in [0, N-1] \\ &z_{i|k} \in \mathbb{Z}_f. \end{aligned} \tag{43}$$

The solution of (43) is the optimal nominal control sequence $v_{0|k}^* = [v_{0|k}^*(0; z_k), \ldots, v_{T-1|k}^*(T-1; z_k)]$ and the first control action, that is, $\widetilde{\kappa}_N(z_k) := v_{0|k}^*(0; z_k)$, represents the optimal control $v_{i|k}$ to be applied to system (40).

The proposed control law applied on the uncertain system (40), according to the control policy adopted, is

$$\begin{aligned} u_{i|k} &= v_{i|k} + K\left(x_{i|k} - z_{i|k}\right) = \kappa_N(x_k, z_k) \\ &= \widetilde{\kappa}_N(z_k) + K(x_k - z_k). \end{aligned} \tag{44}$$

The composite closed-loop system then satisfies

$$x_{i+1|k} = A_d x_{i|k} + B_d \kappa_N(i, x_k, z_k) + B_{\omega_d} d_{i|k}, \tag{45}$$

$$z_{i+1|k} = A_d z_{i|k} + B_d \widetilde{\kappa}_N(i, z_k). \tag{46}$$

For the TRMPC approach, the matrix K in the control policy (39) is designed to stabilize system (30). Consider the following closed-loop system:

$$x_{i+1|k} = \left(A_d + B_d K\right) x_{i|k} + B_d v_{i|k} + B_{\omega_d} d_{i|k}. \tag{47}$$

Hence, the satisfaction of the following condition aims to define the feedback gain K that stabilizes the system.

$$\left(A_d + B_d K\right)^T \widehat{P}\left(A_d + B_d K\right) - \widehat{P} < 0, \quad \widehat{P} > 0. \tag{48}$$

In order to robustly satisfy the mission constrains, they are tightened to allow the trajectories of the uncertain system, affected by disturbance, to lie in a tube centred on the nominal one, where each trajectory is related to a particular realization of the uncertainty at each time step k. The derivations of the nominal state, input, and terminal constrains set $\mathbb{Z}, \mathbb{V}, \mathbb{Z}_f$ are described according to the approach proposed in [57], such that the constraints in (39) of system (30) are satisfied for every realization of the disturbance sequence ω by suitable design of the tube.

We now define $S_K(\infty) := A_K^0 \mathbb{W} \oplus A_K^1 \mathbb{W} \oplus \cdots = \sum_{j=0}^{\infty} A_K^j \mathbb{W}$, where $\oplus$ is the Minkowski sum and $A_K^j \mathbb{W} := \left\{A_K^j d_k | d_k \in \mathbb{W}\right\}$ is the set multiplication; the uncertain set of the error $e_{i|k}$ is the minimal robust positive invariant set for

$$x_{i+1|k} = A_d x_{i|k} + B_{\omega_a} d_{i|k}, \quad d_k \in \mathbb{W}. \tag{49}$$

Then the state and control input vector constraints in (35) are satisfied provided that

$$\begin{aligned} z_{i|k} &\in \mathbb{X} \ominus S_K(\infty), \\ v_{i|k} &\in \mathbb{U} \ominus K S_K(\infty), \end{aligned} \tag{50}$$

where $\ominus$ denotes the Pontryagin set difference. It is obvious that the terminal constraint for system (30) at time instant N is ensured if the normal system (40) satisfies the tighter constraint

$$z_N \in \mathbb{Z} \subseteq \mathbb{X} - S_K(\infty), \quad \mathbb{Z}_f \subseteq \mathbb{Z}. \tag{51}$$

Moreover, these assertions only make sense if the disturbance set $\mathbb{W}$ is sufficiently small to satisfy the following Assumption 3, as defined in [57].

Assumption 3. (Restricted disturbances for constraints satisfaction) $S_K \subset \mathbb{X}$ and $K \times S_K \subset \mathbb{U}$.

The next step is to define a robust positively invariant set S_K for [19] to obtain the tighter constraints acting on the nominal system. Then the constraints are considered for the TRMPC problem. Once the uncertainty set $\mathbb{W}$ is evaluated, an inner approximation of the nominal constraint set can be constructed. In this design, we adopt the following strategy presented in [57].

Algorithm 1. Computation of $\mathbb{Z}$ and $\mathbb{V}$

(1) Define the linear state constraint as: $\mathbb{X} = \left\{x_{i|k} \in \mathbb{R}^n | a x_{i|k} < b\right\}$;

(2) Construct the nominal state constraint inequality $a z_{i|k} \le b - \max\left\{a e_{i|k} | e_{i|k} \in S_K(\infty)\right\} = b - \Phi_\infty$;

(3) Approximate the upper value of Φ_∞ as $\Phi_N = \max\left\{a \sum_{i=0}^{N-1} A_K^i d_{i|k} | d_{i|k} \in \mathbb{W}\right\}$;

(4) Choose a suitable $\alpha \in (0,1)$ and N such that $A_K^N d_{i|k} \in \alpha \mathbb{W}$, compute $\Phi_\infty \le (1-\alpha)^{-1} \Phi_N$;

(5) Compute the nominal state constraint set $\mathbb{Z} := \left\{z_{i|k} \in \mathbb{R}^n | a z_{i|k} \le b - (1-\alpha)^{-1} \Phi_N\right\}$;

(6) Compute the nominal control constraint set $\mathbb{V} := \left\{v_{i|k} \in \mathbb{R}^m | a' v_{i|k} \le b' - K(1-\alpha)^{-1} \Phi_N\right\}$, where $\mathbb{U} := \left\{u_{i|k} \in \mathbb{R}^m | a' u_{i|k} \le b'\right\}$.

Hence, the observer-based model predictive control strategy could be formally described by the following algorithm.

Algorithm 2. Disturbance observer-based model predictive control strategy.

(1) Initialization: at time $k = 0$, set $x_k = z_k = x(0)$ where $x(0)$ denotes the current state.

(2) At time k, considering the current state (x_k, z_k), based on the disturbance estimation $\widehat{\xi}_k$ from the observer (8), solve the nominal optimal control problem (43) to obtain the nominal control vector $v_k := v_{0|k}^*(0; z_k)$ and the control input vector $u_k = v_k + K(x_k - z_k) - \widehat{\xi}_k$.

(3) If the nominal optimal control problem (43) is infeasible, adopt safety/recovery procedure.

(4) Apply the control u_k to the system (45) and (46);

(5) Calculate the estimation $\widehat{x}_{k+1}$ from the observer (8) as successor state x_{k+1} of the system (30), and calculate the successor state z_{k+1} of the nominal system (40).

(6) Set $(x_k, z_k) = (x_{k+1}, z_{k+1})$, set $k = k + 1$, and go to (2).

4. Simulation Results

In this section, a numerical simulation is carried out to verify the effectiveness of the extended sliding mode-based TRMPC approach. Suppose that the satellite is flying at a little eccentric low Earth orbit with altitude of 300 km. The parameters in (1) are given in Table 1 [54].

For the relative position motion between the TM1 and the satellite, define $F_{d,10} = F_{\text{drag}} + F_{\text{thruster}}$, where

$$F_{\text{drag}} = m_0 \times \begin{bmatrix} 2.15 \times 10^{-7} \sin(0.00114t) \\ 0.15 \times 10^{-4} \sin(0.00114t) - 2.35 \times 10^{-4} \\ 0.20 \times 10^{-5} \sin(0.00114t) - 2.05 \times 10^{-5} \end{bmatrix} N. \tag{52}$$

The resolution and the maximum value of the thruster are 10^{-6} N and 0.4 N. Besides, a zero mean white noise with mean squared error being 10^{-8} N is added as the stochastic disturbance.

For the relative position motion between TM1 and TM2, define $F_{d,12} = F_{\text{elec}} + F_{\text{actuator}}$, where

$$F_{\text{elec}} = m_1 \times \begin{bmatrix} 1 \times 10^{-6} \sin\left(0.04t + \dfrac{\pi}{3}\right) \\ 1 \times 10^{-6} \sin(0.05t) \\ 1 \times 10^{-6} \sin\left(0.05t + \dfrac{\pi}{2}\right) \end{bmatrix} N. \tag{53}$$

Table 1: Parameters of satellite used in the simulation.

Symbols	Parameters
m_0	145 kg
m_1	1 kg
m_2	1 kg
ω_0	0.0011569 rad/s
$\tilde{\rho}_{\max}$	0.1 m
$\dot{\tilde{\rho}}_{\max}$	0.1 m/s
K_t	$\begin{bmatrix} 1 & 0.039 & 0.039 \\ 0.039 & 1 & 0.039 \\ 0.039 & 0.039 & 1 \end{bmatrix} \times 10^{-6}$ N/m
D_t	$1.4 \times 10^{-11} I_3$ N/(m/s)

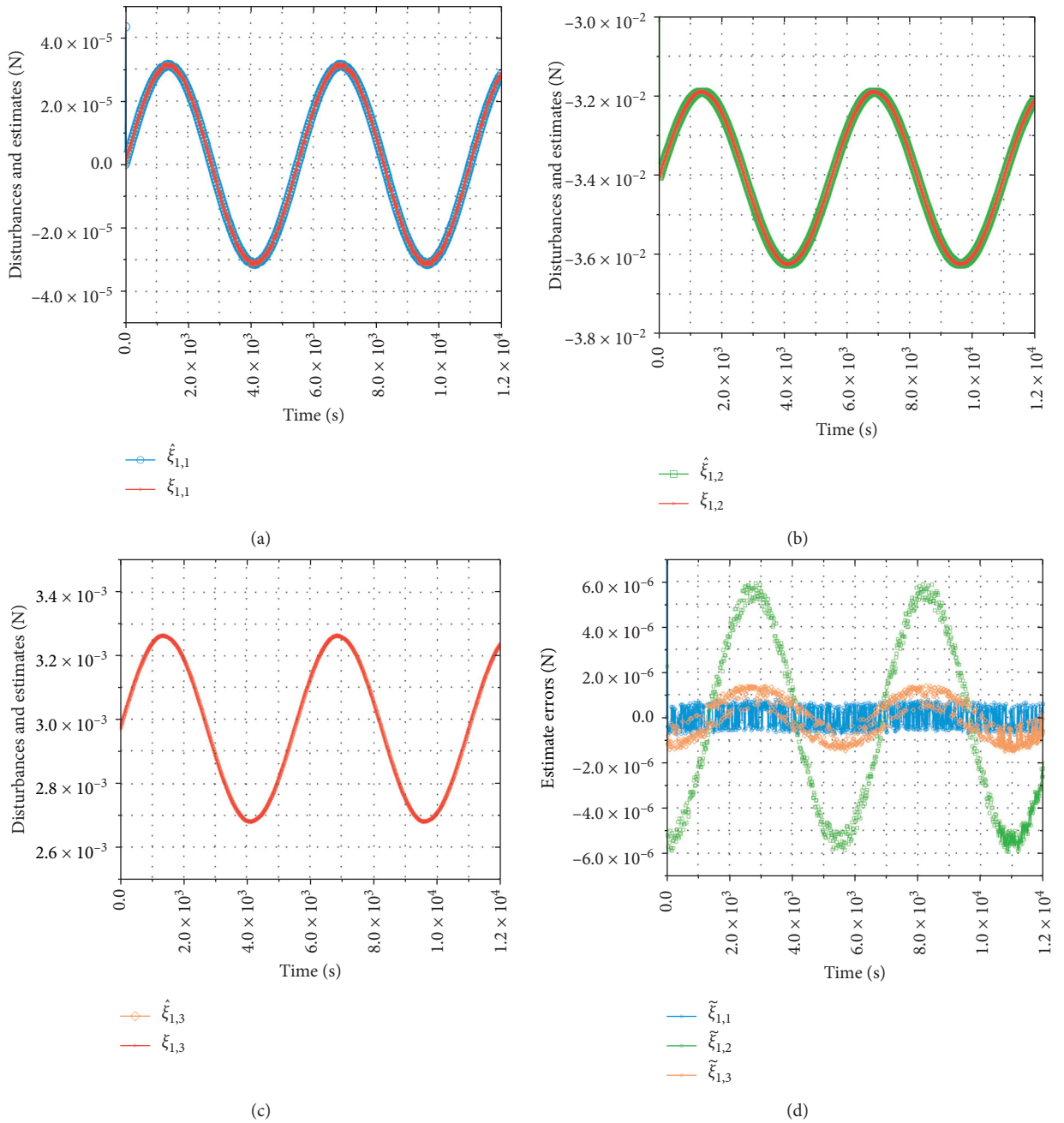

Figure 4: Estimation of the disturbances $\xi_1(t)$ by the ESMO.

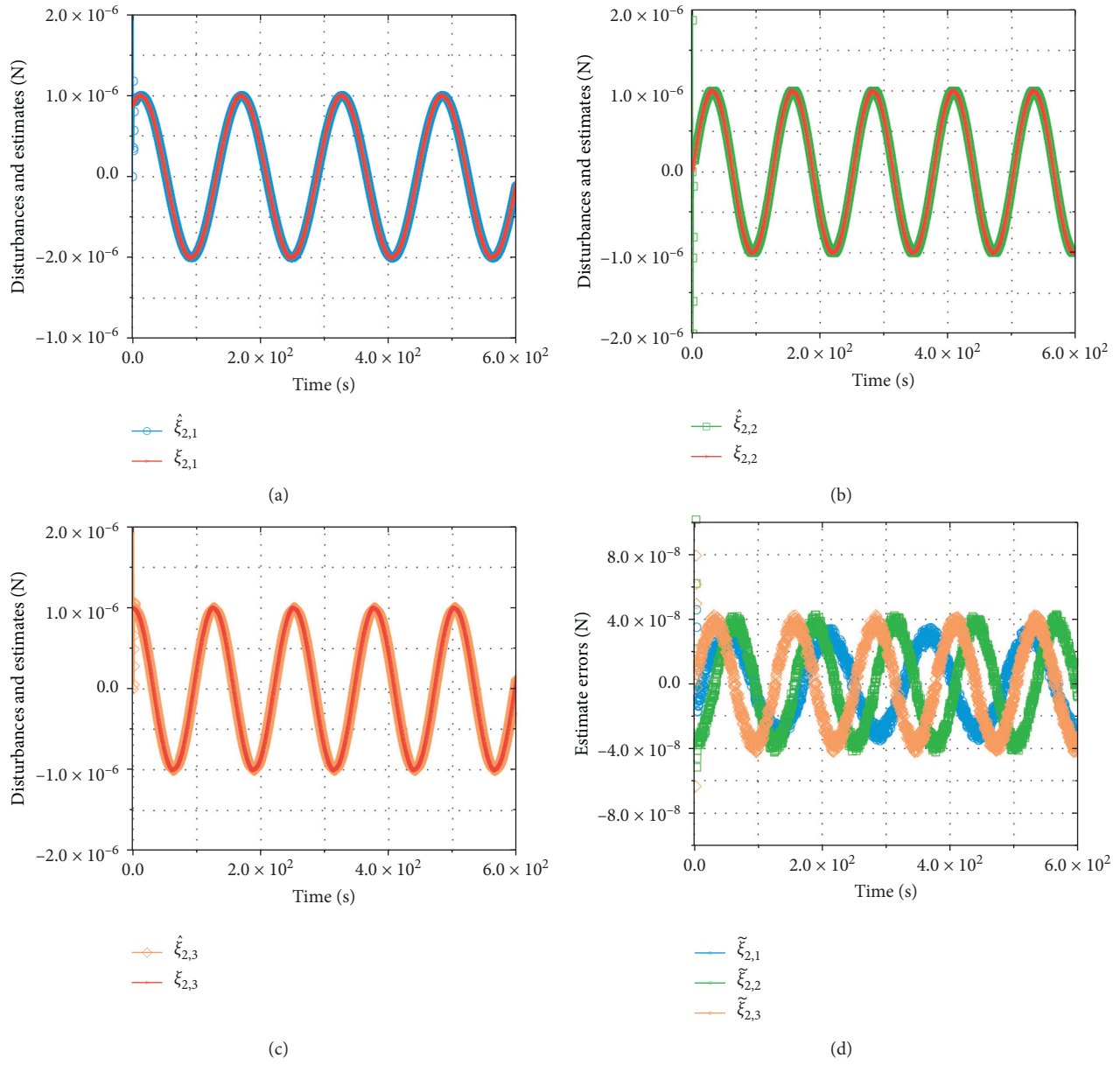

Figure 5: Estimation of the disturbances $\xi_2(t)$ by the ESMO.

The resolution and the maximum value of the thruster are 10^{-7} N and 60×10^{-6} N. Similarly, a zero mean white noise with mean squared error being 10^{-8} N is added as the stochastic disturbance.

The simulation results are shown in Figures 4–10 as follows. Define the estimated error $\tilde{\xi}_i(t) = \hat{\xi}_i(t) - \xi_i(t)$ $(i = 1, 2)$, as shown in Figures 4 and 5, and $\xi_i(t)$ can be estimated precisely by the ESMO. From Figures 6–11, the relative motion variables $\tilde{\rho}_{10}(t)$, $\dot{\tilde{\rho}}_{10}(t)$, $\tilde{\rho}_{12}(t)$, and $\dot{\tilde{\rho}}_{12}(t)$ could be estimated well by the ESMO. In addition, the stable control accuracy of the composite control approach has achieved 10^{-7} or 10^{-8}, which shows that the developed extended sliding mode observer method and tube-based model predictive control law are effective.

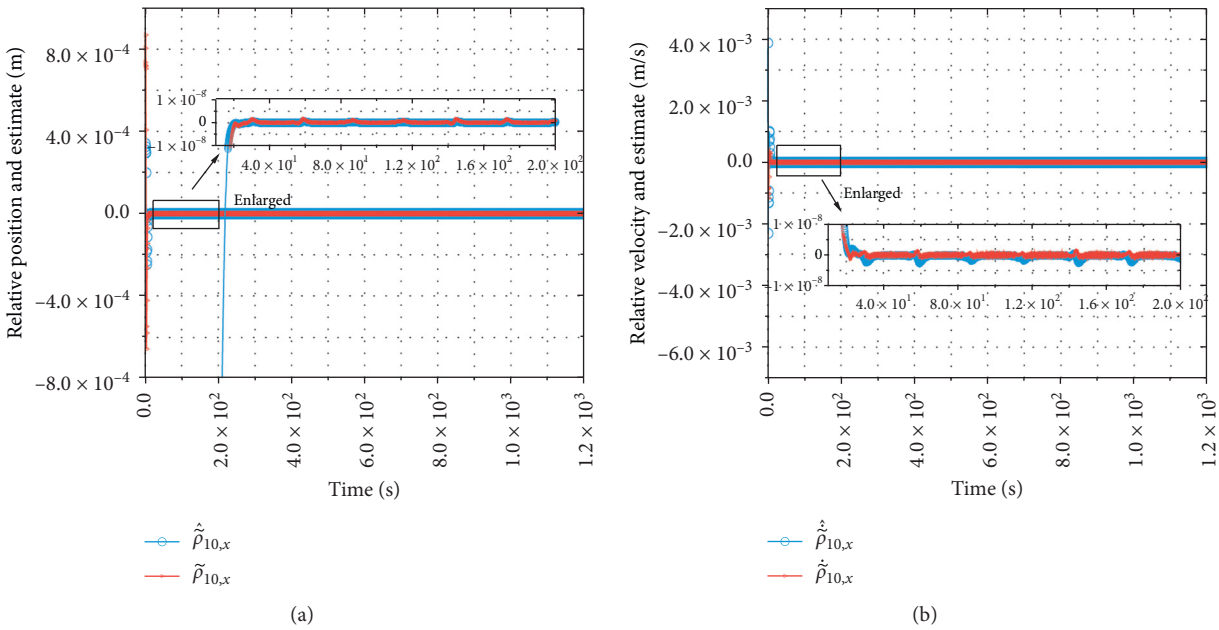

FIGURE 6: Simulated relative positions $\tilde{\rho}_{10,x}(t), \dot{\tilde{\rho}}_{10,x}(t)$ and their estimations between TM1 and the satellite.

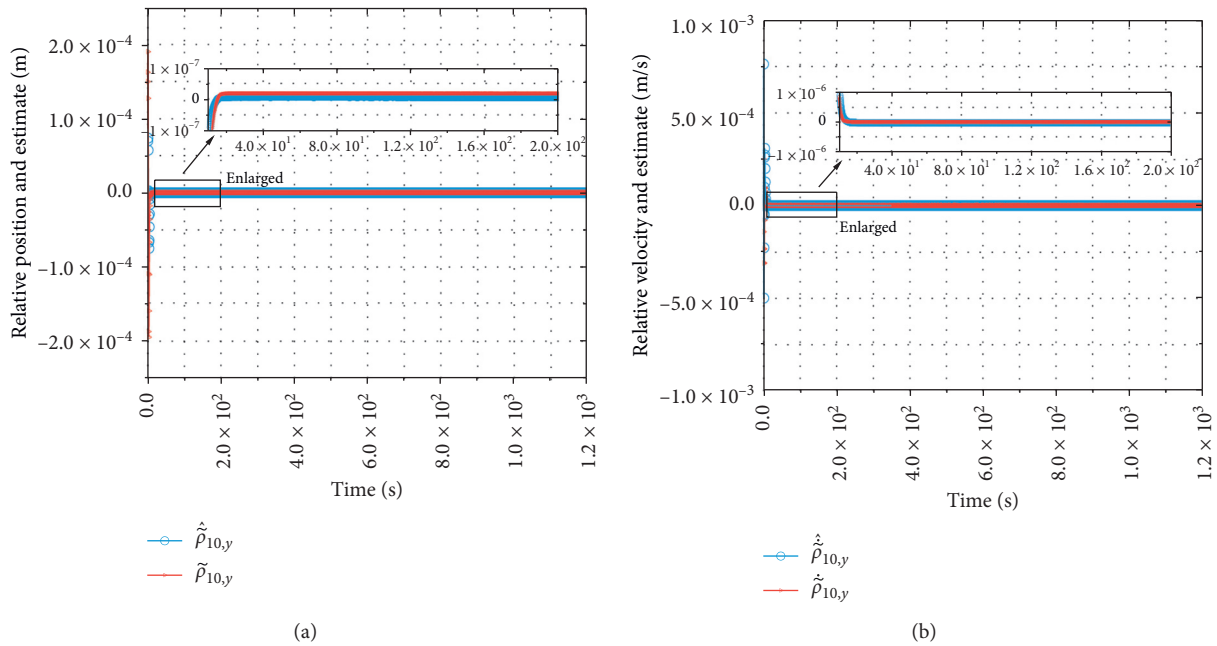

FIGURE 7: Simulated relative positions $\tilde{\rho}_{10,y}(t), \dot{\tilde{\rho}}_{10,y}(t)$ and their estimations between TM1 and the satellite.

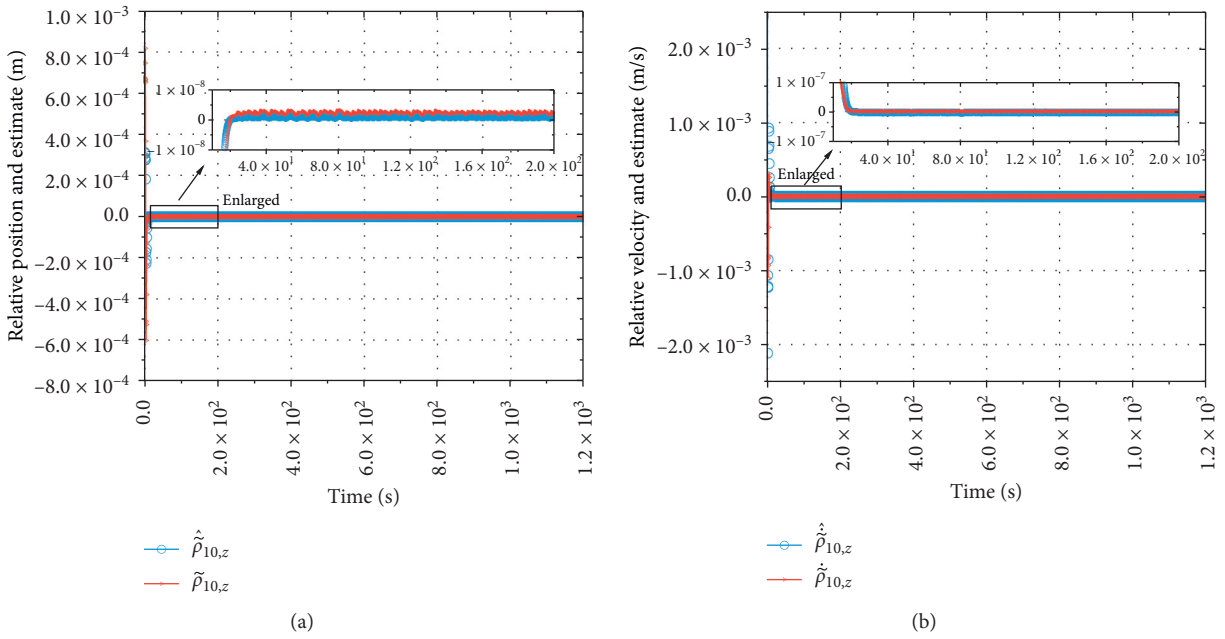

Figure 8: Simulated relative positions $\tilde{\rho}_{10,z}(t), \dot{\tilde{\rho}}_{10,z}(t)$ and their estimations between TM1 and the satellite.

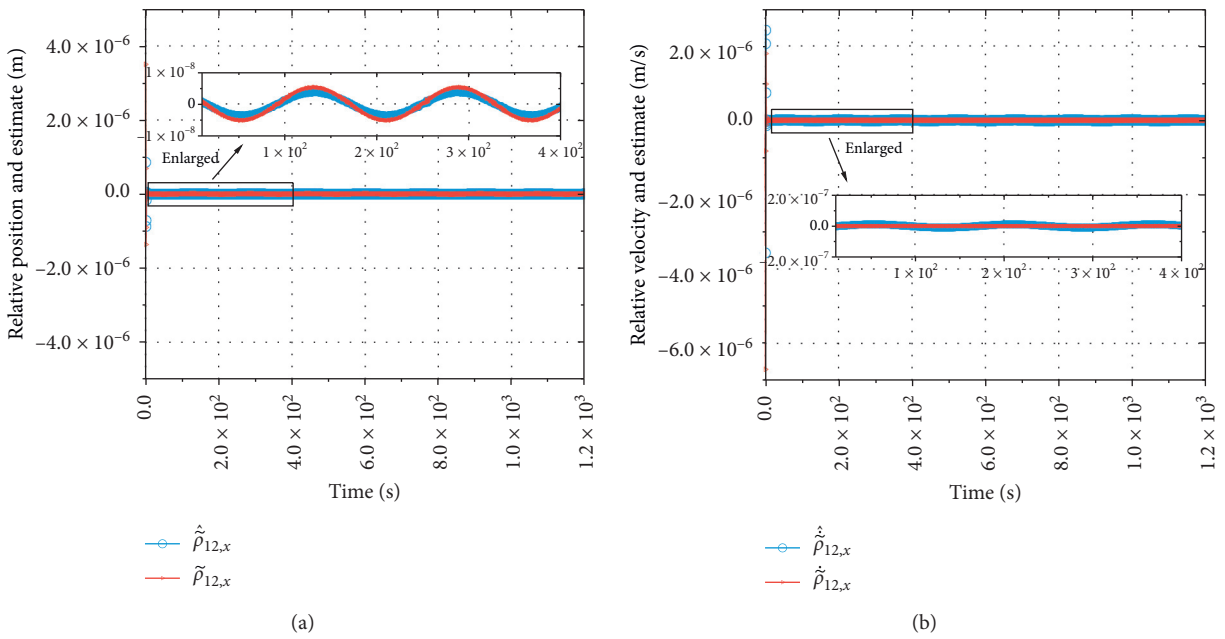

Figure 9: Simulated relative positions $\tilde{\rho}_{12,x}(t), \dot{\tilde{\rho}}_{12,x}(t)$ and their estimations between TM1 and TM2.

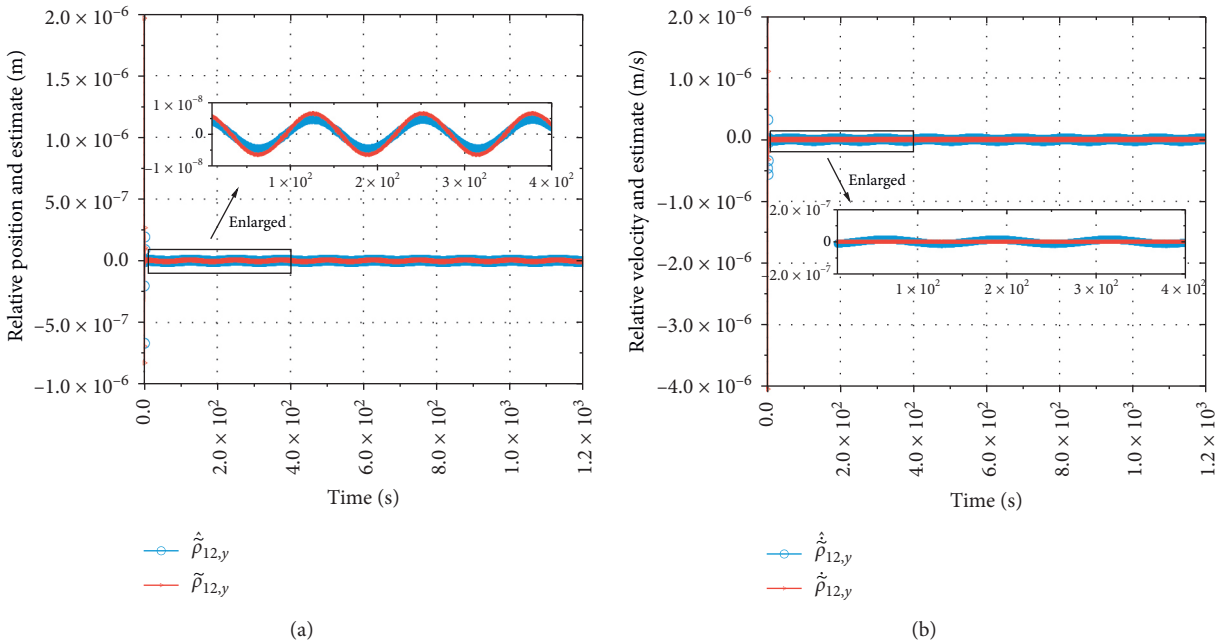

FIGURE 10: Simulated relative positions $\tilde{\rho}_{12,y}(t), \dot{\tilde{\rho}}_{12,y}(t)$ and their estimations between TM1 and TM2.

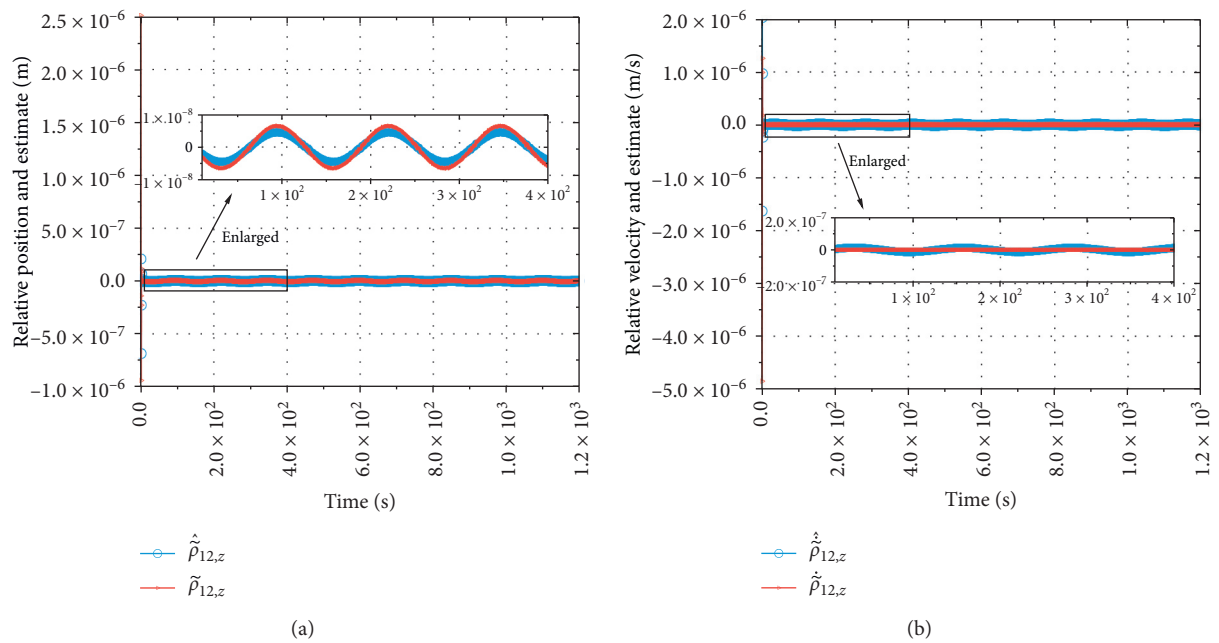

FIGURE 11: Simulated relative positions $\tilde{\rho}_{12,z}(t), \dot{\tilde{\rho}}_{12,z}(t)$ and their estimations between TM1 and TM2.

5. Conclusions

This paper has considered the relative position control of the drag-free satellite with double cube test-masses in the presence of external disturbance, additive stochastic disturbances, actuator quantization error, actuator saturation, and state constraints. An extended sliding mode observer method is adopted to estimate the state vector and external disturbance, based on which a tube-based robust model predictive control scheme is developed. The designed control method can not only cope with the constraints of control and state but also attenuate the effect of additive stochastic noises. Future work will be focused on the consideration of relative attitude dynamics between the test-masses and the satellite.

Data Availability

The data used to support the findings of this study are available from the corresponding author upon request.

Conflicts of Interest

The authors declare that there are no conflicts of interest regarding the publication of this paper.

Acknowledgments

This work was supported by the National Natural Science Foundation of China (61833009, 11972130, and 61690212) and Guangdong Major Project of Basic and Applied Basic Research (Grant no. 2019B030302001).

References

[1] B. Lange, "The drag-free satellite," *AIAA Journal*, vol. 2, no. 9, pp. 1590–1606, 1964.

[2] E. Hardy, M. S. Rodrigues, P. Touboul et al., "Testing the equivalence principle in space: the MICROSCOPE mission," in *Proceedings of the 42nd COSPAR Scientific Assembly*, Pasadena, CA, USA, 2018.

[3] A. N. Marchenko, D. A. Marchenko, and A. N. Lopushansky, "Gravity field models derived from the second degree radial derivatives of the GOCE mission: a case study," *Annals of Geophysics*, vol. 59, no. 6, p. 0649, 2017.

[4] P. Amaro-Seoane, H. Audley, S. Babak et al., "Laser interferometer space antenna," 2017, https://arxiv.org/abs/1702.00786.

[5] J. Conklin and A. N. Nguyen, "Drag-free control and drag force recovery of small satellites," in *Proceedings of the 2017 Annual AIAA/USU Conference on Small Satellites*, Logan, UT, USA, 2017.

[6] A. N. Nguyen and J. W. Conklin, "Three-axis drag-free control and drag force recovery of a single-thruster small satellite," *Journal of Spacecraft and Rockets*, vol. 52, no. 6, pp. 1640–1650, 2015.

[7] C. F. Everitt, D. DeBra, B. Parkinson et al., "Gravity probe B: final results of a space experiment to test general relativity," *Physical Review Letters*, vol. 106, no. 22, p. 221101, 2011.

[8] P. Prieur, T. Lienart, M. Rodrigues et al., "MICROSCOPE mission: on-orbit assessment of the drag-free and attitude control system," in *Proceedings of the 31st International Symposium on Space Technology and Science (ISTS 2017)*, Kobe, Japan, 2017.

[9] E. Canuto, "Drag-free and attitude control for the GOCE satellite," *Automatica*, vol. 44, no. 7, pp. 1766–1780, 2008.

[10] E. Canuto, L. Colangelo, M. Lotufo, and S. Dionisio, "Satellite-to-satellite attitude control of a long-distance spacecraft formation for the next generation gravity mission," *European Journal of Control*, vol. 25, pp. 1–16, 2015.

[11] B. D. Loomis, R. S. Nerem, and S. B. Luthcke, "Simulation study of a follow-on gravity mission to GRACE," *Journal of Geodesy*, vol. 86, no. 5, pp. 319–335, 2012.

[12] J. Baker, J. Bellovary, P. L. Bender et al., "The laser interferometer space antenna: unveiling the Millihertz gravitational wave sky," 2019, https://arxiv.org/abs/1907.06482.

[13] M. Armano, H. Audley, J. Baird et al., "LISA Pathfinder platform stability and drag-free performance," *Physical Review D*, vol. 99, no. 8, Article ID 082001, 2019.

[14] Z. Dang and Y. Zhang, "Relative position and attitude estimation for inner-formation gravity measurement satellite system," *Acta Astronautica*, vol. 69, no. 7-8, pp. 514–525, 2011.

[15] J. Luo, L. S. Chen, H. Z. Duan et al., "TianQin: a space-borne gravitational wave detector," *Classical and Quantum Gravity*, vol. 33, no. 3, Article ID 035010, 2016.

[16] G. D. Racca and P. W. McNamara, "The LISA pathfinder mission," *Space Science Reviews*, vol. 151, no. 1–3, pp. 159–181, 2010.

[17] L. Ji, J. Xiang, and K. Liu, "Model predictive technics based three-axis stabilization control of a drag-free satellite," in *Proceedings of the 2010 3rd International Conference on Computer Science and Information Technology*, IEEE, Chengdu, China, 2010.

[18] W. Fichter, P. Gath, S. Vitale, and D. Bortoluzzi, "LISA pathfinder drag-free control and system implications," *Classical and Quantum Gravity*, vol. 22, no. 10, pp. S139–S148, 2005.

[19] L. Pettazzi, A. Lanzon, S. Theil, and A. E. Finzi, "Design of robust drag-free controllers with given structure," *Journal of Guidance, Control, and Dynamics*, vol. 32, no. 5, pp. 1609–1621, 2009.

[20] Z. Dang and Y. Zhang, "Formation control using μ-synthesis for inner-formation gravity measurement satellite system," *Advances in Space Research*, vol. 49, no. 10, pp. 1487–1505, 2012.

[21] E. Canuto and L. Massotti, "All-propulsion design of the drag-free and attitude control of the European satellite GOCE," *Acta Astronautica*, vol. 64, no. 2-3, pp. 325–344, 2009.

[22] S.-F. Wu and D. Fertin, "Spacecraft drag-free attitude control system design with quantitative feedback theory," *Acta Astronautica*, vol. 62, no. 12, pp. 668–682, 2008.

[23] W. H. Chen, J. Yang, L. Guo et al., "Disturbance-observer-based control and related methods—an overview," *IEEE Transactions on Industrial Electronics*, vol. 63, no. 2, pp. 1083–1095, 2015.

[24] Q. Hou, S. Ding, and X. Yu, "Composite super-twisting sliding mode control design for PMSM speed regulation problem based on a novel disturbance observer," *IEEE Transactions on Energy Conversion*, p. 1, 2020.

[25] S. Ding, W.-H. Chen, K. Mei, and D. J. Murray-Smith, "Disturbance observer design for nonlinear systems represented by input-output models," *IEEE Transactions on Industrial Electronics*, vol. 67, no. 2, pp. 1222–1232, 2020.

[26] X. Zhao, X. Ma, and X. Ma, "A novel disturbance observer for multiagent tracking control with matched and unmatched

uncertainties," *Mathematical Problems in Engineering*, vol. 2019, Article ID 9765353, 9 pages, 2019.

[27] J. Yan, H. Wang, S. Huang, and Y. Lan, "Disturbance observer-based backstepping control of PMSM for the mine traction electric locomotive," *Mathematical Problems in Engineering*, vol. 2018, Article ID 7253210, 10 pages, 2018.

[28] X. Zhang, J. Gao, W. Zhang, T. Zeng, and L. Ye, "Distributed formation control for multiple quadrotor based on multi-agent theory and disturbance observer," *Mathematical Problems in Engineering*, vol. 2019, Article ID 7234969, 11 pages, 2019.

[29] L. Liu, X. Song, Z. Fu, and S. Song, "Disturbance observer-based input-output finite-time control of a class of nonlinear systems," *Mathematical Problems in Engineering*, vol. 2017, Article ID 7202584, 7 pages, 2017.

[30] H. Liang, X. Guo, Y. Pan, and T. Huang, "Event-triggered fuzzy bipartite tracking control for network systems based on distributed reduced-order observers (revised manuscript of TFS-2019-1049)," *IEEE Transactions on Fuzzy Systems*, p. 1, 2020.

[31] P. Du, Y. Pan, H. Li, and H.-K. Lam, "Nonsingular finite-time event-triggered fuzzy control for large-scale nonlinear systems," *IEEE Transactions on Fuzzy Systems*, p. 1, 2020.

[32] Z. Zhu, Y. Pan, Q. Zhou, and C. Lu, "Event-triggered adaptive fuzzy control for stochastic nonlinear systems with unmeasured states and unknown backlash-like hysteresis," *IEEE Transactions on Fuzzy Systems*, p. 1, 2020.

[33] Q. Zhou, S. Zhao, H. Li, R. Lu, and C. Wu, "Adaptive neural network tracking control for robotic manipulators with dead zone," *IEEE Transactions on Neural Networks and Learning Systems*, vol. 30, no. 12, pp. 3611–3620, 2019.

[34] J. Han, "From PID to active disturbance rejection control," *IEEE Transactions on Industrial Electronics*, vol. 56, no. 3, pp. 900–906, 2009.

[35] C. Zhong, Z. Chen, and Y. Guo, "Attitude control for flexible spacecraft with disturbance rejection," *IEEE Transactions on Aerospace and Electronic Systems*, vol. 53, no. 1, pp. 101–110, 2017.

[36] W. Wang, H. Liang, Y. Pan, and T. Li, "Prescribed performance adaptive fuzzy containment control for nonlinear multiagent systems using disturbance observer," *IEEE Transactions on Cybernetics*, vol. 50, no. 9, pp. 3879–3891, 2020.

[37] G. Dong, L. Cao, D. Yao et al., "Adaptive attitude control for multi-MUAVs with output dead-zone and actuator fault," *IEEE/CAA Journal of Automatica Sinica*, 2020.

[38] G. Lin, H. Li, H. Ma et al., "Human-in-the-loop consensus control for nonlinear multi-agent systems with actuator faults," *IEEE/CAA Journal of Automatica Sinica*, 2020.

[39] H. Ma, H. Li, R. Lu et al., "Adaptive event-triggered control for a class of nonlinear systems with periodic disturbances," *Science China Information Sciences*, vol. 63, no. 5, pp. 1–15, 2020.

[40] E. Canuto, A. Molano, and L. Massotti, "Drag-free control of the GOCE satellite: noise and observer design," *IEEE Transactions on Control Systems Technology*, vol. 18, no. 2, pp. 501–509, 2009.

[41] H. Li, Y. Bai, M. Hu et al., "A novel controller design for the next generation space electrostatic accelerometer based on disturbance observation and rejection," *Sensors*, vol. 17, no. 1, p. 21, 2017.

[42] L. Cao, B. Xiao, and M. Golestani, "Robust fixed-time attitude stabilization control of flexible spacecraft with actuator uncertainty," *Nonlinear Dynamics*, vol. 100, no. 3, pp. 2505–2519, 2020.

[43] B. Xiao, L. Cao, S. Xu, and L. Liu, "Robust tracking control of robot manipulators with actuator faults and joint velocity measurement uncertainty," *IEEE/ASME Transactions on Mechatronics*, vol. 25, no. 3, pp. 1354–1365, 2020.

[44] R. Yang and W. X. Zheng, "Output-based event-triggered predictive control for networked control systems," *IEEE Transactions on Industrial Electronics*, vol. 67, no. 12, pp. 10631–10640, 2020.

[45] R. Yang, W. X. Zheng, and Y. Yu, "Event-triggered sliding mode control of discrete-time two-dimensional systems in Roesser model," *Automatica*, vol. 114, Article ID 108813, 2020.

[46] Y. Zhu and W. X. Zheng, "Multiple Lyapunov functions analysis approach for discrete-time-switched piecewise-affine systems under dwell-time constraints," *IEEE Transactions on Automatic Control*, vol. 65, no. 5, pp. 2177–2184, 2020.

[47] Y. Zhu, W. X. Zheng, and D. Zhou, "Quasi-synchronization of discrete-time lure-type switched systems with parameter mismatches and relaxed PDT constraints," *IEEE Transactions on Cybernetics*, vol. 50, no. 5, pp. 2026–2037, 2020.

[48] Y. Zhu and W. X. Zheng, "Observer-based control for cyber-physical systems with periodic DoS attacks via a cyclic switching strategy," *IEEE Transactions on Automatic Control*, vol. 65, no. 8, pp. 3714–3721, 2020.

[49] L. Liu, W. X. Zheng, and S. Ding, "An adaptive SOSM controller design by using a sliding-mode-based filter and its application to buck converter," *IEEE Transactions on Circuits and Systems I: Regular Papers*, vol. 67, no. 7, pp. 2409–2418, 2020.

[50] C. Zhang, J. He, L. Duan, and Q. Kang, "Design of an active disturbance rejection control for drag-free satellite," *Microgravity Science and Technology*, vol. 31, no. 1, pp. 31–48, 2019.

[51] E. Canuto, W. Acuna-Bravo, A. Molano-Jimenez, and C. Perez Montenegro, "Embedded model control calls for disturbance modeling and rejection," *ISA Transactions*, vol. 51, no. 5, pp. 584–595, 2012.

[52] S. V. Raković, "Model predictive control: classical, robust, and stochastic," *IEEE Control Systems Magazine*, vol. 36, no. 6, pp. 102–105, 2016.

[53] Z. Dang, "Modeling and controller design of inner-formation flying system with two proof-masses," *Aerospace Science and Technology*, vol. 30, no. 1, pp. 8–17, 2013.

[54] J. Zhou, L. Liu, and Z. Wang, "Modeling and analysis of ultra-low frequency dynamics of drag-free satellites," *Microgravity Science and Technology*, vol. 31, no. 2, pp. 151–160, 2019.

[55] J. Zhang, P. Shi, and W. Lin, "Extended sliding mode observer based control for Markovian jump linear systems with disturbances," *Automatica*, vol. 70, pp. 140–147, 2016.

[56] Y. Shtessel, C. Edwards, L. Fridman et al., *Sliding Mode Control and Observation*, Springer, Berlin, Germany, 2014.

[57] J. B. Rawlings and D. Q. Mayne, *Model Predictive Control: Theory and Design*, Nob Hill Pub, Madison, WI, USA, 2009.

Hindawi
Mathematical Problems in Engineering
Volume 2021, Article ID 6670277, 5 pages
https://doi.org/10.1155/2021/6670277

Research Article

Research on Array Structures of Acoustic Directional Transducer

Guozhu Zhao,[1] Kaibo Shi ,[2] and Shouming Zhong[3]

[1]*Simulator Training Center Civil Aviation Flight University of China, Guanghan, Sichuan 618300, China*
[2]*School of Information Science and Engineering, Chengdu University, Chengdu, Sichuan 610106, China*
[3]*School of Mathematical Sciences, University of Electronic Science and Technology of China, Chengdu, Sichuan 611731, China*

Correspondence should be addressed to Kaibo Shi; skbs111@163.com

Received 3 October 2020; Revised 8 December 2020; Accepted 17 December 2020; Published 4 January 2021

Academic Editor: Shihong Ding

This paper focuses on the directivity design of array structures of acoustic directional transducers. Based on Huygens principles, the directivity formula of transducer arrays under random distribution in *xyz* space is derived when the circular piston transducers are used as the array element, which is used to analyze the directivity and acoustic pressure of conical transducer arrangements. In addition, a practical approach to analyze the directivity and acoustic pressure of transducer arrays under random arrangements is proposed. *Findings*. The conical transducer arrays show side lobes at higher frequency. Below the frequency of 2 kHz, array directivity shows rapid changes. Above the frequency of 2 kHz, array directivity varies slowly with frequency. Besides, the beam width is $\Theta_{-3\,\mathrm{dB}} \le 29.85^{\circ}$.

1. Theoretical Calculation of Transducer Array Directivity

For the single transducer, its directivity is decided by the ratio of sound wave length λ to size a. Take the circular piston source on the baffle as an example, as shown Figure 1. As for the single transducer, its directivity is expressed as the following formula [1–3]:

$$D(\theta) = \left|\frac{2J_1(ka\sin\theta)}{ka\sin\theta}\right| = \left|\left(\frac{2J_1(\pi d/\lambda)\sin\theta}{(\pi d/\lambda)\sin\theta}\right)\right|. \quad (1)$$

In this formula, J_1 is first-order Bessel function; wave number is $k = 2\pi/\lambda$; a represents sound source radius; and $d = 2a$ represents sound source diameter.

For linear arrays of point acoustic sources that consist of multiple transducers, the directivity is not decided by the ratio of sound wave length λ to transducer size a, but by array element arrangement. It is important to obtain the formula of directivity for transducer arrays in any random arrangements. The following shows the analysis of two relevant formulas [4–6].

2. Comparison of Directivity of Transducer Arrays and Random Array Configurations

According to Huygens principles, the linear array directivity function of n point acoustic sources is derived, as shown in Figure 1. It should be noted that at this point, each unit transducer is regarded as point with no radius, assuming $d = 2a$. It is possible to derive the directivity function of transducer arrays in N lines and M rows, as shown in Figure 2 [1]:

$$D(\alpha,\theta) = \frac{\sin\left((kMd_1/2)\cos\alpha\sin\theta\right)}{M\sin\left((kd_1/2)\cos\alpha\sin\theta\right)} \cdot \frac{\sin\left((kNd_2/2)\sin\alpha\sin\theta\right)}{N\sin\left((kd_2/2)\sin\alpha\sin\theta\right)}. \quad (2)$$

In this formula, d_1 and d_2 represent line space and space between columns; α is angle between the projection of vector $\overrightarrow{OP}$ on XOY and positive x axis; and θ is the angle between vector $\overrightarrow{OP}$ and z axis. The above formula obtains the following conclusion: for this function, it is necessary to demonstrate equidistant distribution in a certain direction (set the spacing distance in x axis or y axis); it needs to be a

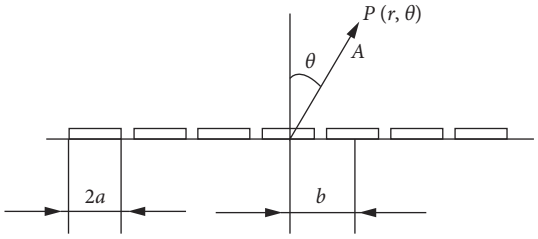

Figure 1: Transducer line arrays.

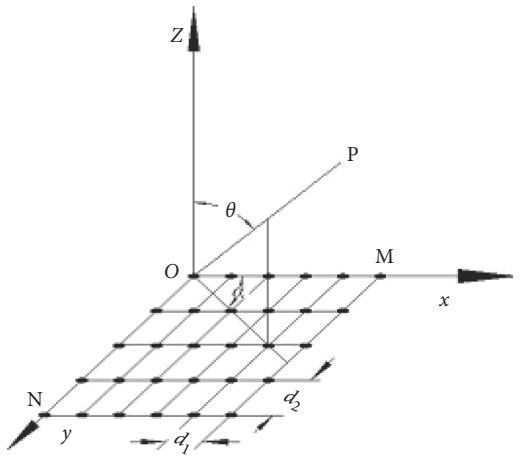

Figure 2: Transducer square arrays.

rectangular distribution instead of random arrays (such as polygon or circular array). When M or N is 1, this formula can calculate the array directivity. When $M = N = 1$, the formula can calculate directivity of single transducer [7–9].

3. Theoretical Calculation of Random Transducer Array Directivity

Figure 3 shows the rectangular coordinate system of directional acoustic transducer arrays. The central point of transducer arrays O is the origin of coordinate. Assuming transducer array within the xoy plane of the three-dimensional coordinate system, any single transducer is at the position Q (x_0, y_0). In the sound field, the distance between any single observation point $P(x_0, y_0, z_0)$ and the origin of coordinate is r, the intersection angle between the point and z axis is θ, and rotation angle is φ. It is likely to obtain normalized directivity function of n circular piston transducer arrays with the radius a and random placements:

$$D(\theta, \phi) = \left| \frac{p_M(\theta, \phi)_\theta}{p_M(\theta, \phi)_{\theta=0}} \right| = \left| \frac{2J_1(ka \sin\theta)}{ka \sin\theta} \right| \left| \sum_{i=1}^{n} e^{jk|x_i \sin\theta \sin\phi + y_i \sin\theta \cos\phi|} \right|. \tag{3}$$

From formula (3), it can be concluded that, for this function, there is no need to set the distance between transducer array elements or rectangular arrangements to obtain the directivity of random array arrangements. It is only necessary to identify the coordinate of each array element. When P (x_0, y_0) is determined, the directivity of random transducer plane layouts can be obtained. Besides,

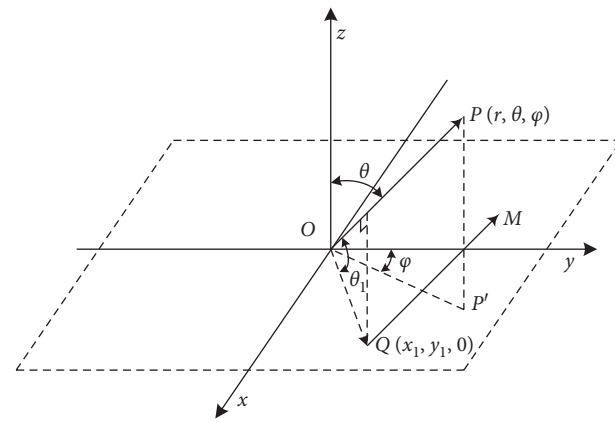

Figure 3: Coordinate system of transducer array.

this formula is relatively complex and difficult to obtain directivity patterns of arrays by conducting research on two-dimensional directivity. Hence, a research method of three-dimensional directivity is used to identify directivity [4–6].

4. Directivity Analysis of Three-Dimensional Transducer Arrangement

As shown in Figure 4, the three-dimensional space is established in the three-dimensional coordinate system with random transducers. O is the central point of the three-dimensional coordinate system. Assume transducer arrays are within the xyz plane of the three-dimensional coordinate system.

If the circular piston transducer with the radius a vibrates at the velocity, $u = u_0 e^{j\omega t}$, where u_0 is the velocity amplitude. Assume it is right at the origin of coordinate O. Then, its sound pressure is generated at observation point P (x_0, y_0, z_0) (the distance from origin of coordinate is r. The intersection angle with z axis is θ. The rotation angle is the position of φ). The resulting sound pressure is

$$p = j\omega \frac{\rho_0 u_a a^2}{2r} \left| \frac{2J_1(ka \sin\theta)}{ka \sin\theta} \right| e^{j(\omega t - kr)}. \tag{4}$$

In this formula, ρ_0 is the density of medium. $k = 2\pi/\lambda$ is the wave number (λ is the sound wave length). Frequency $f = 10000$ Hz. Sound speed is $C_0 = 340$ m/s, $\lambda = C_0/f$.

When circular piston transducer is at any point of xyz space, set r_1 as the sonic path distance between Q and P. Likewise, for at any point of xyz space Q, the sound pressure generated by circular piston transducer with the radium a at point P is

$$p_1 = j\omega \frac{\rho_0 u_a a^2}{2r_1} \left| \frac{2J_1\left(ka \sin\theta_Q\right)}{ka \sin\theta_Q} \right| e^{j(\omega t - kr_1)}. \tag{5}$$

In this formula, θ_Q is the included angle between vector $\overrightarrow{QP}$ and z. In the far field, it is approximately assumed as vector $\overrightarrow{OP} // \overrightarrow{QP}$. The connection between r_1 and r is shown in formula (4). $|\overrightarrow{OQ}| \cos\theta_1$ represents the projection of vector $\overrightarrow{OQ}$ on vector $\overrightarrow{OP}$. From the projection relationship, it can be inferred

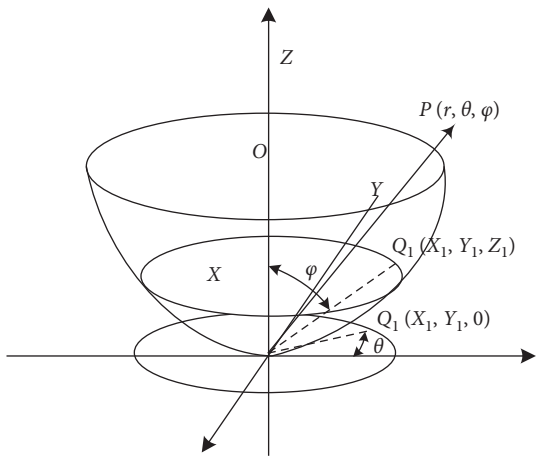

Figure 4: The three-dimensional coordinate system of transducer arrays.

$$r = r_1 + |\overrightarrow{OQ}|\cos\theta_1 = r_1 + r_Q\cos\theta_1. \tag{6}$$

In this formula, r_Q is the module of vector $\overrightarrow{OQ}$ and θ_1 is the included angle between vectors $\overrightarrow{OQ}$ and $\overrightarrow{OP}$. It should be noted that θ_1 may be an acute angle or an obtuse angle. The rectangular coordinate of point P is (x_0, y_0, z_0). The rectangular coordinate of point Q is (x_1, y_1, z_1). Vectors $\overrightarrow{OP}$ and $\overrightarrow{OQ}$ are represented as $\{x_0, y_0, z_0\}$ and $\{x_1, y_1, z_1\}$. Then, included angle cosine in formula (4) is

$$\cos\theta_1 = \frac{x_0x_1 + y_0y_1 + z_0z_1}{\sqrt{x_0^2 + y_0^2 + z_0^2}\sqrt{x_1^2 + y_1^2 + z_1^2}} = \frac{x_0x_1 + y_0y_1 + z_0z_1}{rr_Q}. \tag{7}$$

Formulas (4) and (5) are combined and arranged to obtain

$$r_1 = r - \frac{x_0x_1 + y_0y_1 + z_0z_1}{r}, \tag{8}$$

where, x_0, y_0, and z_0 in formula (6) are converted to circular cylindrical coordinates as the following:

$$\begin{cases} x_0 = r\sin\theta\sin\phi, \\ y_0 = r\sin\theta\cos\phi, \\ z_0 = r\cos\theta. \end{cases} \tag{9}$$

Formula (7) is substituted to formula (6):

$$r_1 = r - (x_1\sin\theta\sin\phi + y_1\sin\theta\cos\phi + z_1\cos\theta). \tag{10}$$

In the far field, the amplitude of formula (2) $r_1 \approx r$, $\theta_Q \approx \theta$. Formula (8) is substituted to formula (2) to obtain the following: the sound pressure generated by any point Q at point P in the xyz space is

$$p_1 = j\omega\frac{\rho_0u_aa^2}{2r}\left|\frac{2J_1(ka\sin\theta)}{ka\sin\theta}\right|e^{j[\omega t - kr + k(x_1\sin\theta\sin\phi + y_1\sin\theta\cos\phi + z_1\cos\theta)]}. \tag{11}$$

If planar transducer arrays consist of n circular piston transducers, the i transducer is in position (x_i, y_i, z_i) of the plane. Each transducer vibrates at the velocity $u = u_ae^{j\omega t}$. The sound pressure generated by n circular piston transducers at point P in the xyz space is shown in the following:

$$p_M = j\omega\frac{\rho_0u_aa^2}{2r}\left|\frac{2J_1(ka\sin\theta)}{ka\sin\theta}\right|e^{j(\omega t - kr)}\sum_{i=1}^{n}e^{jk(x_1\sin\theta\sin\phi + y_1\sin\theta\cos\phi + z_1\cos\theta)}. \tag{12}$$

According to Bessel function, when $x = 0$, $J_1(x)/x = (1/2)$. Based on formula (10), the normalized directivity function of transducers in random space arrangement can be obtained:

$$D(\theta,\phi) = \left|\frac{p_M(\theta,\phi)_\theta}{p_M(\theta,\phi)_{\theta=0}}\right| = \left|\frac{2J_1(ka\sin\theta)}{ka\sin\theta}\right|\left|\sum_{i=1}^{M}e^{jk(x_1\sin\theta\sin\phi + y_1\sin\theta\cos\phi + z_1\cos\theta)}\right|. \tag{13}$$

According to formula (11), it is feasible to calculate the feasibility of circular piston transducers with random arrangement in three-dimensional space. However, the above formula is a function concerned with variables θ and φ, which are hard to identify the directivity of the array. Hence, three-dimensional directivity research method is used in the process. To be more specific, conversion of coordinates is carried out in formula (11).

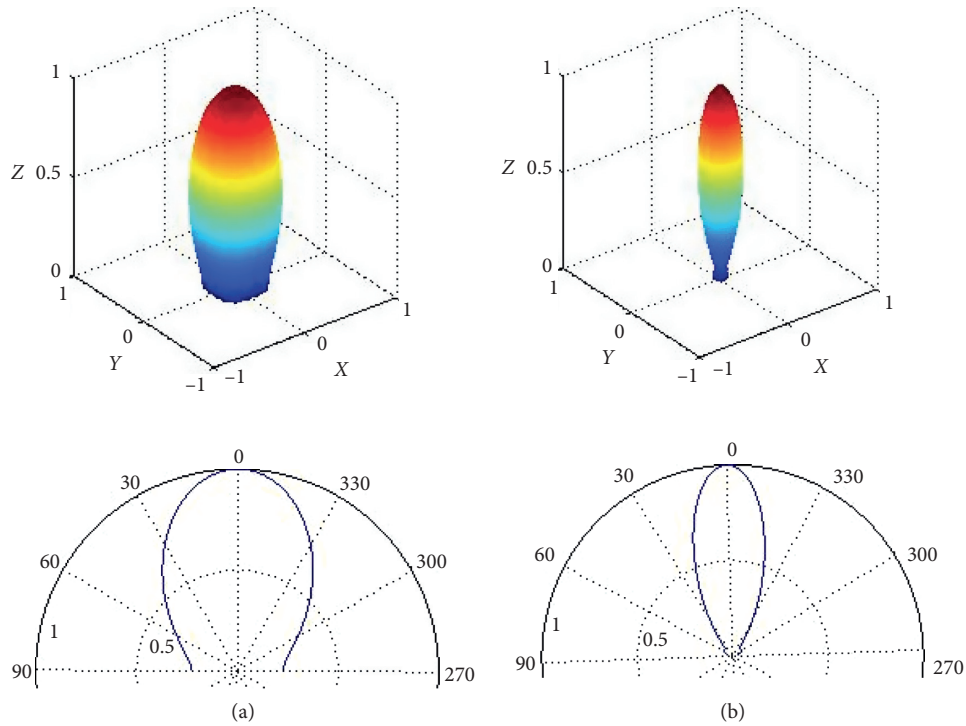

Figure 5: Directivity pattern of acoustic directional dispersion device. (a) 500 Hz. (b) 1 kHz.

$$\begin{cases} x_0 = \sin\theta \sin\phi \cdot D(\theta, \phi), \\ y_0 = \sin\theta \cos\phi \cdot D(\theta, \phi), \\ y_0 = \cos\theta \cdot D(\theta, \phi). \end{cases} \tag{14}$$

Assume the most central transducer is origin of coordinate O (0, 0), then the position coordinate of acoustic directional dispersion system is shown in Figure 4. The rectangular coordinates of acoustic directional transducer array are substituted in formula (11) to calculate the directivity angle of transducer. By changing the frequency, it is feasible to get the result shown in Figure 3.

It is known from Figure 5 that acoustic directional transducer array shows weak directivity at the sound wave frequency level of 500 Hz. If the sound wave frequency level increases, the level of directivity also rises gradually. When the frequency level reaches 4 kHz, apparent sidelobe shows up. When the frequency level reaches 6 kHz, directivity becomes favorable, but sidelobe becomes more apparent as well.

The figure shows that beam width $\Theta_{-3\,\mathrm{dB}}$ gradually narrows as frequency increases. Below the beam width of 2 kHz, frequency change is apparent. Above the beam width of 2 kHz, frequency change is slow. The frequency of dispersion sound wave ranges between 2.1 and 3.4 kHz. When it is above 2 kHz, the beam width of acoustic directional transducer is $\Theta_{-3\,\mathrm{dB}} \leq 29.85^{\circ}$, directional acute angle $(\Theta_{-3\,\mathrm{dB}}/2) \leq \pm 14.925^{\circ}$. Favorable directivity is shown.

5. Conclusion

Based on the Huygens principle of sound waves, this work has derived the formula for the directivity of transducer arrays in random arrangement when circular piston transducers are used as array elements. Based on this formula, it studied the directivity and sound pressure of conical transducer array arrangements. The work provided a way to analyze directivity and sound pressure of transducer arrays in random arrangements for conical transducer and acoustic directional transducers. Findings: conical transducer arrays demonstrate sidelobe at high-frequency levels, but it can be overlooked compared to the main lobe. Below the frequency level of 2 kHz, array directivity changes rapidly. Above the frequency level of 2 kHz, array directivity changes more slowly, and the beam width is $\Theta_{-3\,\mathrm{dB}} \leq 29.85^{\circ}$.

The work expands the formula of calculating the directivity of circular piston transducers with random array arrangements. Based on the digital simulation of computers, it resolves the difficult issues in the directivity design of three-dimensional arrays of acoustic directional transducers, providing positive significance for designing acoustic directional transducer arrays.

Data Availability

No data used to support the study.

Conflicts of Interest

The authors declare that they have no conflicts of interest.

Acknowledgments

This work was financially supported by the Civil Aviation Flight University of China fund project: fault diagnosis of the operating system of the certificate simulator (XM2803).

References

[1] J. Moro and C. M. Sprinkle, "Thin high performance constant directivity waveguide and speaker," U.S. Patent Application 15/236,720, 2017.

[2] G. K. Munch and J. Dyreby, "Loudspeaker transducer arrangement for directivity control," U.S. Patent 9,942,659, 2018.

[3] J. Ahrens and S. Bilbao, "Interpolation and range extrapolation of sound source directivity based on a spherical wave propagation model," in *Proceedings of the ICASSP International Conference on Acoustics, Speech and Signal Processing*, pp. 4662–4666, IEEE, Barcelona, Spain, May 2020.

[4] H. Wang, X. Wang, C. He, and C. Xue, "Directivity theory and analysis of 2D capacitive micro-machined ultrasonic transducer array," *Journal of Nanoelectronics and Optoelectronics*, vol. 12, no. 8, pp. 786–794, 2017.

[5] G. Huang, J. Chen, and J. Benesty, "A flexible high directivity beamformer with spherical microphone arrays," *The Journal of the Acoustical Society of America*, vol. 143, no. 5, pp. 3024–3035, 2018.

[6] X. Zhen-yang, W. Xin-peng, and Z. Jing-yuan, "Research on the directivity of transducer array based on typical array elements," *Journal of Physics: Conference Series*, IOP Publishing, vol. 1237, no. 4, , p. 042063, 2019.

[7] J. Ling, Y.-Q. Chen, Y. Chen et al., "Design and characterization of high-density ultrasonic transducer array," *IEEE Sensors Journal*, vol. 18, no. 6, pp. 2285–2290, 2018.

[8] S. Yan, "Robust time-domain wideband modal beamforming with circular arrays," *IEEE Transactions on Aerospace and Electronic Systems*, In press.

[9] Q. Zhao, W. Zheng, and J. Li, "Research on the directionality of difference frequency sound field based on circular ultrasonic array," *Journal of Physics: Conference Series*, IOP Publishing, vol. 1314, no. 1, p. 012040, 2019.

Hindawi
Mathematical Problems in Engineering
Volume 2020, Article ID 8826630, 8 pages
https://doi.org/10.1155/2020/8826630

Research Article

Sliding Mode Integrated Control for Vehicle Systems Based on AFS and DYC

Chao Lu, Jing Yuan, and Genlong Zha

School of Information Engineering, Suqian University, Suqian 223800, China

Correspondence should be addressed to Chao Lu; luxiaochao6@163.com

Received 22 September 2020; Revised 30 October 2020; Accepted 16 November 2020; Published 10 December 2020

Academic Editor: Shihong Ding

This paper has investigated an integrated control of active front steering (AFS) and direct yaw-moment control (DYC) for vehicle systems. First of all, the desired yaw rate and sideslip angle are estimated by using a two-degree-of-freedom (2-DOF) model of the vehicle system. On this basis, the actual sideslip angle is estimated by means of an observer. Then, the sliding mode control (SMC) is developed for AFS and DYC, respectively, to guarantee that the actual yaw rate and the sideslip angle track their reference signals. Additionally, the disturbance observer (DOB) technique is introduced to further improve the control performance. Finally, the simulation results validate the superiority of the AFS and DYC integrated control by using CarSim software during the following conditions: double lane change and side wind disturbance.

1. Introduction

With the development of electronic technology, the use of control technology to improve the active safety of automobiles has become a hot topic in the automotive field. Active safety can minimize or avoid traffic accidents through vehicle design, while passive safety means that vehicles are designed to minimize the damage to passengers after an accident occurs. In the 90s of the last century, the concept of vehicle stability was proposed [1–3]. Then, the active safety control received considerable attention in the vehicle stability control, such as [4–7]. Among them, AFS catches researchers' eyes since it can directly adjust the steering angle of the drive. Nevertheless, when the moment of the vehicle in control limit is under the sections of high-speed turning, heavy braking, or acceleration, steering will have no effect or limited effect, the car loses the ability to turn, and the initiative will have little effect on the steering. On the contrary, the effect of DYC is very obvious at this time, and it is easy to realize. It does not require a great change in the original structure of the vehicle. This is because the goal of DYC is to adjust the vehicle yaw motion. Thus, the integrated control of AFS and DYC can not only further improve the lateral stability of the vehicle but also reduce the influence of braking on longitudinal dynamics and improve the driving comfort.

In [7], the LQR method was used in the integrated control of AFS and DYC and compared with DYC control. In [8], an integrated control of AFS and DYC with forward and feedback controllers was presented, and the parameters of the feedback controller were obtained by the optimum control theory. Then, the control strategy of AFS based on sliding mode theory and the control strategy of EPS (combined control on both direct yaw moment and variable slip ratio) were presented in [9]. An integrated AFS and DYC control system was developed in [10] based on the fuzzy logic control, which was used for the yaw rate controller to keep the yaw rate in its ideal value. In [11], the model predictive control was used to adopt the hierarchical integrated control structure.

In addition, on the one hand, the sliding mode control (SMC) is popular for rejecting the uncertainties [12–18]. On the other hand, the accurate mathematical model is indeed necessary for SMC [19, 20]. Hence, it is obvious that the SMC method is a very useful tool for active safety control, such as [21–23].

This paper focuses on the investigation of the integrated SMC control for the AFS and DYC system, which is designed to make sure the actual yaw rate and sideslip angle track the desired signals. First of all, the proposed control can drive

the error of the yaw rate and the sideslip angle to zero within a finite time. Then, a disturbance observer (DOB) [24] is constructed for the proposed control to reduce the control gain so as to reduce the chattering. The effectiveness of the proposed control is illustrated by the simulation on MATLAB and CarSim.

As compared with the existing results, the contributions of this paper are twofold. On the one hand, an integrated control of AFS and DYC for vehicle systems has been studied. On the other hand, the Lyapunov stability analysis and simulation results have been given to demonstrate the effectiveness of the proposed strategy.

The rest of the paper is organized as follows. Section 2 introduces the dynamic model of the vehicle and problem statement. The process of control design is given in Section 3. The simulation results are shown in Section 4. Section 5 concludes this paper.

2. Dynamical Model and Problem Statement

2.1. 2-DOF Model. The 2-DOF model is called as the "bicycle model" [25, 26], which is shown in Figure 1.

Then, the model is described as

$$mV_x(\dot{\beta}+r) = -2\left(C_f + C_r\right)\beta + \frac{-2\left(aC_f - bC_r\right)}{V_x}r + 2C_f\delta_f, \tag{1}$$

$$I_z\dot{r} = -2\left(aC_f - bC_r\right)\beta + \frac{-2\left(a^2C_f + b^2C_r\right)}{V_x}r + 2aC_f\delta_f, \tag{2}$$

where C_f and C_r, respectively, are the front and rear tire cornering stiffness, F is the tire force, x means the longitudinal position, y means the lateral position, β is the sideslip angle, a and b mean the distances from the center of gravity to the front and rear axles, V is the velocity, f means "front," r means "rear," r is the yaw rate, I_z is the moment of inertia, δ_f is the front-wheel steering angle, and m is the mass.

2.2. Problem Formulation. It is important to make sure what the ideal reference signal is. Usually, the yaw rate and the sideslip angle are the two important parameters to measure vehicle stability. According to the 2-DOF model, the desired yaw rate and sideslip angle can be calculated as [27]

$$r_d = \begin{cases} r_t, & |r_t| < \dfrac{0.85\mu g}{V_x}, \\ \dfrac{0.85\mu g}{V_x}\operatorname{sign}(r_t), & |r_t| \geq \dfrac{0.85\mu g}{V_x}, \end{cases} \tag{3}$$

$$\beta_d = \begin{cases} \beta_t, & |\beta_t| < \beta_{\max}, \\ \beta_{\max}\operatorname{sign}(\beta_t), & |\beta_t| \geq \beta_{\max}, \end{cases} \tag{4}$$

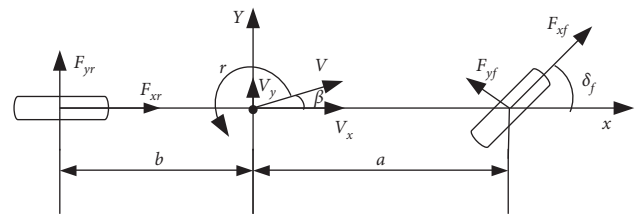

Figure 1: 2-DOF vehicle model.

with

$$r_t = \frac{V_x}{(a+b)\left(1+KV_x^2\right)}\delta_{fd}, \qquad \beta_t = \frac{b - amV_x^2/2C_f(a+b)}{(a+b)\left(1+KV_x^2\right)}\delta_{fd}, \tag{5}$$

where μ is the tire-road friction coefficient, K is a positive constant, δ_{fd} is the angle input from the steering wheel to the front wheel, $\beta_{\max} = \arctan(0.02\mu g)$, and g is the gravitational constant.

The diagram of the integrated control of active front steering and direct yaw moment (AFS + DYC) is depicted in Figure 2, and the vehicle inputs include the vehicle speed V_x and the steering wheel angle δ_{fd} commanded by the driver. According to the 2-DOF vehicle model, the ideal sideslip angle β_d and yaw rate r_d can be calculated, respectively. The CarSim vehicle model is regarded as a real vehicle model, which can output the actual yaw rate r. As a matter of fact, it is difficult to measure the actual sideslip angle directly by some special sensors, and the sensors needed are expensive. On the contrary, the accuracy and stability need to be further improved, thus designing the state observer to estimate the exact value is a good solution.

Remark 1. The DYC algorithm cannot be imposed on the 2-DOF model. This is because the implementation of DYC algorithm is based on the yaw moment M_z generated by the torque difference between left and right wheels, while the 2-DOF model regards the left and right wheels as one wheel such that there is no M_z in the 2-DOF model.

3. Control Design

3.1. Sideslip Angle Observer. The lateral acceleration a_y is expressed as

$$a_y = V_x(\dot{\beta} + tr) = \frac{-2\left(C_f + C_r\right)}{m}\beta + \frac{-2\left(aC_f - bC_r\right)}{mV_x}r + \frac{2C_f}{m}\delta_f. \tag{6}$$

Introduce the variables $x_1 = r$, $x_2 = \beta$, $X = [r, \beta]^T$, $Y = [y_1, y_2]^T = [r, a_y]^T$, and $u = [\delta_f]$. The vehicle model described by equations (1) and (2) can be rewritten as

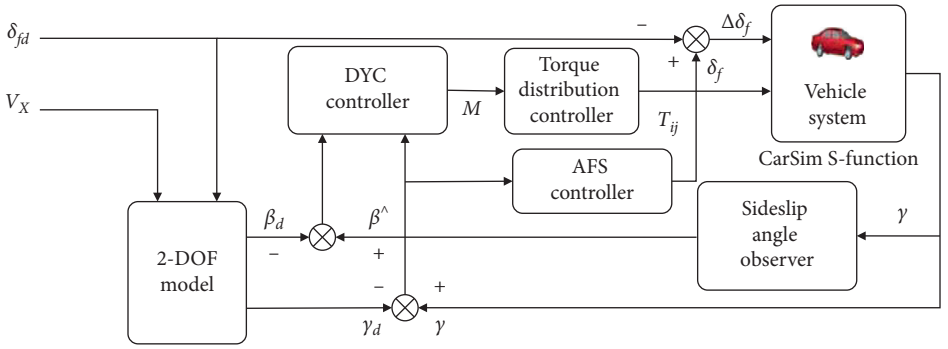

Figure 2: Structure of the AFS + DYC control system.

$$\begin{cases} \dot{X} = AX + Bu, \\ Y = CX + Du, \end{cases}$$

$$A = \begin{bmatrix} \dfrac{-2\left(a^2C_f + b^2C_r\right)}{I_z V_x} & \dfrac{-2\left(aC_f - bC_r\right)}{I_z} \\ \dfrac{-2\left(aC_f - bC_r\right)}{mV_x^2} - 1 & \dfrac{-2\left(C_f + C_r\right)}{mV_x} \end{bmatrix}, \quad B = \begin{bmatrix} \dfrac{2aC_f}{I_z} \\ \dfrac{2C_f}{mV_x} \end{bmatrix},$$

$$C = \begin{bmatrix} 1 & 0 \\ V_x\left(A_{21} + 1\right) & V_x A_{22} \end{bmatrix}, \quad D = \begin{bmatrix} 0 \\ V_x B_2 \end{bmatrix}. \tag{7}$$

Then, the observer is constructed as

$$\begin{cases} \dot{\widehat{x}}_1 = A_{11}y_1 + A_{12}\widehat{x}_2 + B_1u + c_1\left|y_1 - \widehat{x}_1\right|^{1/2}\operatorname{sign}\left(y_1 - \widehat{x}_1\right), \\ \dot{\widehat{x}}_2 = A_{21}y_1 + A_{22}\widehat{x}_2 + B_2u + c_2\operatorname{sign}\left(y_1 - \widehat{x}_1\right) + \dfrac{1}{V_x}\left(a_y - \widehat{a}_y\right), \\ \widehat{a}_y = V_x\left(A_{21} + 1\right)y_1 + V_xA_{22}\widehat{x}_2 + V_xB_2\delta_f, \end{cases} \tag{8}$$

where c_1 and c_2 are positive constants.

Then, the following lemma is obtained, whose proof is similar to that in [23]. Thus, it is omitted here.

Lemma 1. *The output $\widehat{x}_2$ of (8) will track x_2 within a finite time.*

Remark 2. It should be pointed out that the values of the front and rear tire cornering stiffness C_f and C_r are assumed to be constants in the vehicle dynamic model. In fact, their values are dependent on the road condition and normal force on tires, and thus, there are some perturbations for the two parameters. In addition, the model error also exists in the vehicle dynamics. These factors affect the accuracy of the estimation. To fix this problem, the lateral acceleration error $a_y - \widehat{a}_y$ is introduced in the observer (8) to compensate the model error and parameter perturbations.

3.2. Baseline Controller

3.2.1. AFS Controller. The AFS is to control the steering angle of the front wheel in the linear range of the tire. Therefore, the design of the controller is based on 2-DOF. The purpose of the controller is to eliminate the error between the actual vehicle and the ideal vehicle by controlling the front steering angle and to make sure the yaw rate follows the ideal model well.

The active front steering 2-DOF vehicle model is described as

$$\begin{bmatrix} \dot{r} \\ \dot{\beta} \end{bmatrix} = \begin{bmatrix} A_{11} & A_{12} \\ A_{21} & A_{22} \end{bmatrix}\begin{bmatrix} r \\ \beta \end{bmatrix} + \begin{bmatrix} B_1 \\ B_2 \end{bmatrix}\delta_f. \tag{9}$$

The difference between the actual yaw rate and the ideal value is

$$e = r - r_d. \tag{10}$$

Taking the derivative of (10) yields

$$\dot{e} = \dot{r} - \dot{r}_d. \tag{11}$$

We choose the sliding surface as $s_1 = e$. Taking the time derivative of s_1 along system (9) gives

$$\dot{s}_1 = A_{11}r + A_{12}\widehat{\beta} + B_1\delta_f + D_1(t), \tag{12}$$

where $D_1 = -\dot{r}_d + A_{12}\left(\beta - \widehat{\beta}\right)$. One can find a constant γ_{D_1} such that

$$\left|D_1(t)\right| \le \gamma_{D_1}. \tag{13}$$

Theorem 1. *If the AFS controller is constructed as*

$$\delta_f = \frac{1}{B_1}\left(-A_{11}r - A_{12}\widehat{\beta} - k_1\operatorname{sign}\left(s_1\right) - k_2s_1\right), \tag{14}$$

where $k_1 > \gamma_{D_1}$ and $k_2 > 0$, r will finite-time converge to r_d.

Proof. Putting (14) into (12) yields

$$\dot{s}_1 = -k_1\operatorname{sign}\left(s_1\right) - k_2s_1 + D_1(t). \tag{15}$$

Let $V(s_1) = (1/2)s_1^2$. The time derivative of $V(s_1)$ along system (15) is

$$\begin{aligned}\dot{V} &= s_1\dot{s}_1\\ &= -k_1\operatorname{sign}(s_1)s_1 - k_2s_1^2 + D_1(t)s_1\\ &\le -k_1|s_1| - k_2s_1^2 + |D_1(t)||s_1|\\ &\le -\left(k_1 - \gamma_{D_1}\right)|s_1| - k_2s_1^2\\ &\le -\left(k_1 - \gamma_{D_1}\right)|s_1|.\end{aligned} \tag{16}$$

Note that $k_1 > \gamma_{D_1}$. It can be proved that $\dot{V} \le -CV^{1/2}$, $C = \sqrt{2}(k_1 - \gamma_{D_1})$. From [28–30], the sliding variable s_1 will finite-time converge to zero. Hence, the corrective steer angle $\Delta\delta_f$ generated by the controller is determined as

$$\Delta\delta_f = \delta_f - \delta_{fd}. \tag{17}$$

□

3.2.2. DYC Controller. DYC control is to utilize the present antilock brake system to obtain the demanded longitudinal force and steady yaw moment. When the yaw moment is taken into account, the equation of state (9) becomes

$$\dot{r} = A_{11}r + A_{12}\beta + B_1\delta_f + \frac{1}{I_z}M, \tag{18}$$

$$\dot{\beta} = A_{21}r + A_{22}\beta + B_2\delta_f, \tag{19}$$

in which (19) can be rewritten as follows:

$$\delta_f = \frac{1}{B_2}\left(\dot{\beta} - A_{21}r - A_{22}\beta\right). \tag{20}$$

Substituting (20) into (18) produces

$$\dot{r} = \left(A_{11} - \frac{B_1}{B_2}A_{21}\right)r + \left(A_{12} - \frac{B_1}{B_2}A_{22}\right)\beta + \frac{B_1}{B_2}\dot{\beta} + \frac{1}{I_z}M. \tag{21}$$

Then, we select a sliding surface, which is composed of the deviation of the yaw rate and the deviation of the sideslip angle, i.e.,

$$s_2 = r - r_d + \xi(\beta - \beta_d), \tag{22}$$

with $\xi > 0$.

Combining the time derivative of (22) with (21) gives

$$\dot{s}_2 = \left(A_{11} - \frac{B_1}{B_2}A_{21}\right)r + \left(A_{12} - \frac{B_1}{B_2}A_{22}\right)\widehat{\beta} + \frac{1}{I_z}M + D_2(t), \tag{23}$$

with $D_2(t) = (A_{12} - (B_1/B_2)A_{22})(\beta - \widehat{\beta}) + (B_1/B_2)\dot{\beta} + \xi(\dot{\beta} - \dot{\beta}_d) - \dot{r}_d$. Note that $\dot{\beta}$ is often very small, and from the definition of β_d and r_d, $\dot{\beta}_d$ and $\dot{r}_d$ are bounded. Hence, a constant γ_{D_2} can be found such that

$$|D_2(t)| \le \gamma_{D_2}. \tag{24}$$

Theorem 2. *If the DYC controller is constructed as*

$$\begin{aligned}M = I_z\Bigg(&-\left(A_{11} - \frac{B_1}{B_2}A_{21}\right)\gamma\\ &-\left(A_{12} - \frac{B_1}{B_2}A_{22}\right)\widehat{\beta} - K_1\operatorname{sign}(s_2) - K_2s_2\Bigg),\end{aligned} \tag{25}$$

where $K_1 > \gamma_{D_2}$ and $K_2 > 0$, s_2 will finite-time converge to zero.

Proof. Putting (25) into (23) yields

$$\dot{s}_2 = -K_1\operatorname{sign}(s_2) - K_2s_2 + D_2(t). \tag{26}$$

Choose the Lyapunov function as $V(s_2) = (1/2)s_2^2$. Differentiating $V(s_2)$ along system (26) gives

$$\begin{aligned}\dot{V} &= s_2,\\ \dot{s}_2 &= -K_1\operatorname{sign}(s_2)s_2 - K_2s_2^2 + D_2(t)s_2\\ &\le -K_1|s_2| - K_2s_2^2 + |D_2(t)||s_2|\\ &\le -\left(K_1 - \gamma_{D_2}\right)|s_2| - K_2s_2^2\\ &\le -\left(K_1 - \gamma_{D_2}\right)|s_2|.\end{aligned} \tag{27}$$

Note that $K_1 > \gamma_{D_2}$. It can be proved that $\dot{V} \le -C_\gamma V^{1/2}$, $C_\gamma = \sqrt{2}(K_1 - \gamma_{D_2})$, and s_2 finite-time converges to zero. □

3.3. Composite Controller Design. In the following, by using DOB technique and baseline controllers, we will give the composite controllers to enhance the control performance.

3.3.1. AFS Controller Based on a DOB. We can rewrite system (12) as

$$\dot{s}_1 = F(s_1) + G_1(s_1)\delta_f + G_2(s_1)D_1(t), \tag{28}$$

where $F(s_1) = A_{11}r + A_{12}\widehat{\beta}$, $G_1(s_1) = B_1$, $G_2(s_1) = 1$, and $D_1(t)$ is regarded as the unknown disturbance and satisfies $|\dot{D}_1(t)| \le \gamma_{\dot{D}_1}$ with $\gamma_{\dot{D}_1} > 0$ being a constant, which at least holds locally.

Design the nonlinear DOB (NDOB) as

$$\begin{cases}\dot{P} = -L_1G_2P - L_1\left[G_2L_1s_1 + F(s_1) + G_1\delta_f\right],\\ D_1 = \widehat{P + L_1s_1},\end{cases} \tag{29}$$

where P and L_1 are the state and constant.

Let $e_1(t) = D_1(t) - \widehat{D}_1(t)$. Differentiating $e_1(t)$ along systems (28) and (29) gives

$$\begin{aligned}\dot{e}_1 &= \dot{D}_1 - \dot{\widehat{D}}_1\\ &= \dot{D}_1 - \left[-L_1G_2P - L_1^2G_2s_1 + L_1G_2D_1\right]\\ &= \dot{D}_1 - L_1G_2e_1.\end{aligned} \tag{30}$$

Let $V(e_1) = (1/2)e_1^2$. Then, one has

$$\dot{V}(e_1) = e_1\dot{e}_1 = e_1\left(\dot{D}_1 - L_1G_2e_1\right) \le |e_1|\gamma_{\dot{D}_1} - L_1G_2e_1^2. \tag{31}$$

Define a region as $Q_1 = \{e_1 : |e_1| \le (\gamma_{\dot{D}_1}/L_1G_2)\}$. For any $e_1(t) \in R/Q_1$, one has $|e_1| > (\gamma_{\dot{D}_1}/L_1G_2)$. This, together with (31), yields $\dot{V}(e_1) \le -|e_1|(L_1G_2|e_1| - \gamma_{\dot{D}_1}) < 0$. Note that $G_2 = 1$, which means that $e_1(t)$ will reach and stay in the domain

$$Q_1 = \left\{e_1 : |e_1| \le \frac{\gamma_{\dot{D}_1}}{L_1}\right\}. \tag{32}$$

Theorem 3. *Provided that the composite AFS controller is constructed as*

$$\delta_f = \frac{1}{B_1}\left(-A_{11}r - A_{12}\widehat{\beta} - \widehat{D}_1 - k_1\text{sign}(s_1) - k_2 s_1\right), \tag{33}$$

where $k_1 > 0$, $k_2 > 0$, and $L_1 > \gamma_{\dot{D}_1}$, s_1 will finite-time converge to zero.

Proof. Putting (33) into (12) yields

$$\begin{aligned} \dot{s_1} &= -K_1\text{sign}(s_1) - K_2 s_1 + D_1(t) - \widehat{D}_1 \\ &= -K_1 \cdot \text{sign}(s_1) - K_2 s_1 + e_1(t). \end{aligned} \tag{34}$$

From NDOB (29), it is clear that the error $e_1(t)$ is bounded. This means that a constant γ_{e_1} can be found such that $|e_1(t)| = |D_1(t) - \widehat{D}_1| \le \gamma_{e_1}$.

Hence, the corrective steer angle $\Delta\delta_f$ generated by the controller is determined as follows:

$$\Delta\delta_f = \delta_f - \delta_{fd}. \tag{35}$$

□

3.3.2. DYC Controller Based on a DOB. System (23) can be rewritten as

$$\dot{s}_2 = f(s_2) + g_1(s_2)M + g_2(s_2)D_2(t), \tag{36}$$

where $f(s_2) = (A_{11} - (B_1/B_2)A_{21})r + (A_{12} - (B_1/B_2)A_{22})\widehat{\beta}$, $g_1(s_2) = 1/I_z$, $g_2(s_2) = 1$, and $D_2(t)$ is considered as the unknown perturbation, and $|\dot{D}_2(t)| \le \gamma_{\dot{D}2}$. Then, a NDOB is constructed as

$$\begin{cases} \dot{p} = -L_2g_2p - L_2[g_2L_2s_2 + f(s_2) + g_1M], \\ \widehat{D_2} = p + L_2s_2. \end{cases} \tag{37}$$

L_2 is a positive constant.

Let $e_2(t) = D_2(t) - \widehat{D}_2(t)$. Taking the derivative of $e_2(t)$ along systems (36) and (37) gives

$$\begin{aligned} \dot{e}_2 &= \dot{D}_2 - \dot{\widehat{D}}_2 \\ &= \dot{D}_2 - \left[-L_2g_2p - L_2^2g_2s_2 + L_2g_2D_2\right] \\ &= \dot{D}_2 - L_2g_2e_2. \end{aligned} \tag{38}$$

We choose a Lyapunov function as $V(e_2) = (1/2)e_2^2$, whose time derivative along (38) is

$$\dot{V}(e_2) = e_2\dot{e}_2 = e_2\left(\dot{D}_2 - L_2g_2e_2\right) \le |e_2|\gamma_{\dot{D}_2} - L_2g_2e_1^2. \tag{39}$$

Define a region as $Q_2 = \{e_2 : |e_2| \le \gamma_{\dot{D}_2}/L_2g_2\}$. For any $e_2(t) \in R/Q_2$, we have $|e_2| > \gamma_{\dot{D}_2}/L_2g_2$. This, together with (39), yields $\dot{V}(e_2) \le -|e_2|(L_2g_2|e_2| - \gamma_{\dot{D}_2}) < 0$. It is noted that $g_2 = 1$. This means that $e_2(t)$ will stay in the domain

$$Q_2 = \left\{e_2 : |e_2| \le \frac{\gamma_{\dot{D}_2}}{L_2}\right\}. \tag{40}$$

Theorem 4. *Provided that the composite DYC controller is constructed as*

$$\begin{aligned} M = I_z\Bigg(&-\left(A_{11} - \frac{B_1}{B_2}A_{21}\right)r - \left(A_{12} - \frac{B_1}{B_2}A_{22}\right)\widehat{\beta} \\ &- K_1\text{sign}(s_2) - K_2s_2 - \widehat{D_2}\Bigg), \end{aligned} \tag{41}$$

where $k_1 > 0$, $k_2 > 0$, and $L_1 > \gamma_{\dot{D}_1}$, s_2 will finite-time converge to zero.

Proof. Putting (41) into (23) yields

$$\begin{aligned} \dot{s}_2 &= -k_1 sign(s_2) - k_2 s_2 + D_2(t) - \widehat{D}_2 \\ &= -k_1 \cdot \text{sign}(s_2) - k_2 s_2 + e_2(t). \end{aligned} \tag{42}$$

From NDOB (37), it is clear that the error $e_2(t)$ is bounded. This means that a constant $\gamma_{e_2} > 0$ can be found such that $|e_2(t)| = |D_2(t) - \widehat{D}_2| \le \gamma_{e_2}$. The remainder of the proof is similar to that in Theorem 2. □

3.4. Torque Distribution Controller. On the basis of the ideal yaw moment obtained by the DYC controller, the main function of the whole control strategy is to assign the expected yaw moment calculated by the DYC controller to four wheels. The torque distributor designed in this paper is based on the vertical load distribution, taking into account the motor output and road surface conditions of the distribution constraints. First of all, the relationship between the longitudinal force of the tire and the torque of the motor is

$$F_{xij} = \frac{T_{ij}}{R}, \tag{43}$$

which leads to

$$\begin{aligned} T_{fl} &= \frac{F_{zfl}}{F_z}\frac{M_z}{-d_f/2\cos\delta_{fd} + a\sin\delta_{fd}}R, \\ T_{fr} &= \frac{F_{zfr}}{F_z}\frac{M_z}{d_f/2\cos\delta_{fd} + a\sin\delta_{fd}}R, \\ T_{rl} &= -\frac{F_{zrl}}{F_z}\frac{M_z}{2d_r}R, \\ T_{fl} &= \frac{F_{zrr}}{F_z}\frac{M_z}{2d_r}R. \end{aligned} \tag{44}$$

Finally, the torques obtained by formula (44) are constrained as follows:

Table 1: Parameters of the vehicle model.

Symbol	Value
m	1429 (Kg)
b	1.569 (m)
d_r	1.565 (m)
I_z	1765 (Kg·m^2)
C_r	87002 (N/rad)
a	1.05 (m)
d_f	1.565 (m)
R	0.35 (m)
C_f	79240 (N/rad)
n	20

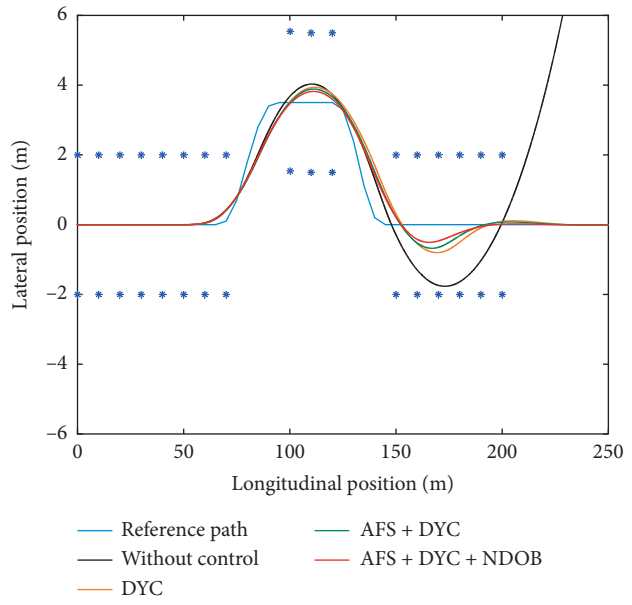

Figure 3: The vehicle trajectory.

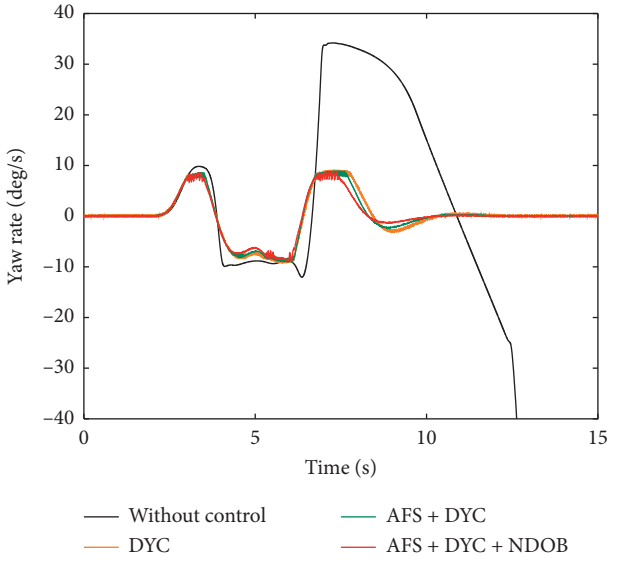

Figure 4: Time history of the yaw rate.

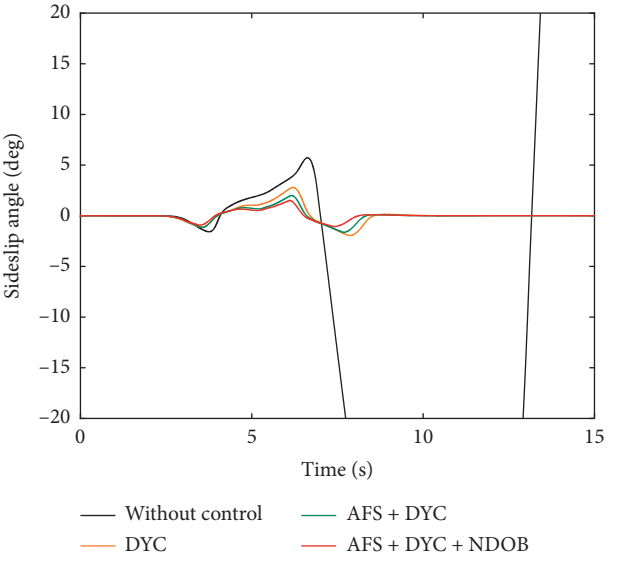

Figure 5: Time history of the sideslip angle.

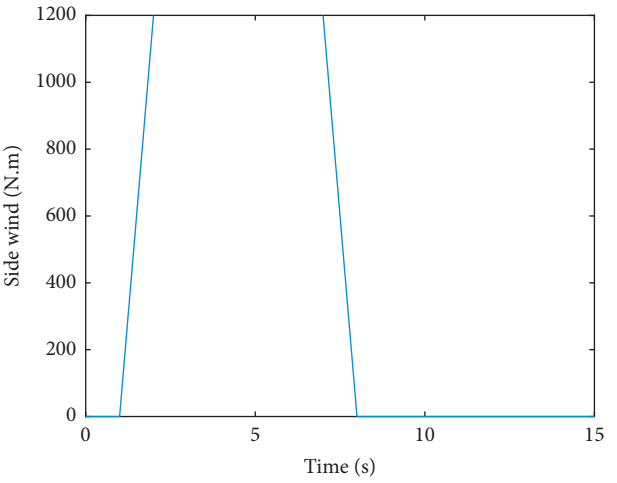

Figure 6: The side wind disturbance input.

$$\left|T_{ij}\right| \le \min\left(\mu R F_{zij}, T_{\max}\right), \tag{45}$$

where F_{zij} is the driving or braking torque, T_{ij} is the vertical load, T_{max} is the maximum motor output torque, μ is the adhesion coefficient of the road, and R represents the effective radius of the tire.

4. Simulation Results

The validity of the AFS and DYC control is shown by using the cosimulation of MATLAB/Simulink and CarSim. The responses are compared with those without any control, with yaw-moment control only, and with the AFS and DYC integrated control. The parameters are given in Table 1.

In the simulation, the initial speed of the vehicle is 80 km/h, and μ is 0.3 in the double lane-changing maneuver, and $\xi = 0.5$.

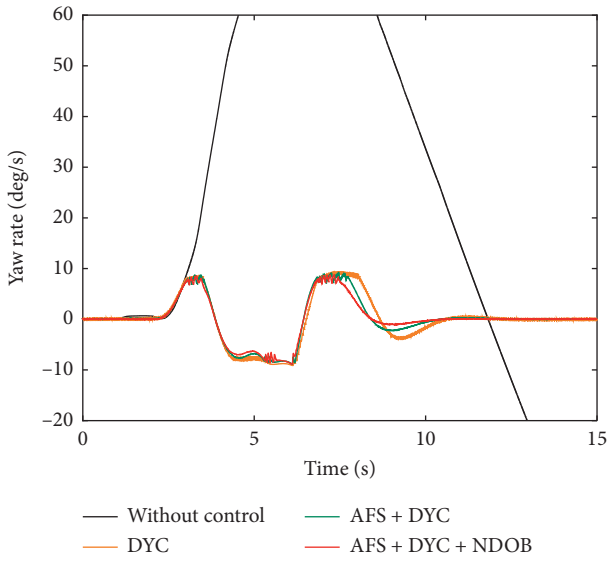

Figure 7: The response curve of the yaw rate.

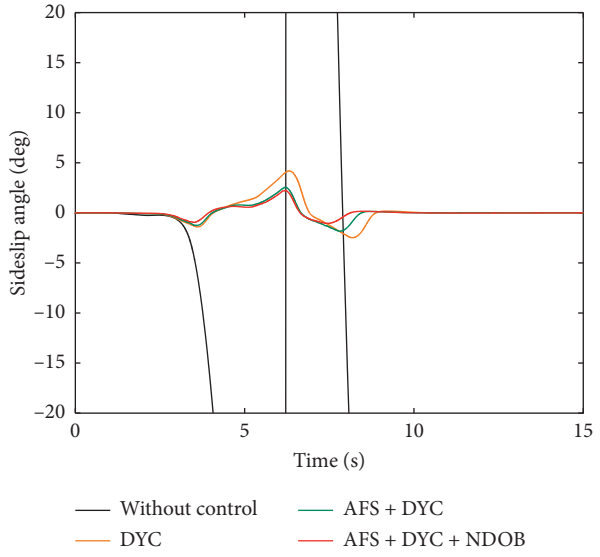

Figure 8: Time history of the sideslip angle.

4.1. Double Lane-Change Maneuver. The simulation results are depicted in Figures 3–5. It can be seen from Figures 4 and 5 that, without any control, the yaw rate and the sideslip angle are larger values deviating from their ideal value, even cannot guarantee the stability of the vehicle. On the contrary, under the other three controllers, the vehicle trajectory can track the expected trajectory, the actual yaw rate can follow the ideal value, and the actual sideslip angle can be controlled in a stable region. Compared with other controllers, the integrated control of AFS and DYC based on the DOB technique can improve the vehicle response, which can also be verified by Figure 3.

4.2. Response to Side Wind Disturbance. The simulation is given under a side wind force, as shown in Figure 6. It can be seen from Figures 7 and 8 that the case without any control

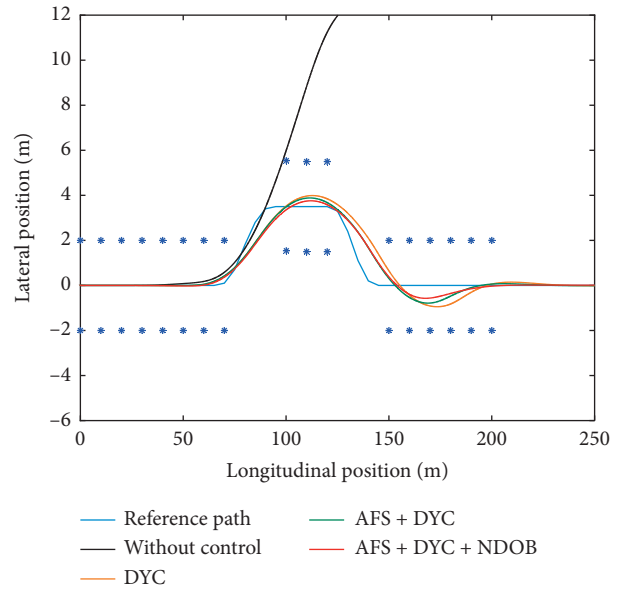

Figure 9: The vehicle trajectory.

fails to keep vehicle's stability, while the case with the yaw-moment control only cannot control well compared with the integrated control. The properties can be clearly seen in Figure 9, which reflects the double lane-change maneuvering under the proposed controllers. At last, it can also be observed from Figure 9 that the integrated control of AFS and DYC based on the DOB technique has better control performance compared with the pure AFS and DYC integrated control.

5. Conclusion

In our study, it has been shown that the AFS and DYC integrated control has better control performance than the DYC control. At the same time, we also confirm that the integrated control of AFS and DYC based on the DOB technique can suppress the large disturbance and have better robustness in comparison with the pure AFS and DYC integrated control [31].

Data Availability

No data were used to support this study.

Conflicts of Interest

The authors declare that there are no conflicts of interest.

Acknowledgments

This work was supported by the Guiding Funds for Industrial Development of Suqian City under grant S201920.

References

[1] A. Zanten, R. Erhardt, and G. Pfaff, "The vehicle dynamics control system of bosch," 1995. SAE Technical Paper, Article ID 950759.

[2] D. Zhang, Y.-P. Shen, S.-Q. Zhou, X.-W. Dong, and L. Yu, "Distributed secure platoon control of connected vehicles

subject to DoS attack: theory and application," *IEEE Transactions on Systems, Man, and Cybernetics: Systems*, p. 1, 2020.

[3] Z. Xu, H. Ni, H. Reza Karimi, and D. Zhang, "A Markovian jump system approach to consensus of heterogeneous multiagent systems with partially unknown and uncertain attack strategies," *International Journal of Robust and Nonlinear Control*, vol. 30, no. 7, pp. 3039–3053, 2020.

[4] C. Doniselli, G. Mastinu, and R. Cal, "Traction control for front-wheel-drive vehicles," *Vehicle System Dynamics*, vol. 23, no. sup1, pp. 87–104, 1994.

[5] D. V. T. Truong and W. Tomaske, "Active front steering system using adaptive sliding mode control," in *Proceedings of the Control and Decision Conference*, vol. 253-258, IEEE, Firenze, Italy, 2013.

[6] Y. Shibahata, K. Shimada, and T. Tomari, "Improvement of vehicle maneuverability by direct yaw moment control," *Vehicle System Dynamics*, vol. 22, no. 5-6, pp. 465–481, 1993.

[7] M. Nagai, M. Shino, and F. Gao, "Study on integrated control of active front steer angle and direct yaw moment," *Jsae Review*, vol. 23, no. 3, pp. 309–315, 2002.

[8] W. Yao, W. U. Maosheng, and Y. U. Datai, "A method to improve braking stability by the integrated control of yaw-moment control and active front steering," *Journal of University of Science Technology Beijing*, vol. 4, no. 4, 2005.

[9] X. Gao and Z. A. Yu, "Coordinated control of AFS and ESP based on vehicle state identification," *International Journal of Vehicle Mechanics and Mobility*, vol. 47, 2007.

[10] X. N. Wen and W. H. Chai, *AFS/DYC Integrated Control Strategy Research Based on Fuzzy Logic*, Changchun University, Changchun, China, 2009.

[11] G. Li, C. F. Zong, and L. Y. Jiang, "Active front steering and direct yaw moment integrated control algorithm," *Vehicle System Dynamics*, vol. 48, 2011.

[12] L. Liu, S. Ding, and X. Yu, "Second-order sliding mode control design subject to an asymmetric output constraint," *IEEE Transactions on Circuits and Systems II: Express Briefs*, vol. 112, p. 1, 2020.

[13] Q. Hou, S. Ding, and X. Yu, "Composite super-twisting sliding mode control design for PMSM speed regulation problem based on a novel disturbance observer," *IEEE Transactions on Energy Conversion*, p. 1, 2020.

[14] Q. Hou and S. Ding, "GPIO based super-twisting sliding mode control for PMSM," *IEEE Transactions on Circuits and Systems II: Express Briefs*, p. 1, 2020.

[15] L. Liu, W. X. Zheng, and S. Ding, "An adaptive SOSM controller design by using a sliding-mode-based filter and its application to Buck converter," *IEEE Transactions on Circuits and Systems I: Regular Papers*, vol. 67, no. 7, pp. 2409–2418, 2020.

[16] S. Ding, J. H. Park, and C. C. Chen, "Second-order sliding mode controller design with output contraint," *Automatica*, vol. 112, Article ID 108704, 2020.

[17] Q. Meng, C. Qian, and R. Liu, "Dual-rate sampled-data stabilization for active suspension system of electric vehicle," *International Journal of Robust and Nonlinear Control*, vol. 28, no. 5, pp. 1610–1623, 2018.

[18] S. Ding, W. Chen, K. Mei, and D. Murray-Smith, "Disturbance observer design for nonlinear systems represented by input-output models," *IEEE Transactions on Industrial Electronics*, vol. 67, no. 2, pp. 1222–1232, 2019.

[19] H. Du, C. Jiang, G. Wen, W. Zhu, and Y. Cheng, "Current sharing control for parallel DC-DC Buck converters based on finite-time control technique," *IEEE Transactions on Industrial Informatics*, vol. 15, no. 4, pp. 2186–2198, 2019.

[20] Q. Meng, T. Zhao, C. Qian, Z. Sun, and P. Ge, "Integrated stability control of AFS and DYC for electric vehicle based on non-smooth control," *International Journal of Systems Science*, vol. 49, no. 7, pp. 1518–1528, 2019.

[21] A. Mehmet and J. Kalkkuhl, "Lateral dynamics emulation via a four-wheel steering vehicle," *Vehicle System Dynamics*, vol. 46, no. 9, pp. 803–829, 2008.

[22] Q. Zhou, F. Wang, and L. Li, "Robust sliding mode control of 4WS vehicles for automatic path tracking," in *Proceedings of Intelligent Vehicles Symposium*, pp. 819–826, IEEE, Vegas, NV, USA, 2005.

[23] S. Ding, L. Liu, and W. X. Zheng, "Sliding mode direct yaw-moment control design for in-wheel electric vehicles," *IEEE Transactions on Industrial Electronics*, vol. 64, no. 8, pp. 6752–6762, 2017.

[24] W. H. Chen, "Nonlinear disturbance observer-enhanced dynamic inversion control of missiles," *Journal of Guidance Control Dynamics*, vol. 26, no. 1, pp. 161–166, 2015.

[25] Y. Ji, H. Guo, and H. Chen, "Integrated control of active front steering and direct yaw moment based on model predictive control," in *Proceedings of Control and Decision Conference*, IEEE, Nanchang, China, 2014.

[26] S. Zhang, S. Ding, and H. Jiang, "Direct yaw-moment control of in-wheel electric vehicle by sliding mode technique," in *Proceedings of Conference on Industrial Technology*, IEEE, Nanchang, China, 2016.

[27] U. Kiencke and L. Nielsen, *Automotive Control Systems*, Springer, Berlin, Germany, 2005.

[28] Z.-Y. Sun, Y. Shao, and C.-C. Chen, "Fast finite-time stability and its application in adaptive control of high-order nonlinear system," *Automatica*, vol. 106, no. 5, pp. 339–348, 2019.

[29] Z. Sun, Y. Shao, C. Chen, and Q. Meng, "Global output-feedback stabilization for stochastic nonlinear systems: a double-domination approach," *International Journal of Robust and Nonlinear Control*, vol. 28, no. 5, pp. 4635–4646, 2018.

[30] C. Chen and Z. Sun, "A unified approach to finite-time stabilization of high-order nonlinear systems with an asymmetric output constraint," *Automatica*, vol. 111, Article ID 108581, 2020.

Hindawi
Mathematical Problems in Engineering
Volume 2020, Article ID 8343940, 11 pages
https://doi.org/10.1155/2020/8343940

Research Article

Disturbance Observer-Based Complementary Fractional-Order Sliding Mode Control for PMSM Drive System

Yong-Hong Lan, Li-Tao Zheng, and Zhao-Hong Wang

School of Automation and Electronic Information, Xiangtan University, Xiangtan, Hunan 411105, China

Correspondence should be addressed to Yong-Hong Lan; 961501563@qq.com

Received 19 August 2020; Revised 21 October 2020; Accepted 23 November 2020; Published 3 December 2020

Academic Editor: Chih-Chiang Chen

In this paper, a disturbance observer-based complementary fractional-order sliding mode control (CFOSMC) scheme is proposed for the permanent magnet synchronous motor (PMSM) drive system. First, to reconstruct the load disturbance and parameter variations, a nonlinear disturbance observer is designed. Next, a disturbance observer-based fractional-order sliding mode with a saturation function control law is designed to reduce the chattering problem in the existing fractional-order sliding mode control (FOSMC) method. Furthermore, to reduce the thickness of the boundary layer, a CFOSMC scheme is designed. By using the fractional-order Lyapunov stability theorem, the existence condition and the chattering problem are analyzed. Compared with the existing FOSMC, the obtained CFOSMC law does not contain any high-order derivatives of tracking error, which is easier to implement. Finally, the numerical simulations and experimental results are provided to show the superiority of the proposed method. To improve the performance of the permanent magnet synchronous motor (PMSM) drive system in terms of tracking rapidity, accuracy, and robustness, a complementary fractional-order sliding mode control (CFOSMC) scheme with disturbance observer is proposed in this paper.

1. Introduction

Permanent magnet synchronous motor (PMSM) has many applications in industries due to its excellent features such as superpower density, high torque to current ratio, fast response, and low noise [1, 2]. However, the PMSM is a typical multivariable coupled high nonlinear system, and its performance is sensitive to external load disturbances and parameter uncertainties. Over the last decades, various design methods have been developed, such as robust control [3], predictive control [4], adaptive control [5], and neural network control [6].

Recently, to improve the control performances in PMSM diver systems, much attention has been given to the disturbance observer-based (DOB) control method. In [7], a DOB state feedback controller was designed for the PMSM system. On the basis of this paper, a sensorless control method for PMSM drive was developed in [8]. In [9], a generalized predictive current control method combined with sliding mode disturbance compensation was proposed to satisfy the requirement of fast response and strong robustness. By combining the adaptive sliding mode control with sliding mode disturbance observer, a hybrid control strategy was proposed in [10]. In [11], a new estimation method of sensor faults and unknown disturbance in current measurement circuits for the PMSM drive system was presented. However, the above-proposed DOB control schemes only focus on the load torque disturbance but lack the estimation of parameter uncertainties.

To counteract the disturbances and uncertainties, sliding mode control (SMC) is a powerful nonlinear control technique, which has been widely used for speed and position control of the PMSM system [12]. To estimate the immeasurable mechanical parameters of PMSM, an intelligent second-order SMC using a wavelet fuzzy neural network estimator was proposed in [13]. Considering the time-varying characteristic and the high-bandwidth property of the uncertainties and disturbances in a PMSM drive

system, a disturbance observer-based SMC scheme was introduced in [14]. To estimate the online stator resistance, a new sliding mode observer for sensorless SMC was presented in [15]. To further improve the performance of the SMC, a robust SMC scheme based on a rapid nonlinear tracking differentiator was proposed in [16]. The second-order SMC design problem was discussed in [17], in which a novel saturation function was used. Based on the conventional SMC, adding a generalized error sliding surface, the complementary sliding mode control (CSMC) was proposed for the fault-tolerant control of a six-phase PMSM drive system in [18]. The complementary sliding mode control method based on Elman neural network was proposed in [19], which can not only reduce the system state to the sliding surface time but also guarantee the system tracking accuracy. Considering that the control system in a PMSM has uncertainties and disturbances, in [20], an adaptive switching gain was proposed. Comparisons of experimental results show that the proposed method has a faster adjustment process than SMC. In [21], a disturbance observer-based CSMC design method was proposed for the PMSM control system of the mine traction electric locomotive.

As we all know, one obvious disadvantage of the SMC method is the chattering phenomenon caused by discontinuous control law and frequent switching action near the sliding surface. Besides, the upper bound of lumped disturbances is not easy to be determined, which could worsen the chattering phenomenon of SMC strategy. Recently, to overcome these drawbacks, some fractional-order sliding mode control (FOSMC) schemes have been widely adopted to weaken the chattering phenomenon and deal with external disturbances. An FOSMC scheme based on parameters auto-tuning for the velocity control of PMSM was proposed in [22]. A robust FOSMC was proposed for the position control of PMSM in [23]. By selecting a proper fractional-order and designing a fractional-order sliding surface, the proposed FOSMC is distinctly more excellent than that of the conventional SMC. To investigate the position regulation problem of PMSM subject to parameter uncertainties and external disturbances, an FOSMC was proposed and the finite-time stability of the closed-loop system was obtained in [24]. Based on the fractional stability theory, a sliding mode control scheme for synchronization of fractional PMSM was developed in [25]. A novel FOSMC for a class of integer-order systems with mismatched disturbances was proposed in [26]. In [27], a disturbance observer-based composite supertwisting sliding mode control was designed for the PMSM speed regulation problem. To improve the convergence rate over the existing sliding mode control method for the trajectory tracking control, an adaptive fast nonsingular integral terminal SMC method was proposed in [28, 29].

Note that the above SMC-based control methods for the PMSM driver system can deal with mismatched disturbance and have better control performance with faster response speed, lower overshoot, and less chattering effect than the traditional control strategy. However, the high-order derivative of the tracking error (or the reference signal) was usually used in the sliding model controller [19, 20, 22]. From a practical point of view, it is difficult to implement. On the other hand, there is still room for improvement when it comes to the chattering phenomenon in classic FOSMC. This observation motivates our current study. In this paper, we mainly investigate a modified FOSMC scheme with a load disturbance observer for the speed control of PMSM. The main contributions are as follows: (1) to estimate the load disturbance and parameter uncertainties, a nonlinear disturbance observer is constructed and the asymptotic stability condition for observation error is also obtained; (2) to reduce the chattering phenomenon in the existing FOSMC method, a disturbance observer-based fractional-order sliding mode with saturation function control law is designed; and (3) to reduce the thickness of boundary layer, a CFOSMC law with disturbance observer is proposed. The tracking performance and robustness of the proposed method are also analyzed and compared with the conventional FOSMC scheme.

The rest of this paper is organized as follows: in Section 2, the mathematic model of PMSM and problem formulation are presented. The nonlinear disturbance observer design and stability analysis are derived in Section 3. In Section 4, the conventional FOSMC for the PMSM drive system is improved and the disturbance observer-based CFOSMC method is derived. The effectiveness of the proposed algorithm is illustrated in Section 5 through numerical simulations and experiment examples. Finally, some conclusions are drawn in Section 6.

2. Mathematical Model of PMSM and Problem Formulation

The mathematics model of a PMSM can be described in the rotor rotating reference frame as follows [10, 22, 23]:

$$\begin{cases} u_q^* = R_s i_q^* + \dot{\lambda}_q + \omega_f \lambda_d, \\ u_d^* = R_s i_d^* + \dot{\lambda}_d q + \omega_f \lambda_q, \\ \lambda_q = L_q i_q^*, \\ \lambda_d = L_d i_d^* + L_m I_{\mathrm{df}}, \\ \omega_f = n_p \omega_r^*, \end{cases} \tag{1}$$

where u_d^*, u_q^* are the d,q-axis stator voltages; i_d^*, i_q^* are the d,q-axis stator currents; λ_d, λ_q are the d,q-axis stator flux linkages; and L_d, L_q are the d,q-axis stator inductances. While ω_f and ω_r^* are the inverter frequency and rotor speed, respectively, L_m is the d-axis mutual inductance; I_{df} is the equivalent d-axis magnetizing current; n_p is the number of pole pairs; and R_s is the stator resistance.

The electric torque is stated as

$$T_e = 3n_p \frac{\left[L_m I_{\mathrm{df}} i_q^* + \left(L_d - L_q\right) i_q^* i_d^*\right]}{2}. \tag{2}$$

Motor dynamics is presented as

$$T_e = J\dot{\omega}_r + B_m \omega_r + T_l, \tag{3}$$

where T_l is the load torque, B_m is the viscous friction coefficient, and J is the moment of inertia.

By using the field-oriented mechanism with $i_d = 0$ [10, 22], we can simplify the electric torque as

$$T_e = k_p^* i_q^* = \frac{3n_p L_m I_{\mathrm{df}}}{2} i_q^*. \tag{4}$$

Substituting (3) into (4), one can obtain the state equation of servo drive:

$$\begin{cases} \dot{\omega}_r = -a\omega_r + bi_q - c, \\ a = \dfrac{B_m}{J}, b = \dfrac{k_p^*}{J}, c = \dfrac{T_l}{J}. \end{cases} \tag{5}$$

Considering the uncertainties and time-invariant parameters, we can rewrite (5) as

$$\dot{\omega}_r = -(a + \Delta a)\omega_r + (b + \Delta b)i_q - (c + \Delta c), \tag{6}$$

where $\Delta a, \Delta b, \Delta c$ are the time-invariant parameters.

The tracking error $e(t)$, in terms of the desired reference speed $\omega_r^*(t)$ and the measured actual output speed $\omega_r(t)$, is defined as

$$e(t) = \omega_r^*(t) - \omega_r(t). \tag{7}$$

The time derivative of $e(t)$ is

$$\begin{cases} \dot{e}(t) = -ae(t) - bi_q(t) + \phi(t) + d, \\ \phi(t) = a\omega_r^*(t) + c + \dot{\omega}_r^*(t), \\ d = \Delta a\omega_r(t) - \Delta bi_q(t) + \Delta c, \end{cases} \tag{8}$$

where d is time-variant uncertainties such as mechanical parameter variations, friction force, load disturbances, speed distortion, and current harmonics. It is assumed that

$$|d| \le \Lambda(>0), \lim_{t\longrightarrow\infty} \dot{d} = d^*, \tag{9}$$

where d^* is a constant.

In this paper, the control objective is to find a suitable FOSMC input $i_q^*(t)$ such that the output speed $\omega_r(t)$ can track the desired reference speed $\omega_r^*(t)$ asymptotically in the presence of any arbitrary initial conditions and uncertainties.

3. Disturbance Observer Design

To estimate time-variant lumped uncertainties and load torque disturbance, we use the following nonlinear disturbance observer [30]:

$$\begin{cases} \dot{p}(t) = -l\widehat{d} + l[\,ae(t) + bi_q(t) - \phi(t)\,], \\ \widehat{d} = p(t) + le(t), \end{cases} \tag{10}$$

where $\widehat{d}$ is the estimation of d and $l > 0$ is the observer gain.

Estimation error of the disturbance observer is defined as

$$\widetilde{d} = \widehat{d} - d, \tag{11}$$

and error dynamics of disturbance observer is governed by

$$\dot{\widetilde{d}} = \dot{\widehat{d}} - \dot{d}. \tag{12}$$

It can be derived from (10)–(12) that

$$\dot{\widetilde{d}} = -l\widetilde{d} - \dot{d}. \tag{13}$$

Since $l > 0$ and $\lim_{t\longrightarrow\infty}\dot{d} = d^*$, we have $\lim_{t\longrightarrow\infty}\widetilde{d} = -(d^*/l)$.

Now, we give the following result.

Lemma 1. *For nonlinear system (8), suppose that the disturbance observer is formulated as (10); then, the disturbance estimation error $\widetilde{d}$ is bounded.*

Remark 1. It follows from Lemma 1 that the observer gain l can change the bound of the disturbance estimation error. Clearly, it should be selected as large enough.

4. Disturbance Observer-Based CFOSMC Scheme Design

Considering that the disturbance observer (10) can estimate the load torque disturbance accurately, we will replace d with $\widehat{d}$ in the following synthesis.

4.1. Traditional FOSMC. Fractional calculus is a generalization of integer-order integration and differentiation to noninteger-order ones. Let $\mathscr{D}^\alpha$ denote the fractional-order derivative, which is defined as in Definition 1.

Definition 1 (see [31]). The Caputo derivative is defined by

$$\mathscr{D}^\alpha f(t) = \frac{1}{\Gamma(n-\alpha)} \int_{t_0}^{t} (t-\tau)^{-\alpha+n-1} f^{(n)}(\tau)\mathrm{d}\tau, \tag{14}$$

where n is the first integer which is not less than α, that is, $\alpha \in [n-1, n)$. $\Gamma(\cdot)$ is the well-known Gamma function, which is defined by $\Gamma(z) = \int_0^\infty e^{-z}t^{z-1}\mathrm{d}t$.

Definition 2 (see [31]). The definition of the fractional integral is described by

$$\mathscr{D}^{-\alpha} f(t) = \frac{1}{\Gamma(\alpha)} \int_{t_0}^{t} (t-\tau)^{\alpha-1} f(\tau)\mathrm{d}\tau, \quad \alpha > 0. \tag{15}$$

To proceed with the discussion, the following lemmas will be used.

Lemma 2 (see [32]). *Autonomous system is as follows:*

$$\mathscr{D}^\alpha x(t) = Ax(t), \tag{16}$$

with $x(t_0) = x_0$ and $0 < \alpha < 1$, is asymptotically stable if and only if $|\arg(spec(A))| > (\alpha\pi/2)$, where spec(A) is the spectrum (set of all eigenvalues) of A. Also, the state vector $x(t)$ decays towards 0 and meets the condition $\|x(t)\| < Mt^{-\alpha}$, $t > 0$, $M > 0$.

Lemma 3 (see [33]). *Let $x(t) \in \mathbb{R}^n$ be a vector of a differentiable function. Then, for any time instant $t \ge t_0$, the following relationship holds:*

$$\frac{1}{2}\mathscr{D}^{\alpha}\left(x^{T}(t)Px(t)\right) \leq x^{T}(t)P\mathscr{D}^{\alpha}x(t), \quad \forall \alpha \in (0,1], \tag{17}$$

where $P \in \mathbb{R}^{n\times n}$ is a positive definite matrix.

Lemma 4 (see [34]). *Let $x(t) = 0$ be an equilibrium point for the nonautonomous fractional-order system $\mathscr{D}^{\alpha}x(t) = f(x(t), t)$, where $f(x(t), t)$ is locally Lipschitz in $x(t)$. Assume that there exists a Lyapunov candidate $V(x(t), t)$ satisfying*

$$\begin{aligned} \alpha_1 \|x(t)\|_2^a \leq V(x(t), t) \leq \alpha_2 \|x(t)\|_2^{ab}, \\ \mathscr{D}^{\beta}V(x(t), t) \leq -\alpha_3 \|x(t)\|_2^{ab}, \end{aligned} \tag{18}$$

where $\alpha_1, \alpha_2, \alpha_3, a$, and b are positive constants and $\beta \in (0, 1)$. Then, the equilibrium point is Mittag–Leffler stable.

Remark 2 Mittag–Leffler stability implies asymptotic stability [34].

Clearly, the fractional-order operator has more degrees of freedom than that with integer order. It is likely that a better performance can be obtained with the proper choice of order [22, 23].

As presented in [22, 23], a traditional fractional-order sliding surface S can be chosen as

$$S = \lambda e(t) + \mathscr{D}^{\alpha}e(t), \tag{19}$$

where $\lambda > 0$ and $0 < \alpha < 1$.

Taking the time derivative on both sides of (19) and using $\widehat{d}$ to estimate d, we have

$$\begin{aligned} \dot{S} &= \lambda \dot{e}(t) + \mathscr{D}^{\alpha+1}e(t) \\ &= \lambda\left(-ae(t) - bi_q(t) + \phi(t) + \widehat{d}\right) + \mathscr{D}^{\alpha+1}e(t). \end{aligned} \tag{20}$$

The equivalent control law can be selected as

$$i_q = u_{\text{eq}} = \frac{1}{\lambda b}\left(-a\lambda e(t) + \lambda\phi(t) + \lambda\widehat{d} + \mathscr{D}^{\alpha+1}e(t)\right). \tag{21}$$

As usual, we adopt the following approach law [22]:

$$\dot{S} = \varepsilon S + \rho \operatorname{sgn}(S), \tag{22}$$

where $\varepsilon > 0, \rho > 0$, and $\operatorname{sgn}(\cdot)$ denotes the sign function, which is defined as

$$\operatorname{sgn}(S) = \begin{cases} 1, & S \geq 0, \\ 0, & S = 0, \\ -1, & S < 0. \end{cases} \tag{23}$$

From (21) and (22), the final controller can be designed as

$$\begin{aligned} i_q &= u_{\text{eq}} + u_v \\ &= u_{\text{eq}} + \varepsilon S + \rho \operatorname{sgn}(S) \\ &= \frac{1}{\lambda b}\left(-ae(t) + \phi(t) + \widehat{d} + \mathscr{D}^{\alpha+1}e\right) \\ &\quad + \varepsilon S + \rho \operatorname{sgn}(S). \end{aligned} \tag{24}$$

When the sliding mode occurs, system (19) can be represented as

$$\mathscr{D}^{\alpha}e(t) = -\lambda e(t). \tag{25}$$

Thus, by Lemma 2, system (25) is asymptotic stable.

Remark 3. As pointed out in Lemma 2, the state $e(t)$ of the fractional-order system (25) decays towards 0 like $t^{-\alpha}$. But, in the case of the integer-order system, it decays towards 0 like e^{-t}. It means that the energy transfer is slower with fractional-order sliding surface than that with integer-order one [22, 23]. Therefore, the fractional-order sliding surface is smoother compared with the integer-order one. As a result, the chattering can be better attenuated with a fractional-order controller.

Remark 4. It is worth pointing out that if $d = 0$, then the fractional-order sliding mode controller (24) is reduced to

$$\begin{aligned} i_q &= u_{\text{eq}} + u_v \\ &= u_{\text{eq}} + \varepsilon S + \rho \operatorname{sgn}(S) \\ &= \frac{1}{\lambda b}\left(-ae(t) + \phi(t) + \mathscr{D}^{\alpha+1}e\right) \\ &\quad + \varepsilon S + \rho \operatorname{sgn}(S), \end{aligned} \tag{26}$$

which is the same as the one proposed in [22].

It can be seen that the $\operatorname{sgn}(\cdot)$ function is involved in (26). As pointed out in [23], the chattering phenomenon will be caused. In the following, a saturation function $\operatorname{sat}(\cdot)$ is adopted to further reduce the chattering problem, which is described as follows:

$$\operatorname{sat}(S) = \begin{cases} 1, & S \geq \Phi, \\ \dfrac{S}{\Phi}, & -\Phi < S < \Phi, \\ -1, & S \leq -\Phi, \end{cases} \tag{27}$$

where $\Phi > 0$ denotes the thickness of the boundary layer. Clearly, when the saturation function is used, the final controller (24) can be modified as

$$\begin{aligned} i_q &= \frac{1}{\lambda b}\left(-ae(t) + \phi(t) + \widehat{d} + \mathscr{D}^{\alpha+1}e(t)\right) \\ &\quad + \varepsilon S + \rho \operatorname{sat}(S). \end{aligned} \tag{28}$$

The Lyapunov function is defined as

$$V(t) = \frac{1}{2}S^2. \tag{29}$$

Calculating the derivation of (29) and invoking (20) and (28), it yields

$$\begin{aligned}\dot{V}(t) &= S\dot{S}\\ &= S\left(\lambda\dot{e}(t) + \mathscr{D}^{\alpha+1}e(t)\right)\\ &= S\lambda\left(-ae(t) - bi_q(t) + \phi(t) + \widehat{d}\right) + \mathscr{D}^{\alpha+1}e\\ &= -\varepsilon S^2 - S\,\mathrm{sat}\left(\frac{S}{\Phi}\right) \le 0.\end{aligned} \tag{30}$$

According to the Lyapunov stability theorem, the reaching condition of the sliding mode controller is satisfied, which indicates that the system will converge to the switching manifold asymptotically.

Remark 5. Note that the high-order derivative $\mathscr{D}^{\alpha+1}e$ is used in fractional-order sliding model controller (24) and (28). From a practical point of view, it is difficult to implement.

Remark 6. From (19) and (27), it can be seen that the sliding mode surface S will finally maintain on the steady state of $|S| \le \Phi$. That is, the closed-loop system is in a steady state with $|e(t)| \le (\Phi/\lambda)$. Though the large Φ can reduce the chattering mostly, it also can increase the ultimate bound of the tracking error $e(t)$. To trade off the chattering and control performance, conservative λ and Φ are always selected by trial and error.

4.2. Disturbance Observer-Based CFOSMC. As stated in Remark 6, there exists a boundary layer Φ of S in a steady state. In this state, the boundary layer is also the tracking error boundary layer for a given λ. In this section, to further reduce the thickness of the boundary layer, a complementary fractional-order sliding mode controller is designed.

Borrowed from [18–20], the complementary fractional-order sliding mode surface is defined as

$$\overline{S} = S_g + S_c, \tag{31}$$

where

$$S_g = \mathscr{D}^{\alpha}e(t) + 2\lambda e(t) + \lambda^2\mathscr{D}^{-\alpha}e(t), \quad \lambda > 0, \tag{32}$$

$$S_c = \mathscr{D}^{\alpha}e(t) - \lambda^2\mathscr{D}^{-\alpha}e(t), \quad \lambda > 0. \tag{33}$$

Taking the α order time derivation on both sides of (32) and (33), respectively, we have

$$\mathscr{D}^{\alpha}S_g = \mathscr{D}^{2\alpha}e(t) + 2\lambda\mathscr{D}^{\alpha}e(t) + \lambda^2 e(t), \tag{34}$$

$$\mathscr{D}^{\alpha}S_c = \mathscr{D}^{2\alpha}e(t) - \lambda^2 e(t). \tag{35}$$

From (31) to (35), we can obtain

$$\overline{S} = S_g + S_c = 2\left(\mathscr{D}^{\alpha}e(t) + \lambda e(t)\right), \tag{36}$$

$$\mathscr{D}^{\alpha}S_g - \mathscr{D}^{\alpha}S_c = 2\lambda\left(\mathscr{D}^{\alpha}e(t) + \lambda e(t)\right) = \lambda\overline{S}. \tag{37}$$

The Lyapunov function candidate is chosen as

$$V_c(t) = \frac{1}{2}\left(S_g^2 + S_c^2\right). \tag{38}$$

Taking the α order derivative of (38) and using Lemma 3 as well as (32) to (37), we have

$$\begin{aligned}\mathscr{D}^{\alpha}V_c(t) &\le S_g\mathscr{D}^{\alpha}S_g + S_c\mathscr{D}^{\alpha}S_c\\ &\le S_g\mathscr{D}^{\alpha}S_g + S_c\left(\mathscr{D}^{\alpha}S_g - \lambda S_c\right)\\ &= \left(S_g + S_c\right)\left(\mathscr{D}^{\alpha}S_g - \lambda S_c\right)\\ &= \overline{S}\left(\mathscr{D}^{2\alpha}e(t) + 2\lambda\mathscr{D}^{\alpha}e(t) + \lambda^2 e(t) - \lambda S_c\right)\\ &= \overline{S}\left(\mathscr{D}^{2\alpha-1}\dot{e}(t) + 2\lambda\mathscr{D}^{\alpha}e(t) + \lambda^2 e(t) - \lambda S_c\right)\\ &= \overline{S}\left[\mathscr{D}^{2\alpha-1}\left(-ae(t) - bi_q(t) + \phi(t) + \widehat{d}(t)\right)\right.\\ &\quad \left. + 2\lambda\mathscr{D}^{\alpha}e(t) + \lambda^2 e(t) - \lambda S_c\right].\end{aligned} \tag{39}$$

Therefore, if the complementary fractional-order sliding mode controller is designed as

$$i_q = i_{\mathrm{eq}} + i_v, \tag{40}$$

where

$$\begin{aligned}i_{\mathrm{eq}} = \frac{1}{b}\left[\left(-ae(t) + \phi(t) + \widehat{d}(t)\right) + 2\lambda\mathscr{D}^{1-\alpha}e(t)\right.\\ \left. + \lambda^2\mathscr{D}^{1-2\alpha}e(t) - \lambda\mathscr{D}^{1-2\alpha}S_c\right],\end{aligned} \tag{41}$$

$$i_v = \frac{\rho}{b}\mathscr{D}^{1-2\alpha}\mathrm{sat}\left(\overline{S}\right), \quad \rho > 0, \tag{42}$$

then

$$\mathscr{D}^{\alpha}V_c(t) \le -\rho\overline{S}\,\mathrm{sat}\left(\overline{S}\right) \le 0, \tag{43}$$

which means that $\overline{S}$ will approach zero in a finite-time duration and the system is globally stable.

Remark 7. Note that the CFOSMC scheme (41) can be rewritten as

$$\begin{aligned}i_{\mathrm{eq}} = \frac{1}{b}\left[\left(-ae(t) + \phi(t) + \widehat{d}(t)\right) + 2\lambda\mathscr{D}^{1-\alpha}e(t)\right.\\ \left. + \lambda^2\mathscr{D}^{1-2\alpha}e(t) - \lambda\left(\mathscr{D}^{1-\alpha}e(t) - \lambda^2\mathscr{D}^{1-3\alpha}e(t)\right)\right].\end{aligned} \tag{44}$$

Since $0 < \alpha < 1$, the highest order derivative of $e(t)$ in controller (44) is less than 1, which is easier to implement in practice than FOSMC (24) and (28).

Remark 8. When $(1/3) < \alpha < 1$, the fractional-order differentiation of $e(t)$ is contained in controller (44). It can be viewed as a low-pass filter and reduce the amplitude of high-frequency fluctuations of $e(t)$ [23]. When $\alpha = (1/2)$, especially, controller (44) is a fractional-order $PI^{(1/2)}D^{(1/2)}$ controller. As we all know, fractional-order PID is a trade-off between higher precision (provided by a higher order of integrator) and stability (provided by a higher order of

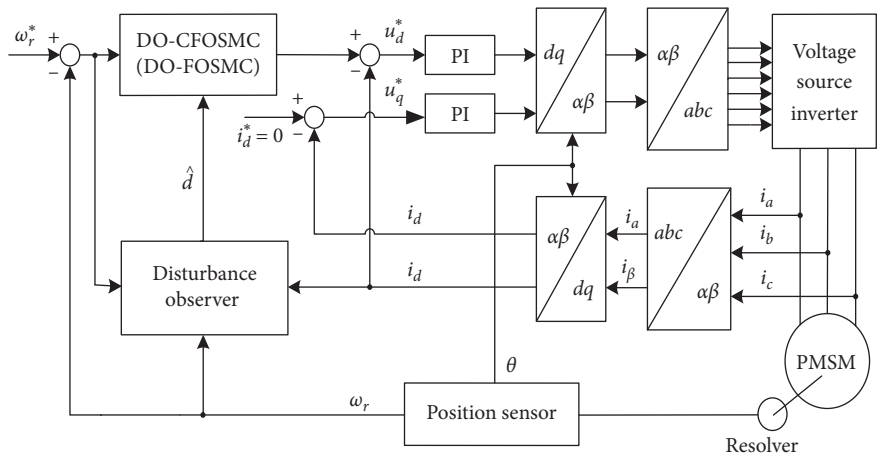

Figure 1: Block diagram of the PMSM position control system.

differentiator). Hence, CFOSMC (41) is more smoother than the conventional FOSMC (24) and (28). On the other hand, there are several parameters in the fractional-order sliding mode controller (42). As we all know, one of the difficulties in SMC-based controller design is the determination of the controller parameters. In this paper, we obtained them by trial and error. In fact, even with the effort and knowledge of the control designer, it can not guarantee that the set of parameters is optimal.

Remark 9. When the system is in a steady state, the sliding surface function $\overline{S}$ will finally maintain on the state of $|\overline{S}| \leq \Phi$. From (27) and (36), we can see that the closed-loop system is in a steady state with $|e(t)| \leq (\Phi/2\lambda)$. Compared with disturbance observer-based FOSMC with saturation function, CFOSMC (41) can eliminate the chattering problem further.

5. Simulations and Experiments

In this section, the numerical example and experimental results are presented to demonstrate the validity of the proposed method.

5.1. Numerical Simulation Results. The configuration of the overall simulation control system is shown in Figure 1, in which DO-FOSMC means the disturbance based FOSMC with saturation function (controller (28)), and DO-CFOSMC is the proposed disturbance observer-based CFOSMC (controller (40)). The performances of the proposed DO-CFOSMC are analyzed and compared with that of DO-FOSMC.

The parameters of the PMSM system are set as follows: rated power $P = 10$KW, pole pairs is $p = 3$, friction factor is $B = 0.001$ (N · m · s/rad), stator inductance is $L = 0.0153$ H, rotor moment of inertia is $J = 0.0021\,\text{kg} \cdot \text{m}^2$, permanent magnet flux is $\phi_f = 0.82$ wb, and stator resistance is $R = 0.56\Omega$. The parameters of DO-CFOSMC and DO-FOSMC are selected as $l = 5, \Phi = 0.01, \lambda = 8000, \rho = 3000$. From the simulation results, we found that the best selection range for the fractional-order of the proposed FOSMC method is $\alpha \in [0.50 \quad 0.60]$. In the following, we set $\alpha = 0.50$.

The initial rotation speed of the motor is given as $r_{f1} = 1200$ r/min. When $t = 0.6$ s, the rotation speed is set to $r_{f2} = 1000$ r/min. The initial load torque of the motor is $0\,\text{N} \cdot \text{m}$ while $t = 0.8$ s, and the load torque is $10\,\text{N} \cdot \text{m}$, which can be viewed as an external disturbance.

The numerical simulation results are shown in Figures 2–4. Figure 2(a) indicates the actual speed responses of the proposed DO-CFOSMC and conventional DO-FOSMC in the presence of the above load disturbance. Figure 2(b) shows the rotation speed response when the PMSM motor just started. In the time $t = 0.6$ s, the reference rotation speed has a sudden change. The rotation speed response is depicted in Figure 2(c). Figure 2(d) shows the rotation speed response at $t = 0.8$ s, in this time, the external disturbance load is added suddenly. From Figure 2, it can be seen that the output can both track precisely the reference input signal. But, under the DO-FOSMC method, the speed response is faster and more stable, whereas the chatter amplitude occurring in conventional DO-FOSMC is bigger than that in DO-CFOSMC.

With respect to the DO-FOSMC method, the three-phase current of the stator is shown in Figure 3. The current frequency is inversely proportional to the rotation speed, while the current amplitude is proportional to the rotation torque and changes rapidly as the load torque varies. The variation of electromagnetic torque is shown in Figure 4 as the speed and load torque change. It can be indicated that the motor has a faster and small overshoot torque response with the DO-CFOSMC than that in DO-FOSMC.

In order to evaluate the robustness of the proposed DO-CFOSMC scheme under parameter variations, numerical simulations are also carried out. The tested PMSM electric parameters are the mutual inductance $L_m = 0.0158$, viscous friction coefficient $f_m = 0.006$ and stator resistance $R_m = 0.75$. The parameters of the controllers (DO-CFOSMC and DO-FOSMC) are set the same as before.

Figure 5 shows a comparison of the speed responses between the proposed DO-CFOSMC and conventional DO-FOSMC methods under parameter variations. It is observed

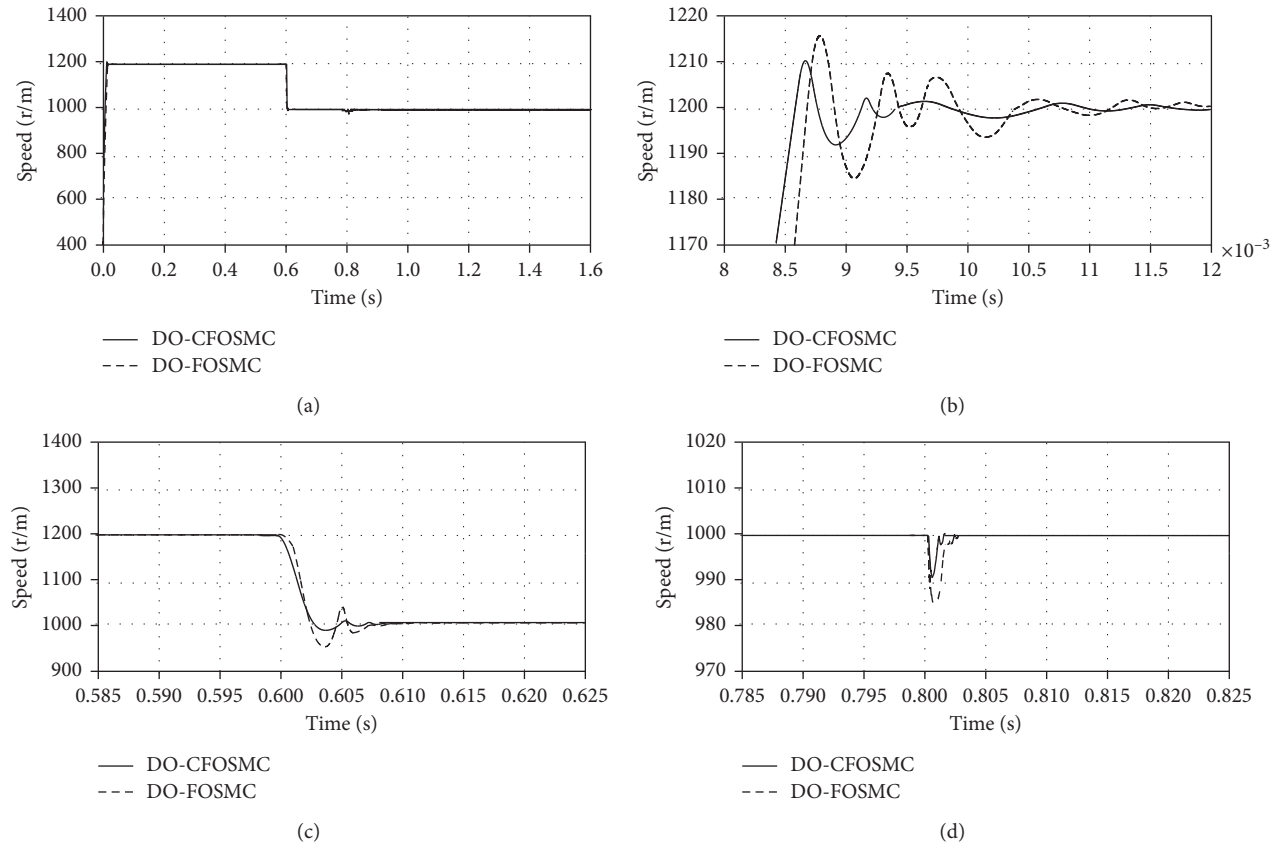

Figure 2: Rotation speed responses.

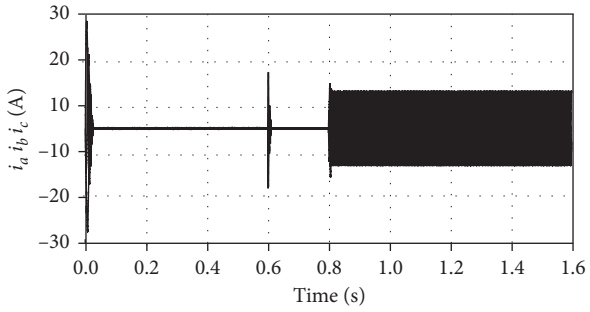

Figure 3: Three-phase stator current.

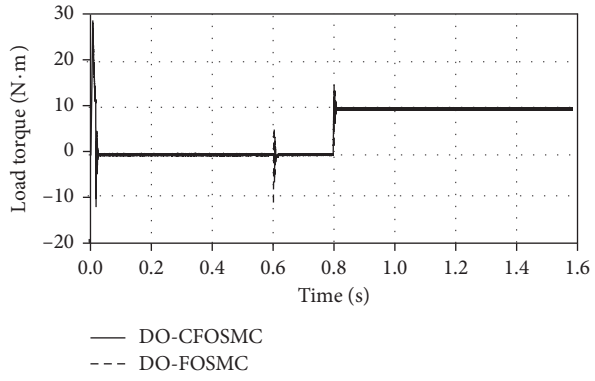

Figure 4: Load torque responses.

that both controllers can make the output speed track the desired reference speed accurately. But the DO-CFOSMC can realize the closed-loop system more robust to parameter variations and guarantee a better tracking performance.

According to the above numerical simulations, the effectiveness of the proposed DO-CFOSMC scheme with respect to the rejection of external disturbance and parameter variations has been verified. The results show that the proposed DO-CFOSMC scheme gives better tracking performances than that of the conventional DO-FOSMC.

5.2. Experimental Results. To further investigate the effectiveness of the proposed control scheme, some real-time experiments are carried out. The PMSM speed control platform is illustrated in Figure 6. The main chip of the inverter adopts the TMS320F28335 digital signal processor (DSP).

The initial rotation speed of the motor is 0 r/min, and the rotation speed is 800 r/min at 4 s. The load torque of the motor is 0 Nm. Figures 7(a) and 7(b) show the dynamic responses of the speed and torque, respectively. From Figure 7(a), it can be seen that the DO-CFOSMC method has a smaller overshoot and a shorter settling time than that of the conventional DO-FOSMC method. Figure 7(b) shows that when the PMSM motor just started, the maximum load torque under the DO-

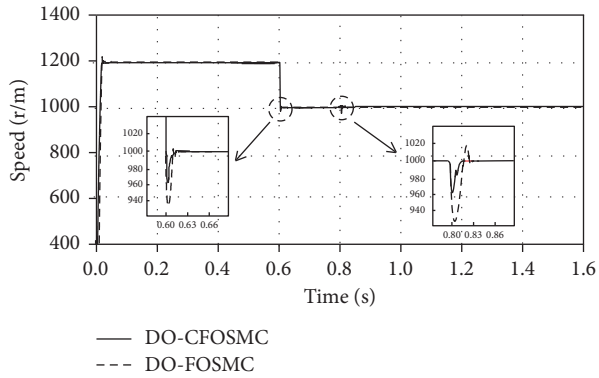

Figure 5: Rotation speed responses under parameter variations.

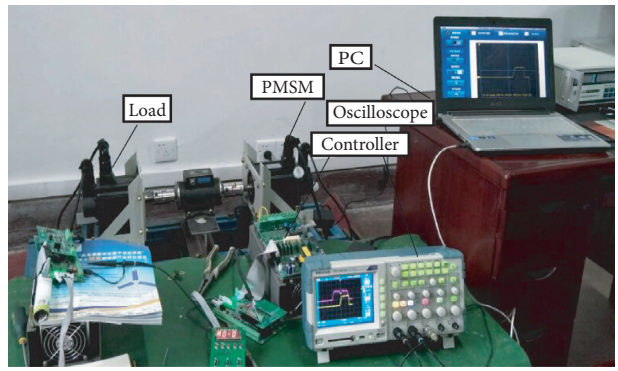

Figure 6: PMSM speed control platform.

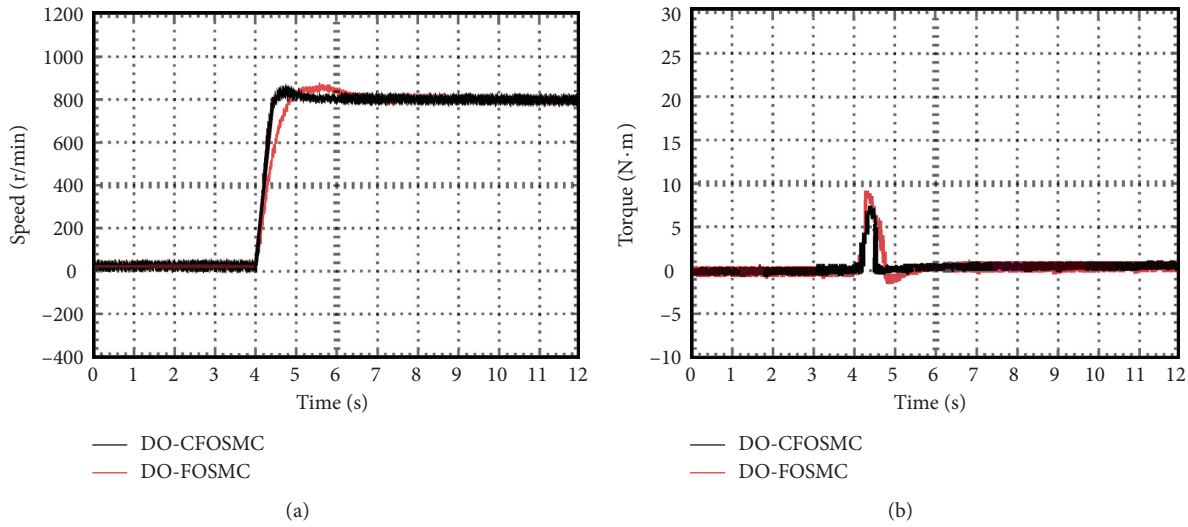

Figure 7: Experimental results of the startup procedure.

FOSMC method is 9 Nm, whereas the DO-CFOSMC method reduces it to 7 Nm. Moreover, the adjustment time required for the load torque to return to its original value decreases obviously with the DO-CFOSMC method.

When a load disturbance torque $T_l = 14$ Nm is added and removed suddenly at 0.8 s and 1.2 s, respectively, the dynamic responses of the speed and torque are shown in Figures 8 and 9, respectively. From these figures, we can see that, under the DO-CFOSMC method, the fluctuation maximum values of the speed and torque are smaller, while the recovering time against load disturbance is shorter than that of the conventional DO-FOSMC method.

The above experimental results show that the DO-CFOSMC method achieves a smaller fluctuation

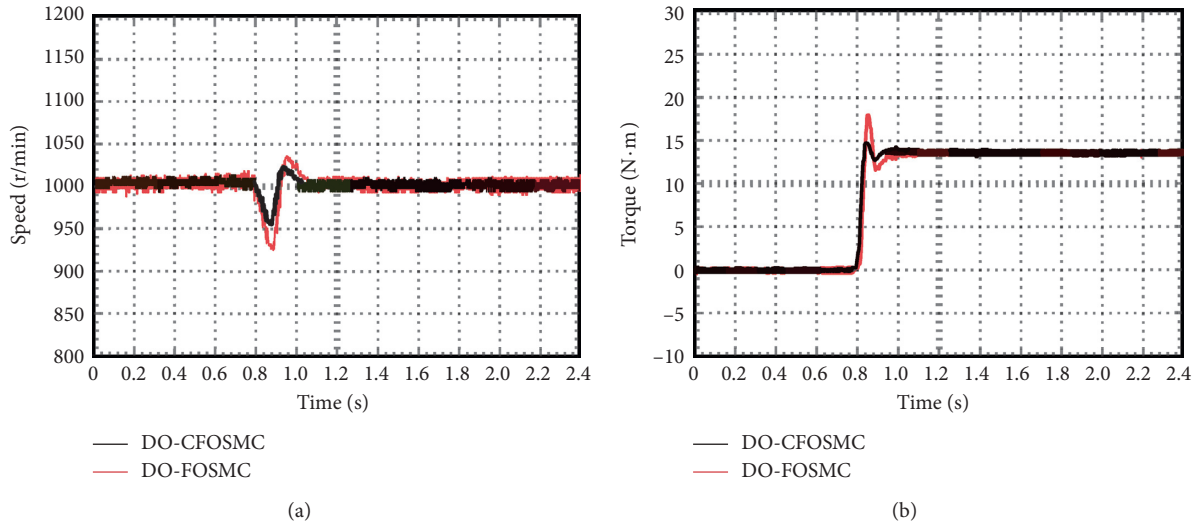

Figure 8: Experimental results of adding sudden load torque.

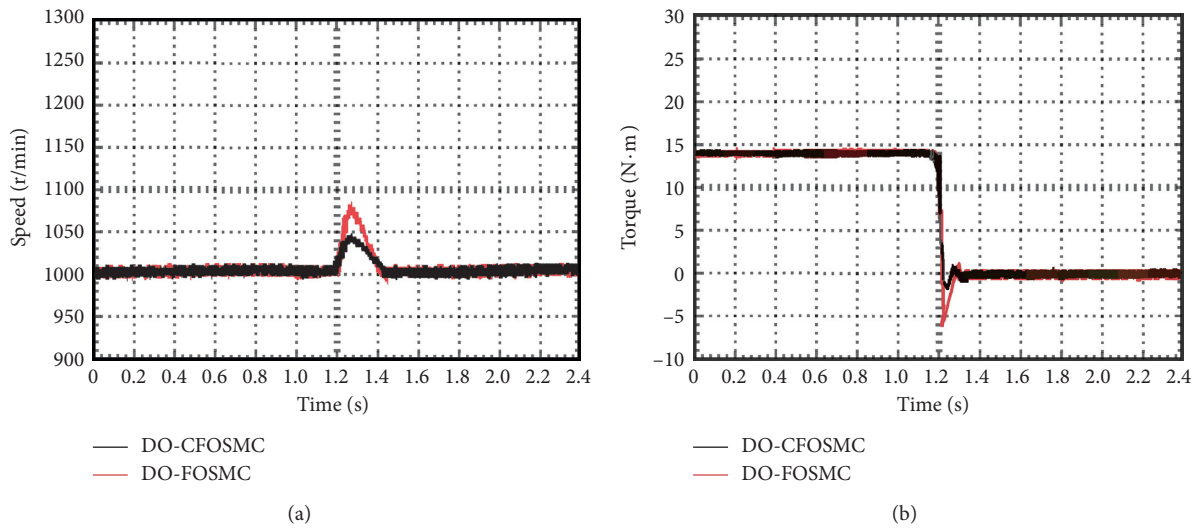

Figure 9: Experimental results of removing sudden load torque.

overshoot with respect to the rotation speed response. In addition, the DO-CFOSMC method guarantees that the adjustment time required for the load torque to return to its original value is smaller than that with the DO-FOSMC method. Therefore, the proposed DO-CFOSMC scheme exhibits a satisfactory tracking rapidity, accuracy, and robustness.

6. Conclusion

In this paper, in order to improve the antidisturbance capability of the PMSM drive system, a disturbance observer-based CFOSMC method has been presented, in which a nonlinear observer was employed to estimate the model uncertainties and load disturbance, while the CFOSMC scheme was utilized to improve the performance of the PMSM in terms of the tracking rapidity, accuracy, and robustness. Both numerical simulations and experimental results have shown the effectiveness of the proposed method. Our future work includes adaptive nonsingular integral terminal CFOSMC with disturbance observer for PMSM. Moreover, the fuzzy logic inference scheme to tune the gains of switching control law will also be included.

Data Availability

No data were used to support this study.

Conflicts of Interest

The authors declare that they have no conflicts of interest.

Acknowledgments

This work was supported in part by the National Natural Science Foundation of PR China (61573298) and Hunan Provincial Natural Science Foundation of China (2020JJ6037).

References

[1] S. Bolognani, R. Oboe, and M. Zigliotto, "Sensorless full-digital PMSM drive with EKF estimation of speed and rotor position," *IEEE Transactions on Industrial Electronics*, vol. 46, no. 1, pp. 184–191, 1999.

[2] A. Djerioui, A. Houari, M. Ait-Ahmed, M.-F. Benkhoris, A. Chouder, and M. Machmoum, "Grey Wolf based control for speed ripple reduction at low speed operation of PMSM drives," *ISA Transactions*, vol. 74, pp. 111–119, 2018.

[3] S. Mandra, K. Galkowski, and H. Aschemann, "Robust guaranteed cost ILC with dynamic feedforward and disturbance compensation for accurate PMSM position control," *Control Engineering Practice*, vol. 65, pp. 36–47, 2017.

[4] T. Turker, U. Buyukkeles, and A. F. Bakan, "A robust predictive current controller for PMSM drives," *IEEE Transactions on Industrial Electronics*, vol. 63, no. 6, pp. 3906–3914, 2016.

[5] J. Chen, W. Yao, Y. Ren, R. Wang, L. Zhang, and L. Jiang, "Nonlinear adaptive speed control of a permanent magnet synchronous motor: a perturbation estimation approach," *Control Engineering Practice*, vol. 85, pp. 163–175, 2019.

[6] S. Gao, H. Dong, B. Ning, T. Tang, and Y. Li, "Nonlinear mapping-based feedback technique of dynamic surface control for the chaotic PMSM using neural approximation and parameter identification," *IET Control Theory & Applications*, vol. 12, no. 6, pp. 819–827, 2018.

[7] A. A. Aishwarya, A. J. Vrunda, A. W. Rahee, and A. A. Godbole, "Speed control of PMSM using disturbance observer," *IFAC-papers OnLine*, vol. 49, no. 1, pp. 308–314, 2016.

[8] X. Lu, H. Lin, and J. Han, "Load disturbance observer-based control method for sensorless PMSM drive," *IET Electric Power Applications*, vol. 10, no. 8, pp. 735–743, 2016.

[9] X. Liu, C. Zhang, K. Li, and Q. Zhang, "Robust current control-based generalized predictive control with sliding mode disturbance compensation for PMSM drives," *ISA Transactions*, vol. 71, no. 2, pp. 542–552, 2017.

[10] Y. Deng, J. Wang, H. Li, J. Liu, and D. Tian, "Adaptive sliding mode current control with sliding mode disturbance observer for PMSM drives," *ISA Transactions*, vol. 88, no. 4, pp. 113–126, 2019.

[11] G. Huang, E. F. Fukushima, J. She, C. Zhang, and J. He, "Estimation of sensor faults and unknown disturbance in current measurement circuits for PMSM drive system," *Measurement*, vol. 137, pp. 580–587, 2019.

[12] S. H. Ding, J. H. Park, and C. C. Chen, "Second-order sliding mode controller design with output constraint," *Automatica*, vol. 112, Article ID 108704, 2020.

[13] F.-J. Lin, Y.-C. Hung, and K.-C. Ruan, "An intelligent second-order sliding-mode control for an electric power steering system using a wavelet fuzzy neural network," *IEEE Transactions on Fuzzy Systems*, vol. 22, no. 6, pp. 1598–1611, 2014.

[14] W. Xu, Y. Jiang, and C. Mu, "Novel composite sliding mode control for PMSM drive system based on disturbance observer," *IEEE Transactions on Applied Superconductivity*, vol. 26, no. 7, pp. 12905–12910, 2016.

[15] A. Hosseyni, R. Trabelsi, A. Iqbal et al., "An improved sensorless sliding mode control/adaptive observer of a five-phase permanent magnet synchronous motor drive," *International Journal of Advanced Manufacturing Technology*, vol. 93, no. 4, pp. 1029–1039, 2017.

[16] Z. Zhou, B. Zhang, and D. Mao, "Robust sliding mode control of PMSM based on rapid nonlinear tracking differentiator and disturbance observer," *Sensors*, vol. 18, no. 4, pp. 1031–1043, 2018.

[17] K. Mei and S. Ding, "Second-order sliding mode controller design subject to an upper-triangular structure," *IEEE Transactions on Systems Man and Cybernetics Systems*, vol. 15, pp. 1–11, 2018.

[18] F.-J. Lin, Y.-C. Hung, and M.-T. Tsai, "Fault-tolerant control for six-phase pmsm drive system via intelligent complementary sliding-mode control using TSKFNN-AMF," *IEEE Transactions on Industrial Electronics*, vol. 60, no. 12, pp. 5747–5762, 2013.

[19] X. Zhao and H. Jin, "Complementary sliding mode control for permanent magnet linear synchronous motor based on elman neural network," *Transactions of China Electrotechnical Society*, vol. 4, pp. 1–10, 2018.

[20] Y. Huang, W. Huang, S. Chen, and Z. Liu, "Complementary sliding mode control with adaptive switching gain for PMSM," *Transactions of the Institute of Measurement and Control*, vol. 3, no. 2, pp. 319–3250, 2019.

[21] J. Yan, H. Wang, S. D. Huang, and Y. H. Lan, "Load disturbance observer-based complementary sliding mode control for PMSM of the mine traction electric locomotive," *International Journal of Fuzzy Systems*, vol. 21, no. 1, pp. 1051–1058, 2019.

[22] B. Zhang, Y. Pi, and Y. Luo, "Fractional order sliding-mode control based on parameters auto-tuning for velocity control of permanent magnet synchronous motor," *ISA Transactions*, vol. 51, no. 5, pp. 649–656, 2012.

[23] J. Huang, H. Li, Y. Q. Chen et al., "Robust position control of PMSM using fractional-order sliding mode controller," *Abstract and Applied Analysis*, vol. 2012, no. 4, ArticleID 512703, 33 pages, 2012.

[24] H.-R. Li, Z.-B. Jiang, and N. Kang, "Sliding mode disturbance observer-based fractional second-order nonsingular terminal sliding mode control for PMSM position regulation system," *Mathematical Problems in Engineering*, vol. 2015, Article ID 370904, 14 pages, 2015.

[25] C.-L. Li and L. Wu, "Sliding mode control for synchronization of fractional permanent magnet synchronous motors with finite time," *Optik*, vol. 127, no. 6, pp. 3329–3332, 2016.

[26] J. Wang, C. Shao, and Y.-Q. Chen, "Fractional order sliding mode control via disturbance observer for a class of fractional order systems with mismatched disturbance,," *Mechatronics*, vol. 53, pp. 8–19, 2018.

[27] Q. Hou, S. Ding, and X. Yu, "Composite super-twisting sliding mode control design for PMSM speed regulation problem based on a novel disturbance observer," *IEEE Transactions on Energy Conversion*, vol. 99, p. 1, 2020.

[28] L. Yu and W. Zhang, "Adaptive non-singular integral terminal sliding mode tracking control for autonomous underwater vehicles," *IET Control Theory and Applications*, vol. 11, no. 8, pp. 706–710, 2017.

[29] L. Qiao and W. Zhang, "Trajectory tracking control of AUVs via adaptive fast nonsingular integral terminal sliding mode control," *IEEE Transactions on Industrial Informatics*, vol. 16, no. 2, pp. 1248–1258, 2020.

[30] W.-H. Chen, "Disturbance observer based control for nonlinear systems," *IEEE/ASME Transactions on Mechatronics*, vol. 9, no. 4, pp. 706–710, 2004.
[31] I. Podlubny, *Fractional Differential Equations*, Academie Press, New York, NY, USA, 1999.
[32] D. Matignon, "Stability results on fractional differential equations with applications to control processing," in *Proceedings of Computational Engineering in Systems and Application Multiconference Rouen, France*, pp. 963–968, 1996.
[33] A. D. Manuel, A. C. Norelys, A. Javier et al., "Using general quadratic Lyapunov functions to prove Lyapunov uniform stability for fractional order systems," *Communications in Nonlinear Science and Numerical Simulation*, vol. 22, no. 3, pp. 650–659, 2015.
[34] Y. Li, Y. Chen, and I. Podlubny, "Mittag-Leffler stability of fractional order nonlinear dynamic systems," *Automatica*, vol. 45, no. 8, pp. 1965–1969, 2009.